Resolved stars in external galaxies

Nial Rahil Tanvir

Resolved Stars in External Galaxies

by

Nial Rahil Tanvir

A Thesis Submitted to the University of Durham

for the Degree of Doctor of Philosophy.

May 1992

Abstract

In this thesis we apply techniques based on the resolution and photometry of stars to estimate the distances to external galaxies. Two critical rungs of the distance ladder, the local group galaxies M31 and M33, and the Virgo Cluster are selected for study.

The existing Cepheid distances to local group galaxies, which are important calibrators of secondary indicators, are still controversial, largely due to uncertainty in the correction for extinction due to dust. We apply modern techniques of crowded field photometry to CCD images in order to find new estimates of the reddening, and hence extinction, and also to recalibrate previous photometry. In the process, we consider several means of enhancing and evaluating the results from these methods.

In M31 we present BVR photometry for ~ 2300 stars to a limit of $V \sim 23.^m5$. The majority of stars are red-giants from an old disk population, but there is also a clear main-sequence. After accounting for age and metallicity effects, we use the colour of the main-sequence to deduce a value for the reddening of $E_{B-V} = 0.09 \pm 0.05$, where the error is largely from the uncertainties in the photometric zero-points. Correcting a scale error in the original photographic Cepheid photometry, and accounting for the low metallicity thought to apply to this field, we find a distance modulus of $\mu_0 = 24.^m44 \pm 0.^m16$.

For M33 we find B and V photometry for ~ 4500 stars to $V \sim 22.^m5$. In this case the field is characterised by a very young population of bright blue stars. By plotting colour magnitude diagrams for different portions of the field, we demonstrate that the reddening is a function of position. Applying the correct extinction to each Cepheid individually we get a distance modulus of $\mu_0 = 24.^m5 \pm 0.^m25$.

We use the new technique of ground-based image-sharpening to study galaxies in the Virgo Cluster, which is, arguably, the point at which the main disagreement in the extragalactic distance scale hinges. The technique is assessed with regard to its potential for astronomical observations, and several developments described. The best results obtained during bright time tests achieved $\sim 0.''3$ FWHM seeing.

Moderately deep images of two galaxies have been obtained, both with $0.''6$ seeing. In the first, IC3583, we do not find any convincing candidates for brightest supergiants, and conclude a lower limit for the distance of $\mu_0 = 30.^m7$. Observations of the second galaxy, NGC4523, go deeper and are supplemented by colour and narrow-band information. Three good candidates are found for yellow supergiants, and we estimate a distance of $\mu_0 = 30.^m6$. The implications of such a low distance to Virgo, and hence high value of the Hubble constant, are discussed.

Preface

The work presented in this thesis was carried out between 1988 to 1992, while the author was a research student under the supervision of Dr. R. Fong in the Physics Department at the University of Durham.

Some of the work was done in collaboration with various colleagues, but the major part of this thesis is a description of the author's contribution to these studies. None of this work has been submitted for a degree to Durham or any other university.

Certain results have appeared in the following papers:

Tanvir, N.R., Shanks, T., Major, J.V., Doel, A.P., Myers, R.M., Dunlop, C., Redfern, M.R., Devaney, N., O'Kane, P., 1991, *The Distance to the Virgo Cluster Via Image-Sharpening*, published in *IInd Rencontres de Blois:Physical Cosmology*, eds. Blanchard, A., Celnikier, L., Lachièze-Rey, M., Trân Thanh Vân, J., Editions Frontières..

Shanks, T., Tanvir, N.R., Doel, A.P., Dunlop, C., Myers, R.M., Major, J.V., Redfern, M.R., Devaney, N., O'Kane, P., *A High-Resolution, Ground Based Observation of a Virgo Galaxy.*, *Observational Tests of Cosmological Inflation*, eds. Shanks, T., Banday, A.J., Ellis, R.S., Frenk, C.S., Wolfendale, A.W., NATO ASI C348.

Tanvir, N.R., Shanks, T., Major, J.V., Doel, A.P., Myers, R.M., Dunlop, C., Redfern, M.R., Devaney, N., O'Kane, P., 1991, *Monthly Notices of the Royal Astronomical Society*, **253**, 21p.

Shanks, T., Tanvir, N.R., Major, J.V., Doel, A.P., Dunlop, C., Myers, R.M., 1992, *Monthly Notices of the Royal Astronomical Society*, **256**, 29p.

"The observer looks out through the swarm of stars which surrounds him, past the borders and across empty space, to find another stellar system - the nebula Messier 31."

– Edwin Hubble, *The Realm of the Nebulae.*

"Space is big. Really big. You just won't believe how vastly hugely mindbogglingly big it is. I mean you may think it's a long way down the road to the chemist, but that's just peanuts to space."

– Douglas Adams, *The Hitch Hiker's Guide to the Galaxy.*

Contents

Chapter 1

Introduction

Modern cosmology began with the observational work of astronomers in the early years of this century. These included Slipher, Wirtz, Leavitt, Curtis, Shapley and, most notably, Edwin Hubble. Hubble's first contribution was to finally settle the debate on the nature of the spiral nebulae. By observing individual Cepheid variable stars in the largest of the spiral nebulae, he confirmed that they were in fact external stellar systems, that we now know as the galaxies of the local group (Hubble 1925). His second contribution, even more closely associated with his name, was that of demonstrating the universal expansion. Hubble had estimated the distances to galaxies beyond the local group, as far as the Virgo Cluster of galaxies, by attempting to measure the luminosities of their brightest stars. These he plotted against their velocities, derived from redshifts, and found a roughly linear relationship (See Hubble and Humason 1931; Hubble 1936). The gradient of this line, we now know as the 'Hubble constant', or H_0.

Despite the simplicity and importance of the central result, the expansion rate of the universe remains very difficult to measure with any accuracy. This is largely due to the problem of measuring the distances to remote astronomical objects. Hubble's original value of 520km s^{-1} Mpc^{-1}, has been greatly reduced in the subsequent years. The first major revision came in the early 1950s when Walter Baade used the newly commissioned 200 inch telescope to search for RR Lyrae variables in the bulge of M31. When none were found at the expected magnitudes, he was forced to reconsider

Hubble's Cepheid distance scale. He concluded that there were two types of Cepheid, population I, found in young disk systems, and roughly four times fainter population II variables, found in older halo systems and globular clusters (see Baade 1956). Shapley's calibration of the Cepheid period-luminosity relationship, which had been used by Hubble, was much nearer to the population II variables, whereas those actually observed in M31 were population I. Thereby the distance to M31 was increased by almost a factor of three. Then, in 1958, Allan Sandage showed that many of the objects identified as bright stars in distant galaxies, were in fact misidentifications of HII regions and clusters. Thus Hubble had systematically underestimated the distances of more remote galaxies as well. This realisation reduced the value of the H_0 by about another factor of three.

In the 1970s the debate over the cosmological distance ladder resurfaced. The argument has often been seen as polarized between two camps; those who believe in a value of 100km $s^{-1}Mpc^{-1}$, championed by de Vaucouleurs (1983 and references therein), and those who advocate a value nearer 50km s^{-1} Mpc^{-1}, notably Sandage and Tammann (1990 and references therein). This controversy, with its association with the questions of the age and size of the universe, is perhaps the best known in cosmology. It was also one of the prime motivations for the Hubble Space Telescope, which, it was hoped, by resolving Cepheids in the Virgo Cluster, would be able to provide a much more precise value for H_0.

1.1 The Age Problem

Whilst the Hubble constant and the distances to external galaxies are interesting in their own right, there is a very particular motivation for their study which comes from considering their context in the standard 'Big-Bang' model of the Universe (which is outlined in appendix D). In the simplest cases, the Friedmann models, the age of the universe can be calculated as a function of H_0 and q_0 for the three different values of the curvature constant, k. In particular, for $k = 0$, the case of a spatially flat 'Einstein-deSitter' universe, the age at any given epoch is given by:

$$t_0 = \frac{2}{3H_0}$$

We emphasize this value since it has become fashionable in recent years to weight highly the arguments for globally Euclidean geometry, particularly within the context of inflationary scenarios (eg. Guth 1991).

A very serious problem in modern cosmology is that of reconciling the measured value of the Hubble constant, the measured ages of individual objects, and the theories which have been proposed for the form and density of the material content of the universe. This is easily seen by taking an 'typical' value for H_0 of 75km $s^{-1}Mpc^{-1}$, which leads to an age of t_0 =8.7Gyr assuming $\Omega_0 = 1$. This value is considerably less than the ages, for example, of globular clusters in our galaxy. These are calculated, on the basis of physical models of stellar evolution, as 16 ± 2Gyr (eg. Vandenberg 1988).

A resolution of this conflict must involve either modifying the stellar models, adopting a new cosmological model or accepting a lower value for H_0. Several attempts have been made at the first of these, by allowing for possible effects of hitherto ignored physical processes. Mechanisms which increase the mixing of the stellar material such as helium diffusion, and the motion of exotic 'WIMPS', do reduce lifetimes by burning the fuel more rapidly, but only by around 10%. Mass loss during the red-giant stage has also been suggested as a means by which the evolutionary time-scale of a star of given luminosity could be reduced, although, again the effect of this does not seem to be large (eg. Renzini 1991).

The most obvious changes in the standard cosmological model involve a lower value for Ω_0. However, even reducing Ω_0 to 0.1, with the same value for H_0, only increase the corresponding age of the universe to $\sim$ 11.8Gyrs. A recently popular variant to this approach is the further adoption of a small, but non-zero cosmological constant Λ, which then still permits spatially a flat universe, whilst also providing a greater age (eg. Peebles and Ratra 1988).

The possibility of a much lower value for the Hubble constant has been discussed by Shanks (1985). It is suggested that $H_0 \sim 25 kms^{-1}Mpc^{-1}$ would solve the age problem and allow the universe to be flat, without requiring the existence of exotic dark matter. This second point arises because the baryon density, Ω_b, and the expansion rate, H_0, are jointly constrained by the

primordial nucleosynthesis of light elements (eg. Boesgaard and Steigman 1985). These imply that high values of H_0 lead to low values of Ω_b, a prediction which has led to the development of various models in which the missing mass is made up of plausible, but as yet undiscovered, 'Cold Dark Matter' particles.

It was against this background that we began our program of observations to better determine the Hubble constant. The approach we have taken is to address two of the most important rungs of the extra-galactic distance ladder. Firstly, the distances to the local group galaxies M31 and M33, which are principal calibrators of secondary distance indicators, such as the Tully-Fisher relation. Secondly, the Virgo Cluster, which is the nearest cluster with large populations of both spiral and early type galaxies, and thus the stepping stone to more distant clusters via, for example, the $D_n - \sigma$ relation and supernovae. In the following sections we therefore review the status of current distance estimates to local group galaxies (§1.2), and the Virgo Cluster (§1.3).

1.2 Distances to Local Group Galaxies

The distances to the nearest external galaxies, those in the Local Group, are measured by 'primary' indicators, which themselves can be calibrated mainly in our galaxy, by geometrical methods, or by theory. From the point of view of H_0 and the distance ladder, the main interest in the distances to the nearby galaxies is in their use in the calibration of secondary distance indicators. In this respect the galaxies M31 and M33 are traditionally particularly important. For example, Pierce and Tully (1988) base their calibration of the Tully-Fisher relation on just these two galaxies and NGC2403. Furthermore, even the new population II distance indicators, the 'planetary nebula luminosity function' and 'surface brightness fluctuations' methods, have been calibrated in M31 and its satellites. These, and several other secondary distance indicators, are discussed further in §1.3.

Here we review the recent evidence produced by the primary indicators, for the distances to M31 and M33, and also include a discussion of the very important question of the effect of extinction

due to interstellar dust on these estimates.

1.2.1 Cepheid Variables

Foremost amongst the primary distance indicators are the Cepheid variable stars. These stars, in common with other important classes of variable stars, notably RR Lyraes and W Virginis stars, are standard candles by virtue of the correlation between their periods and magnitudes. Our confidence in their reliability has been built up from observations and theoretical modelling over the last seventy years.

Cepheids occupy an area of the Hertzsprung-Russell diagram known as the instability strip. In evolutionary terms they are fairly massive stars which have left the main sequence and are proceeding to cross the HR diagram through alternate periods of shell and core burning. The pulsations arise as the star oscillates about hydrostatic equilibrium, resulting in successive phases of expansion, leading to cooling, leading now to contraction, leading to heating and so on.

Apart from being good standard candles, they are also very bright, reaching up to $M_V \sim -7$ at maximum light. Furthermore, both the amplitude of the variability and the dispersion about the mean period-luminosity relation are wavelength dependent, being greatest at short wavelengths. This lends itself to the strategy of observing in the blue to obtain periods, and observing in the red or near infra-red, where the extinction is also less, to obtain photometry. A good illustration of this property is given in the review by Madore and Freedman (1991), who show comparative plots for LMC Cepheids in seven passbands from B to K.

Until recently, however, the Cepheid distance scale was still heavily reliant on old photographic results. In a study using CCDs, Metcalfe and Shanks (1991) have recalibrated the original photographic photometry for the galaxies M31 and M33, arriving at the following distances:

$$\mu_0(M31) = 24.63 \pm 0.06$$

$$\mu_0(M33) = 24.7 \pm 0.15$$

A more detailed discussion of this, and other related work, can be found in chapter 3.

1.2.2 RR-Lyrae Variables

These population II variables reside on the horizontal branch in the HR diagram. Thus their average absolute magnitudes are almost independent of period. Historically, they have provided a valuable confirmation of the population I Cepheid distance scale to the Magellanic Clouds. Because of their faintness by comparison with the Cepheids, ($M_V \sim 0.8$) they have not been extensively used in the study of more distant galaxies; however, Pritchet and van den Bergh (1987) have detected RR Lyraes in the halo of M31 and derive a distance

$$\mu_0(M31) = 24.34 \pm 0.15$$

Pritchet (1987) also reports their preliminary RR Lyrae distance to M33 of

$$\mu_0(M33) = 24.45 \pm 0.2$$

1.2.3 The Hertzsprung-Russell Diagram

The Hertzsprung-Russell diagram is a powerful tool in the estimation of distances. Since the locus of the main sequence is fixed in the diagram (for a population of fixed metallicity), it can be used as a distance indicator itself. Indeed this is the principal route by which the few nearby stars and clusters with direct distance estimates, can be used to jump to the large number of more distant clusters required to calibrate the Cepheid and RR Lyrae distance scales. This method has so far been applied as far as the LMC (Schommer *et al.* 1984). It is difficult to apply to more remote systems since the main sequence becomes almost vertical at bright magnitudes in optical colours.

A second method of distance estimation based on the HR diagram is the use of the tip of the red-giant branch as a standard candle. In stellar evolutionary terms the red giant branch is the locus of stars as they come off the main-sequence rising up to the point where the helium core flash occurs. The tip of the red-giant branch is at a fairly constant magnitude and hence can be used as a distance indicator. This method is rather sensitive to factors such as age and metallicity, and

is best carried out in infra-red passbands. Mould and Kristian (1986) apply this method to both M31 and M33 to obtain

$$\mu_0(M31) = 24.4 \pm 0.25$$

$$\mu_0(M33) = 24.8 \pm 0.3$$

A final use of the HR diagram, and one which features prominently in this work, is the use of the colour excess of the main sequence at bright magnitudes to estimate reddening. As already mentioned, the main sequence becomes almost vertical in $B - V$ for stars brighter than about $M_V \sim -2$. This means that it can be used to estimate reddening in a way which is essentially independent of the distance modulus. The reddening can be used to estimate the extinction due to dust to these stars, which is perhaps the principal source of uncertainty in the local extragalactic distance scale.

1.2.4 Novae

Novae are stars which undergo periodic explosive increases in brightness, when they can reach magnitudes up to $M_V \sim -9.5$ (Cohen 1987). They are relatively common, and their transient nature has the benefit of allowing good photometry even in distant galaxies. In principle the maximum luminosity-rate of decline relationship for novae can be derived from novae for which distances are found geometrically, and they are therefore primary indicators. Cohen (1985), calibrates the relationship from spatially resolved nova shells in our galaxy, to arrive at a distance to M31 of $\mu_{AB}(M31) = 24.35 \pm 0.2$. It has been pointed out, however, by Ford and Ciardullo (1988), that this calibration makes the unreasonable assumption that nova shells are typically spherical and uniform, and that more realistic models would tend to push this distance estimate out. The method has been extended to the Virgo Cluster by Pritchet and van den Bergh (1987B), who express their result as

$$\mu_0(Virgo) - \mu_0(M31) = 6.8 \pm 0.4$$

on the basis of six well observed light curves.

1.2.5 Extinction Due to Dust

A common problem encountered in estimating distances, is in quantifying the degree to which the light which reaches us from a 'standard candle' is attenuated by interstellar 'dust'. This 'dust' consists of small grains of matter, such as ices, silicates and graphite. The effect of the dust is a function of the wavelength of the incident radiation, and the properties of the dust, such as typical size and composition. It is most pronounced at short wavelengths, so the light from stars which has travelled through dust appears redder than it would otherwise. Observation of reddening is one of the main tools which is used to estimate the total extinction, which can then be used to correct the photometry. The standard reddening relations used in this thesis are summarised in appendix F.

As discussed above, one of the largest sources of uncertainty in the distances to M31 and M33 is the level of the extinction corrections which should be applied, particularly to the observations of the Cepheids. Our intention is to obtain new limits on these corrections from observations of the reddening of the main sequence in these galaxies. These observations will determine the total reddening, however, it is also interesting, at the low galactic latitudes of M31 and M33, to consider the expected contribution from dust in our galaxy. This should provide us with a lower limit to the total reddening, and hence a consistency check on our results.

Traditionally, the dust in the galaxy has been modelled as a 'slab' within the disk, possibly with some patchiness. This approach has led to several laws for galactic extinction, each of which is a refinement of a basic 'cosecant' law. These are discussed in Rowan-Robinson (1985), suffice to say here that they do not give consistent answers.

There are a number of methods which have been used to estimate the line of sight extinction within our galaxy experimentally. The first is to use colours of objects, typically standard stars, to estimate the reddening. This method produces good, relatively high resolution results, but has not been used to produce large scale maps of extinction.

Second is the technique pioneered by Burstein and Heiles (1978, 1984), based on combining maps of HI column density with galaxy counts, to account for variable gas to dust ratio. Their

whole sky maps of extinction became the standard in the 1980s.

Finally, we look at a new technique based on the all sky IRAS map at $100\mu m$, which detects the cold dust component directly (Fong *et al.* , 1987, Rowan-Robinson*et al.* (1991), hereafter RR91). RR91 offer the following relationship between extinction and observed flux for galactic latitude $|b| > 5°$:

$$A_V = 0.06 I_{100}$$

By examining their data directly, which has had subtracted a model for the contribution due to zodiacal dust in the plane of the ecliptic, it is possible to very easily arrive at a value for the extinction for any given point in the sky.

Although elegant, two notes of caution should be sounded regarding the use of this latter method. Firstly, there remains a small conflict between the reddening predicted by RR91 for the north polar cap, of $A_V = 0.^m05$, and that obtained by several studies of standard field stars, which conclude essentially zero reddening (Hilditch *et al.* 1983, Knude 1985) This would be resolved if there was a zero-point error in the *IRAS* method, which might arise, for example, from a uniform infra-red background. Secondly, Mather *et al.* (1990) report a discrepancy between the preliminary results from the *DIRBE* experiment on *COBE* for the south ecliptic pole region, and those inferred from *IRAS*, of greater then a factor of 2. RR91 interpret this as a possible scale error for extended emission, and calculate a correction factor for their processed data of ~ 1.8 at $100\mu m$. Since the relationship between I_{100} and A_V is derived by comparison with the HI column density, assuming a constant gas to dust ratio, this should have no effect on the implied reddening. However, until these questions are fully resolved, some caution will be required in using the *IRAS* reddening results.

The actual predictions from all these methods are given in the relevant chapters on M31 and M33 (numbers 3 and 4 respectively).

1.3 Distance to the Virgo Cluster

The Virgo Cluster, both historically and scientifically, holds a pivotal position in the extragalactic distance scale. Traditionally its distance is estimated from secondary indicators which are calibrated in the Local Group and other nearby groups of galaxies. As discussed in §1.4, the distance to Virgo can then be used to calibrate other indicators which are then used to step to large enough distances to estimate H_0.

Here we review the principal secondary distance indicators which have been applied to Virgo, and also discuss the 'brightest star' distance indicators, which become viable for high-resolution imaging of Virgo.

1.3.1 The Tully-Fisher Relation

In the last 15 years a variety of new methods of distance determination have been suggested which rely on proposed relationships between the velocity dispersions of galaxies and their magnitudes and sizes. The first of these was the Tully-Fisher relation (Tully and Fisher 1977). This is the most important for the distance scale as it relates the magnitude of spiral galaxies to the 21cm HI line width. Thus, unlike some of the other relationships which apply to late types, it can be calibrated by nearby galaxies, and used in absolute distance estimates.

The original formulation was in terms of photographic magnitudes. The HI $21cm$ line width is a measure of the velocity dispersion due to the differential Doppler shift from one side of the galaxy to the other. Since then, the technique has been extended to the broad photo-electric bands, including the infra-red (eg. Aaronson and Mould 1986 and references therein). It has also been tested, and found robust, in a variety of environments (eg. Biviano *et al.* 1990).

A paper by Pierce and Tully (1988), which uses CCD photometry obtained in B, R and I, and H band aperture photometry, arrives at a Virgo distance of $(m - M)_{Virgo} = 30.96 \pm 0.20$. However, a similar study by Kraan-Korteweg *et al.* (1988), reaches the significantly greater value $(m-M)_{Virgo} = 31.6 \pm 0.15$. The conflict between the two seems to arise largely from their different

treatment of biases and selection criteria used to define the cluster members.

1.3.2 Planetary Nebulae

Recently Jacoby and collaborators (Jacoby, Ciardullo and Ford 1990, and references therein) have reconsidered the possibility of using planetary nebulae as distance indicators. Previous work had concentrated on the empirically observed limiting magnitude of planetaries in the OIII line. This was regarded as a rather poor method due to the large scatter of the actual brightest PN in different galaxies. ($\sim 0.^m 5$).

Their new approach relies on fitting a model to the bright end of the PN luminosity function. This appears to yield consistent results when applied to groups of galaxies (notably the M96/Leo Group) which are approximately at the same distance. The justification of a constant luminosity function is based on the fact that the lifetimes of planetary nebulae are highly dependent on the mass of their progenitor stars. This explains the apparent cut-off in the maximum brightness of observed PNs. The life-times can also be convolved, in a semi-empirical way, with a stellar mass function to yield an expected luminosity function for the planetaries. The very sharp cutoff in the maximum PN magnitude means that the maximum likelihood fits to the data should provide strong upper limits on the distances, with a larger uncertainty on the lower limits.

Their primary calibration object is the bulge of M31. Candidates are identified as objects seen in narrow band OIII images, but not in the off band continuum. They are further subjected to the criteria of being pointlike and not visible in an H_α image. This ensures against any contamination by HII regions and should mean that all identifications are PNs. They thus claim to be able to produce complete, homogeneous samples. Their result for the Virgo Cluster is $\mu_0(Virgo) - \mu_0(M31) = 6.61$.

The most obvious weakness in the technique is the lack of empirical confirmation that it can be applied to give relative distances between galaxies of significantly different morphological types. A good test of this would be if the spiral galaxies in the M96 Leo Group could be studied for Cepheids. A reliable Cepheid distance would provide the stepping stone from the early-type members of the

group, using PNLF and several other indicators, to the Virgo Cluster.

1.3.3 Surface Brightness Fluctuations

It is clear that even in instances in which a galaxy cannot be resolved into individual stars, the 'texture' of the surface brightness will reflect the degree of crowding of the stars. In very distant galaxies any observed pixel variance will be entirely due to photon noise and larger scale structures. In nearer galaxies however there will be a progressively larger contribution to the variance from the number statistics of the stars in each pixel. Thus by measuring the surface brightness fluctuations in an image of a galaxy, one, in principle, gets a distance estimate. In order to use this technique accurately one must define galaxy types which can be regarded as standard in respect to the stellar luminosity function and distribution of stars, and also overcome the observational problems of rejecting spurious contributions to the variance from contaminating objects such as globular clusters.

An ambitious attempt at this project has been made by Tonry and co-workers (see Tonry 1991, and references therein). They originally intended to calibrate the relationship using theoretical stellar isochrones; however they subsequently concluded that much more consistent results were obtained with an empirical calibration using M31 and M32. The standard fields they observed were the central regions of ellipticals and the bulges of nearby spirals. The results for the I-band were found to be the most consistent, and, if the empirical calibration is used, display impressive correlation with the results from PNLF and IRTF, but not $D_n - \sigma$.

Technically they calculate the power spectrum of the variations with respect to a smoothed surface. This consists of a contribution from point sources and a white noise component. The strength of the point source contribution is essentially their distance indicator. Their result for the distance of the Virgo Cluster can be expressed

$$\mu_0(Virgo) - \mu_0(M31) = 6.57$$

Once again, this method suffers from the difficulty of calibrating in galaxies of a different type to those on which it is applied, and which may, for example, have differing star formation histories. One might also worry that there could be systematic, distance dependent, errors associated with the procedure for processing the raw image in order to obtain the variance.

1.3.4 Supernovae

Supernovae are very attractive candidates as distance indicators because of their extreme brightness. For example, type 1a are roughly ten thousand times more luminous than the brightest supergiants and novae. This allows them, in principal, to be used to probe directly the distances of objects considerably beyond the local peculiar flows, as discussed in §1.4. Type I supernovae are thought to occur when an accreting white dwarf in a binary system reaches the Chandrasekhar limit for the ignition of its carbon core. This process of formation seems to explain the apparent standard candle properties of these events.

Although supernovae have more often been used as secondary indicators, they can, once again, in principle, be calibrated as primary indicators. For example, Branch (1979) uses the Baade-Wesselink method to deduce a maximum blue absolute magnitude of

$$M_B = -19.6 \pm 0.6$$

whilst Arnett, Branch and Wheeler (1985) develop a theoretical model which predicts

$$M_B = -19.1 \pm 0.3$$

Using the recent compilation of Capaccioli *et al.* (1990), who find an average maximum B magnitude for 10 Virgo supernovae of $\sim 12.1 \pm 0.1$ (although using an unusual extinction parameter $R_B = 1.8$), and a compromise calibration of $M_B = -19.3$, we arrive at

$$\mu_0(Virgo) = 31.4$$

We should note, however, that both of these methods of calibration have been criticized as unreliable (eg. Fukugita and Hogan 1991).

1.3.5 Brightest Stars

Brightest stars form one of the original classes of standard candle proposed, and used, by Hubble (1936). Although Hubble's own observations were hampered by difficulties in distinguishing stars from bright HII regions and clusters, modern studies (eg. Sandage and Carlson 1988; Humphreys 1988) suggest that brightest stars, with due care, are good distance indicators. The problem in applying them to Virgo is the confusion due to crowding at such distances. Images with higher resolution should be able to remove this confusion, and hence provide a new distance estimate to Virgo based on stellar distance indicators. This was one of the main goals of the HST distance scale program, and also the original motivation for the work presented in this thesis in chapter 7. Here we briefly review the current understanding of the nature of these objects, which is of interest in explaining their standard candle properties.

Supergiant stars are observed over a broad range of colours and their very bright absolute magnitudes makes them attractive as potential distance indicators. Hertzsprung-Russell diagrams of the brightest stars, a composite example for local group galaxies is shown in Humphreys (1983), show that there appears to be an upper envelope to their magnitudes. In terms of bolometric luminosity, this envelope is observed to decrease with decreasing effective temperature down to $T_{eff} \sim 15,000$K and thereafter remain fairly level. This observation was originally unexpected since simple calculations lead to the conclusion that the evolution of super-bright stars should take place at almost constant luminosity. Furthermore this upper luminosity envelope is, for the most part, considerably below the classical 'Eddington limit', the luminosity at which radiation pressure will dominate gravitation attraction.

The commonly offered explanation of this (eg. Maeder, 1983) is that the most massive stars must experience very high rates of mass-loss as they move redward across the HR diagram, which, for stars with $M \gtrsim 50M_{\odot}$, reverses their paths turning them blueward again. This is supported by the fact that these stars are observed to generate strong winds (eg. Chiosi and Maeder, 1986, and references therein) and some, notably the class of luminous blue variables, are highly unstable. Recently Lamers and Fitzpatrick (1988) showed that detailed model atmosphere calculations reduce the Eddington limit, and indeed that there exists a minimum at $T_{eff} \sim 10^4$K. This, they claim,

is the explanation of the high levels of mass loss seen in these stars. Thus, the picture is that the brightest stars, hotter than this minimum point, are those near their Eddington limit, which for the bluest stars is close to the classical value, whereas the cooler stars have their masses fixed by the fact that they have already evolved past the minimum point.

These theoretical developments help to support the idea that brightest stars can be treated as standard candles, which had previously been based primarily on the empirical evidence gathered from studies of the stellar content of nearby galaxies. The results of these efforts to calibrate the brightest star magnitudes, and the practical use of brightest stars as distance indicators is described in detail in §7.1.

1.4 The Distance Scale Route to H_0

In order to discover H_0 via the normal distance scale route, it is required to obtain the distance and redshift to some object which is sufficiently massive and/or far away, that it is unaffected by perturbations in the Hubble flow. In recent years, it has become increasingly evident that this necessitates using objects well beyond the Virgo Cluster which has been shown to be taking part in the local bulk flow (eg. Faber *et al.* 1989). As suggested above, the distance scale relies on a series of estimators to build a ladder from nearby objects out to more remote ones. Each rung is used to calibrate the indicators which are going to be used to reach the next rung. Crucial to this process is the use of the local group galaxies, notably M31 and M33, to reach the Virgo Cluster.

In order to step out beyond Virgo various estimators can be used to give relative distances to other, more remote, clusters. Since Virgo has large numbers of both early and late type galaxies, both population I indicators, such as the Tully-Fisher, and population II indicators, such as the $D_n - \sigma$ relation, can be used. Working in clusters has the advantage of providing large numbers of objects and hence good statistics. It is also easier in clusters to handle the various biases which arise when using distance estimators which have an intrinsic dispersion. A reasonable consensus now exists in the relative distances between Virgo and more distant clusters, notably the Coma Cluster. For example, Sandage and Tammann (1990) have used a variety of methods, including

the $D_n - \sigma$ relation for early type galaxies, the Tully-Fisher method, $m_1 0$ and supernovae, to obtain the relative distances between Virgo and Coma, and other distant clusters, to arrive at the following expression

$$H_0 = 52(21.9\mathrm{Mpc}/r_{virgo})\mathrm{km\,s^{-1}\,Mpc^{-1}}$$

For comparison, we note, that their value for the relative Virgo Coma distance of 3.8 in distance modulus, compares well with the original $D_n - \sigma$ result of Dressler *et al.* (1987) of 3.65 and the Capaccioli *et al.* (1990) supernovae result of 3.75 ± 0.2.

1.5 Contents of Thesis

1.5.1 Crowded Field Photometry of M31 and M33

The above discussion describes how distances to external galaxies are generally found by stepping out, building on the distances to nearby objects. M31 and M33 are our cosmological next-door neighbours and are of particular importance in the calibration of the secondary distance indicators, such as the Tully-Fisher relation and Planetary Nebulae. Despite its importance and proximity, the distance to M31 is still reliant to some extent on the original photographic study of Baade and Swope (1963). One source of substantial uncertainty is in the estimation of the extinction due to dust towards M31 and, in particular towards the Cepheids. The situation in M33 is rather similar, and both merit a renewed study of their resolved stellar content.

We were able to make use of existing deep CCD images of regions of M31 and M33 obtained with the prime focus camera on the 2.5m Isaac Newton Telescope (INT). Our approach here was to perform crowded field photometry on the resolved stars in these fields, to produce Hertzsprung-Russell diagrams. The main interest is in estimating the reddening from the position of the main sequence, and, in the case of M31, the distance from the position of the tip of the red giant branch. We are also able to make comparisons with the photometry obtained by previous authors, and

hence reconsider their distance estimates. The diagrams also contain useful information on the stellar populations in these two galaxies.

Chapter 2 details the method of crowded field photometry, reporting some developments which were made during the course of the study, and evaluating the algorithms and the data. Chapter 3 and chapter 4, present and discuss the results for M31 and M33 respectively.

1.5.2 Image Sharpening and the Virgo Cluster

As we have indicated, it is at the Virgo Cluster that the greatest discrepancies arise for the cosmological distance ladder. Observationally, the large number of member galaxies offer good statistics for all distance indicators, and its high galactic latitude, close to the galactic north pole, mean that extinction corrections are small.

Our aim is to provide new, direct, estimates of the distance, from ground-based image-sharpening observations of resolved stars in Virgo galaxies. In the first instance, observations of brightest stars will provide a new, independent route to the Virgo distance. Ultimately, by observing Cepheids, a whole rung of the distance ladder can be removed, with consequent improvement in the distance scale as a whole, and our value of the Hubble constant. In chapter 5, we describe the techniques of image sharpening, and the instrumental setups used. In chapter 6, we present the results of the technical studies of image sharpening which were conducted to prove the feasibility of its application to faint object astronomy. In chapter 7, the astronomical observations are described, which relate to the two Virgo galaxies, IC3583 and NGC4523 for which we have obtained deep images.

All observations in this program were taken at the $f/11$ GHRIL Nasmyth focus of the 4.2m William Herschel Telescope (WHT), on La Palma.

Chapter 2

Techniques of Crowded Field Photometry

2.1 Introduction

In astronomy, the term photometry denotes the measurement of the intensity in a given waveband of an astronomical source, which ultimately leads to an apparent magnitude for that source. In this thesis we are particularly concerned with the photometry of stars, which are essentially point sources, and hence have images which are simply an appropriately scaled PSF. From this it follows that the proportion of light from a star which falls within a particular aperture centred on the star, is a constant. Hence the relative magnitudes of stars can be determined from measurements of intensity within an aperture, providing an estimate of the diffuse sky background behind the object can be made and subtracted, and that the PSF is constant across the image. This fact has been at the heart of traditional stellar photometry.

In situations where the stellar images begin to 'crowd' together, there is a danger that light from neighbouring stars will 'contaminate' the aperture. This is minimised by using small apertures, but here problems may arise due to pixel quantization and increased Poisson noise, and the additional

question of the effect on sky estimation must also be considered. The extreme crowding which is encountered in many observations of globular clusters and external galaxies require new levels of sophistication to accomplish good photometry. This has resulted in the development of techniques of 'profile fitting' stellar photometry (eg. Penny and Dickens 1986; Mighell 1989; Buonanno and Iannicola 1989; Stetson 1987, hereafter S87). Here we describe the technique, which was applied to the analysis of star fields in M31 and M33 (described in chapters 3 and 4), and attempt to evaluate its success.

Prompted by the some of the problems faced during this work, several aspects of the method have been investigated, with the aim of enhancing the algorithms. These can be split into the four areas of object location, sky determination, PSF determination and error analysis. In fact, these developments were a continuous process resulting, usually, from encountering specific problems. Where improvements have been achieved, they are not necessarily applied throughout the analyses of the M31 and M33 fields.

2.2 Profile Fitting Photometry

The advent of linear, digital electronic imaging devices has led to the production and application of computer codes which attempt perform profile fitting photometry. Several such codes now exist, the principles being similar in each. The basic idea of these techniques is to use knowledge of the point spread function to obtain more accurate photometry for stars whose profiles 'overlap'.

We concentrate on the DAOPHOT package, which is perhaps the most widely used, in part because it is relatively well automated. The sequence of computations in a 'standard' DAOPHOT reduction (as outlined in the DAOPHOT USER GUIDE, Stetson, 1987) is as follows:

1. 'FIND' the objects down to a given detection limit. The detection algorithm convolves the image with a gaussian function of similar width to the PSF, and looks for enhancements above local sky. This procedure smooths the noise and optimizes the detection of point-like sources, whilst reducing the weight of sharper (eg. cosmic rays) or broader (eg. galaxies)

objects. Two image classification parameters are calculated for each object, 'ROUND', which measures the ellipticity of the object, and 'SHARP', which measures its 'peakiness'. Limiting the allowed range of these numbers serves for preliminary star/non-star separation.

2. Perform aperture photometry with the 'PHOT' routine, and estimate the sky values. This routine allows a large number of aperture magnitudes corresponding to different radii, to be acquired automatically. The sky value is calculated from the pixels in a specified annulus around the object centre, using an estimator of their modal value.

3. Find the 'PSF' using the bright stars on the frame as templates. The quality of the PSF is improved iteratively by successively subtracting the nearby neighbours from around the template stars, using the current best PSF, and then re-extracting the PSF from these 'cleaned' templates.

   The PSF is defined out to a fixed radius, 'PSFRADIUS', and is allowed to vary smoothly across the frame.

4. Reduce the frame in large groups of candidate stars by simultaneously fitting the PSF, using the routine 'NSTAR'. This routine minimises the non-linear least squares residuals allowing the stars within a group to vary in position and magnitude. The fitting is done within a region called the 'FITTINGRADIUS' around the centre of each star in the group. By making the fitting radius small, the errors introduced by contamination are further reduced.

   The grouping of stars (performed by the 'GROUP' and 'SELECT' routines) is intended to allow multiple reduction of many close stars at one time. Reduction of all the stars in the frame in one large group is usually impractical on grounds of the required computer time. The 'GROUP' algorithm aims to include in a group all stars whose photometry will be critically affected by other stars in the group. Thus, a faint star at a given separation from a bright star might be included in its group, whereas two stars of similar magnitude and separation might not be grouped together, as their influence on each other will be less. The threshold for determining the 'critical overlap' is user defined. The 'SELECT' routine allows different 'critical overlaps' to be used for different groups, thus allowing for a variable degree of crowding over the frame.

5. Optionally supplement the given uncertainty estimates, by using the 'ADDSTAR' routine to test the photometry on simulations. Basically, this employs the principle that a few stars may be added artificially to a frame without increasing the crowding, and, by repeating the reduction procedure on the artificial frame, thus allows precise comparison of *true* magnitude against recovered magnitude. The routine uses the PSF which has been generated for the frame, and scales it to the required magnitude, with the addition of photon noise.

Although the NSTAR routine does actually fit the PSF to each star in the central regions, the critical aspect of the algorithm is the subtraction of the contribution from the wings of each star from the fitting regions of the neighbouring stars. Thus, this is similar to finding small aperture magnitudes but with additional account being taken of the light which would be thrown into the aperture from nearby stars. We should add that the fitting procedure does also have the advantage of refining the centroid determinations. From this perspective, the advantage of DAOPHOT profile fitting is that it allows fainter stars to be measured with better precision than would otherwise be the case. The measurements of brighter stars are less likely to be improved by this method, and indeed might be expected to show somewhat larger errors than typical aperture photometry, due to the use of a small fitting radius in the automated reduction. We now go on to describe various extensions of this basic approach.

2.3 Object Location

The DAOPHOT FIND routine is an optimised algorithm for detection of point sources on a noisy background. It also works well in crowded fields, but with some inevitable loss of performance. An alternative approach, which might be expected to be more suited to crowded field situations, is to employ image-deconvolution to detect objects. This can be done using a preliminary PSF from the frame.

In fact, the INT data, presented in chapters 3 and 4, does not lend itself to deconvolution as the PSF is poorly sampled, typically $\sim$ 2 pixels FWHM. Instead, we tested the technique using a simulation. To make this as realistic as possible, a PSF was used which was obtained from

another, well sampled, WHT frame. Stars were placed on the image according to a power law luminosity function (slope 0.5), in random positions. Sufficient stars were put down so as to create an unresolved background of faint sources. The background sky, and the counts from the stars themselves, were both subject to realistic photon noise.

This frame was then analysed by both the normal FIND routine, and also by locating objects as local enhancements after the image was processed by maximum entropy deconvolution (using the KAPPA MEM2D routine, which in turn uses the MEMSYS3 library; Berry 1991). The limiting threshold in each case was taken so that only ~1% of the detections were spurious. With this criterion, the deconvolution technique identified 26% more stars, in total, than FIND. Perhaps surprisingly, there were a few stars detected by FIND which were missed by the deconvolution method.

A similar experiment is reported by Weir (1991), in which he finds a slightly smaller gain of 19%. The difference may not be significant, but could reflect the fact that his simulation uses a simple gaussian PSF, rather than a real one. The more extended wings, in the latter case, might be expected to favour the deconvolution method. Clearly there is a useful gain to be had with this approach, which would be particularly well suited to well sampled, high signal to noise, crowded images; an obvious example being globular cluster fields.

2.4 Sky Estimation

The determination of a good sky level is critical in all photometry. It is even more important in crowded fields, since estimators not only become very noisy, but can easily introduce systematic biases. As we shall see below, the method of estimating sky should depend on the type of photometry one is attempting and also on the nature of the results one is trying to get; there is no universally applicable 'best' method. Although we are primarily interested in profile fitting photometry, it is also instructive to compare this with the same problem for aperture photometry.

2.4.1 Aperture Photometry

In the case of aperture photometry the aim is to answer the question 'what would be the count found in the aperture in the absence of the object of interest?'. These counts could consist of diffuse sky light, unresolved background sources, image defects etc. This value can then be subtracted from the measured counts in the aperture to yield an aperture magnitude. Depending on the method of calibration, it may then be necessary to add a correction to account for the fact that some of the light is inevitably lost outside any finite aperture. (Traditional photoelectric photometry used an aperture ~ 5 times greater than the seeing.) The correction is clearly a function of seeing and can be obtained empirically from bright stars on the frame, or theoretically (see Stetson 1990 for discussion).

Since most objects of interest are not transient, it is usually impossible to get a definite answer to the question raised above. Instead, an estimator must be used which derives a sky value by looking at another part of the image, usually close to the object. This procedure may be done either automatically or interactively, but in both cases we need to consider two questions. Firstly, where and how large a region of the image do we sample? This is particularly relevant to situations in which the sky background varies rapidly, and must be balanced against the noise which is introduced if only a small number of pixels are used. Secondly, what statistic should be used to provide the estimate of sky?

Although it may depend on particular circumstances, it will generally be best to choose a region close to the object, which contains several times the number of pixels which are in the aperture containing the object. This will ensure that the random noise is sufficiently low, whilst, hopefully, minimising the likelihood of including areas which are not typical of that in which the object resides. Taking a user specified annulus around the object, as is done in DAOPHOT, provides a good method of defining the sky sample, which also compensates, to first order, for any large scale gradients.

All other things being equal, an unbiased estimate of the level within the sky sample is given by the *mean*, and it can be argued that, since any given star is in an arbitrary position, this is the best

statistic to use. However, we would contend that the fact that an object is identified in the first place, by whatever algorithm is used to find it, actually, to a certain extent, selects the nature of the sky behind it. For example, in the case of DAOPHOT the SHARPness and ROUNDness figures are used to reject 'non-stellar' objects. This means that we will exclude objects which are 'merged' to the point of giving non-stellar images; we are biased against objects which are too obviously contaminated, and it will no longer be appropriate to use the *mean* as an estimator. Interestingly, this is obviously a magnitude dependent process, since a bright star will be less affected by close neighbours.

Alternative statistics, which would tend to reject bright contaminating stars, and hence be more appropriate to the selected objects, are the *clipped mean*, the *median* and the *mode*. These could reasonably be applied either for all the pixels or on the basis of sub-samples of pixels of the same size as the object aperture. The DAOPHOT algorithm actually uses an approximation to the modal value of the pixels in the annulus, formed from $3 \times median - 2 \times mean$.

The above argument applies to the automatic case, but if the sky region is defined interactively, then the experimenter will be the judge of what constitutes an 'object' and the 'sky'. In this case, the aim is to select areas which appear as though they are similar to the background of the star in question. However, we must worry that even this procedure could introduce a bias in the results.

In passing we note that, by implication, in these approaches, if two objects are close enough together as to appear single by the object finding criteria, then the photometry we are obtaining is for a 'double' object. The upshot of this is that as we go fainter we expect to suffer from more and more objects which are effectively 'double'.

One way of evaluating algorithms for estimating sky for aperture photometry, is by taking the frame in question and simulating the sky calculation procedure at a set of random points on the frame. For each point the sky is estimated with the chosen algorithm and compared to the actual value in an aperture at the point. This essentially allows us to gauge the degree to which the estimator answers the question of the value of the sky in the absence of the object. To get a realistic result, we must reject any points which would have been eliminated if an object had

indeed been present in the aperture. As we have already seen, this would actually depend on the magnitude of the target objects, so perhaps the best that can be done is to aim at close to the limiting magnitude. (This approach has recently been incorporated into a STARLINK program PHOTOPT, (Eaton 1992, Starlink User Note 45.4.))

2.4.2 Profile Fitting Photometry

The determination of sky values for profile fitting photometry is a rather different problem. In this instance, we would like to determine a value of sky which would be found if *none* of the detected stars, within a group, existed. This is because the contributions of the other stars in the group to the sky level behind a particular star, should be accounted for in the reduction process.

The DAOPHOT program uses essentially the same values for sky found for the aperture photometry routines for the profile fitting. The only difference is that the sky values for groups of stars are averaged and then this value is applied to the group as a whole. In order to test and possibly improve this method of estimation, for the M31 data, the following procedure was carried out.

Once a satisfactory PSF was obtained using bright stars, which are hopefully to first order immune from the effects of small errors in the sky level, an artificial frame was created using the PSF and all the stars which came out of a previous NSTAR run. This image was subjected to the same analysis as the originals and, in particular the sky estimates were compared to the now known levels. The discrepancies between the calculated sky value and the *true* value for each group of stars in the simulation were then used as first order corrections to the sky estimates which had been found on the real images.

In fact, the corrections derived in this way, were generally less than 1% of the sky value, but this was still useful for the PSF generation and in the photometry of the fainter stars. Interestingly, for this data, the sky estimate was found to be generally better in cases in which the histogram of sky pixels was more skewed, which presumably means more crowded. This must reflect the behavior of the approximator for the *mode*, namely $3 \times median - 2 \times mean$, which is used by DAOPHOT.

In regions of rapidly varying sky background, which typically arise due to bright and dark nebulosity, unresolved background stars and the wings of bright, saturated stars, any estimate formed by sampling the sky around the star, is liable to be imprecise. In particular, an estimate formed for the whole group of stars is almost certain to be in error. This was the situation for the M33 fields.

A more robust method, by which we can iterate towards better sky subtraction, involves directly subtracting a sky frame from the image before attempting the photometry. The sky frame is created from the star subtracted image, which has been created using the aperture magnitudes. However, it is not sufficient to use this image directly since any errors in the initial magnitudes will then be simply fed back into the sky-subtracted image. Instead we note that any errors in the photometry due to a poor sky value will leave a scar at the position of the star in the subtracted image. This scar may be either positive or negative, but will be such that the value within the fitting radius will be equal to the initial, incorrect, estimate of the sky. Beyond the fitting radius, however, in the wings of the PSF, the influence of any errors will be considerably less. Thus, by smoothing the star subtracted image we can produce a sky image in which the actual effects of the bad photometry are ironed out. The smoothing should not be so heavy as to erase the actual background structure, however this should not be too difficult since we know that the background is at least already convolved with the PSF. The sky frame thus created uses information about the background level much closer to the object in question, and is thus less affected by larger scale variations in that level.

Using the directly sky subtracted frame, and fixing the sky values to zero for the subsequent NSTAR run, should produce improved photometry. This can then be repeated several times, until the sky frame converges. By this means most problems caused by rapidly varying backgrounds can be accounted for. As usual, stars which are seen on the subtracted image should be located and added to the reduction list. Any stars which are added in this way should be excised from the sky image prior to subtraction. In the case of the M33 data, the improvement when using this method was marked.

A working recipe for performing this procedure is as follows:

1. Produce the PSF for the frame in the standard way, using the brightest stars, optionally adding theoretical wings.

2. GROUP the stars in the standard way.

3. Find provisional photometry using the NSTAR routine.

4. Subtract these stars from the true image.

5. Examine this image, noting the subtraction problems. Typically these will be most evident on the brightest images. Systematic underestimation of sky, for example, will result in an overestimate of magnitudes of the stars, and the subtracted image will have a small residual pit at the location of the star.

6. Now smooth the image so that the scars are largely erased, but the real structure is left largely intact.

7. Now subtract this approximation to the true sky from the original image to leave just the detected stars. It is also important to add a constant to the frame before putting it through NSTAR since the fitting algorithm weights pixels according to the expected noise. This in turn depends on the intensity, read-out noise and photons per ADU.

8. Now go back to step 1 or 2, depending on degree of satisfaction with the PSF, until step 5 reveals that the scars are no longer serious. One word of caution here is that there may be instances in which some scars do not appear to improve beyond a certain limit. This is most likely to be due the objects which are not quite point-like (eg. close blends, compact images of galaxies or nebulae.), and thus there will be an inevitable residual pit.

A similar procedure has also been suggested by Parker (1991). Instead of performing the sky subtraction explicitly, his recipe simply takes the sky from a small aperture in the subtracted image. In fact this is similar to the smoothing step in the procedure described here. The sky from the small aperture should give a good approximation to the sky directly behind the image, being much smaller than the original annulus used by DAOPHOT, but also large enough to be insensitive to the subtraction scar. Once again this can be iterated towards the 'true' sky values. Presumably

the version of DAOPHOT used in this case has been modified so as not to find the group sky by averaging the skies for all the stars, since that would nullify the advantage of the technique.

The outcomes of the two techniques should be very similar, with the only differences being due to any discrepancies between calculating the sky from an estimate of the modal value within the aperture, as compared to the particular smoothing procedure adopted.

2.5 Determination of the PSF

To quote Stetson (DAOPHOT User Guide): 'Obtaining a point-spread function in a crowded field is an art, not a science'. This has certainly proved true in the very crowded fields discussed in chapters 3 and 4.

As described above, DAOPHOT, uses an empirical PSF found by using the bright stars on the frame as templates. For computational reasons this is held in the form of a parametrized, best-fitting gaussian, and a look-up table of residuals. This procedure for finding the PSF becomes difficult in very crowded images, especially if there are few outstanding, bright stars. The main problem is to produce a PSF which has sensible wings, since this is critical to the performance of the profile fitting photometry, and yet is most susceptible to poor accounting of the neighbouring objects of the template stars.

A simpler alternative is to use theoretical or model PSFs. These remove the need to find uncontaminated field stars, except such as are required to parameterise the model. For example, Buonanno and Iannicola (1989), in their ROMAFOT package, employ an analytic Moffat function (Moffat 1969), whilst Penny's original STARMAN package used the sum of a Gaussian and a Lorentzian (Penny and Dickens 1986, although subsequent enhancements include an empirical PSF option). The problem with this analytic approach is primarily that it is not able to accommodate unusual PSFs. Examples, which are commonly met, are diffraction spikes, slightly trailed images, images produced by stacking offset parent frames or images in which the PSF varies, perhaps due to focus changing across the chip.

Prompted by the difficulty in defining the PSF from the images of M33, especially the V frame, we have investigated the use of a new form of analytic profile, namely that predicted by studies of atmospheric seeing. In chapter 5 we shall see that the PSF of a long exposure image is given by the Hankel transform of the combined optical transfer function of the telescope and atmosphere. Using a program written by Dr A.P.Doel, PSFs were generated by this means for a variety of values of the seeing, and compared to the stars on the frame.

In this case, these were still found to be imprecise in the cores, probably due to the fact that the images were stacked. A compromise solution was found by creating a 'hybrid' PSF which uses the empirical data to define the cores, where the confidence is high in any case, and the analytical PSF to give the wings. The wings should be much less affected by problems such as trailing, so the analytic PSF should be applicable. Although it is hard to test quantitatively, this hybrid PSF was judged to be superior to the empirical PSF from the appearance of the star subtracted images.

For observed PSFs, at greater radii than are needed for our photometry, the wings tend to an inverse square power law form (King 1971), probably due to scattering processes. Since this is unlikely to be altered significantly by seeing or any of the other factors which affect the central regions, it would be possible to extend the hybrid method, if required, by 'grafting' on such an outer halo. The onset and form of this halo is perhaps best determined from the outer parts of the images of saturated stars.

2.6 Error Analysis

There are many sources of error associated with any photometric measurement, and it is valuable to attempt to quantify them. Amongst these are the limits of the calibration procedures, typically bias subtraction, flat-fielding, and conversion of magnitudes onto a standard system, although possibly also including linearity corrections, preflash subtraction etc. These generally rely on control observations and remaining errors will be systematic and hence will not be evident in the scatter of the measurements off the reduced frame. A detailed discussion of these type of errors is given by Newberry (1991).

Further errors may be introduced by image defects, cosmic rays, saturated stars and, of course, crowding. In the case of crowded field photometry error determination is not trivial, since conventional error analysis, based on the counting statistics of the photons, is likely to significantly underestimate the true uncertainty. This is because of the additional problems of varying sky background, due to nebulosity and the unresolved stellar component, blends, poor cross-identification of stars over different passbands, and problems of sky and PSF determination (see previous sections). A powerful weapon at our disposal is the ability, primarily by virtue of the digital nature of the image and reduction system, to generate simulated images on which to carry out the analysis.

The basis of these simulations is adding artificial stars (in this case with DAOPHOT ADDSTAR), defined by a PSF, position and magnitude, to a data frame. This frame is then subject to essentially the same analysis as the original data and the recovered magnitudes and positions are compared to those input. By suitable choices of simulation and analysis we can investigate not only the total spread, but also the contributions due to distinguishable sources of error.

For the M31 B,V and R images, three different types of experiment were conducted:

1. Add isolated stars to a flat sky frame (including poisson noise), to estimate the minimum possible errors in the absence of all crowding effects and cosmetic defects.

2. Create an artificial frame, based on the original images, by adding the whole output photometry list to a flat sky frame. This should highlight the extra problems due to crowding of detected objects. In principle, these frames could also be used to test the PSF derivation procedure, to see how accurately the input profile itself was recovered.

3. Add synthetic stars to the real frames to gauge the extra problems of unresolved stars, image defects etc. This analysis will also contain the likelihood that a given 'star' is in fact not single, but a line-of-sight double, as was discussed above with regard to sky estimation. It is valuable to produce these results for a given luminosity/colour distribution for the input stars, which corresponds roughly to the expected distribution on the frame. Since this requires many simulated stars to get good statistics, it is usually necessary to produce several new frames, each with only a small number of artificial stars, so as not to increase the crowding.

Before going on to describe the results of these tests, we should note three important points regarding their interpretation. Firstly, with respect to the third type of experiment, if the derived PSF, which is used to generate the artificial stars, is not very realistic, the results of this analysis should still be valid. This is because the most likely problems with the PSF will be in the form of the wings rather than the cores, because of the good statistics for the cores of the stars. Thus the crucial step is not the fitting of the star itself, but of the estimation of the contribution from the wings in the profiles of neighbouring stars. If the derived PSF is in fact getting this wrong, then the recovered magnitudes of the artificial stars will also be systematically wrong, and the error will be evident. Thus the circularity in using the derived PSF to test the photometry, is of second order, and it is, therefore, difficult to 'cheat' with this method of error determination.

Secondly, despite the potency of simulations in investigating the errors and completeness of our photometry, care should be taken in considering what they mean quantitatively. This is simply because what we have actually studied is the error and completeness distribution of the recovered magnitudes from a population of simulated stars of a given magnitude. It will not, in general, be true that these distributions will apply well to the actual recovered magnitudes of real stars, particularly when working at faint detection limits. A simple example of a case where our error analysis would break down, is in a situation in which there is a steep rise in the numbers of stars just below the detection limit. In these circumstances there would typically be many false detections of stars which were in fact due to chance intensity peaks in the background distribution of the population of faint stars. This would have the result of increasing the slope of the luminosity function at the faint end. Far from improving the situation, applying the derived completeness correction to the faint end stars would bump the slope up even further, increasing the error. Now, it would be possible to investigate the likelihood of any given simulated star, which was set fainter than the nominal detection limit, appearing in the catalogue by chance. However, to actually then account for this effect in the data, we would have to make some assumption about the luminosity function below the detection limit. Since we are actually trying to calculate the LF above the detection limit, this appears to be a rather risky business. In conclusion, it is safest to stick to stars reasonably above the detection limit when interpreting the errors derived from simulations.

Thirdly, even allowing that, at least for the bright end, the error bars and completeness estimates are similar for real stars as for artificial stars, we must still take care in applying these results to the HR diagram. In order to get the completeness as a function of colour and magnitude, one would conventionally take the product of the survival fractions in both bands at the appropriate magnitude bins. However, this is not correct for crowded field photometry, since the probability that a star is not detected it is usually determined by its position with respect to its neighbours, and hence not an independent function of passband. Put simply, if a star is missed in one band it will usually be because it is too close to a brighter star, and hence will probably be missed in another band too.

Now we come back to the actual outcomes of these simulations for the M31 data. Firstly, we consider the results for isolated stars (simulation 1 above), which are shown in figure 2.1. We plot the points as a function of the input magnitude rather than output magnitude, to help resist the temptation to assume that the spread is really applicable to the observed magnitudes. It can be seen that in all three passbands, genuinely isolated stars should be confidently detected down to faint limits, with good photometry. For example, at $B = 23^m$, the position of the stars are recovered to better than $0.''1$, and the magnitudes to better then $0.^m05$, in this sample. In reality somewhat greater precision could be obtained for these stars by, for example, large aperture photometry. This is because the profile fitting parameters have been optimised for the crowded fields.

For the simulation of the whole frame (number 2 above), we show just the V band result as a representative example (figure 2.2). This shows the effects of crowding begin to erode the quality of the photometry even in this 'easy' case, where the stars are all point-like and unmerged to start with, sitting on a flat background. Fainter than $V = 23.^m5$, we begin to see the onset of the detection limit

The plots for the stars which are placed down on the original data frames (figure 2.3) show the errors increased again. In particular there are now some evident outliers, even at higher magnitudes, which are the result of blending. The completeness is also affected for the same

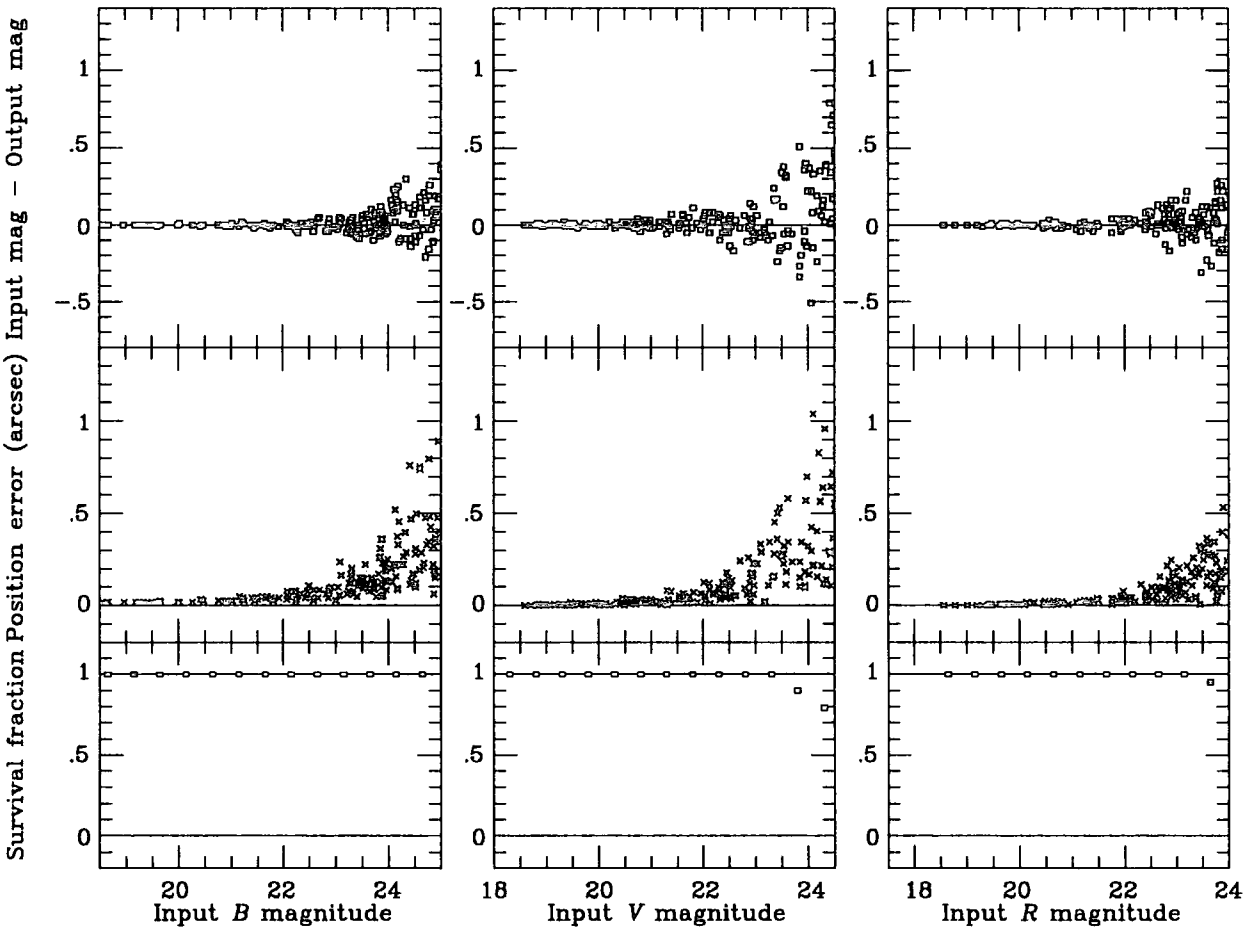

Figure 2.1: Results of simulations for M31 B, V and R band, isolated stars. The plots show the errors in the magnitude and position, and the completeness as a function of the input magnitude of the artificial stars. This indicates the unavoidable errors due to photon counting statistics.

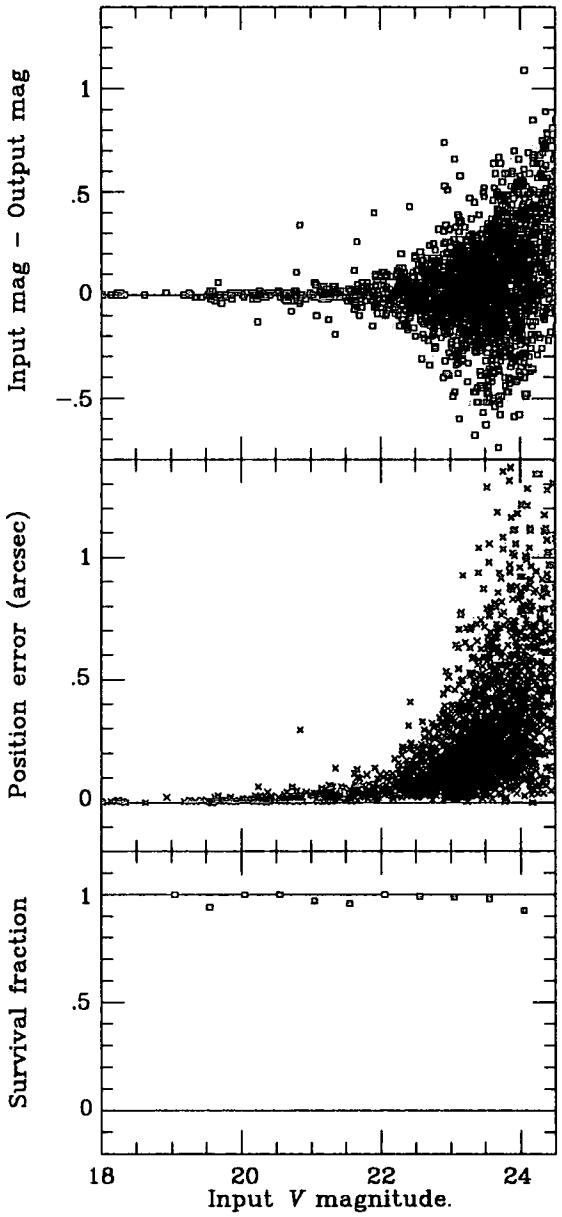

Figure 2.2: Results of simulations for M31 V band, data, in which a whole frame full of stars has been generated from the NSTAR output for the real V image. The plots show the errors in the magnitude and position, and the completeness as a function of the input magnitude of the artificial stars.

reason, namely that some of the artificial stars end up merged with stars which are brighter than them, and hence are regarded as being lost. Despite this, the error for 23^m artificial stars in the B image, for example, is still generally less than $0.^m2$. Thus it appears that the errors associated with the crowded field photometry, in these frames, are only about twice those which would apply to the case of isolated stars.

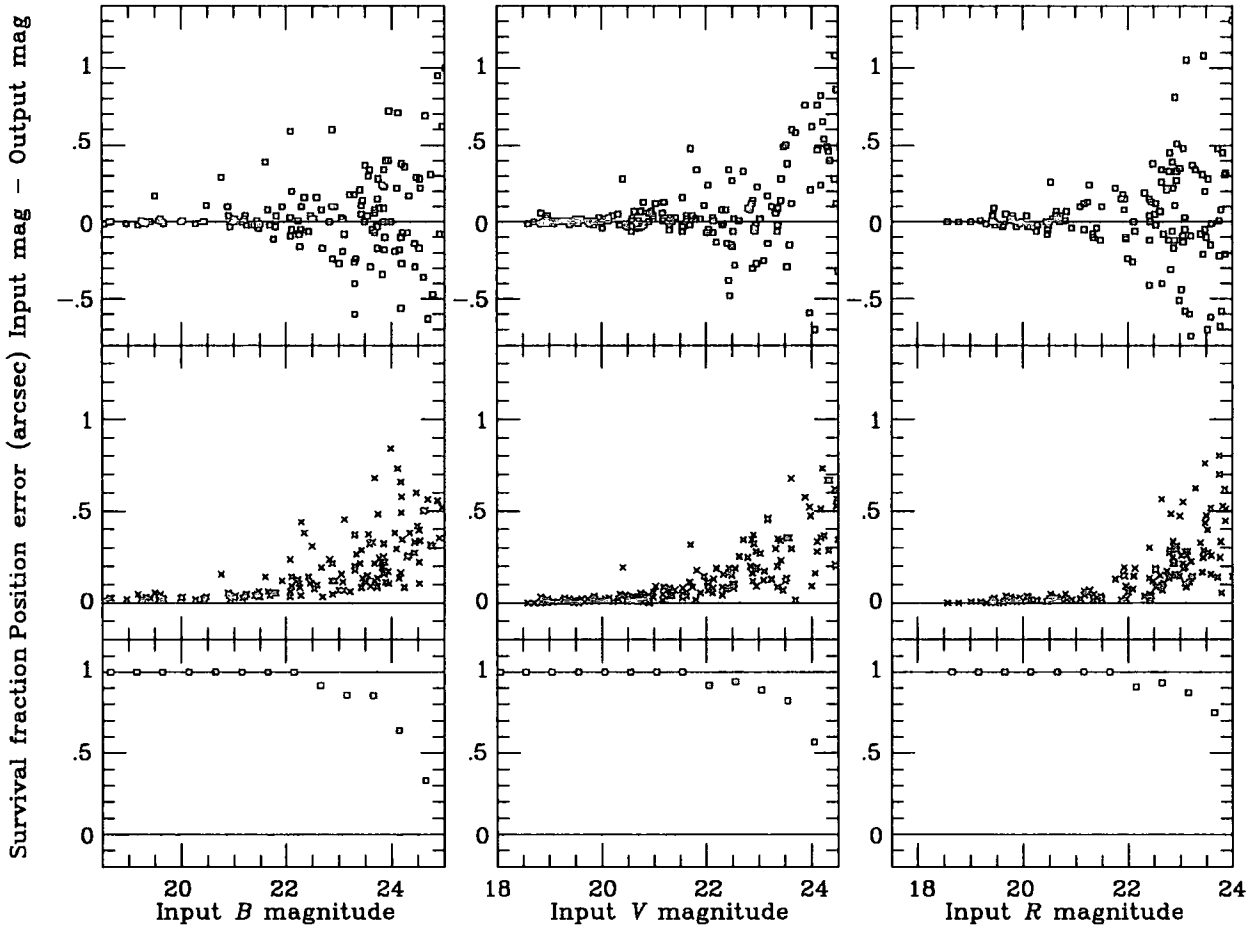

Figure 2.3: Results of simulations for M31 B, V and R band, stars which are placed, at random, on the original images. The plots show the errors in the magnitude and position, and the completeness as a function of the input magnitude of the artificial stars. These plots indicate the scale of the errors which we can expect in our actual photometry.

Thus, despite the above comments regarding the applicability of these results, they should give a fairly good impression of the spread and scale error for the real data at least at brighter

magnitudes. This, incidentally, is another test of any systematic effect of the sky subtraction procedure, described in §2.4.

The M33 data suffers from even more serious crowding than in the M31 fields. In this case the isolated star photometry should be of a similar quality to that for M31, but the analysis of the artificial stars added to the real frames (figure 2.4), show that the real errors are much higher. This is due to both the increased crowding and fluctuating background. Both the B and the V frames show a large ($\sim 0.^m1$ to $0.^m2$) spread by 20^m, although the cut-off at 21^m simply represents the faint end of the range of magnitudes which were input. Several outliers are due to mergers, although it is noticeable that they are such as to not have a significant effect on the positional error.

2.7 Conclusions

We have outlined the principles of crowded field photometry with particular reference to the DAOPHOT package which was used in the analyses presented in chapters 3 and 4. We have considered the following new methods for accomplishing parts of the reduction procedure, all of which offer improvements in some circumstances:

- object detection after maximum-entropy deconvolution of the image. In simulations this recovered $\sim 25\%$ more stars than the traditional 'FIND' method, with no additional spurious detections.
- sky subtraction by iteratively creating a background sky frame from the star subtracted image. This was vital for the undulating background on the M33 field.
- using the wings from a 'seeing theory' analytic profile, to generate a hybrid PSF. This helps extend the PSF when it becomes difficult to define it empirically off the frame.

Finally, we used simulations to investigate the photometric errors for the actual M31 and M33 fields studied in the subsequent chapters. These results also demonstrated the additional contri-

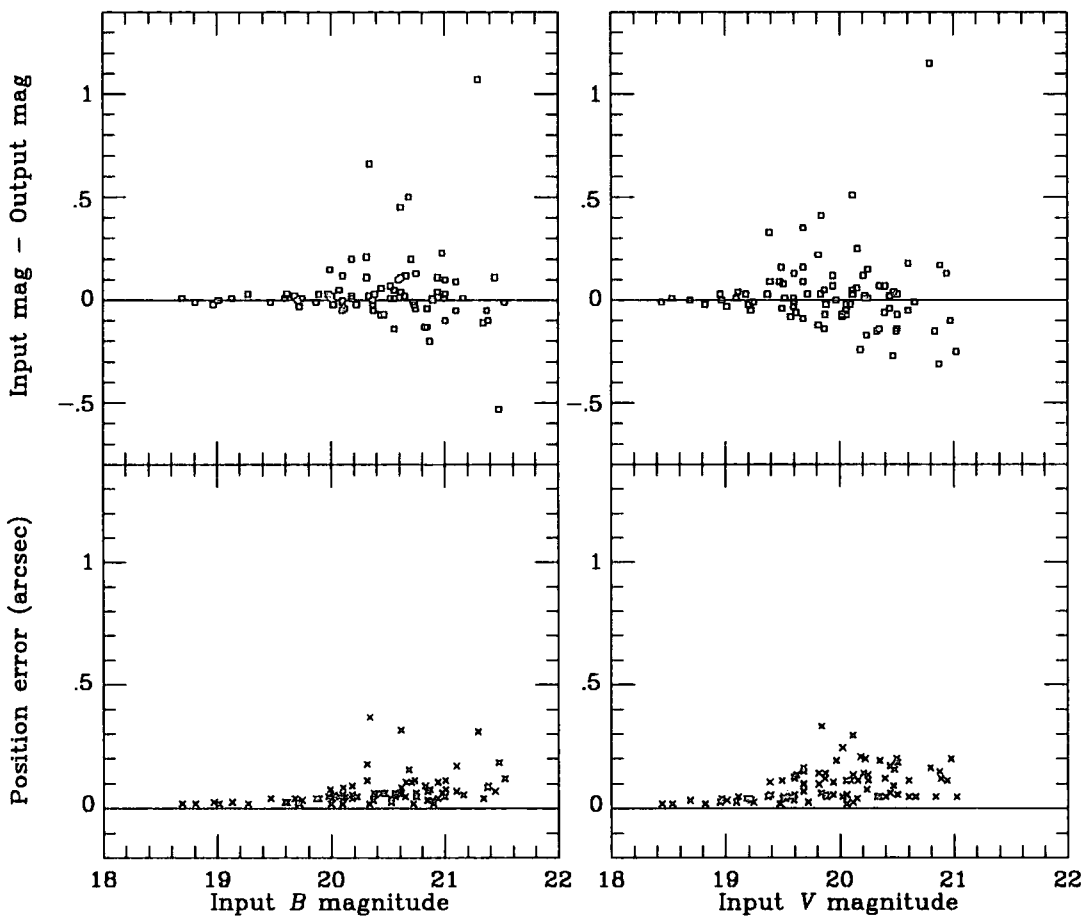

Figure 2.4: Results of simulations for M33 B and V band, stars which are placed, at random, on the real images. The plots, which show the errors in the magnitude and position, demonstrate the dominant effect of crowding on the uncertainty in the photometry.

bution to the errors due to the crowding and variable background, over and above the inevitable errors due to counting statistics.

Chapter 3

Resolved Stars in M31

3.1 Introduction

The spiral galaxy Messier 31, the Andromeda galaxy, is the furthest object visible to the unaided eye, and may be regarded as the sister galaxy of the Milky-Way. It is classified as a type Sb, and is inclined at $\sim 76°$ to our line of sight. Apart from the intrinsic interest in M31 as a large stellar system, it plays a pivotal rôle in the calibration of secondary distance indicators, and hence in the whole distance scale.

In particular, Baade's field IV, in which our fields are contained, has been the site of several studies, the first by Baade and Swope (1963, and hereafter BS63). It is a disk field situated around 20kpc south west of the nucleus, well away from the main areas of dust and nebulosity. Its interest lies in the presence of several clusters and associations which make up part of the outermost spiral arm of the galaxy. It was originally chosen by Baade as being a good field in which to search for Cepheids, and indeed it turned out to be so. Also, unlike the first three fields studied by Baade, it was considered to be sufficiently far from the centre of the galaxy so that variable internal extinction would not pose a serious problem. The results presented in BS63 gave a true distance modulus $\mu_0 = 24.20$, which had been corrected for the effect of reddening of $E_{B-V} = 0.16$.

More recently, the stellar populations of M31 have been the subject of a number of observational campaigns with modern detectors. Humphreys (1979) found spectral classifications and $UBVR$ photoelectric photometry for several of the brightest supergiants in field IV, concluding that their properties and distribution were similar to the spiral arm features found locally. A very large scale $UBVR$ photographic survey by Berkhuijsen *et al.* (1988) catalogued 11438 stars in the field of M31, down to a limiting magnitude of $18.^m8$ in V. Spectroscopic and photometric surveys for the most luminous red supergiants (Humphreys *et al.* 1988) and blue supergiants (Humphreys *et al.* 1990) have also been made for the whole of M31. Massey, Armandroff and Conti (1986) used UBV and narrow band CCD photometry for giant stars in OB associations in M31, to identify Wolf-Rayet stars, which were followed up spectroscopically, whilst the late-type population of the disk (actually in Baade's field III) has been studied by Richer and Crabtree (1985) and of the bulge by Rich *et al.* (1989). In a similar, but shallower, study to that presented here, Hodge, Lee and Mateo (1988) obtained $UBVR$ photometry for another CCD field within field IV, which has some overlap with ours.

A comparison of the colour magnitude diagrams of disk and halo fields was presented by Crotts (1986). He studied two disk fields, both at $\sim 18kpc$ from the centre of M31, but one on the major axis and one on the minor axis, thus the difference between them was inferred to be the difference in the halo populations. The halo population has also been studied by Mould and Kristian (1986) and, to very deep limiting magnitudes of $V_{lim} \sim 25.^m4$, by Pritchet and van den Bergh (1988). Pritchet and van den Bergh (1987A) were also the first to identify RR lyrae stars in M31, from which they concluded $\mu_0 = 24.34 \pm 0.15$ assuming $A_B = 0.31$.

Welch *et al.* (1986) find a distance to M31 using H band photometry of seven of the Cepheids from fields III and IV. Revising their figure to comply with an LMC true distance modulus of 18.5, they conclude $\mu_0 = 24.29 \pm 0.08$, after subtracting $A_H = 0.05$. Most recently, Freedman, and Madore (1990, and hereafter FM90), have reported their findings from a new CCD survey of the Cepheids in Baade's fields I, III and IV, arriving at a value $\mu_0 = 24.42$. Unfortunately, they have not yet published their full photometry, meaning any more detailed comparison with their results is not possible. However, their conclusions regarding the evidence for the requirement of

metallicity corrections are discussed in detail in this chapter, and revised moduli estimated on that basis.

The images used here were originally obtained by Drs. N. Metcalfe and T. Shanks for the purpose of recalibrating the secondary photometric sequences used by Baade and Swope in monitoring the Cepheids. By making the assumption that the BS63 Cepheid photometry is subject to the same systematic errors as the rest of the field, they produced new values for the Cepheid apparent distance moduli (Metcalfe and Shanks 1991, hereafter MS91). Specifically they obtained $\mu_{AB} = 24.56$, $\mu_{AV} = 24.62$ and $\mu_{PLC} = 24.71$. From this they concluded a very small value for the reddening, and hence deduced $\mu_0 = 24.63$, or $\mu_0 = 24.66$ for the above value of the LMC distance. However, they further commented that 'the main uncertainty in the true distance modulus of M31...is the value of the reddening'.

Our objective is to obtain deep BVR photometry from these images. The considerable crowding on these frames called for some sophistication in the method of photometry, particularly in order to get reasonably accurate results for the fainter stars. It was decided to use the profile fitting photometry routine DAOPHOT (Stetson 1987). The advantages of these techniques are discussed in chapter 2.

The motivation for this work is primarily to address the critical issue of the reddening which we shall do by consideration of the colour of the main sequence in the colour magnitude diagram. Our photometry should also enable us to check the MS91 corrections and thus allow a new distance estimate to be obtained. As discussed in chapter 2, there there is potential for scale errors with crowded field photometry, which might produce problems at the faint end.

Finally, we study the general stellar content of the field, and compare our results to the predictions of other similar work and theoretical models. The additional R band photometry and the use of a control field to assess foreground contamination, help test the consistency of these results.

3.2 Data

This section describes the experimental details of data acquisition and analysis. A plate of the R image of the M31 field is shown in figure 3.1. The field is fairly uniform, containing two or three small OB associations.

3.2.1 Observations

The data consists of CCD images taken at the $f/3.29$ prime focus of the 2.5m Isaac Newton Telescope, on La Palma, in November 1986. Broad band Mould-KPNO B, V and R filters were used.

The fields were centred around:

$$00^h35^m03^s, +39°40'45'', (B1950.0)$$

Which corresponds to galactic coordinates:

$$l^{II} = 120°, b^{II} = -23°$$

The details of the exposures given in table 3.1.

PASSBAND	EXPOSURE (s)	CHIP	SEEING ('')	CALIBRATION (Magnitudes/ADU)
B	4 × 800	RCA	2.0	30.92
V	1 × 1000	GEC	1.6	31.80
R	2 × 1000	GEC	1.1	32.41

Table 3.1: Summary of INT observations of M31.

The values given in the fourth column are only approximate as the FWHM of the PSF was

Figure 3.1: R band image of the M31 field. East is at the top and North on the right. The dimensions are $195'' \times 265''$.

found to vary somewhat across the frames. This variation was worst in the case of the RCA chip, being of order 15% in the FWHM. This could be due to a slight tilt of the camera with respect to the focal plane. Fortunately it was approximately linear from bottom left to top right, and so could be dealt with in the normal reduction procedure.

3.2.2 Pre-Processing

The basic pre-processing and calibration of these frames is described fully in MS91. The standard de-biasing and flat-fielding were done using appropriate control frames taken on the night. Photometric calibration was tied to the Landolt (1983a,b) standard stars, which were observed between exposures, for the Johnson BV and Kron-Cousins R systems. Since the seeing was found to vary through the nights, total magnitudes were required for the standard stars. These were obtained by taking the intensity within large apertures (15″ to 20″, radius), where the curve of growth met the background, for standard stars with similar seeing to the data frames.

Once produced, the frames were shifted, stacked upon each other, and cut to a common size of $3.4' \times 4.5'$, or a total area of $\sim 15.3\Box'$. This corresponded to the area formed by the overlap of all the images. (which had been offset from each other.) Thus the final working area was only 61% of the original field of view of the RCA chip ($\sim 24.2\Box'$). A further $\sim 3\%$ was lost due to the presence of saturated stars which were cut out of the image.

3.2.3 Control Field

In order to form an estimate of the contamination of foreground and background objects in the CM diagram, a control field was observed away from M31. These observations were acquired in October 1989, also at the INT.

This was centred at:

$$00^h25^m00^s, +41°00'00'', (B1950.0)$$

This is 3° from the centre of M31 and out of the plane of the disk. This corresponds to $\sim 40kpc$ at the distance of M31 and hence we would expect very little contamination from objects in M31 itself.

Details of the exposures are given in table 3.2.

PASSBAND	EXPOSURE (s)	CHIP	SEEING (″)
B	1 × 1000	RCA	1.2
V	1 × 500	RCA	1.1
R	1 × 500	RCA	1.0

Table 3.2: Summary of INT observations of M31 control field.

3.2.4 Reduction

The DAOPHOT 'FIND' routine was used to identify all 3.5σ detections in each band. This amounted to some 1300 stars in B, 2300 in V and 3500 in R. Roughly this limit corresponds to $B \sim 24.^m3$, $V \sim 22.^m9$ and $R \sim 23.^m6$. The different detection rates between the bands are partly accounted for by the differences in seeing and depth in each image, but in the main reflect the numerical dominance of the underlying red-giant population in this region.

The different pixel sizes of the two chips meant that accurate linear transformations had to be constructed to allow comparison of positions. This was done by using the centroid positions of ten of the brighter stars in the field to define the transformation coefficients. These candidate lists were then merged with any detections within 1″ of each other on different bands being counted as one star. This gave a grand total of around 5000 stars since most of the stars were found in more than one band.

The standard reduction procedure, described more completely in chapter 2, was followed. Preliminary aperture photometry was carried out on these stars, using the PHOT routine. The

apertures used ranged from a diameter of 2″, where quantisation effects are dominant, to 9″ when crowding errors become very severe. The reference magnitudes, which are used in the subsequent analysis, was chosen to be the compromise aperture 4″. This is not a critical decision since these magnitudes only serve as the first approximations for the iterative fitting procedure.

Stars for which DAOPHOT failed to obtain aperture magnitudes were investigated and usually turned out to be at sites of image defects such as charge transfer columns. These candidates, which typically amounted to a hundred on each frame, were dropped from the lists.

An initial point-spread function was generated for each frame from large numbers of bright stars used as templates. The radius of this PSF was chosen to be around 4″. With these first order PSFs the neighbours around the best 20 or so template stars were subtracted (in the manner described in chapter 2). These 'neighbour-subtracted' frames were than used to find a better PSF. This time the PSF variation with position was allowed for by setting the appropriate flag.

This procedure was repeated several times to iterate towards the true PSF. On each occasion the PSF was examined and any template stars which gave cause for concern , such as indications that they weren't point like, were dropped from the list. The corrections to sky estimation by comparison with an artificial frame, as described in chapter 2, were applied throughout.

The best PSFs in each band were then used to reduce the whole lists of candidate stars. The stars were grouped into sets of close neighbours of less than sixty members. The DAOPHOT routine which performs the grouping works with a user defined threshold, and groups according to brightness weighted nearest neighbour algorithm. The 'SELECT' routine was employed so that as many stars as possible were reduced in large groups, thus making full use of the multiple profile fitting. This said, examination of simulated results using different critical overlaps did not show a strong dependence on crowding.

After the NSTAR fitting routine was run, care was taken to ensure that any stars which had 'migrated' to other groups during the iterative fitting procedure, were removed. This migration occurs because of the extreme crowding, and because of the loose candidate selection criteria. Essentially very faint candidates run the risk of being dragged towards a nearby bright star during

the iterative profile fitting. If this occurs within a group then the program automatically deletes the fainter star, but occasionally migrations occur to neighbouring groups and these must be dealt with separately.

It was found that a smaller spread in magnitudes resulted when a small fitting radius of 1. $''$3 was used. This is consistent with the errors being dominated by crowding. In this situation a small fitting radius minimises the influence of contamination, although it sacrifices something to poisson noise. (This is similar to the use of very small apertures to get the most reliable aperture photometry in crowded fields.)

Having obtained the final magnitudes the three lists were again put through a merging program to make sure that the stars originally identified as being the same on each frame, ended up as having the same measured positions to a tight tolerance (1$''$). This procedure should reduce the occasions in which the photometry for supposedly one star is actually for more than one star.

This produced a total number of 2294 stars which 'survived' in at least two passbands. Here 'survival' depends on both whether NSTAR output a magnitude for the star, and also if the output position was such that the star coincided with the position on the other band, as described above. For this reason, the numbers in any given pair of passbands are somewhat less than the total number. This is seen clearly in the colour-magnitude diagrams presented below.

The reduction procedure for the control field followed the same basic steps outlined above. The lower level of crowding meant that the task was simpler, with no need to correct the sky values. In fact the precision of these results is not critical since they are only required to give an estimate of the average numbers of foreground stars in areas of the colour-magnitude diagram.

3.3 Results

A complete table of all the stars for which magnitudes were obtained in at least two passbands is included in appendix A. The remainder of this section is devoted to the presentation of this data in graphical form, and comparison with previous work and simulations.

3.3.1 Comparison With Other Photometry

Since the original photographic studies of Baade, several workers have observed this field with electronic detectors. Here we compare directly with the original BS63 magnitudes (together with Arp's photoelectric sequence reported therein), the interactive aperture photometry obtained from the same images as analysed here by MS91, and the independent CCD photometry of HLM88. These are shown in figures 3.2, 3.3 and 3.4.

From the figures we conclude that the agreement with MS91 is good, as expected, whilst that with BS63 is less so. Even in the case of MS91, the scatter at the faint end is $0.^m1$ to $0.^m2$, demonstrating the level of uncertainty simply due to the measuring process. The bright end agreement is, of course, ensured, since we are using the same zero-point for the magnitude scale as MS91. In the V band we see no systematic effects down to the magnitude at which MS91 cut off. In the B band there is clear evidence of a small systematic scale error, which results in an overestimate of the brightness with the aperture photometry of $\sim 0.^m07$ by 22^m. From the discussion given in chapter 2, this may indicate a tendency to underestimate the sky with the interactive photometry of this field. It would not be surprising that such an effect varies from image to image, since the observations differ in several ways, most notably the seeing. The B band scale error seen in the BS63 comparison is not as sudden as that seen in the full MS91 comparison, as presented in their paper.

This suggestion is on lent support by the fact that the comparison of our photometry with that of HLM88 reveals no obvious scale error, in any band, to fainter magnitudes. These plots also give us reassurance regarding the zero-points of our photometry. Formally, using a magnitude weighted fit for the indicated range of magnitudes, gives:

$$B_{\text{This work}} - B_{\text{HLM88}} = 0.02 \pm 0.01 \ ; B_{\text{This work}} < 22$$

$$V_{\text{This work}} - V_{\text{HLM88}} = 0.00 \pm 0.01 \ ; V_{\text{This work}} < 21.5$$

$$R_{\text{This work}} - R_{\text{HLM88}} = -0.03 \pm 0.02 \ ; R_{\text{This work}} < 21$$

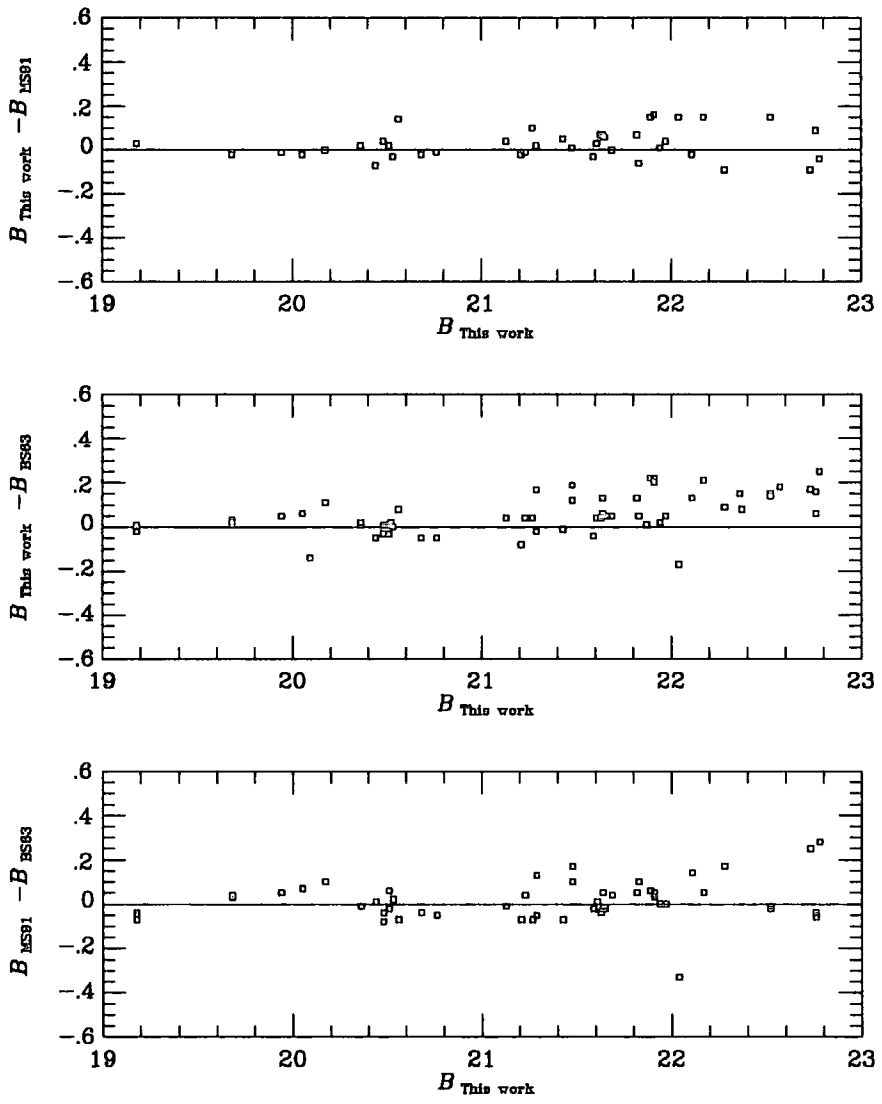

Figure 3.2: Comparison of B band photometry between this work, MS91 and BS63. The Arp photoelectric photometry is shown as filled boxes. Also see MS91 for their full comparison with BS63 from both their CCD fields.

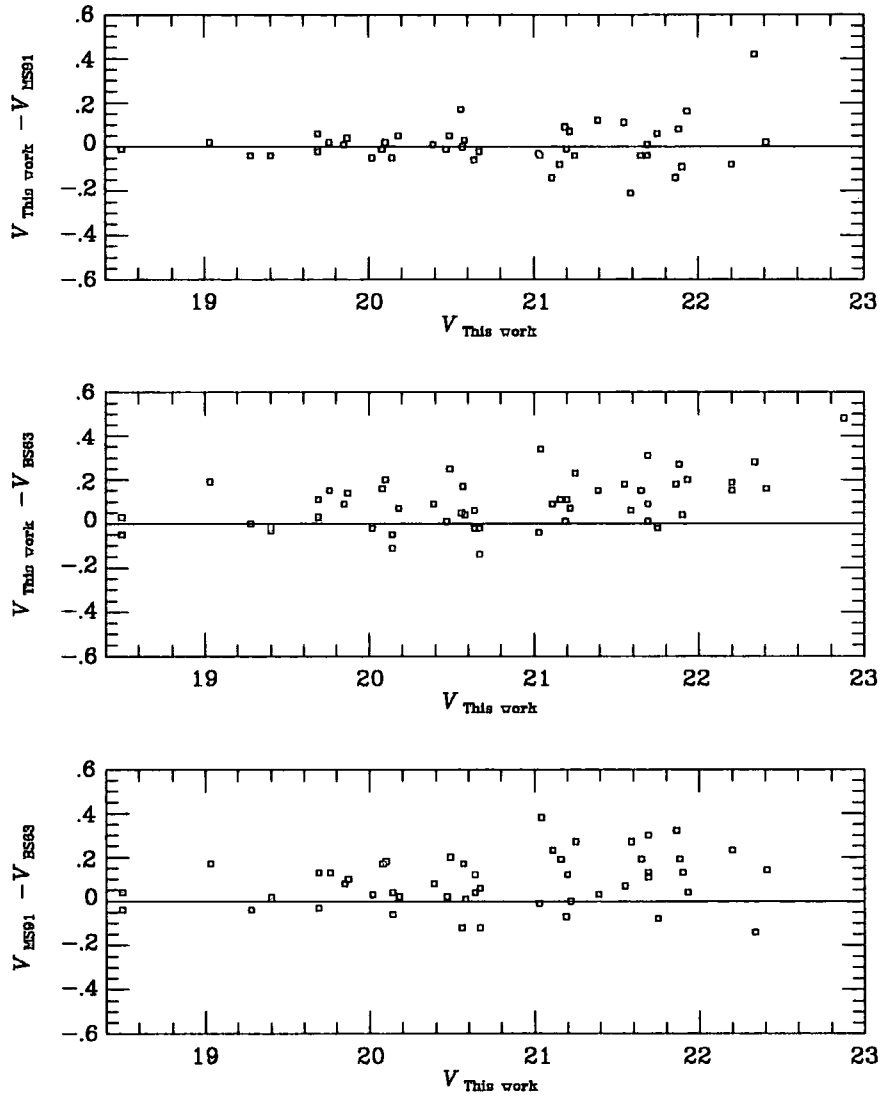

Figure 3.3: Comparison of V band photometry between this work, MS91 and BS63. The Arp photoelectric photometry is shown as filled boxes. Also see MS91 for their full comparison with BS63 from both their CCD fields.

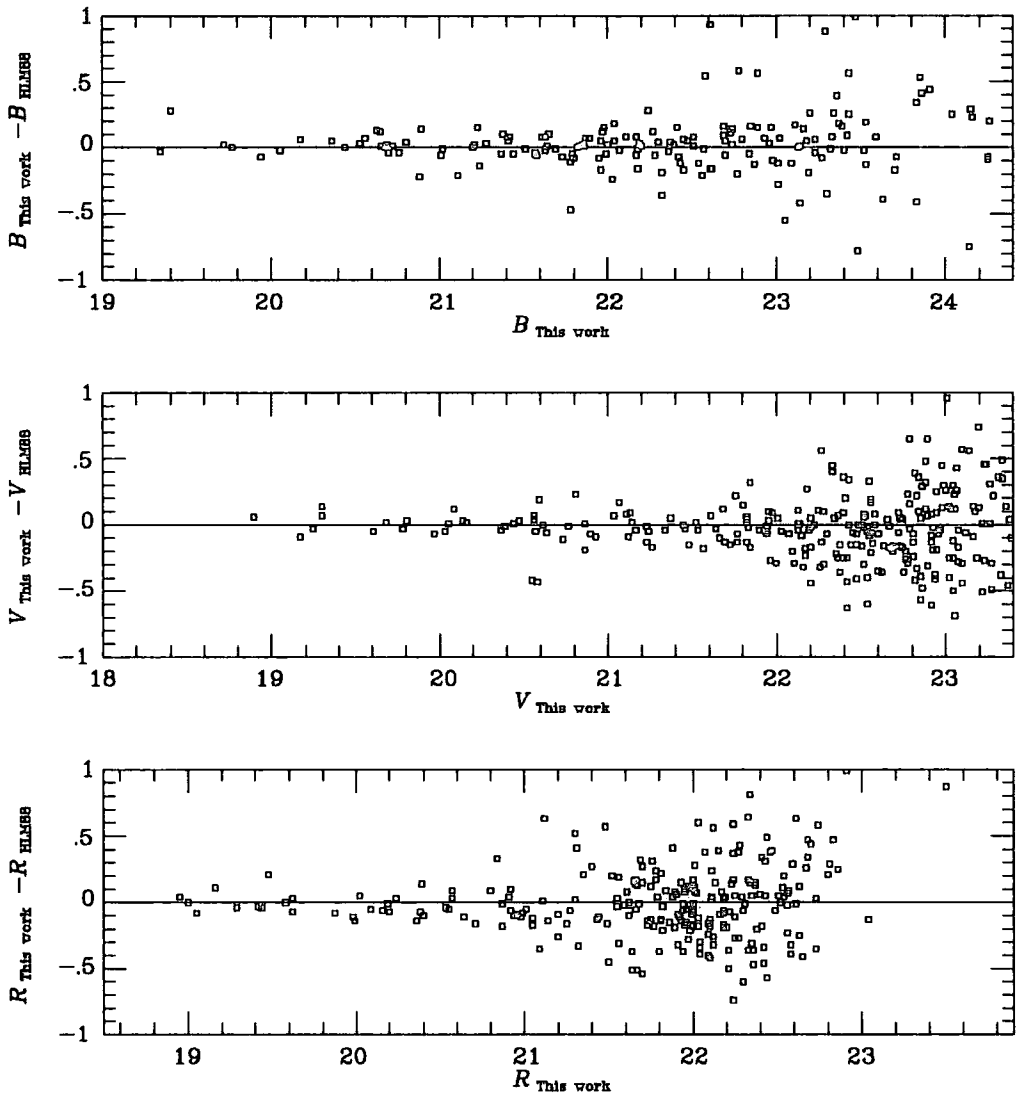

Figure 3.4: Comparison of our photometry with that of Hodge, Lee and Mateo (1988), in the B, V and R passbands. The agreement in terms of the zero-points and scale offsets is very good, although an increasingly large scatter is seen at faint magnitudes.

The consequences of these comparisons for the interpretation of the BS63 Cepheid results are discussed later.

3.3.2 The Colour-Magnitude Diagram

The final colour-magnitude diagrams for all the stars photometered in our field, are shown in figure 3.5. As discussed above, the number appearing in each diagram varies due to differing completeness dependent on the pair of passbands concerned. In particular, there is a noticeable reduction in the number of faint red stars for which B band magnitudes were obtained. This is due to the faintness of these stars in the B band and also to the poorer seeing.

Each diagram shows a clear, reasonably tight, main sequence (MS) running almost vertically up the left hand side. Also the red-giant branch (RGB) is well populated, and shows considerably more spread than the main-sequence. Several brighter stars are also seen; these are a combination of foreground stars, asymptotic giant branch (AGB) stars, and possibly some stars on the instability strip and other evolved stars. These are discussed in more detail in future sections. The results for the V versus $B-V$ diagram are given again below in table 3.3 , which shows more clearly the relative numbers of stars in different regions of the diagram.

3.3.3 Error Analysis

From a measurement standpoint, apart from the evident effect of poisson noise, contamination by blended images will tend to produce objects which are brighter than they should be. Blended images may often also have a more neutral colour, particularly if the primary object is blue where there is a good chance that any faint overlapping object will be red. This may be enhanced during the cross identification process, which would preferentially pick up cases where two faint stars of opposite colours happened to be close together. In an attempt to quantify the expected spread due to errors in the photometry, from all sources, we have constructed a diagram purely of results from synthetic stars, in the manner described in chapter 2. No attempt is being made here to duplicate

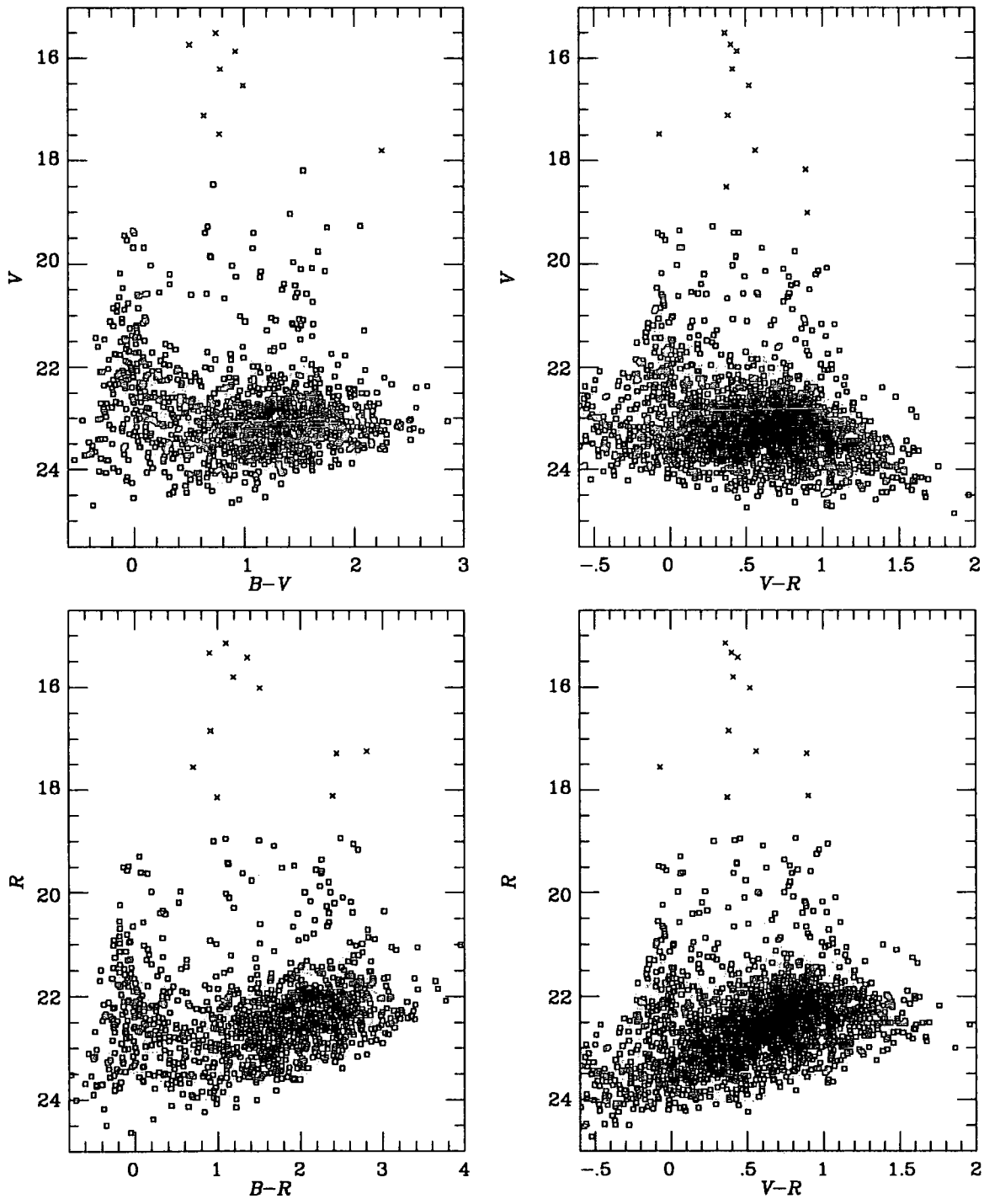

Figure 3.5: Colour-magnitude diagrams for all stars in the M31 field. The crosses represent stars which were saturated in the main images, and whose magnitudes were retrieved from short exposure frames.

15.25			1					
15.75			1	1				
16.25				1				
16.75				1				
17.25			1	1				
17.75						1		
18.25			1		1			
18.75			1					
19.25		3	2	1	2	1		
19.75		3	2	1	2			
20.25		3	2	4	6			
20.75		12	2	1	4			
21.25	2	17		4	10	1		
21.75	1	23	9	7	5	3		
22.25	3	45	15	28	31	13	4	
22.75	5	29	46	71	113	36	1	
23.25	8	30	55	113	137	68	16	1
23.75	10	17	42	60	56	17	2	
24.25	2	5	22	12	7			
24.75	1	1		3				
25.25								
	-0.50	0.00	0.50	1.00	1.50	2.00	2.50	3.00

Table 3.3: The numbers of stars recovered in each colour and magnitude bin for the $(V, B-V)$ diagram. The bin axis labels represent the bin centre values.

the real results, simply to indicate the extent of the errors in the most interesting regions of the diagram.

These results are shown in figure 3.6, with the small dots being the input magnitudes, and the open symbols the recovered magnitudes. Every effort was made to ensure the reduction process was as realistic as possible, however, it should not be forgotten that these are really errors on a model, not the data itself.

This analysis clearly reproduces the relative appearances of the different diagrams, such as the separation of the two populations. Much of the spread of the main sequence and red-giant branches can, thus, be explained by random measurement errors. In particular the errors at the bright end of the MS should be very small, implying features seen there in the diagram are real.

Although the giant branch is greatly broadened by photometric errors, this is due principally to the poor B band magnitudes, for these red stars, and, therefore, the magnitude of the tip in the V and R bands is fairly sharp.

3.3.4 Colour-Colour Diagram

Figure 3.7 shows the $(B-V, B-R)$ and $(B-V, V-R)$ colour-colour diagrams. These show clearly the distinction between the main-sequence stars, which are clustered around $(0, 0)$, and the red-giant population. The good correspondence between the two colours gives an impression of the errors. Since the numbers are dominated by fairly faint stars this good correlation suggests that we have generally found reliable photometry for these stars.

The greater apparent scatter in the second diagram is due to the fact that in this case all photometric errors will tend to move points in a direction perpendicular to the stellar locus, whereas, in the $(B-V, B-R)$ case the errors will be more aligned with the stellar locus.

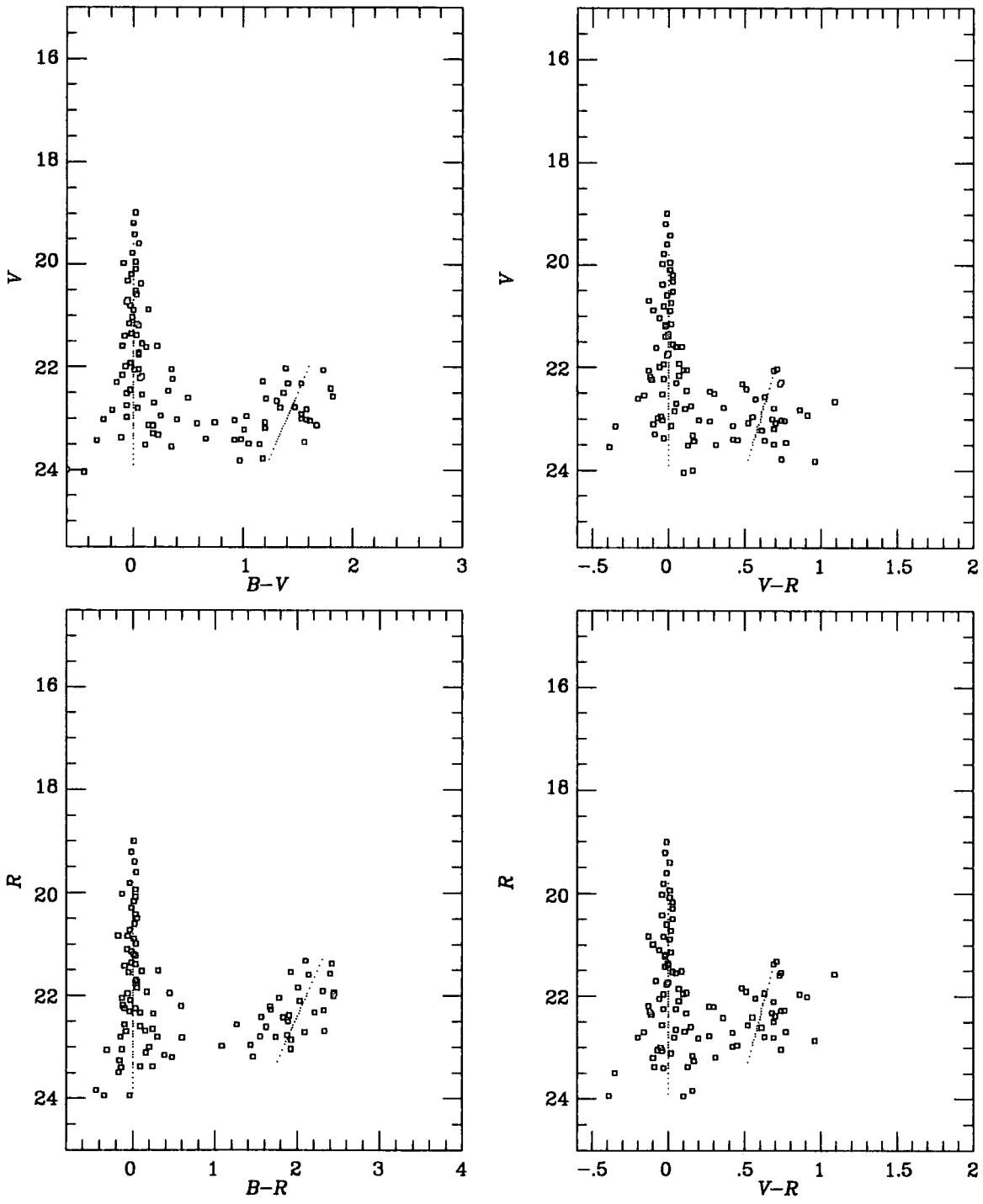

Figure 3.6: Colour-magnitude diagrams for artificial stars reduced in the same manner as for the real stars to show the expected effects of photometric errors on the retrieved magnitudes. The small dots show the input positions.

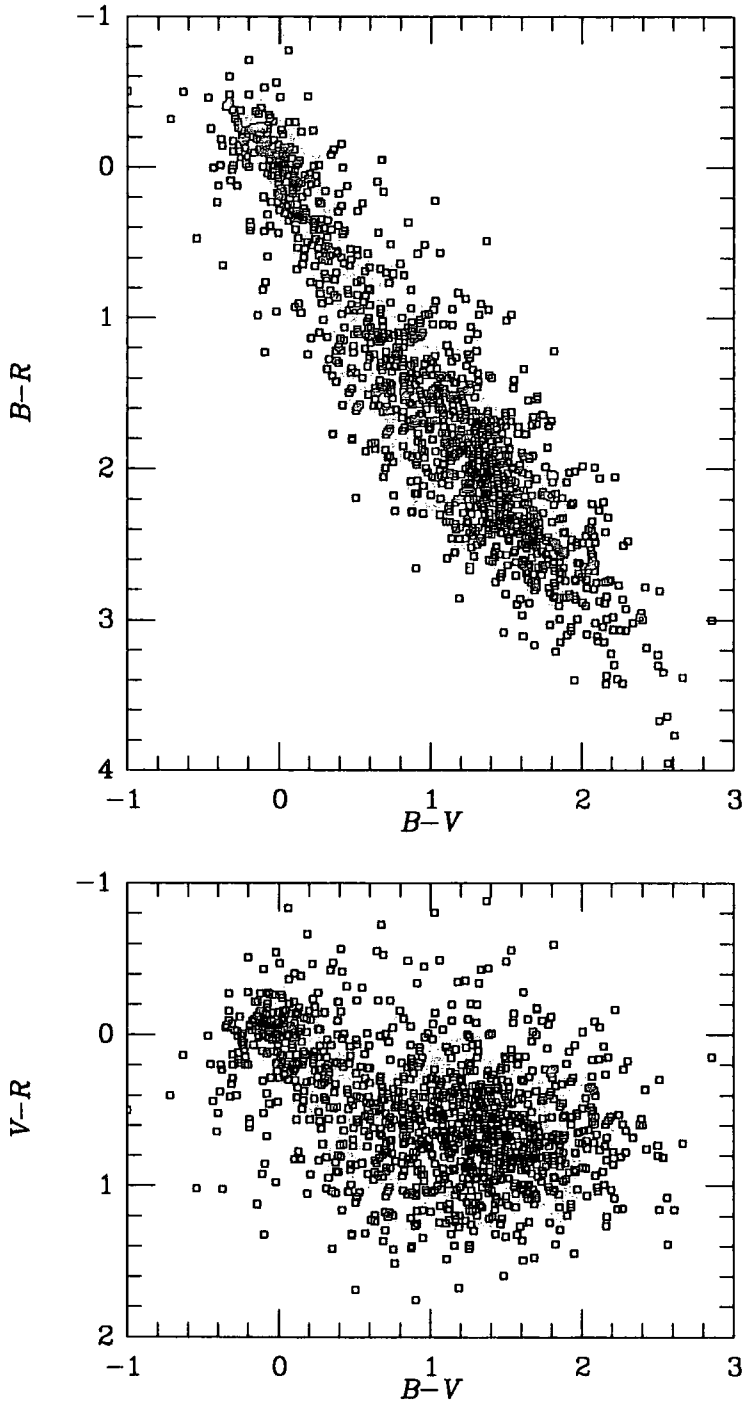

Figure 3.7: Two colour-colour diagrams for all stars in field. These show clearly the separation between the main sequence stars and the red-giant branch.

3.3.5 Control Field

In the case of the control fields, the total area covered was 24□′. The colour-magnitude diagrams for the control field are shown in figure 3.8. The same information is shown for the $(V, B-V)$ data in table 3.4.

14.00	0	1	0	0	0
16.00	0	2	7	0	0
18.00	0	3	13	5	1
20.00	1	5	6	7	0
22.00	1	12	38	33	10
24.00	18	28	27	18	9
	0.05	0.55	1.05	1.55	2.05

Table 3.4: Control field results for foreground stars in a 24□′ field. The numbers are given for bin centres in V magnitude and $B-V$ colour.

It is interesting to compare this data with the predictions of the Bahcall and Soneira model for stellar number counts. These are tabulated in Ratnatunga and Bahcall (1985), as summarised in table 3.5.

We see a reasonable agreement for the $V = 20^m$ bin, and brighter, within the inevitable errors from counting statistics. There is some evidence for a slight enhancement in the numbers of blue and intermediate colour stars. The drop off in the number of faint red objects is likely to be due to the effect of incompleteness. This still leaves, however, a large excess of objects with blue and intermediate colours, in the two faint magnitude bins.

From deep galaxy number count studies (eg. Metcalfe *et al.* 1991) we know that the faint galaxy population forms a similar feature to this in terms of both colour and number density. For example, they find that for the magnitude range $22 < R_{\rm CCD} < 22.5$ that the galaxy distribution peaks at $(B-R)_{\rm CCD} = 1.3$ with a number density which translates to an expected number in our field of ~ 17 objects with colours $(B-R)_{\rm CCD} < 2$. This compares to an observed number in that

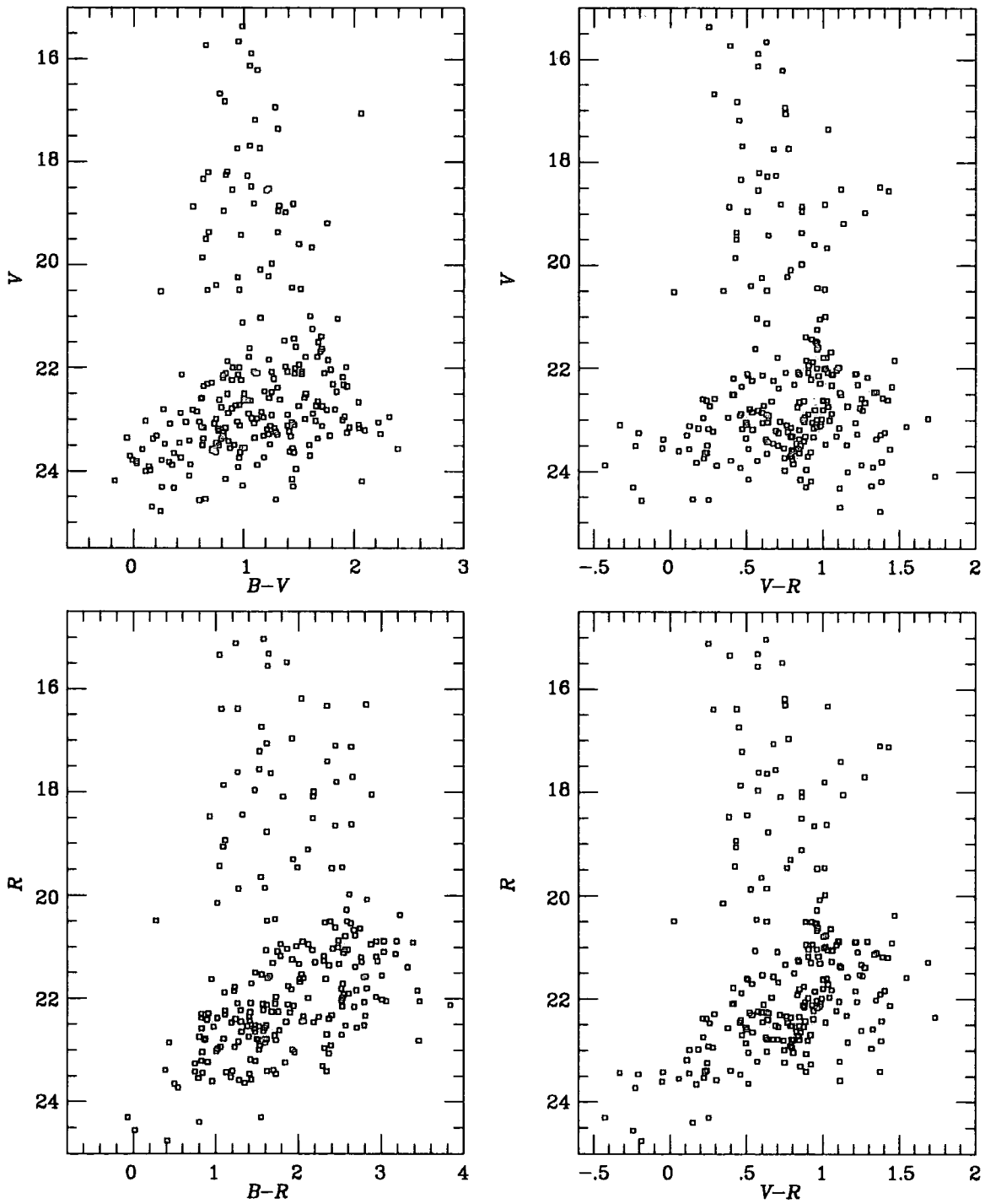

Figure 3.8: Colour-magnitude diagrams for the M31 control field. The bright objects are all foreground stars in our galaxy, whilst at fainter magnitudes there are an increasing number of unresolved, background galaxies.

14.00	1.5	0.5	0.1
16.00	3.6	2.4	0.5
18.00	2.9	6.7	3.6
20.00	1.9	4.6	14.9
22.00	2.2	2.6	34.6
24.00	1.0	2.6	57.6
	$(B-V) < 0.8$	$0.8 < (B-V) < 1.3$	$1.3 < (B-V)$

Table 3.5: Bahcall and Soneira predictions for foreground stars in the direction of M31, in a 24□′ field. The numbers are given for bins in V magnitude and $B-V$ colour.

bin of 26 objects. Thus our faint blue objects are well explained as background galaxies which are sufficiently small and faint as not to be distinguishable from point-like sources, with the object finding algorithm used (essentially DAOPHOT 'FIND' with the addition of the discriminating statistics of 'NSTAR').

The reasonable agreement between the results and expectations here, raises questions about the similar study of Crotts (1986). In his comparative study of disk and halo populations of M31, he observed two control fields, with projected distances of 35.5kpc and 21.5kpc, from the centre of M31, respectively. Comparing the results from these two fields, Crotts noted that the inner field had considerably more objects than the outer one and that many of these were blue in colour. In order to explain the difference between the two fields he suggests that the inner field is sampling a remote disk population in M31, for which he must also invoke significant warping of the disk. Since Crotts' photometry (Thuan-Gunn g, r) reaches a similar depth to that presented here, we see that a possible explanation is simply the detection of the onset of the faint galaxy population in the inner field. There is still no obvious reason why the same objects are not detected in the outer field however.

Reconsidering the data in the main diagram (figure 3.5) we see that contamination by foreground stars in our galaxy account for most of the objects of intermediate colour, especially at the

bright end. They can also account for some of the stars in the bright red plume of evolved stars in M31. A recent large area photographic survey by Berkhuijsen *et al.* (1991) of $\sim$ 12000 stars brighter than $V \sim 20$ (complete to $V \sim 18.8$) in fields on and off M31, confirms this result. To their limits they find nearly all objects bluer than $B - V < 0.4$ to be in M31, but only 1/3 of stars with $B - V > 1.5$ to be so.

The fainter, generally bluer, population of background galaxies would be largely swamped in the red-giant branch. However, since they come in at a somewhat brighter magnitude, and would be expected to have a broader range of colours, they could account for some of the 'fuzziness' around the edges of the red-giant grouping. We would expect them to suffer from roughly twice the amount of extinction due to dust internal to M31 as the young disk stars.

3.4 The Effect of Absorption by Dust

The question of extinction due to dust towards the stars in M31 is clearly important in deriving a true distance modulus to that system. The methods of estimating reddening and extinction are reviewed in chapter 1, and the standard relations given in appendix F. Here we consider their implications for both the extinction toward, and that within M31.

3.4.1 Foreground Extinction

Firstly we consider the foreground, 'line of sight', extinction. Rowan-Robinson (1986) summarizes the results of the standard extinction laws for the galactic latitude of M31 ($b \sim 23°$):

$$A_B(Sandage - Tammann) = 0.22$$

$$A_B(deVaucouleurs) = 0.41$$

$$A_B(Tully - Fisher) = 0.41$$

The large discrepancy in the predictions of these different models for even the *average* extinction, suggests that the question of the extinction to our small fields is best dealt with by direct observation.

Using the colour excess of late-type field stars, McClure and Racine (1969) found a value for the reddening in the direction of M31 of $E_{B-V} = 0.11 \pm 0.02$. A similar technique was used by Humphreys (1979) for six spectroscopically confirmed foreground stars within field IV itself, giving answers in the range $0.02 < E_{B-V} < 0.07$, with one outlier. Burstein and Heiles (1984) find a value of $A_B = 0.32^m$ for the foreground extinction, using a combination of galaxy counts and HI maps. This would imply a reddening of $E_{B-V} = 0.08$. Finally, using the IRAS maps of Rowan-Robinson *et al.* (1991), we find that the intensity in the region of M31 is around 3.3MJySr^{-1}, but for the square degree in which our field lies is only 2.95MJySr^{-1}. From this, we arrive at an extinction of $A_V = 0.18$ or $E_{B-V} = 0.06$. This value is towards the lower of the cosecant law estimates, although inspection of the I_{100} map reveals a complicated structure on small scales. For example, M31 appears to be in something of a window in the IRAS cirrus.

On the face of it this seems to be a painting a reasonably consistent picture with foreground reddening in the region of $E_{B-V} = 0.^m08$ for the general vicinity of M31, but a little lower for the particular area of our field. However, we should note that there are two reasons for taking the IRAS estimate as an upper limit. Firstly, there would be expected to be some contribution to the IRAS flux from M31 itself. This is clearly seen in other parts of M31. Secondly, there remains a conflict between the reddening predicted for the north polar cap by RR91, compared with from stellar photometry (see §1.2.5), which might suggest that a lower value for the reddening prediction is appropriate.

In contrast to these arguments, which tend to favour a reduced value of the galactic reddening, revising the photoelectric results of Humphreys (1979), for foreground stars in the direction of M31, appears to come to the opposite conclusion. Comparing the photometry of MS91 (private communication) directly for the same stars suggests that her 10″ aperture photometry, gives unreliable results, much worse than the quoted formal errors indicate. The actual numbers are tabulated below (table 3.6), where we have also taken the opportunity to update the intrinsic colours appropriate to the spectral type of the stars, according to Fitzgerald (1970). (Note that the MS91, short exposure, photometry is used here since these stars are bright and generally saturated on the long exposures. All are in field IV, but some of them are off the CCD image which is the subject of the

main part of this study.) Formally this result gives $E_{B-V} = 0.125 \pm 0.047$, but this would change significantly if one or more of the outliers were dropped.

Star	Classification	$(B-V)_{MS91}$	$(B-V)_0$	E_{B-V}
B69a	G8: V	0.87	0.74	0.13
B81	G2 V	0.74	0.63	0.11
B79	G5 V	0.77	0.68	0.09
B38	G5-G8 V	1.00	0.72	0.28
B49	G8-K0 V	0.96	0.76	0.20
A179	F8-G0 V	0.50	0.56	-0.06

Table 3.6: Reddening calculated from foreground stars using the MS91 photometry with the Humphreys (1979) spectral identifications. This table should be compared to H79 table 4

Subsequently Humphreys *et al.* (1988) and Humphreys *et al.* (1990) have adopted foreground extinctions of $A_V = 0.2$ and $A_V = 0.3$ respectively, on the basis of these being the lowest values found for any individual super-giants in their surveys. Similarly, Massey *et al.* (1986) adopt $E_{B-V} = 0.08$ for the foreground, being the lowest value found in their sample of OB associations.

Considering all the evidence for foreground reddening, noting the large error bar on the result from the foreground stars in field IV itself, we conclude an estimate of $A_V = 0.2 \pm 0.05$ is likely to bracket the true value.

3.4.2 Absorption within M31

The question of the additional reddening due to dust within M31 which obscures the particular stars in which we are interested, is best answered by examining the stars themselves. It is conventional, in this respect, to assume that the internal reddening is likely to be the same for the Cepheids as it is for the young giant stars. Both are expected to have similar small scale heights compared to that of the interstellar dust. For example, Allen (1973) gives the scale heights of O stars and classical Cepheids as $\sim 50pc$, compared to $\sim 120pc$ for interstellar gas and dust.

Although M31 is highly inclined to our line of sight ($\sim 76^{\circ}$), the remoteness of field IV, at around $18kpc$, is expected to mean that internal extinction in M31 is fairly low. BS63 originally derived a value for the total reddening of $E_{B-V} = 0.16^{m}$, from the colours of the Cepheids. This was corroborated by the H79 value of $E_{B-V} = 0.14$, obtained for four of the brightest red super-giants in this field.

These conclusions must now be re-examined in light of more recent CCD photometry. Firstly considering the Cepheids; the re-analysis of the BS63 data by MS91 now appears to suggest lower reddening from the colours of the Cepheids. This is illustrated by the fact that, to within the photometric errors, they obtain the same distance modulus for the $P - L_B$ relation as the the $P - L_V$ relation, consistent with zero-reddening. A similar result is reported by Freedman and Madore (1990), who obtained practically identical apparent moduli, for field IV, in four bands ($\mu_{AB} = 24.59$, $\mu_{AV} = 24.57$, $\mu_{AR} = 24.63$ and $\mu_{AI} = 24.58$). However, we should recall the H band results of Welch *et al.* (1986) gave $\mu_{AH} = 24.34$. We also note that our small scale error relative to MS91, implied by the B band data presented here, would tend to increase the reddening by these arguments, but still be broadly consistent with zero.

However, the reddening derived from the Cepheids themselves must be treated with caution. Firstly, the natural spread in colours of the Cepheids, due to the width of the instability strip, requires that large numbers of Cepheids are observed to give good confidence limits. FM90 calculate that around 50 would be required to give the reddening to $0.^{m}01$, this compares to only 13 actually observed. Secondly, variations in metallicity can alter the apparent distance moduli so that the reddening thus estimated is seriously in error. The effect is discussed in more detail later.

With regard to the spectroscopic evidence, we have again re-tabulated the H79 data with the revised MS91 photometry, this time for the M31 super-giants (table 3.7). In this instance, the intrinsic colours are from Flower (1977), except for F-type supergiant star A207, which we take from the more recent work of Böhm-Vitense (1981). This gives the formal answer of $E_{B-V} = 0.175 \pm 0.036$, although we should note that the external error due uncertainties in zero-point determination, spectroscopic identification and ascription of intrinsic colours is likely to be larger than this internal error. For completeness we mention further results from the CCD/spectroscopic

study of Humphreys *et al.* (1988) of M giants. Two of these are located in field IV, and these give the high, but uncertain, values $A_V = 0.83 \pm 0.22$ and $A_V = 0.88 \pm 0.44$.

Star	Classification	$(B-V)_{MS}$	$(B-V)_0$	E_{B-V}
A207	F5 Ia(-Ib)	0.63	0.40	0.23
B59	B2: Ia	0.05	-0.16	0.21
B24	B0 I	-0.06	-0.25	0.19
A240	A2 Ib	0.12	0.05	0.07

Table 3.7: Revised reddenings to individual giant stars in field IV, using MS91 photometry and H79 spectral classification.

A final independent estimate of the reddening is given by HLM88 of $E_{B-V} = 0.13 \pm 0.04$ from their $(U-B), (B-V)$ diagram for stars in field IV. Considering all the values given above for the total reddening, clearly shows it to still be uncertain. An alternative approach, which we concentrate on here, is to estimate the reddening from the position of the main-sequence in our colour-magnitude diagram, and to take this to apply to the Cepheids also. This method is developed in the next section.

3.5 The Young Population

The appearance within the diagram of two principal features, the main sequence and the red giant branch, is indicative of the presence, in this field, of at least two population components, one old and one young. The older stars are considered later (§3.6) later whilst the young stars are discussed here. Our interest is primarily in the question of the implications of our results for the reddening and the Cepheid distance. In particular, we consider the important effect of metallicity on the correct interpretation of both of these.

3.5.1 Evolution of Massive Stars

The cartography of the HR diagram, and in particular, the position and spread of the main-sequence are dependent, in a complex way, on the parameters which determine stellar evolution, chiefly helium and heavy metal abundance, mass-loss and convective overshoot. The main-sequence is very steep in our diagrams since for these stars the broad band BVR filters are sampling the Rayleigh-Jeans tail of the black body spectrum, resulting in an almost constant ratio of fluxes between the bands.

Metallicity affects the position of the MS in the sense that higher values of Z, the heavy element abundance, result in somewhat redder stars. However, they also become fainter, resulting in only a small change in the actual locus. (eg Lattanzio, 1991). Variations in metallicity are unlikely to contribute to the observed spread, as they will be dominated by the other effects discussed below.

Evolution also tends to redden the MS, as stars become both brighter and somewhat redder during their core hydrogen-burning life. It is this effect which produces the familiar curved isochrones which fit to the CM diagrams of open clusters. The subsequent evolution, beginning with the shell hydrogen-burning phase, is relatively rapid. For massive stars the details of this evolution are rather sensitive to the input physics of the models (eg. De Loore, 1988, Chiosi and Maeder, 1986). This makes precise comparisons, at the present time, rather unproductive, and instead we look at the general features common to all the models.

Firstly the star moves rightwards across the CM diagram, as its envelope expands, proceeding up the red-giant branch. At this stage the star begins to burn helium in its core, which gradually takes over from the shell hydrogen-burning as the main mechanism for energy generation, and pushes the star back bluewards across the CM diagram. For the massive stars, such as we are studying, there will be a shorter but stable lifetime on the core helium-burning main sequence (typically $10\% - 20\%$ that of the H-burning lifetime). These stars will be considerably brighter than they were during their hydrogen-burning phase, but their colour depends strongly on their heavy-metal abundance. Low metallicity will result in very blue stars, comparable with the H-burning MS, whilst more metal rich populations will have a much redder He-burning MS.

Thus, for metal poor stars, this could give rise to the appearance of two turn-off points, one for the core H-burning and one for the core He-burning. There is clearly the potential for ambiguity here in estimating the ages. The helium abundance is also important; for the MS high abundance has the opposite effect from metallicity, whilst for the He MS, lower Y has the same effect as lower Z.

3.5.2 The Metallicity

We see, then, that estimates of the abundances are required if we are to understand the features we see in the CM diagram. From the BS63 data, Iben and Tuggle (1975) find a metallicity for the Cepheids of $Z = 0.02$, which is similar to solar metallicity, $Z = 0.017$ (Vandenberg, 1985). In order to arrive at this they assumed that the derived reddening of E_{B-V} $=0.^m16$ was correct, but that the distance modulus was $(m - M)_V$ $=24.^m4$, found by fitting the theoretical blue edge of the instability strip to the observed distribution of mean luminosities of the Cepheids. However, since then, not only has the BS63 photometry been reappraised, as discussed above, but further studies of supernova remnants and HII regions in M31, have shown an abundance gradient with galactic radius (Blair *et al.* 1981, 1982). FM90 argue that this, more recent evidence, implies a lower metallicity for this part of M31 of only $Z = 0.3Z_\odot \sim 0.005$, although they attach an uncertainty, due to dispersion of the metallicity-radius relation, of $\pm 0.3Z_\odot$. In passing, we note there is an encouraging consistency in the metallicity estimate by FM90, based on Blair *et al.* , for field III, which they give approximately solar abundance, with an independent estimate by Richer and Crabtree (1985) based on the ratio of carbon stars to M super-giants.

Using this information, FM90 attempted to test the predicted theoretical dependence of the Cepheid period luminosity relations on metallicity (Stothers, 1988). This dependence is mainly in account of the effects of line-blanketing on the colours, particularly in the B band. The effect of metallicity on the stellar evolution, will be to change the demography of the observed population of Cepheids within the instability strip (Becker *et al.* 1977). From their new (as yet unpublished) photometry, FM90 derived distance moduli for Cepheids in Baade's fields I, III and IV. The lack of apparent dependence of derived modulus with metallicity (fields I and III are closer to the centre of

M31 and have higher abundances) leads them to claim a contradiction with the models, and that, therefore, metallicity corrections are not required when using Cepheids as distance indicators.

This result has come under serious criticism by Feast (1991). He highlights various anomalies in their analysis, for example, the transforms used to go from theory to broad band R and I magnitudes were those for the Johnson system, not that of Kron-Cousins as appropriate to their data. However, most critical seems to be the use by FM90 of a predictive equation for the situation in which the reddening has been calculated from the $B-V$ colours of the Cepheids themselves. This amplifies the effect of the metallicity on the derived distance modulus, because a relatively small change in the reddening produces a roughly three times larger change in the implied extinction. Thus, taking the example of the low metallicity field IV, the effect is predicted to give rise to the appearance of *negative* reddening, which would lead to a conclusion of a much greater true distance modulus if translated into a negative extinction. However, this is not how FM90 actually calculate the extinction, which is inferred instead from fitting to the apparent moduli from all four ($BVRI$) of their photometric bands. Since the main effect of metallicity variations is on the level of line blanketing in the B band, this method would not be expected to be nearly so sensitive to metallicity.

FM90 also claim that restricting their data to just the B and V, shows a similar contradiction with theory. However, in this case the test fails again since even small errors in the photometry will be amplified, in the same way as the reddening, resulting in very large errors in the derived distance modulus. A better approach is to use the extinction derived by methods other than the $B-V$ colours of the Cepheids, and then test for the effect of metallicity directly. Feast (1991) plots this graph, and shows a better agreement with theory, although the scatter is still large.

3.5.3 Fitting Theoretical Sequences

In order to arrive at a picture of the star formation history of this region we first split the data according to those stars which appear to be in OB associations and those in the field. Á priori, we would expect the cluster stars to be younger with possibly higher amounts of dust and heavy

metals. These data are discussed in §3.5.6.

Here we turn our attention to the remaining field stars, which are plotted in figure 3.9, with the cluster stars removed. We notice that there is now appears a distinct gap of around 1^m between the few brightest blue stars and the rest of the main-sequence.

As a starting point we have taken the apparent Cepheid distance modulus derived by MS91 for the V band of μ_{AV} =24.^{m}7, Which, we shall see, is the value obtained below (§3.5.7) from the Cepheid distance, although this is not critical. We use this to overlay the theoretical isochrones of Bertelli *et al.* (1990), for a 90Myr, 200Myr and 500Myr population. These employ sophisticated evolution models, which include account of convective overshoot and mass-loss, and which have proved successful in reproducing the observed loci of clusters in the CM diagram. These particular set of isochrones are for abundances: $X = 0.75$, $Y = 0.246$ and $Z = 0.004$, which is reasonably consistent with the available data. We should note that, after leaving the main sequence, the evolution across the diagram is rapid, with the more stable periods being at the turning points on the loci. Thus, the true turn-off the main sequence is, actually, lower than the apparent turn over of the isochrones.

Our purpose is to show that the young field population is plausibly consistent with a burst of star formation, at about 100 to 150 Myrs in this model, with possible additional older components. Furthermore, the bright blue stars are now explained as being evolved, core helium-burning giants, from this most recent burst. This, in fact, is additional confirmation of the low metallicity, since higher metallicity tends to move the core helium-burning sequence redward. We hesitate to be more specific about the ages or masses of these stars, since they depend very much on the degree of convective overshoot built into the models. Roughly speaking, in more traditional models, which do not account for convective overshoot, a star at a given point in the diagram will be half the age and hence more massive (eg. Maeder and Mermilliod 1991). A recent argument in favour of reducing the degree of convective overshoot has been put by Stothers and Chin (1991), who claim that anomalies in traditional models can now be explained by new opacity measurements.

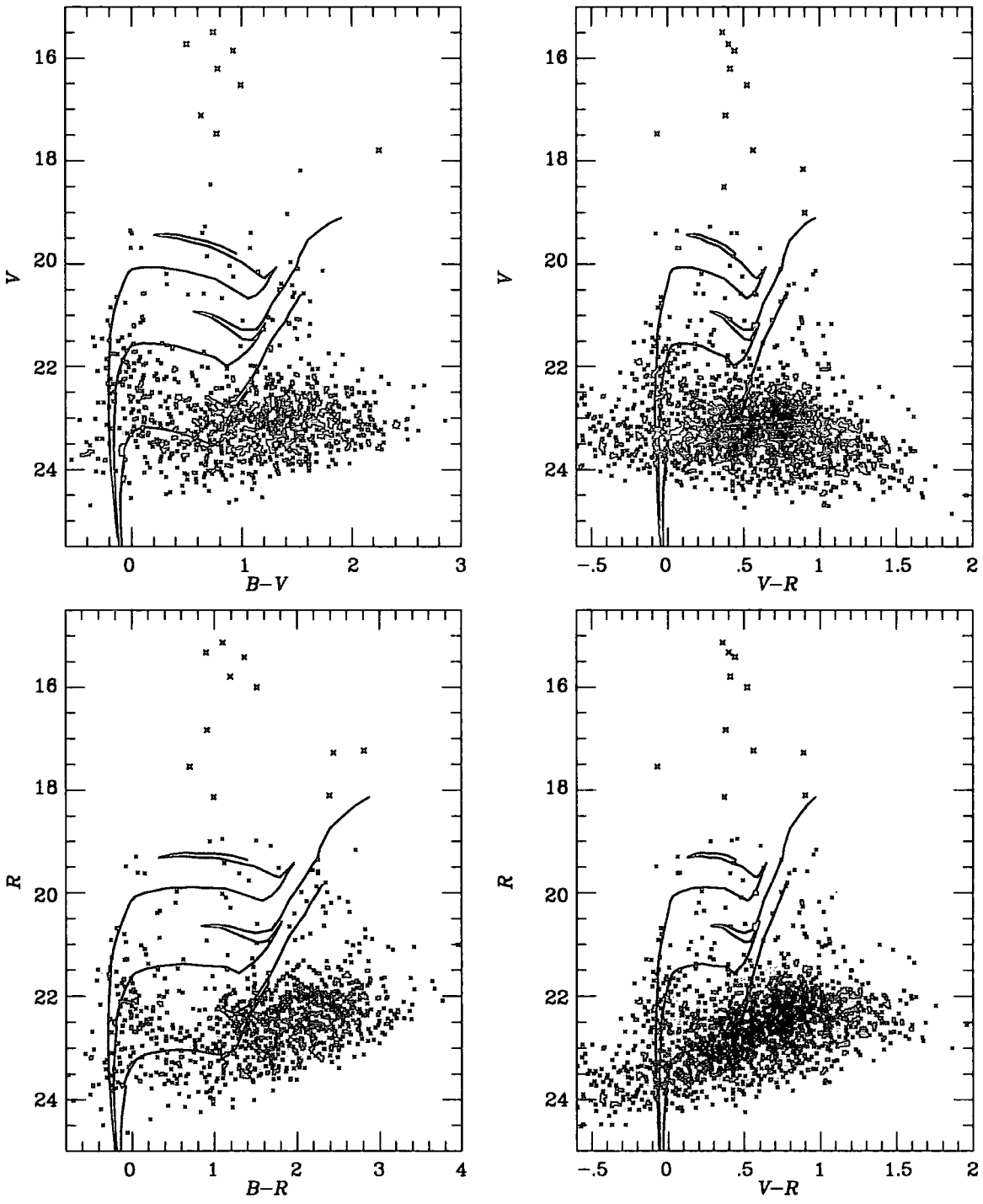

Figure 3.9: M31 colour-magnitude diagrams with the cluster stars removed. The theoretical isochrones of Bertelli *et al.* (1990) are overlaid for ages of 90,200 and 500 Myrs. The model is for $Z = 0.004$ and includes convective overshoot.

3.5.4 Luminosity Function

The luminosity function for the blue ($B-V<0.4$) stars, taken from the (V,$B-V$) diagram, is shown in figure 3.10. This result is in good agreement with that of HLM88 with regard to the slope and normalisation of the raw counts, although we find a somewhat shallower slope after correcting for completeness. This is the outcome of the very large corrections applied by HLM88, due in part to their shallower images and worse seeing, but mainly to the fact that they are incorrectly calculated, in the manner described in section 2.6.

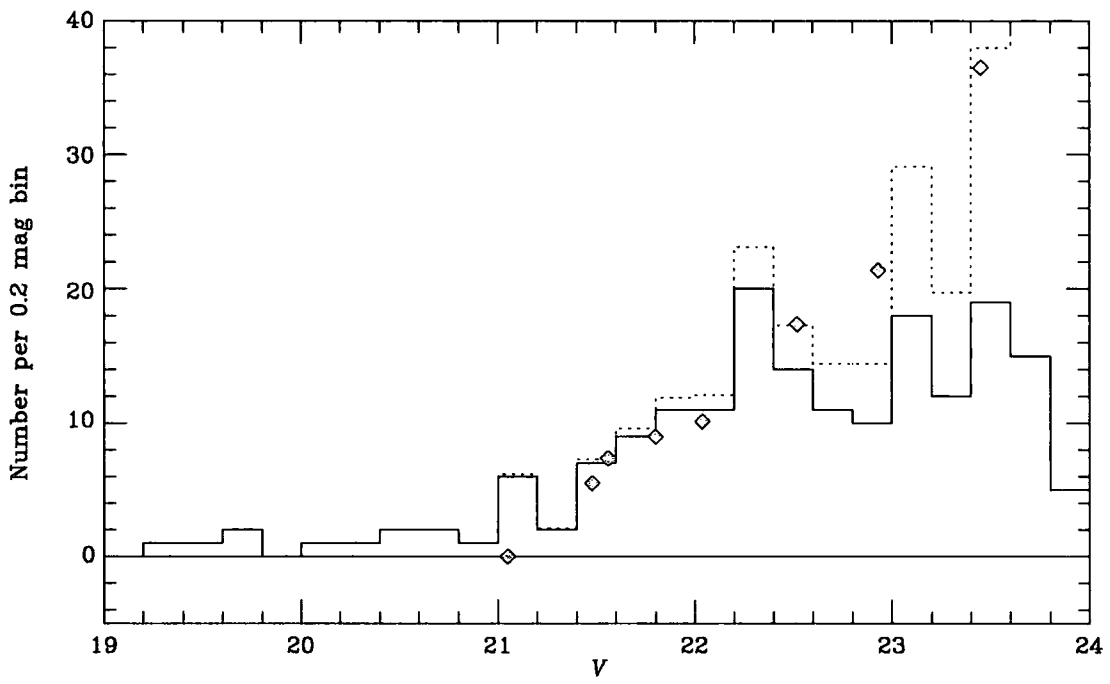

Figure 3.10: Luminosity histogram for the blue ($B-V<0.4$) stars from which the foreground component, derived from the control field, has been subtracted. The dotted line indicates the effect of applying the completeness corrections, which are calculated from simulations. The diamonds show the luminosity function from the theoretical models of Bertelli *et al.* (1990), for a 100Myr population.

Interestingly, again using the tables of Bertelli *et al.* (1990), we find surprisingly good agreement with the predicted luminosity function for a single age population of $100Myrs$. Here, their model uses $Z=0.004$, and assumes a Salpeter IMF with $\alpha=2.35$. However, given the error bars due to counting statistics, and the uncertainty introduced by the completeness correction, we prefer to

retain the conservative assumption that there could be a spread of ages older than 100Myrs.

3.5.5 Estimate of the Reddening

Clearly the almost vertical nature of the main-sequence at these absolute magnitudes, means that the reddening estimate is, to first order, insensitive to the uncertainty in the distance modulus. We are also helped by the use of three passbands rather than two in the reduction of the influence of photometric errors.

We have already discussed how age and metallicity will affect the position and spread of the sequence. Two additional factors which might effect the fit, due to their influence on the MS, are differential reddening and photometric errors. Now, field IV was chosen in the hope that differential reddening would be small and given the lack of dust clouds or sites of very recent star formation, we still expect this to be the case, at least for the young component. The effect of photometric errors, on the other hand, has already been seen, and makes identifying the MS impossible at the faint end. At intermediate magnitudes the MS is more clearly seen, but here there is some worry that blending will have some tendency to scatter stars preferentially redward. We suggest that, in this range, at least the *ridge* line of the MS should be well defined. In other words, that the modal position, if not the mean, should not be systematically shifted.

Our method, then, is to attempt to fit, by eye, a colour magnitude envelope corresponding to the small width due to a spread of ages, simultaneously to the three diagrams. This, once metallicity effects have been accounted for, will produce a single reddening estimate. The idea is to fit to the modal line (which can be fairly well identified from a histogram) of the sequence in the region where there are reasonable numbers of stars, but errors are still low. In practice this means $20.5 < V < 22.5$. We are aided in the fitting by also considering the $(B-V,V-R)$ colour-colour diagram for that range of stars, for which photometric errors will tend to scatter in the directions perpendicular to the reddening vector, and hence offer good discrimination of the effect in which we are interested.

There are several methods one could imagine for deriving an envelope for the main-sequence.

Here we have chosen to use the composite cluster loci of Mermilliod (1981). By plotting a range of these, covering the maximum range of ages present in the data, we can proceed to draw an envelope. The R band magnitudes are extrapolated from the tables of Johnson (1966) using the transforms of Fernie (1983). In order to correct these from solar metallicity to that which we are assuming for field IV, we move the envelopes blueward by $\Delta(B-V) = 0.03$ and $\Delta(V-R) = 0.01$, which come from figures given in Green *et al.* (1987).

The results of this procedure are shown in figure 3.11. The sequences have been moved to $\mu_{AV} = 24.7$, which is, again, not critical, and $E_{B-V} = 0.09$, which we consider to be the best compromise fit. The reddenings derived from each colour are slightly inconsistent, in the sense that the reddening appears greater in the $B-V$ colour and less in the $V-R$ colour. However, we feel that this discrepancy is within the errors of the photometric zero-points ($\sim 0.^m02$), and that we can say with some confidence that $E_{B-V} = 0.09 \pm 0.05$, even allowing for the remaining uncertainty in the metallicity.

3.5.6 OB Associations

In our field there are two prominent clusters or associations of bright blue stars. One of these, denoted A, is very tight and contains one very bright star which is classed by BS63 as a semiregular variable. Cluster B, is looser, although it has more members, but no particularly striking individual star. There is also a lesser cluster, which we have denoted C.

Figures 3.12, 3.13 and 3.14 show the colour magnitude diagrams for these clusters, where, once again we have overlaid the theoretical loci for the 90, 200 and 500Myr populations. The small numbers of stars, and the field contamination, mean that it is difficult to provide unambiguous interpretations for these plots. However, the bright evolved star in A is indicative of a younger age for that cluster, in which case, the two bright blue stars would be turning off the main sequence. Although, for our adopted composition, younger isochrones are not given, from comparison with the tables of other abundances, we deduce an age in the region of 40-60Myrs, for such a turn-off point, in these models. Similarly, for cluster B, the two bright blue stars are brighter than

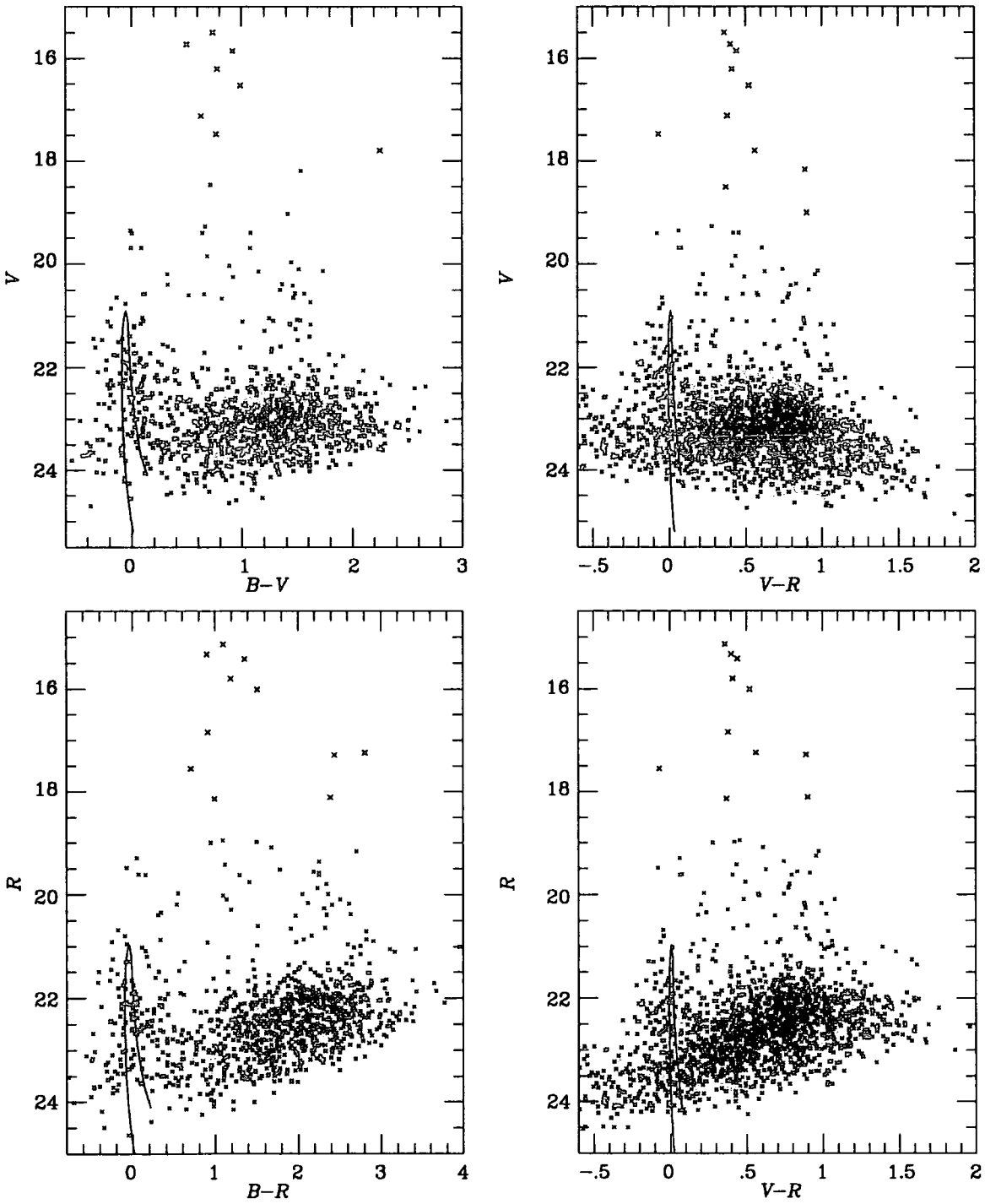

Figure 3.11: Colour-magnitude with the main sequences, with the observed loci for several open clusters superimposed (Mermilliod 1981). The loci have been shifted to $\mu_{AV} = 24.7$, $E_{B-V} = 0.09$ and corrected for the metallicity effect.

the turnoff point for a 100Myr population, which also indicates a younger age, in the region of 60-80Myrs.

3.5.7 Revised Cepheid Moduli

We are now in a position to make a new estimate of the Cepheid distance to M31, based on the revised magnitude scale, the estimate of the extinction and the evidence for low metallicity. Following MS91 we adopt a simple linear offset to account for the scale errors in the BS63 photometry. Unlike MS91, we will correct the B as well as the V magnitudes. The calibration lines (figure 3.15) represent a least squares fit to the points, but are constrained to go through $B = 21.0$ and $V = 18.5$, which can be seen in MS91 to be where the BS63 scale is effectively okay.

We correct the mean magnitudes of all the Cepheids brighter than $B = 22.3$ and $V = 21.8$, with the exception of numbers 11 and 27 (from BS63), which have been identified by Iben and Tuggle (1975) as probable overtone pulsators. This leaves thirteen stars in each band, and the resultant apparent moduli, from fitting the relations given in appendix E, are $\mu_{AB} = 24.74$ and $\mu_{AV} = 24.71$ (see figure 3.16). As expected, the greater dispersion is in the B band. To these we add the metallicity corrections of Stothers (1988), which are discussed above, to get:

$$\mu_{AB} = 24.83 \pm 0.08$$

$$\mu_{AV} = 24.70 \pm 0.05$$

Where the error bars are those calculated from the P-L relation fits. Note that we do not reconsider the P-L-C relation due to the uncertainty in its fundamental coefficients and also potential problems accounting for metallicity effects, outlined by Feast (1991).

Finally, we apply our extinction estimates ($A_B = 0.36$, $A_V = 0.28$) to each of these moduli, and perform a weighted average of them to find:

$$\mu_0 = 24.44 \pm 0.16$$

Here the error is still dominated by the extinction uncertainty.

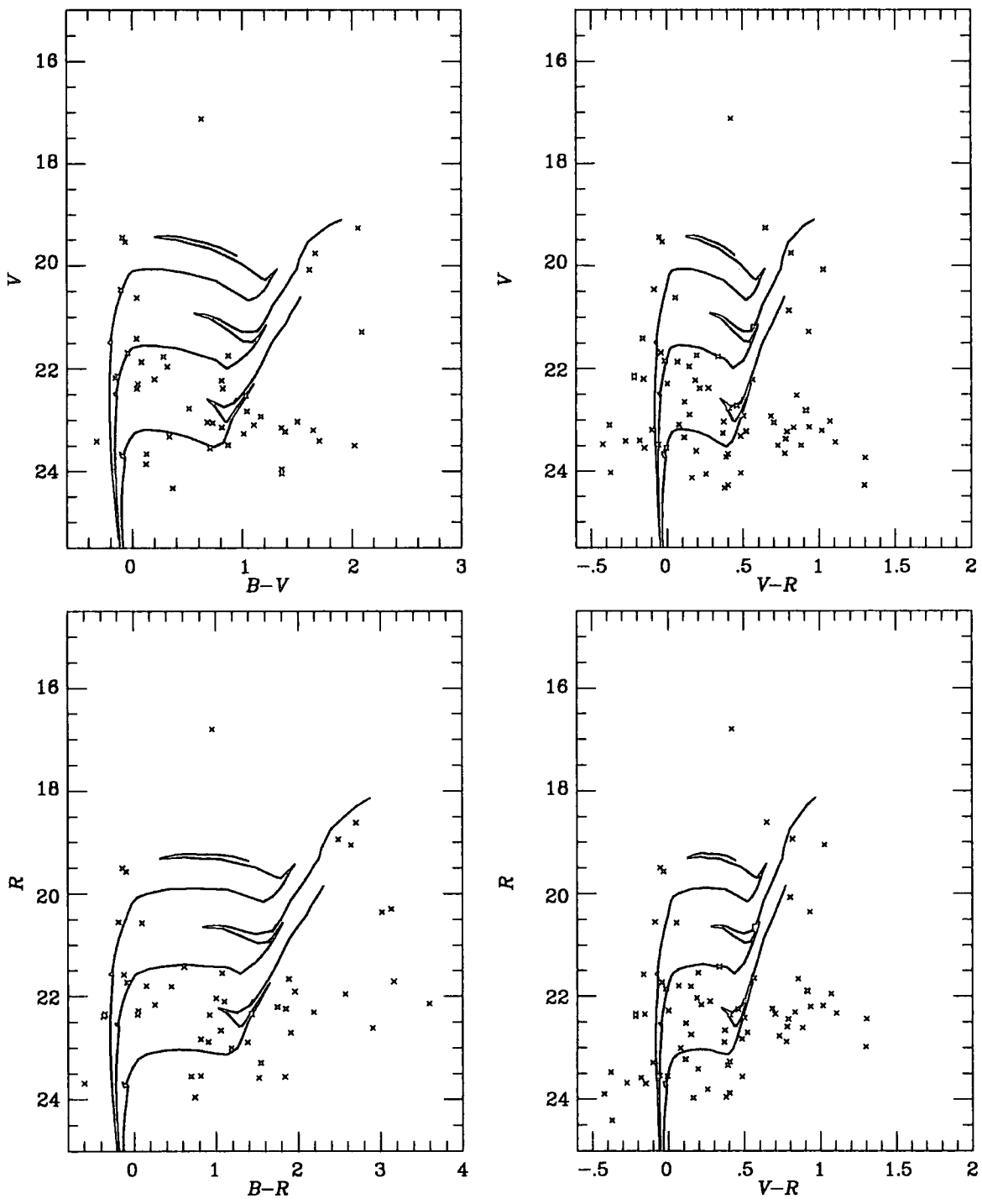

Figure 3.12: Colour-magnitude diagram for stars in cluster A. The theoretical loci are as for figure 3.9.

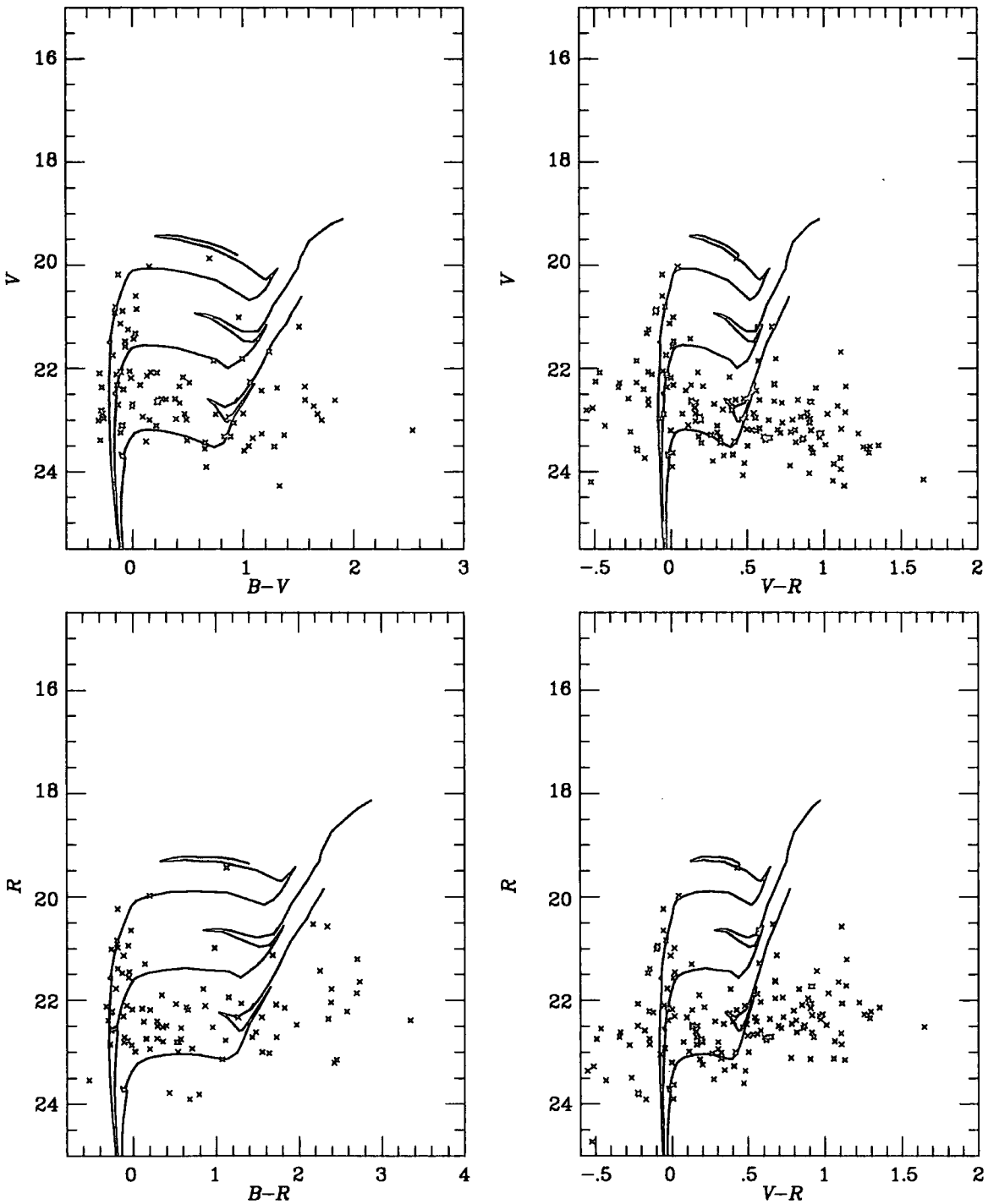

Figure 3.13: Colour-magnitude diagram for stars in cluster B. The theoretical loci are as for figure 3.9.

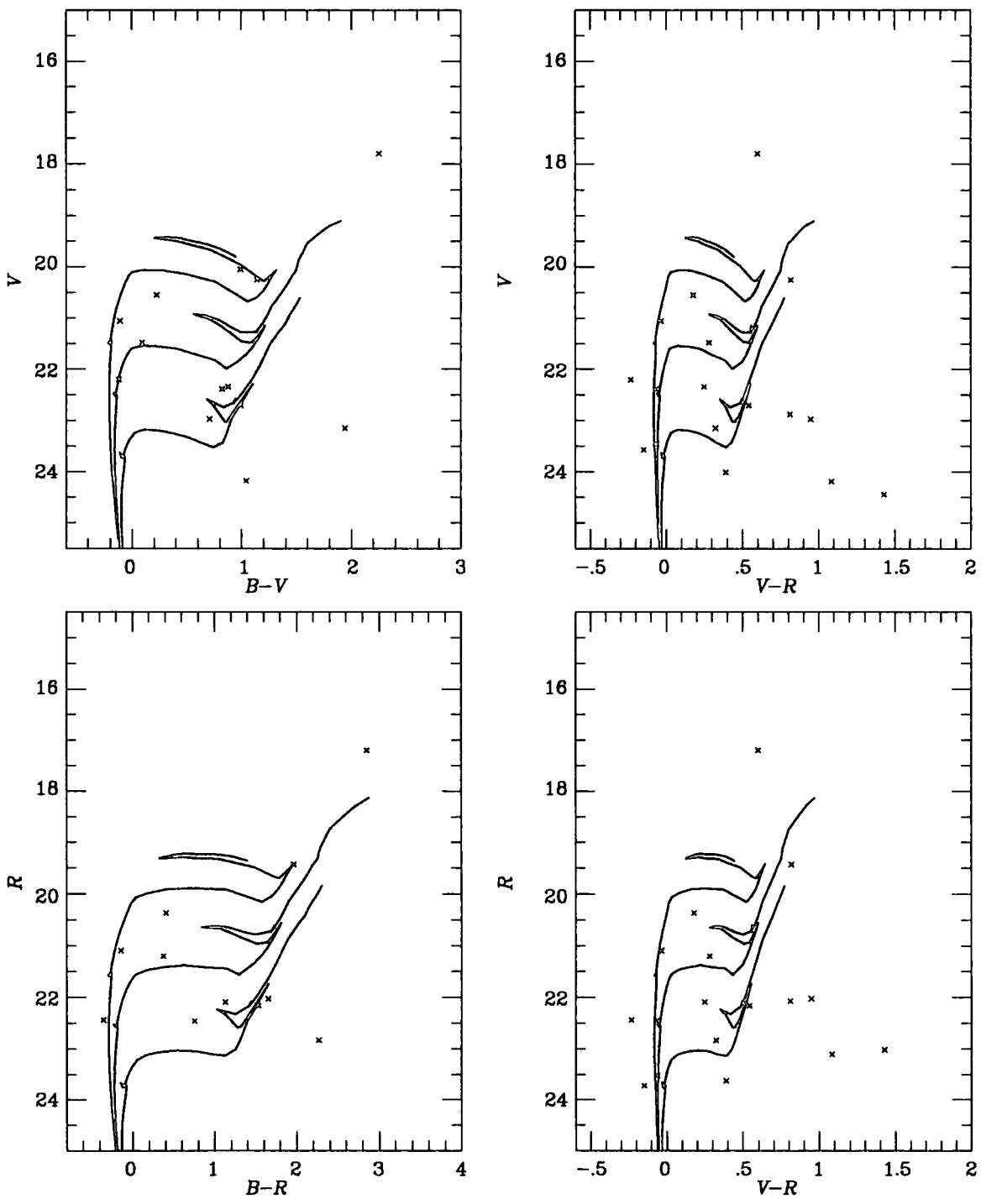

Figure 3.14: Colour-magnitude diagram for stars in cluster C. The theoretical loci are as for figure 3.9.

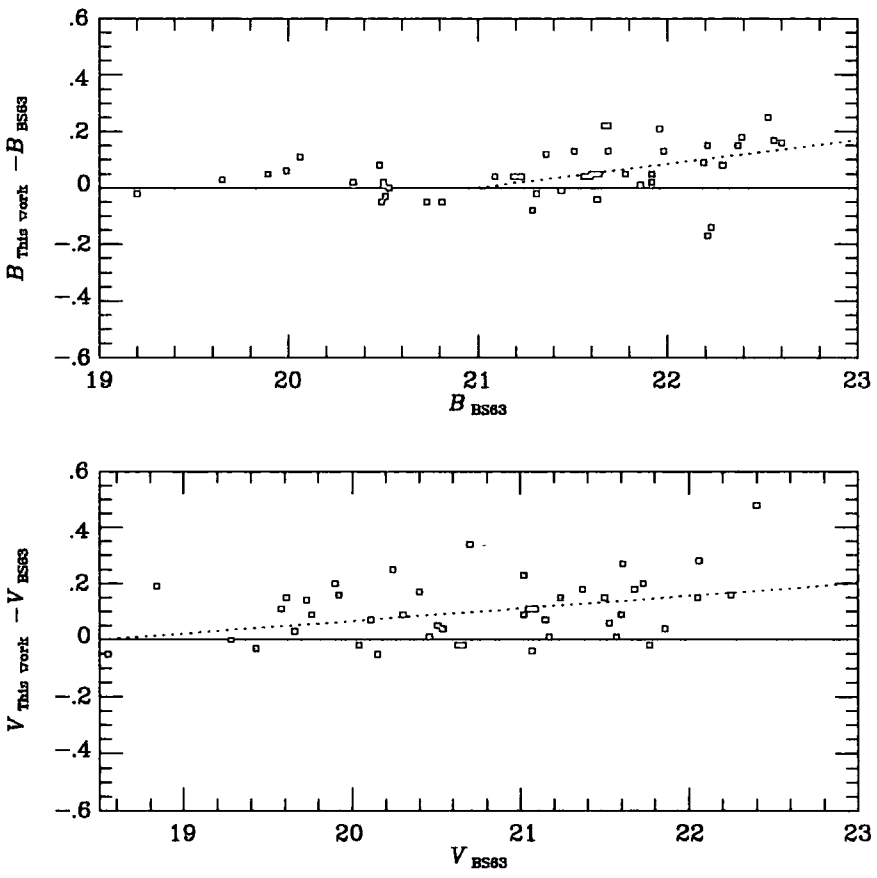

Figure 3.15: The correction lines which are applied to the BS63 photometry to correct for the scale error.

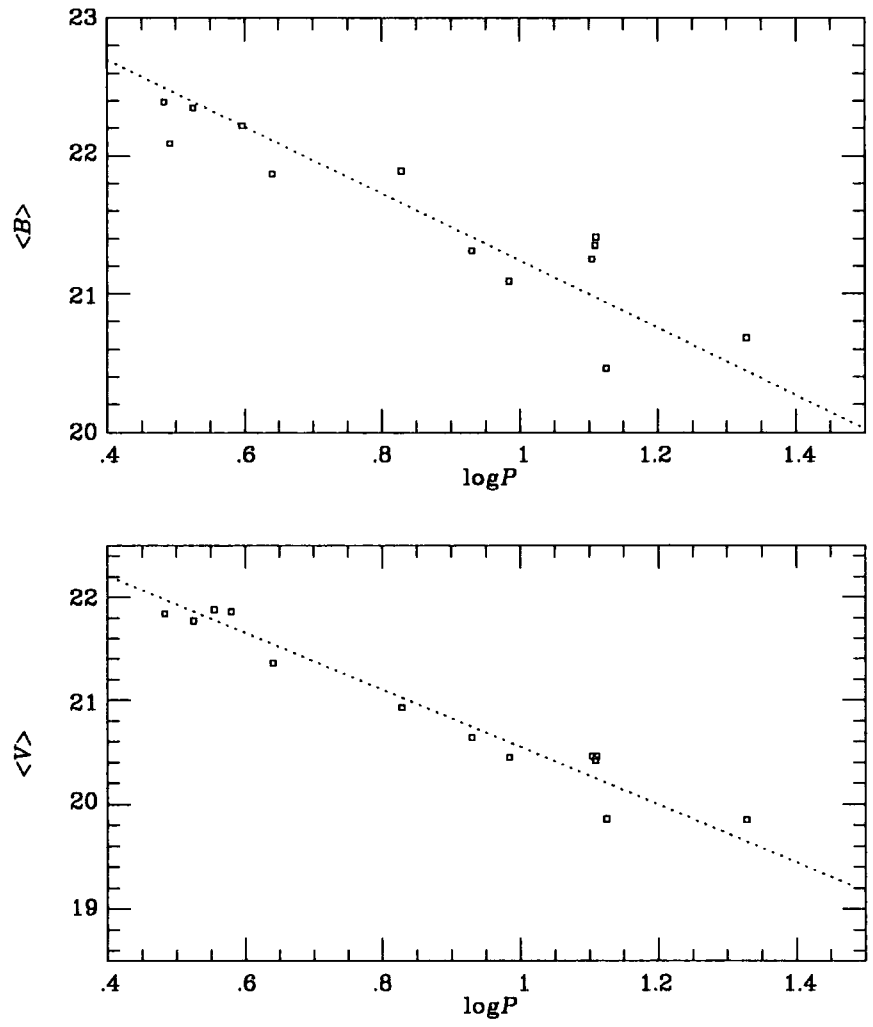

Figure 3.16: The P-L relation fits to the corrected B and V band Cepheid magnitudes.

3.6 The Old Population

3.6.1 The Locus of the Red-Giant Branch

The red giants form the largest population found in our CM diagram. As with the main sequence, the position and spread of this branch would be expected to depend on age and metallicity, in addition to the effects of errors.

This situation is complicated by several factors which will tend to broaden the width of this branch. Firstly, there is contamination of the main red-giant branch, which we assume to be predominantly an old disk population, by young evolved stars, foreground and background objects and also halo giants. Secondly, there will will be a greater spread due to differential reddening due to the much larger scale height for older stars. Thirdly, we see from the error analysis, that, because they are faint in the B band, the red-giants will be more affected by measurement errors than blue giants of a similar V band magnitude.

A comparison of the red-giant branch loci of several old clusters (From Sandage, 1986) is shown in figure 3.17. From this we deduce a value for the metallicity of $[Fe/H] \sim -1.6 \pm 0.2$, which is similar to the mean metallicity of the sub-dwarf population in the solar neighbourhood (Laird *et al.* , 1988).

3.6.2 Luminosity Function

The V band and R band luminosity functions for the red ($V - R > 0.^m3$) stars are shown in figure 3.18. Only the $V - R$ diagrams were used since they had significantly more red stars. The solid line is the raw counts with just the control field (smoothed) subtracted. The dotted line shows the effect of completeness corrections, up to the point where they become greater than a factor of two. Beyond this point, apart from the intrinsic errors becoming very large, there are likely to be problems with spurious stars entering the count, artificially increasing it.

Both diagrams have a similar shape, showing a slow rise due to the extended red plume of

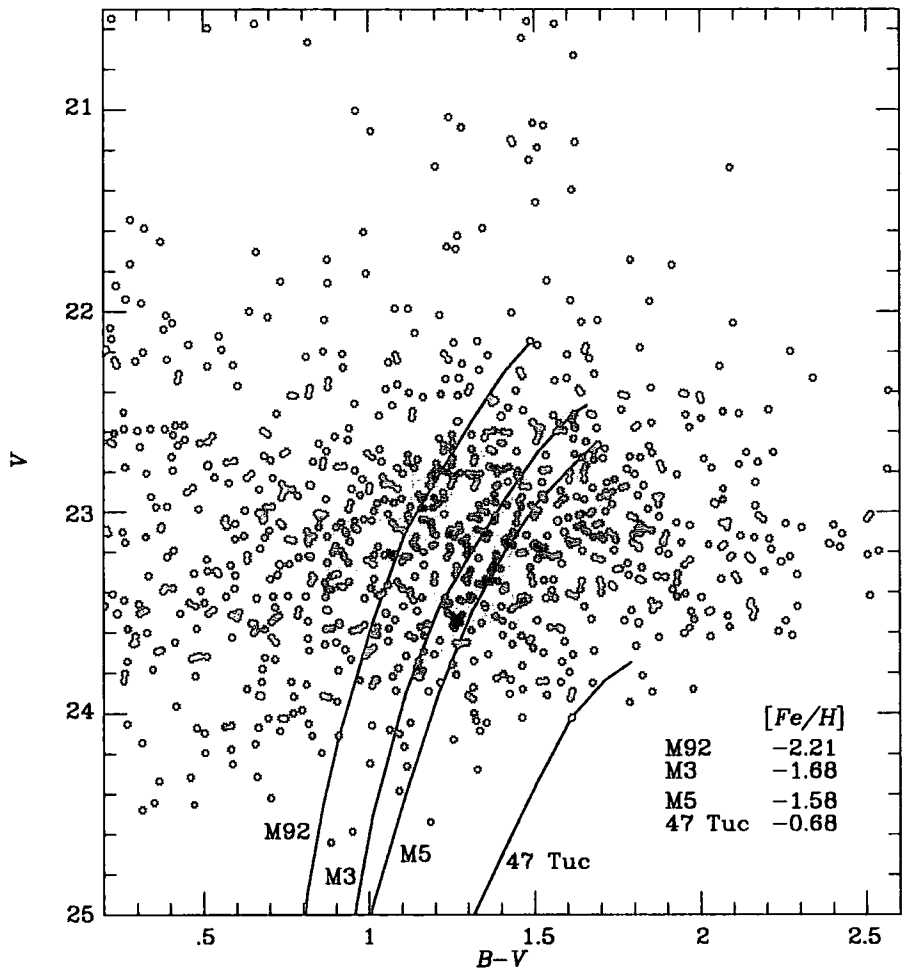

Figure 3.17: The red-giant branch with the loci of several galactic globular clusters are overlaid. ($\mu_{AV} = 24.7$ and $E_{B-V} = 0.09$ have been assumed).

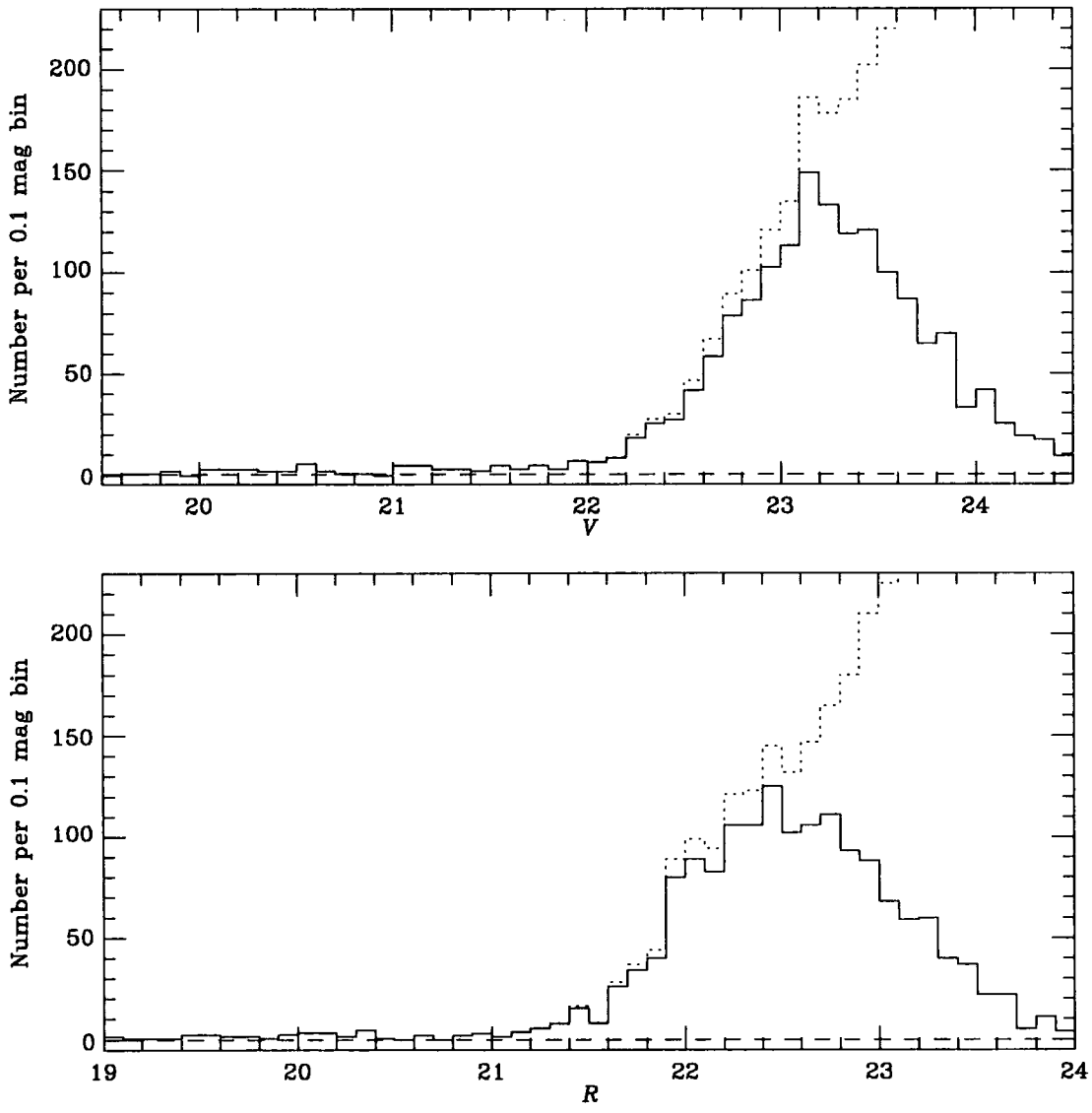

Figure 3.18: Luminosity histograms of red ($V-R > 0.^m3$) stars in the $V-R$ diagrams. The top plot is for the V band and the bottom for the R band. The dotted line shows the effect of completeness corrections.

young evolved stars, followed by a step and then steady rise as the old red-giant population comes in. The V plot is sharper than the R since the locus of the branch in the V diagram will be flatter. Towards the faint end, the slope becomes fairly constant, which is similar to the behavior seen by Pritchet and van den Bergh (1988) for M31 halo stars.

3.6.3 Distance to M31 from the Position of the Tip of the Red Giant Branch

The tip of the red giant branch occurs because of the helium core flash after which stars evolve rapidly away from the RGB and onto the horizontal branch. Its position in the HR diagram, for low mass stars, is at a constant magnitude largely independent of the actual mass of the star. For this reason it has been used as a distance indicator.

The procedure for estimating the apparent magnitude of the tip of the RGB is to take the luminosity function in the selected passband and subtract from it a contribution from foreground objects, derived from the control field. As we have seen, the situation is complicated when studying disk systems by the existence of a younger population of evolved stars (AGB). However, we can usefully gain a relative distance modulus by direct comparison with a similar population of stars in the LMC. Reid, Mould and Thompson (1987, hereafter RMT87) made a photographic study of the Shapley Constellation III area in the LMC, obtaining V and I magnitudes of $\sim$ 12000 stars, to a limiting I magnitude of 18^m. Morphologically this field is similar to our own, with a admixture of young evolved stars forming a plume brighter than the old red giant branch. The value they found for the metallicity of $[Fe/H] \sim -1.1 \pm 0.2$, somewhat higher than our value for the M31 old population.

They identified a step in the luminosity function of red stars, which occurred at $I = 14.^m6$ and $V = 16.^m3$, as the tip of the red giant branch. From this they deduce an LMC distance modulus of $\mu_0 = 18.42 \pm 0.15$, using the globular cluster calibration of Frogel *et al.* (1983). Whilst our number statistics are rather poor, we notice a similar feature appears in our luminosity function, occurring at $V = 22.^m2$. This would imply a difference in V band distance modulus between M31

and the LMC of $\Delta\mu_{AV}(M31 - LMC) \sim 5.^m9$.

The question of the appropriate value for the extinction to be applied to the M31 data is not straight forward. The value for the reddening based on the position of the main sequence, which is derived above (§3.5.5), may not be applicable to the older stars observed on the giant branch. Whether some of these stars are actually in the halo, or if they are largely part of the old disk population, they will certainly be spread over a much larger scale height than the young disk stars. Furthermore, since we are looking at the brightest tip of the giant branch, we are preferentially seeing the brighter, nearer stars, for which the reddening is at a minimum. This suggests that we should, in fact, adopt only the foreground reddening in this case. This we take to be $A_V = 0.^m2$, and also using the RMT87 value for the LMC extinction of $A_V = 0.15$, together with our adopted LMC modulus of $\mu_0 = 18.5$, to obtain $\mu_0 = 24.^m35$. Finally we correct for the difference in metallicity between the two populations (from Bertelli *et al.* 1990):

$$\mu_0 = 24.6 \pm 0.35$$

where the error bar is estimated to account for the uncertainty in identifying the position of the red-giant branch tip, recalling, in particular, the worry about contamination by young evolved stars, and also the metallicity correction.

3.7 Conclusions

We have presented our BVR photometry and colour magnitude diagrams of $\sim$ 2300 resolved stars from deep INT CCD images in Baade's Field IV in M31. The agreement with previous photometry of this field is fairly good, although we find a small scale offset in the B band when compared to the interactive aperture photometry of Metcalfe and Shanks (1991), using the same data. Better agreement is found with the profile fitting photometry of Hodge *et al.* (1988)

Several stellar populations are identified, an old disk component, a young to intermediate age field component and OB association stars, which are probably younger than the field. By considering theoretical isochrones we suggest that the young background field stars are $\sim$100Myrs

and older (dependent on the model), and agree with the previous evidence for low metallicity in this region. Using these values for the metallicity and age spread, we fit an envelope to the main sequence to estimate the reddening. Although the results from the different colours disagree slightly, this can be explained by the zero-point errors of the photometry, and we conclude $E_{B-V} = 0.09 \pm 0.05$. This, we note, is consistent with there being a small amount of internal reddening, in addition to the best available estimates for the foreground reddening ($E_{B-V} = 0.07 \pm 0.02$).

Recalibrating the original Baade and Swope (1963) photometry for the Cepheids, we arrive at new apparent moduli, which we correct for the effects of metallicity and extinction. This gives (assuming $\mu_0(\mathrm{LMC}) = 18.50$):

$$\mu_0 = 24.44 \pm 0.16$$

Here the error is largely from the uncertainty in the extinction, which in turn suffers from the photometry zero-point errors. Clearly, tieing down these zero-points more precisely would considerably reduce the final error. We should, however, be aware of two objective problems which could still systematically bias this result. Firstly, there is the question of the number of Cepheids which are components of binary systems. This has been put at $\sim 25\%$ of all Cepheids by Madore (1977). Secondly, it has recently been proposed that a significant number, perhaps the majority, of short period Cepheids (< 6 days) are in fact pulsating primarily in the first overtone mode (Böhm-Vitense 1988). For example, from a study by Mateo *et al.* (1990) of three short period Cepheids in the LMC cluster NGC2157, two were classed as overtone pulsators. Both of these effects would tend to introduce anomalously bright Cepheids into the sample, particularly at the faint end, and hence bring the distance modulus down. So, although we have already dropped the two most likely problem stars from the sample, we might still worry about the remaining short period variables. Since, even now, we are limited to only 13 Cepheids in each band, this does suggest that a larger sample might be required before such effects can be confidently accounted for.

Finally, we have discussed the old disk population which make up the majority of the red stars in our diagram. By comparison with galactic globular clusters we estimate a metallicity for these stars of $[Fe/H] = 1.6 \pm 0.2$. This allows us to form another, less precise, estimate of the M31

modulus from comparing the tip of the red-giant branch with that in the LMC (Reid *et al.* 1987):

$$\mu_0 = 24.6 \pm 0.35$$

Chapter 4

Resolved Stars in M33

4.1 Introduction

Messier 33, or NGC598, is an Scd spiral galaxy situated in the constellation of Triangulum, inclined to our line of sight at $\sim 39°$. It is a member of the local group of galaxies, but is smaller and dimmer than M31 and the Milky Way. Van den Bergh (1991) cites two authors (Duncan 1922, and Wolf 1923) who observed variable stars in M33. Apparently neither appreciated the full import of these discoveries and it was left to Hubble (1926) to draw the conclusion that M33 was thus proven to be a separate stellar system beyond our own galaxy.

The images of M33 were obtained for the same program of recalibration of photographic Cepheid sequences as those of M31 (Metcalfe and Shanks 1991, hereafter MS91). They concluded that $\mu_0(M33) = 24.73 \pm 0.15$, and again, as with M31, found little reddening (here, and subsequently, references to M33 distance moduli are recalculated according to a consistent LMC modulus of $\mu_0 = 18.50$). This followed similar projects by Sandage (1983), Cristian and Schommer (1987 and hereafter CS87), who found $\mu_0(M33) = 24.05 \pm 0.15$ with $A_B = 0.65$, and Sandage (1988) who found $\mu_0(M33) = 24.20 \pm 0.15$ using $A_B = 0.6$. Since then, new multiband CCD photometry for many of the individual Cepheids has been published by Freedman, Wilson and Madore (1991 and

hereafter FWM91). Their results are in good agreement with MS91 regarding the true distance modulus $\mu_0(M33) = 24.64 \pm 0.09$, although, in this case, reddening of $E_{B-V} = 0.10 \pm 0.09$ is deduced from the Cepheids themselves. Their Cepheids are also taken from Hubble's original sample, with roughly half of the variables which have full photometry being in field 9.

Although less thoroughly surveyed than M31, there have been several other recent studies of the resolved stellar content of M33. Humphreys (1980) presents spectroscopic and photometric data for 22 supergiants in M33. Humphreys, Massey and Freedman (1990) obtained spectra and photometry for a further eight early-type supergiants. Mould and Kristian (1986) observed a halo field at an estimated 7kpc from the centre of M33. By fitting to the tip of the red-giant branch they found a low value of the metallicity of $[Fe/H] \sim -2.2$ and a distance of $\mu_0 = 24.8 \pm 0.3$. Wilson, Freedman and Madore (1990, and hereafter WFM90) presented photometry for resolved stars in four CCD fields in M33 to a depth of $V = 21^m$. The Cepheid photometry of FWM91 is a subset of these results.

Once again, the range of values from the literature is fairly broad, particularly with regard to the important factor of extinction. As with M31, our approach is to perform careful profile fitting photometry of resolved stars, with the main aim of estimating the reddening, and hence the extinction, from the colour excess of the locus of the main sequence. In this chapter we present the full CM diagram for the resolved stars in our field, and compare the photometry to previous studies. We also consider the available evidence of the amount of extinction due to dust in M33, and go on to use the position of the main sequence to estimate the reddening in our field as a function of location in the field. Finally the consequences for the Cepheid distance of M33 are discussed.

4.2 Data

The chosen field was field 9 of Humphreys and Sandage (1980), which contains sequences around eight of Hubble's (1926) original Cepheids. A plate showing the CCD image is shown in This field differs from field IV in M31 in that it is much closer to the nucleus of the galaxy, at 4′.5, or only

around 1kpc. It is also a region of more active star formation, in part reflecting the quiescent nature of M31 in this respect (eg. van den Bergh 1964). This would lead us to expect a much higher proportion of young blue stars. The prominent dark nebulae testify to the dustiness of this region. It remains to be seen, however, what effect this has on the reddening to the field stars and Cepheids, both in the global level and differentially. The crowding problems are even more severe than in M31, in the sense that the density of objects of a given magnitude is much higher, and the background intensity within the field is steeply ramped and varying.

4.2.1 Observations

The observations were made at the INT, on a good photometric night, during the same run as those of M31. The field was centred at:

$$01^h30^m43^s, +30°20'50'', (B1950)$$

which corresponds roughly to galactic coordinate:

$$l^{II} = 134°, b^{II} = -31°$$

The observations are summarised in table 7.1.

PASSBAND	EXPOSURE (s)	CHIP	SEEING $''$	CALIBRATION mags/ADU
B	3 × 800	RCA	1.25	30.93
V	2 × 500	RCA	1.20	30.40

Table 4.1: Summary of INT observations of M33.

The seeing was more uniformly good for these images than for M31. This was fortunate, given the crowding problems in this field. On the minus side, the sampling of the point-spread-function,

Figure 4.1: V band image of the M33 field. East is at the top and North is on the right. The dimensions are $230'' \times 357''$. Note the large background gradient, due to the proximity to the centre of the galaxy.

with such large (0.″74) pixels for the RCA chip, is less than ideal.

4.2.2 Data Reduction

Once again, the basic processing of these images; that is bias subtraction, flat-fielding and calibration of the colour terms and zero-points; was done by Dr N. Metcalfe. In each case the images were shifted by integer pixels, to overlap, and then were stacked. The final frames covered an area of $22.8\square'$.

The standard DAOPHOT reduction procedure was carried out as described in chapter 2. Using FIND, almost 7000 candidate stars were identified on each frame, down to a 3.5σ detection limit. Aperture photometry was acquired for these stars, using PHOT. A list of around 20 stars on each frame were used as templates to find provisional PSFs.

The presence in this field of large amounts of varying nebulosity, both bright and dark, led us to further question the validity of the standard DAOPHOT method of sky determination. It was found that, apart from the overall gradient of the background, stars which were being grouped together for reduction had significantly varying sky values. In order to ensure better sky estimation, and particularly to prevent a single mean value of sky being taken for each group, as happens in the standard DAOPHOT algorithm, the variations were removed by subtracting a background sky frame. This sky frame is created by smoothing a preliminary version of the star-subtracted image, as is described in chapter 2. The sky frame is iterated towards the 'true' sky by successively subtracting the stars with better photometry. Subsequent processing was carried out on these, background subtracted, images.

A further difficulty encountered on these fields, particularly the V frame, was an almost complete lack of good stars with which to generate the PSF. This makes the likely errors in the wings of the PSF even more severe. The solution adopted was to construct a hybrid PSF which consisted of the empirical profile in the core, but with an appropriately grafted theoretical form for the wings. Once again, this procedure is also described in more detail in chapter 2.

Finally, unlike M31, the B and V star candidate lists were not merged initially, relying instead

on performing the cross-identification from the final lists of photometry. This was considered sufficient since the original images were very similar, in terms of seeing, depth and CCD format, so few extra candidates would have been found by merging. The criterion for being regarded as the same object was to have centroids within 1″ on the different frames. This process produced a grand total of 4454 stars for which photometry was obtained in both passbands. In most other respects the reduction followed the procedure outlined for the M31 fields.

Since the DAOPHOT routines produce magnitudes relative to an arbitrary zero-point, it was required, finally, to tie our photometry to the sample of the stars supplied by Dr. Metcalfe (see figures 4.3 and 4.4). This placed the magnitudes on the standard Johnson magnitude system, and also corrected them to total light. The fitting of the points was performed using a magnitude weighted, least squares algorithm, for stars brighter than $V = 19.^m8$ and $B = 20.^m1$.

One problem which was evident in the M33 data was that of a high proportion of 'discrete' objects being measurably non-pointlike. This manifested itself in high values for the SHARP parameter, produced by NSTAR, when compared to the same distribution obtained from a frame made up exclusively of crowded artificial stars (see chapter 2). This also resulted in rather poor subtraction of images in some cases. It is most likely due to the situation where effectively many of the stars we are looking at are in fact merged objects at our resolution. It would seem that there is very little that can be done about this problem, except simply to apply a SHARPness cut to the final photometry to exclude suspected 'extended' stars.

4.3 Results

A complete list of all the stars for which both B and V photometry was obtained, is given in appendix B.

4.3.1 The Colour-Magnitude Diagram

We first present the full colour magnitude diagram for all $\sim$ 4500 stars which were successfully photometered in both bands (figure 4.2). The filled points in the diagram represent those stars deemed to have the most secure photometry. These were chosen as having SHARP values in the range -0.1 to 0.1, on both frames, and being cross-identified to better than 0.″5. In fact, whilst this excludes some outliers, and many of the fainter stars there is little evidence for a tightening of the diagram. This might be expected since, if a star is effectively multiple in this field there is a good chance that the components will have similar colours. In any case, it suggests that other factors are dominant in spreading the locus of the main sequence.

It is immediately clear that, although we have produced photometry for a larger numbers of stars than in the M31 case, due to the crowding it has not been possible to go as deep. We also see that, as expected, the diagram is dominated by blue stars. Indeed, a high proportion of the redder stars which are found at the bright end are likely to be foreground contamination.

In order to appreciate the numerical distribution of stars we also show the same data in tabulated form in table 7.2.

4.3.2 Comparison of Photometry

In figure 4.3 and figure 4.4 we plot the magnitudes obtained here against those obtained by other authors for stars which we have in common. The first comparison is with the results obtained by MS91 from interactive aperture photometry of the same images. The scatter seen here gives a good impression of the size of the random errors which are simply due to the different measurement techniques. The zero-point is the same in both bands, since it was defined so as to ensure agreement at the bright end. Fainter than these magnitudes a scale dependent offset appears, particularly evident in the V data, but also in the B. This is most likely due to the different methods of sky determination, as discussed in chapter 2, although it should also be said that identification of some of the faintest stars, from Sandage's plates, was difficult and might have caused some of the discrepancies.

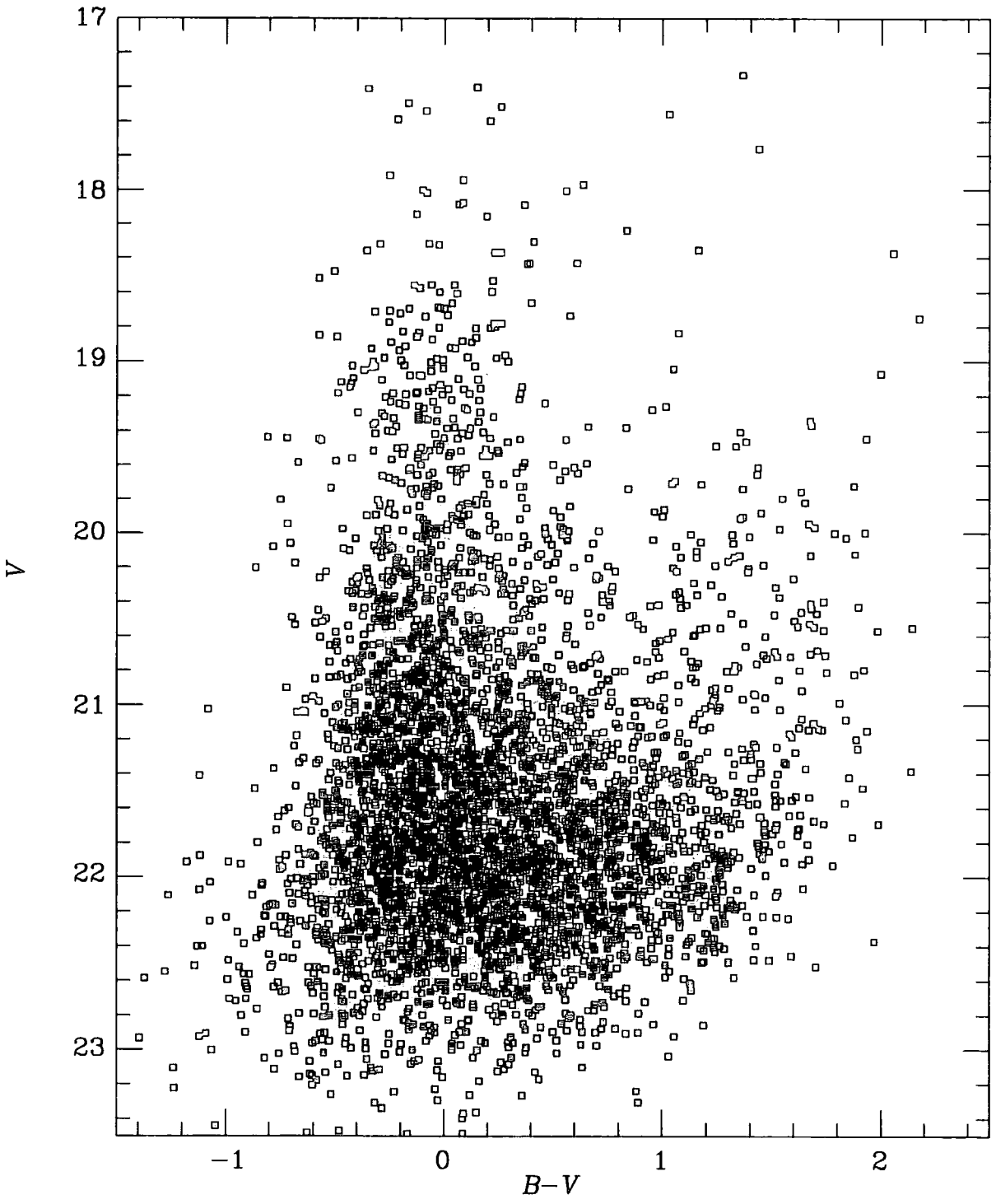

Figure 4.2: Colour magnitude diagram for all $\sim$ 4500 stars in M33 field. The filled symbols represent stars which are particularly secure (see text).

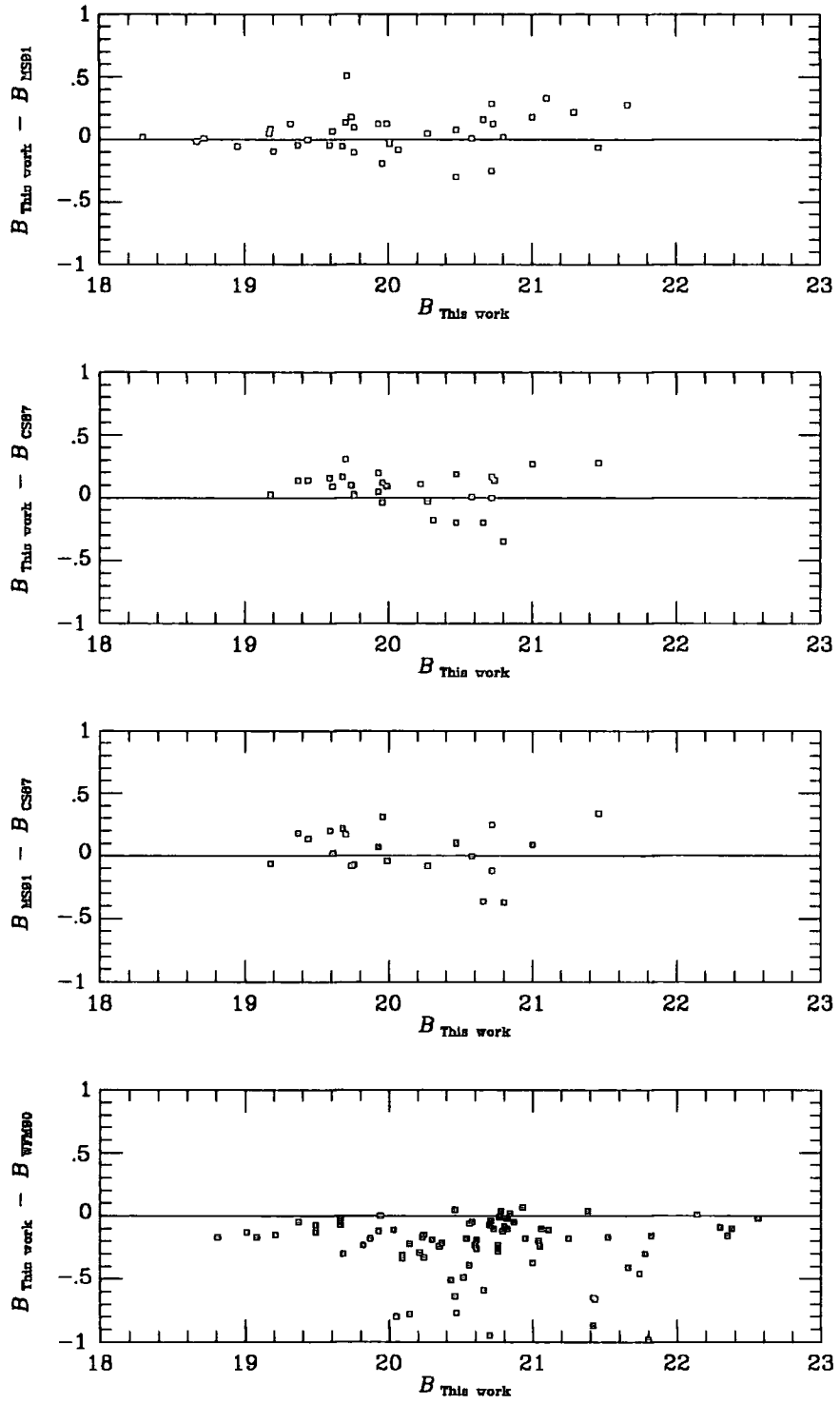

Figure 4.3: These plots show the comparisons between the different sets of CCD photometry, for the B band.

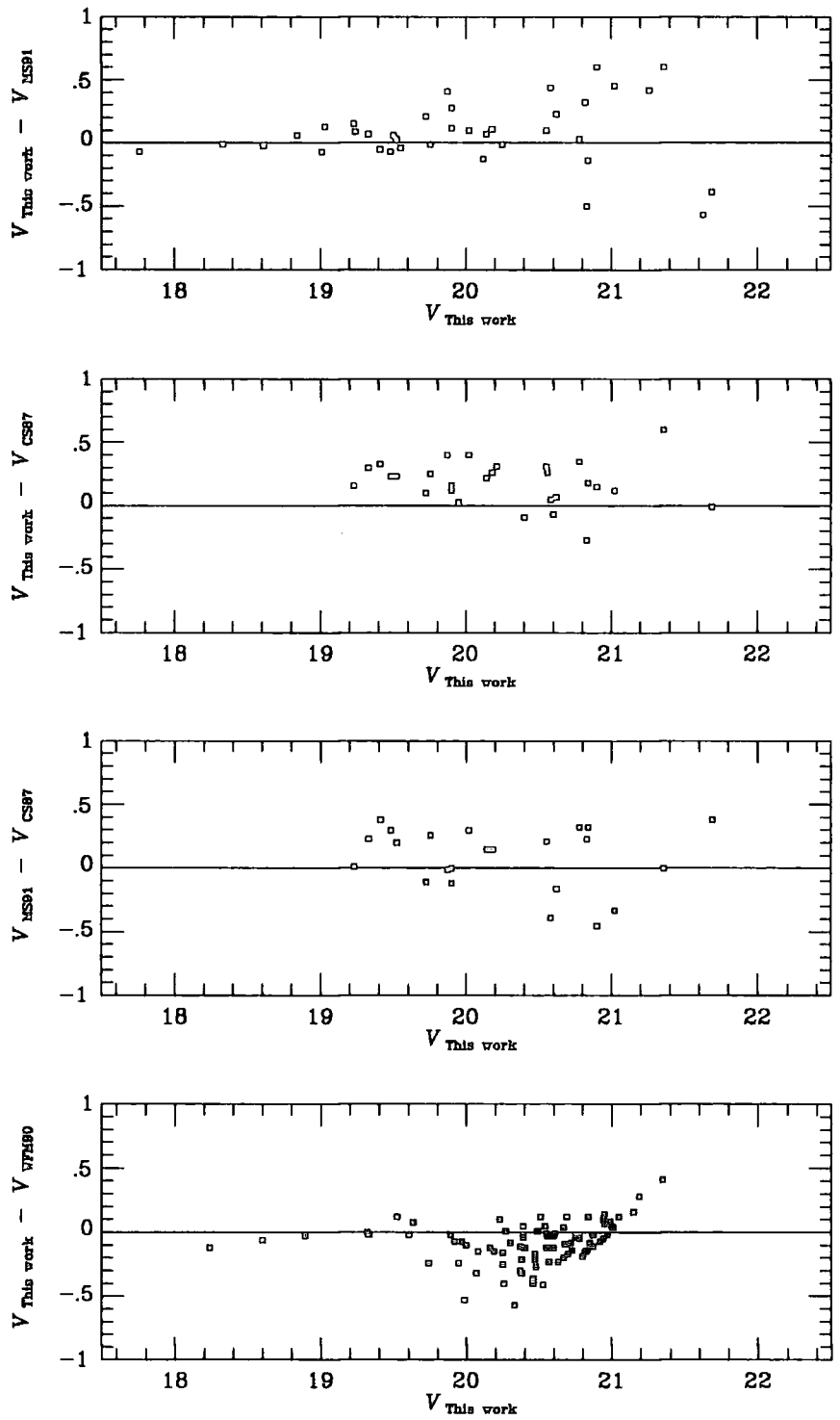

Figure 4.4: These plots show the comparisons between the different sets of CCD photometry, for the V band.

17.25		2	1			1		
17.75		3	3	1	1	1		
18.25	1	7	8	3	2			1
18.75	3	26	21	1	1			1
19.25	9	51	28	3	4	4	4	
19.75	7	51	49	14	7	8	7	
20.25	17	115	69	37	20	17	9	
20.75	29	167	103	56	33	25	15	1
21.25	49	269	243	114	67	31	15	1
21.75	99	323	322	244	119	68	15	
22.25	102	261	280	214	104	43	2	
22.75	57	80	84	63	18	1	1	
23.25	16	20	15	4	3			
23.75		3						
	-0.60	-0.20	0.20	0.60	1.00	1.40	1.80	2.20

Table 4.2: Tabular form of the colour-magnitude diagram for all M33 stars. The number of stars is given for each V and $B-V$ bin.

Now we come to the comparison of our data with previously published independent observations. Restricting ourselves to other CCD data, this amounts to the work of CS87 and WFM90. For completeness we have plotted the CS87 data against both us and MS91. Again a large scatter is seen in both comparisons, although it is interesting to note that it is somewhat less in the comparison with this work, presumably because they also used profile fitting photometry. The absence of bright stars in this comparison makes the estimate of the actual zero-point offset less certain. However, formally, using a magnitude weighted fit for the same range of magnitudes used to define the zero-point, we find high offsets of

$$B_{\text{This work}} - B_{\text{CS87}} = 0.10 \pm 0.05$$

$$V_{\text{This work}} - V_{\text{CS87}} = 0.21 \pm 0.07$$

Turning to the WFM90 data, we see the opposite tendency, in that they find the zero-points fainter, particularly in the B band. In this case there are a larger number of stars in common and less scatter, reducing the uncertainty in the offsets:

$$B_{\text{This work}} - B_{\text{WFM90}} = -0.14 \pm 0.03$$

$$V_{\text{This work}} - V_{\text{WFM90}} = -0.03 \pm 0.03$$

The obvious importance of this point for both our analysis and because of the consequences for the results on the M33 Cepheids of FWM91, who use the same data as WFM90, further discussion is merited.

We consider first the B band discrepancies. The formal error claimed by WFM90 for their zero-point is $0.^m03$, with an additional contribution of $0.^m03$ from the aperture corrections. They do find good agreement between the measurements obtained on two photometric nights, although this is using the same transformations for each night. They find only six 'uncrowded' stars in common with CS87, with only one brighter than $B = 21.^m8$, making comparisons difficult. Although all of these stars are found to be brighter by CS87 than WFM90, by amounts ranging from $0.^m1$ to $0.^m7$, they interpret this as being largely a scale error, with only a small zero-point difference of $0.^m11 \pm 0.^m05$. How this estimate is actually arrived at is not made clear, and our comparison seems to indicate a true zero-point offset in the B of nearer $0.^m25$ between CS87 and WFM90.

The calibration used by MS91 also has a small formal error of $0.^m02$. The transformations arrived at are claimed to be similar to previous observations with the same chip. We also notice that the same zero-point applied to the data for M31, (presented in chapter 3) and also NGC2403 and SA45, discussed in MS91. This provides several other independent checks with the photoelectric and CCD photometry, some of which is for brighter and less crowded stars than those in the M33

field itself. (all for B brighter than $20.^m0$) In all these cases the disagreement is small, and tends, if anything, to be in the opposite sense to that with WFM90.

$B_{\rm MS91} - B_{\rm SA45} = 0.04 \pm 0.04$ reported in Sandage (1983).

$B_{\rm MS91} - B_{\rm Arp} = 0.01 \pm 0.07$ for Arp, reported in Baade and Swope (1963).

$B_{\rm MS91} - B_{\rm HLM} = 0.02 \pm 0.01$ for Hodge, Lee and Mateo (1988).

$B_{\rm MS91} - B_{\rm TS68} = -0.01 \pm 0.14$ for Tammann and Sandage (1968).

$B_{\rm MS91} - B_{\rm HSS} = 0.01 \pm 0.01$ for Humphreys, Sitko and Sitko (1987).

The problem with the V zero-point is mainly in comparison to CS87. Once again WFM90 appear to have underestimated their disagreement with CS87, quoting $0.^m17$ from just four points, whereas we again find nearer $0.^m25$. Repeating the exercise of comparing to other sources of photoelectric photometry gives:

$V_{\rm MS91} - V_{\rm SA45} = 0.00 \pm 0.03$

$V_{\rm MS91} - V_{\rm Arp} = -0.04 \pm 0.06$

$V_{\rm MS91} - V_{\rm HLM} = 0.00 \pm 0.01$

$V_{\rm MS91} - V_{\rm TS68} = -0.01 \pm 0.14$

$V_{\rm MS91} - V_{\rm HSS} = -0.04 \pm 0.03$

which, again, are all in good agreement.

We conclude then, that, unless there was an undetected variation in photometric conditions on the night of the observations, the weight of evidence suggests an error in the B zero-point adopted by WFM90, and both B and V zero-points adopted by CS87, which go beyond the quoted uncertainties. For the rest of this study we shall continue with the MS91 zero-points, but ascribe an uncertainty of ± 0.05 to each as a reflection of the of the disagreement between the different sources. We note that this covers any uncertainty in the MS91 zero-points which arose in the M31 analysis.

Now we turn our attention, briefly, to the faint end of the magnitude range. Here, there appears to be a systematic tendency for WFM90 to obtain fainter magnitudes. This may well be due to the fact that they had significantly better seeing for their observations (averaging $0\farcs7$), which may have enabled them to de-blend stars which we have classed as single. Despite the large scatter, this explanation is given some support by examination of the plots. These show that most of the points lie on a roughly horizontal line, but with a group of outliers below them. The picture in the V band is obviously distorted by the fact that WFM90 selected only stars with V brighter than $21.^m0$ for explicit tabulation.

4.3.3 Foreground Contamination

No control field was observed specifically for M33, since it was felt that foreground contamination would have negligible effect on the diagram, which is dominated by young blue stars. In fact we would expect a rather similar distribution of foreground stars as with M31, but with a somewhat lower normalisation because of the higher galactic latitude ($\sim 31°$ compared to $\sim 23°$). This is reflected in the Ratnatunga and Bahcall (1985) predictions for M33 given in table 7.3. The only point of note from this is that foreground contamination can apparently account for most of the yellow and red stars in the bright, $V = 18^m$, bin.

18.00	1.2	2.7	2.3
20.00	1.8	1.4	7.6
22.00	2.0	1.8	16.0
	$B-V < 0.8$	$0.8 < B-V < 1.3$	$1.3 < B-V$

Table 4.3: Bahcall and Soneira predictions for foreground stars in the direction of M33, in a 22.8□′ field. The numbers are given for bins in V magnitude and $B-V$ colour.

4.3.4 Error Analysis

Once again simulations were performed to provide some indication of the level of the errors and completeness. The plots showing the error on the magnitude as a function of the input magnitudes of the artificial stars are shown in chapter 2. In figure 4.5 we show a small section of a simulated colour-magnitude diagram. The input stars are the small points and the large points show the output photometry. The range of input magnitudes was chosen to cover the most important area of the diagram from the point of view of studying the main sequence. The stars were given the colour $B-V=0$, in order to give an approximate representation of the main sequence.

On the whole, the scatter about the original locus is small, especially at the bright end, and considerably less than is exhibited in the real diagram. For example, for the bin $19.5 < V < 20$, the *rms* scatter is 0.11 (the average colour being only $B-V=0.005$), compared to an *rms* scatter in the real data of 0.29, for stars bluer than $B-V=0.7$. This suggests that factors other than photometric/crowding errors must be responsible for the width of the main-sequence in this field.

4.4 Discussion

4.4.1 Stellar Populations

In this instance, unlike M31, there is no evidence of an older population. The extreme crowding on these images means that the effects of incompleteness begin around the magnitude of the tip of

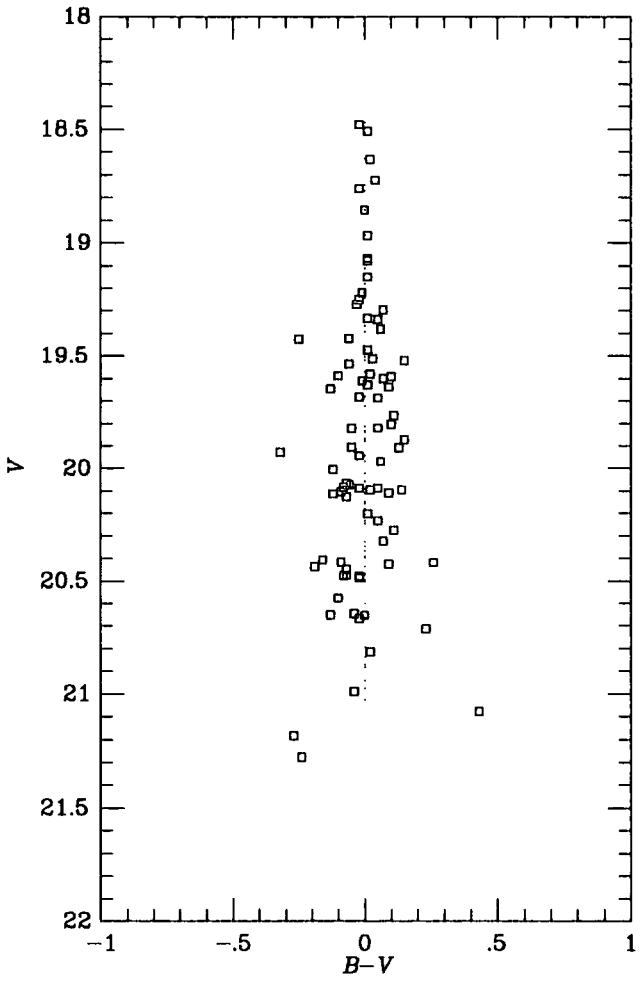

Figure 4.5: Colour-magnitude diagram for artificial stars added to the M33 field. The small points represent the input distribution, and the open squares show the retrieved photometry.

the red-giant branch. Thus we confine our discussion to the young stars.

Regarding the metallicity, this is estimated by WFM90 as $Z \sim 0.01 - 0.02$. The basis for this is the work of McCall, Rybinski and Shields (1985) on the chemistry of giant HII regions in several galaxies. Thus we shall take the metallicity to be approximately solar.

The discussion of stellar evolution in chapter 3 applies to 'intermediate mass' stars (less than $\sim 10 M_{\odot}$), and is therefore appropriate for the lower part of the M33 diagram. The most luminous stars, however, are classified as 'high mass' stars and some additional considerations should be mentioned.

In fact the evolution of these stars is even less certain than those of lower mass, primarily because of the importance of mass-loss, due to stellar winds, and increased convective overshoot (eg. Chiosi and Maeder 1986; Doom, De Greve and De Loore 1986). Winds are thought to be sufficient to significantly reduce the mass of the star during its lifetime, with one result being the apparent cut-off of the maximum mass (and hence luminosity) of red-giants, discussed later. These winds have been observed directly by satellite-based, ultra-violet spectroscopy (eg. Bianchi, Hutchings and Massey 1991).

Because of this, and the large spread of the main sequence evident in the diagram, it is not fruitful to attempt any direct comparisons of theory with observations here. Suffice to say that evolution in this part of the HR diagram is largely vertical, and so varying ages will not contribute significantly to the width of the main sequence.

4.4.2 Reddening

Once again we would like to estimate the reddening from the position of the main sequence. In this case the situation is complicated by the spread of the main-sequence. We have already seen that this is unlikely to be due to photometric errors, or the existence of a range of stellar ages in the field. One possibility is that it is caused by differential reddening, which might arise either as a depth effect, or across the field. The visible dust lanes and steep background ramping away from the centre of the galaxy both suggest this as a likely possibility. Before considering our own

results we should examine the previous evidence.

The reddening to M33 has, perhaps, an even more controversial history than that toward M31. M33 is at a somewhat higher galactic latitude (31° compared to 23°) and is also significantly less inclined than M31. For this reason, the reddening is in general expected to be lower. However, our M33 field is much closer to the centre of that galaxy, and the visible presence of regions of high extinction (the dark nebulae) might lead us to expect higher values.

As with M31, it is instructive to compare the previous estimates of extinction found by other methods, starting with those for the foreground contribution. Firstly the standard cosecant laws of galactic extinction (from Rowan-Robinson, 1986) give:

$$A_B(\text{de Vaucouleurs}) = 0.31$$

$$A_B(\text{Sandage}) = 0.11$$

$$A_B(\text{Fisher \& Tully}) = 0.25$$

Comparing these values to those in the literature we find that a recent study, by Johnson and Joner (1987), concludes: $E_{B-V} = 0.077 \Rightarrow A_B = 0.31$. This value, derived from a study of 314 foreground field stars close to M33, may be considered as superseding similar previous studies (Humphreys 1980, McClure and Racine 1969). Burstein and Heiles (1984), using HI column densities, normalised by galaxy counts, find $A_B = 0.18$, or $A_V = 0.14$. From the IRAS $100\mu m$ map of Rowan-Robinson*et al.* (1991), we find a flux in an area round M33 of $\sim 4.5\text{MJySr}^{-1}$, which translates to $A_V = 0.27$. As argued in chapter 3, this estimate might be regarded as an upper limit. In this case the effect of taking zero reddening at the NGP reduces A_V to 0.22 and $E_{B-V} \sim 0.07$.

Although these values are not in agreement, the latter work casts doubt on the technique of Burstein and Heiles, since there appears to be good agreement between the IRAS map and the HI map. This would contradict the Burstein and Heiles assumption of variable gas to dust ratio. Thus, these observations seem to point to a foreground reddening in the region of $E_{B-V} = 0.06$ to 0.09, or extinction of $A_V = 0.24 \pm 0.05$.

Now we come to the reddening inclusive of that within M33. Humphreys (1980) finds high values of around $A_V = 0.8$ from the colours of spectroscopically confirmed supergiants and also HI observations, although there is a large scatter in the results for individual stars. Bianchi, Hutchings and Massey (1991) obtain $A_V = 0.3 - 0.5$ for young OB stars observed with IUE.

WFM90 fit to the main sequence in each of their four fields. Although the scatter in their diagrams is also large, they estimate $E_{B-V} = 0.30 \pm 0.05$, for the field which overlaps ours. If we reset their data onto our magnitude scale zero-points, this becomes $E_{B-V} \sim 0.2$.

FWM91 are able to use their $BVRI$ distance moduli to derive an average reddening of $E_{B-V} = 0.1$, although this goes higher, to $E_{B-V} = 0.2$ when all the H band data (Madore *et al.* 1985) is included. However, if we simply adjust the zero-points of their photometry to bring it into line with our zero-points, then the main effect is to brighten the Cepheids in B, which reduces μ_{AB}. This would then tend to suggest a lower value for the average reddening, but would also mean that the curve defining the extinction law would no longer fit so well to their points.

MS91 also estimate a low value for the reddening by comparing their result for μ_{AB} with published values for μ_{AI}. Although these data are derived from other areas of M33, and the values show considerable scatter, the average is around $\mu_{AI} = 24.8$, which is close to the Freedman (1988) value of $\mu_{AI} = 24.7$.

We turn now to consider what our results might add to this question. We do not benefit here from the use of the R data which previously gave a self-consistency check for the M31 result, but have the advantage of a much larger number of bright main-sequence stars. Since the full diagram exhibits such a large spread, we tried splitting the frame up into 24 roughly square, equal areas. The colour-magnitude diagrams for each of these is shown in figure 4.6.

Plotted on the diagrams is the locus, including age spread, of the unreddened main-sequence, assuming a V band distance modulus of 24.7. (This locus is adapted from Mermiliod 1981, in the same manner as described in chapter 3.) It is immediately apparent that, in many areas the main sequence is tighter, closer to the width expected by photometric errors, and in those cases, its location clearly varies as a function of position in the field.

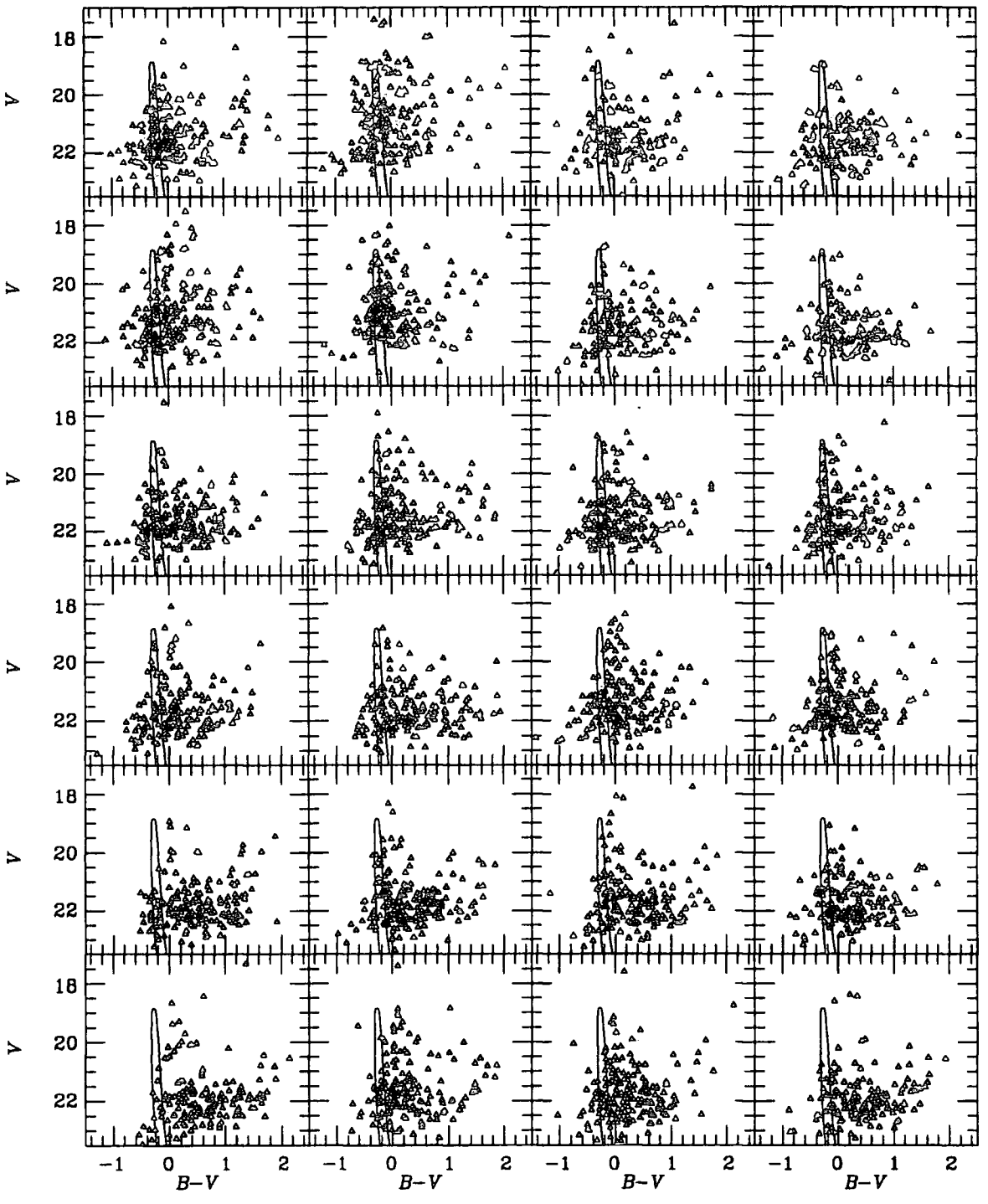

Figure 4.6: Colour-magnitude diagrams for each area of the M33 field. The unreddened envelope of the main sequence shows how the reddening appears to depend upon position on the field.

We might ask if this variation could be a facet of the data reduction. However, whilst it is possible to conceive of problems with the photometry which would depend on position, it is more difficult to see how this could significantly affect the colour. This is particularly so in this case since the images were taken on the same night, with the same detector and in similar seeing. Thus most problems would be expected to be present in both passbands. In order to test this, we have split up the small sample of simulated star results, into two sets, one for the top half of the image and one for the bottom. (See figure 4.7). Apart from confirming that there is no significant bias in the colour due to position, this figure is also interesting in that it shows the relative photometric errors for the two halves of the frame. Not surprisingly, the situation in the bottom half, which was generally less crowded, is better.

Just considering those areas where the sequence is reasonably tight, the variation in reddening is from $E_{B-V} = 0.05$ to 0.35, with errors on the eyeball fitting procedure of ~ 0.05. This is consistent with a small amount of foreground reddening, but with an addition of up to 0.3 magnitudes of internal reddening. It is also in good agreement with the corrected result of WFM90 for the position of the main sequence, taking into account that the overlap area was mainly the lower half of our field. We also note that, perhaps surprisingly, the regions of lower reddening are actually those closer to the centre of the galaxy, in this field. An alternative factor which could contribute a little to a variation in the position of the main sequence, namely a metallicity gradient, would also require the situation where the lower metallicity was in the inner regions of the galaxy.

4.4.3 Cepheid Distance

The existence of significantly variable reddening makes us wary of recalibrating the Cepheid moduli as a whole. Instead we shall limit ourselves to the small sample of Cepheids for which new CCD mean intensities have been found by FWM91, which are on our field. For these, we have adjusted the BV zero-points to those found by MS91, and have found a value for the reddening by fitting the main-sequence, by eye, to the ridge line in the particular region of each Cepheid. These are summarised in table 7.4.

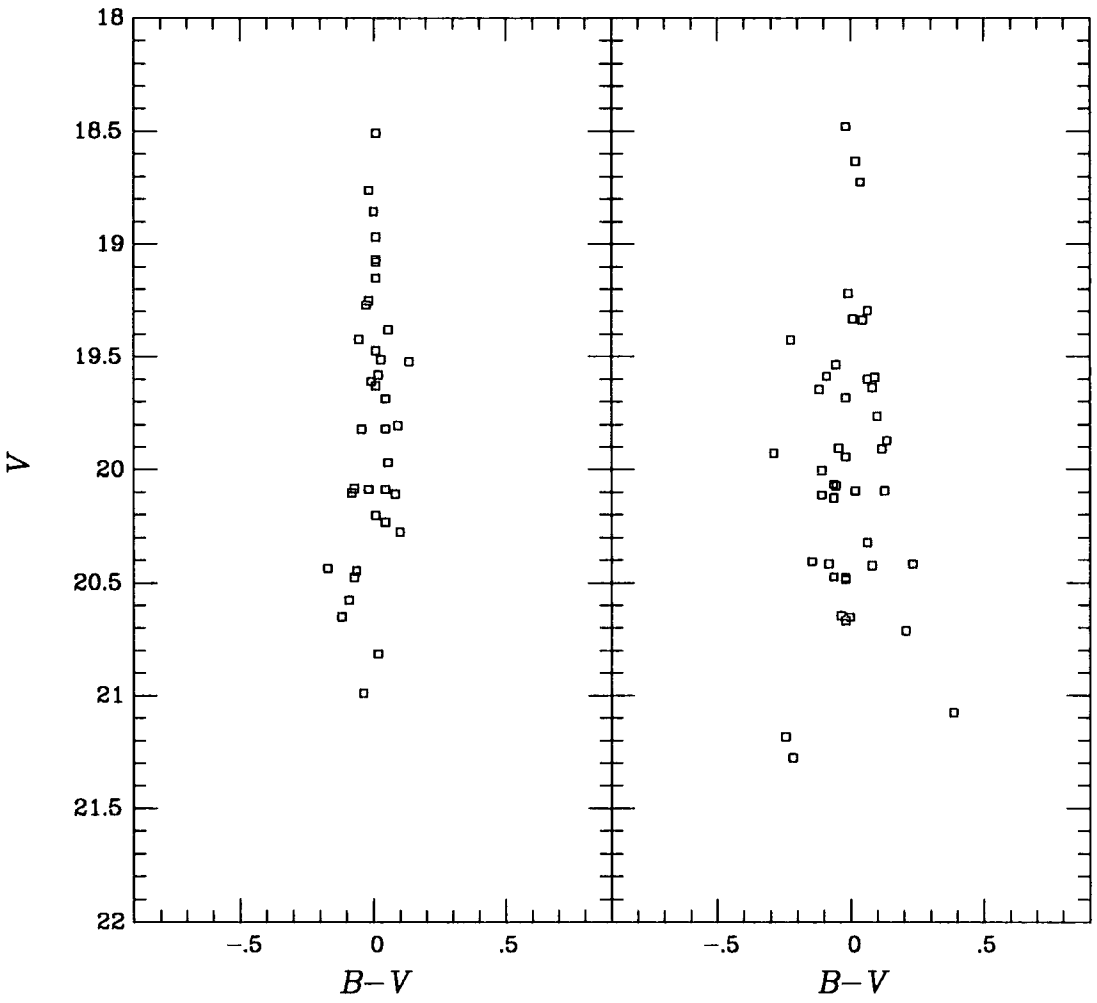

Figure 4.7: Artificial star data split into the bottom half of the field, on the left, and the top half, on the right. This shows how the photometric errors generally increase going up the frame.

Cepheid	log P	B	V	R	I	A_V
V30	1.663	20.34	19.21	18.59	18.15	0.5
V31	1.572	19.92	19.14	18.64	18.14	0.6
V33	1.312	-	20.00	19.47	18.98	0.6
V41	1.255	20.50	19.79	19.33	18.99	0.7
V42	1.482	20.74	19.73	19.18	18.62	0.4
V44	1.479	20.64	19.69	19.19	18.91	0.6

Table 4.4: The FWM91 mean-light Cepheid photometry, recalibrated onto our adopted magnitude scale in B and V. The estimated V extinction is also given.

Putting these values in the MF91 relations given in appendix E, we arrive at new values for the distance modulus of M33. The errors are dominated by the remaining uncertainty in the zero-points, which contribute substantially to the uncertainty in the reddening. $\mu_0(M33) = 24.40 \pm 0.45$, from the B data. $\mu_0(M33) = 24.47 \pm 0.35$, from the V data; $\mu_0(M33) = 24.57 \pm 0.25$, from the R data. $\mu_0(M33) = 24.64 \pm 0.2$, from the I data.

4.5 Conclusions

We have obtained BV photometry for $\sim$ 4500 resolved stars in field 9 of M33. The resulting colour-magnitude diagram has been used to demonstrate that the locus of the main sequence in the colour-magnitude diagram varies across the field, implying differential reddening. The reddening, estimated by this method for each Cepheid, is generally higher than the global estimates proposed by other recent studies. This results in a somewhat lower distance modulus, of

$$\mu_0 = 24.5$$

although with a large uncertainty of ± 0.25. Here we have weighted the BV photometry more highly because of the comparisons we have been able to make for that data, including several independent determinations of the zero-points. We have also assumed a value of $\mu_0(LMC) = 18.5$

(see appendix E).

Clearly one of the most important questions which has been left is that of confirming the zero-points of the magnitude scale, which contribute the majority of the quoted uncertainty. The large variations between different authors, and the sensitivity of the results, particularly for the extinction, make it an important matter to re-examine the existing zero-points.

These results have also highlighted the apparent discrepancy with the published I and R band photometry, which have tended to produce higher values of μ_0. In fact, the moduli from all four bands would agree very well if the extinction were reduced by 0.3 in A_V. Whilst this is at the limit of the formal errors, it would appear, from figure 4.6, to require zero foreground reddening, in conflict with the best current estimates which say it should be $E_{B-V} \approx 0.07$. However, we should note that random phase H band photometry of M33 Cepheids (Madore *et al.* 1985) gives $\mu_0(M33) = 24.4 \pm 0.2$, closer to our B and V band moduli.

Chapter 5

High Resolution Imaging

5.1 Introduction

Both lines of enquiry presented in this thesis are concerned, at some level, with the practical meaning of spatial resolution, as understood in optical astronomy. In this chapter we discuss this concept, and its relationship, in a qualitative sense, to the information contained in an image; wherein is provided the motivation for high-resolution imaging. The background physics of atmospheric image degradation is introduced, which leads to the well known problem of limiting resolution on ground-based telescopes. The solution provided by image-sharpening is outlined.

We give a detailed description of the image-sharpening devices used in this work, the TRIFFID and MARTINI, both of which are designed to be placed at the $f/11$ GHRIL focus of the WHT. There is particular reference to the aim of the program of technical observations, described fully in chapter 6, and to the enhancements required for faint object work, which is described in chapter 7. Other routes to high-resolution imaging are considered together with the current status of results.

5.2 Discussion of Resolution

In optical terms, there are two instrumental factors which contribute to determining the information content of a given exposure. One is the light gathering power and the other is the resolving power of the instrument. The resolution is a measure of the degradation of the image due to the inevitable blurring of detail which occurs in its formation. In fact, these two factors are related since improved resolution will often mean a higher signal to noise ratio, whilst high signal can, in some sense, be traded off for resolution via reconstruction techniques.

In any imaging device the resolution is limited by the diffraction at the entrance pupil. Fundamentally this is a quantum mechanical process, and is a manifestation of Heisenberg's *Uncertainty Principle.* In ground-based astronomical telescopes, there is a further deterioration due to the effect of turbulence in the air through which the light travels. (Of course, there will usually be some effect due to instrumental imperfections in optics and tracking too.) Since, at least for large telescopes, the atmospheric contribution is dominant, the final resolution is generally referred to simply as the 'seeing'.

5.2.1 The Point-Spread Function

The resolution inherent in an image, and hence characteristic of the instrument and observing conditions used to obtain it, can be quantified in several different ways. Astronomers usually consider resolution in terms of the point spread function (PSF). This is an idealisation of the two dimensional image formed by a single point source. It is equivalent to the power spectrum of the aperture function of the telescope. Clearly this perspective is natural since distant stars, when viewed from the Earth, are effectively point-like objects. In fact, the situation is frequently simplified by adopting only some convenient measure of the width of the PSF, such as the full-width-at-half-maximum (FWHM), to describe the resolution.

Typical seeing from good ground based sites is around 1″ FWHM at visible wavelengths. This corresponds to the diffraction limit of a small ~12cm telescope. By comparison, the diffraction limit of a 4m telescope is ~0.″03.

5.2.2 The Coherence Parameter r_0

Another description of resolution is in terms of the coherence parameter, r_0. This can be thought of as the correlation length of spatial variations of the wavefront. It becomes particularly important in seeing theory, which is described later. In basic seeing theory, discussed below, it is equivalent to the diameter of a hypothetical aperture whose diffraction limit is the same as the observed seeing. Re-writing the standard formula, we have for r_0 in m:

$$r_0 = \frac{\lambda}{4\theta},$$

where λ is the wavelength in μm and θ is the FWHM of the PSF in *arcsecs*. Thus, for example, seeing of $1''$ corresponds roughly to r_0 =15cm when working in the R band.

5.2.3 The Modulation Transfer Function

Perhaps a more physical approach, which reflects the fact that resolution can be considered in terms of the removal of the high spatial frequencies, is to use the modulation transfer function (MTF). This is defined as the ratio of the intensity modulation in the image to that in the source, as a function of angular frequency. That is to say, if our source is a sine wave intensity pattern, of a given angular frequency, then the MTF for that frequency is the amplitude of the sine wave in the image divided by the amplitude in the source. This must be normalised, and it is sensible to do so by setting the MTF to unity at zero spatial frequency. (See, for example, Steward, 1983)

The MTF turns out to be equivalent to the modulus of the Fourier transform of the line spread function, and is thus closely related to the PSF (see below). It is also given by the auto-correlation function of the aperture function. The optical transfer function (OTF) is the analogue of the MTF for two-dimensional imaging, and is thus identical to the MTF for point sources.

The particular value of transfer function approach lies in the fact that the combined transfer function for a complex system is simply given by the product of the transfer functions for the components of the system. Thus, for example, the transfer function appropriate to the production of an image by a ground based telescope, is obtained by multiplying the transfer function of the

telescope optics by the transfer function for the atmosphere. Having obtained the overall OTF in this way, the point spread function is then given by the Hankel transform:

$$\mathrm{PSF}(\mathbf{r}) = 2\pi \int_0^\infty \mathrm{OTF}(\rho)\mathrm{J_o}(2\pi\rho r)d\rho,$$

where $\mathrm{J_o}(x)$ is the zero order Bessel function.

5.2.4 The Strehl Ratio

It is instructive to now also define the Strehl ratio, which is frequently used as the description of resolution in optical papers. This defined as the integral of the observed MTF divided by the integral of the diffraction limited MTF. Equivalently, this can be expressed as the central intensity of the observed PSF divided by the central intensity of the diffraction PSF for a given aperture. Thus a high Strehl ratio corresponds to good resolution.

5.2.5 What is 'Resolved'?

The question of whether a particular detail or object within an image can *be resolved* is much more ambiguous, and consequently the source of misunderstanding. The Raleigh Criterion suggests that we call two images "resolved" if the central peaks coincide with, or are beyond, the first minimum of the other's diffraction pattern. Apart from the fact that this convention can only be applied to true diffraction images, it is clear that in any real situation our ability to separate cannot be decided in such a concrete manner. For example, if we have a lot of noise the two images may not be resolved until they are further apart, whilst an arbitrarily close pair could be told apart given sufficiently low noise and a precise knowledge of the PSF.

Some progress could be made with this hypothetical problem by taking the standard statistical approach of testing against a null hypothesis that a given image is single. However, in real astronomy, when dealing with extended objects and complex systems of stars, on top of experimental uncertainties, such as imprecise knowledge of the PSF, no single, quantitative approach can be

used. The particular case of resolving point-like objects is discussed below.

5.2.6 Object Detection in Crowded Fields

In much of this work we are particularly concerned with the problem of identifying and photometering individual stars in crowded regions. The practical aspects of this process were examined in detail in chapter 2. Here we consider, briefly, the question of what we mean by 'crowding' in this context. This is also relevant to the feasibility of the astronomical image-sharpening observations of Virgo Cluster galaxies, described in chapter 7.

By crowded we really mean that the object itself is likely to appear partly merged with other visible objects; that is to say, objects of a comparable brightness. In real situations there will often be, in crowded regions, a background of fainter stars, below the detection threshold, whose number variance from place to place provides a fluctuating sky brightness. These, however, will generally contribute little to the crowding as we are considering it here.

It follows, then, that it is perfectly possible to observe, without confusion, an object which sits on a very dense background of other sources, providing it is sufficiently brighter than those sources. Thus the question of whether a particular star field is 'resolved' must also be thought of in terms of whether the particular stars of interest, probably close to the detection limits, are crowded with respect to other objects of a similar brightness. We are not interested in the density of background, much fainter, objects except in as much as they contribute to the fluctuations of the background.

Now, the more common limitation in identifying and obtaining photometry is that of acquiring sufficient signal from the object relative to the noise created by photon counting statistics. The tighter the PSF, the less likely it is that it could be mimicked by a noise spike.

The advantage of increased resolution, then, is two-fold. Firstly the signal-to-noise ratio is increased over the poor resolution case, whether or not there is crowding. Secondly, if there is crowding, that will also be reduced, with the effect of increasing statistical confidence in the integrity of our object identification and photometry.

Unfortunately, in practice, as we shall see later, the present techniques of image-sharpening often significantly reduce the signal obtained for an object, and hence offer little or no advantage for isolated objects. Thus the benefit must be primarily in the terms of the second, still very important, factor, of reducing the confusion in crowded fields.

5.3 Overview of the Optical Effects of Atmospheric Turbulence

Although there is ample empirical evidence to motivate the study of image-sharpening, and other forms of ground-based high resolution imaging, it is useful to consider, briefly, the background physics of the subject. For detailed overviews of the general theory of seeing, refer to Young (1974), Woolf (1982) and Roddier (1981).

Turbulence in the atmosphere is understood in terms of the non-linear Navier-Stokes equation which governs fluid flow. The energy which powers the flow, is naturally injected at large scales, of the order of 10m. This energy subsequently 'cascades' up the spatial frequency domain to smaller scales, until it is lost via viscous dissipation on mm scales. These scales are referred to as the outer (L_0) and inner (l_0) scales of turbulence, respectively. Between these extremes the turbulence can be described by the Kolmogorov (1961) power spectrum for velocity fluctuations

$$P(\vec{k}) \propto k^{-\frac{11}{3}}$$

where k is the modulus of the wavevector $\vec{k}$.

Temperature inhomogeneities, which may be the cause of turbulence in the first place, are only smoothed out on these smallest of scales. These are typically of the order of a few hundredths of a degree in the upper atmosphere, and a few tenths nearer the ground. The small dependence of the refractive index of air on temperature has the effect of varying the path-length through adjacent parts of the atmosphere. It is this, then, that is responsible for the corrugation of the initially flat wave-fronts which pass through it.

Following, for example, Tartarski (1961), assuming the Kolmogorov spectrum, the structure function, $D_N(\rho)$, or mean square difference of refractive index between points separated by a distance ρ, is given by:

$$D_N(\rho) = \langle (N(\vec{r}) - N(\vec{r}+\vec{\rho}))^2 \rangle = C_N^2 \rho^{\frac{2}{3}}$$

Here, C_N is the refractive index structure constant, which is a measure of the strength of the variations. The distribution of C_N with altitude is of considerable importance to the effectiveness of image-sharpening. We can now write the formal definition of the coherence parameter, r_0, following Fried (1965), in which the integral over the atmospheric path of the C_N determines the degree of coherence.

$$r_0 = \left[0.423 \left(\frac{2\pi}{\lambda} \right)^2 \sec\theta \int_0^H C_N^2(h) dh \right]^{-\frac{3}{5}},$$

where h is the height in the atmosphere, H is the total height of the atmosphere which influences seeing, λ is the wavelength of the light and θ is the zenith angle of the source.

It is interesting to note the wavelength dependence

$$r_0 \propto \lambda^{\frac{6}{5}},$$

which also demonstrates the wavelength dependence of intrinsic seeing, for a large aperture

$$\theta \propto \lambda^{-\frac{1}{5}}$$

5.3.1 Imaging through Turbulence

When these deformed wave-fronts are focussed to form an image it is significantly degraded from the Airy pattern expected from considerations of pupil plane diffraction alone. Moreover, its position, shape and intensity will vary on rapid time-scales ~10ms. The relative importance of atmosphere and optics depend on the size of the imaging aperture. For small apertures the diffraction will dominate, whilst, as the aperture is increased, the long term image will approach a minimum size determined only by the statistics of the turbulence.

The transfer function for the atmosphere, for a 'long exposure', following Fried (1966), is given

by

$$TF_{LE}(\rho) = exp\left[-3.44\left(\frac{\lambda\rho}{r_0}\right)^{\frac{5}{3}}\right]$$

The interest of image-sharpening lies primarily in the fact that a 'snapshot', short-exposure, image freezes out the time-variation and thus may be superior, in sharpness, to an integrated image. What is actually seen, in such a snapshot, is a, so called, 'speckle pattern'. A grouping of small, imperfectly formed, near diffraction images.

In fact, for large apertures there is rarely much improvement in the snapshot since the image is formed from light which has traversed well separated paths through the atmosphere, and hence the pattern itself contains many, widely separated speckles. For smaller apertures, however, the effect is evident since the tilt of the wave-front is well correlated over small scales, and the, now fewer but larger, speckles may be grouped offset from the nominal centre. There may also be occasions when, by chance, the image consists of essentially one speckle.

Visually, this amounts to saying that for small apertures the blurring of the integrated image is primarily caused by image motion, whereas for larger apertures motion is not significant compared to the size of the instantaneous speckle pattern. Small apertures also increase the proportion of time where the image is not broken up. We see below how we can utilise these two properties of ground based images to achieve improvements in resolution.

This difference is reflected in the transfer function for the short exposure, which is modified, in the near field approximation, to:

$$TF_{SE}(\rho) = exp\left[-3.44\left(\frac{\lambda\rho}{r_0}\right)^{\frac{5}{3}}\left(1-\left(\frac{\lambda\rho}{D}\right)^{\frac{1}{3}}\right)\right],$$

where D is the diameter of the imaging pupil.

5.4 Image-Sharpening

In this section we describe the principles behind the image-sharpening devices used in this work. The generic term for high-resolution techniques which work by high speed monitoring and removing

distortions of the image is adaptive correction. In the case where the correction is applied by optical means, this becomes 'adaptive optics'. The related term, 'active optics', applies to the simpler task of mechanically minimising optical aberrations on time scales of seconds. Systems which offer this facility, such as the ESO New Technology Telescope, generally work by directly deforming the primary mirror itself.

Here, by 'image-sharpening', we shall usually mean the simplest form of adaptive correction, that of tilt correction. As it sounds, this is the case where the global tilt of the wavefront over an aperture is removed. Optically, this tilt would be responsible for moving the image centroid from its nominal position. Thus the technique corresponds to superimposing the short exposure images. This form of high-resolution imaging offers the most immediate promise of applications in many areas of astronomy. We shall also give some consideration to image-sharpening by frame-selection, where only particularly sharp images are added to give the final, high resolution, image.

5.4.1 The Expected Gain from Tilt Correction

We have seen that the resolution achieved with large ground based telescopes is generally considerably worse than their nominal optical limit, due to the effect on the incoming light rays of turbulence in the atmosphere. The wave-fronts are deformed in a complex and rapidly varying manner. This results in an interference pattern of speckles which fluctuates and dances in the image plane

There are several means by which some of this lost information can be added back into the image to enhance its resolution. The simplest of these works by removing the dancing motion of the speckle pattern which otherwise contributes to the blurring (The next stage of sophistication is selecting only those frames which are particularly sharp for inclusion in the integrated image. See §5.4.3) For faint images there are too few photons to follow the very rapid movements so a brighter nearby object must be used as a guide.

The theory of atmospheric seeing suggests that, as expected, the quality of the sharpened image depends on the intrinsic seeing at the time of the exposure. A detailed analysis (originally Fried

1965, 1966, also see Wang 1977) shows the expected relationship between aperture size and the achieved resolution in long and short exposure images (figure 5.1).

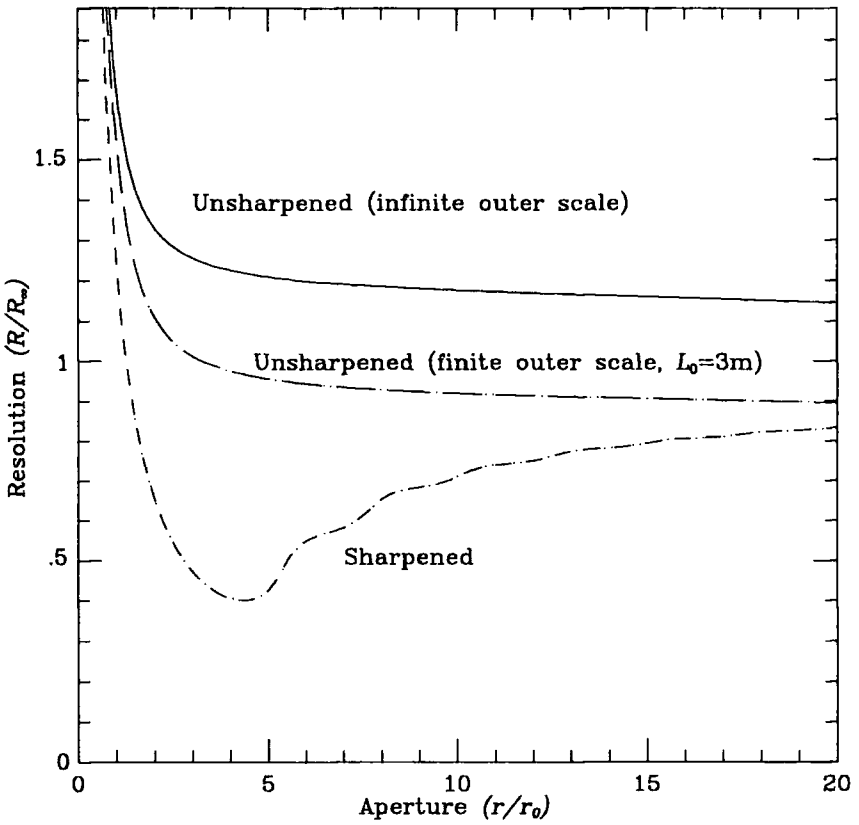

Figure 5.1: Theoretical 'Fried' curves showing the relationship between the resolution of an image, normalised to the infinite aperture result, and the pupil size, normalised by r_0. Also shown is the modified long exposure curve for the case of a particularly small outer scale of turbulence of L_0 =3m.

Fried's analysis makes the simplifying assumptions that all the turbulent effects occur in a single layer in the near field of the telescope, and that the outer scale of turbulence is infinite. A relaxation of either of these assumptions will result in a reduction in the effectiveness of image-sharpening. Regarding the first, there is certainly evidence that turbulence is largely confined to discrete layers reasonably low in the atmosphere (eg. Coulman 1986; Guryanov 1984; Young 1974). The second assumption is now considered not to be generally valid. In particular, Doel (1990) has investigated the effect of a finite outer scale, using the results of Valley (1979), and finds that with that extra degree of freedom, observational data obtained with MARTINI are much better fit by

the theoretical curves (for values of 1m< L_0 <10m). An example of the effect of reduced outer scale of turbulence is also shown in the figure. A similar result, of L_0=2m, is found by Nightingale and Buscher (1991) using their interferometric seeing monitor at La Palma.

The Fried curves clearly show that the maximum benefit from image sharpening is obtained when the entrance pupil is set to about $4r_0$. At this point the best trade-off occurs between the speckle size (diffraction limit) and the number of speckles. The improvement in resolution is around a factor of two to three for the sharpened image over the unsharpened large aperture image. In practical terms, this implies that, for the optimum sharpening, an aperture of between 30cm and 1m will usually be appropriate. For large telescopes, the improved resolution would have to be weighed against such a light loss. In passing, we note that reducing the aperture of the telescope might also have some advantage in reducing the effects of any small aberrations in the optics.

5.4.2 Isoplanicity and Conjugate Focus

Apart from the improvement in resolution, the other consideration, from an observational point of view, is the question of over how large a field of view is image-sharpening effective. This is important since in many situations the object used to monitor the seeing motion will not be of any astronomical interest in itself, but simply a nearby bright star. The region around such a star which would be sharpened in such circumstances is known as the isoplanatic patch.

To construct a simple model for predicting isoplanicity, we return to the assumption of turbulence in one layer in the near field. A consequence of this is that wave-fronts passing through any particular patch of this layer, even if their sources are well separated, will be deformed in a similar manner. So, if the beams from different objects within the field can be collected such that each beam coincides at the height of the turbulent layer, the required correction for wave-front tilt should be the same across the field. This would correspond to a large isoplanatic patch, as would be desired.

Now, since the turbulent layer, in general, may be many kilometers above the observatory, we have to collect the light from each source from different areas of the primary mirror. We are only

able to do this because of the restriction to using small optimum apertures, and by virtue of using a much larger primary collecting area. This is one rationale behind using a 4m class telescope, even if we are stopping down the primary and reducing its collecting power. This is illustrated in figure 5.2.

In optical terms we want to place the aperture plate at the conjugate focus of the turbulent layer. That is to say, at a position within the apparatus, at which the layer itself is focussed. If this is achieved then it will be effectively as if the aperture plate were itself fixed at the height of the layer, as we require. Thus the size of the isoplanatic patch will depend on the distance between the conjugate focus of the aperture plate and the turbulent layer. A rough guide would be that the amount of correlation between the wavefronts from adjacent objects, would be proportional to the degree of overlap of their beams when they pass through the turbulent layer. This simple model also allows us to predict that there will be higher correlation, and hence more effective sharpening, in the direction perpendicular to the line joining the two stars, than in the radial direction.

The degree to which the turbulence can actually be considered to be in just one layer, and our ability to identify the position of the optimum conjugate focus, will, to a large extent, determine the usefulness of this technique for general astronomy. This question is investigated, empirically, in chapter 6.

An attempt at a more realistic theoretical treatment has been given by Valley (1980), who derives the expected form of the isoplanatic patch for a Hufnagel (1974) model of the structure functions. Unfortunately, this calculation makes the implicit assumption that the aperture stop is fixed in the pupil plane, and thus does not make any predictions regarding the gain to be made by optimising the conjugate focus position.

There are two previous experimental studies of interest. Firstly Christian and Racine (1985) simply observed the correlations between the motions of star trails in a deliberately trailed photograph taken at the CFHT. They found good correlation at $1'$ separation. Secondly, the recent work of McClure *et al.* (1991) investigated the variation of stellar PSFs across a CCD image taken using the HRCAM at CFHT. The deterioration with distance from the guide star is small, from $0.27''$

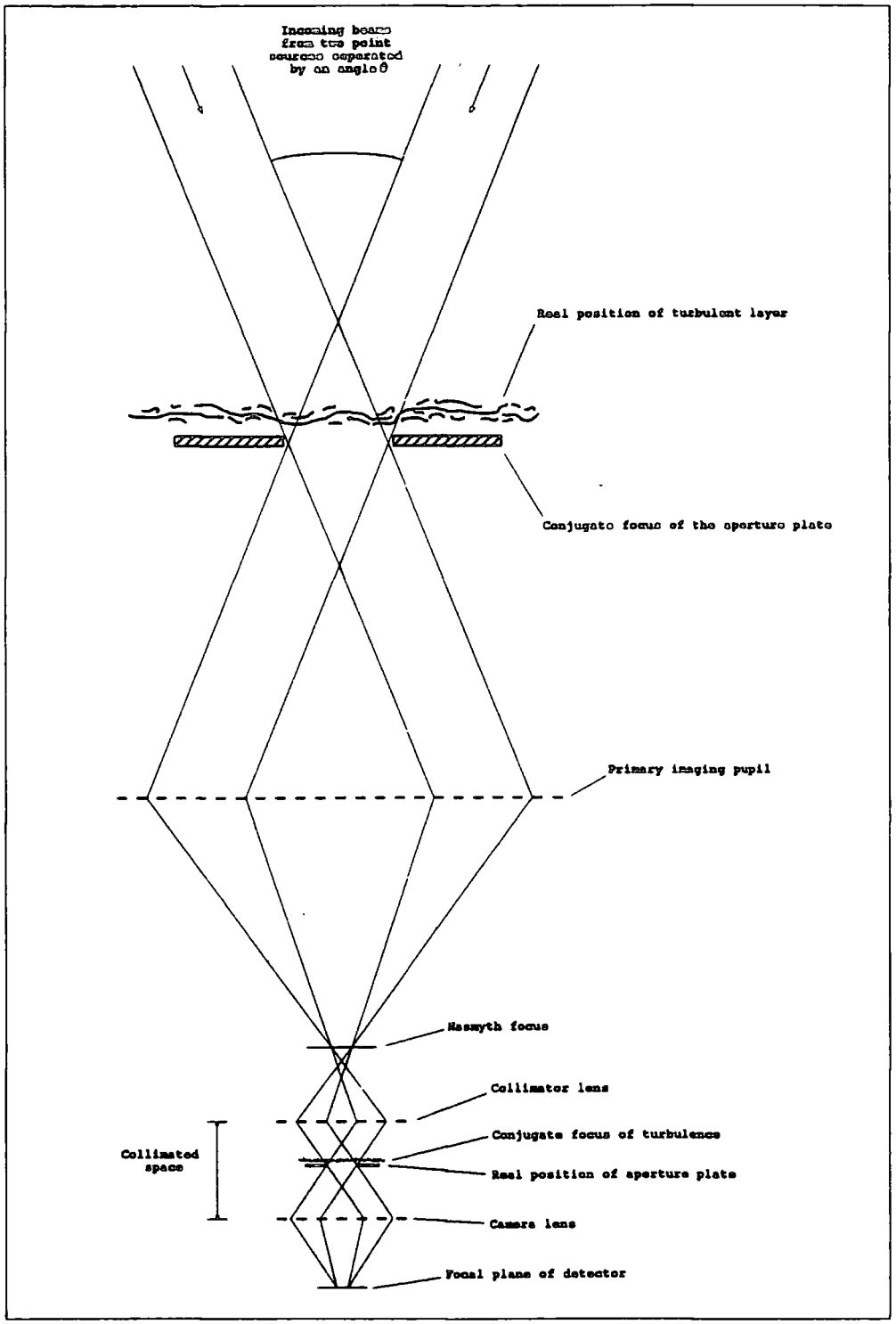

Figure 5.2: Schematic diagram showing the effect of putting the aperture plate at the conjugate focus of the turbulence on the isoplanicity. In this simple model the amount of overlap of the two beams, as they traverse the turbulent layer, will determine the degree to which their tilts are correlated.

to 0.33″ at a distance of 100″. However, it is not made clear what the correct unsharpened seeing should be, and hence leaves the question as to what is limiting the resolution in the sharpened case.

5.4.3 The Expected Gain from Frame Selection

Fried (1978) has also calculated the chances of getting an particularly sharp instantaneous image, what he calls a 'lucky exposure'. This he defines as instances in which the phase shifts of the wavefront over the imaging aperture are nowhere greater than $1 radian$. We may consider this as times when, by chance, only one speckle is seen in a short exposure. This is also a function of aperture size, as indicated in figure 5.3.

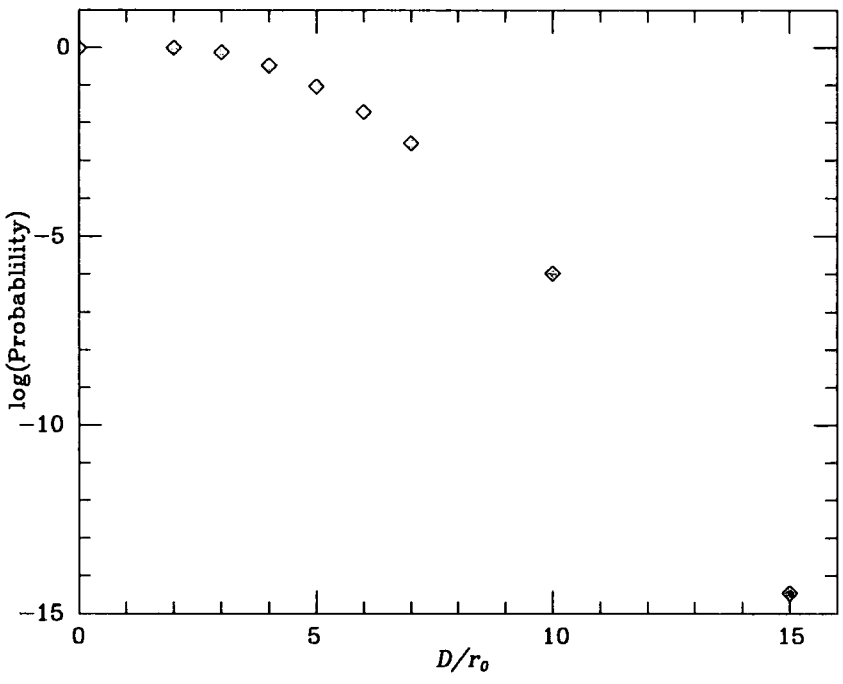

Figure 5.3: The theoretical probability of a particularly sharp or 'lucky' image in a short exposure, is a strong function of the aperture size. A 'lucky' exposure amounts to an image in which there is just a single speckle. Thus, although larger apertures are much less likely to provide lucky exposures, they will be sharper when they occur

This offers us another technique of image-sharpening; one which is, in principle, only limited by

the size of the telescope, but which suffers from similar problems of balancing loss of signal against increased resolution. In order to apply this technique to real-time sharpening, a fast shutter would be required.

We notice that at the optimum aperture for tilt-correction there is a roughly 40% chance of obtaining a lucky short-exposure. Since this is about $4r_0$, the lucky exposure method could give up to a factor of 4 improvement with such a configuration. The question of isoplanicity also arises in this connection, as the correlation of the instantaneous image widths will also depend on separation. Since the speckle pattern depends on the small scale corrugations of the wave-front, it is easy to imagine that correlation between two partially overlapping beams will be less for these small scale distortions than for the gross tilt. A detailed analysis (Valley 1980) confirms this expectation for higher order Zernike terms. Thus the isoplanatic patch size for frame-selection is predicted to be less than for tilt correction.

5.4.4 Time Scales of Image Motion

The time-scales of image motion are not addressed by seeing theory since they are thought to depend mainly on the wind speed, which may vary independently of any measurable parameters, such as r_0. Specifically, to a good approximation, the turbulent atmosphere is considered as a 'frozen' phase screen flowing across the field of view. Experience has shown that coherence times of a few tens of milliseconds are typical, which would correspond, very roughly, to wind speeds of around 10ms^{-1}. Our experimental setups are designed to read-out comfortably faster than this, although, clearly, the shorter the coherence time, the greater difficulty the sharpening algorithm has in following the image motion. Thus, wind speeds could have a significant effect on the performance of image-sharpening devices. In particular, monitoring devices which read-out slower than $\sim$ 30Hz may, in some circumstances, not be sufficient to stop the image motion.

5.4.5 Post Exposure versus Real Time

Since it has had a bearing on the experimental work we have conducted, we shall discuss briefly the debate between the post-exposure and real-time sharpening. The advantages of real-time sharpening (with adaptive optics) are primarily that the corrected wavefront may be imaged onto a variety of detectors. This means, for example, that high efficiency CCDs, infra-red cameras or spectrographs can all be used.

Post-exposure correction has the one main benefit of allowing 'future' as well as 'past' photons to be used in calculating the centroid position. This improves the precision of the monitoring, and allows fainter guide stars to be used. It is also easier to use multiple monitoring objects (see chapter 6).

5.4.6 Previous Studies of Image-Sharpening

A review and discussion of the groups currently active in the design of image-sharpening instruments is provided by Doel (1990). The work of several of these groups is considered, briefly, below, and in the subsequent chapters.

The earliest experiments with image-sharpening date from the 1950s, however, it has only been the advent of fast electronic detectors and the availability of powerful computers to cope with the data analysis, that has allowed more thorough studies. The parameters of image-sharpening, and optimisation of algorithms, have been examined by several previous authors, although, perhaps, thus far, the emphasis has been on obtaining the ultimate preformance in terms of resolution, rather than considering problems of practical astronomy.

Nieto, Llebaria and di Serego Alighieri (1987) investigated the use of a 30Hz photon counting device for simple, post-processing, recentering and frame selection. Lelievre *et al.* (1988) report further developments of this device, which was used to achieve 0.″26 seeing at the CFHT, by means of 10% frame selection.

McClure and Racine and collaborators, have researched into several aspects of the performance

the their instrument, the HRCAM, on the CFHT. Some of these contributions are mentioned elsewhere in this thesis, we note here two general papers McClure *et al.* 1989, Racine and McClure 1989. Briefly, the HRCAM is a common user image-sharpening camera, which consists of a single tip-tilt mirror, which can correct the over the whole 3.6m aperture of the telescope. The best resolutions obtained are around 0.″3, found with a stopped down aperture.

Taken as a whole, the results from HRCAM suggest that the good seeing is to a some extent due to a long-term campaign to reduce dome seeing, which includes active cooling of the telescope enclosure. For example, statistics given in the CFHT Bulletin no.25 (1991) show a median seeing for HRCAM of $\sim$ 0.″61 compared to that for the non-image-sharpening FOCAM of $\sim$ 0.″79. Similar statistics for the last decade show a monotonic improvement in achieved seeing. Racine *et al.* (1991), have attempted to quantify the different contributions to the observed image spread. They concluded that the dominant local effect was mirror seeing which added 0.″4 for each 1°C differential in temperature between the mirror and the atmosphere. They also suggested that at present the limit on the best seeing is due to aberrations introduced by the optical system, and reported that a correcting lens is currently being produced to rectify this.

A long term program to evaluate the contributions to seeing using a Shack-Hartmann wavefront sensor on a 0.62m mirror is reported by Iye *et al.* (1991). They also found a dependence on the mirror to ambient air temperature difference, but further discovered that the degradation was significantly reduced when the mirror was flushed with a laminar wind.

Previous results from the TRIFFID group are summarised by Devaney 1989. Of particular interest is the development of optimal filtering algorithms for post-processing recentroiding. Similarly, technical results from MARTINI are given by Doel 1990. These have validated the principle of image-sharpening, obtaining seeing improvements on test objects using post-exposure techniques. The best seeing found by these authors is again around 0.″3, with the best improvements approaching a factor $\sim$ 2.

5.5 Other Methods of High-Resolution Imaging

There are several other approaches to high-resolution imaging. These fall into four classes, those which use adaptive optics to correct higher-order distortions, those which use interference methods, the use of space based observatories and the use of computer image-deconvolution techniques.

5.5.1 Higher Order Adaptive Optics

An extension of the adaptive optics solution is to attempt to correct for higher order distortions, and, ultimately to flatten the full wave-front. These techniques have two variants, the 'modal' and 'zonal' approaches. The first analyses the wavefront by decomposing it, generally into Zernike polynomials. The lower order polynomials correspond to standard aberrations, such coma, tip-tilt and piston. To date most efforts in this direction have been aimed at near infra-red imaging where the technical problems are not as great as in the visible. (eg. Roddier, Northcott and Graves, 1991). The alternative 'zonal' approach is more closely related to the present MARTINI device (see §5.7), in that the tilt is measured independently over small portions of the wavefront. This may hold more promise for the future development of partial wavefront correction in the visible, given the status of current technology.

In either case, the form of the physical optics which flatten the wave-front, will have to be more versatile. One possibility is to use a segmented mirror, similar to the present MARTINI, but with considerably more moveable segments. Another is based on a flexible mirror which can be contorted so as to flatten the wave-front completely.

The obvious advantage of this approach is that it lends itself to utilizing the full aperture of the telescope, with the increased light-gathering and resolution that this provides. The disadvantage is that in order to monitor and correct the wave-front on smaller scales ($\sim r_0$), correspondingly brighter magnitude limits are imposed for the monitor. A prototype full aperture system, called COME-ON, has been successfully used to produce diffraction limited (0.″37) images in the L band (3.5μm) on the ESO 3.6m telescope (Reported by Beckers 1990).

5.5.2 Interferometric Techniques

Other high-resolution methods are based on interferometric techniques. For example, speckle interferometry was developed by Labeyrie (1970). In its original form, a series of very short exposures is taken of the object. These are used to produce a diffraction screen which is illuminated by a collimated laser, to produce, in effect, a fourier transform of the image. Although phase information is lost in in this method, these results can be used to infer aspects of the structure of the source.

Several, computer intensive, algorithms have been proposed to retrieve this information, in order to reconstruct true images. For a review of recent developments in this field, see Aitken (1989). We note only that these schemes are still restricted to relatively bright objects, and, unlike adaptive optics, cannot make use of monitoring objects.

Other uses of interference methods include those which are being developed for use with large, multiple aperture, ground based telescopes, most notably ESOs VLT. This project is to build four 8m class telescopes, which are arranged so that they will allow an interferometric mode of operation. One of the requirements for this system would be to use simpler forms of image-sharpening to produce near diffraction limited images, before combining the beams to form the final image. This project is reviewed by Lena (1991).

The COAST instrument, which is under development at the MRAO, is a less ambitious attempt to obtain long baseline, interferometric images in the visible. This instrument will ultimately consist of four 1m mirrors which image light to a common focus. Test observations, based on this principle, at the WHT, have resolved detail on the surface of the nearby red-giant Betelgeuse (Buscher *et al.* 1990).

5.5.3 Space Based Observatories

The advantage of placing telescopes in space is obviously that they are no longer affected by the atmosphere at all, but only limited by the entrance pupil diffraction, and optical aberrations. This

was the motivation behind the 2.5m Hubble Space Telescope, which was launched by the space shuttle in 1990. Unfortunately the expected performance, of sub-0.″1 resolution has so far not been possible due to the accidental inclusion of a significant amount of spherical aberration in the grinding of the mirror (eg. Groth 1991). Nonetheless, the present images are comparable with those produced by image-sharpening techniques.

5.5.4 Image Deconvolution Techniques

Optical images are conventionally regarded as a convolution of a true intensity distribution with a PSF, and the additional contribution of noise. Deconvolution techniques attempt to resurrect the 'best guess' at the true distribution from a given image, using knowledge of the PSF and a model of the noise. The criteria as to what constitutes the 'best guess' distinguish the different algorithms. For example, the 'Maximum Entropy' method (eg. Narayan and Nityananda, 1986), seeks to find the least structured image which would be consistent with the data, with the given prior knowledge.

The development of these techniques was stimulated by the advent of digital detectors and image-processing using computers. Particular interest has been generated recently with regard to their application to HST images. The relatively stable PSF produced by the HST, combined with its sharp central peak, lend its images to this analysis.

It is clear that deconvolution techniques should be regarded as a form of enhancement, by which information in the image is brought out and made more accessible to, say, the eye. Like any technique of enhancement we must take extra care in interpreting what is seen. Perhaps the principal use will be for object finding (see chapter 2) and subjective descriptions, rather than in answering quantitative questions.

5.6 The TRIFFID Camera

The TRIFFID (TRansputer Instrument For Fast Image Deconvolution) camera, was largely designed and built by Dr. Mike Redfern's group in Galway (Devaney 1989). It is based around a photon counting IPD device, which records the arrival positions of individual photons, and packages these events into 1ms frames. This data rate is amply fast enough to cope with the time-scales of atmospheric motion. Although it is ultimately intended to work in pseudo real-time, the data presented here is all post-processed to provide a final sharpened image. Apart from the advantage of allowing subsequent optimisation of sharpening techniques, the post-exposure approach has the advantage of allowing the algorithm to make use of 'future' as well as 'past' information, in tracking the image motion. At the present time, due to the lack of availability of fast, reliable shutters, it is also considerably easier to carry out frame-selection sharpening by post-processing the data.

The detailed design has evolved greatly during the series of observations discussed in chapter 6, so we will, in this section, deal with the most recent system, and discuss any notable differences in the sections describing the relevant observations.

5.6.1 Configuration on the Optical Bench

The Ground Based High Resolution Imaging Laboratory (GHRIL) is situated on one of the Nasmyth platforms of the WHT. This is a dedicated focus for the purpose of high-resolution experiments and observations. It is equipped with an optical bench and standard optical components. The TRIFFID (see figure 5.4) is configured so that the $f/11$ beam from the Nasmyth focus is first collimated by a 300mm telephoto lens (actually $f5.6$). There are typically the following components positioned in the $\sim$ 30mm wide parallel beam:

1. An atmospheric dispersion corrector (Dainty *et al.*). This device employs two, counter-rotating prisms, to optically remove the effects of differential refraction in the atmosphere on the images. If not used then this effect would elongate the PSF by $\sim 0.''3$ for broad band images at a zenith angle $z \sim 30°$.

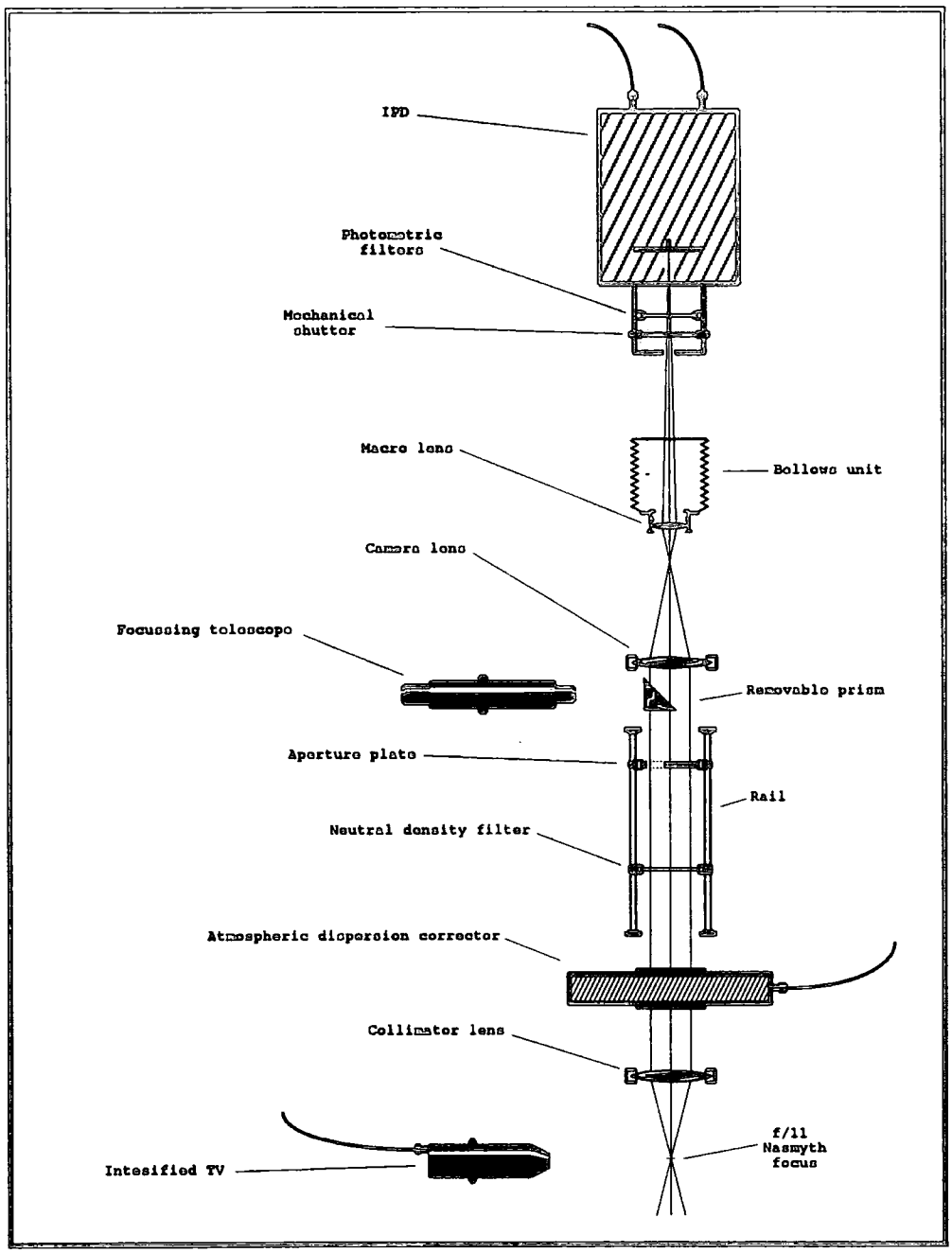

Figure 5.4: Diagram illustrating a typical configuration of the TRIFFID apparatus. The size and conjugate focus position of the aperture can be easily altered, as can the field scale. The focussing telescope and TV camera are used only for set-up purposes

2. The aperture plate. A range of sizes is available and also a double aperture for focussing purposes, as discussed below. The position of the plate determines the position of the conjugate focus.

3. Any filters which can't be put in the filter box; however these are placed carefully, at a slight angle to the beam, to minimise the possibility of ghosting.

The light is refocussed by another telephoto lens (actually 400mm, $f5.5$) to an $f/15$ beam. This is finally re-imaged by a macro-lens onto the IPD detector. This final relay lens is mounted on an adjustable bellows unit, allowing the field scale to be varied by adjusting the position of the IPD and refocussing the lens appropriately. There is a filter box immediately in front of the IPD housing, in which can be inserted spectral or neutral density filters.

Optionally an artificial star (created using an optical fibre) can be positioned at the main telescope focus. This was useful for focussing the back-end and investigating the saturation characteristics of the IPD.

The beam could also be diverted to an intensified TV camera for use in finding and, on one occasion, tracking faint reference stars. This arrangement also allowed the images to be easily recorded on video.

5.6.2 Position of the Conjugate Focus

The desired aperture plate is located in the 27.3mm diameter parallel beam. With this arrangement we are free to set the position of the conjugate focus of the aperture plate in the atmosphere. For practical purposes, the holder for the aperture plate was mounted on a rail, along which several standard conjugate focus positions were marked. Thus we can optimise the isoplanatic patch by attempting to match the conjugate focus to the average height of turbulence.

5.6.3 Alignment and Focussing of Components

This has proved a particular problem since, initially, the Nasmyth mirror flat was not correctly positioned, resulting in severe difficulties on our first TRIFFID run, discussed in chapter 6. Although subsequently the whole WHT optics were re-aligned, a careful setting up procedure was developed after that first run to ensure there would be no problems in the future. Firstly an alignment telescope was set up precisely looking down the centres of two targets marking the mechanical altitiude axis. This was then used to position each component in the optical train in turn. The artificial source was located on this axis, close to the nominal focus, where it could then be used to focus the rest of the optics. A further small telescope was at hand to check that the beam was parallel. Finally, the telescope itself was focussed onto the object by use of a double aperture Hartmann plate. This was placed in the parallel beam, with the result that the image on the IPD split into two, unless the focus was good.

5.6.4 Description of IPD

As mentioned previously the IPD photon counting device was chosen as the main imaging detector, primarily because of its high time-resolution, which is better than that of the IPCS or standard video cameras. Other advantages are:

1. it is considered to be linear up to its saturation point;
2. it has a reasonably flat response over the detector surface;
3. although delicate it is more robust than, at least, the IPCS;
4. A big advantage of the IPD is that, when cooled, it has a very low dark current of only around 30 events per second. This means that observations are generally sky noise limited even for the small apertures which are used in image-sharpening.

The disadvantages result from a combination of problems with the detector itself, and with the accompanying electronics box:

1. the spatial resolution afforded by the IPD, is less than ideal, having only about 100 resolution elements across. This meant that there was a strong restriction in field size of $\sim 30''$ if we were to retain adequate sampling of the PSF.

2. another problem with the IPD is its saturation characteristics. These arise due to a combination of detector dead-times. For the whole device this dead-time is only of the order of $\sim 1\mu s$; but for smaller areas estimates range from 10ms to 100ms. Clearly this might represent a big problem for the interpretation of control experiments since the FWHM for the bright stars would not be reliable.

   In fact the situation is better for actual astronomical observations since we could afford some saturation of the central reference star without having a too detrimental effect on the calculations of centroid position (as long as we did not risk it being so bright as to saturate the whole device).

3. the quantum efficiency is low compared to a CCD being only of order a few percent.

4. there are several cosmetic problems. The worst of these is a grid pattern, thought to arise in the electronics box. This grid consists of spurious events which have coordinates preferentially along lines and columns 128,128 etc. The grid is particularly strong near to bright stars and also in line with bright stars in the horizontal and vertical directions. It is not simply a flat fielding problem, and hence is difficult to remove.

5.6.5 Field Rotation

The rotation of the field at the Nasmyth focus is caused by the standard cassegrain field rotation, combined with that produced by the beam being diverted at a tangent along the altitude axis and hence depending only on the elevation of the telescope. The actual equations are as follows (eg. Devaney 1989):

$$\text{Cumulative Rotation} = \text{Parallactic Angle} + \text{Zenith Angle Increase}$$

Where:

$$\text{Parallactic Angle} = arctan\left(\frac{cos(\text{Lat})sin(\text{LHA})}{cos(\delta)sin(\text{Lat}) - sin(\delta)cos(\text{Lat})cos(\text{LHA})}\right)$$

and:

$$\text{Zenith Angle} = 90 - arcsin(sin(\delta)sin(\text{Lat}) + cos(\delta)cos(\text{Lat})cos(\text{LHA}))$$

Although optical derotators were available for the later runs, the extra light-loss they would have contributed made it worth-while to take the rotation out in the reduction process.

5.6.6 Data Acquisition System

This is described in detail by Devaney (1989), who also wrote the control software for the instrument. The data were gathered with an INMOS T414 transputer system with three FIFOS, and stored on an IBM PC hard disk. The saturation rate of the interface was 60k events per second. Our data were recorded as a series of (x,y) coordinate pairs. These were grouped together in 1ms frames. Initially each (x,y) address comprised a pair of 9 bit words, but later the least significant bit was dropped. This gave, then, 256 pixel resolution, which is fairly near to the nominal 100 element resolution of our IPD.

The data were transferred to the Durham Starlink VAX system in this byte format, prior to the analysis. To facilitate calculations it was then processed again to a two-byte integer format, held in a customised Starlink HDS file. This allowed us to use fortran integer arithmetic for the manipulations. The software written to perform the subsequent analysis, is described in appendix C.

5.7 Description of the MARTINI Instrument

MARTINI, or Multiple Aperture Real Time Image Normalisation Instrument, uses adaptive-optics to correct for the global image motion seen in time resolved images of astronomical objects (Doel *et al.* 1990). The prototype system has been developed in Durham by a team under the late Dr. David Brown and Dr. John Major. The advantages of this method over the post-processing approach is that it allows use of high efficiency integrating cameras.

5.7.1 Configuration of MARTINI

The MARTINI instrument (figure 5.5) also makes good some of the light loss which arises from the requirement of stopping down the aperture to something approaching the Fried optimum. It achieves this by virtue of using six sub-apertures and normalising the image from each independently. Thus in good seeing, with $r_0 \sim 20$cm, the effective collecting area is that of a 2m telescope. From the $f/11$ Nasmyth focus of the WHT, the light is incident on the ring of six small mirrors. These are moveable by means of three piezo-electric actuators attached behind each mirror. These, in turn, are situated behind an aperture plate, which provides a choice of eight apertures in the range 42cm to 133cm. The light path is then folded, for reasons of compactness, by means of a toroidal mirror, which refocusses the light to an off-axis image.

At this focus (or shortly before it) the beam is split, one portion to the integrating CCD camera and the other to the photon counting IPD device. This division of the light can be done in several ways, and is discussed in more detail below. The light which is sent to the CCD passes through a camera-collimator arrangement. This provides a parallel beam for the insertion of an atmospheric dispersion corrector and filter wheel. It also serves to allow an adjustable field scale by means of simply altering the focal length of the camera lens.

The light from each sub-aperture/mirror is focussed onto a separate area of the IPD detector surface, by means of a split lens. Thus the IPD monitor sees six independent images of the monitoring object, in a hexagonal arrangement. The IPD has a time resolution of $\sim$ 100kHz, and a spatial resolution of $\sim 0\farcs03$ in its normal configuration. The coordinates of each photon arrival

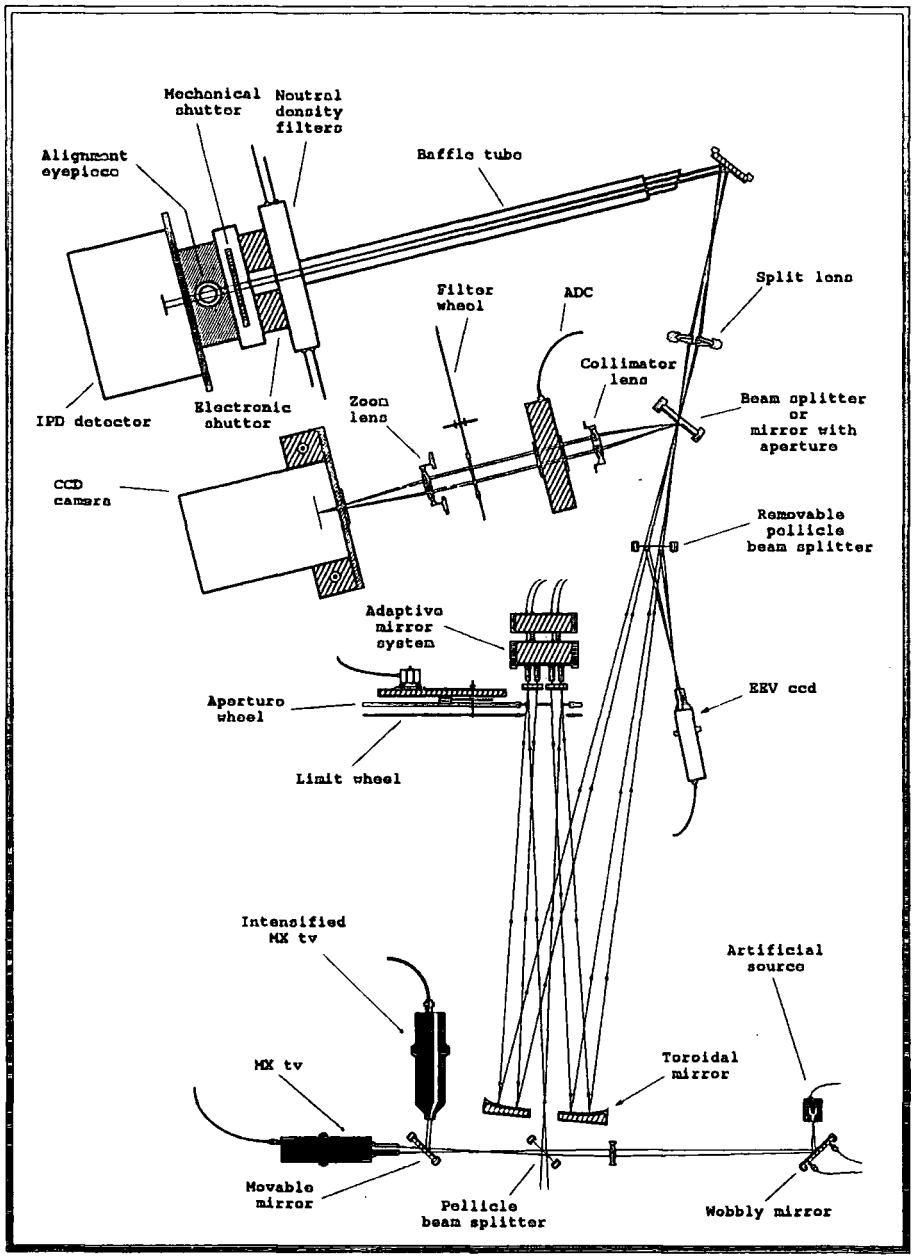

Figure 5.5: Diagram illustrating a typical configuration of the MARTINI apparatus. The light from the telescope enters from the bottom to be focussed in the centre of the toroidal mirror. The precise configuration may be altered to accommodate different beam-splitter arrangements etc.

event are sent back to a computer which then attempts to track the image motion and hence feed this information back to the adaptive mirrors.

It should be noted that the conjugate focus position for the MARTINI instrument is fixed by the design, and hence the isoplanatic patch cannot presently be optimised experimentally. The actual position is conjugate to a height of 3.5km above the telescope, which was chosen as being the best compromise.

5.7.2 Modifications for Faint Object Work

The original MARTINI design used an optical beam splitter to divide the light between the CCD and IPD. This is an appropriate arrangement in the situation in which the monitoring object is of intrinsic interest. However, for faint object work, when the monitor is simply a fortuitously placed foreground star, it has several disadvantages:

1. some of the light from the target is diverted away from the CCD requiring proportionally longer integration times.
2. some of the light from the monitor is diverted from the IPD meaning that brighter monitors are needed to achieve the same sharpening.
3. the light from the bright monitor, which is registered on the CCD may often saturate a portion of the device leading to cosmetic problems on read-out.

In response to these problems it was decided to manufacture a mirror with a small hole in its centre, which could be used as an alternative to the beam-splitter. In this configuration the light from the monitor passes through the hole to the IPD and the remainder goes exclusively to the CCD. A prototype version of such a mirror was tested in the March 1990 run, but was unfortunately found not to have met the specification. Thus we had to resort to a 70:30 beam splitter, which resulted in a factor of ~ 3 less in signal to noise ratio over what we had hoped for. A new mirror was subsequently tested in November 1990 and performed well. Another solution to some of these problems is to use a dichroic beam-splitter which diverts shorter wavelengths to the

blue sensitive IPD leaving the longer wavelengths for the CCD. In some circumstances this has the advantage of leaving the monitor star image on the CCD.

The MARTINI CCD itself is currently an uncoated 'B'-grade GEC chip, which has shown itself to have poor cosmetic qualities as well as being insensitive shortwards of 5000Å. For the 1991 run this was replaced by a large-format, blue-coated EEV chip provided by the observatory.

5.8 Techniques of Post-Exposure Analysis

There are two orders of image-sharpening which have been applied in post-exposure analysis of the type of data acquired by TRIFFID. Firstly, there is that of centroid correction, to remove image motion, in essence the same as MARTINI tilt correction. Secondly, there is a smaller investigation of the application of 'lucky-exposure' selection to include only periods of particularly fine seeing in a final integrated image.

The computational questions which must be addressed in carrying out these procedures are:

1. How should one calculate the displacement of a given frame from the nominal position?

   This splits into two problems: how should one use the photons on the frame to calculate an offset? and how to use the noisy sequence of offsets from the frames prior and subsequent to the frame of interest, to obtain a more confident offset?

   The latter of these questions has been considered in detail by Redfern *et al.* (1989) who describe the use of a modified Wiener digital filter to optimally extract the true signal of the image motion from the noise. Such filters have been employed on this data, with the parameters either input or determined by a variety of heuristic optimisation techniques. A variety of simpler filters, such as a running mean, have also been investigated, on our data.

   The question of the best way to determine offsets has also been addressed. Basically there are two possibilities: firstly, one could calculate centroids for one or more bright monitoring objects on the frame and use this information to deliver an offset. This is essentially the MARTINI approach. There remains a choice in the method of windowing on the object to

calculate the centroid. This method must be efficient since the number of photons in the centroid determination may be low. The methods which have been tried are a top-hat window function, a triangular window function, and a gaussian weighting function. In all cases it is important that the window follow the centroid fairly closely to take out the longer term motions. Of these, the top-hat function frequently showed evidence of statistical sharpening, in that the window function could clearly be seen in the final image (although this had very little effect on the achieved seeing.) The two weighted functions got over this problem.

Secondly there is the option is to create a mask, from an integrated image, and to cross-correlate each frame in turn with this mask, selecting the strongest signal to be the true offset position. This is particularly good in the case of objects such as globular clusters, where there may not be a single bright object to monitor on.

2. How should one obtain an estimate of the seeing in a frame?

   This is easiest done in the case of a monitoring object by calculating the standard deviation in the photon positions at the same time that the centroid is calculated.

   In the case that the cross-correlation technique is used an estimate of the quality of the frame, for the purposes of frame selection, can be taken from the strength of the signal, normalised to the number of photons. This said, one should also take into account the number of photons in the frame, since that determines the confidence we have in the statistics.

   In both cases we note that the most important requirement is to get a measure of the relative seeing, for use with frame selection and to gauge stability of conditions. The actual seeing is much better derived from the final integrated image.

3. Can one be sure that there is no contribution of self-sharpening? That is to say; if the photons used to obtain the statistics are also used in the final image then there is a non-independence in the values of the final seeing.

   In principal, this problem can be largely overcome by separating, randomly, the photons in a frame into two independent groups. The larger group can then be used to calculate the offset and the smaller can contribute to the final image. This can be considered to have the same

effect as the beam-splitter in the MARTINI system. If a large proportion is chosen to go into the calculation group, typically 90%, then the quality of the sharpening is not affected.

The smaller group will frequently contain too few photons to create a satisfactory image, so, either it is just used to test that the sharpening process does not input significant self-sharpening, or the beam-splitter process can be repeated to create further images which can be coadded.

Before assessing the final improvement with image-sharpening, as a function of the techniques used and the statistical quality of the data, we should also be aware of the following effects which we would like to be able to disentangle:

- Telescope/instrument motion included in the unsharpened image, which enhances the apparent improvement after sharpening.
- Seeing conditions changing on time scales shorter than an individual long exposure or series of exposures.
- Contributions from the local atmospheric motion; ie. dome/mirror seeing.
- Problems with focus of instrument.
- Properties of the detector, such as resolution, non-linear response and dynamic range, stability and integrity.
- Optical aberrations in the telescope and instrument which may be position dependent.
- Differential atmospheric refraction.

These must all be considered along with the parameters of the atmospheric theory, in evaluating the results. Having said this, in our work on the technical aspects of image-sharpening, using bright multiple star systems, we have concentrated on an empirical analysis. That is to say we hope, in the main, to consider the question of what would be the actual advantages and dis-advantages to an astronomer using image-sharpening, over normal methods of observation. This is as opposed

Chapter 6

Technical Investigations of Image-Sharpening

6.1 Introduction

As implied in the previous chapter, there are two motivations for technical investigations of image-sharpening. The first is to ascertain the ultimate potential of the method and to compare this to the theoretical predictions. The second is the evaluation of the actual gains to be made, and constraints involved in, using current image-sharpening technology for real astronomical observations. Both necessitate the optimisation of the algorithms employed in the sharpening procedure.

The data on which this program is based were gathered exclusively using the TRIFFID, over several observing seasons. The main results of this program come from data obtained in February/March 1990 (§6.3), however, we also include a shorter discussion of earlier results, which also contributed to our understanding of the technique and in the development of the instrument.

6.2 Early Observations - 1988,1989

In April 1988, we were allocated time, on a good-seeing override basis, during the commissioning period of the WHT. Our intention was to investigate the potential of astronomical image-sharpening. At the same time we made the first attempts at image-sharpening observations of two Virgo Cluster galaxies. These observations were, in fact, the first light at the GHRIL.

In April 1989 we were allocated two discretionary nights to further develop the prototype TRIFFID camera. In the event, both of these nights were lost to bad weather, although some useful testing was possible on the optical bench. The main part of this section is, therefore, concerned with the 1988 observations.

6.2.1 Observing Procedure

The observing procedure was determined in part by the special conditions governing our time allocation. For six successive nights it was first decided whether or not there was any observational potential, both in terms of the weather and also the status of the hardware. On four of these nights we went on to conduct a 'seeing' test. This consisted of acquiring one or two double stars using the normal TV camera and with the full 4.2m mirror, which we usually proceeded to video for future reference. These were chosen from catalogues so that their separation was such as to give a good indication of the quality of the 'seeing'.

In particular, on each occasion we observed a double star ADS8231 with a listed separation of 0.5″. (Redfern (private communication) subsequently analysed this data, from the video of night 1, putting the separation at $\sim 0.65''$. The same recording gives an estimate of 'seeing' of 0.4″ for a 5s integration. This is exceptionally good for an uncorrected image.)

For three of these tests this double star was clearly resolved, and the 'seeing' was then judged to be better than 0.″75, as stipulated for our override. We were then left in control of the telescope for the remainder of a four hour period, which began at the start of the 'seeing' test. In fact we gathered useful data on the first two of these sessions, but on the third were subsequently wiped

out by cloud. The very best conditions, by eye and backed up by the video record, were on night 1 when we observed '7°27''. The second night we observed NGC4639, but conditions were then not so good. On both occasions the objects were fairly near the meridian which is very desirable to cut down the effects of the atmosphere, in particular that of differential refraction.

Unexpected problems were encountered due to residual misalignment of the WHT optics, most severely the Nasmyth flat. The upshot of this was that it was very difficult to acquire and guide on the objects, especially given the small (~11.″7) field of view of the IPD. In the end we had to use the approach of locating nearby bright stars and blind offsetting from these in order to obtain the faint monitoring objects. Having found the object in the intensified TV we made final adjustments in order to centre the reference star in the IPD. We then attempted to focus by eye using the oscilloscope display, as, at that time, no more precise method was available.

We selected the subaperture of 1.4m which corresponds to a Fried optimum r_0 of around 35cm. This was regarded as a reasonable compromise between our desire for sharp images and our requirement of adequate signal. During exposures one observer was left in the GHRIL cage as guiding had to be done with the handset, by following the object using the intensified TV.

In order to retain as high a count rate as possible, the observations were performed without a filter. In fact the response of the IPD itself runs from about 4000Åto 6500Å, peaking at 5000Å (eg. Doel 1990). The flat field, obtained during morning twilight, showed little small scale structure, but could not be used to calibrate large-scale sensitivity variations since there was evidence of some light leak.

6.2.2 Results and Examination of the Raw Data

In most of our analysis we are primarily concerned with '7°27''since it had the best conditions and also the brightest reference star which meant that we could be more confident of the quality of the statistics from that run.

To begin with we can gain some insight from examining the data directly. In figure 6.1 we have

plotted the X position of the star centroid, determined in 5ms bins, for two separate 5s sections of the data. This reveals that early in the run there is a significant contribution to the motion by resonant oscillations, which subsequently damp down. This is most likely due to vibrations of the GHRIL enclosure itself whilst people were leaving it early in the run. These regular ($\sim$ 4Hz) vibrations are also evident when one simply views a 'movie' of the results. The residual, presumably largely atmospheric motions, appear to be very small.

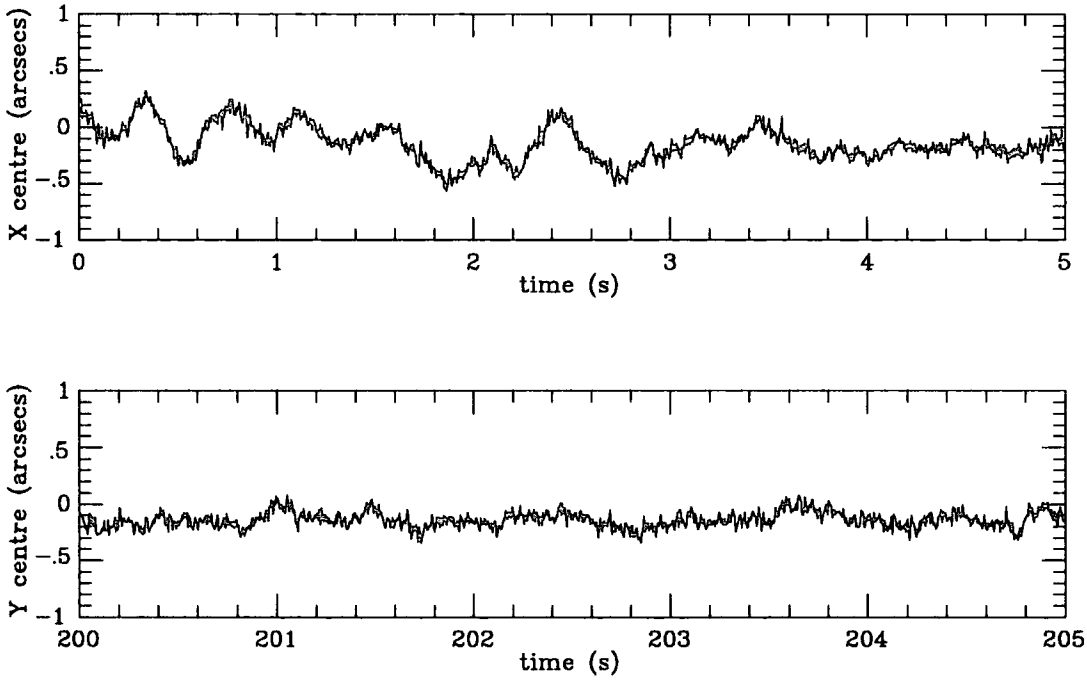

Figure 6.1: Graphs showing the centroid motion in one direction for two five second data sets of the '7°27''data. The first is at the start of the run and shows the regular vibrations imprinted on the seeing motion. The second is 200s into the run after the vibrations had damped down. The centroids displayed here were determined for 5ms frames.

The autocorrelation function of the centroid motion, after the vibrations had died down, is shown in figure 6.2 This shows a fairly long correlation time (half life) of around 0.2s. This is consistent with the low wind on that night.

It is also of interest to examine the photometric stability, indicated by the plot of photon arrival rate for the first 300s of the run (figure 6.3). This shows that the rate was fairly constant, with

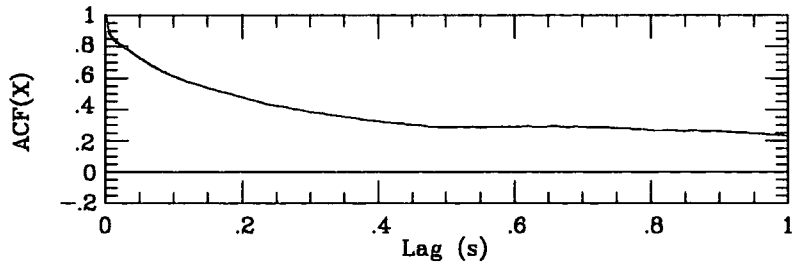

Figure 6.2: Graph showing the auto-correlation function of centroid motion in one direction for a stretch of the '7°27"data, after the initial period which showed regular oscillations.

only small fluctuations, which is again consistent with the good conditions.

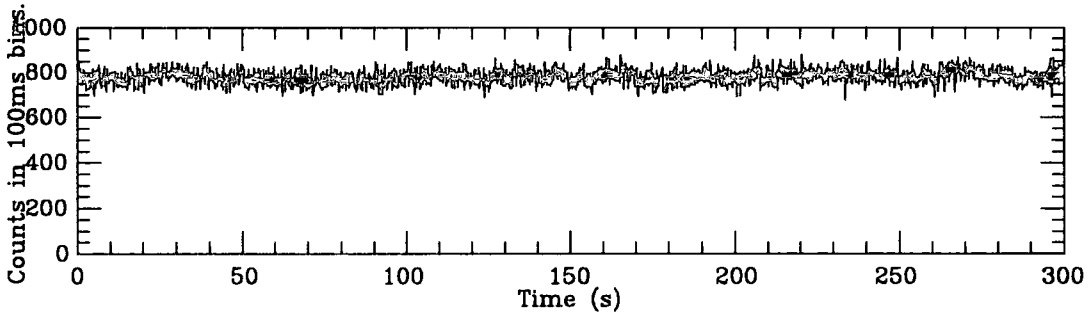

Figure 6.3: The count rate in 100ms bins for a 300s section of the '7°27"data. This shows that the photometric conditions were fairly stable, with only small short-scale fluctuations.

There were two anomalies evident in the data due to electronic problems. Firstly, there was a 'grid' effect where some extra, spurious counts were recorded preferentially in certain rows and columns. At least some of these extra events arose when a photon was apparently counted twice. Although this effect was also seen in the flat field, its severity depended in a complex way on the objects in the field, and hence it could not be calibrated out. The second anomaly, which was probably due to a buffering problem, manifested itself as a unusually high count in a 1ms frame, roughly every 10000 events, followed by several frames with a low count. Both of these effects, once understood, were adequately accounted for in the software analysis.

6.2.3 Sharpening Analysis

In terms of the sharpening procedure, the long coherence time means that we are able to use relatively long periods to evaluate the star motion and hence will not suffer from the effects of noise in the centroid determination. This also means that we should be insensitive to the precise choice of sharpening algorithm, which indeed turned out to be the case.

The actual improvement achieved was from 0.″50 FWHM for an image with just the long term telescope drift removed, to 0.″43 for the sharpened image. This level of improvement is consistent with the small amount of motion seen in the centroid plots shown above. Taken at face value, the unsharpened result corresponds to r_0 ~25cm, in which case our sub-aperture is around 5-6 r_0. The standard predicted improvement (Fried, 1966) would still be a factor of ~ 2.

There are several possible reasons why we have failed to achieve this. Firstly, it may have been that on this night there was a small outer scale of turbulence, which effectively reduces the long exposure image size for a given r_0. Secondly there could be problems with optical aberrations due to the provisional optical alignment of the telescope. Finally, there must be a possibility that we were not in perfect focus, due to the eyeball procedure which was employed. This latter point is backed up by the superior results obtained with the video camera and also by a lack of time correlation of image-widths.

Using the statistics from the full half hour, derotated, image, we calculate that the signal-to-noise ratio for a $B \sim 21.5^m$ star would be around 5σ. Although this is reasonably deep, given the small field of view and that much of this is taken up with the image of the monitoring star, it is not surprising that no other objects were detected to this limit.

In the case of NGC4639, the seeing deteriorated by the time we started integrating to 0.9″. This meant that the aperture of 1.4m was now much less well matched, and that the small improvement of only around 8% could be explained because of that.

Finally, it is interesting to note that not only were the atmospheric conditions very favourable, particularly on night 1, but that, in addition, the air temperature was relatively warm which may

have helped to reduce the contribution of local turbulence or 'dome seeing'.

6.2.4 Developments of the TRIFFID Camera.

In consequence of the 1988 and 1989 runs several developments were made with the TRIFFID camera. Firstly, the initial catadioptric lenses were found to limit the field of view to a maximum of 18″ and so were replaced by commercial camera telephoto lenses. Secondly, an SLR Macro lens was used, in conjunction with a belows unit, to give a offer a variable field scale. Thirdly, mounts for the various optical components were manufactured to ensure correct internal alignment within the instrument, and, by means of a sliding rail, to allow a variable conjugate focus position to be selected for the aperture plate. Fourthly, an optical fibre attached to an LED was used to provide an artificial star, which then became the primary alignment and focussing reference. Finally, a new, two-hole, aperture plate was manufactured, to enable precise focussing via a Hartmann method, described below. These improvements combined to greatly increase the speed and reliability of the set-up and alignment procedures.

In April 1989 we also had the opportunity to test the linearity of the IPD. In principle this device suffers from saturation due to both a device dead-time and a pixel dead-time after detections. Now, in fact, the device dead-time is very short, in the region of $10\mu s$ and so is unimportant for our typical count rates, which are usually less than $10000s^{-1}$. Saturation due to the pixel dead-time is a more likely possibility, particularly on occasions when the field of view is large. This will have the effect of flattening the tops of bright stars, and, hence, artificially degrading the measured resolution. In order to quantify this effect we used the artificial star image and monitored the count rate as a function of the neutral density in front of the IPD. Because this image is naturally flat topped it was possible to translate this rate into a rate per pixel. This is plotted in figure 6.4, and it shows that the device is linear to rates of about $50s^{-1}$ in a pixel, and thereafter becomes increasingly saturated.

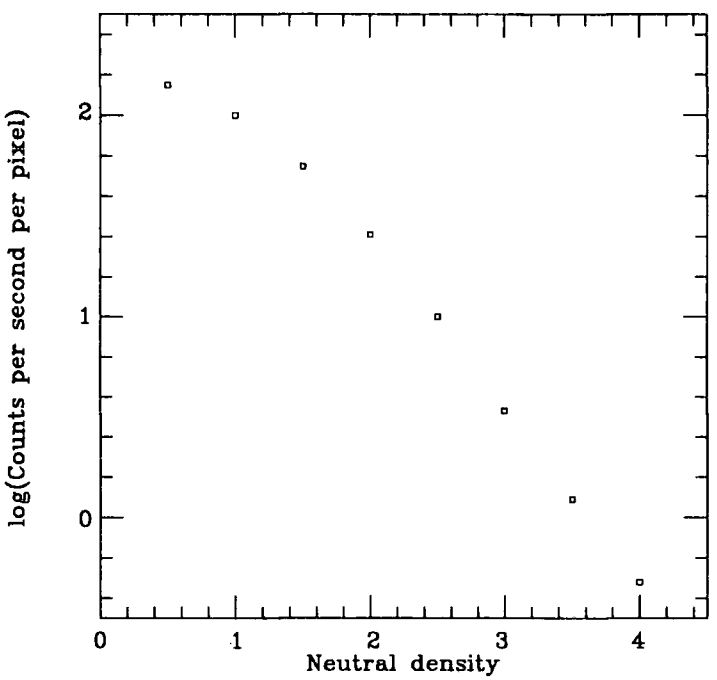

Figure 6.4: Plot showing the variation of detected count rate per pixel as a function of the amount of neutral density in front of the detector. This shows that the device is linear up to about 50 counts per second in any single pixel. Saturation becomes serious as one approaches 100 counts per second in a pixel. Note that an increase of 1 in the neutral density index does not in this case correspond to a factor of 10 in attenuation, presumably because they are not strictly neutral out to red wavelengths.

6.3 TRIFFID Observations, February/March 1990

These observations were conducted on three and a half nights from the 3^{rd} of February, and two nights from the 3^{rd} of March. The first night was officially grey, but, thereafter the time was bright. One full night was lost to the weather, and all other nights suffered from periods lost through cloud. Most of the observations were conducted in high wind and some of them with patchy cloud cover. For this reason we must show a degree of caution in drawing general conclusions, particularly from the worst affected data.

Special care was taken, before and during these runs, in developing reliable focussing procedures during this run. A Hartmann type method was adopted using a double aperture plate, placed in the collimated beam. When this was observed out of focus, separate images of a test star were seen. The telescope focus was tracked through its nominal position and the separation of the images noted. Care was taken to only track in one direction, since tests appeared to show a small amount of backlash.

All observations were conducted with a B filter, and neutral density was employed to equalize the count rates in different apertures. This was to ensure that statistical noise would have little effect on the differences between the results in each aperture.

The main systems which were observed are listed in table 6.1, and shown in figures 6.5 to 6.9. These maps in fact show the data unsharpened but with long term (> 10s) motion removed.

In the following sections we draw upon this data to attemp to answer some of the questions raised in chapter 5. In particular, we want to validate the predictions of seeing theory in terms of the resolution gain and the isoplanicity. We also want to develop the computer algorithms in order to deliver the maximum gain in circumstances in which there is only a low count rate from the monitoring object.

System	RA(2000)	Dec(2000)	Night	Exposures	Notes
ADS7187	09^h07^m	$+22°58'$	4 Feb	16× 60s	High wind, cloud.
ADS8495	12^h17^m	$+39°36'$	4 Feb	12× 60s	High wind, cloud.
ADS4186	05^h35^m	$-05°23'$	5 Feb	20× 60s	(Trapezium) Cloud towards end.
ADS6650	08^h11^m	$+17°38'$	6 Feb	9× 120s	Good conditions.
M67	08^h51^m	$+11°45'$	4 Mar	7× 120s	Fair conditions.

Table 6.1: Basic data for the multiple star systems observed in the program of technical image-sharpening investigations.

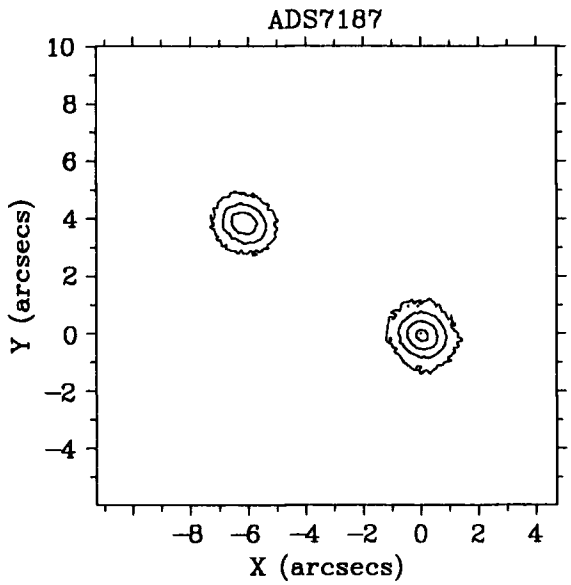

Figure 6.5: Map of ADS7187 binary system.

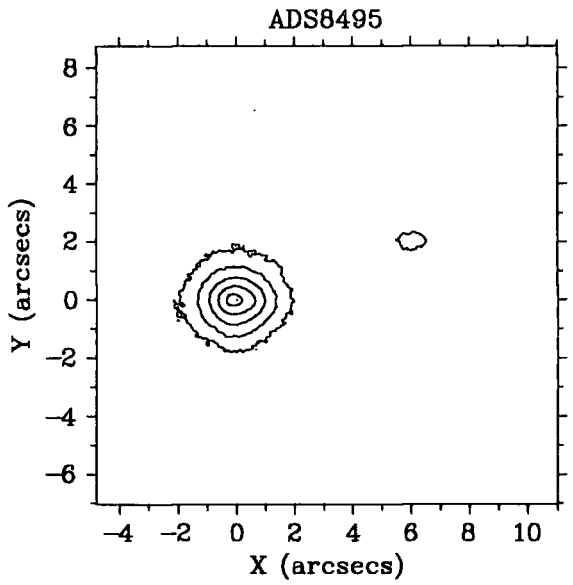

Figure 6.6: Map of ADS8495 binary system.

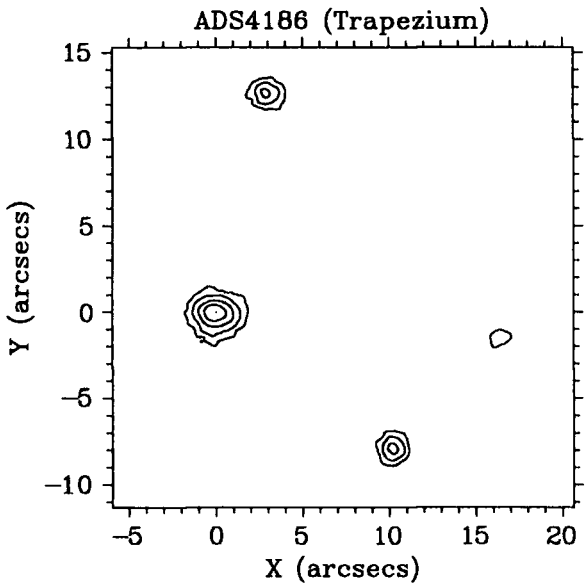

Figure 6.7: Map of ADS4186 quadruple system.

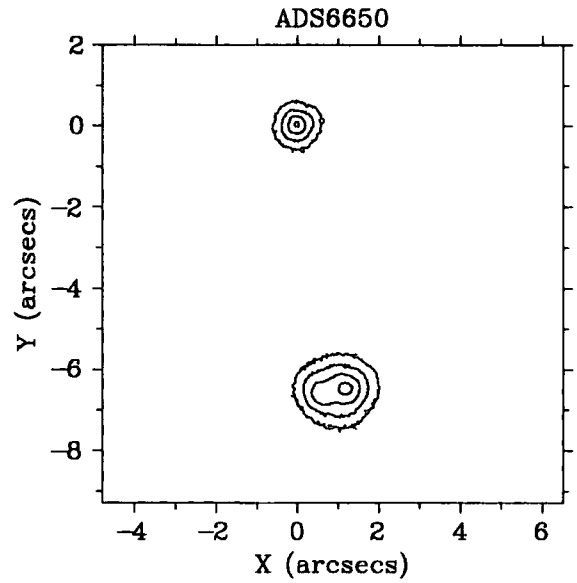

Figure 6.8: Map of ADS6650 triple system.

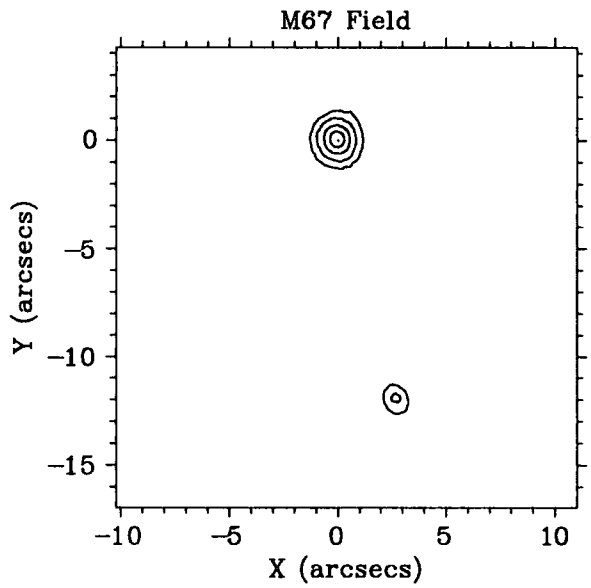

Figure 6.9: Map of M67 field around photometric standard star Schild 108 (Schild 1983).

6.3.1 Time Series.

We first present basic time-series graphs for one exposure for each object. The exposures are chosen to be ones showing better sharpening gain, but are in other respects typical. The plots give some evidence of the stability of the conditions, in terms of transparency and seeing, and also give an indication of the expected improvement from the relative amount of motion compared to the short exposure widths. The following points should be noted in interpreting these plots:

- The count rate is that in 100ms bins.
- The X centroid position is that determined by the filtering algorithm.
- The auto-correlation functions are determined more sparsely (every 100ms) after the first 0.5s.
- The time-series of the centroids is made stationary for the purposes of the ACF, by subtracting the 10s running mean from the data.
- The dispersion is shown in 100ms bins and is calculated around the filtered centroid positions.
- Since the dispersions are calculated within a window a value for the FWHM of the image is not implied. The interest in this plot is in the variations of the seeing.

ADS7187.

In this instance (figure 6.10) the rapidly varying conditions and patchy cloud manifest themselves in a fluctuating count rate and seeing (around 1″). The correlation time for image motion is relatively short, consistent with the strong wind that night. The correlation time for the image width is actually quite long due to the long term changes in the seeing, however there is also evidence of somewhat increased correlation at very short scales, which is likely to be due to the predicted, 'lucky exposure' type fluctuations.

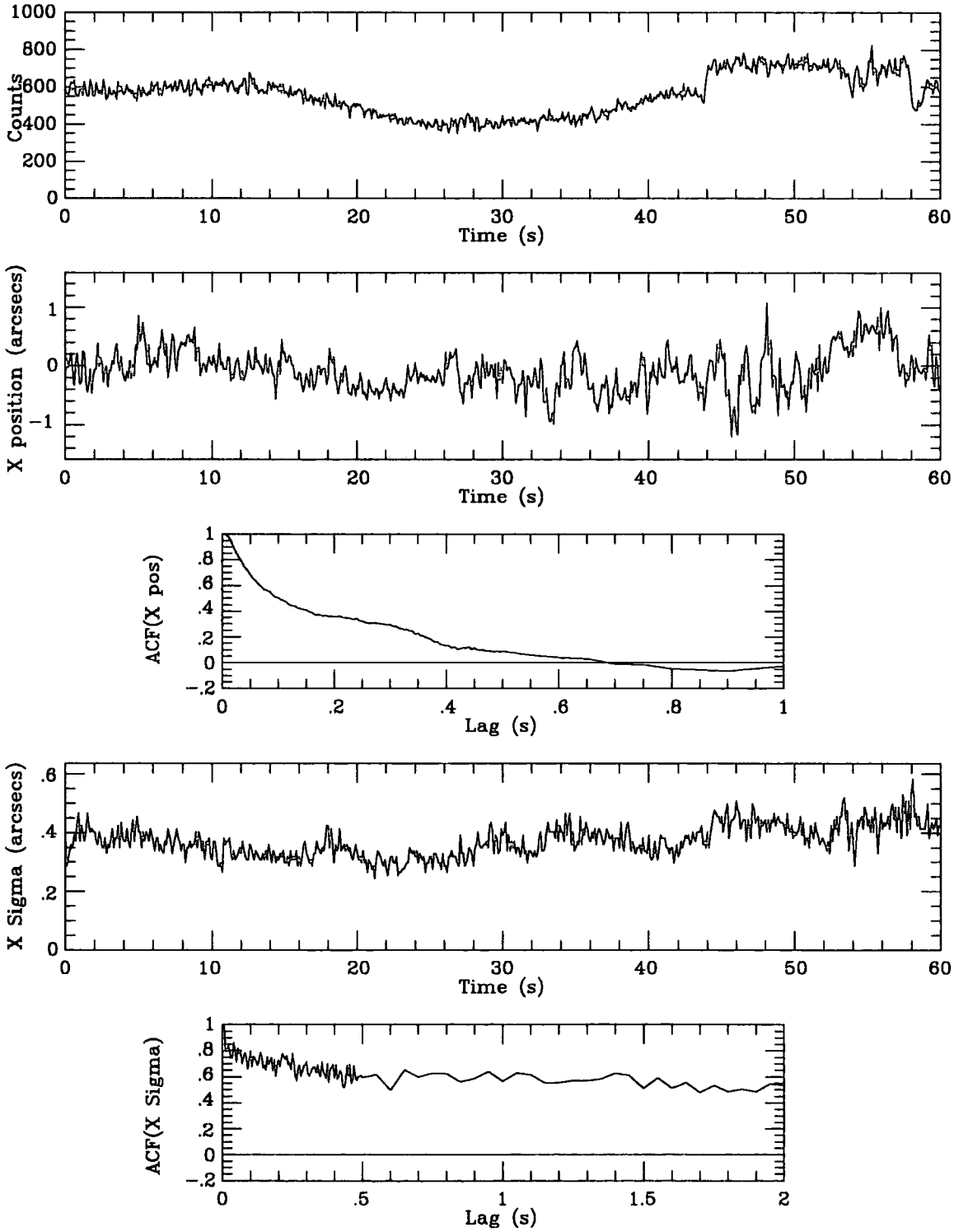

Figure 6.10: Time series data for one observation (50cm aperture) of ADS7187. Note the variable count rate and width of the star.

ADS8495.

Observations of this system (figure 6.11) also suffered the same problems of varying conditions as those of ADS7187, although, in this instance, the particular run shown is one of the better ones. The short correlation times for image motion and image width are again apparent, as is the extended tail on the image width ACF due to longer term seeing changes.

ADS4186

Although generally somewhat better conditions than the previous observations, the count rate varies dramatically during the particular run shown here (figure 6.12). Fortunately the correlation length is a little longer, for both motion and width, and shows less evidence for long term variations of width. The images of this system were noticeably affected by distortions, probably from the optical apparatus, and so the widths may not be representative of the actual seeing.

ADS6650

This triple star system (figure 6.13) is a nice test object for image-sharpening. It consists of a tight double of $\sim 0.6''$ separation, and a more distant ($6''$) single object. The interest lies in the visual appearance of the separation of the close pair when sharpening is performed on the isolated star.

Conditions for this run were notably better, reflected in the stability of the counts and width, and the long correlation time for image motion and width. This suggests that these data would be a fairer test of the potential of image sharpening in 'typical' good observing conditions. The ambient seeing was around $0.''6$ to $0.''7$.

M67

These observations were also obtained in fairly stable conditions, and again the coherence time is long, at least for centroid motion (figure 6.14). The relatively low count rate for these observations mean that there may be some loss of sharpening due to insufficient statistics. The unsharpened

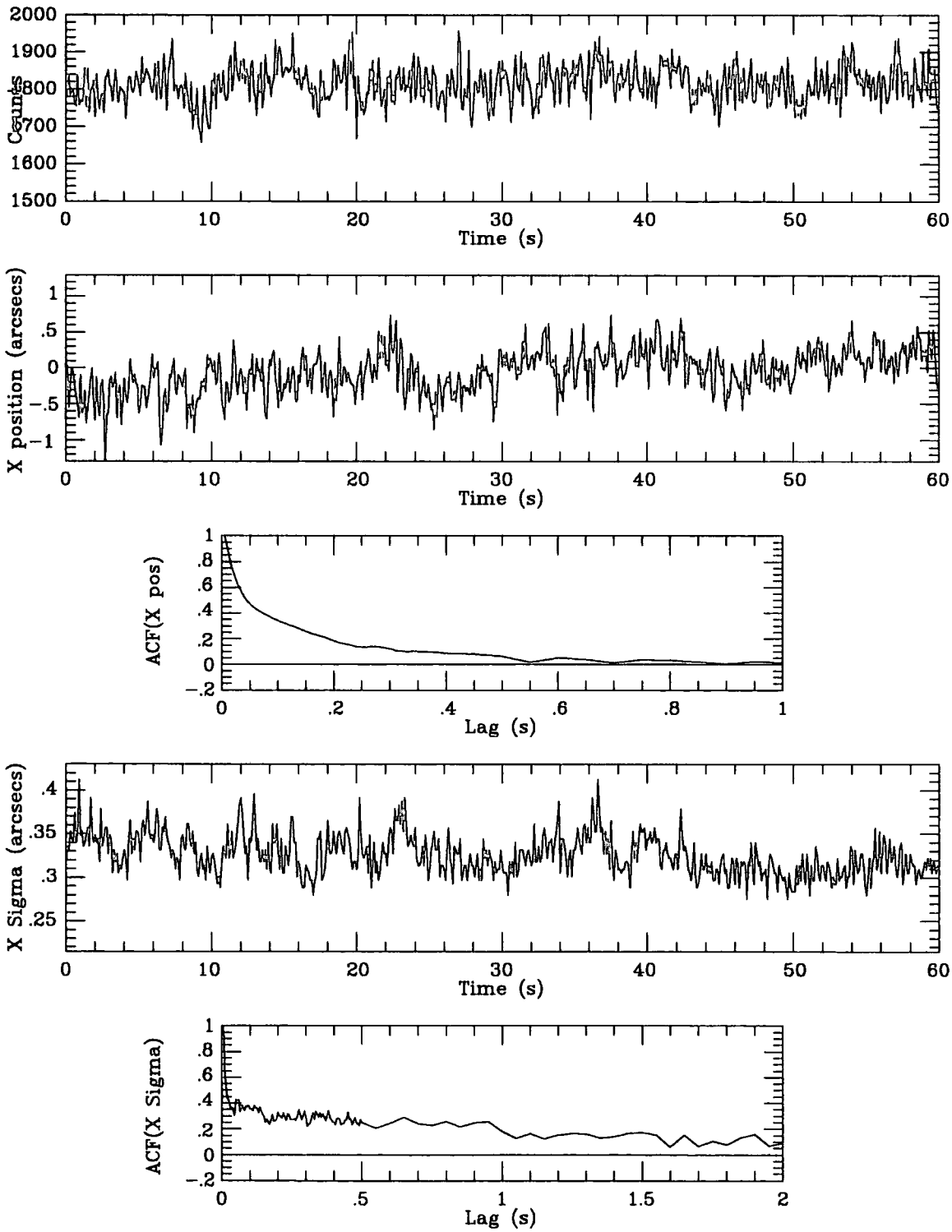

Figure 6.11: Time series data for one observation (25cm aperture) of ADS8495.

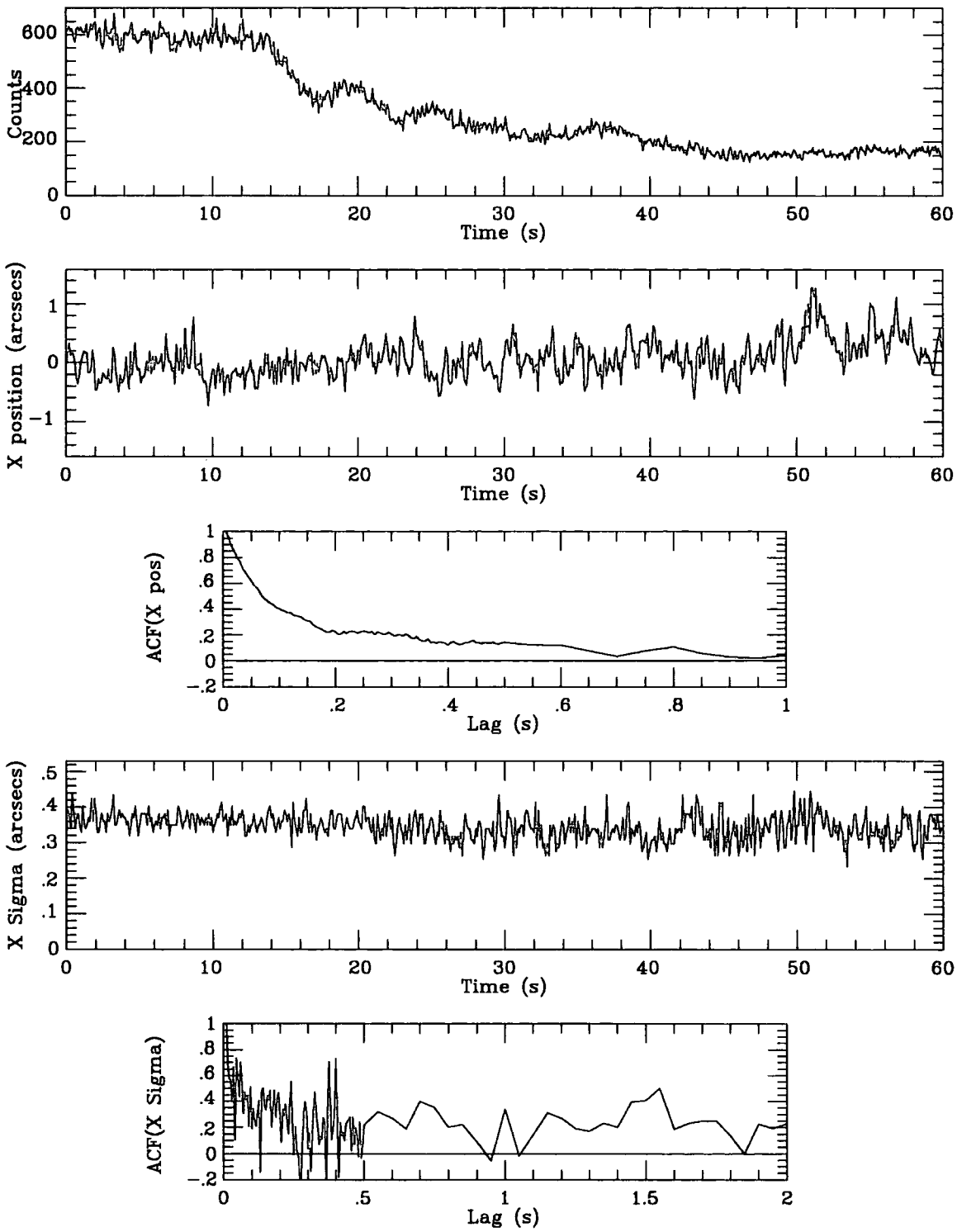

Figure 6.12: Time series data for one observation (25cm aperture) of ADS4186 (The Trapezium).

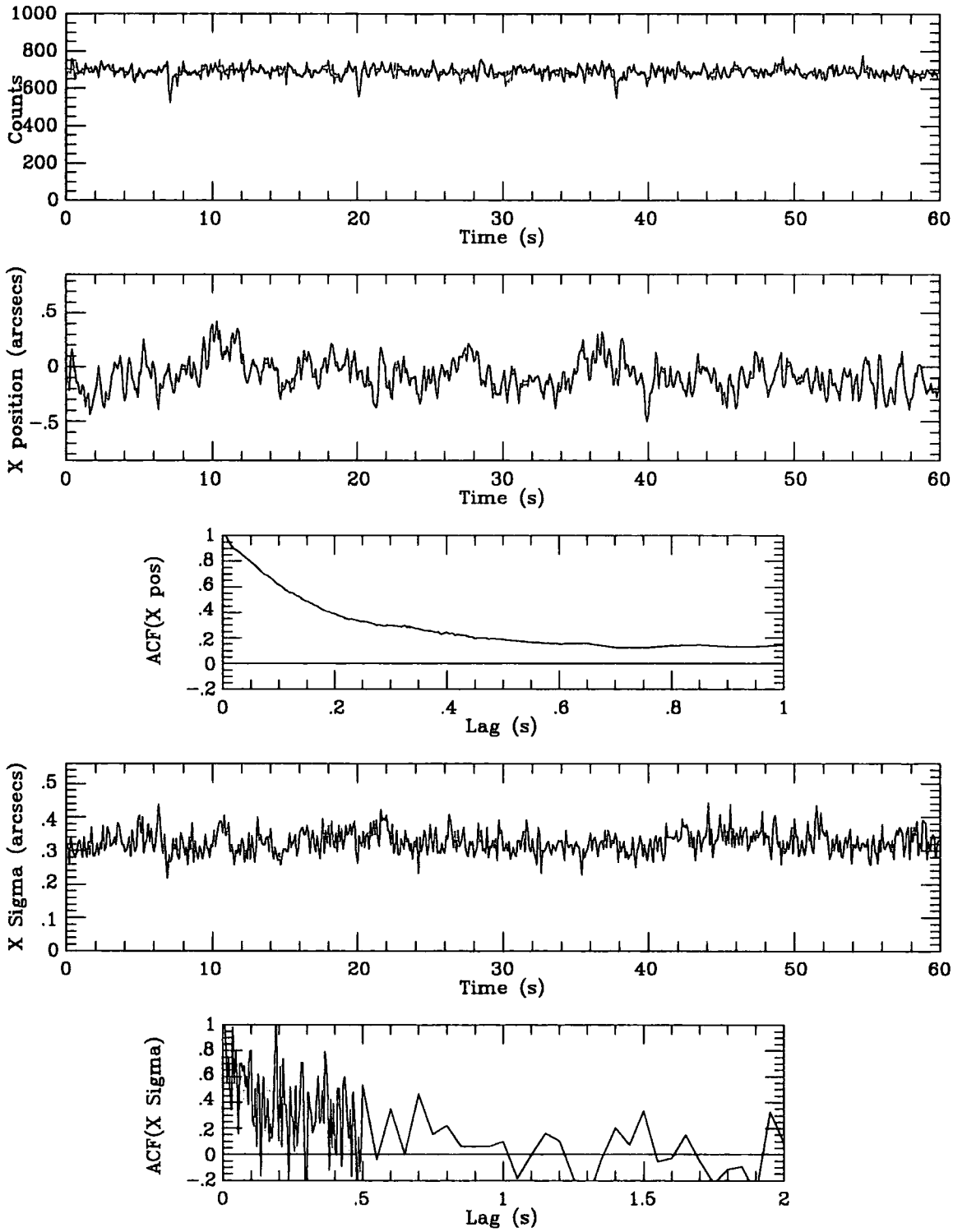

Figure 6.13: Time series data for one observation (50cm aperture) of ADS6650. Note the particularly long correlation length for image motion.

seeing for these observations was around 1″.

6.3.2 Dependence on Size of Aperture.

As shown above, most of our observations suffer from the ambient seeing varying on time scales less than the series of exposures, and in some cases, within a given exposure. In these cases the comparison of resolution improvement with seeing theory predictions is not clearly seen in standard plots. An alternative comparison, which is less affected by these problems, is to plot instead the ratio of sharpened to unsharpened seeing as a function of aperture. These graphs are shown in figures 6.15 to 6.18. In each case, the unsharpened seeing is actually found after passing a 10s top-hat filter through the photon event data in order to remove telescope tracking errors. We should note that with this plot the minimum sharpening ratio is not necessarily at the optimum aperture, since the unsharpened seeing is also expected to have a small aperture dependence.

For each data set we have plotted a theoretical curve which is a reasonable fit to the points. The curves have three parameters, Fried's r_0 seeing parameter, the outer scale of turbulence L_0, and a constant base level which is added in quadrature to the seeing. The base level is intended to reflect effects such as optical aberrations or local seeing which are increasing the measured widths. The three parameters are constrained such that the long term, large aperture seeing must be consistent with the average of the raw data. Clearly one could add further complications, such as aberrations dependent on aperture size, or accounting for the manifestly varying seeing, but here we seek simply to demonstrate plausibility.

These results confirm the qualitative predictions of seeing theory for tilt correction, that the improvement is a function of aperture size, with a minimum at around $4r_0$. They also suggest that the level of improvement is less than predicted, possibly because of a small outer scale of turbulence (between 1m and 10m in our examples), and additional aberrations which contribute between 0.″3 and 0.″6 to the image size. On the positive side, the intrinsic r_0 is reasonably large (between 10cm and 18cm) for observations in the B band. Furthermore, the apparent variation in the base level may indicate that it is caused by local seeing effects, which are varying from night

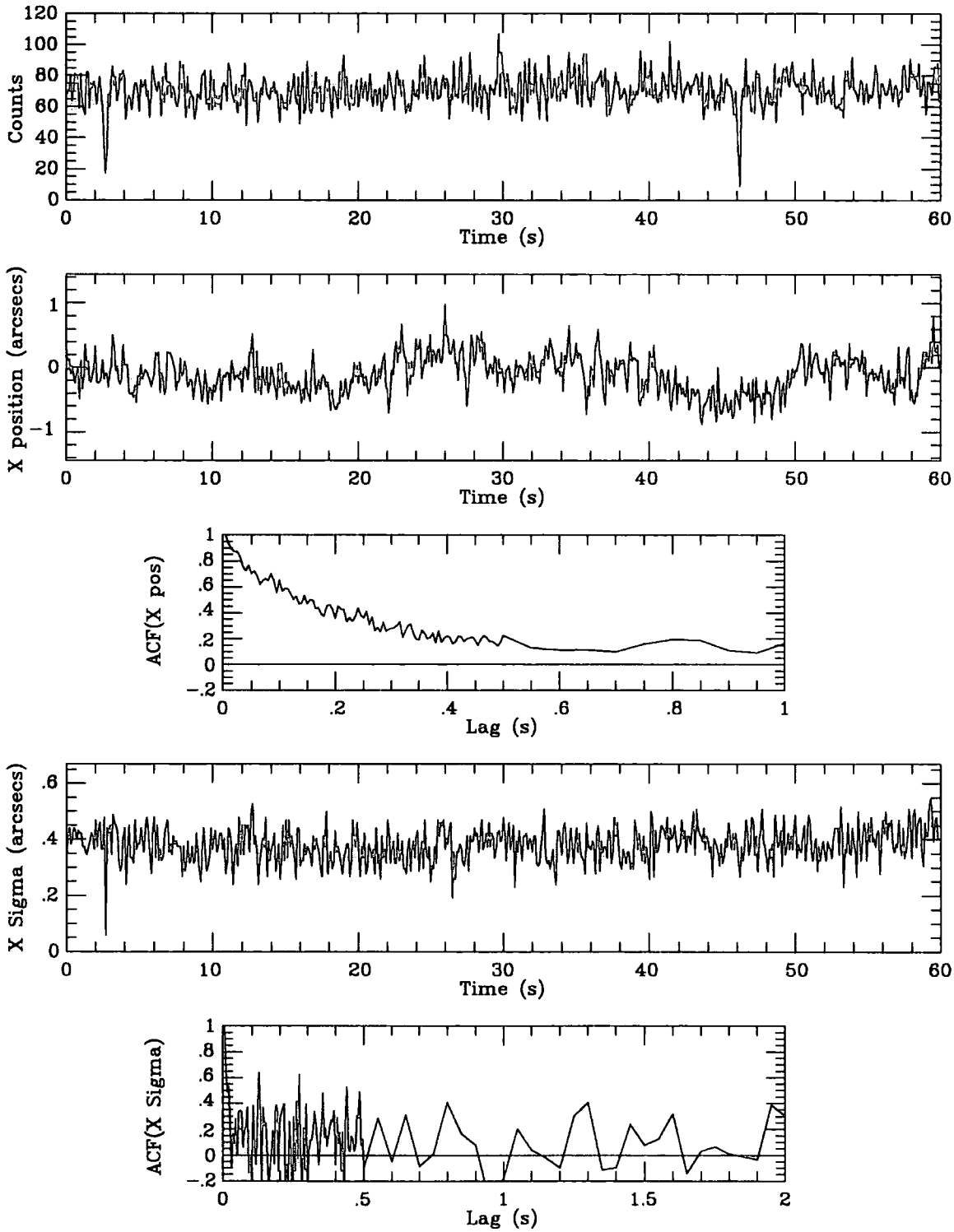

Figure 6.14: Time series data for one observation (25cm aperture) of the M67 field (Schild 108).

to night, and, thus, may be controllable.

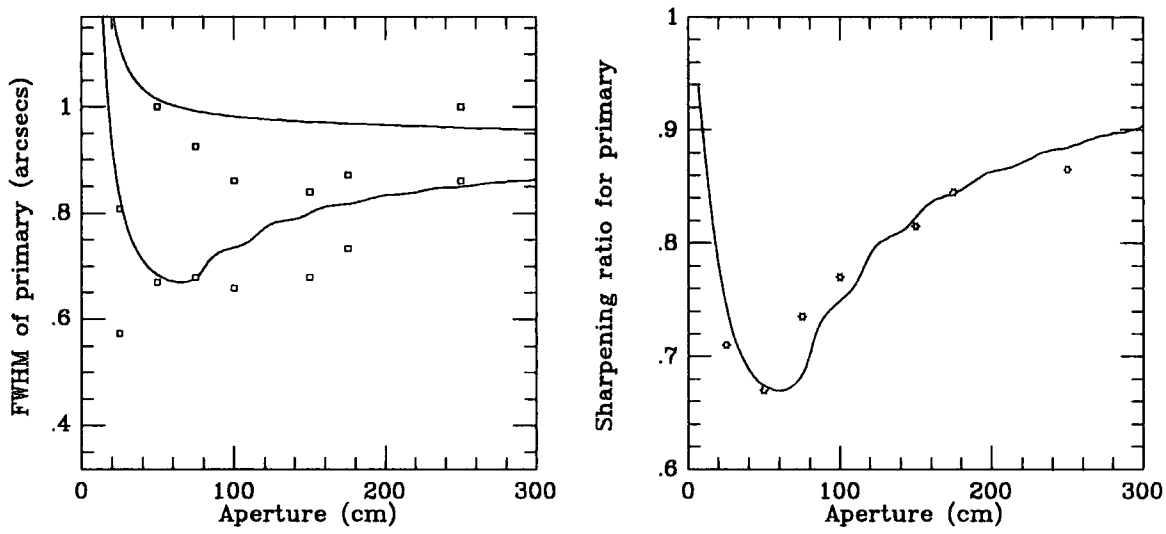

Figure 6.15: Sharpening plots for ADS7187. The parameters for the theoretical curve are r_0 = 15cm, L_0 = 10m and *base* =0.″6. Open squares represent the unsharpened seeing, and solid squares show the result of sharpening.

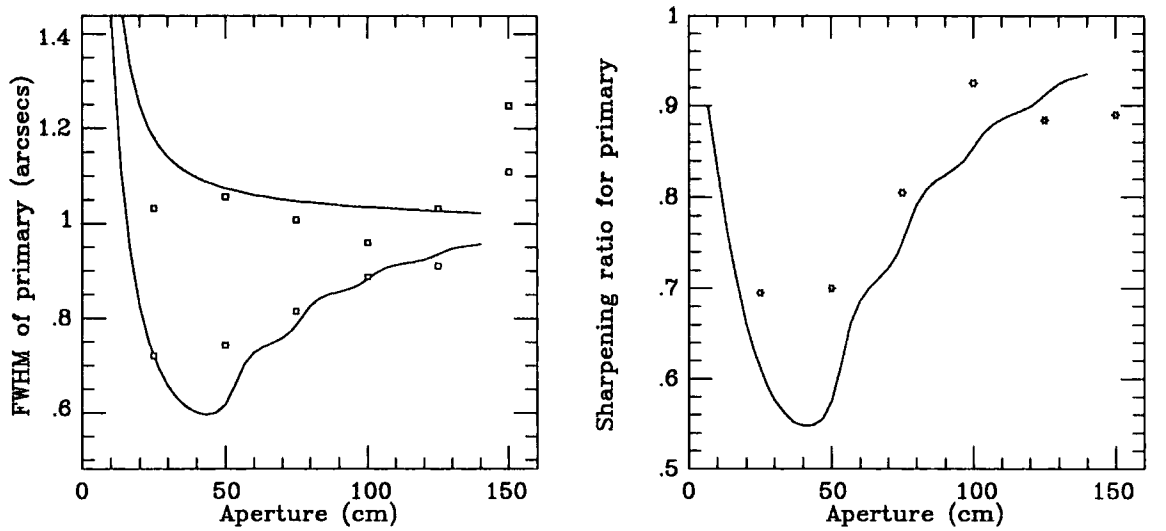

Figure 6.16: Sharpening plots for ADS8495. The parameters for the theoretical curve are r_0 = 10cm, L_0 = 1m and *base* =0.″4. Open squares represent the unsharpened seeing, and solid squares show the result of sharpening.

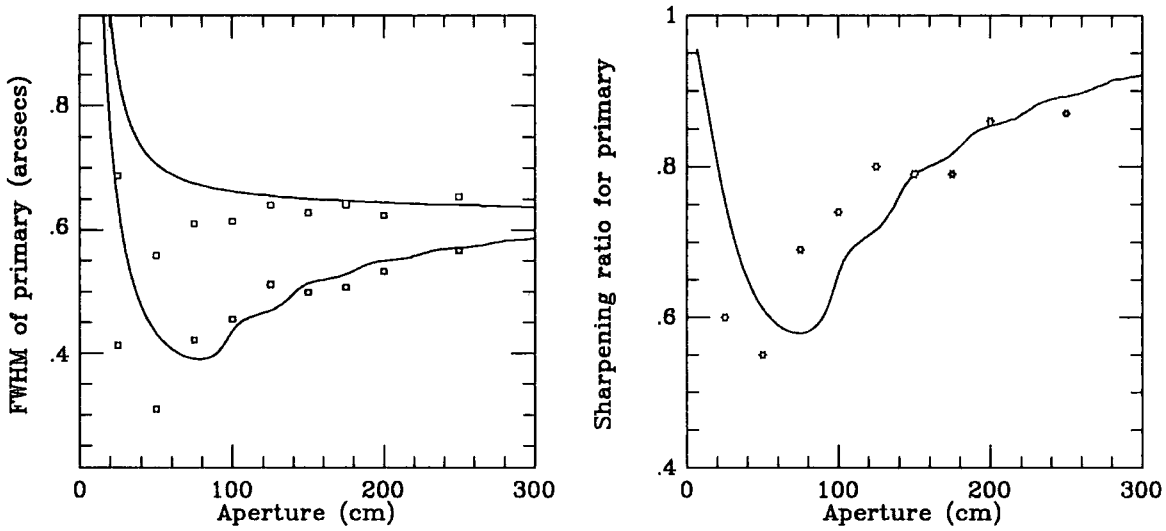

Figure 6.17: Sharpening plots for ADS6650. The parameters for the theoretical curve are r_0 = 18cm, L_0 = 3m and *base* =0.″3. Open squares represent the unsharpened seeing, and solid squares show the result of sharpening.

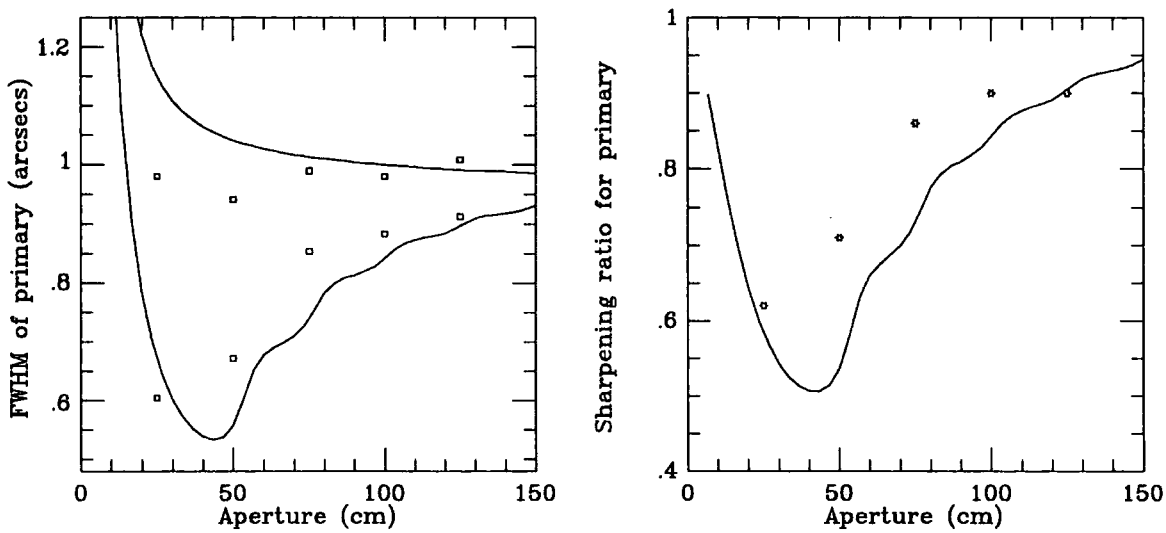

Figure 6.18: Sharpening plots for M67/Schild 108. The parameters for the theoretical curve are r_0 = 10cm, L_0 = 1m and *base* =0.″3. Open squares represent the unsharpened seeing, and solid squares show the result of sharpening.

6.3.3 Optimisation of Sharpening Algorithms.

In order to perform controlled tests of sharpening algorithms it is preferable to concentrate on a single good run where we have some confidence that the factors affecting performance are well constrained. The following sections consist of examples of the effects of different algorithms on the sharpening for just one observation of ADS6650, with a 50cm aperture. The stable conditions prevailing during these observations mean that this data is useful for demonstrating certain technical aspects of image-sharpening, independent of worries such as rapid seeing variations and other problems which afflict some of the other data.

The factors which we would like to understand the effects of are:

- different filtering algorithms.
- different spatial windowing functions.
- artificial sharpening.
- count rate.
- frame selection sharpening.
- multiple object 'cross-correlation' sharpening.
- real time sharpening.

The Achieved Gain with Simple Centroid Superposition

Figure 6.19 gives a visual impression of the improvement to be gained from simple centroid-superposition sharpening. The perspective plots show the effect of going from unsharpened to sharpened, together with intermediate top-hat smoothing of the data for comparison. The sharpening in this case was performed with a symmetric exponential filter of decay constant 30ms and a cut-off at 50ms. The monitoring was performed on the isolated star; the behaviour of the double star image, which is less sharpened, shows the effects of non-isoplanicity. The final plot is for the

10% of photon events which were 'beam-split' (see §5.8), demonstrating that artificial sharpening is negligible in this instance.

Figure 6.19(d) will be used in the rest of this section as the 'standard' performance against which other enhancements will be compared.

The Danger of Artificial Sharpening

As already described in the §5.8 there is a danger with post-exposure image-sharpening, of creating artificially sharp images by simply putting photon events into small images, rather than using the photon events to follow the motion of the image. Our technique for quantifying and hence avoiding this problem is to only use 90% of the available photons in determining the image motion, and applying that estimate to the remaining 10% of photons. The independence of these 10% 'beam-split' photons, should mean that any errors in estimating the image motion will be reflected in poorer images, as opposed to the artificially sharp images produced by the 90%.

Figure 6.20 shows two examples of artificial sharpening, one mild and one severe, along with the unsharpened and correctly sharpened images. The most severe case, which was produced with a 5ms top-hat filter, shows that whilst the primary star is artificially sharpened, both the secondary and the beam-split primary are blurred.

The Effect of Different Filtering Algorithms

It was clear from figure 6.19 that the difference in sharpening using a close to optimal filter and a rather long duration (150ms) top-hat smoothing, is only small. This is further illustrated in figure 6.21. Very little difference is seen between the images; even the two 'heuristic' algorithms which use different 'success criteria' to vary the parameters of the filter as it is running, show negligible improvement.

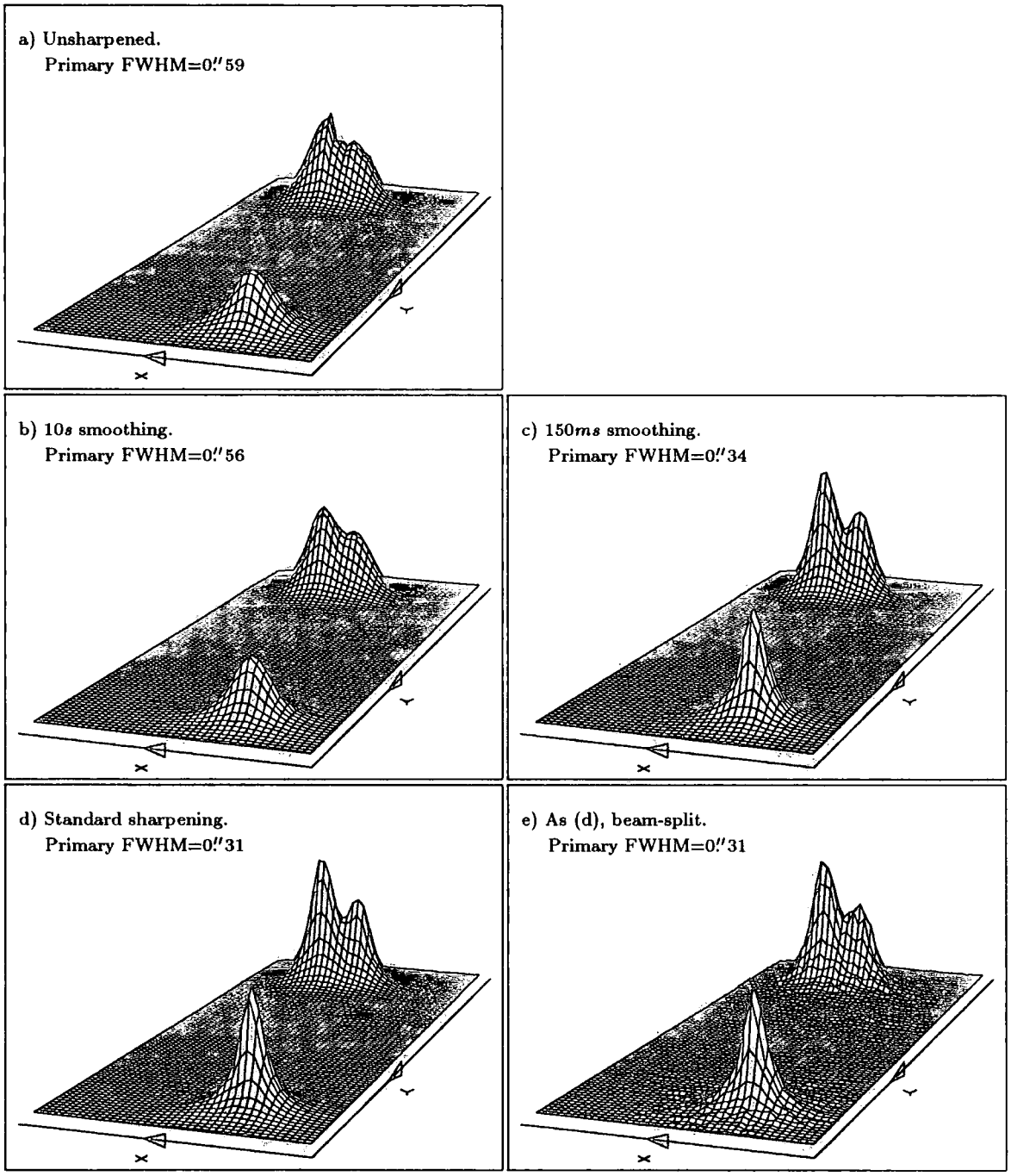

Figure 6.19: 3D perspective view of effect of simple centroid superposition sharpening on ADS6650. A good improvement is seen, although most of this is already gained in the 150ms smoothing case.

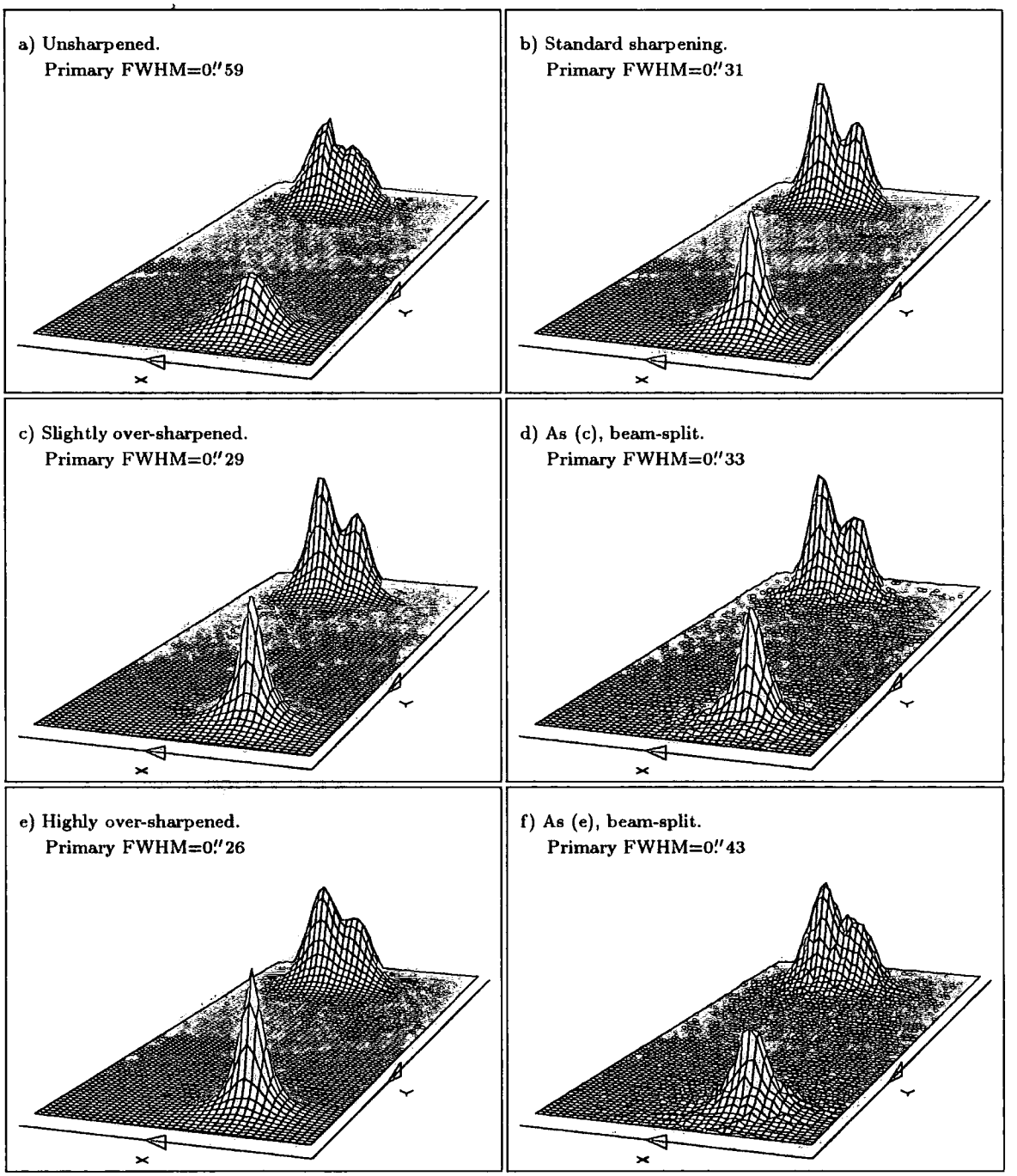

Figure 6.20: 3D perspective view of effects of artificial sharpening on ADS6650. This arrises when, for example, too few photons are used in calculating each centroid.

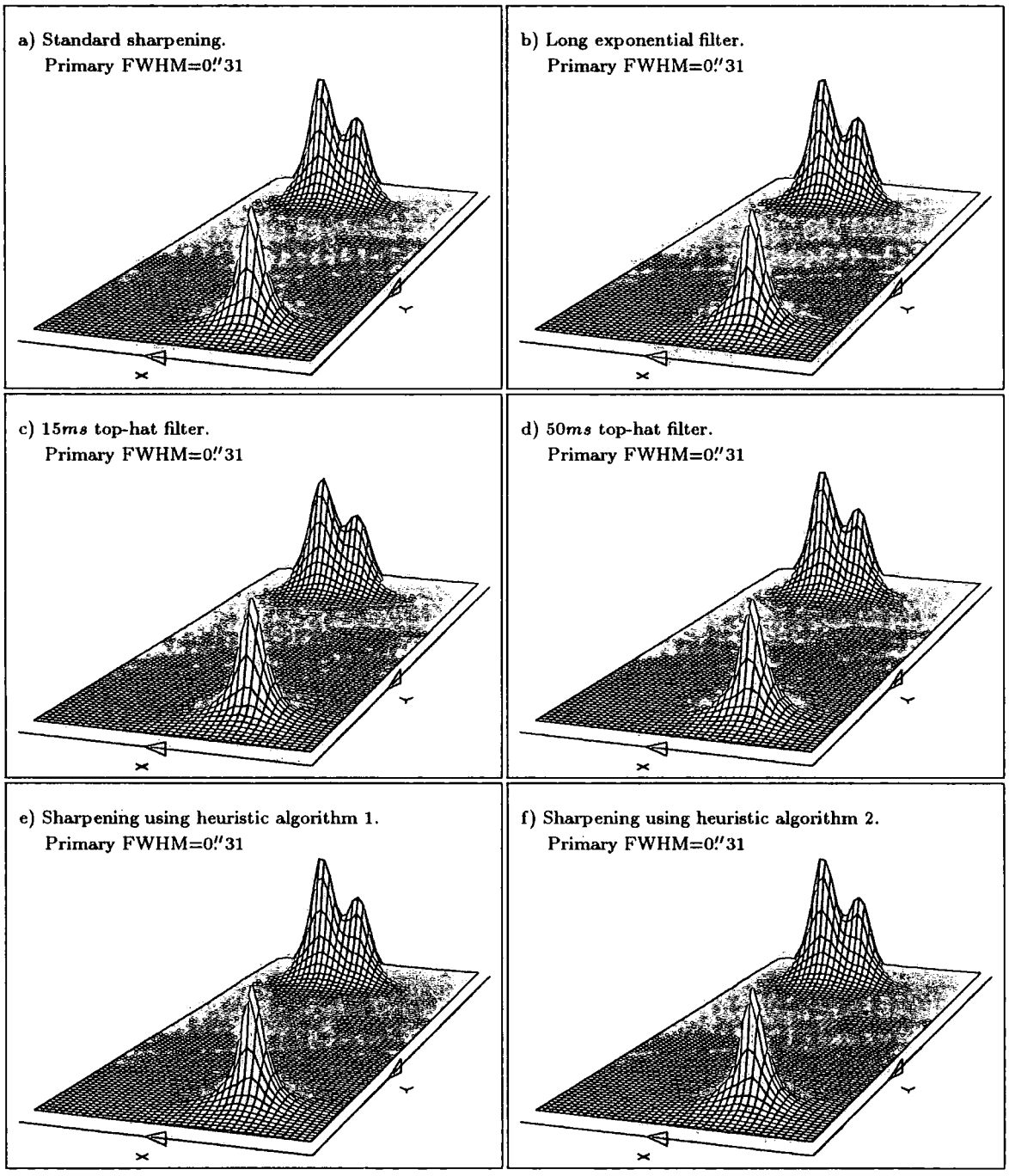

Figure 6.21: 3D perspective view of effect of different filtering algorithms on sharpening of ADS6650. Little gain is made, in this case, from optimising the filtering.

The Effect of Different Window Functions

Another choice to be made for the centroid-superposition technique is that of the window function through which to look at the data for the purpose of finding the centroids. We must choose a functional form; top-hat or gaussian, say; a size, and also the means by which the window follows the image motion. In figure 6.22 we compare the window function used in the standard sharpening (triangular weighting, 2.″15 diameter) which a range of top-hat windows of differing radius. The advantage of the weighted window is clearly seen.

The Effect of Cross-Correlation Sharpening

Rather than simply using the photons from one star, it may be useful to use information from all the objects in the field. This can be done be cross-correlating the photon events within each frame with a mask which is created from an integrated image. In this case we would expect to significantly improve the sharpening on the tight binary, which previously suffered due to the isoplanicity, but to be less effective on the original monitor star. This is indeed seen, in figure 6.23, as is a small amount of artificial sharpening, particularly when using the shorter exponential filters (decay lengths 10ms and 5ms) on the double star.

The Effect of Reduced Count Rate

The photon rate is important to the effectiveness of image-sharpening purely because the centroids cannot be calculated with few photons. Figure 6.24 illustrates how the effectiveness of a given set of sharpening parameters depends on count-rate. Little effect is seen in this instance down to about 50% of events used, but thereafter the sharpening suffers. It should be added that the sharpening at low count rates could be improved somewhat by extending the length of the filter.

This experiment tends to confirm that we can require a count rate of around 500 per second in a monitoring star to retrieve essentially all the information pertaining to the motion of the image. This value is, of course, for good conditions with a long time constant, and a double sided filter. A real-time predictive filter should probably be given at least twice this rate to work on,

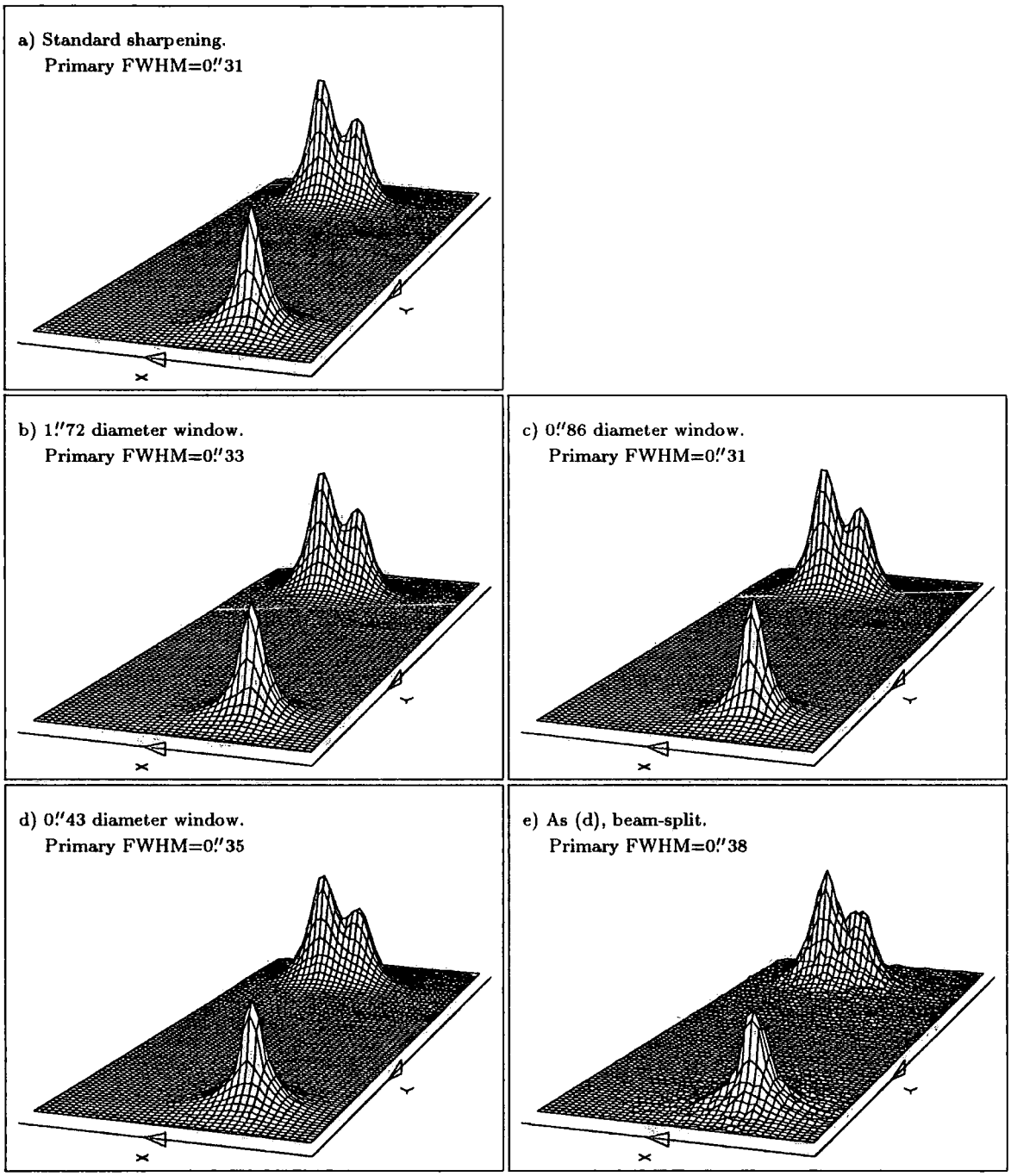

Figure 6.22: 3D perspective view of effect of different spatial window functions on sharpening of ADS6650.

The triangular weighted window, in (a), gives the best results.

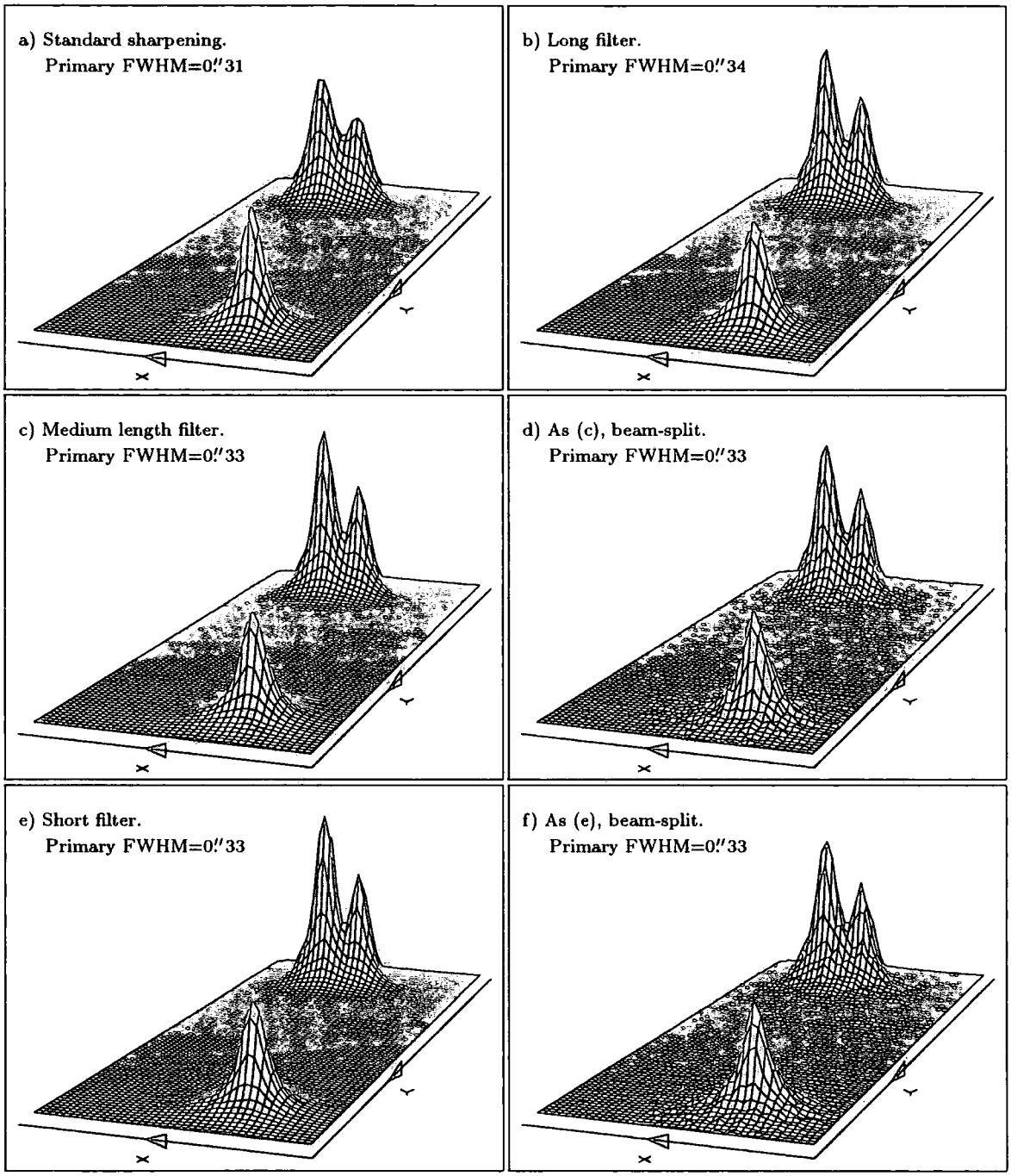

Figure 6.23: 3D perspective view of effect of cross-correlation technique on sharpening of ADS6650. As expected, the tight binary greatly improved in this case.

and proportionally more if the time constant of motion were shorter.

The Effect of Frame-Selection Sharpening

Frame-selection sharpening can, in principle, be used to obtain images approaching the diffraction limit. The technique relies simply on selecting, perhaps rare, moments of particularly good seeing, for inclusion in the integrated image. (The theoretical basis of this is described in section 5.4.3) Figure 6.25 shows the effect of various degrees of frame selection, where, here, a frame is effectively around 25 photons. It is clear that even this simple experiment has yielded significant gains in resolution, even though there is evidence of artificial sharpening from the beam-split integrations. The improvement for the tight pair is less marked, again due to isoplanatic degradation.

Simulation of Real Time Sharpening

Using this data we can also investigate the expected performance of real time sharpening algorithms. These can only take data from prior to the present when estimating the current centroid position, so, generally, they form a centroid for some time before the present and then extrapolate using a predictive term.

Of particular interest is the CUSPS algorithm used by MARTINI. This has been described in some detail by Doel (1990). Basically a cumulative index of photon offsets is kept, which is used as the input to a closed-loop digital filter. This smooths the signal to eradicate noise. The output signal is modified by the addition of a velocity term and hysteresis correction before being applied to the adaptive mirrors.

Our results (figure 6.26) show that the form of window used in calculating the centroids from the monitor photons is quite important. In particular, a large, unweighted window gives poor results, whilst a small, gaussian weighted window function gives good results. Furthermore, the best results achieved with the CUSPS algorithm, with this given photon rate in the monitor, by optimising the filter parameters, is only around 10% worse than the post-processed results. This gives us confidence in the potential of the real-time system. Further enhancements to the CUSPS

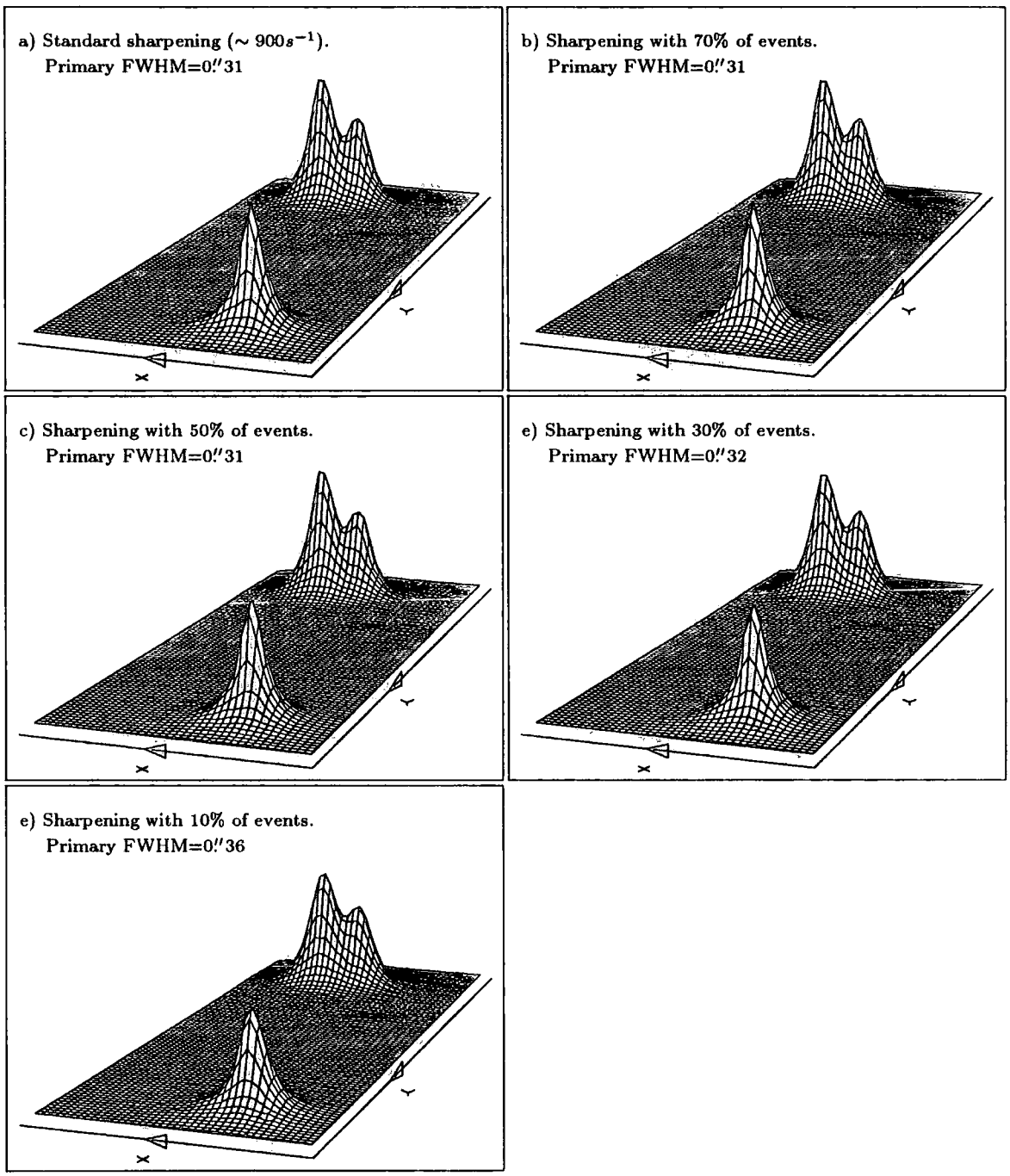

Figure 6.24: 3D perspective view of effect of reduced count rate on sharpening of ADS6650. Only the lowest count rate is badly affected.

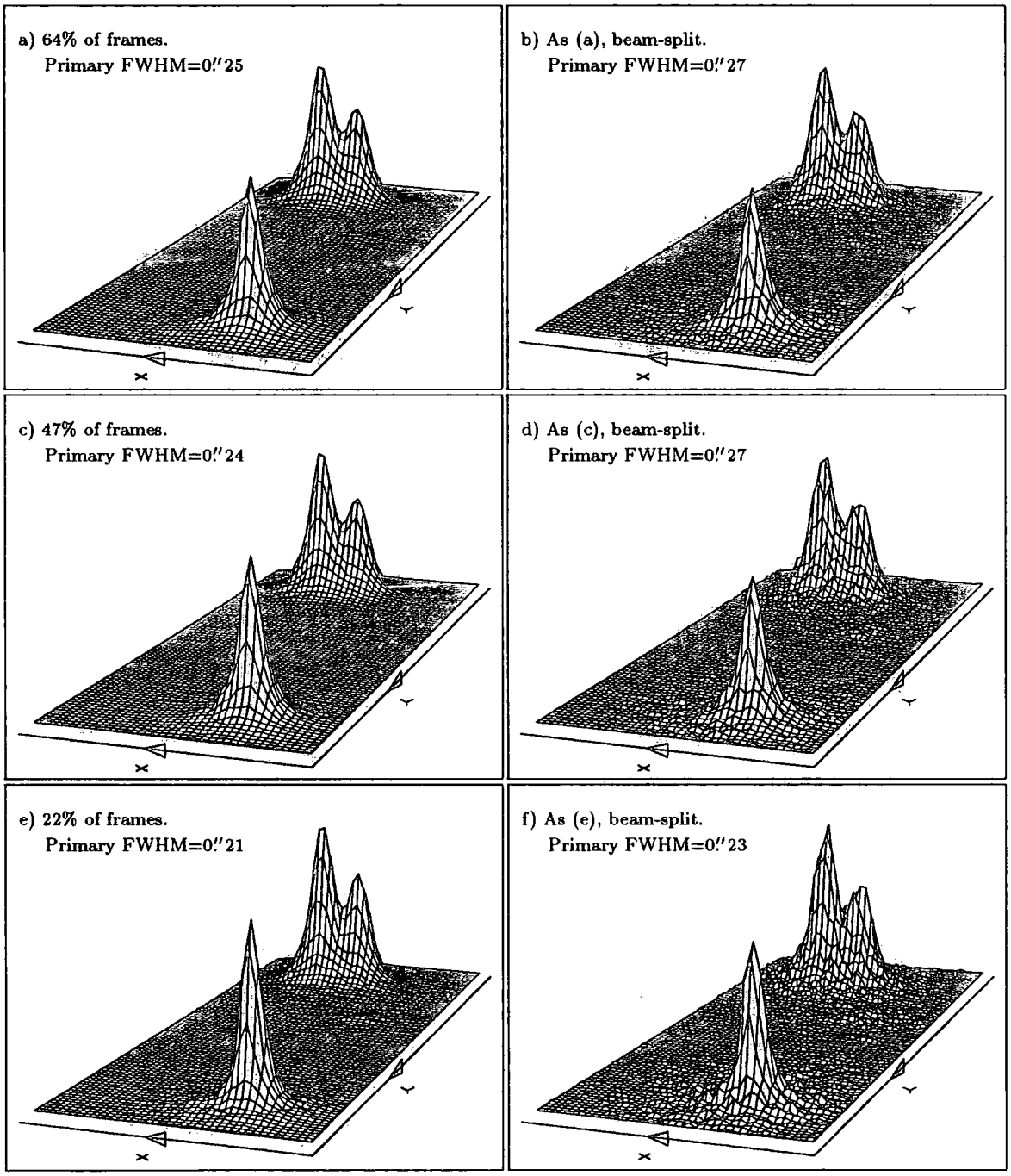

Figure 6.25: 3D perspective view of effect of frame-selection on sharpening of ADS6650.

algorithm would be possible with the use of a faster processor (CPU speed currently limits the amount of real-time processing which can be performed).

6.3.4 Isoplanicity and Conjugate Focus.

The most useful system for studying these issues is the Trapezium, or ADS4186. This celebrated small cluster of young stars, in the heart of the Orion Nebula, has four bright components which provide six independent baselines over which to test isoplanicity. Our method is to find the cross-correlation coefficient for the image motion of each pair of images. This avoids problems of measuring profiles which are particularly severe in this instance due to the non-circular shape of some of the images. It also allows us, relatively easily, to distinguish between the correlation of motions radial to the line between the stars, and that transverse. According to the standard theory, outlined in chapter 5, the isoplanatic patch for transverse motion should be larger than that for radial.

We chose to perform this analysis for the small, 25cm, aperture, which should minimise the isoplanatic patch and hence give greatest sensitivity in determining the optimum conjugate focus. Four conjugate heights were used, namely 0km, 1km, 3.5km and 5km above the telescope. The results of this analysis are shown in figure 6.27. Here a correction has been made for the lack of correlation due to errors in the centroid determination. That is to say, the true correlations between the signals for each star would be worse than those in the plots to an extent dependent on the magnitudes of the two particular components. The expected deterioration due to this effect can be estimated by extrapolating the autocorrelation curves for each star to zero-lag and comparing to the observed zero-lag coefficient. The corrected values are of more interest since they give a truer picture of the physical form of the isoplanatic patch. In practice, when performing image-sharpening, the problem of poor photon statistics applies only to the monitoring star motion. Note also that the data were smoothed with a 10s running mean to get a reasonably stationary series.

The effect of isoplanicity is clearly seen with correlation decreasing with base-line separation in all the plots. For the 0km conjugate, following Valley and Wandzura (1979), we have plotted the

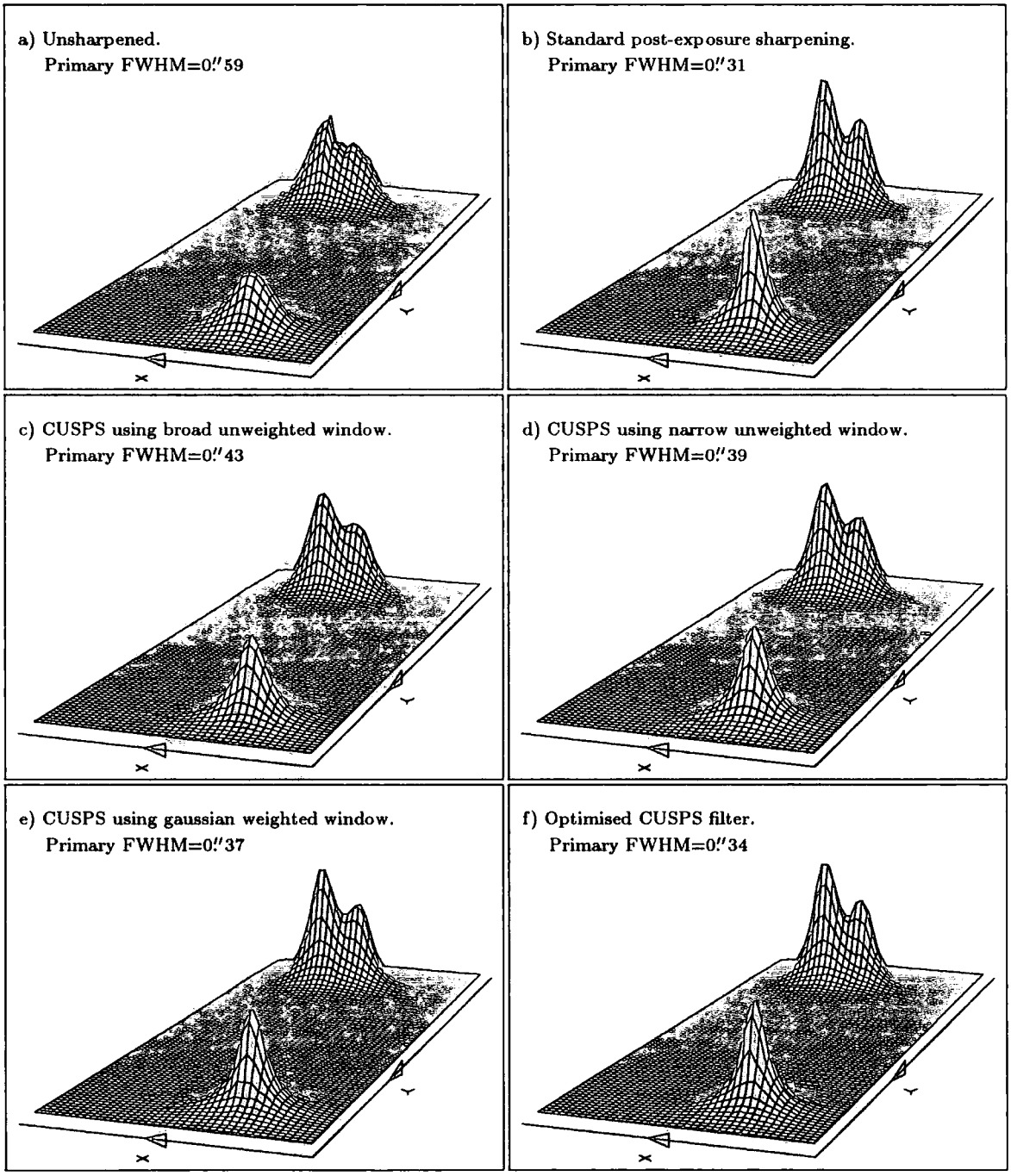

Figure 6.26: 3D perspective view of effect of results from simulation of the CUSPS real-time sharpening algorithm. The best real-time result, with an optimal filter and gaussian weighted window, is only 10% worse than the standard post-exposure result.

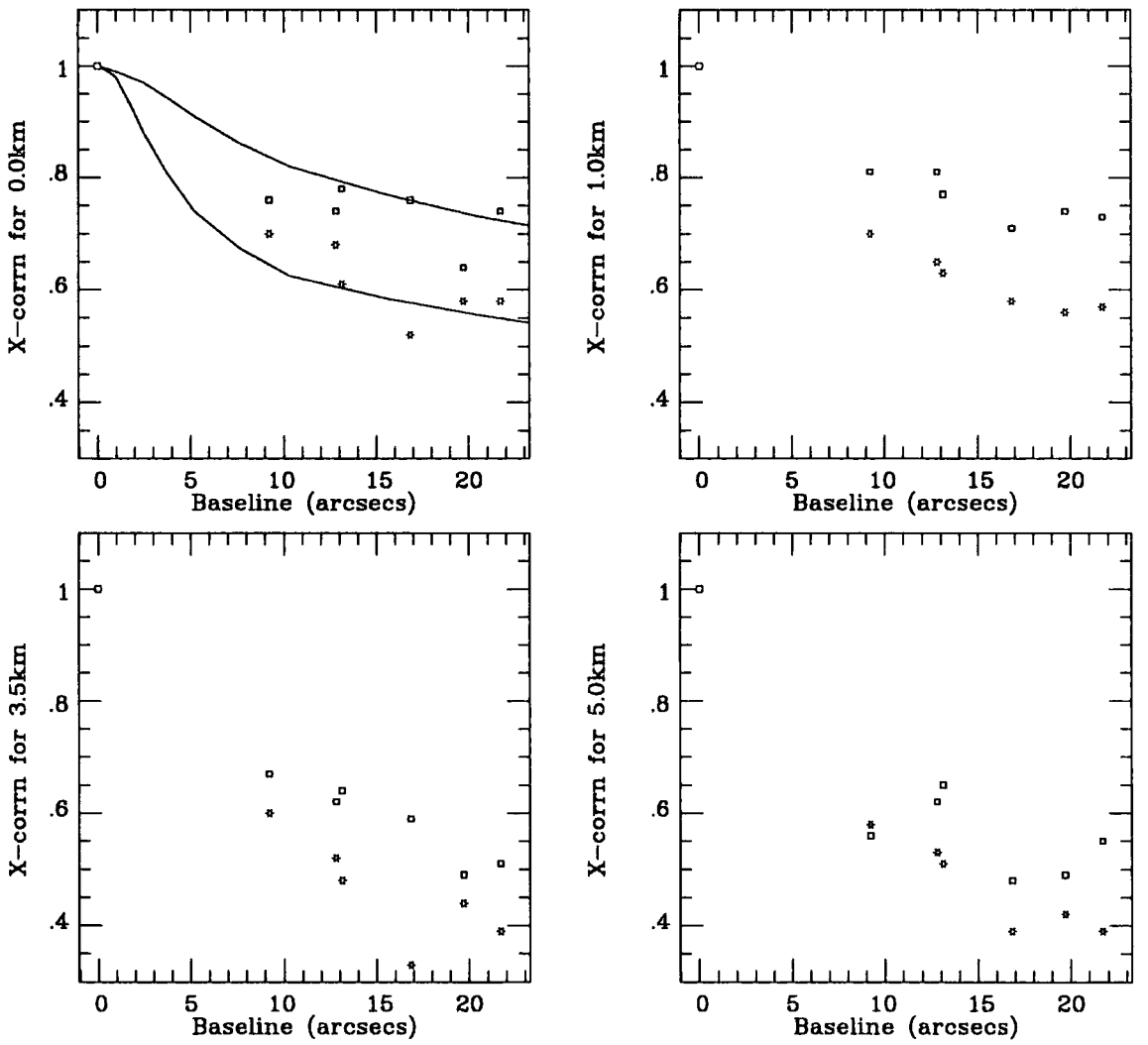

Figure 6.27: Cross-correlation coefficients as a function of base-line for Trapezium data. The open squares are the coeficients for the transverse motion and the stars are for the radial. The theoretical curve for the zero-height conjugate, based on the method of Valley and Wandzura (1979), is in good agreement with the data. We deduce that the optimum conjugate focus, on this night, was low, in the region of 0-1km

predictions of the Hufnagel atmospheric model, with the appropriate parameters. The qualitative agreement is very good, with our data apparently showing a slightly smaller difference between the transverse and radial correlations. The good agreement of the two close baselines at $13 arcsecs$ in all the graphs is gratifying. The apparently higher scatter of the other points is expected since they are all between stars of lower combined luminosities. The steepness of decline is also seen to be a function of the conjugate focus position, as expected. In this instance the best results are found for the lower values, namely $0km$ and $1km$, whilst the higher positions of $3.5km$ and $5km$, show a much sharper decline. This may be related to the weather conditions on the night which were such that there was a strong blustery wind, which was blowing sporadic wisps of low, fast-moving cloud across the observatory.

In order to interpret these graphs, we note that it can be shown that a correlation coefficient of 0.5 corresponds to the break even point for image-sharpening, and any lower will result in an actual deterioration of the secondary image. (Zero correlation would result in roughly a factor of $\sqrt{2}$ deterioration.) Clearly, on this night, there was not much gain to be had for secondary objects, especially for high conjugate foci. Once again, however, we could question how typical these conditions are, and should also recall that a small aperture was deliberately used to highlight any lack of isoplanicity.

6.4 Conclusions

As has already been indicated, it is not clear that all of our observations can be regarded as a fair tests of image-sharpening. This is because of the atypical weather conditions, high winds and patchy cloud, for several of the runs (when, incidentally, other telescopes on the site were not observing). Nonetheless we have been able to draw some important conclusions regarding the technical basis of image sharpening.

- In each case there is some sharpening improvement, which goes through a minimum at small apertures, thus verifying the basic prediction of seeing theory for tilt correction. The form of the relationships between aperture and improvement can be roughly explained by the

standard theory with the addition of a finite outer scale of turbulence and a baseline to the image width.

- The time-scales of the motion vary from around 40ms to 200ms, dependent on wind speed. Generally, the best seeing conditions were also on still nights. The time-scales of image width variation are less easy to quantify. Generally the component due to turbulence seems to be on somewhat shorter scales than the image motion, but in some data sets there is evidence of changes in the intrinsic seeing conditions on scales of seconds.

  High winds, although not necessarily affecting the intrinsic seeing, would be expected to reduce the correlation time of the image motion, making sharpening more difficult. In addition to this it is likely that high winds close to the ground will increase the amount of local turbulence, deteriorating the seeing, and reducing the isoplanaticity. For comparison, a correlation between wind speed and seeing at the University of Hawaii 2.2m telescope has been reported by Henry *et al.* (1987). Furthermore, the geography of the Observatory on La Palma, with the telescopes being situated on the rim of the Caldera, may make certain wind directions particularly bad for producing local seeing.

- There is apparently a tendency for the best seeing to be found when the external air temperature is high relative to the dome, suggesting that the dome seeing due to the temperature differential relative to the telescope is significant. This is consistent with findings at other sites. Undoubtedly a campaign to monitor the correlation between seeing and temperature differentials, to audit the heat sources near the telescope, and, ultimately, to attempt to control dome seeing by passive or active cooling, could be of great benefit to the high-resolution effort at the WHT.

- We have demonstrated the potential of using cross-correlation of star motions in multiple component systems to investigate the functional form of the isoplanatic patch. The basic, expected, characteristics are well reproduced in the observations of ADS4186. This data also shows a clear difference in the isoplanicity for radial and transverse motions, with transverse motions being more highly correlated, as predicted. The optimum conjugate focus for this observation was low, around 1km, with improvement out to $> 23''$ even for a small, 25cm,

aperture. The higher conjugate, at 5km, ceases to offer any sharpening improvement at around 15″. Clearly, until such time as further data are available relating to the constancy of the turbulent structure of the atmosphere, and also the size of local effects, it would be an advantage to be able to optimize the conjugate focus empirically.

- Regarding optimization of sharpening algorithms, our results for ADS6650 showed that, when the time constant is long, optimal temporal weighting in the filter is less important than optimal spatial weighting in determining centroids. We have also demonstrated the potential of cross-correlation sharpening, particularly useful for instances of several monitoring objects, and simple frame-selection.

- Simulation of real-time sharpening, in the form of the CUSPS algorithm used by MARTINI, showed that there is a small but evident degradation of $\sim$ 10% compared to post-exposure sharpening. This was minimised when using a gaussian weighted window, of roughly the width of the unsharpened image, and optimising the filter coefficients.

- As discussed in chapter 5, it is difficult with current technology to envisage a good real-time frame selection system using a fast shutter. However, our experience clearly points to the potential value of a slow shutter, which could be operated manually or automatically, to remove more extended periods of poor seeing, of the order of seconds to tens of seconds, without terminating the exposure.

- With regard to the monitoring star, we suggest a rule of thumb that 1000 counts per second is required for real-time sharpening, in reasonable conditions. This corresponds to a V magnitude of around 12.5 for an observation with a 1m sub-aperture. Ultimately, however, it would be recommended that the optimum aperture be found empirically on the night. This could be done with the MARTINI instrument by creating an aperture plate with 6 different sub-apertures and simultaneously sharpening each image of the monitor.

We should also ask what are the practical implications for astronomy. One point to take on board is the crucial role of good conditions. This statement is not as tautological as it first seems, since, on top of the proportional improvement in the achieved seeing which theory suggests we

should obtain, good seeing conditions also ensure:

1. large apertures can be used, increasing light gathering power, and also, very importantly, the photon rate from the monitor.

2. stable seeing conditions seem to often mean longer coherence times for the seeing motion, allowing more photons to be used in calculating centroid offsets.

3. large apertures would also be expected to provide a larger isoplanatic patch.

The following chapter (7), describes how real-time image-sharpening methods were applied to the astronomical project of high-resolution imaging of Virgo Cluster galaxies.

Chapter 7

Image-Sharpening Observations of Virgo Cluster Galaxies

7.1 Introduction

This chapter is devoted to the program of astronomical observations which we have undertaken using image-sharpening methods. Our primary aim has been to obtain high-resolution images of Virgo Cluster galaxies in order to identify their individual stars. These are used to put new constraints on the distance to the Virgo Cluster. The extension of stellar distance indicators as far as Virgo is vital step in determining the value of H_0. All the image-sharpening observations reported here were carried out with the MARTINI instrument (see chapter 5).

In choosing targets for image-sharpening, certain constraints must be born in mind, in the context of the particular setup which is used. These arise in connection with the requirement of monitoring the seeing, usually with a nearby reference star. Firstly, in order that sufficient information be gathered to determine the shape of the wave-front, there will always be a limiting magnitude of monitor, be it the object of interest or otherwise. Furthermore, this limit will depend

on the seeing directly and also indirectly in the influence the seeing has on the choice of aperture. [1] In Virgo we are fortunate in that the large number of galaxies has allowed us to make a reasonable short-list of good targets which have the required overlapping foreground star.

A second factor is that of isoplanicity. In the usual case, where the monitor is not the object of interest, the astronomical target must be close enough to the reference star to benefit from the sharpening. Once again this will have some dependence on the aperture, with larger apertures expected to give a larger isoplanatic patch. As described in chapter 5, it may also be possible to optimise the isoplanatic patch by positioning the apertures close to the conjugate focus of the turbulence.

Finally, there is the question of the means by which part of the light is diverted to the real-time detector and the rest to the integrating camera. Usually a mirror with a small unsilvered hole is used to separate the monitor star-light spatially from the rest of the field. However, in some circumstances, usually when the monitor is itself of interest, it is necessary to use a either a conventional or dichroic beam-splitter. The latter has the advantage if the observations are at long wavelengths, since then all the short wavelength light can go to the blue sensitive IPD.

7.1.1 Feasibility Considerations

Our aim, then, is to use image sharpening observations to produce high-resolution, ground-based images of Virgo cluster galaxies, to search, in the first instance for brightest stars, and ultimately for Cepheids. It has been traditionally assumed that the resolution of the HST would be required in order to make progress on the identification of stars in Virgo Cluster galaxies. In reality, as we argue below, the situation may not be as bad as this.

[1] One proviso to this is that, in the case of the TRIFFID, where all the light is incident on the IPD, it may be possible to use several objects as monitors. The most obvious application of this is in observing globular clusters, which will frequently have several stars in the field which can be used to determine an average shift. An example of this was given for the ADS6650 triple star system, described in chapter 6.

Brightest Stars

We saw in chapter 1 that the long-standing suggestion that the brightest supergiants are standard candles is now receiving new theoretical motivation. The modern observational basis for their use as distance indicators has been built up, in the main, by two ongoing parallel programs, one by Sandage and Carlson (1988 and references therein, hereafter SC88) and the other by Humphreys and collaborators (Humphreys 1988 and references therein, hereafter H88). Both these groups have surveyed the stellar content of nearby resolved galaxies, and have arrived at similar calibrations for the red and blue supergiant magnitudes, which are outlined below.

In general terms, these stars are sufficiently bright that, if they are single, they are unlikely to be crowded by other stars, but may well be confused by nebulosity or regions of variable background intensity. Typically in the magnitude range $M_R \sim -9^m$ to -10^m, they should be easily detectable with modern detectors, to distances considerably beyond Virgo, even in poor seeing. The primary problem, then, is to deconfuse brightest stars from nebulosity, and imposters such as clusters, foreground stars, background galaxies etc. There are several means by which this may be achieved, without necessarily having very high spatial resolution. For example, narrow band, emission-line images allow the identification of regions of nebulosity. Similarly, broad band colours can be used, in conjunction with statistical arguments, to account for contamination by point-like continuum objects.

Of the different classes of supergiant stars, the best standard candles are thought to be the red supergiants. Here, both SC88 and H88 give $M_V \sim -8.^m2$ (or $M_R \sim -9.^m1$), for all galaxies brighter than $M_V \sim -16^m$. Furthermore, both authors suggest that taking the mean of the three brightest red supergiants in a galaxy, say, is an even better standard candle, with $M_V(3) \sim -8^m$. The colours of these stars are very red. Taking the intrinsic colours from Johnson (1966), and transforming these to put the R photometry in the Kron-Cousins system (Fernie, 1983), we find $(B-R)_0$ in the range 2.5 to 3. This makes them easy to identify, and means that contaminated objects will usually not be included in the sample on colour grounds. Frequently these stars are also semi-regular variables.

Thus, selection of the reddest objects should reliably identify such stars, with the only likely contaminants being foreground M-dwarves. The level of foreground contamination can be estimated from control fields nearby the galaxy, or from other surveys of galactic stars, and appropriate account taken in the statistics. For example, the Bahcall and Soneira model (from results given in Ratnatunga and Bahcall, 1985, hereafter RB85) predicts, for high galactic latitudes, 0.25 stars per $\Box'$, with $B - V > 1.3$, in the range $21^m < V < 23^m$, and 0.12 stars per $\Box'$, in the range $19^m < V < 21^m$. This may be compared to the stellar number counts of Metcalfe *et al.* (1991). They find that, in the range $19^m < R < 20.^m5$, the distribution of colours is double peaked, with most stars being around $B - R = 2.^m2$, around 0.2 stars per $\Box'$, but a smaller number peaked at $B - R \sim 0.^m8$.

The other well studied class of supergiants are the blue BA stars. In this case, however, there is a clear tendency for the most luminous supergiants to be found in the brightest galaxies, with a flattening at the brighter end of the host galaxy magnitude range. This suggests that the luminosity function for these stars, as they approach the upper limit, does not drop as steeply as that of the red stars. Sandage (1988) suggests that the very brightest blue supergiants, which are only seen in host galaxies brighter than $M_B \sim -19^m$, are in fact close to their Eddington limit, and hence reliable standard candles with $M_B = -10^m$. Their colours mean that there is only a small chance of confusion with foreground or background objects. Furthermore, he claims that most of these stars are irregular variables and hence they should be easy to identify. This point is contended, however, by H88, who does not find the variable stars are necessarily the brightest, and, in any event, claims they show a large dispersion in their magnitudes. Several authors have also argued that blue supergiant stars, even in nearby galaxies, are more susceptible to being composite systems which are mistakenly identified as single (eg. Humphreys and Aaronson, 1987, Heydari-Malayeri and Hutsemékers, 1991). These arguments, combined with the lack of bright galaxies in our short-list of target galaxies (see below), would seem to make them less suitable as distance indicators for our project.

Finally, following H88, we note that there is an additional class of stars which have not hitherto been considered as distances indicators, namely, the intermediate F, G and K-type 'yellow'

hypergiant stars. These stars would be also be expected to be bound by the upper envelope of luminosity, and have the advantage of being more than half a magnitude brighter than the red supergiants in the R band ($M_R \sim -9.^m7$ to -9.^{m}8, Humphreys 1983). In this case, the colours of these stars range from $(B-R)_0$ =0.^{m}4 to 2.^{m}4. The main drawbacks of these stars are the problems of misidentification with foreground stars and clusters in the host galaxy. Firstly, considering the foreground contamination, it is likely to be less of a difficulty for Virgo than more nearby galaxies. RB85 find 0.19 stars per □′, for $B - V < 1.3$, in the range $19^m < V < 21^m$ and 0.26 stars per □′ in the range $21^m < V < 23^m$. Perhaps more serious is confusion with star clusters, which will have similar colours, and are likely to be unresolved at Virgo distances. In fact, the globular cluster contamination should not be so important for us since small galaxies generally have few bright globular clusters. For example, Harris (1991) finds only one globular cluster brighter than $M_V = -8^m$ in a sample of seven small local group galaxies (which include the LMC and M33). The brightest yellow supergiants should be a full magnitude brighter than this. This still leaves the possibility of open clusters. Here, we can only argue that for a bright cluster to have such an intermediate colour, it would probably have to be a group of young blue stars which happened to have a maximum brightness red supergiant within it. Thus the final combined magnitude would be almost as great as a brightest yellow supergiant, and the error from the misidentification would be small. This reasoning also suggests that such objects could probably be distinguished from single stars from their position in a $(B - V, V - R)$ colour-colour diagram.

Cepheid Variables

Going fainter from the brightest stars inevitably leads to greater crowding problems. The Cepheid variables, appear in the range $M_B \sim -2^m$ to $M_B \sim -6^m$ and they become progressively redder as they become brighter, ranging from $(B - R)_0$ =0.^{m}8 to $(B - R)_0 \sim 1.^m8$. The linear relation between period and luminosity is maintained up to $M_B \sim -5^m$ or $M_R \sim -6.^m5$ (Madore and Freedman 1991).

Thus, the brightest Cepheids are $\sim$ 3 magnitudes fainter than the brightest supergiants in the R band. Despite this we contend that they can be detected in good seeing ground-based observations,

for the following reasons. Firstly, the most distant galaxy with a Cepheid distance is currently M101, at 7.2Mpc (Cook *et al.* 1986). This galaxy is clearly resolved in 1.″2 seeing, which implies similar ease of resolution for Virgo in 0.″6 seeing if it is closer than 14Mpc and in 0.″3 seeing out to 28Mpc. Furthermore, over a whole galaxy there is a good chance of finding some variables in relatively 'quiet' areas. This is certainly the case for one of the M101 Cepheids, which would be uncrowded even in 2″ seeing. As we have seen, in chapter 6, such seeing, in the region of 0.″3 to 0.″8, has been regularly attained with image-sharpening at the WHT.

Secondly, their very variability is a good signature of their presence, so they cannot easily be mistaken for foreground or background objects. Furthermore, with modern digital detectors, it is a relatively simple matter to align and difference images. The variables then show as point sources standing on a much more uniform background. The large variability of the B band magnitude, which is typically $\sim 1^m$ but can be up to 2^m (see Sandage 1971), gives the possibility of detecting Cepheids in this manner even with moderate seeing. Thus, for simply identifying Cepheids and obtaining light curves, the level of crowding may be only of secondary importance. This naturally complements high-resolution studies, since the image-sharpening is most productive at long wavelengths, where the variability and dispersion about the P-L relationship, and also the extinction corrections, are least. In addition it would be possible, by taking a sequence of appropriately separated exposures, to add and subtract alternate images to select out variables of the expected periods for the brightest Cepheids, that is to say, in the region of 30 to 100 days.

The large number of galaxies in Virgo help us to select a good sample of galaxies, which would be required to tie down the statistics of any results obtained from these methods. The location of Virgo, close to the north galactic pole, also has the advantage of only requiring a small correction for foreground extinction, and, in the case of the brightest stars, less contamination by galactic stars than would be the case working at lower galactic latitudes.

7.2 Candidate Virgo Galaxies

As already described, the essential criterion for image-sharpening candidates is that they have a sufficiently bright, overlapping monitor star. Although the precise requirements depend on observing conditions, we took this to mean $B \lesssim 13.^m5$ as the rule of thumb guide-line. The large number of galaxies in Virgo allowed us to draw up a short-list which is a subset of the galaxies identified by Sandage and Bedke (1985, hereafter SB85) as being useful for resolution by the Hubble Space Telescope. These are generally low surface brightness, face-on, late-type galaxies which are judged to be in the Virgo core. The data for the short-listed galaxies and their monitoring stars are given in tables 7.1 and 7.2.

Galaxy	Rating (SB85)	RA(1950)	Dec(1950)	Type	B_T	Vel (kms^{-1})
IC3583	Excellent	$12^h34^m12^s$	$+13°32'00''$	SmIII	13.9	1120
NGC4411A	Good	$12^h23^m57^s$	$+09°08'55''$	SBc(s)II	13.4	1277
NGC4411B	Good	$12^h24^m15^s$	$+09°09'40''$	Sc(s)II	12.9	1266
NGC4523	Excellent	$12^h31^m17^s$	$+15°26'30''$	SBd(s)III	13.6	262
NGC4535	Good	$12^h31^m48^s$	$+08°28'25''$	SBc(s)I.3	10.5	1961
NGC4639	Good/Fair	$12^h40^m21^s$	$+13°31'53''$	SBb(r)II	12.2	972
'7°27''	Excellent	$12^h24^m38^s$	$+07°32'23''$	Scd(s)II	13.6	932

Table 7.1: Basic data for the short list of Virgo galaxies which are good targets for image sharpening with MARTINI.

Additional factors to be considered in selecting from this list are the confidence that the galaxy is a cluster member, for example, from its redshift, and the existence of other, fainter field stars which can be used to gauge PSF variation within the image. The data given in these tables for the guide stars comes partly as a result of our observations and was not all known prior to them. This is one of the reasons that there has been a change in our favoured targets with time as described below.

Galaxy	RA(1950)	Dec(1950)	B_{Star}
IC3583	$12^h34^m13^s$	$+13°31'38''$	13.5
NGC4411A	$12^h23^m57^s$	$+09°08'51''$	13.5
NGC4411B	$12^h24^m10^s$	$+09°10'24''$	13.5
NGC4523	$12^h31^m18^s$	$+15°27'01''$	12.9
NGC4535	$12^h31^m20^s$	$+08°27'00''$	-
NGC4639	$12^h40^m25^s$	$+13°31'18''$	13.5
'7°27''	$12^h24^m44^s$	$+07°31'50''$	11.5

Table 7.2: Basic data for the guide stars in each galaxy.

7.3 Observations of IC3583 - Feb/March 1990

These observations took place on the four nights from 27^{th} of February 1990, starting dark, but getting brighter. The first night had very poor conditions and the only work done was in the way of instrumental tests. These tests persuaded us that the prototype mirror, to split the light from the monitor and object, was not functioning well, and that we should revert to the 70-30 beam-splitter for the remainder of the observations. The second night was lost completely. The third night offered the best conditions, and on this night we observed the Virgo galaxy IC3583 and several control objects. The fourth night was less good, with the dome shut for about half of the night. This prohibited us from observing Virgo on that night, but allowed several more control observations to be carried out.

7.3.1 Instrumental Setup

The standard MARTINI setup is described in chapter 5. As mentioned above it was found that the conventional beam-splitter had to be used for the observations, which reduced throughput by a factor of ~ 3. In addition, the only detector available was the MARTINI development CCD, which is a 'B'-grade EEV chip, with $\sim 8e^-$ read-out noise and poor cosmetic qualities. The format

is 575x400 pixels, which was configured to give a scale of 0.″12 per pixel.

One problem which was experienced on this run was that occasionally the guide star image in one of the apertures would jump completely out of the 3″ IPD field and would proceed to wander across the CCD. This usually coincided with a small power glitch associated with the movement of the dome. This was particularly problematic as the exposures could not be terminated, but had to be aborted, resulting in several images being lost. For this reason we were obliged to use relatively short exposure times (see below), which meant that the images suffered from being read-out noise limited. It also meant that some of the images had short trails which resulted when 'run-away' monitor stars were reacquired, by chance, before the exposure was aborted. These trails had to be removed in the data-reduction procedure.

7.3.2 Log of MARTINI IC3583 Observations

Our final choice of target Virgo galaxy candidate was IC3583, which has a monitoring star of magnitude $B = 13.^m5$ at its edge. This is an SMIII dwarf galaxy, with an apparent magnitude of $B = 13.^m9$ and a recession velocity close to the cluster mean. It was chosen since the guide star was positioned at the edge of the galaxy so that the field clearly covered parts of the galaxy from the centre to the outskirts. There is also a convenient 18.″5 double star close to this field which is useful for conducting test exposures.

Before turning to our main target we observed the nearby double to help gauge both the seeing improvement and the isoplanicity as a function of aperture. This observation was also used to obtain a precise field scale for the detector. The results of these exposures are summarised in table 7.3. These observations were interpreted as showing that the sharpening performance was in the region of 30% to 50%, with little deterioration at the larger aperture. The isoplanicity is rather confused since the secondary star, at 18.″5, is somewhat broader than the primary in the unsharpened image as well as the sharpened image. This may be due to an increase in aberrations towards the edge of the field, or, possibly, the secondary may not be point-like. In any event, the sharpening of the secondary is still good, and the isoplanicity appears to be better for the wider

aperture, as expected.

Aperture (cm)	FWHM of Primary (″)	FWHM of Secondary (″)
58 (unsharpened)	0.76	0.79
58 (sharpened)	0.52	0.59
89 (unsharpened)	0.68	0.71
89 (sharpened)	0.55	0.60

Table 7.3: Real time sharpening results for the IC3583 double star.

Table 7.4 lists the R band (KPNO-Mould) exposures which were taken of the galaxy IC3583 with the MARTINI system. The length of the exposures were kept to $\leq$600s in order to minimise the number of frames affected by lost mirrors, as discussed in the section above. This was not an ideal situation since, particularly with the setup as it was, with the beam-splitter, our data was very read-out noise dominated. Time constraints, and poor conditions on the last night, meant that it was unfortunately not possible to make exposures in other filters, as had been intended.

Frame Num.	Aperture (cms)	Exposure (s)	Seeing (″)
1	89 × 6	300	0.57
2	89 × 6	600	0.64
3	89 × 6	600	0.66
4	75 × 6	600	0.54
5	75 × 6	600	0.56
6	75 × 6	600	0.58
7	89 × 6	600	0.56
8	89 × 6	600	0.57

Table 7.4: Log of MARTINI exposures on IC3583 (all KPNO-Mould R band).

7.3.3 Reduction of MARTINI IC3583 Images

The images obtained by MARTINI of IC3583 were such that a relatively large amount of processing was required to produce the final image. The reasons for this were:

1. There existed a strong, slowly varying, 'pick-up' pattern on all of the images.
2. Coinciding with the bright monitoring star was an increase in the bias level, of around 1 ADU, which decayed slowly back to the normal level over many of the subsequently read-out rows of the CCD.
3. Each image typically had several radiation events, which, because of the count rate, produced not just a single hot pixel, but had a significant halo extending over a number of pixels. Further, two of the images had problems with wandering mirrors which had been lost by the tracking monitor during power glitches. Since both the radiation events and the 'run-away' mirrors produced bad data over a fairly large number of pixels, the images could not be simply stacked. Also the images themselves did not all have the same average intensity, due to different exposure times, apertures and varying transparency, and hence could not be cleaned by simple median filtering
4. The field is quite strongly vignetted in a way which is certainly aperture dependent, time dependent and possibly wavelength dependent. This resulted in the twilight flat-fields being inconsistent amongst themselves, and not very applicable to the images.

The following steps were taken to overcome these problems and to create and calibrate the final image.

1. A stacked bias frame was created from 9 zero-exposure images which were offset to a zero average (excluding blemishes) in the bias strip region.
2. This bias frame was lightly smoothed, to reduce the pixel to pixel noise and the residual pickup pattern. This did not significantly affect any large scale features, which were not, in any case, strong.

3. The bias frame zero-point was offset to each image and flat-field frame in turn, using the good columns in the bias strips, taking care to avoid radiation events, and then subtracted.

4. The pickup pattern on each image was largely removed by taking a 2D Fourier transform of the image, 'zapping' the rows and columns which were a result of the, approximately sinusoidal, pattern and transforming back. ('Zapping' consists of linearly interpolating over the region in question.)

5. By trial and error selected the best flat-field images for each aperture (ie. 75cms and 89cms.) These were normalised to unity in the central, unvignetted, regions and divided into the appropriate images. Some transient bad columns were zapped. Because of the time dependent nature of the vignetting, the results were judged not to have a flat response right to the edge of the frames, and that a border around the images was cut off.

6. A representative intensity was obtained by examination of a large area in each image, avoiding blemishes. The images were then co-added using an algorithm which identified bad data by normalising each image to a common intensity and recording deviant pixels. A 5x5 box around each bad pixel was then cut out of the appropriate image, and replaced by an average of the same area (pixel by pixel) in the other frames. This procedure was designed to remove radiation events and the tracks of 'run-away' mirrors, including any lower level halos. The images were then rescaled back to their true intensities prior to final stacking.

7. The central step in the bias, although small compared to the noise, was largely removed by empirically fitting a wedge to the data and subtracting this.

8. The same de-biassing and flat-fielding scheme was applied to the images taken of the M92 standard stars, and this was used to calibrate the CCD magnitude scale. The preliminary result was that 1 ADU in the final image corresponded to a magnitude of $28.^m6$. By this means a magnitude of $R_{\rm CCD}=12.^m7$ was found for the monitoring star.

   However, this zero-point was not considered very reliable, so subsequent service observations were taken on the JKT by Dr. D.H.P. Jones. These observations gave accurate B and R magnitudes for the monitoring star of $B_{\rm J}$ $=13.^m5$, $R_{\rm KC}$ $=12.^m6$. This corresponds to

a zero-point on the co-added frame of $28.^m5$ per ADU, which is a slight revision of the original zero-point. For the MARTINI observation the sky brightness off the galaxy was 20.5 $R\,mags/\Box''$ and on a typical region the surface brightness of the galaxy was 20.9 R mags/$\Box''$.

7.3.4 Efficiency of MARTINI

One disappointing fact to emerge from the analysis of the JKT images was that, after taking into account the different aperture sizes, and the expected losses due to the MARTINI optics, the final efficiency of MARTINI seemed to be down by about a factor of three from the JKT camera. There are several possible explanations of this:

- it is quite possible that the 'B'-grade CCD was simply insensitive;
- the losses in the optics were more severe than had been calculated;
- some of the light was being obstructed and not reaching the detector; or
- there may have been unusually high atmospheric extinction on that night.

One clue may lie in the examination of the ghost image. This is formed due to a second reflection of the light from the monitoring star from the back of the beam-splitter (9mm thick). Since this travels a somewhat greater distance to the detector, it is out of focus, thus producing the characteristic hexagonal pattern. In other words, there is one out of focus image for each aperture. This light should be subject to, at worst, the same vignetting as the rest of the image; however, the actual variation in the intensity in each of the sub-images is considerably greater than this. In fact, there is almost a factor of three between the highest and lowest. A possible explanation of this is that there was some obstacle in the beam blocking part of the light. This would also seem to account for at least some of the loss in throughput. Since MARTINI is a prototype system, and was thus simply laid out on the optical bench with no cover, it is conceivable that this could have happened despite the care taken in setting the apparatus up.

7.3.5 Object Finding

In order to locate candidate objects in this image, it was first smoothed with a gaussian filter of the same width as the PSF. This was unsharp masked by subtracting a more highly median filtered image of the galaxy. The same procedure was performed on an artificial image which only contained noise, equivalent to that measured off the real data (7.8ADUs per pixel). The threshold was then set so as to exclude the highest peak on the noise frame. This method is optimised to search for point-like objects. By this means, point-sources were detected down to a limiting magnitude of $R \sim 22^m$ over most of the frame, although this limit was not entirely uniform due to vignetting at the edge of the field and enhanced noise in certain regions of high surface brightness, which had to be accounted for.

As a test of this technique, a set of artificial stars of varying magnitude, and complete with photon noise, were placed on the image (using DAOPHOT ADDSTAR, see chapter 2). This was then subject to the same analysis as before. This confirmed that stars down to a magnitude limit of $R = 22.^m3$ were recovered over much of the frame. The artificial stars were modelled on the PSF of the monitor star, using the PSF routine in DAOPHOT. All of the objects which found were in the region of the galaxy. This is indicative of the fact that contamination by foreground and background objects is small. The actual area of galaxy visible in the image is $\approx 0.6\Box'$. The R magnitudes obtained for these objects, and their coordinates on the frame, are listed in table 7.5. This should be referred to the finding chart and plate for IC3583 (figures 7.1 and 7.2).

7.3.6 Discussion

Brighter than $R = 21.^m5$ all the objects appeared extended, or, at least, situated in 'knotty' regions, except for two. These are labelled 4 and 11 and had magnitudes $R = 20.^m8$ and $R = 20.^m9$ respectively. Using JKT photometry we find colours for these stars of $B-R > 0.^m8$ and $B-R = 0.^m2$ respectively, with the former being a lower limit due to being undetected in the B image. Fainter than $R = 21.^m5$ it becomes difficult to reliably differentiate point sources, so, whilst these objects may be considered candidate stars, we shall concentrate on the brighter objects.

Figure 7.1: Final processed 4500s MARTINI CCD image of IC3583. North is at the bottom, and East towards the right, with the long dimension being 70″. The bright central object is the B=13.^{m}5 monitoring star, for which the seeing is 0.″6. The hexagonal pattern towards the bottom of the image is a ghost reflection of the monitor star. The hatched pattern across the middle is a by product of the Fourier masking technique used to remove the pickup pattern from the data.

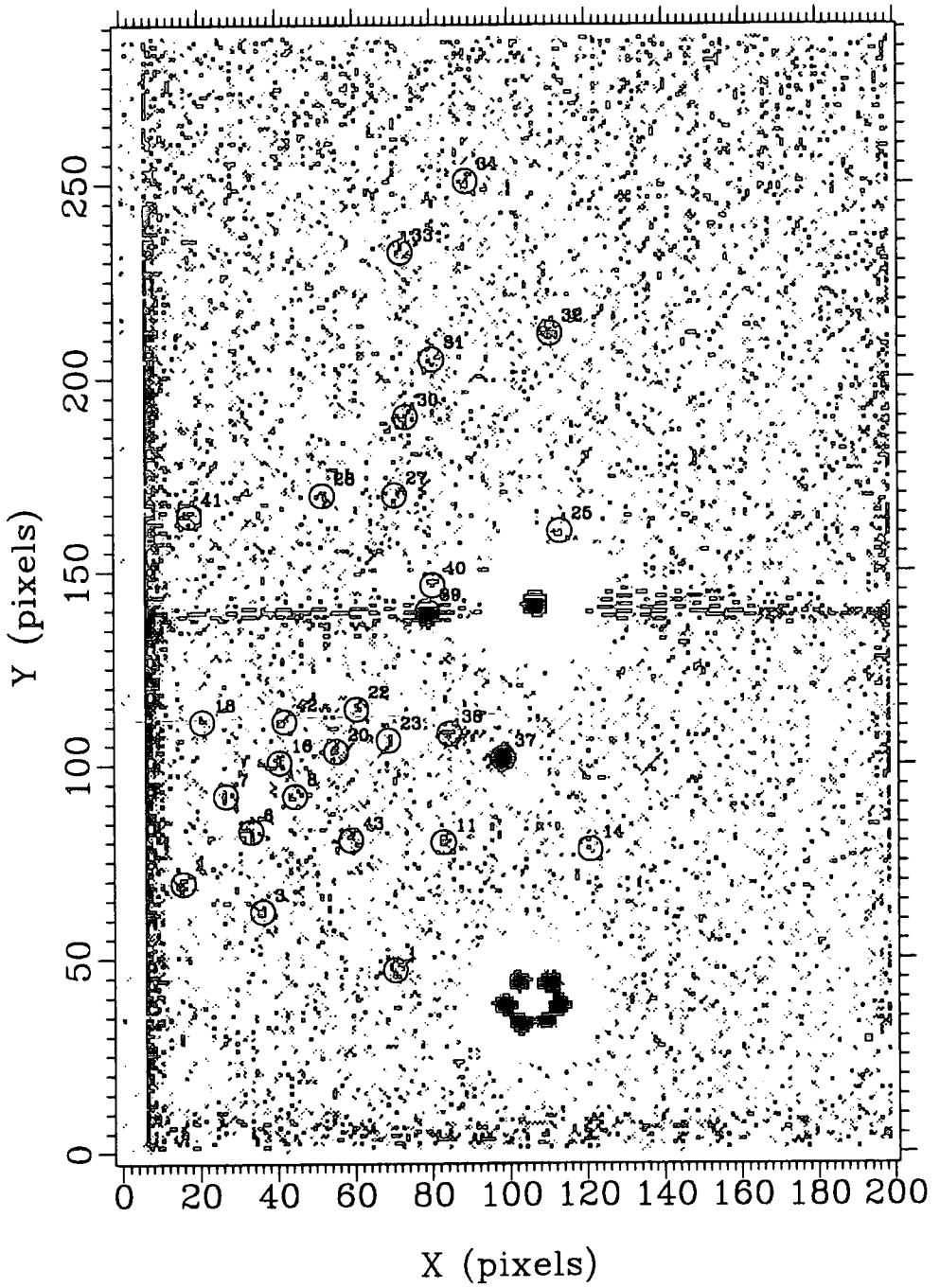

Figure 7.2: Finding chart for discrete objects identified in IC3583. The pixels have been binned 2×2, and an unsharp mask has been subtracted to reveal the objects. All the objects are in the main body of the galaxy which extends to the left of the monitor star.

ID	X	Y	R mag	Notes
37	196	203	19.7	Probable HII region.
39	158	279	19.9	Probable HII region.
4	31	138	20.8	Point-like, $B-R>0.^m8$.
11	165	159	20.9	Point-like, $B-R=0.^m2$.
40	160	292	21.3	Associated with 39.
20	110	206	21.4	Extended.
30	147	380	21.5	Extended.
32	221	423	21.5	Extended.
34	178	501	21.5	Extended.
38	169	216	21.6	Associated with 37.
7	53	184	21.7	
43	117	161	21.7	
14	241	156	21.8	
42	83	222	21.8	
1	140	94	21.9	
8	89	183	21.9	
18	41	222	21.9	
25	226	320	21.9	
3	72	124	22.0	
6	66	165	22.0	
22	121	228	22.0	
27	141	339	22.0	
16	81	201	22.1	
33	144	464	22.1	
23	137	212	22.2	
31	160	409	22.2	
28	103	339	22.3	
41	35	328	22.3	

Table 7.5: The 28 discrete objects identified in IC3583 field.

Now, from §7.1, we know that it would be unlikely that there would be a globular cluster in this galaxy which was brighter than the brightest stars. However, it would surprising if we did not find open clusters and HII regions which were. Although the broad band colours of HII regions are not fixed, they certainly can appear blue, as, in most cases, will young clusters or OB associations. Thus, one of these categories of object is a likely explanation of object 11, especially given the problems of identifying blue supergiants even in nearby galaxies.

Object 4 is a better candidate for being either yellow supergiant or a red supergiant within a cluster, which we have suggested should look similar to a yellow supergiant in terms of the R magnitude and $B-R$ colour. It would seem unlikely to be a single red supergiant given that it so outshines the other detected objects. However, firstly, until a narrow band image is obtained for this galaxy, there remains the possibility that it is a compact HII region. Secondly, the number of foreground stars expected in this magnitude range and this area is approximately 0.3, meaning that there is a reasonable chance of finding one. Once again further broad and narrow band images would help to resolve this uncertainty, but, until such time, this object, cannot be considered a good candidate supergiant either.

By comparison with similar galaxies, such as the LMC (Humphreys and Davidson 1979, hereafter HD79) we see that there would, in fact, be expected to be around 20 stars brighter than $M_R = -9^m$, including some, notably the blue and yellow hypergiants approaching $M_R = -10^m$ (This is based on the same sources for the temperature-colour relations as are given above.) Thus, even if we allow that IC3583 might be a somewhat smaller galaxy and that some stars might have escaped detection due to being within the HII region complexes, close to the monitoring star or ghost image, or in the outer regions of the galaxy outside the field of view, these results suggest a lower limit for the distance modulus of IC3583 of $\mu_{AR} = 30.^m7$, with the extinction correction expected to be small.

7.4 Observations of NGC4523, June 1991

On this occasion, our allocation was for a half night over-ride during a five night MARTINI run, from 1-5 June. The first nights were troubled by poor conditions and instrumental problems, so that, in the end, most of the useful data was gathered on the last night.

7.4.1 Instrumental Setup

The instrument set-up was similar to previous runs. In this case we used a large (1280x1180), blue-coated EEV CCD, provided by the RGO, which has a low, $\sim 5e^-$, readout noise per pixel. We also benefited from greatly increased automation of the mechanisms, and remote control from the main control room. This has the considerable advantage of reducing the heat sources in the vicinity of the instrument, which had, on occasions, added visibly to the local seeing.

With a pixel scale of 0.″139 per pixel, the entire MARTINI field of view, as dictated by the size of the hole in the toroidal mirror, was about 800 pixels across. This also meant that we suffered from the full effects of the vignetting introduced by the MARTINI system, meaning that good flat fields were required. A larger choice of beam-splitters were available on this run, including a large dichroic and several mirrors with holes. Most of the observations were taken with a mirror with a 4″ hole. These new features were expected to effectively increased the signal to noise by a factor ~3, for the same exposure time, over the previous year. In fact, an even greater improvement was seen, as the additional inefficiency problems, noted for the IC3583 observations, did not reappear.

On the earlier nights we, once again, experienced the phenomenon of rapidly varying underlying seeing conditions, on time-scales of a few seconds to several minutes. Visually it appeared that the more rapid variations corresponded to the seeing disk 'blowing up', often to the point where the star could hardly be distinguished on the real-time display. These conditions make the observations difficult, and also raise again the question of whether the performance of image-sharpening in such circumstances, purely in terms of the adherence to Fried theory, is the same as during more stable periods. It also provides further support for the idea that a useful enhancement to the system would be a shutter which could be operated, either automatically or manually, during an exposure

to cut out the periods of poor seeing. Such a system could also be useful for rare occasions when the monitor star is lost completely from the IPD field of view and must be reacquired.

7.4.2 Log of NGC4523 Observations

This galaxy was chosen, from the short-list, as the primary target for several reasons. Firstly, the somewhat brighter monitoring star ($B \sim 12.^m9$) than IC3583, and most other candidates, offered better scope for sharpening. Secondly, there are, fortuitously, three fainter foreground stars in the field of view, providing good calibration of the variation of seeing across the frame due to isoplanatic degradation. In particular, there is a 16^m star at a distance of only 24.″7 from the monitor. The main drawback of this galaxy is its low red-shift, of 262km s^{-1}, which, it may be argued, reduces the confidence that it is a genuine cluster member.

The data was obtained on the last night of the run which had the best conditions, and was also after certain technical problems had-arisen on earlier nights. Just after twilight the unsharpened seeing was measured to be $\sim$ 0.″8. The details of the exposures, which were taken with the Harris filter set, are given in table 7.6.

The seeing for the first image was very good, but thereafter it deteriorated steadily, so that, for some of the later images (frames 4 and 5), it was not even possible to run with the adaptive optics. The isoplanicity was less good, with the field star showing consistently broader images than the monitor. Nevertheless, the first image, taken alone, goes deeper than the previous season's image of IC3583. Most of the analysis was done on an image which was the sum of the first two images. This summed frame had a measured seeing for the monitor of 0.″60, and for the secondary of 0.″76 at $\sim$ 25″.

Approximate photometric calibration, to the Kron-Cousins R scale, was achieved by observing a standard star field in M92, immediately following the Virgo observations. Twilight flat-fields and bias frames were also recorded to aid reduction of the data.

Frame Num.	Filter	Aperture (cms)	Exposure (s)	Seeing on monitor (″)	Seeing on secondary (″)
1	R	75 × 6	300	0.53	0.71
2	R	75 × 6	600	0.64	0.82
3	R	75 × 6	600	0.82	1.10
4	R	110 × 6	300	1.63	1.66
5	R	110 × 6	300	1.45	1.62
6	R	110 × 6	600	1.34	1.53
7	B	110 × 6	600	1.45	1.53
8	B	110 × 6	600	1.30	1.37
9	H_α	110 × 6	600	1.39	1.40

Table 7.6: Log of exposures on NGC4523.

7.4.3 INT Images of NGC4523

Unfortunately the B and H_α images from MARTINI were of poor quality, being both short exposures and in worsening seeing. In addition, the R band calibration was of uncertain reliability as conditions had not been photometric. For this reason Dr. N. Metcalfe kindly acquired additional R, B and H_α images of NGC4523, with the RCA chip on the 2.5m Isaac Newton Telescope. The seeing for these images was around 1″ to 1.″5. The B band photometry was calibrated to the standard Johnson B, but the H_α remained on an arbitrary scale.

7.4.4 Reduction of NGC4523 Images

The basic pre-processing was much more straight forward than had been the case for IC3583. This consisted of the standard steps of bias subtraction and flat-fielding, and additionally cropping the images to cut down the storage requirements. The first two images, which had the best seeing, were co-added, with cosmic-ray removal, to produce a final 900s image. The sky surface brightness

off the galaxy was 20.8Rmags/$\Box''$, and 20.9Rmags/$\Box''$ on a typical region of the galaxy.

Object location proceeded in a similar manner to IC3583. The image was first unsharp-mask subtracted (with bright objects deleted from the mask), and then smoothed. Object location was on the basis of applying a threshold to the resultant image. The threshold was set according to the results of performing a similar procedure on a simulated frame which was flat with an appropriate amount of Poisson noise. This was done as a function of position to take into account the higher noise in the body of the galaxy, and around the edge of the field where there was vignetting.

Over the whole field 85 objects were found with this method, although a few of these are not associated with NGC4523. This is a larger number than found for the IC3583 observations, at least in part due to the increased depth of the exposure. These positions were used to get automated aperture photometry from all the MARTINI R images, and, after obtaining a precise coordinate transform, the INT B and H_α images. This was pursued even if, as was frequently the case, the object in question would not have been confidently detected in the B or H_α images. Thus the objects for which B or H_α magnitudes could not be obtained, were cases where the photometry program failed through insufficient signal.

The plate and finding chart for the detected objects is shown in figures 7.3 and 7.4. The details of these objects are given table 7.7. Note that the R magnitudes given here are extrapolated from $0.''8$ aperture magnitudes to total for the stellar objects and are $2.''5$ aperture magntitudes for non-stellar objects. The criterion for being described as stellar is having a 'Sharp' parameter (column 7) which is less than 0.3. This is defined as $R(0.''8) - R(2.''5)$, but renormalised so that the bright (16^m) foreground star has sharpness parameter 0. The colours are all found within $2.''5$ apertures, which is limited by the INT images. In column (8) we list our preferred identification for the objects brighter than $R = 21.^m5$, based on the sharpness parameter and colours.

7.4.5 Discussion

The fact that we are resolving discrete sources down to $R \sim 23.^m1$, suggests that we can be fairly confident that we have detected some of the brightest stars in NGC4523. This only assumes

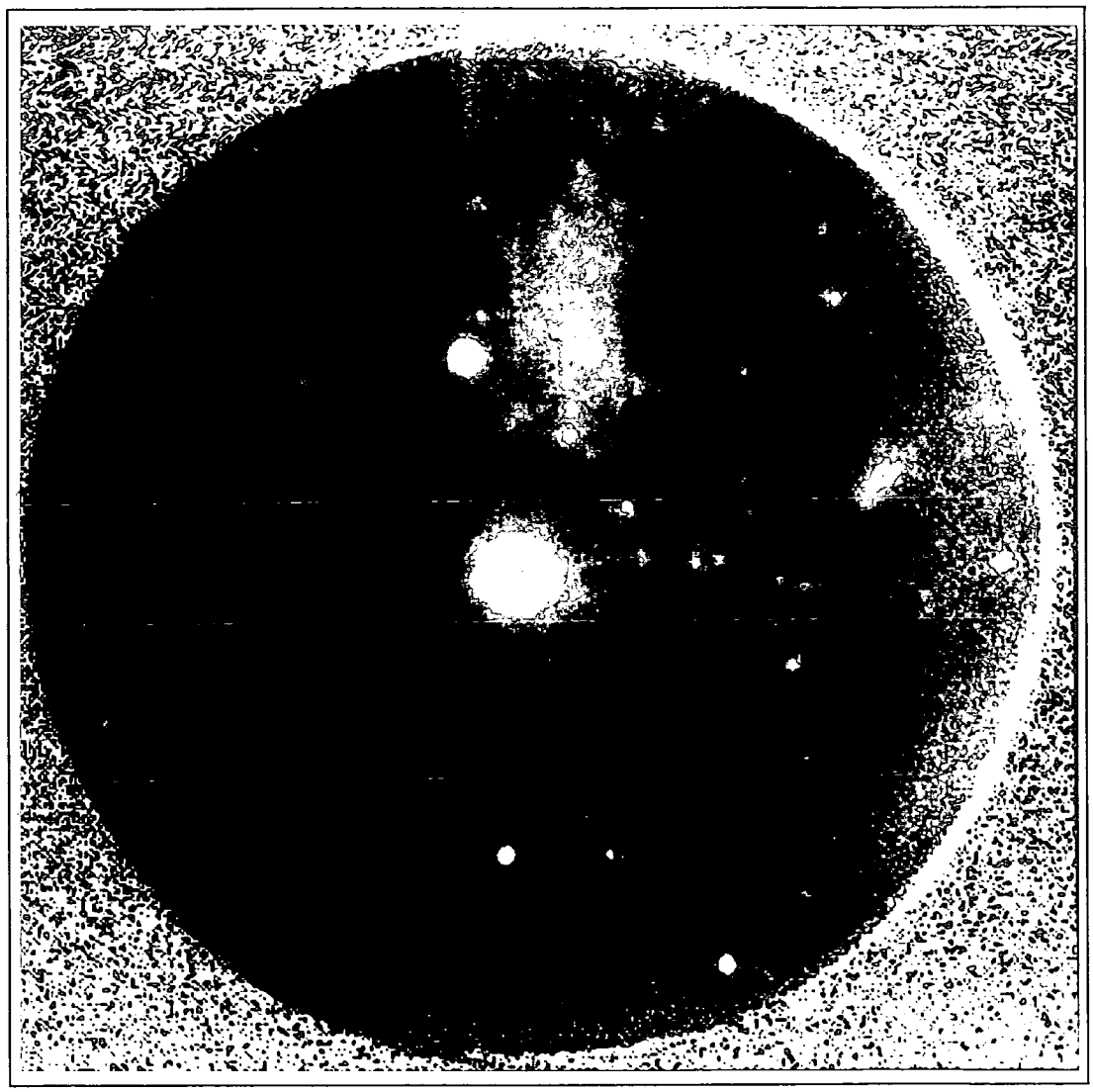

Figure 7.3: Final processed 900s MARTINI CCD image of NGC4523. North is at the bottom, and east towards the left. The bright B =12.^{m}9 monitoring star is at the centre of the 110″ field of view, and has a FWHM of 0.″6.

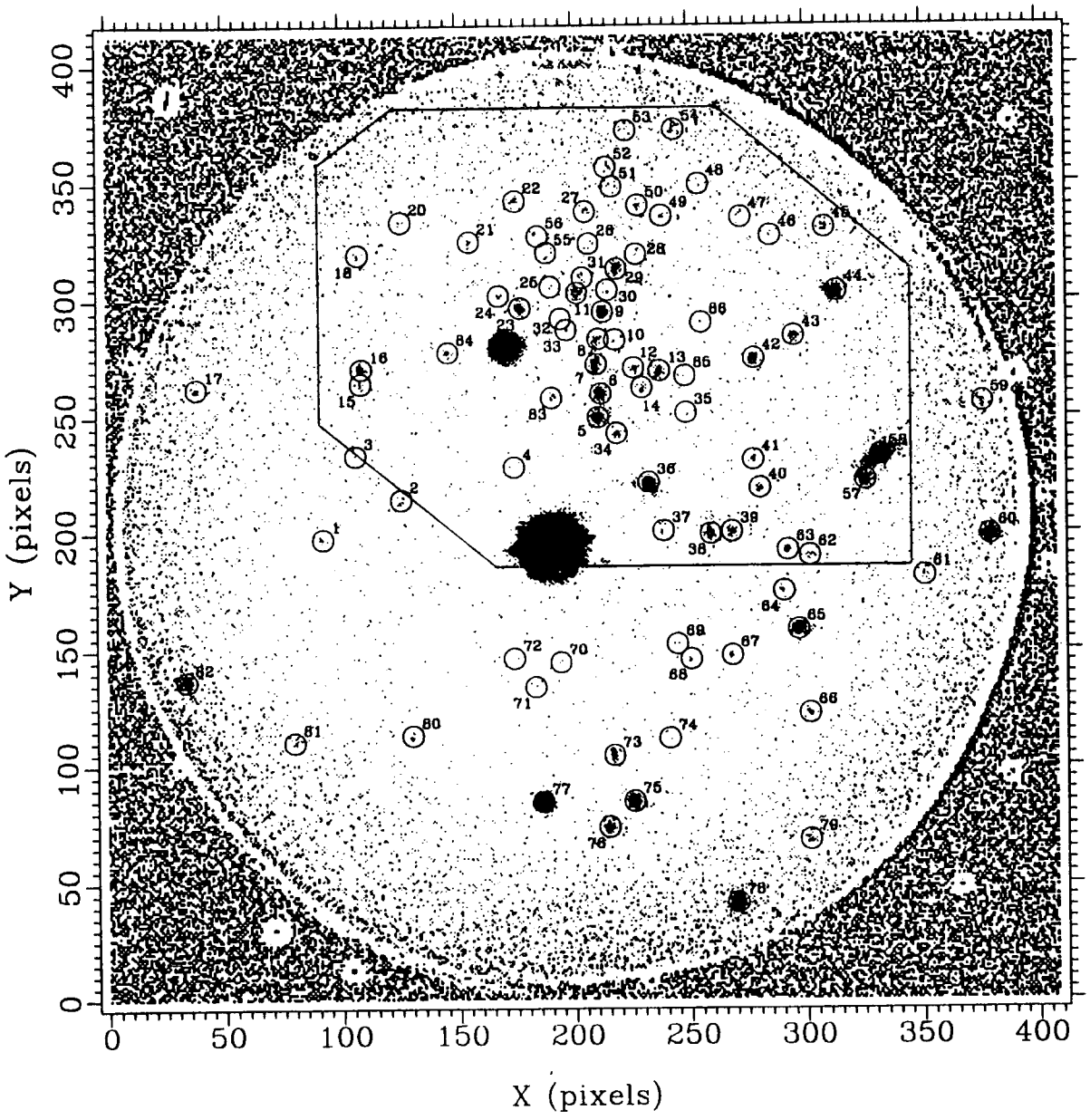

Figure 7.4: Finding chart for discrete objects identified in the NGC4523 field. Once again, the pixels are binned 2 × 2 and an unsharp mask subtracted for clarity. The $\sim 1\square'$ area which is judged to contain the galaxy is shown.

ID	X	Y	R	$B-R$	$R-H_\alpha$	Sharp	Notes
(1)	(2)	(3)	(4)	(5)	(6)	(7)	(8)
77	372	169	18.2	2.21	0.31	0.04	Foreground star
78	540	83	18.6	2.65	-0.31	0.09	Foreground star
58	664	465	19.6	1.59	0.23	0.77	Diffuse
44	627	606	20.2	2.41	0.26	0.72	Diffuse
82	68	272	20.3	1.99	0.79	0.63	Diffuse
65	593	317	20.3	0.66	2.09	0.45	HII region
60	758	397	20.4	2.44	-0.91	0.64	Diffuse
9	426	589	20.4	0.18	0.86	0.30	Blue stellar object
75	451	169	20.5	2.16	0.34	0.34	Foreground star
36	466	442	20.5	0.43	1.80	0.88	Diffuse
10	437	566	20.5	-0.04	1.87	1.23	Diffuse
57	651	445	20.6	0.61	1.17	0.89	Diffuse
5	421	499	20.6	1.37	1.16	0.37	Yellow star
7	420	546	20.7	0.10	2.25	1.02	Diffuse
59	752	511	20.8	1.05	0.97	0.79	Diffuse
22	350	684	20.8	-0.17	2.09	0.88	HII region
6	424	519	20.9	0.19	2.29	0.33	HII region
23	354	593	21.0	0.25	2.31	0.42	HII region
51	433	697	21.0	0.10	0.85	1.11	Diffuse
83	381	516	21.0	-0.18	-	0.98	Diffuse
45	617	661	21.0	-	0.94	0.53	Diffuse
38	518	398	21.0	0.33	2.29	0.43	HII region
16	217	541	21.1	1.56	0.87	-0.02	Yellow star
37	478	401	21.1	0.49	0.64	0.79	Diffuse
39	536	400	21.2	0.04	1.36	0.86	Diffuse
84	293	555	21.2	0.38	1.42	0.58	HII region
8	421	566	21.3	-0.50	2.85	0.70	HII region
42	556	549	21.3	1.76	-0.23	0.30	Yellow star
52	429	711	21.3	-0.04	1.17	1.01	Diffuse

55	378	639	21.3	0.48	1.41	0.86	HII region
62	604	379	21.3	1.01	1.61	0.68	HII region
11	404	606	21.4	-0.18	1.76	0.20	HII region
32	390	583	21.4	-0.24	1.99	0.96	HII region
29	438	627	21.4	-0.34	2.94	0.54	HII region
76	429	148	21.4	1.40	0.74	0.36	Diffuse (off galaxy)
80	260	226	21.4	1.24	0.92	0.51	Diffuse (off galaxy)
17	77	524	21.4	1.20	1.71	0.41	HII region
33	394	574	21.4	-0.12	2.25	0.83	HII region
61	702	362	21.4	0.43	0.26	0.87	Diffuse
40	561	438	21.5	0.55	2.18	0.48	
13	474	539	21.5	-0.19	1.97	0.43	
54	489	745	21.5	-0.13	2.86	0.75	
53	447	743	21.6	-0.01	2.77	0.99	
54	489	745	21.6	-0.13	2.86	0.75	
64	581	349	21.6	-0.33	-	0.74	
12	452	542	21.7	-0.62	2.25	0.55	
27	412	674	21.7	0.47	0.32	0.54	
30	430	608	21.7	-0.70	0.63	0.76	
66	602	245	21.7	-	1.64	0.27	
56	369	655	21.7	-0.10	1.76	0.95	
43	590	568	21.8	0.77	2.41	0.43	
48	508	700	21.8	-0.24	1.69	1.06	
50	457	680	21.8	-0.53	-	0.28	
2	251	428	21.8	0.19	2.16	0.55	
73	434	208	21.8	-	-	0.23	
79	602	136	21.8	-	-	0.22	
4	348	457	21.8	-0.25	1.43	1.23	
41	555	462	21.8	1.20	0.31	0.27	

81	158	220	21.8	-	1.42	0.62	
67	536	295	21.9	0.72	2.13	0.07	
31	408	618	22.0	-0.92	2.75	0.73	
15	217	529	22.0	0.88	-	0.09	
34	437	485	22.1	0.79	-	0.37	
69	489	306	22.1	-	1.28	0.55	
49	477	671	22.2	0.54	-	0.16	
1	184	395	22.2	0.41	1.15	0.27	
18	215	638	22.2	0.59	2.03	0.27	
35	497	503	22.2	0.20	-	0.64	
26	415	647	22.3	-	1.87	1.08	
28	456	639	22.3	-0.99	2.02	0.68	
74	481	223	22.3	-	1.03	0.68	
21	310	650	22.4	-	2.48	0.11	
68	501	293	22.4	0.33	1.73	0.54	
71	366	268	22.4	-	-	0.53	
85	495	534	22.4	-0.65	-	0.85	
14	459	525	22.5	-	-	-0.07	
47	544	670	22.5	-	-	0.09	
70	388	289	22.5	0.26	1.51	-0.01	
24	337	603	22.5	-0.69	2.01	-0.27	
3	213	466	22.7	-	1.72	0.33	
86	510	583	22.7	-	-	0.62	
46	570	654	22.8	-	2.38	0.01	
25	380	610	22.8	-	-	-0.85	
72	348	292	23.0	-	-	0.30	
20	251	667	23.1	-	-	-0.78	

Table 7.7: Data for the 85 discrete objects identified in the NGC4523 field. The columns are described more fully in the text.

that the distance modulus $\mu_0 \lesssim 32$, that we expect there to be several bright supergiants with $M_R < -9^m$ and that the supergiants don't all conspire to be more crowded than the objects we see.

Since the classification of the fainter objects, given the limitations of the INT B and H_α exposures, becomes difficult below about $R = 21.^m5$, we shall again concentrate our attention on the brighter ones. Here we see that there are 4 objects which are within a $1\square'$ area around the body of the galaxy, which are classified as stellar, by virtue of being point-like and having low H_α flux, and hence are candidate supergiants (5,9,16,42). Three of these have intermediate colours, whilst one (9) is blue. Once again, as with the similar object found in IC3583, there would seem to be a good chance that object 9 is an open cluster or OB association. In this instance, we can, however, rule out the possibility of it being an HII region due to its low H_α emission.

Although a larger area of galaxy is seen in this image than that of IC3583, it would still be unlikely that there was more than one foreground star in that magnitude range, especially given that the vignetting reduces the actual area that they could be recovered on. Again, we consider that globular clusters are also ruled out statistically. This still leaves an excess of objects (5,16,42) with colours around $B - R = 1.^m6$, which, therefore, seem to be good candidate yellow supergiants.

A systematic calibration of the yellow supergiant magnitudes is lacking, so, once again, we consider the HD79 results for the LMC, which is a morphologically similar galaxy. Here we find the average magnitude of the brightest three yellow supergiants is $M_R = -9.^m6$. This we can compare to the equivalent quantity in NGC4523, namely $R = 21^m$, to arrive at a distance modulus $\mu_{AR} = -30.^m6 \pm 0.^m3$. Where the estimated error accounts for photometric uncertainty and a dispersion similar to that for other supergiant standard candles. The extinction corrections are likely to be small for a face on galaxy at high galactic latitude. We notice that this distance would make the blue object (9) $M_R = -10.^m2$, which, in fact, would still be plausible for the brightest blue supergiant (in the LMC the equivalent number is $M_R = -9.^m9$). We also note that the possibility that one of our yellow objects is a contaminated red supergiant would not substantially alter out conclusion, although this could be addressed by future V band imaging.

Clearly this modulus must be regarded as provisional pending further studies of the three candidate supergiants, and deeper B band imaging to search for red supergiants by their colours. If any of these objects turns out not to be a star in NGC4523, although, as we have seen, it is unlikely that they are all misidentified, then that would have the effect of increasing the distance estimate.

7.5 Conclusions

We have so far obtained moderately deep images of two Virgo galaxies, IC3583 and NGC4523, in $\sim 0.''6$ seeing with the MARTINI instrument. The astronomical potential of image-sharpening is thus demonstrated, although we note that instrumental problems and a lack of good, stable conditions have so far prevented us reaching the performance, both in terms of depth and resolution, which we believe possible.

The IC3583 image shows objects down to $R = 22.^m3$. Of the brighter ($R < 21.^m5$) images, only two are point-like. One of these is blue, and is probably an open cluster or HII region. The other object is less easy to classify, without good colour or line-emission information, but may be a foreground star or HII region. By comparison with the numbers of bright supergiants in the LMC, we conclude that a lower limit to the distance of this galaxy of $\mu_0 = 30.^m7$ is suggested from this image.

Although a considerably shorter total 'good-seeing' integration (900s compared to 4500s), the NGC4523 image goes roughly 1^m deeper, and shows correspondingly more objects. This was brought about by several improvements in the instrumental setup between the two runs. It also covers a greater field, thanks to a large format CCD, albeit vignetted at the edges. In this case we benefit from having deeper B images and also H_α which enables us to reject non-stellar objects with more confidence. Of the point-like objects which show little line-emission, one is blue, and hence probably an open cluster, and three are of intermediate colour. It is very unlikely that all three of these yellow objects are foreground, so we tentatively identify them as candidate yellow supergiants, and infer a distance for this galaxy of $\mu_0 = 30.^m6$. If this is the case, then many of the

fainter objects on this frame would be expected to be red supergiants, something which could be tested with a deeper B exposure. Alternatively, if it is that one or more of these objects has, in fact, been misidentified, then that would tend to imply a larger distance.

Further observations are required to clarify this situation. More colours, narrow band observations and even spectroscopy, would enable much stronger statements to be made about the brightest stars in the two galaxies already studied. Deeper, higher resolution images would also allow us to begin searching for variable stars; recalling that the brightest Cepheids have absolute magnitudes $M_R \sim -6.^m5$, they should appear at $R = 24^m$–25^m if our low distance to NGC4523 is correct. Ultimately, a larger sample of galaxies must be observed to beat down the errors on the distance estimates, and also to get a clearer idea of the distribution of the galaxies in the line of sight.

Finally, we note that a recent preprint by Pierce, McClure and Racine, claims to have resolved stars in another Virgo galaxy, NGC4571, using the HRCAM at CFHT. Again the candidate brightest stars have magnitudes $R \approx 21$, and their inferred distance is $\mu_0 = 30.^m9 \pm 0.^m2$. This result is in good agreement with our observations of NGC4523, and provides further confirmation of the viability and importance of this program. The value of H_0 which would be concluded from this low Virgo distance would be in the region of 80–90kms^{-1}. As discussed in chapter 1, this would have serious implications for cosmology.

Chapter 8

Conclusions

This thesis has been concerned with applying modern observational tools to the study of resolved stars in external galaxies, with the primary aim of estimating their distances. Specifically, we have employed techniques of profile-fitting photometry to analyse crowded fields in M31 and M33, and have developed, and used, the method of image-sharpening to search for the brightest supergiants in two Virgo Cluster galaxies, IC3583 and NGC4523. The motivation for this work arose from the continuing controversy over the extragalactic distance scale, and, in particular, the implications for cosmology of high values of the Hubble constant. Here we reiterate the main results and conclusions of this work, and elaborate, briefly, on their consequences and the prospects for future work.

8.1 Techniques of Crowded Field Photometry

In chapter 2, we showed that the large numbers of resolved stars in the CCD fields of M31 and M33 mean that errors are dominated by crowding rather than photon shot noise, and necessitate the use of profile-fitting photometry. We outlined the standard reduction procedure, using the DAOPHOT software, and considered three particular areas where improvements could be made. Firstly, we showed, in simulation, that significantly ($\sim 25\%$) more stars could be found, in well sampled, high signal-to-noise data, by locating objects on a maximum entropy deconvolution of the image, than

with DAOPHOT 'FIND' on the original image. Secondly, we discussed, at some length, the method of creating a background sky frame by iteratively subtracting the known stars. This technique is particularly valuable in situations of rapidly varying background intensity. Finally, we considered the use of the theoretical seeing profile in determining the wings of the point-spread function, as an alternative to the empirical method.

8.2 The Distances to the Nearby Galaxies M31 and M33

Chapters 3 and 4 presented the results of the profile fitting photometry of Cepheid fields in M31 and M33. Our intention was to provide new estimates of the extinction, which has previously been the most serious point of contention in the distances to both of these galaxies, from the colour excess of the main-sequence stars.

In the case of M31 BVR photometry was obtained for $\sim$ 2300 stars, to a limit of $V \sim 23.^m5$, in Baade's field IV. The dominant population in this field are red-giants from an old disk population. From the position of the red-giant branch we estimated a metallicity of $[Fe/H] = -1.6 \pm 0.2$. The main sequence was also evident, implying the presence of a younger stars. By comparison with theoretical loci we found a (model dependent) age of the youngest field stars of $\sim$ 100Myrs, and also supported previous suggestions that this field has low metallicity. The position of the main-sequence, with due account of age and metallicity effects, was used to provide an estimate of the reddening of $E_{B-V} = 0.09 \pm 0.05$. Finally, we recalibrated the original photographic Cepheid photometry of Baade and Swope (1963) and, in conjunction with the estimated extinction, found μ_0(M31) = 24.44 ± 0.16.

Field 9 in M33 posed an even more difficult data reduction task. In this case, BV photometry was obtained for $\sim$ 4500 stars, although to a brighter limit of $V \sim 22.^m5$. The detected stars were all from a young population, largely on the main-sequence. By splitting the frame up into 24 smaller areas, we showed that the reddening appeared to be dependent on position, and was up to $E_{B-V} \sim 0.2$. The highest values were, perhaps surprisingly, at the end of the field most distant from the nucleus. We compared our photometry with the recently published results of Wilson *et al.*

(1990), and discovered significant zero-point offsets, especially in the B band where it amounted to $0.^m14$. Our zero-points were, however, in better agreement with those of most other authors. This is important since the same zero-points were used by Freedman *et al.* (1991) in their new, direct, $BVRI$ observations of the M33 Cepheids. Recalibrating their Cepheid BV photometry, accordingly, and applying individual extinction estimates to each of the 6 Cepheids in the frame, we found $\mu_0(\mathrm{M33}) = 24.5 \pm 0.25$.

The errors on both these estimates are still dominated by the extinction. However, we feel that the error in the extinction is now in a large part due to the photometric zero-point uncertainty, as highlighted by the comparisons of different authors. Clearly, this is a matter which could ofton be addressed with only a small expenditure of telescope time. It is, however, also true that the Cepheid sample sizes used in both these studies, are less than ideal, and observations of further fields are called for.

8.3 The Technique of Astronomical Image Sharpening

In chapter 5 we outlined the theory of atmospheric seeing and described the gains predicted for wave-front tilt correction. The two image-sharpening cameras which we have used, the TRIFFID and MARTINI, were described, along with some of the experimental procedures and instrumental modifications developed during the course of the observing programs.

In chapter 6 we went on to describe our investigations of the image-sharpening technique, which mostly used bright multiple star systems as control objects. The basic prediction of a maximum sharpening gain at small apertures, typically 25cm to 50cm in the B band, was confirmed, although the level of improvement was not as good as expected. Two factors were suggested to explain this: firstly, much of the data was acquired in atypical weather conditions, and, secondly, local 'dome' or 'mirror' seeing could be imposing a baseline to the resolution.

The best gain was from $0.''59$ FWHM seeing to $0.''31$. Simple experiments with frame selection, on this data set, improved this figure to $0.''23$ using the best 22% of frames. Simulations of

the CUSPS real-time sharpening algorithm were shown capable of producing 0.″34, although this required careful optimisation of the parameters.

Observations of the Trapezium allowed investigation of the functional form of the isplanatic patch. These results showed that the optimum conjugate focus on that night was low, in the region of 0km to 1km, and followed, reasonably well, model predictions.

Work still needs to be done in several basic areas, such as more reliable evaluation and control of 'dome' seeing, and empirical study of the turbulent structure of the atmosphere. In addition, several interesting developments may broaden the scope of image-sharpening in the near future. These include:

- High quantum efficiency photon counting devices (eg. avalanche photo-diodes), to replace the IPD. This would allow $\sim 2^m$ fainter monitoring stars and greatly increase the number of potential targets.
- Higher order wave-front correction, possibly making use of commercially available segmented mirrors;
- Application to the near infra-red. Here the intrinsic seeing is better, and the optimum aperture larger. Furthermore the timescales of motion are longer, and the isoplanicity is greater. This has led to considerable effort on image-sharpening in the near infra-red, and, in any event, is also a good argument for observing at the longest wavelengths compatible with the project.

In the longer term, we have noted several ambitious programs aimed at performing ground-based, long base-line, interferometry in the optical and infra-red to produce ultra high resolutions. These could ultimately be aided by the use of laser guide star technology, which it is hoped, in principle if not yet in practice, will enable measurement of the full wavefront corrugation.

8.4 The Distance to the Virgo Cluster

Finally, in chapter 7, we reported the first attempts, using the MARTINI instrument, to extend stellar distance indicators to the Virgo Cluster. So far we have obtained moderately deep CCD images of two Virgo galaxies, with $\sim 0.''6$ resolution. For IC3583, we showed a finding chart for 28 discrete objects which we identified, with $R < 22.3$. Of the brighter objects ($R < 21.5$), only two were classed as possible brightest supergiants, but both cases it was thought unlikely. The first because it was blue, and hence probably an open cluster, and the second because there is a good chance of finding either a compact HII region or foreground star in the field, with such a magnitude. Based on the number of detected objects, we concluded a lower limit for the distance modulus of this galaxy of $\mu_0(\mathrm{IC3583}) \gtrsim 30.^m7$.

In the NGC4523 field, we located 85 discrete objects to $R < 23.1$, most being within the area of the galaxy. Here, deeper colour and line-emission information allowed much more confident rejection of unwanted objects, and resulted in the identification of three convincing candidates for being yellow supergiants. Using their average magnitude, and comparing it to the same quantity in the LMC, we deduced a distance modulus of $\mu_0(\mathrm{NGC4523}) = 30.6$.

These results have demonstrated that the possibility now exists of using resolved stellar distance indicators to address the Virgo Cluster distance with ground-based observations. The combination of high resolution, from image-sharpening, and multi-band exposures can be used to tackle the problem of identifying brightest stars. Given the short (900s) NGC4523 exposure time, and our experience of achieving even better seeing, we are also optimistic of being able to reach the brightest Cepheids with ground-based observations. We have argued that this could be complemented by lower resolution shorter wavelength studies, which should be able to identify Cepheids from their variability, irrespective of crowding, and hence provide light curves.

8.5 The Hubble Constant and Cosmology

We argued in chapter 1 that the Virgo Cluster was central to the distance scale as it is where the population I and population II distance scales come together, and it allows us to step to much more distant clusters, beyond the effects of local peculiar flows. Taking the average of our NGC4523 and the Pierce *et al.* NGC4571 distances, we arrive at 14.2Mpc for the Virgo Cluster. This, by most estimations, corresponds to a Hubble constant in the region of 80 – 90 $\mathrm{kms^{-1}Mpc^{-1}}$. If this is genuinely the case then we are faced with the well known problem for high values of H_0, of being unable to reconcile the age of the universe in the 'standard' $\Omega_0 = 1$, $\Lambda = 0$ model of the Big Bang, with the ages of stars predicted from stellar evolution theory. Either the stellar physics is seriously wrong, or we are forced to revise our cosmological model. Simply lowering the value of Ω_0 would probably force us to abandon inflation, would also contradict the recent COBE detections of fluctuations in the microwave background radiation (Smoot *et al.* , preprint), In any case, this would not increase the age sufficiently. Instead, it seems that, at least, a non-zero cosmological constant would have to be invoked.

However, before entertaining these possibilities seriously, it is necessary to make further observations to confirm or refute our preliminary analysis of NGC4523. Even then, distances to only one or two galaxies are not sufficient to rule out the possibility of confusion by depth effects, given that the spiral galaxies are known to be more widely distributed than the early types, and may even extend away from the cluster along filaments. For the present, then, the distance scale remains, very much, a central and exciting problem in cosmology.

Appendix A

BVR Photometry for Stars in M31

The following table contains the full details of the Johnson B, V and Kron-Cousins R photometry obtained for all the stars in M31 which were included in the final colour-magnitude diagram presented in chapter 3 (ie. all the stars which were matched on at least two of the passbands, according to the criteria for cross-identification).

Num	X	Y	B	V	R
1	73.8	5.3	24.71	23.06	22.48
2	144.1	17.0	-	23.48	22.84
3	91.9	39.0	24.19	23.25	22.56
4	17.8	42.1	25.10	23.32	22.58
5	339.9	43.4	23.68	21.77	20.86
6	326.6	55.0	23.45	23.53	22.86
7	116.3	59.1	22.56	21.07	20.66
8	86.0	60.5	-	23.00	22.11
9	276.3	62.5	24.66	23.28	22.23
10	270.6	65.5	24.71	23.34	22.55
11	53.7	92.8	23.81	23.51	23.29
12	28.8	106.9	24.36	23.16	22.15
13	7.8	131.2	24.80	23.13	23.15
14	267.3	148.7	24.33	23.62	23.10
15	246.6	189.9	24.35	23.25	22.58
16	117.5	194.2	23.66	22.89	22.05
17	89.8	212.6	24.53	22.94	22.21
18	81.3	259.4	25.12	23.06	22.51
19	251.6	297.4	24.22	23.31	22.30
20	191.2	300.0	-	23.44	23.12
21	40.3	304.3	23.81	23.30	22.96
22	40.1	338.2	24.23	23.72	23.68
23	37.7	356.8	24.26	22.86	22.24
24	87.9	429.0	23.19	23.08	22.78
25	16.6	434.9	23.14	22.81	22.25
26	27.0	437.6	24.25	22.80	21.95
27	238.3	5.3	25.21	23.53	23.49
28	274.5	6.3	24.95	23.54	22.34
29	278.3	8.5	25.17	23.58	23.44
30	98.3	7.8	25.40	23.19	22.11
31	356.0	9.8	24.91	23.52	23.52
32	12.1	13.9	-	23.42	22.75
33	316.0	61.2	24.55	23.14	22.32
34	254.8	70.7	24.57	22.85	22.17
35	257.6	80.9	24.51	22.72	22.33
36	128.1	116.7	24.84	23.94	22.18
37	278.6	130.3	24.52	23.02	22.35
38	92.2	160.3	-	23.21	22.47
39	196.7	165.9	25.03	23.39	22.67
40	198.2	169.4	24.61	23.04	22.20
41	244.4	175.4	24.28	23.37	22.12
42	9.0	180.7	24.35	23.33	22.78
43	54.8	205.8	25.72	23.22	22.42
44	211.3	216.3	24.65	23.35	23.02
45	210.8	219.6	24.80	22.92	22.24
46	107.0	328.9	23.52	22.58	21.87
47	106.5	334.0	24.62	23.33	23.10
48	231.3	344.4	24.56	22.88	21.86
49	105.5	345.1	23.11	22.93	22.61
50	105.4	348.0	22.46	22.06	22.21
51	101.0	365.9	24.73	23.56	23.19
52	62.6	420.1	-	23.33	22.31
53	130.8	429.7	23.61	23.22	22.43
54	186.3	430.7	-	23.52	23.22
55	275.3	452.6	24.70	23.64	22.40
56	76.1	468.8	24.04	23.31	23.27
57	76.7	471.5	23.98	23.08	22.01
58	5.1	482.6	24.09	23.20	22.81
59	244.1	482.3	25.35	23.42	22.83
60	311.5	483.1	25.64	23.81	22.43
61	310.3	486.0	24.17	22.78	21.81
62	166.2	484.4	-	23.05	22.67
63	336.2	13.6	22.98	22.57	22.98
64	331.9	18.5	23.70	22.92	22.45
65	207.8	18.5	-	23.90	23.08
66	306.2	56.1	22.93	22.80	22.61
67	309.5	60.3	22.76	22.50	22.54
68	148.7	70.4	24.15	24.22	24.50
69	263.8	80.4	-	24.17	23.29
70	55.5	107.7	25.01	22.94	22.36
71	52.3	110.7	22.70	22.52	22.53
72	42.0	151.0	24.83	23.55	23.49
73	7.9	165.5	24.12	23.64	23.20
74	16.2	161.3	25.24	23.18	22.68
75	18.3	163.6	24.85	23.64	22.57
76	282.4	196.3	24.19	23.48	22.44
77	285.5	199.7	24.45	23.73	23.34
78	237.2	205.4	24.97	24.31	23.56
79	238.4	208.1	24.76	24.02	23.86
80	353.0	277.4	-	23.90	23.76

Num	X	Y	B	V	R
81	356.0	285.2	23.64	23.48	23.05
82	271.0	332.5	25.19	23.02	22.45
83	353.9	339.3	21.23	21.15	21.29
84	256.3	352.9	24.62	22.90	22.18
85	8.4	411.2	24.16	22.93	22.03
86	328.7	465.6	23.44	23.07	22.22
87	255.5	20.9	24.76	23.06	22.25
88	211.3	23.5	25.76	23.47	22.84
89	211.6	26.9	24.84	24.25	23.71
90	23.5	53.8	22.11	21.11	20.60
91	216.2	55.2	24.73	23.44	22.69
92	215.9	58.9	24.55	23.59	22.56
93	210.7	60.4	24.10	22.84	21.97
94	173.9	64.3	25.40	23.80	23.38
95	331.7	71.0	21.75	21.71	21.75
96	12.5	78.9	24.81	23.46	22.60
97	13.3	84.4	25.19	23.17	22.75
98	355.4	103.2	21.35	21.43	21.53
99	275.0	185.2	-	23.27	22.76
100	279.0	189.8	-	24.24	22.64
101	51.3	212.8	24.51	22.67	21.97
102	47.3	214.8	23.91	23.45	22.41
103	233.7	338.1	24.43	23.35	22.71
104	353.5	352.7	23.07	21.99	21.59
105	352.2	350.2	24.12	23.05	22.03
106	347.7	351.8	24.48	23.38	22.44
107	349.8	358.3	23.91	23.32	23.00
108	349.3	364.3	-	22.78	22.01
109	20.8	7.8	25.66	23.57	23.17
110	282.8	26.5	22.07	21.94	22.12
111	12.6	46.5	24.79	22.93	22.10
112	292.0	125.0	25.14	23.06	22.69
113	284.9	122.3	23.91	23.10	22.62
114	33.5	137.1	25.12	24.42	23.35
115	66.2	208.1	25.28	23.49	23.24
116	61.7	210.8	-	23.14	22.84
117	59.0	209.3	23.48	23.78	23.66
118	68.2	218.4	24.91	23.08	22.42
119	82.1	218.0	25.04	23.26	23.33
120	17.9	299.1	24.69	23.10	22.72
121	20.6	302.9	24.91	23.48	22.85
122	143.4	306.4	24.26	23.39	21.98
123	140.0	308.6	25.33	23.75	23.32
124	9.5	346.5	24.27	23.12	22.65
125	12.0	350.5	24.70	23.45	22.50
126	267.5	371.3	24.30	23.22	22.53
127	272.4	374.8	24.61	23.84	22.33
128	27.3	424.4	23.83	22.88	22.47
129	305.5	432.2	23.75	23.51	23.27
130	257.2	11.6	-	23.33	23.19
131	267.2	49.7	24.92	23.49	22.40
132	264.9	56.6	23.97	22.88	21.93
133	264.0	60.7	23.82	22.84	21.79
134	27.5	143.7	24.03	23.33	22.04
135	28.4	147.5	24.77	23.16	22.40
136	23.5	148.4	24.60	23.29	23.49
137	99.7	234.2	22.93	21.59	20.87
138	95.6	231.1	24.53	23.66	22.44
139	125.1	280.6	24.55	24.07	22.75
140	132.5	282.4	24.88	23.43	22.72
141	134.9	282.2	24.34	23.10	21.99
142	86.4	413.1	-	22.61	22.30
143	82.7	407.4	23.88	23.24	22.01
144	13.6	426.8	24.55	23.13	22.42
145	26.6	85.3	23.32	23.33	23.36
146	24.3	95.5	24.31	23.17	23.37
147	20.9	97.0	24.47	23.11	22.57
148	16.4	99.2	23.06	22.20	21.66
149	11.5	95.8	-	23.58	23.60
150	122.7	106.9	24.85	23.83	23.17
151	121.1	110.3	24.42	23.17	23.27
152	116.1	115.2	24.23	23.21	23.28
153	28.7	122.6	24.55	23.56	22.81
154	118.0	164.2	21.89	21.81	21.87
155	34.8	154.7	24.81	22.78	22.03
156	31.7	158.6	24.17	23.42	22.00
157	38.1	211.2	25.01	22.96	22.61
158	278.5	15.4	24.25	23.59	23.10
159	108.5	235.6	23.92	22.99	22.23
160	104.1	245.6	22.04	20.56	19.99

Num	X	Y	*B*	*V*	*R*
161	52.2	313.8	24.02	23.26	22.70
162	53.3	317.7	24.21	23.63	22.70
163	135.8	10.9	25.65	23.62	22.92
164	138.3	10.5	25.06	23.74	24.08
165	261.1	39.6	23.66	23.06	22.84
166	258.2	46.6	21.29	20.14	19.52
167	251.1	52.6	24.20	23.04	22.28
168	257.3	54.7	24.83	23.03	22.80
169	47.4	105.1	24.25	22.72	22.02
170	43.2	108.7	25.54	23.04	22.31
171	97.6	102.6	24.68	23.33	22.71
172	99.8	116.1	24.18	23.35	22.73
173	94.2	111.9	24.01	22.82	22.13
174	32.1	246.8	25.34	23.88	23.39
175	38.0	247.4	24.59	23.43	22.36
176	45.1	256.6	25.17	23.68	23.46
177	33.5	273.7	24.64	23.61	22.58
178	28.4	269.2	25.07	23.71	23.00
179	28.4	275.0	-	23.84	23.09
180	346.4	308.8	25.16	23.08	22.36
181	14.0	30.0	25.34	23.46	23.01
182	17.5	33.1	24.56	22.70	21.83
183	19.2	106.6	24.13	23.61	23.24
184	19.4	114.0	25.40	23.33	22.99
185	23.9	116.2	24.91	23.65	23.85
186	21.0	121.3	24.89	23.14	22.23
187	267.2	23.5	-	24.09	24.07
188	262.8	24.1	23.44	23.29	22.80
189	279.6	41.1	22.70	22.60	22.68
190	263.6	27.8	24.55	22.58	22.06
191	269.5	31.1	25.52	23.85	23.61
192	270.8	38.6	23.56	21.94	20.96
193	251.5	40.0	24.24	23.05	21.77
194	235.5	44.8	-	23.35	22.33
195	234.7	49.0	25.37	23.22	23.15
196	238.4	51.1	24.47	23.58	22.80
197	348.8	42.2	23.31	23.70	23.33
198	345.0	56.4	24.20	22.78	22.43
199	341.7	50.9	-	23.40	23.11
200	338.0	56.3	25.42	24.09	22.94
201	347.2	192.4	24.91	23.71	23.42
202	0.0	0.0	23.81	23.13	-
203	350.6	201.4	23.35	22.90	22.54
204	355.6	210.7	22.07	21.97	21.99
205	352.9	205.3	22.40	22.31	22.22
206	51.4	227.7	24.92	23.77	23.09
207	53.2	232.2	-	24.08	22.97
208	52.5	237.3	25.49	23.25	22.72
209	63.9	231.8	25.36	23.55	24.15
210	68.9	238.8	-	22.35	22.06
211	59.3	267.1	-	23.33	23.52
212	78.5	268.3	24.52	23.84	23.42
213	74.6	275.5	24.34	23.22	22.00
214	65.9	273.5	23.76	23.38	23.47
215	63.4	269.8	25.23	23.76	22.51
216	77.1	417.2	24.76	23.63	22.31
217	15.1	476.7	-	23.20	23.26
218	225.5	108.2	25.06	23.84	23.50
219	216.6	112.2	-	22.77	21.94
220	120.3	131.5	24.66	23.21	22.10
221	121.2	138.6	25.07	23.19	22.65
222	117.2	144.8	24.81	23.83	23.20
223	229.5	217.8	25.08	23.62	23.39
224	234.0	222.5	-	23.37	23.72
225	255.0	479.4	-	23.32	22.36
226	251.4	479.7	24.98	23.05	21.91
227	276.8	477.5	-	22.99	22.34
228	271.3	479.2	23.54	22.83	22.11
229	65.0	244.8	24.18	22.51	21.59
230	65.8	248.9	25.36	23.41	22.63
231	59.7	249.2	24.05	22.73	22.27
232	62.3	251.7	25.91	23.05	22.91
233	56.7	251.8	24.38	23.12	22.90
234	52.3	254.6	24.13	22.56	22.37
235	48.9	249.8	24.63	24.07	23.94
236	59.8	258.1	23.34	22.75	22.67
237	51.1	245.5	24.78	23.52	23.02
238	308.8	68.6	22.29	22.37	22.25
239	315.8	77.3	22.93	22.86	23.23
240	321.3	75.9	22.20	22.20	22.35

Num	X	Y	*B*	*V*	*R*
241	310.6	80.7	24.26	23.21	22.88
242	325.7	77.1	23.24	23.05	23.71
243	328.9	79.9	-	23.23	23.32
244	319.3	92.1	22.74	22.19	21.85
245	306.0	94.7	22.84	22.83	23.09
246	57.0	337.9	23.36	23.10	22.82
247	51.5	347.3	25.47	23.67	23.39
248	54.8	348.9	25.01	23.41	22.04
249	60.5	351.9	23.94	23.51	22.87
250	121.3	479.8	24.01	23.00	22.48
251	122.1	484.7	23.63	22.41	22.03
252	218.2	5.7	25.50	23.62	22.96
253	221.3	7.3	23.96	22.49	21.78
254	237.7	30.9	25.86	23.88	23.17
255	229.1	9.6	24.41	22.80	22.00
256	234.8	15.5	24.77	24.02	23.24
257	248.1	12.8	22.48	21.28	20.98
258	246.7	20.7	24.55	22.73	21.87
259	244.8	25.4	24.92	22.75	22.60
260	239.4	27.0	-	22.86	22.14
261	72.2	71.6	25.21	23.91	23.99
262	69.3	73.5	24.44	23.63	23.17
263	68.5	76.1	24.47	22.94	22.17
264	68.4	96.6	22.02	21.65	21.47
265	61.8	80.0	24.29	23.15	22.34
266	59.2	89.1	20.52	20.20	19.97
267	6.3	312.8	-	23.47	22.34
268	13.4	317.8	24.41	23.72	22.36
269	18.8	320.0	23.27	22.92	22.86
270	23.4	321.1	21.63	21.86	21.81
271	27.4	320.9	-	23.89	22.54
272	36.2	317.0	23.79	23.38	22.57
273	123.1	440.5	21.74	20.38	19.55
274	43.6	384.1	24.37	23.49	22.44
275	39.2	389.7	23.88	23.75	23.41
276	36.8	392.0	-	23.07	22.33
277	31.1	393.3	23.83	22.44	21.78
278	36.5	395.9	23.91	23.14	22.68
279	25.9	395.3	-	23.28	22.42
280	33.5	399.1	-	23.65	23.54
281	35.3	403.7	25.36	24.04	23.59
282	25.1	405.9	22.89	21.62	20.92
283	27.2	408.6	23.86	23.31	22.46
284	93.0	340.1	-	23.70	22.52
285	83.1	363.8	24.43	23.14	22.71
286	85.5	344.7	22.98	22.67	22.25
287	80.9	347.3	-	23.71	23.37
288	87.9	349.3	24.46	23.78	23.35
289	94.4	347.8	23.51	22.66	22.44
290	82.4	366.7	23.85	23.27	23.28
291	88.5	357.6	-	23.75	23.30
292	97.2	357.8	24.88	23.06	22.04
293	96.2	361.8	24.04	23.08	23.53
294	90.5	364.3	24.46	23.17	22.62
295	99.8	354.2	-	23.80	23.27
296	350.2	24.8	24.04	23.11	22.92
297	354.1	24.6	-	23.98	23.61
298	346.6	28.7	-	23.62	22.86
299	332.9	28.3	-	22.53	22.13
300	326.5	28.0	25.53	23.01	21.85
301	326.7	32.4	22.47	22.24	22.13
302	329.6	42.2	24.77	23.52	22.64
303	329.0	25.1	24.15	23.22	22.67
304	326.8	6.0	24.02	22.39	21.49
305	328.3	12.3	24.11	22.81	22.42
306	322.8	12.5	-	23.15	22.72
307	315.0	18.2	21.57	21.56	21.38
308	311.0	6.7	24.05	22.55	21.98
309	312.6	9.0	24.25	22.63	21.92
310	309.7	23.5	24.97	23.82	23.35
311	303.4	14.3	25.47	23.07	22.47
312	291.1	14.7	23.72	24.04	23.63
313	118.8	269.1	-	23.67	23.42
314	136.1	276.2	23.11	21.99	21.88
315	106.6	279.1	23.75	22.29	21.78
316	111.3	277.9	23.63	22.29	21.89
317	95.9	434.3	-	23.61	22.50
318	103.6	441.5	21.23	20.57	20.09
319	102.5	447.2	24.66	23.12	22.67
320	97.8	448.3	-	23.64	22.77

Num	X	Y	B	V	R
321	166.9	14.7	-	22.68	22.50
322	162.7	18.0	22.52	22.20	22.17
323	173.6	14.0	22.67	22.12	22.43
324	180.2	17.9	24.64	22.92	22.19
325	157.3	27.0	24.67	23.20	22.99
326	165.2	29.8	22.05	22.24	21.65
327	153.1	29.0	24.90	23.34	22.36
328	196.7	26.1	24.37	23.65	22.87
329	187.4	24.1	25.83	23.60	22.44
330	191.4	24.4	-	23.88	24.49
331	190.4	28.1	24.83	22.99	22.30
332	54.3	157.4	-	23.40	22.49
333	54.8	165.9	-	23.31	23.17
334	52.6	170.9	24.21	22.58	21.71
335	47.3	163.5	24.04	22.80	22.56
336	49.4	172.2	25.01	23.76	22.59
337	55.8	177.3	24.37	22.41	21.51
338	43.3	165.4	22.57	22.47	22.69
339	60.3	174.4	24.52	22.93	22.11
340	58.5	179.4	25.54	23.16	22.56
341	37.0	165.1	-	22.77	22.38
342	35.5	172.3	21.48	20.67	20.29
343	27.8	168.6	24.69	23.79	23.01
344	31.1	171.1	23.63	22.50	22.34
345	50.5	198.1	24.22	23.35	22.86
346	85.7	232.2	-	23.88	22.62
347	77.6	244.6	25.23	23.70	22.90
348	84.9	246.9	23.09	22.98	22.80
349	81.7	247.7	24.69	23.36	23.03
350	79.5	250.1	23.97	23.38	22.71
351	85.8	268.0	23.40	23.33	23.04
352	91.0	243.5	25.07	23.89	24.24
353	88.7	255.9	23.91	22.86	22.23
354	94.1	257.8	24.93	23.19	22.64
355	96.6	249.0	-	23.72	23.15
356	99.5	264.6	24.01	22.60	22.15
357	90.9	271.1	22.36	22.14	22.37
358	233.5	238.0	-	22.92	23.43
359	228.7	254.2	24.94	23.24	22.38
360	230.5	259.7	21.21	21.19	21.30
361	230.6	265.2	-	23.21	22.30
362	234.7	283.3	-	23.25	22.27
363	234.1	270.5	23.97	23.16	22.35
364	80.7	303.4	25.43	23.43	22.94
365	79.9	308.6	24.59	22.94	21.70
366	74.0	345.4	24.69	23.68	22.89
367	74.2	318.5	23.02	22.61	23.18
368	76.4	320.4	25.75	23.89	22.60
369	79.7	326.8	22.43	22.34	22.38
370	66.5	326.2	25.10	23.28	22.33
371	71.0	326.5	25.85	23.25	22.09
372	63.0	322.2	-	22.78	22.33
373	57.5	327.9	24.62	23.05	22.38
374	73.4	332.0	24.54	23.10	22.74
375	72.1	339.6	25.04	23.07	22.04
376	75.9	339.6	25.37	23.56	22.88
377	159.1	111.9	-	23.12	22.88
378	134.2	145.0	-	23.33	22.81
379	157.4	128.2	25.13	23.05	22.46
380	147.0	119.5	-	23.40	23.38
381	151.0	126.8	25.42	23.32	22.28
382	151.3	131.5	24.12	22.87	22.22
383	147.5	134.5	25.38	23.08	22.91
384	156.2	134.7	24.44	23.41	23.56
385	143.8	145.0	23.66	22.53	22.29
386	135.9	118.9	25.07	23.81	23.61
387	133.7	122.6	24.95	23.09	22.37
388	131.3	126.0	23.25	22.11	22.20
389	127.6	125.2	25.32	24.00	23.61
390	131.9	132.9	24.87	24.05	23.55
391	139.2	135.7	25.53	23.11	22.35
392	136.4	138.9	-	23.24	23.15
393	137.4	141.9	-	23.49	23.00
394	301.8	26.6	24.10	23.84	23.52
395	297.9	26.8	-	23.12	22.60
396	299.2	30.9	25.25	24.25	23.08
397	292.2	38.2	-	23.16	22.20
398	294.4	43.3	24.20	22.79	22.00
399	308.7	41.7	23.18	23.16	23.40
400	293.6	47.3	25.37	23.69	22.89

Num	X	Y	B	V	R
401	312.1	44.6	24.18	22.42	21.61
402	290.4	49.5	24.12	22.81	22.29
403	284.6	48.6	25.24	23.93	23.38
404	290.9	57.7	22.73	21.25	20.39
405	321.2	35.8	24.78	23.22	23.37
406	285.7	59.7	-	23.06	22.37
407	319.9	33.2	23.10	23.41	23.08
408	284.4	65.3	21.13	21.03	21.02
409	290.0	67.8	23.79	23.09	21.92
410	278.9	68.2	25.14	24.08	22.95
411	290.1	72.1	24.63	22.93	21.85
412	338.2	62.7	23.62	22.99	22.38
413	347.4	69.2	24.05	22.55	21.87
414	341.8	71.2	24.51	23.69	22.66
415	349.7	73.7	23.44	22.74	22.17
416	355.2	71.6	24.01	23.23	22.80
417	349.3	79.2	24.76	23.10	22.41
418	347.2	91.6	24.32	23.18	22.80
419	350.5	96.4	24.08	24.15	23.69
420	338.6	96.5	22.37	22.39	22.46
421	337.6	85.4	24.77	24.32	23.83
422	335.3	88.5	24.56	23.51	22.95
423	331.4	93.3	21.19	21.46	21.45
424	328.5	88.4	23.48	23.44	23.18
425	325.3	106.8	-	22.88	22.11
426	316.4	108.3	21.39	20.25	19.47
427	229.0	29.9	25.15	23.33	22.91
428	225.3	34.1	24.65	23.27	22.91
429	223.9	39.2	24.50	23.06	22.47
430	220.1	29.6	25.14	22.97	22.29
431	224.2	43.4	25.73	23.95	22.70
432	189.1	66.8	24.80	23.53	22.41
433	218.2	43.0	24.04	23.22	22.65
434	211.9	37.0	24.70	22.87	22.18
435	184.1	60.4	24.70	23.36	22.61
436	207.3	38.8	-	23.60	22.75
437	198.6	38.7	24.54	22.53	21.65
438	190.9	62.5	24.09	22.58	21.90
439	196.3	43.5	-	23.30	22.80
440	198.1	46.8	-	22.90	22.57
441	198.4	53.3	24.74	23.21	23.11
442	192.9	49.8	24.70	22.96	22.53
443	190.7	70.7	24.55	24.56	24.11
444	182.9	69.2	24.83	23.13	23.13
445	192.2	56.8	24.44	22.73	22.02
446	117.0	364.8	23.61	23.05	22.41
447	117.7	368.5	-	22.64	21.90
448	120.9	368.7	24.02	22.77	22.00
449	120.0	374.6	23.69	22.05	21.02
450	116.2	375.5	-	22.75	22.05
451	117.4	378.3	24.40	23.02	22.00
452	118.7	383.9	24.45	22.80	22.00
453	100.3	371.9	24.27	23.49	23.11
454	103.1	394.4	24.03	22.60	21.64
455	97.6	370.8	-	23.42	22.65
456	91.3	397.3	-	23.67	22.60
457	94.0	401.9	23.72	23.04	22.37
458	102.7	407.5	24.59	23.91	24.64
459	105.8	409.4	24.95	22.89	22.61
460	27.5	340.8	-	22.41	21.88
461	35.2	344.9	-	24.06	22.77
462	39.4	343.0	24.46	23.01	22.66
463	32.8	352.0	23.01	23.21	22.65
464	20.1	382.7	22.47	22.09	21.90
465	17.9	352.4	24.78	23.37	22.41
466	16.7	355.0	24.24	23.01	23.37
467	15.1	364.2	24.31	22.65	22.00
468	21.0	365.5	21.28	21.61	21.70
469	20.3	373.5	20.66	20.85	20.91
470	23.8	383.2	24.08	22.52	21.99
471	77.5	483.8	23.70	22.77	22.13
472	30.7	457.7	23.92	22.78	22.19
473	28.7	463.6	20.69	20.57	20.39
474	19.8	463.1	23.60	23.03	22.75
475	17.8	455.4	24.26	22.82	22.15
476	36.9	465.5	24.06	23.65	23.62
477	40.1	466.0	23.40	24.40	23.90
478	46.4	470.7	22.95	21.69	20.79
479	14.6	470.6	-	22.99	22.34
480	56.7	476.2	20.04	19.40	18.95

Num	X	Y	B	V	R
481	58.1	470.5	-	21.78	21.38
482	8.0	471.6	24.33	22.99	21.98
483	68.6	477.7	-	23.51	22.90
484	67.4	483.1	22.68	23.01	23.17
485	37.8	42.1	24.41	23.09	22.31
486	188.9	106.5	23.82	22.55	21.76
487	118.7	334.6	24.04	23.31	22.72
488	225.3	380.5	23.35	22.88	22.80
489	352.3	389.2	24.49	23.38	22.14
490	43.1	417.2	23.94	22.69	21.92
491	344.7	456.0	24.17	24.06	23.50
492	45.9	145.4	23.68	22.17	21.32
493	108.7	190.9	23.80	24.06	24.18
494	60.9	192.8	24.87	23.78	22.97
495	203.2	213.9	-	23.13	22.85
496	9.8	267.6	25.53	23.93	23.14
497	138.9	386.1	24.35	22.87	21.99
498	143.1	389.0	24.57	23.47	23.18
499	288.2	60.3	23.89	23.14	22.78
500	345.2	119.2	22.40	22.19	22.29
501	112.1	136.5	24.75	22.74	22.10
502	188.9	268.4	-	24.04	23.35
503	190.6	270.7	24.64	23.49	23.06
504	261.4	322.7	24.01	22.79	22.33
505	201.3	359.3	-	23.35	22.70
506	239.7	471.4	24.07	22.91	22.17
507	339.4	481.5	24.74	23.14	22.12
508	180.0	81.3	24.20	22.52	21.92
509	236.7	186.9	24.05	22.86	22.15
510	241.6	187.2	-	23.94	24.07
511	223.6	304.4	23.14	23.24	22.94
512	229.9	310.3	21.02	21.13	21.14
513	80.3	54.8	22.78	21.16	20.17
514	197.3	246.9	-	23.38	22.97
515	280.2	280.1	25.12	23.47	22.66
516	275.7	279.7	24.63	23.34	22.61
517	115.1	302.7	25.09	23.36	22.55
518	296.1	306.3	-	23.05	22.17
519	292.8	306.2	-	23.14	23.14
520	37.3	439.1	24.73	24.07	23.77
521	33.8	442.9	24.77	23.15	23.43
522	40.4	446.1	-	22.65	22.46
523	341.4	463.0	-	23.55	22.85
524	39.2	364.8	23.26	23.64	23.44
525	35.5	365.9	24.43	23.13	22.17
526	71.7	369.1	-	23.54	23.20
527	73.9	375.7	25.09	23.66	23.10
528	67.4	376.4	22.74	22.58	22.69
529	0.0	0.0	24.16	23.33	-
530	88.2	379.4	24.90	23.02	22.25
531	91.4	381.7	25.02	24.11	23.05
532	177.2	400.1	23.46	23.09	22.76
533	200.7	76.9	24.59	23.12	22.17
534	200.4	82.3	-	23.40	22.09
535	203.3	85.8	-	23.28	22.75
536	280.7	95.7	20.51	20.64	20.69
537	277.5	90.5	-	23.80	23.64
538	291.0	93.9	25.19	23.87	22.80
539	264.0	91.3	25.26	23.83	22.51
540	266.2	95.2	24.05	23.23	22.67
541	261.6	101.3	21.17	20.25	19.76
542	264.8	107.7	24.81	23.02	21.99
543	23.9	244.1	24.25	23.60	23.15
544	20.1	246.8	25.01	23.11	22.92
545	26.7	245.1	25.55	23.16	22.60
546	297.4	395.0	23.61	23.56	23.56
547	273.2	366.4	23.16	23.53	23.30
548	346.0	424.4	-	23.34	22.57
549	349.8	425.5	24.82	24.09	22.91
550	333.6	431.0	24.84	23.58	22.18
551	356.0	473.7	-	24.74	24.24
552	343.8	477.9	24.46	23.55	23.89
553	239.2	74.5	23.74	22.04	20.98
554	236.2	71.4	24.43	23.15	22.52
555	83.2	102.6	-	23.21	23.09
556	194.0	156.8	23.93	22.86	22.54
557	5.2	248.4	24.47	22.51	21.73
558	10.4	232.1	-	23.57	22.43
559	7.4	239.9	24.66	23.16	23.64
560	27.5	303.6	-	23.22	22.35

Num	X	Y	B	V	R
561	28.7	313.9	24.74	23.50	22.86
562	97.8	327.1	24.27	22.58	21.10
563	99.7	336.8	25.02	22.85	22.02
564	289.8	366.3	24.13	23.78	22.75
565	295.1	382.1	24.63	22.90	22.00
566	290.2	383.2	24.16	22.06	21.05
567	63.1	438.6	24.93	23.66	22.63
568	68.6	442.0	23.86	22.78	21.89
569	72.3	443.2	-	23.49	22.62
570	81.5	444.8	-	22.57	22.03
571	78.4	446.8	24.29	23.42	22.98
572	199.7	265.3	24.54	23.42	23.01
573	202.0	274.6	24.13	22.62	21.67
574	202.7	277.5	22.74	22.31	22.31
575	59.0	274.2	24.13	23.25	22.55
576	50.8	281.3	25.62	23.47	22.47
577	78.8	386.2	-	22.54	21.95
578	82.2	387.9	-	22.82	22.35
579	268.7	452.3	22.00	22.11	22.10
580	264.4	454.9	-	23.46	22.82
581	261.9	460.0	-	23.60	22.07
582	246.3	215.9	-	22.80	22.68
583	260.7	231.0	22.27	22.16	22.30
584	18.9	281.4	-	23.27	23.02
585	25.7	285.3	-	24.35	23.40
586	11.8	288.8	24.29	22.92	22.56
587	16.7	291.9	22.19	22.30	22.19
588	321.3	322.2	-	23.52	22.97
589	323.6	319.0	-	23.99	22.64
590	228.3	402.5	-	23.29	22.96
591	222.8	140.7	25.89	23.61	23.39
592	224.3	143.8	23.26	23.30	23.56
593	221.9	147.0	-	23.37	22.84
594	224.7	153.3	25.03	23.29	22.86
595	215.9	149.9	24.55	23.11	22.52
596	14.4	251.2	-	23.84	23.50
597	15.5	257.6	24.47	22.20	21.05
598	41.3	49.0	25.60	23.52	23.61
599	37.6	49.5	24.83	23.48	22.56
600	33.6	50.2	24.15	22.81	22.43
601	37.8	55.5	23.99	22.31	21.69
602	66.9	393.2	22.98	22.37	21.81
603	68.4	396.6	25.31	23.54	23.45
604	62.3	398.4	21.83	20.49	19.58
605	66.4	402.2	24.36	23.17	21.97
606	10.7	64.2	23.75	23.24	22.99
607	13.6	72.0	23.92	22.70	22.12
608	18.4	72.8	24.41	22.56	21.73
609	15.7	224.9	24.36	22.41	21.52
610	16.9	219.1	24.43	22.91	22.34
611	18.5	228.4	23.91	22.66	22.47
612	24.2	229.3	24.17	22.60	22.02
613	18.8	233.3	24.44	23.19	22.65
614	30.5	230.1	21.61	20.10	19.35
615	20.4	236.3	24.74	23.34	22.37
616	28.9	236.5	24.86	23.69	22.46
617	313.9	253.8	23.95	23.14	22.20
618	307.9	256.4	24.70	24.33	23.96
619	301.8	254.9	24.25	23.55	23.55
620	282.3	364.1	-	22.99	22.53
621	294.1	345.5	24.80	23.92	22.52
622	286.6	352.9	23.94	23.12	22.55
623	55.2	402.6	22.58	22.78	22.58
624	59.7	410.6	24.58	23.44	22.80
625	53.2	414.0	24.84	23.26	22.83
626	46.0	407.8	23.27	23.26	23.73
627	170.1	452.5	23.44	22.21	21.44
628	178.0	453.1	-	23.43	22.39
629	178.3	462.9	24.15	22.65	21.95
630	173.2	458.2	-	22.91	22.94
631	119.0	316.4	24.34	23.07	22.41
632	139.8	317.5	25.24	23.16	22.66
633	123.6	328.3	24.51	23.88	22.97
634	135.9	319.1	25.05	23.16	22.31
635	158.2	290.2	23.30	23.50	24.01
636	152.5	294.7	23.57	23.81	23.82
637	141.2	294.2	21.65	21.69	21.66
638	244.2	86.5	-	24.11	22.94
639	246.5	91.1	-	23.12	22.36
640	252.0	91.3	-	23.23	22.24

Num	X	Y	*B*	*V*	*R*
641	238.2	96.4	24.62	22.51	21.75
642	245.6	108.4	24.82	23.57	22.15
643	241.0	101.2	25.93	23.42	23.12
644	246.7	100.5	25.48	24.38	24.00
645	243.9	105.4	25.34	23.14	22.36
646	174.6	132.1	24.71	23.18	23.02
647	176.9	138.2	25.49	23.30	22.27
648	173.0	139.1	24.68	23.01	22.50
649	175.0	141.7	-	23.50	23.81
650	184.9	155.2	-	24.22	23.61
651	190.9	136.2	23.46	22.83	21.63
652	74.0	363.4	24.44	22.98	22.18
653	68.8	364.5	23.64	22.90	22.20
654	63.7	364.4	24.46	23.23	22.34
655	58.6	367.1	24.81	23.32	22.56
656	56.6	370.0	24.67	23.86	23.01
657	60.8	374.5	-	24.15	22.55
658	50.9	381.1	22.74	22.81	22.91
659	55.6	382.8	22.06	22.11	22.20
660	53.7	385.5	24.05	22.69	21.89
661	309.7	131.0	23.68	22.97	22.07
662	312.4	133.1	25.09	23.15	22.87
663	301.8	129.4	20.77	20.55	20.41
664	304.4	138.0	23.08	22.64	22.96
665	302.4	139.4	23.40	22.72	21.93
666	304.3	142.7	24.06	23.69	22.64
667	289.7	142.8	24.20	22.42	21.75
668	291.8	131.0	23.67	23.47	22.91
669	266.0	336.5	25.53	24.59	23.24
670	262.6	337.9	25.22	23.27	23.20
671	269.4	340.6	24.29	22.83	21.94
672	262.0	342.5	-	23.86	23.41
673	274.0	343.6	23.43	22.00	21.56
674	274.6	346.9	-	23.26	22.26
675	275.3	352.2	23.91	22.81	22.10
676	252.1	345.3	23.91	23.62	23.51
677	271.2	353.9	23.88	23.03	22.21
678	243.1	304.4	22.90	23.13	23.03
679	244.6	307.0	23.08	23.19	22.27
680	254.4	327.0	23.29	23.69	23.17
681	256.3	314.0	23.61	22.75	22.12
682	261.4	315.2	23.23	22.02	21.35
683	228.2	120.0	22.57	23.03	23.03
684	217.7	127.6	-	23.31	23.06
685	213.4	123.1	24.38	22.58	21.90
686	210.0	118.3	22.11	21.87	22.05
687	208.6	123.6	23.54	22.26	21.79
688	211.4	129.1	24.31	22.79	22.44
689	53.9	117.9	24.57	22.50	22.34
690	45.8	121.9	24.49	22.84	22.56
691	73.8	145.1	24.37	23.09	22.22
692	37.9	127.7	25.00	23.18	22.25
693	68.8	148.1	23.23	22.51	22.10
694	49.9	138.4	-	23.22	23.31
695	62.8	138.8	24.37	22.85	22.51
696	68.3	139.8	24.64	22.76	21.79
697	53.5	144.8	24.36	23.00	22.06
698	71.6	137.3	-	23.04	22.38
699	57.3	144.7	-	23.48	22.92
700	271.6	223.4	24.36	23.49	23.54
701	263.6	189.5	-	23.98	23.24
702	265.8	201.9	24.34	22.95	22.41
703	262.2	204.4	-	23.51	23.27
704	252.6	209.1	24.73	22.92	21.97
705	256.6	209.8	25.55	23.58	23.04
706	261.8	209.8	24.74	23.23	22.55
707	249.8	210.5	24.26	22.87	22.10
708	82.3	9.1	24.55	23.58	23.05
709	59.6	31.5	24.52	23.39	22.49
710	76.4	12.1	25.60	23.31	22.53
711	75.0	20.5	24.69	23.92	23.49
712	74.8	24.8	25.52	23.54	22.89
713	61.3	17.4	24.57	22.79	21.78
714	61.9	25.5	25.13	23.64	22.05
715	136.4	72.3	25.30	23.39	23.28
716	137.3	77.6	25.34	23.49	23.02
717	114.4	96.6	24.46	24.14	23.33
718	119.6	74.6	25.72	24.54	22.86
719	125.0	77.2	25.03	22.37	21.65
720	119.5	79.3	23.90	22.23	21.15

Num	X	Y	*B*	*V*	*R*
721	124.1	95.2	-	23.54	23.18
722	250.5	275.2	24.90	23.59	23.53
723	249.0	279.3	25.68	23.53	23.26
724	248.6	287.1	22.09	22.07	22.08
725	243.9	293.8	23.93	23.60	23.35
726	258.9	299.3	23.85	23.18	22.56
727	258.2	288.1	-	22.64	22.27
728	226.5	291.8	24.79	23.51	22.22
729	263.2	291.1	24.79	23.22	22.63
730	231.3	293.3	22.60	22.87	22.71
731	231.3	298.2	-	23.74	22.63
732	267.9	294.7	24.78	23.15	22.26
733	43.4	281.8	24.67	22.33	21.65
734	74.6	295.5	24.21	23.31	22.76
735	37.5	284.3	25.02	23.61	22.58
736	37.6	291.3	-	23.05	22.47
737	50.3	289.8	24.45	22.44	22.46
738	39.2	296.0	24.57	23.31	22.45
739	53.3	294.0	24.73	23.57	23.19
740	35.7	296.6	25.19	23.32	23.00
741	57.9	291.6	25.39	23.24	22.65
742	62.4	290.9	24.45	23.58	23.52
743	60.5	294.3	23.58	23.82	23.77
744	67.9	290.2	-	23.47	23.90
745	64.7	293.5	22.69	22.57	22.56
746	39.8	6.7	24.44	23.10	22.64
747	35.4	7.8	24.29	23.21	22.68
748	39.8	11.6	24.72	23.42	23.02
749	36.9	14.1	24.40	22.95	22.10
750	36.7	18.2	24.75	23.09	22.25
751	34.0	18.8	-	23.48	23.11
752	54.6	8.6	23.84	22.39	21.46
753	32.2	22.4	24.77	24.00	23.16
754	43.8	17.6	25.04	23.28	23.06
755	25.6	13.7	24.68	23.28	23.00
756	46.4	12.2	24.90	23.52	23.96
757	53.2	20.3	24.53	22.97	22.15
758	52.0	27.0	25.48	24.02	23.17
759	46.1	32.8	25.15	23.58	22.25
760	53.8	13.3	-	23.04	21.96
761	54.2	30.9	25.64	24.02	22.53
762	225.0	58.5	-	23.55	23.23
763	221.6	66.0	25.33	23.90	22.78
764	205.5	94.9	24.69	23.69	23.41
765	218.5	70.9	20.48	19.40	18.98
766	213.5	67.7	24.53	23.27	22.01
767	224.6	79.5	24.20	22.81	21.98
768	218.3	81.8	23.75	23.51	23.65
769	208.8	75.6	24.84	23.14	22.53
770	200.8	67.0	23.79	22.32	21.55
771	208.6	94.2	25.52	24.64	23.82
772	217.8	87.5	24.61	23.68	23.58
773	213.8	92.4	21.91	21.59	21.29
774	349.1	168.9	-	23.02	22.59
775	343.8	170.8	24.13	22.51	21.95
776	336.2	168.9	-	22.76	22.45
777	356.4	180.0	25.12	23.58	23.66
778	329.1	166.8	24.75	23.07	21.94
779	331.3	173.6	22.10	22.32	22.12
780	334.0	177.0	24.94	24.11	23.21
781	324.9	189.7	24.30	23.37	22.65
782	43.4	427.1	24.16	23.04	21.92
783	40.7	429.7	24.89	23.42	23.13
784	43.7	434.2	22.32	22.22	22.00
785	50.5	431.8	-	23.29	23.15
786	46.8	441.0	24.16	22.54	21.55
787	54.2	427.4	24.94	23.65	22.53
788	69.7	458.8	22.28	21.04	20.16
789	60.6	427.9	-	24.25	22.84
790	61.8	459.0	24.02	23.87	23.05
791	55.4	446.3	22.90	22.79	22.66
792	43.8	453.3	24.89	23.55	22.41
793	49.5	446.7	22.17	22.34	22.44
794	56.0	454.1	21.87	20.13	19.16
795	45.7	448.7	-	24.34	23.43
796	86.4	279.9	24.30	23.52	23.20
797	85.1	285.1	23.56	22.89	22.61
798	84.2	294.4	-	22.94	23.11
799	90.3	288.7	21.73	21.72	21.82
800	82.1	297.6	25.52	23.49	22.43

Num	X	Y	B	V	R
801	86.3	301.0	23.81	23.07	22.33
802	89.3	303.6	25.19	24.10	23.42
803	93.3	302.4	24.99	22.95	22.32
804	91.2	306.9	23.89	22.92	22.62
805	96.5	300.4	24.97	23.89	23.30
806	95.6	309.8	24.79	24.44	23.02
807	92.9	314.4	-	23.09	22.01
808	90.6	316.1	24.20	22.88	22.25
809	112.3	319.1	24.02	23.49	22.44
810	107.1	304.9	23.96	22.76	22.56
811	105.9	297.0	24.87	23.86	23.39
812	16.5	181.8	24.00	23.05	22.12
813	13.3	209.3	24.27	23.39	23.13
814	26.1	192.7	24.21	23.04	22.01
815	16.3	213.4	24.03	22.95	22.56
816	10.9	198.2	25.07	23.37	23.54
817	23.0	199.0	23.13	22.21	22.00
818	31.1	189.0	24.16	23.08	22.53
819	32.6	193.2	23.42	23.15	22.64
820	10.7	196.3	24.86	23.12	22.71
821	23.3	205.6	-	22.77	22.21
822	34.3	196.8	-	23.68	22.86
823	30.4	197.4	24.62	23.32	22.56
824	28.2	206.0	24.33	24.70	23.68
825	21.0	211.2	23.39	21.85	21.31
826	293.5	108.8	23.06	23.46	22.82
827	285.1	114.5	24.57	23.16	22.90
828	272.8	113.2	22.33	22.53	21.91
829	268.7	119.5	24.68	23.17	22.72
830	265.6	118.3	24.60	23.57	24.38
831	303.0	119.5	21.58	21.48	21.24
832	307.0	120.4	20.95	21.06	21.13
833	264.8	123.1	-	24.02	23.13
834	269.7	129.1	23.96	22.60	22.05
835	267.0	132.9	-	22.92	23.75
836	307.1	312.3	19.41	19.40	19.48
837	316.4	308.7	25.60	23.18	22.82
838	298.0	325.8	24.87	23.34	22.46
839	295.5	328.5	24.23	22.38	21.61
840	305.3	333.2	24.67	23.30	22.68
841	194.1	223.3	23.82	22.22	21.92
842	192.8	262.1	24.38	23.96	22.80
843	201.8	230.1	23.41	22.16	21.40
844	194.2	240.6	22.17	22.25	22.45
845	189.6	243.0	21.78	22.09	22.16
846	188.4	246.3	22.72	22.03	21.27
847	184.7	249.6	19.77	19.69	19.62
848	177.9	245.8	23.36	23.25	22.43
849	182.6	255.6	24.13	23.79	23.31
850	187.3	256.5	23.09	23.81	23.41
851	58.9	47.6	-	22.83	21.25
852	67.2	44.9	24.96	22.39	21.00
853	70.7	40.6	-	23.52	23.38
854	76.1	42.0	24.17	22.85	21.94
855	55.3	61.5	24.65	23.02	21.96
856	49.2	65.2	-	23.21	23.01
857	37.2	87.9	24.77	23.91	23.21
858	44.7	68.4	-	22.91	22.14
859	37.5	70.2	23.84	23.21	22.38
860	38.1	72.8	-	22.73	22.46
861	41.6	79.4	24.64	23.58	23.17
862	128.9	230.2	22.64	22.00	21.49
863	143.6	243.0	24.24	24.26	23.29
864	72.2	113.8	24.99	23.17	22.14
865	107.9	145.5	23.90	22.95	22.35
866	62.8	116.5	-	22.88	22.57
867	68.9	123.2	24.92	23.45	22.23
868	71.0	126.6	23.21	23.04	22.92
869	76.1	118.1	24.89	23.82	23.51
870	72.9	129.4	25.56	23.60	22.16
871	79.9	126.8	23.60	22.33	21.64
872	90.1	145.2	24.05	23.09	22.67
873	88.5	135.9	24.36	23.11	23.12
874	98.6	137.8	23.89	24.03	22.91
875	83.8	143.7	24.20	22.58	21.69
876	327.0	128.9	22.08	22.20	22.48
877	346.1	152.1	24.13	22.82	22.10
878	320.0	139.0	24.09	22.94	22.04
879	320.7	142.6	22.40	22.70	22.41
880	319.5	146.5	23.73	23.13	22.47

Num	X	Y	B	V	R
881	339.1	132.7	23.68	22.77	22.30
882	344.2	133.9	22.75	22.59	22.42
883	347.3	136.7	-	23.91	22.74
884	329.0	149.9	23.58	22.22	21.43
885	341.0	150.3	23.45	22.70	21.50
886	351.2	135.8	24.56	23.23	23.66
887	333.9	155.5	22.60	22.59	22.62
888	342.2	156.8	23.36	22.83	22.41
889	336.6	157.6	23.67	23.00	22.35
890	333.0	158.9	24.32	22.79	21.97
891	126.6	391.1	24.91	23.11	23.23
892	120.0	396.7	23.83	22.45	21.81
893	137.9	395.0	23.98	22.63	21.84
894	147.1	404.0	25.04	23.42	22.82
895	127.2	419.7	23.43	22.85	22.41
896	148.7	393.4	23.13	22.72	21.99
897	155.8	395.0	20.72	20.39	20.19
898	128.1	411.1	22.37	21.09	20.40
899	350.3	240.9	-	22.97	22.27
900	337.7	254.1	24.19	23.09	23.01
901	332.4	250.9	24.53	23.03	21.95
902	340.2	257.8	25.10	23.40	23.58
903	327.8	268.2	24.44	22.92	21.97
904	343.8	282.4	24.45	22.84	21.95
905	337.6	270.8	-	23.01	22.38
906	333.5	266.2	24.70	23.08	22.93
907	331.1	269.5	23.24	22.42	21.75
908	331.8	279.0	24.42	22.42	21.70
909	186.8	34.5	25.37	23.84	22.95
910	148.0	44.2	23.92	22.61	22.06
911	105.2	98.4	-	23.79	22.88
912	236.6	136.3	24.67	22.79	22.26
913	299.2	147.9	24.10	23.51	23.03
914	299.7	152.4	22.45	22.70	22.69
915	283.7	153.4	24.25	22.49	21.62
916	77.2	167.5	24.15	22.78	23.66
917	268.3	170.6	24.55	22.92	22.11
918	236.8	170.8	24.89	23.74	23.47
919	100.9	185.0	24.02	23.04	22.30
920	63.1	198.6	24.03	22.93	22.22
921	318.0	202.9	22.34	22.29	22.29
922	296.3	206.2	-	23.14	22.31
923	285.1	217.1	23.78	23.05	22.35
924	324.2	221.8	-	24.14	23.97
925	312.9	246.5	23.87	22.83	21.91
926	263.3	262.7	24.23	23.24	22.50
927	170.9	265.1	-	23.11	22.17
928	306.0	270.3	23.90	22.48	21.32
929	209.7	281.4	24.10	22.58	21.77
930	205.9	285.1	24.37	22.73	21.64
931	200.9	286.4	25.73	23.19	22.38
932	210.8	294.3	22.03	22.05	22.10
933	195.5	308.0	25.60	24.28	23.15
934	338.4	310.0	25.33	23.71	23.18
935	208.3	312.4	22.32	22.40	22.58
936	202.5	334.3	-	23.59	23.81
937	326.9	346.5	24.84	22.96	22.27
938	311.3	347.1	-	22.95	22.03
939	327.4	352.5	25.00	23.57	23.04
940	321.2	367.0	24.24	23.52	22.33
941	321.0	371.9	24.27	22.85	22.21
942	194.8	374.0	22.69	22.69	22.40
943	195.5	386.9	-	23.02	22.85
944	264.4	387.9	24.24	23.53	22.32
945	348.2	409.9	21.80	21.88	21.49
946	356.5	417.7	24.71	23.44	22.27
947	261.5	440.0	25.24	23.31	22.77
948	257.0	445.7	19.34	19.35	19.29
949	299.6	458.5	-	23.81	22.87
950	263.1	475.5	23.60	23.19	22.63
951	238.6	477.8	21.24	21.22	21.09
952	126.6	33.1	25.22	23.33	22.37
953	97.7	81.7	24.00	22.69	21.94
954	109.8	100.2	24.92	24.45	23.56
955	233.6	139.6	24.13	23.42	22.54
956	250.9	155.6	24.66	23.17	23.01
957	319.4	158.8	-	23.28	23.40
958	252.5	168.6	24.60	24.10	23.23
959	312.6	170.1	20.76	19.69	19.08
960	210.7	168.5	24.27	23.58	22.65

Num	X	Y	B	V	R
961	211.6	172.0	24.33	23.22	22.49
962	212.5	191.8	23.78	23.31	23.17
963	310.8	199.7	23.29	22.21	21.65
964	75.7	206.3	24.04	23.22	22.50
965	100.8	208.2	24.70	24.19	22.60
966	313.9	208.1	21.95	21.87	21.80
967	73.1	214.3	24.44	22.92	22.32
968	334.6	217.1	21.65	21.69	21.73
969	268.1	259.9	23.92	23.07	22.01
970	288.1	269.0	23.27	22.60	22.25
971	334.5	313.1	24.86	23.83	23.61
972	220.3	339.1	21.80	22.09	22.12
973	119.9	349.5	23.15	22.62	22.04
974	121.1	360.0	24.87	23.47	22.87
975	269.2	386.4	23.76	23.81	23.53
976	244.2	408.8	24.80	23.39	22.83
977	302.2	414.2	19.68	19.68	19.61
978	206.5	423.3	-	23.71	22.14
979	216.4	425.2	23.04	22.78	22.55
980	304.0	453.8	24.50	23.21	22.74
981	250.2	460.7	-	24.00	24.20
982	198.8	462.4	23.85	23.58	23.51
983	191.8	468.2	22.46	22.41	22.57
984	163.7	470.0	-	22.62	22.61
985	189.3	480.1	23.45	23.12	22.18
986	86.6	46.2	24.92	22.70	22.87
987	182.2	51.8	24.37	23.04	22.69
988	98.3	154.7	25.35	22.79	21.71
989	100.1	157.8	25.03	23.15	22.48
990	285.3	160.3	25.38	24.26	23.11
991	109.0	169.8	24.93	23.65	22.74
992	105.5	170.6	24.38	22.57	21.76
993	88.2	201.9	24.05	23.69	23.21
994	334.9	226.2	22.04	21.76	21.43
995	332.8	229.1	23.03	22.23	22.04
996	245.9	268.2	-	23.35	22.85
997	229.3	319.2	21.96	22.06	22.21
998	135.4	337.2	23.27	23.72	23.53
999	213.5	366.1	20.05	20.18	20.24
1000	311.0	373.6	23.53	22.40	21.62
1001	173.5	381.3	-	23.26	22.30
1002	240.3	386.9	23.57	22.70	22.54
1003	207.0	412.1	24.20	23.72	22.73
1004	203.2	415.2	-	24.01	23.91
1005	299.8	452.1	-	22.88	22.11
1006	291.5	460.6	21.97	21.90	22.10
1007	287.2	458.6	-	23.45	22.30
1008	269.8	463.6	24.72	23.35	22.51
1009	231.3	473.0	24.42	23.43	22.68
1010	201.0	482.7	24.99	23.43	22.38
1011	112.2	9.4	25.12	23.38	23.47
1012	116.4	14.4	24.70	23.19	22.79
1013	84.8	28.7	24.33	22.79	22.33
1014	136.7	34.1	22.59	21.61	21.62
1015	139.4	37.7	23.69	22.42	21.68
1016	165.8	48.8	24.09	23.15	22.22
1017	162.8	50.7	24.09	22.58	22.06
1018	160.9	54.2	24.42	23.05	22.81
1019	156.4	59.2	23.45	22.71	22.10
1020	97.5	92.4	24.37	22.69	21.90
1021	99.6	96.7	24.42	22.74	21.92
1022	296.7	171.4	23.64	23.41	23.22
1023	299.3	174.4	22.36	21.70	21.21
1024	107.3	179.6	-	22.72	22.04
1025	122.6	214.3	23.80	22.43	21.45
1026	327.2	241.0	23.09	23.41	23.69
1027	181.5	263.8	22.50	22.26	22.15
1028	181.1	267.2	23.85	23.00	23.49
1029	192.8	293.8	24.21	23.56	23.78
1030	171.5	302.0	24.09	23.43	22.61
1031	171.2	305.8	22.39	22.32	22.18
1032	133.1	355.2	24.36	23.54	22.95
1033	135.9	355.3	-	22.84	21.91
1034	334.3	372.7	-	23.40	22.70
1035	329.7	374.4	-	23.70	23.29
1036	348.7	373.9	23.33	22.98	23.45
1037	230.8	377.9	22.97	22.59	22.11
1038	238.1	382.9	23.47	22.99	22.52
1039	347.8	380.6	22.45	22.37	22.13
1040	345.5	387.3	23.31	22.61	21.83

Num	X	Y	B	V	R
1041	285.9	426.0	21.59	21.75	21.68
1042	170.2	446.0	24.66	23.29	22.50
1043	208.2	487.0	25.17	24.05	22.89
1044	206.3	483.4	25.21	23.81	23.27
1045	117.8	23.8	23.58	22.64	22.07
1046	121.9	24.6	24.00	22.18	21.35
1047	116.9	32.7	24.39	22.92	22.02
1048	96.2	51.7	23.99	22.73	22.72
1049	89.3	50.3	25.21	23.24	22.59
1050	87.5	72.5	24.46	23.32	22.95
1051	80.5	81.2	24.51	22.99	22.04
1052	277.8	151.1	-	22.49	21.56
1053	151.0	158.3	22.90	22.90	22.72
1054	151.8	154.4	23.72	22.69	22.05
1055	181.7	162.3	23.96	23.45	22.34
1056	180.0	273.0	24.95	23.79	22.59
1057	187.7	279.5	25.24	23.65	22.81
1058	295.3	290.8	24.03	22.83	22.30
1059	222.4	297.4	-	22.29	21.62
1060	184.0	360.4	23.01	23.11	23.54
1061	185.0	367.1	24.43	23.26	22.04
1062	176.9	364.5	24.71	23.00	22.36
1063	176.5	369.5	23.91	22.34	21.20
1064	335.3	360.9	24.99	23.34	22.95
1065	338.0	369.6	-	23.39	23.28
1066	195.8	413.0	-	23.97	22.98
1067	199.3	416.9	25.66	23.49	22.28
1068	292.1	430.0	24.59	23.21	22.30
1069	264.0	431.3	-	22.88	21.98
1070	261.3	433.3	24.39	22.97	22.50
1071	222.3	432.3	24.20	23.56	22.71
1072	214.2	435.0	23.57	22.33	22.25
1073	278.1	460.1	-	22.89	22.08
1074	279.9	463.6	21.83	21.55	20.92
1075	283.5	464.3	23.99	23.42	22.10
1076	178.1	31.2	24.68	23.73	23.58
1077	181.4	34.0	24.74	22.81	22.51
1078	95.8	63.8	24.55	23.65	22.60
1079	98.3	67.7	24.58	22.84	21.94
1080	241.3	152.4	23.93	22.33	21.43
1081	130.6	175.6	24.29	23.81	22.96
1082	126.9	177.8	24.05	22.41	21.95
1083	128.6	183.0	24.19	22.60	21.33
1084	123.9	191.9	23.99	23.26	22.25
1085	184.1	289.9	22.80	21.81	21.12
1086	180.9	294.7	21.43	21.42	21.30
1087	208.8	444.9	24.10	22.97	22.29
1088	210.7	447.5	23.20	22.28	21.55
1089	174.9	480.3	-	22.54	21.95
1090	178.6	39.5	24.92	23.46	22.66
1091	182.6	41.7	25.30	23.45	22.30
1092	183.6	38.7	24.08	22.81	22.47
1093	100.4	51.0	24.62	23.61	23.33
1094	104.1	61.0	23.92	22.52	21.85
1095	84.6	87.2	-	23.62	22.58
1096	80.8	87.7	23.83	22.17	21.56
1097	200.3	96.0	24.61	22.81	22.26
1098	197.2	96.8	-	23.49	22.75
1099	203.4	103.9	24.65	23.01	22.01
1100	100.8	194.8	-	22.86	22.12
1101	103.9	198.5	-	23.56	23.07
1102	105.9	201.5	24.13	23.97	23.59
1103	255.9	256.4	24.06	22.87	22.28
1104	149.9	307.0	24.14	22.77	22.09
1105	342.0	339.8	-	23.22	22.58
1106	333.8	340.5	23.93	22.52	21.82
1107	331.3	344.9	23.64	22.15	21.76
1108	306.4	345.9	23.95	23.12	22.43
1109	305.6	350.7	23.44	22.39	21.94
1110	303.4	354.3	-	23.24	21.98
1111	257.2	384.7	21.89	21.93	21.91
1112	252.8	403.0	-	23.31	22.81
1113	219.1	412.6	23.01	21.40	20.38
1114	332.2	409.2	21.80	22.03	21.97
1115	336.1	410.6	-	22.86	21.74
1116	337.8	408.5	21.63	21.76	21.75
1117	336.8	417.3	22.18	22.24	22.12
1118	182.5	446.8	21.57	21.65	21.67
1119	320.0	455.9	-	24.03	23.85
1120	323.4	460.2	24.07	23.01	22.06

Num	X	Y	B	V	R
1121	312.0	461.6	24.06	23.58	22.25
1122	307.5	465.8	24.33	22.67	21.91
1123	231.2	154.7	24.11	23.50	22.27
1124	231.6	157.9	-	23.31	22.60
1125	238.4	165.9	-	23.56	22.28
1126	275.9	168.6	-	23.83	22.66
1127	272.4	162.3	24.40	22.68	21.75
1128	278.4	162.7	22.68	22.50	22.60
1129	100.2	175.2	24.42	22.77	22.04
1130	104.1	162.4	24.70	23.47	23.07
1131	99.9	163.4	23.85	22.20	21.21
1132	204.9	170.8	24.74	23.21	22.40
1133	205.8	175.8	23.84	22.63	22.00
1134	307.0	249.9	24.61	23.23	22.71
1135	300.7	247.7	24.27	23.26	22.89
1136	295.3	269.4	23.70	22.40	21.50
1137	341.0	290.4	25.46	23.34	23.18
1138	346.5	292.3	20.53	19.85	19.42
1139	309.5	340.5	24.29	23.35	22.46
1140	210.5	397.8	24.55	23.35	22.68
1141	216.9	396.5	23.74	22.73	22.70
1142	274.8	423.3	21.99	22.01	22.06
1143	276.5	425.5	-	22.96	22.61
1144	288.7	435.2	24.02	23.09	23.01
1145	285.7	441.7	-	23.24	22.59
1146	349.2	446.9	21.87	20.41	19.62
1147	355.2	445.1	20.89	21.11	20.96
1148	354.9	448.1	21.38	21.50	21.66
1149	356.2	457.1	23.45	22.36	21.62
1150	295.0	469.3	22.58	21.15	20.26
1151	300.1	470.7	23.89	22.74	21.85
1152	278.6	176.1	22.63	22.24	22.45
1153	285.9	177.1	25.17	23.34	23.00
1154	286.9	180.4	24.32	24.05	23.48
1155	283.4	183.8	23.18	22.42	21.94
1156	264.5	270.7	23.46	23.35	23.35
1157	271.1	272.0	-	23.03	22.29
1158	264.5	276.0	24.02	23.51	22.43
1159	229.8	366.8	22.08	22.36	22.39
1160	264.3	413.7	21.96	21.93	21.92
1161	261.2	396.6	22.54	22.25	21.93
1162	257.5	404.3	23.61	23.70	22.85
1163	263.0	408.0	20.71	20.76	20.80
1164	254.9	424.1	23.27	23.17	23.57
1165	250.0	419.0	22.61	21.08	20.20
1166	180.3	471.8	24.05	22.65	22.24
1167	170.3	476.6	24.33	22.71	22.10
1168	103.9	25.3	24.64	22.88	22.17
1169	101.9	29.0	24.76	23.28	22.66
1170	98.2	30.7	24.85	23.36	22.02
1171	97.9	34.0	23.82	22.55	22.02
1172	314.2	152.0	-	22.55	22.54
1173	313.1	158.2	21.88	21.71	21.61
1174	312.6	162.5	22.26	22.34	22.48
1175	259.0	173.5	24.35	23.08	22.66
1176	280.0	266.5	23.48	22.15	21.70
1177	180.2	300.0	-	23.53	22.62
1178	185.3	308.4	-	23.24	22.45
1179	186.2	315.2	23.88	23.39	22.77
1180	187.7	320.1	20.89	20.85	20.94
1181	175.3	318.4	23.97	23.05	22.15
1182	178.0	321.4	22.84	22.61	22.18
1183	173.1	321.2	21.41	21.47	21.45
1184	169.2	319.2	20.63	20.59	20.65
1185	178.0	328.3	22.70	23.01	22.81
1186	183.3	324.0	23.68	22.38	21.43
1187	134.7	344.0	22.96	21.46	20.64
1188	316.6	360.9	-	22.98	22.49
1189	310.6	368.2	25.07	24.06	23.01
1190	312.8	362.7	24.13	23.01	22.03
1191	316.9	367.9	24.20	23.72	22.98
1192	355.2	395.0	24.69	22.49	21.63
1193	351.0	397.1	23.90	22.90	22.35
1194	351.0	405.0	23.76	23.46	23.17
1195	195.3	397.7	22.20	22.40	22.68
1196	201.7	402.0	25.29	23.13	21.86
1197	109.3	67.0	24.95	23.15	22.78
1198	112.8	69.0	25.21	23.83	23.45
1199	108.6	74.7	24.36	22.67	21.99
1200	104.1	73.8	24.42	23.36	22.86

Num	X	Y	B	V	R
1201	102.5	69.9	24.92	23.43	22.97
1202	163.3	72.9	24.63	23.03	20.24
1203	158.3	83.2	25.42	23.84	23.01
1204	163.1	83.1	24.46	22.97	20.11
1205	81.9	169.8	24.35	23.02	22.46
1206	86.1	173.1	-	23.32	23.50
1207	102.6	215.9	24.70	23.71	22.97
1208	155.8	91.3	-	23.34	23.58
1209	107.3	13.1	23.80	21.95	20.89
1210	106.7	17.9	24.75	23.24	22.11
1211	111.9	16.5	24.32	23.12	22.82
1212	298.4	192.1	-	22.92	22.34
1213	300.4	196.1	24.13	23.53	23.07
1214	308.9	187.8	25.23	23.04	22.50
1215	185.3	384.2	22.77	22.34	22.13
1216	180.2	384.3	23.81	22.94	22.09
1217	151.9	141.4	24.93	23.11	22.88
1218	218.3	166.9	22.86	22.27	21.86
1219	222.2	172.2	23.47	23.57	22.24
1220	223.6	178.1	22.13	20.57	19.79
1221	221.1	189.1	24.00	22.80	21.96
1222	222.7	184.0	24.26	23.21	22.21
1223	223.1	187.2	-	23.05	23.69
1224	154.9	327.9	24.62	23.54	22.65
1225	143.8	336.1	23.83	22.72	21.92
1226	147.1	338.4	24.47	22.89	22.31
1227	277.4	393.3	22.62	22.63	22.51
1228	273.9	396.0	24.08	22.70	21.98
1229	271.2	408.4	-	23.14	23.47
1230	275.1	401.2	21.20	21.10	20.87
1231	267.5	402.3	23.75	22.79	22.07
1232	156.1	432.1	-	23.12	22.83
1233	82.8	189.8	19.94	19.27	19.00
1234	82.8	195.6	23.54	22.47	21.94
1235	77.8	194.2	24.15	22.70	22.05
1236	80.0	197.9	22.73	22.58	22.63
1237	91.4	194.0	25.04	23.34	22.97
1238	212.0	376.1	-	22.80	22.45
1239	214.8	378.6	20.75	20.91	21.01
1240	213.9	382.9	-	22.61	21.78
1241	216.6	383.6	22.24	22.07	21.90
1242	208.2	385.9	-	22.65	21.73
1243	205.0	381.4	23.53	23.41	23.00
1244	201.8	385.1	22.30	22.08	22.54
1245	204.2	387.1	22.70	21.19	20.53
1246	239.0	402.6	23.42	22.46	22.11
1247	242.9	402.6	25.39	24.13	22.74
1248	233.5	409.4	-	22.42	22.04
1249	226.7	409.9	-	23.16	21.94
1250	228.2	414.2	22.91	22.04	21.44
1251	238.5	415.5	25.11	23.21	22.01
1252	235.3	417.6	24.11	23.19	22.34
1253	338.8	436.2	24.19	23.73	23.54
1254	331.0	441.7	24.82	23.12	22.06
1255	340.0	443.7	21.01	21.20	21.25
1256	330.7	447.4	22.93	22.58	23.01
1257	330.7	454.0	-	23.66	23.26
1258	334.7	453.7	-	23.36	23.00
1259	311.4	285.1	-	23.58	23.48
1260	310.8	289.2	24.62	23.24	22.02
1261	320.0	288.5	20.68	20.58	20.35
1262	310.2	292.9	25.60	23.45	22.71
1263	335.5	290.4	23.33	22.24	21.69
1264	327.1	284.3	23.88	23.01	22.72
1265	330.6	287.7	23.87	22.61	21.89
1266	348.6	328.5	-	23.19	22.82
1267	349.9	332.8	25.27	24.16	22.68
1268	341.1	334.1	25.49	23.22	22.63
1269	133.9	363.5	-	22.77	22.41
1270	134.2	367.5	24.75	23.44	22.24
1271	131.9	371.5	24.01	23.74	23.78
1272	128.8	374.2	-	24.02	23.18
1273	132.3	375.6	24.73	23.61	23.09
1274	330.3	390.3	21.08	21.43	21.50
1275	338.5	393.6	23.91	22.86	22.32
1276	321.2	210.1	21.42	19.76	18.94
1277	333.3	212.1	23.79	23.66	22.89
1278	328.4	216.6	-	23.23	22.44
1279	336.2	206.0	25.40	24.05	23.56
1280	176.3	342.7	23.36	22.97	22.06

Num	X	Y	B	V	R
1281	173.8	344.4	23.15	22.99	22.79
1282	170.8	358.5	23.32	23.11	22.81
1283	156.9	355.4	24.03	23.07	22.10
1284	151.8	344.3	22.11	20.64	19.87
1285	154.1	357.6	-	23.11	22.45
1286	133.9	159.1	-	22.93	22.14
1287	311.1	403.8	-	23.12	22.22
1288	315.1	402.2	-	23.43	22.48
1289	137.0	49.9	20.92	20.03	19.62
1290	135.6	62.9	24.69	23.10	22.55
1291	218.4	193.6	24.06	23.80	22.97
1292	225.4	200.1	-	23.67	23.67
1293	217.4	205.9	-	22.95	22.18
1294	223.0	203.7	24.31	22.95	22.35
1295	286.7	244.1	19.36	19.45	19.50
1296	279.8	245.2	19.48	19.54	19.57
1297	281.3	251.8	22.27	21.96	21.81
1298	285.0	253.2	22.62	21.74	21.55
1299	290.8	256.6	22.43	22.38	22.17
1300	174.1	114.7	-	24.10	22.94
1301	170.3	97.5	23.69	22.87	22.57
1302	178.8	96.1	23.58	22.75	22.03
1303	173.6	106.2	23.15	22.66	21.96
1304	180.6	100.4	23.52	22.62	22.08
1305	178.4	107.2	-	23.03	22.82
1306	220.1	356.0	24.66	23.29	23.02
1307	225.9	347.3	23.31	22.25	22.75
1308	205.7	347.3	-	22.61	22.48
1309	205.9	350.3	21.97	22.11	22.24
1310	223.5	349.7	22.57	22.70	22.85
1311	212.6	354.1	20.65	20.80	20.84
1312	220.2	350.1	24.14	23.32	22.71
1313	216.8	353.9	-	21.85	21.28
1314	177.5	337.5	22.90	22.59	22.74
1315	202.5	312.8	22.87	22.65	22.51
1316	198.0	317.5	23.59	22.43	22.33
1317	176.8	333.6	22.54	22.81	22.41
1318	193.7	319.7	22.19	22.32	22.31
1319	202.0	325.4	24.55	23.50	23.00
1320	191.6	334.0	20.56	19.87	19.44
1321	187.9	337.4	20.80	20.88	20.98
1322	183.7	333.1	21.21	21.24	21.39
1323	198.7	339.7	23.64	22.88	22.93
1324	180.7	336.5	22.62	22.16	21.78
1325	206.5	307.4	22.85	22.58	22.86
1326	212.6	308.1	22.27	22.14	22.16
1327	214.8	310.7	21.35	21.32	21.48
1328	221.2	313.8	22.17	22.18	22.18
1329	218.8	317.9	21.51	21.57	21.56
1330	223.5	318.2	21.57	21.74	21.77
1331	222.1	322.5	22.92	21.68	20.57
1332	218.6	332.7	22.89	22.66	22.49
1333	215.6	322.9	-	22.63	21.72
1334	213.9	326.6	22.78	22.27	22.50
1335	220.5	330.3	23.09	22.67	21.94
1336	293.9	210.4	23.65	23.32	22.84
1337	292.4	214.3	23.28	22.77	22.36
1338	290.9	219.2	20.67	20.62	20.57
1339	316.4	232.7	21.99	22.13	22.35
1340	294.9	223.6	22.02	22.17	22.39
1341	291.9	225.5	21.46	21.42	21.58
1342	301.8	222.0	23.20	22.38	22.10
1343	300.4	230.0	24.84	23.19	23.29
1344	304.0	232.9	20.36	20.47	20.55
1345	308.0	229.9	24.09	22.93	22.24
1346	309.7	225.9	23.72	23.04	22.67
1347	318.2	225.9	21.69	20.08	19.05
1348	311.7	240.7	25.52	23.50	22.62
1349	236.9	435.1	23.68	23.01	22.52
1350	237.8	438.9	22.41	22.02	22.02
1351	248.4	430.9	24.13	22.90	22.03
1352	224.3	442.2	24.36	23.20	22.94
1353	224.9	446.6	23.77	23.40	22.49
1354	225.4	451.7	21.37	21.39	21.20
1355	233.1	458.0	23.48	23.33	23.72
1356	233.9	460.9	24.05	23.04	22.25
1357	349.5	6.7	-	23.74	23.50
1358	254.9	33.2	-	23.93	23.88
1359	301.4	44.9	24.65	23.27	22.61
1360	93.7	56.5	-	23.33	23.14

Num	X	Y	B	V	R
1361	106.3	88.9	-	22.89	22.02
1362	301.4	102.4	-	23.46	23.57
1363	45.8	114.6	-	23.60	22.57
1364	107.7	152.8	-	23.69	23.00
1365	270.3	178.8	-	23.17	22.29
1366	346.9	186.7	-	23.40	23.60
1367	115.7	200.1	-	24.36	22.90
1368	4.4	202.6	-	23.73	23.22
1369	225.5	284.5	-	23.16	22.58
1370	6.5	293.1	-	22.89	22.45
1371	180.6	412.1	-	23.18	22.37
1372	326.3	436.5	-	23.82	22.59
1373	326.3	475.8	-	23.20	22.06
1374	211.2	9.7	-	23.18	22.50
1375	208.2	11.0	-	23.63	23.63
1376	319.6	58.7	-	23.66	23.59
1377	87.9	162.5	-	23.93	22.98
1378	5.7	184.9	-	24.28	23.61
1379	345.3	236.5	-	23.54	22.22
1380	150.1	250.6	24.39	23.38	23.01
1381	106.5	269.4	-	24.00	22.79
1382	148.6	278.9	-	23.73	24.07
1383	150.4	281.1	-	23.64	22.01
1384	216.9	288.8	-	24.20	24.73
1385	238.2	363.0	-	23.80	23.52
1386	38.0	382.0	24.33	22.27	21.79
1387	186.7	434.1	-	23.26	22.46
1388	5.5	449.0	24.07	22.75	22.41
1389	334.7	18.0	-	23.24	22.81
1390	205.6	16.4	-	24.07	22.95
1391	204.3	19.5	-	23.26	23.63
1392	145.8	68.9	-	23.68	24.10
1393	298.9	79.0	-	24.23	23.81
1394	301.6	79.8	-	23.83	24.00
1395	296.8	81.9	-	23.13	22.20
1396	336.8	103.8	-	22.93	21.92
1397	334.7	107.1	-	22.98	22.24
1398	331.9	111.9	-	24.19	23.15
1399	38.0	269.3	-	23.14	21.89
1400	313.3	271.3	-	23.61	23.14
1401	315.7	273.3	-	23.79	23.68
1402	355.3	281.5	-	24.13	23.30
1403	101.6	285.0	-	22.54	21.44
1404	100.5	291.4	-	23.36	23.24
1405	124.7	400.7	24.29	23.21	23.25
1406	106.6	418.1	23.30	23.09	22.16
1407	292.8	483.3	24.47	23.56	22.39
1408	258.5	19.6	-	23.87	23.05
1409	215.9	23.2	-	23.43	22.83
1410	207.2	26.4	-	23.45	22.69
1411	212.7	53.4	-	24.24	23.72
1412	172.8	66.6	-	24.52	23.95
1413	333.5	66.6	-	24.00	24.02
1414	265.3	154.1	-	23.34	22.92
1415	259.8	156.9	-	23.41	22.72
1416	247.4	196.6	-	23.19	22.62
1417	58.0	220.9	-	23.34	23.42
1418	215.9	267.2	-	23.92	22.56
1419	26.0	4.2	24.00	23.12	22.63
1420	284.6	29.2	-	23.17	22.97
1421	288.7	121.2	-	24.34	24.16
1422	288.8	123.1	-	23.46	22.19
1423	38.6	140.2	-	23.38	23.12
1424	36.0	142.9	24.65	22.87	22.06
1425	15.6	300.3	-	23.95	22.51
1426	125.0	302.9	-	23.38	22.92
1427	9.7	353.3	-	23.62	22.18
1428	263.2	370.1	-	23.64	22.61
1429	266.9	373.1	-	23.55	23.22
1430	24.9	425.7	-	23.20	22.78
1431	22.8	428.7	-	23.98	23.91
1432	308.6	429.7	-	24.43	23.65
1433	209.0	466.5	-	23.49	22.72
1434	208.9	470.6	-	24.04	22.87
1435	258.5	6.3	-	23.54	22.10
1436	19.4	144.9	-	23.93	23.25
1437	123.0	281.2	-	23.93	22.90
1438	127.9	283.0	-	23.76	23.38
1439	11.4	430.7	-	22.46	22.37
1440	9.5	436.2	-	23.12	23.44

Num	X	Y	B	V	R
1441	23.5	83.1	24.90	23.08	22.28
1442	29.6	86.0	-	23.47	23.34
1443	119.5	111.8	-	23.00	22.89
1444	110.6	122.2	-	24.49	23.48
1445	119.8	161.5	-	23.00	22.10
1446	274.2	16.8	24.64	24.06	23.84
1447	277.4	20.4	23.98	22.60	22.19
1448	280.7	20.6	23.28	23.72	23.28
1449	111.9	237.4	-	23.93	22.51
1450	313.0	386.1	-	23.52	23.03
1451	221.1	475.1	-	23.15	22.28
1452	137.0	22.0	-	23.17	22.55
1453	248.3	54.8	-	22.92	21.92
1454	39.1	104.2	-	22.82	24.17
1455	36.7	106.4	-	24.23	23.40
1456	101.8	112.2	-	23.24	23.00
1457	91.8	107.6	-	23.49	22.87
1458	95.8	109.9	-	23.32	23.34
1459	41.4	251.4	-	23.52	23.00
1460	48.0	260.9	-	23.92	24.06
1461	29.1	272.2	-	24.40	22.82
1462	353.1	309.6	-	23.21	22.69
1463	12.3	23.9	-	23.39	22.65
1464	77.0	428.2	22.35	20.73	19.99
1465	82.2	433.9	-	23.58	22.43
1466	92.9	440.5	-	23.25	22.67
1467	12.9	123.3	25.45	23.91	23.04
1468	277.6	34.7	-	23.62	24.09
1469	349.6	45.7	-	23.15	22.85
1470	349.0	52.2	-	23.79	23.24
1471	333.8	48.0	-	23.48	22.27
1472	355.4	200.5	24.17	22.96	22.01
1473	57.4	236.6	-	23.34	23.90
1474	75.5	267.0	-	23.58	22.82
1475	76.5	273.9	-	22.70	22.15
1476	68.3	412.6	-	23.76	22.69
1477	93.0	479.5	-	23.18	22.51
1478	104.1	483.1	-	21.54	20.65
1479	24.9	471.1	-	24.16	22.70
1480	38.6	474.5	-	22.61	21.72
1481	21.5	473.0	-	24.26	23.03
1482	19.1	476.4	22.75	22.68	23.52
1483	30.5	478.8	-	22.67	22.12
1484	18.8	478.4	-	22.73	22.32
1485	222.4	111.8	24.96	23.43	23.98
1486	125.7	142.0	-	23.58	23.24
1487	235.0	220.8	-	22.68	21.82
1488	237.3	222.5	23.85	23.01	22.34
1489	224.8	220.1	-	23.06	22.61
1490	227.4	222.3	-	24.42	24.00
1491	230.2	225.8	-	24.17	24.01
1492	226.7	228.0	-	23.64	22.76
1493	259.3	485.1	-	23.65	22.74
1494	270.6	485.2	24.98	23.82	22.42
1495	70.4	249.5	-	23.89	23.68
1496	65.5	258.1	24.54	23.59	22.43
1497	65.2	261.0	-	23.65	23.70
1498	315.6	79.7	-	23.76	24.13
1499	50.4	332.6	-	23.74	23.29
1500	52.1	340.6	-	24.31	23.88
1501	49.7	344.4	-	23.35	23.20
1502	52.1	359.1	-	23.64	22.46
1503	131.6	464.9	-	21.53	21.75
1504	128.8	468.0	-	21.94	22.13
1505	128.0	470.2	-	21.95	21.81
1506	231.8	14.9	-	23.46	22.72
1507	241.3	20.8	-	23.65	23.21
1508	250.1	9.0	-	22.40	21.67
1509	10.0	314.9	-	23.59	23.26
1510	15.5	319.9	-	23.75	22.92
1511	30.3	328.8	-	23.57	23.30
1512	16.4	327.1	-	23.82	23.37
1513	20.4	329.0	-	22.97	22.20
1514	30.7	322.4	-	23.18	22.52
1515	128.0	456.2	-	22.24	21.40
1516	119.6	452.7	-	23.73	23.16
1517	122.2	457.0	-	22.44	22.01
1518	129.8	436.4	22.54	22.57	23.11
1519	138.6	438.8	-	23.03	22.76
1520	40.5	387.4	-	23.26	23.38

Num	X	Y	B	V	R
1521	35.0	412.8	-	22.98	22.41
1522	30.3	412.5	-	24.22	24.16
1523	93.6	337.6	-	22.99	22.55
1524	88.3	341.9	-	23.71	23.25
1525	84.4	339.7	-	23.66	23.00
1526	87.8	344.2	-	23.42	23.25
1527	82.1	349.7	-	23.29	22.42
1528	88.2	361.0	-	23.72	23.62
1529	342.5	32.2	-	23.79	22.77
1530	316.7	13.6	-	23.08	22.20
1531	310.4	20.6	-	23.56	23.17
1532	303.5	11.2	-	23.22	22.33
1533	129.1	259.8	25.12	23.63	23.49
1534	132.3	260.5	-	23.28	22.72
1535	125.8	261.6	-	23.92	24.31
1536	126.9	263.4	-	23.25	23.23
1537	124.6	264.2	-	22.75	23.34
1538	125.5	271.0	-	23.23	22.61
1539	133.1	268.4	-	23.13	22.95
1540	112.0	284.0	-	23.71	23.17
1541	102.8	456.4	-	23.03	22.14
1542	98.5	438.1	-	23.45	23.30
1543	99.1	454.1	-	23.53	23.08
1544	92.1	454.9	-	23.18	22.40
1545	163.3	5.8	-	24.00	23.39
1546	165.3	9.7	-	23.54	23.11
1547	160.4	25.3	-	23.34	22.76
1548	199.6	26.7	-	23.42	24.17
1549	182.2	20.5	-	23.47	22.04
1550	188.2	15.8	-	24.27	23.46
1551	165.9	36.5	-	23.58	23.23
1552	193.1	15.0	24.84	22.70	21.80
1553	162.6	41.3	-	23.42	22.84
1554	196.9	12.2	-	23.90	22.94
1555	54.8	153.4	-	23.19	22.39
1556	47.3	174.8	-	23.70	22.88
1557	36.0	178.4	-	23.30	22.58
1558	88.4	234.8	-	23.93	23.10
1559	81.2	238.3	-	24.33	22.77
1560	82.1	242.5	-	23.21	22.49
1561	83.4	253.2	-	24.13	23.53
1562	91.6	241.7	-	23.30	23.36
1563	99.0	256.1	-	23.83	24.06
1564	93.9	250.0	-	23.25	22.75
1565	103.7	264.0	-	23.61	23.18
1566	228.2	240.2	-	24.02	23.38
1567	243.4	274.5	25.36	23.84	22.90
1568	229.2	250.2	-	23.35	23.33
1569	238.0	243.7	-	23.94	23.51
1570	225.5	261.3	-	24.65	23.62
1571	242.0	241.3	24.80	23.39	23.40
1572	249.4	240.9	-	24.35	23.24
1573	233.7	275.7	-	23.77	23.86
1574	238.3	275.6	-	23.67	23.58
1575	231.5	281.7	-	23.40	23.83
1576	77.9	304.8	-	24.19	23.70
1577	74.3	306.9	-	23.95	23.57
1578	67.9	314.2	-	23.65	22.60
1579	74.1	350.7	-	23.36	22.67
1580	69.6	322.1	-	23.21	22.04
1581	77.0	343.2	-	23.37	22.88
1582	84.5	329.3	-	23.41	22.49
1583	84.3	330.7	-	22.92	22.89
1584	62.0	326.3	-	24.09	23.43
1585	156.1	110.5	-	23.96	22.87
1586	149.5	123.4	-	23.57	23.23
1587	143.6	130.8	25.51	23.89	23.59
1588	295.9	24.3	-	23.53	23.33
1589	302.3	32.5	-	23.32	24.01
1590	295.1	33.6	-	23.76	22.94
1591	296.2	53.7	-	23.89	22.97
1592	281.1	53.8	24.34	23.09	22.24
1593	353.1	68.4	-	23.30	23.23
1594	343.2	93.5	-	23.19	22.36
1595	335.8	95.5	23.13	23.01	23.16
1596	328.3	96.6	-	23.22	22.79
1597	325.6	88.2	-	24.35	23.47
1598	330.0	99.8	-	24.45	23.06
1599	327.0	103.7	23.70	22.71	22.20
1600	220.5	45.8	-	24.03	22.77

Num	X	Y	B	V	R
1601	215.4	39.9	-	23.57	23.13
1602	208.9	32.6	-	23.53	23.02
1603	99.9	380.7	-	23.75	23.42
1604	94.4	397.6	24.74	23.43	23.32
1605	27.5	344.2	-	23.13	22.52
1606	23.9	345.1	-	23.04	22.98
1607	26.2	353.9	23.26	23.81	22.79
1608	16.3	359.9	-	23.19	23.45
1609	25.9	378.9	24.14	22.98	22.48
1610	79.0	487.8	22.53	22.48	22.28
1611	23.4	446.5	-	23.95	24.52
1612	35.0	462.8	-	23.86	23.20
1613	13.9	462.9	-	23.73	22.83
1614	15.0	465.2	-	22.74	22.95
1615	73.8	480.9	22.67	22.68	22.44
1616	10.6	455.3	-	23.38	22.79
1617	9.9	469.1	-	23.31	22.24
1618	57.0	483.1	-	21.38	21.09
1619	45.9	479.5	-	22.99	22.78
1620	143.7	109.7	-	23.31	23.09
1621	207.7	248.7	-	22.35	22.05
1622	186.0	354.7	-	23.36	22.75
1623	158.6	419.5	-	22.86	22.19
1624	298.2	429.7	-	23.08	22.33
1625	74.9	453.3	23.30	23.65	23.70
1626	234.0	180.6	-	24.26	23.22
1627	112.7	189.8	-	23.80	23.62
1628	203.6	209.3	-	22.78	23.12
1629	177.1	221.1	-	22.18	22.27
1630	180.5	225.7	-	22.52	22.40
1631	142.0	225.6	-	23.29	23.27
1632	168.4	255.2	-	23.57	23.62
1633	258.5	276.7	-	23.21	23.71
1634	280.2	288.2	-	23.15	22.06
1635	309.1	420.1	-	23.28	23.25
1636	304.4	422.3	-	23.08	21.88
1637	206.3	113.0	-	23.37	23.44
1638	208.9	111.1	-	23.38	22.93
1639	345.7	115.3	-	23.95	22.92
1640	214.5	248.6	-	23.35	22.56
1641	212.8	251.6	-	23.91	22.43
1642	213.8	252.8	-	23.13	23.52
1643	186.6	271.4	-	23.52	23.82
1644	266.8	322.3	-	23.58	22.84
1645	245.6	357.7	-	23.57	23.11
1646	201.1	362.7	-	23.89	23.11
1647	246.9	400.6	24.88	22.76	22.81
1648	240.9	468.5	-	23.48	22.35
1649	245.8	470.2	-	24.00	22.47
1650	338.5	487.3	-	23.17	22.09
1651	333.8	485.1	-	23.49	23.16
1652	181.5	88.0	-	22.90	22.65
1653	200.9	134.8	24.33	23.03	22.88
1654	76.9	52.4	-	24.32	23.07
1655	202.4	247.3	-	23.55	23.37
1656	195.8	249.0	-	23.09	22.61
1657	203.4	252.7	-	23.27	22.42
1658	113.1	290.5	-	23.11	22.40
1659	301.4	300.1	-	22.74	22.23
1660	238.8	346.1	23.45	22.81	23.36
1661	154.2	426.2	-	23.62	23.27
1662	150.1	429.4	23.95	23.65	23.24
1663	336.4	469.0	25.28	23.35	22.23
1664	336.0	472.4	-	23.43	22.83
1665	41.4	363.3	-	23.49	22.25
1666	76.2	368.1	-	24.07	23.26
1667	75.3	370.8	-	23.51	23.24
1668	93.0	378.8	25.31	23.22	22.56
1669	198.5	83.7	-	23.07	22.48
1670	258.0	92.0	-	23.46	23.30
1671	298.5	398.3	-	23.47	23.11
1672	279.4	372.9	-	22.78	21.84
1673	186.0	405.6	-	23.82	23.39
1674	342.6	423.8	-	23.36	22.80
1675	346.0	429.5	-	22.97	21.35
1676	335.2	429.9	-	23.00	23.05
1677	344.7	479.6	-	24.03	22.74
1678	350.3	477.2	-	23.31	22.57
1679	348.2	479.9	-	24.14	23.47
1680	341.5	475.5	-	24.12	24.49

Num	X	Y	B	V	R
1681	246.9	72.9	-	23.55	22.75
1682	85.7	110.7	-	23.40	22.72
1683	199.2	148.4	-	23.13	22.73
1684	11.0	228.4	24.45	23.40	23.00
1685	30.9	309.7	-	23.64	23.37
1686	35.9	309.9	-	23.57	22.78
1687	97.8	324.2	-	23.23	22.94
1688	92.0	327.4	-	23.80	23.81
1689	99.6	331.9	-	22.79	22.45
1690	291.6	372.8	-	23.68	23.76
1691	291.2	380.1	-	23.50	23.18
1692	65.8	435.8	-	23.38	22.84
1693	201.3	259.8	-	23.85	22.95
1694	200.3	270.6	-	23.46	22.62
1695	57.4	277.2	-	23.42	22.68
1696	54.5	282.4	-	24.16	23.96
1697	74.0	387.3	-	23.97	22.70
1698	265.9	443.5	-	23.86	23.95
1699	254.5	458.5	-	24.22	22.80
1700	256.9	459.9	-	23.84	23.51
1701	258.6	227.3	-	23.03	22.23
1702	21.4	288.8	-	24.22	22.63
1703	21.9	292.2	-	23.03	23.06
1704	319.2	327.1	-	23.66	22.31
1705	327.2	322.3	24.82	23.12	22.34
1706	227.2	387.4	-	23.25	22.53
1707	224.8	401.1	-	23.73	22.77
1708	225.5	391.0	-	23.55	22.28
1709	234.2	391.0	-	23.33	22.36
1710	223.6	394.5	-	24.26	23.21
1711	208.9	148.1	-	23.13	22.01
1712	351.5	218.6	-	23.84	24.07
1713	351.6	220.9	-	23.85	23.42
1714	355.0	227.6	24.78	23.98	24.14
1715	355.0	236.6	22.94	23.01	23.27
1716	354.3	233.5	-	23.40	23.22
1717	8.5	255.8	-	23.55	22.78
1718	54.5	394.7	-	23.67	23.64
1719	9.7	70.5	-	23.94	24.19
1720	8.3	221.1	-	23.65	23.94
1721	321.2	254.8	-	23.50	22.77
1722	304.7	255.2	-	24.04	24.41
1723	284.7	337.4	-	23.30	21.97
1724	291.8	340.9	-	23.29	22.49
1725	58.7	406.4	-	23.69	23.29
1726	55.2	411.7	-	23.41	23.15
1727	50.3	408.3	-	23.84	23.23
1728	53.8	419.4	-	24.86	23.00
1729	50.4	422.4	-	23.42	22.72
1730	47.2	421.7	24.30	23.11	22.64
1731	175.4	449.9	-	23.29	22.74
1732	181.9	453.3	-	23.03	23.18
1733	184.8	456.7	24.15	22.98	22.63
1734	184.4	462.5	-	23.25	22.52
1735	189.2	462.7	-	23.18	22.78
1736	126.6	317.6	-	23.39	22.96
1737	129.0	324.9	-	23.56	23.73
1738	151.1	298.0	24.66	23.43	22.20
1739	148.6	300.6	-	23.07	22.20
1740	241.0	108.5	-	23.42	23.44
1741	248.8	107.2	-	24.07	23.64
1742	189.2	132.8	-	23.33	23.11
1743	192.9	133.1	-	22.78	22.34
1744	183.5	149.6	-	23.17	23.34
1745	182.8	152.4	-	23.01	22.37
1746	179.4	150.1	-	24.18	24.20
1747	53.9	368.7	24.79	24.48	23.46
1748	49.4	371.3	-	24.53	23.40
1749	53.3	373.3	-	24.46	22.79
1750	50.8	378.5	24.17	22.98	22.53
1751	52.5	379.4	-	22.99	22.35
1752	294.8	144.8	-	23.61	23.06
1753	264.7	341.3	-	23.69	23.67
1754	275.1	360.1	-	24.47	23.76
1755	253.0	340.8	-	23.96	22.66
1756	248.0	340.5	-	23.57	22.71
1757	270.8	356.7	-	23.07	23.23
1758	247.3	307.1	-	22.27	23.12
1759	251.3	311.5	-	23.61	23.33
1760	251.6	318.7	-	22.05	22.11

Num	X	Y	B	V	R
1761	247.7	326.3	24.26	23.07	22.06
1762	249.6	329.0	-	24.39	24.09
1763	231.6	122.3	-	23.21	22.39
1764	218.3	119.8	-	22.82	22.01
1765	42.1	126.4	-	23.48	22.84
1766	37.0	131.3	-	23.66	23.09
1767	44.4	132.4	-	23.75	23.13
1768	58.0	131.2	-	23.73	24.08
1769	62.2	131.8	-	23.73	23.94
1770	51.2	141.3	-	23.28	22.90
1771	260.0	191.1	-	23.73	23.04
1772	254.6	195.4	-	23.28	22.26
1773	260.7	199.4	-	23.23	22.30
1774	252.9	204.7	-	23.45	22.70
1775	255.8	214.6	-	23.30	22.75
1776	269.2	215.3	-	24.28	23.88
1777	267.0	208.5	-	22.78	21.86
1778	263.6	219.1	-	23.95	22.89
1779	266.3	219.9	23.83	23.29	23.08
1780	265.0	223.8	-	23.27	24.19
1781	79.9	11.1	-	23.72	23.17
1782	77.5	17.5	24.00	23.26	22.72
1783	64.2	18.7	-	23.59	23.26
1784	116.6	99.6	-	23.50	22.69
1785	141.6	63.6	-	24.22	22.70
1786	126.5	81.2	-	23.57	22.51
1787	116.7	84.3	-	23.57	22.65
1788	127.1	86.8	-	23.45	22.73
1789	254.7	280.8	-	24.33	23.25
1790	260.3	297.0	-	24.04	24.48
1791	234.1	297.0	-	23.23	23.49
1792	267.4	292.0	-	23.96	24.08
1793	43.0	287.2	-	23.36	22.24
1794	31.5	286.7	-	23.42	22.88
1795	35.5	300.4	-	24.39	23.13
1796	47.8	298.0	-	24.07	23.10
1797	30.9	17.2	24.52	23.32	22.76
1798	40.8	21.2	-	23.68	23.00
1799	26.8	16.4	-	23.83	23.13
1800	27.0	23.4	-	23.85	23.52
1801	47.1	23.7	-	23.70	23.93
1802	225.7	63.2	-	24.34	23.42
1803	224.6	73.3	23.25	22.38	21.85
1804	203.8	70.8	-	23.89	23.34
1805	226.0	83.6	-	23.20	22.39
1806	224.9	86.7	-	23.49	22.48
1807	207.9	91.1	-	24.08	23.74
1808	354.0	165.8	-	22.90	22.12
1809	353.3	168.8	-	23.14	22.74
1810	351.4	171.1	-	23.24	22.80
1811	337.6	171.1	-	22.66	22.19
1812	355.0	184.2	-	23.74	24.22
1813	327.4	180.6	-	23.99	22.94
1814	332.7	184.5	-	22.66	21.88
1815	328.4	186.0	-	22.70	21.50
1816	332.8	186.7	-	22.43	22.93
1817	336.7	186.6	-	22.98	22.48
1818	41.2	422.8	-	23.90	24.03
1819	66.8	462.5	-	23.85	22.99
1820	49.1	449.9	-	23.54	22.26
1821	61.7	452.1	-	23.69	22.43
1822	96.9	303.9	-	24.32	24.22
1823	101.0	302.9	23.98	22.96	22.52
1824	98.5	309.8	-	23.63	23.90
1825	102.3	298.1	-	23.79	23.47
1826	103.6	313.8	-	23.49	22.52
1827	19.5	181.6	-	23.27	23.20
1828	40.8	197.4	-	23.47	22.41
1829	257.2	114.1	23.79	22.75	22.45
1830	284.0	105.5	-	23.09	22.20
1831	255.6	123.6	-	22.74	21.97
1832	282.9	110.7	-	22.97	23.41
1833	274.8	108.5	-	23.78	24.10
1834	268.6	124.1	-	23.53	22.45
1835	298.0	115.5	-	24.01	23.67
1836	258.5	116.3	24.08	22.82	21.83
1837	261.8	113.6	-	23.25	22.46
1838	272.3	307.4	-	22.92	22.51
1839	281.2	303.5	-	22.87	22.15
1840	279.8	308.6	-	22.60	22.65

Num	X	Y	B	V	R
1841	296.6	319.9	-	22.74	23.28
1842	198.5	222.1	-	23.12	22.19
1843	204.5	224.3	24.60	23.17	22.86
1844	196.7	236.6	-	23.00	22.46
1845	195.1	263.1	-	24.04	23.15
1846	192.2	243.8	-	22.39	22.36
1847	182.7	243.5	-	22.83	22.47
1848	173.1	228.1	-	22.57	22.68
1849	180.4	244.1	-	22.91	22.34
1850	181.7	232.7	-	22.95	22.54
1851	173.0	239.5	-	22.39	21.79
1852	186.1	225.6	-	22.81	23.04
1853	171.8	235.1	-	22.38	21.45
1854	197.2	255.0	-	23.73	23.05
1855	59.0	43.3	-	22.83	22.66
1856	58.8	55.5	-	22.67	21.83
1857	39.0	84.1	-	23.68	23.02
1858	44.5	85.2	24.49	23.14	22.37
1859	148.9	217.2	-	21.96	21.69
1860	142.8	217.0	-	22.57	22.12
1861	137.6	232.4	-	22.86	21.95
1862	132.8	248.3	-	23.30	22.63
1863	136.6	244.5	24.67	23.00	22.27
1864	138.3	249.8	-	23.83	23.68
1865	132.6	238.5	-	23.42	23.07
1866	101.2	148.8	-	24.12	23.47
1867	68.4	115.8	-	23.74	23.33
1868	72.1	122.7	-	23.71	22.31
1869	84.5	131.1	-	24.24	24.15
1870	79.4	136.3	-	23.12	22.22
1871	94.5	132.6	-	23.40	22.89
1872	101.4	136.5	-	23.20	23.14
1873	88.1	147.2	-	23.70	22.50
1874	326.2	132.5	23.22	22.34	22.13
1875	331.5	136.9	23.21	22.39	22.50
1876	335.9	137.3	-	23.14	22.91
1877	340.1	128.6	-	23.25	22.47
1878	343.3	142.3	-	23.72	22.95
1879	337.4	144.3	-	22.70	21.98
1880	347.5	130.7	-	23.70	24.06
1881	135.6	415.2	-	23.48	22.69
1882	133.1	386.4	-	22.91	22.12
1883	133.3	409.3	-	23.17	22.71
1884	140.1	409.6	-	22.51	21.65
1885	136.7	408.5	-	22.91	22.02
1886	140.2	396.1	-	23.19	22.24
1887	138.6	401.6	-	23.83	23.38
1888	152.5	400.5	24.30	22.97	22.49
1889	156.1	403.8	-	23.49	22.87
1890	345.6	245.0	-	23.06	21.86
1891	352.3	246.2	-	23.97	22.96
1892	327.4	262.1	-	23.08	23.36
1893	342.7	245.7	-	23.23	22.71
1894	345.8	249.2	-	23.44	22.53
1895	326.6	275.5	-	23.68	23.17
1896	329.1	250.9	-	22.65	22.53
1897	345.1	257.8	-	23.39	22.72
1898	346.3	266.7	-	23.45	22.92
1899	324.5	273.6	23.94	23.66	22.93
1900	343.6	277.0	-	23.93	23.82
1901	340.4	273.4	-	23.72	22.35
1902	353.7	266.7	-	23.73	23.99
1903	334.2	271.0	-	22.70	22.63
1904	353.8	262.2	-	23.24	22.90
1905	123.1	35.0	-	23.51	23.46
1906	150.8	49.0	-	24.45	23.42
1907	147.9	94.3	-	23.75	22.95
1908	248.1	152.1	-	24.00	23.53
1909	321.9	162.8	-	24.27	23.23
1910	247.6	163.5	24.81	24.15	23.23
1911	70.7	167.8	-	23.23	22.24
1912	226.9	168.3	-	24.50	22.54
1913	78.8	177.3	-	23.09	21.93
1914	313.6	178.3	-	23.43	24.13
1915	203.5	189.2	-	22.91	22.80
1916	206.8	192.8	-	23.01	22.49
1917	340.0	215.0	-	23.21	22.19
1918	327.2	225.5	-	24.07	23.81
1919	331.3	235.8	-	22.92	22.42
1920	186.5	297.8	-	24.07	23.60

Num	X	Y	B	V	R
1921	210.3	337.6	23.02	22.93	22.74
1922	141.1	353.3	-	23.58	23.15
1923	122.9	353.5	-	23.44	22.27
1924	250.6	374.4	-	23.82	23.10
1925	151.9	384.5	22.60	21.17	20.09
1926	190.5	399.5	-	23.30	22.58
1927	339.1	400.8	-	23.68	22.99
1928	334.9	403.6	23.16	22.65	22.09
1929	277.9	412.4	-	23.25	22.68
1930	211.6	422.4	-	23.14	22.60
1931	204.5	438.7	-	23.83	22.96
1932	258.2	453.8	-	23.45	22.49
1933	109.2	97.5	-	23.55	23.50
1934	149.1	106.7	-	23.75	23.21
1935	277.6	144.6	-	23.29	22.95
1936	172.7	145.8	-	23.19	22.54
1937	135.7	165.5	-	22.93	21.96
1938	133.9	170.2	-	23.16	22.40
1939	307.4	168.9	-	24.72	23.66
1940	74.2	171.1	-	23.27	22.95
1941	231.9	189.7	-	23.61	23.80
1942	211.5	195.4	-	23.85	23.88
1943	0.0	0.0	21.32	19.27	-
1944	198.2	211.1	-	22.37	22.93
1945	264.1	257.3	-	23.97	23.11
1946	174.3	267.2	-	23.86	23.84
1947	175.6	270.7	-	24.17	23.54
1948	284.5	272.2	24.50	23.19	22.59
1949	321.9	279.2	24.76	24.18	23.44
1950	291.8	284.9	-	22.77	22.82
1951	332.7	309.9	-	23.53	22.88
1952	233.1	330.7	-	23.50	22.14
1953	230.6	330.8	-	22.97	23.04
1954	325.8	338.6	-	23.45	23.79
1955	326.0	340.5	-	23.44	21.89
1956	126.9	355.5	-	24.07	24.08
1957	354.2	382.3	-	23.59	23.31
1958	327.9	382.9	-	24.10	23.37
1959	329.3	384.9	-	23.23	22.49
1960	196.1	391.0	-	23.35	22.48
1961	317.6	394.9	-	23.16	22.58
1962	351.7	416.1	-	22.96	22.22
1963	213.3	428.2	-	23.46	22.70
1964	192.2	434.0	-	23.65	23.72
1965	209.9	455.8	24.78	23.61	22.96
1966	250.5	463.5	-	23.00	22.01
1967	200.9	464.5	-	23.13	22.49
1968	162.3	472.2	-	22.64	22.71
1969	192.3	477.6	-	23.28	22.39
1970	183.7	48.9	-	23.10	23.00
1971	326.0	158.3	23.51	23.61	23.09
1972	326.9	161.2	-	23.50	22.96
1973	287.4	156.9	-	23.62	23.69
1974	200.8	182.5	-	22.94	22.24
1975	289.1	186.2	-	23.92	24.48
1976	290.5	188.9	-	23.66	22.21
1977	335.5	238.4	-	23.74	22.44
1978	311.2	279.8	-	23.25	22.21
1979	287.4	303.3	-	23.27	22.82
1980	338.9	315.5	-	23.33	23.41
1981	132.1	336.3	-	23.47	22.30
1982	304.3	374.3	-	24.30	23.70
1983	196.3	381.8	-	23.20	22.65
1984	194.2	382.0	-	23.85	22.79
1985	168.5	379.7	-	23.64	23.63
1986	206.6	414.9	-	23.47	23.55
1987	276.7	435.0	23.66	22.93	22.05
1988	279.3	436.5	-	22.86	22.30
1989	280.8	439.2	-	23.24	22.32
1990	174.6	442.5	-	23.67	23.40
1991	296.8	453.1	-	23.88	23.80
1992	200.3	479.9	-	23.83	22.77
1993	141.6	36.2	-	23.23	22.18
1994	102.6	94.4	-	24.29	23.62
1995	129.6	105.0	-	23.50	23.41
1996	134.2	102.2	-	22.80	22.48
1997	141.6	175.1	-	23.15	22.53
1998	137.9	173.9	-	23.17	22.08
1999	135.7	177.1	-	23.01	22.63
2000	305.4	178.0	-	23.01	21.87

Num	X	Y	B	V	R
2001	300.3	178.8	-	23.99	23.56
2002	304.3	182.0	-	23.70	23.03
2003	272.4	237.9	-	23.55	23.70
2004	276.3	237.4	23.55	22.52	21.66
2005	326.6	245.5	-	23.61	23.42
2006	177.0	263.6	-	24.04	23.89
2007	196.2	292.6	-	23.52	22.27
2008	199.1	299.0	20.17	20.02	19.98
2009	201.7	302.5	-	23.64	22.71
2010	145.7	379.1	23.63	22.77	21.95
2011	146.2	375.0	-	23.65	22.88
2012	330.9	372.0	-	23.21	22.38
2013	174.7	385.6	24.58	23.91	23.90
2014	271.2	418.3	-	23.30	22.95
2015	268.3	422.7	-	23.61	24.03
2016	284.1	421.0	-	23.39	23.14
2017	305.2	449.3	-	23.69	22.70
2018	158.8	476.2	-	23.23	22.71
2019	163.3	477.6	-	23.13	22.76
2020	151.9	37.2	-	23.23	22.22
2021	147.4	34.9	-	23.08	22.66
2022	89.3	52.1	-	23.40	22.63
2023	88.6	75.0	-	23.69	22.69
2024	184.9	97.7	-	23.00	23.80
2025	187.4	99.2	-	23.10	22.96
2026	190.4	99.2	-	23.55	22.67
2027	273.9	148.4	-	23.88	22.52
2028	179.9	158.6	-	23.00	23.05
2029	296.2	163.6	-	23.47	23.20
2030	298.9	165.2	-	23.51	22.59
2031	313.8	183.5	-	23.72	23.61
2032	135.7	191.1	-	22.72	22.10
2033	138.0	192.4	-	22.30	22.31
2034	142.0	194.8	-	21.97	21.42
2035	194.0	194.4	-	21.97	22.10
2036	73.7	198.8	-	24.20	23.95
2037	218.8	294.2	-	22.76	23.28
2038	181.9	364.4	-	22.95	22.46
2039	223.4	360.1	-	23.05	22.32
2040	221.4	366.7	-	22.28	22.61
2041	222.3	364.9	-	22.32	21.64
2042	242.4	379.3	23.95	23.47	23.04
2043	244.5	376.5	23.48	22.24	21.66
2044	187.4	391.3	23.14	23.40	23.28
2045	183.2	391.5	-	23.67	23.27
2046	185.8	394.6	-	24.37	23.66
2047	282.4	406.5	-	23.16	22.47
2048	186.9	422.9	23.70	23.44	23.29
2049	193.3	424.4	-	23.70	24.00
2050	261.8	429.9	-	23.14	22.44
2051	255.4	434.2	-	23.65	22.60
2052	218.8	433.2	23.75	23.56	22.50
2053	319.0	431.9	-	23.40	22.29
2054	315.8	434.5	-	24.05	23.31
2055	319.7	435.1	-	23.98	23.41
2056	94.8	70.8	-	24.27	23.80
2057	241.6	143.0	-	21.92	21.18
2058	127.8	190.5	-	22.84	21.87
2059	135.3	201.1	-	22.23	21.79
2060	246.7	256.5	-	23.52	22.84
2061	239.7	261.6	-	23.66	22.72
2062	246.9	260.1	-	23.19	22.65
2063	179.3	288.0	-	23.84	23.36
2064	325.3	387.8	-	22.84	22.97
2065	294.6	410.2	-	23.72	23.02
2066	292.8	412.2	-	24.24	23.47
2067	206.4	451.8	-	23.35	22.76
2068	156.9	461.3	-	21.60	21.52
2069	179.1	480.4	-	23.30	22.17
2070	176.4	43.5	24.07	23.17	21.90
2071	199.5	102.7	-	23.12	22.97
2072	204.0	100.9	-	23.45	22.45
2073	177.5	175.2	-	22.64	21.76
2074	186.1	183.9	-	22.18	22.23
2075	190.0	184.1	-	22.48	22.17
2076	98.3	190.8	-	22.98	22.29
2077	251.1	254.2	-	23.76	23.86
2078	252.7	258.6	-	23.65	23.26
2079	259.3	258.8	-	23.31	22.64
2080	329.9	305.1	-	23.15	22.93

Num	X	Y	B	V	R
2081	153.6	309.6	-	23.36	22.66
2082	301.8	346.6	-	23.57	24.01
2083	306.1	357.8	-	23.99	23.28
2084	250.9	379.9	23.53	21.74	20.71
2085	253.3	387.8	-	23.34	22.30
2086	260.6	383.0	23.87	22.75	21.96
2087	251.1	406.4	-	23.14	22.32
2088	249.1	411.3	-	23.13	22.11
2089	218.1	401.6	23.74	23.12	22.16
2090	220.3	404.8	-	23.69	23.55
2091	330.2	406.0	-	23.58	21.99
2092	191.3	444.5	21.11	20.60	20.02
2093	186.5	443.4	-	23.30	22.78
2094	186.5	448.0	-	24.15	23.46
2095	322.0	447.1	-	24.24	23.44
2096	318.7	449.3	-	23.42	22.90
2097	315.4	454.0	-	24.13	23.64
2098	312.1	464.8	-	22.59	21.77
2099	311.2	469.0	-	23.78	23.17
2100	199.9	470.0	23.67	22.98	23.50
2101	195.1	473.0	-	23.10	22.41
2102	138.8	482.4	-	22.67	22.17
2103	143.5	104.5	-	23.00	22.71
2104	140.8	98.1	-	23.32	22.31
2105	145.4	101.6	-	22.92	22.23
2106	229.2	159.0	-	23.40	22.73
2107	229.3	164.1	-	23.41	22.81
2108	105.9	159.4	-	23.01	22.21
2109	96.0	169.6	-	23.58	22.54
2110	204.0	166.1	-	23.36	23.13
2111	298.4	263.1	-	23.23	22.96
2112	301.0	266.5	-	24.05	22.51
2113	301.0	273.2	-	23.55	22.98
2114	341.7	301.5	25.80	23.54	22.73
2115	320.5	345.2	-	21.97	21.19
2116	213.9	389.1	-	23.19	22.49
2117	279.6	424.8	-	23.35	22.46
2118	272.0	431.9	23.90	22.67	22.25
2119	290.8	442.7	-	23.88	23.58
2120	343.7	450.6	-	24.05	23.64
2121	352.9	455.8	-	22.92	22.10
2122	348.3	460.4	-	23.63	23.08
2123	294.5	475.6	-	24.06	22.53
2124	267.0	268.7	-	23.82	23.16
2125	268.6	273.2	-	23.37	23.11
2126	267.7	276.8	-	23.79	22.98
2127	229.1	359.0	-	23.95	22.85
2128	230.9	362.2	-	23.64	22.35
2129	232.2	369.3	-	22.99	22.20
2130	226.3	369.2	-	23.17	22.06
2131	228.4	373.7	-	22.85	21.96
2132	261.4	401.0	-	23.36	22.74
2133	177.5	468.9	-	22.97	22.84
2134	173.8	470.8	-	23.59	24.02
2135	184.0	469.3	-	24.00	23.35
2136	100.7	23.5	-	23.90	23.86
2137	308.5	162.2	-	23.42	23.69
2138	260.8	167.4	-	23.15	22.50
2139	256.3	178.7	-	23.56	23.51
2140	278.0	270.6	-	23.77	23.06
2141	181.3	302.2	-	23.44	23.24
2142	181.0	305.7	-	23.33	23.01
2143	182.6	309.7	-	22.93	22.04
2144	185.6	312.7	-	23.74	23.91
2145	128.5	349.2	-	24.04	23.90
2146	127.2	337.2	22.70	23.33	23.20
2147	128.5	344.0	-	23.17	22.91
2148	139.1	342.3	-	23.80	23.45
2149	132.3	348.6	-	24.07	22.92
2150	0.0	0.0	21.41	19.97	-
2151	313.2	366.1	-	23.30	23.23
2152	344.7	396.1	25.32	23.23	22.69
2153	345.1	401.7	-	23.96	22.48
2154	343.3	403.3	-	23.52	23.93
2155	110.3	72.5	-	23.15	22.53
2156	99.7	73.2	24.94	23.39	22.39
2157	158.6	69.1	25.05	23.54	23.23
2158	152.2	76.1	-	23.20	22.05
2159	93.9	176.7	-	23.85	23.01
2160	159.9	95.9	-	23.67	23.38

Num	X	Y	B	V	R
2161	154.1	97.7	-	24.43	23.83
2162	150.9	98.8	-	24.38	23.41
2163	298.9	184.9	-	23.25	22.43
2164	299.9	188.1	-	23.55	22.81
2165	304.8	187.9	-	23.45	22.64
2166	306.0	190.8	23.20	22.79	22.60
2167	309.4	192.9	23.32	22.75	22.22
2168	155.4	144.2	-	23.70	23.03
2169	214.3	164.7	-	23.77	22.86
2170	228.9	182.6	24.81	23.55	22.70
2171	158.5	328.6	-	22.84	22.03
2172	155.3	325.5	-	24.05	22.94
2173	146.3	330.4	-	22.84	22.96
2174	139.4	334.7	-	24.22	23.07
2175	280.7	390.7	-	24.42	23.40
2176	271.0	399.7	-	20.20	19.25
2177	275.0	407.9	-	22.88	21.99
2178	169.6	425.5	-	23.34	22.39
2179	153.6	435.6	-	23.02	22.55
2180	170.6	434.0	-	22.66	22.19
2181	91.5	188.8	-	22.63	21.98
2182	219.6	372.3	22.58	21.85	22.07
2183	335.0	438.5	-	22.91	22.99
2184	338.1	458.5	-	22.92	22.18
2185	325.8	290.3	24.91	23.23	22.46
2186	332.6	289.5	-	23.42	22.56
2187	346.1	331.6	-	24.10	23.16
2188	338.5	327.0	-	23.55	22.30
2189	130.2	363.8	-	23.31	22.51
2190	134.3	378.1	-	23.79	22.85
2191	138.4	372.3	-	23.45	22.82
2192	337.7	381.9	-	23.71	23.86
2193	325.9	394.4	-	21.66	21.67
2194	342.3	207.9	-	24.17	23.62
2195	329.6	202.3	-	23.68	23.27
2196	327.2	208.0	-	20.88	20.07
2197	169.1	349.0	-	22.96	22.41
2198	172.1	349.3	-	23.20	23.20
2199	167.0	352.7	-	22.85	21.71
2200	172.5	354.5	-	23.20	22.28
2201	156.6	351.4	-	23.53	22.50
2202	135.8	153.9	-	22.92	22.44
2203	129.9	158.4	-	23.06	21.75
2204	140.0	158.3	-	22.75	22.25
2205	144.8	158.2	-	24.17	23.80
2206	143.8	163.1	-	23.58	22.26
2207	146.8	165.6	-	23.12	22.75
2208	157.0	170.3	-	22.87	21.97
2209	309.9	409.9	-	23.55	22.47
2210	322.0	402.3	-	23.74	22.99
2211	321.5	405.2	-	23.46	23.40
2212	229.0	198.7	-	23.26	22.50
2213	211.6	205.9	-	22.61	21.80
2214	214.8	211.3	-	22.93	22.21
2215	211.6	201.6	-	22.73	21.87
2216	205.1	203.0	-	23.11	22.90
2217	201.3	199.9	-	22.42	22.33
2218	202.9	195.8	-	22.81	22.67
2219	284.1	249.0	22.40	22.20	22.35
2220	273.2	247.0	-	21.85	21.86
2221	275.0	250.9	-	22.72	22.26
2222	273.6	254.7	-	22.90	22.75
2223	166.8	93.6	-	23.22	22.78
2224	176.1	91.9	-	23.30	22.75
2225	175.8	96.5	-	22.73	22.00
2226	173.8	111.2	-	23.17	22.25
2227	169.3	107.3	-	22.72	22.03
2228	171.9	108.4	-	22.76	22.33
2229	203.1	339.6	-	24.16	22.51
2230	225.1	352.5	-	23.48	22.47
2231	201.8	344.9	24.21	23.32	23.14
2232	211.4	345.9	-	22.43	21.87
2233	204.3	354.1	-	22.76	22.60
2234	200.9	319.2	-	23.19	22.66
2235	198.0	323.9	-	22.36	22.71
2236	190.8	325.7	21.97	21.00	20.99
2237	189.6	329.7	-	23.18	22.68
2238	195.4	335.4	22.71	22.97	22.78
2239	183.3	338.4	23.87	22.87	22.33
2240	183.9	329.9	-	22.63	21.96

Num	X	Y	B	V	R
2241	195.7	341.3	-	24.03	23.13
2242	213.5	328.9	-	22.61	22.03
2243	225.1	326.1	-	22.63	22.25
2244	213.4	333.2	-	24.18	23.12
2245	291.6	204.1	-	24.28	22.98
2246	287.3	223.4	-	22.81	21.89
2247	311.2	229.2	-	23.38	22.59
2248	310.9	235.8	23.38	21.29	20.36
2249	315.2	235.2	-	23.44	22.33
2250	239.7	426.1	-	22.86	22.20
2251	232.9	430.1	-	23.22	22.35
2252	235.0	442.1	-	21.52	21.25
2253	244.1	442.6	-	22.50	21.76
2254	230.6	438.4	-	23.45	22.72
2255	250.3	434.2	-	24.15	23.29
2256	247.3	442.2	-	22.98	23.13
2257	228.9	442.1	-	23.50	22.31
2258	251.3	440.8	-	23.37	23.04
2259	243.1	448.7	-	22.39	21.93
2260	225.7	439.8	-	23.60	22.65
2261	242.1	452.2	-	22.70	22.23
2262	238.9	454.0	-	22.55	21.85
2263	218.3	440.9	23.28	22.76	22.70
2264	9.4	90.4	25.05	24.19	-
2265	163.3	300.1	23.05	23.03	-
2266	49.0	325.9	22.51	22.67	-
2267	66.8	410.9	24.83	23.72	-
2268	50.9	374.0	23.82	23.49	-
2269	226.1	12.8	24.06	22.66	-
2270	81.9	425.9	19.72	18.19	-
2271	102.8	144.9	24.13	22.93	-
2272	164.3	150.6	24.20	23.17	-
2273	159.5	153.3	23.64	23.07	-
2274	164.3	156.3	23.60	22.86	-
2275	259.7	474.3	24.72	24.02	-
2276	98.1	37.5	25.47	23.50	-
2277	334.8	209.6	23.78	23.97	-
2278	79.3	460.6	20.44	19.03	-
2279	162.1	325.4	23.68	22.86	-
2280	352.8	90.2	23.61	23.56	-
2281	160.8	392.2	21.85	21.91	-
2282	162.1	396.7	23.05	23.00	-
2283	311.7	474.5	24.23	23.42	-
2284	162.5	348.6	23.01	22.57	-
2285	163.1	432.8	23.69	23.01	-
2286	200.1	398.0	24.82	23.10	-
2287	291.5	102.5	22.21	21.94	-
2288	310.3	111.1	21.04	19.29	-
2289	158.0	40.3	23.20	22.42	-
2290	154.5	43.9	19.18	18.46	-
2291	208.9	326.5	22.73	21.86	-
2292	304.3	199.7	25.24	23.12	-
2293	279.0	256.9	23.99	22.94	-
2294	306.4	239.2	25.32	23.06	-

Appendix B

BV Photometry for Stars in M33

The following table gives the complete Johnson B and V band photometry obtained for all the stars included in the M33 colour-magnitude diagram presented in chapter 4.

Num	X	Y	B	V	$B-V$
1	67.3	3.0	22.97	22.18	0.79
2	276.6	4.7	22.89	22.45	0.43
3	72.3	4.9	21.25	20.20	1.05
4	9.8	7.0	23.10	22.45	0.65
5	143.8	9.7	23.38	22.80	0.58
6	254.7	11.6	22.64	22.11	0.54
7	269.8	16.4	22.93	21.75	1.18
8	102.3	17.6	22.24	22.09	0.14
9	87.5	18.8	22.06	22.00	0.06
10	186.2	27.8	23.06	23.34	-0.29
11	30.4	31.9	22.81	22.29	0.51
12	293.7	33.7	23.17	22.64	0.53
13	6.5	34.6	23.79	22.90	0.89
14	37.2	47.0	22.66	21.90	0.75
15	22.2	47.7	23.15	23.16	-0.01
16	286.4	56.7	20.24	20.19	0.05
17	245.7	57.4	22.75	21.98	0.77
18	193.4	63.7	22.43	22.25	0.18
19	32.0	64.1	22.98	22.42	0.56
20	193.0	68.9	22.38	22.28	0.10
21	283.6	73.3	22.92	22.08	0.85
22	239.8	76.3	22.54	21.96	0.58
23	13.2	76.5	23.26	23.29	-0.03
24	170.5	78.3	22.64	22.01	0.63
25	219.4	80.3	21.26	21.41	-0.15
26	223.7	82.4	22.89	21.90	0.99
27	305.9	87.0	22.16	21.91	0.24
28	255.6	88.4	21.94	22.15	-0.21
29	196.7	89.1	22.90	22.43	0.47
30	128.5	91.2	22.45	22.48	-0.03
31	266.0	92.4	22.83	21.74	1.09
32	278.0	92.4	21.69	21.83	-0.14
33	193.2	92.7	20.80	20.61	0.19
34	45.9	95.2	21.63	21.32	0.31
35	301.2	106.1	23.02	22.16	0.86
36	16.5	107.0	23.82	22.40	1.43
37	289.9	111.2	20.93	21.25	-0.32
38	204.0	116.3	22.64	22.13	0.51
39	307.7	117.0	22.32	22.25	0.07
40	34.7	118.2	22.79	21.53	1.26
41	106.6	132.8	22.90	22.61	0.29
42	14.0	136.0	22.49	21.91	0.58
43	87.7	140.6	22.76	22.63	0.13
44	111.3	153.4	22.20	21.88	0.32
45	273.0	155.1	23.01	22.27	0.74
46	124.1	172.6	22.24	21.65	0.59
47	163.6	179.9	20.80	20.67	0.13
48	87.1	185.1	21.39	21.35	0.04
49	250.9	185.8	22.58	22.00	0.58
50	280.7	188.8	21.57	21.74	-0.17
51	135.8	198.0	22.33	21.15	1.19
52	275.1	203.5	21.46	21.69	-0.23
53	97.3	204.9	22.95	22.52	0.43
54	234.4	206.3	22.88	22.31	0.57
55	175.2	210.8	23.16	21.87	1.28
56	130.3	215.7	22.19	22.04	0.16
57	50.4	217.1	21.43	21.59	-0.16
58	298.7	217.0	22.80	21.91	0.90
59	282.2	221.4	21.57	21.94	-0.37
60	87.1	223.0	21.87	22.28	-0.41
61	307.1	230.5	21.68	21.12	0.56
62	89.4	232.2	23.10	21.65	1.45
63	289.7	237.6	22.32	22.38	-0.07
64	17.9	238.6	20.22	20.40	-0.17
65	181.9	240.6	22.21	22.50	-0.28
66	283.4	243.6	22.11	22.14	-0.04
67	279.8	250.1	22.61	22.03	0.58
68	308.0	254.6	21.91	21.86	0.05
69	139.6	255.9	21.62	21.40	0.22
70	211.2	261.8	21.17	20.92	0.25
71	307.5	275.6	22.57	22.67	-0.10
72	292.8	281.7	23.44	23.84	-0.40
73	140.4	282.6	21.95	22.20	-0.26
74	241.2	283.2	22.37	22.53	-0.16
75	271.1	285.3	21.40	21.80	-0.40
76	55.3	298.1	21.91	21.78	0.13
77	277.8	302.0	20.21	20.47	-0.26
78	197.7	305.7	22.29	22.23	0.06
79	152.8	307.5	19.68	20.23	-0.54
80	190.4	311.9	21.46	21.96	-0.50

Num	X	Y	B	V	$B-V$
81	250.5	325.3	21.54	22.93	-1.39
82	257.4	326.0	22.13	22.06	0.07
83	216.8	326.8	21.41	21.58	-0.17
84	262.1	329.9	22.69	22.50	0.19
85	166.4	331.2	22.96	22.08	0.88
86	215.5	332.0	21.62	20.63	0.99
87	197.5	331.8	20.99	21.62	-0.62
88	172.9	340.7	23.35	22.36	0.98
89	212.1	347.7	22.61	21.42	1.19
90	239.9	349.6	22.25	21.73	0.52
91	44.0	357.1	21.39	20.79	0.60
92	166.3	363.4	20.89	20.91	-0.02
93	211.7	368.9	20.52	20.65	-0.13
94	132.9	372.4	21.46	21.58	-0.11
95	303.5	375.3	22.86	21.90	0.96
96	262.8	389.1	21.55	21.57	-0.02
97	303.4	400.5	23.69	22.41	1.28
98	170.0	403.1	20.97	21.30	-0.33
99	93.2	409.1	22.16	21.86	0.30
100	25.5	411.7	20.31	20.40	-0.09
101	298.5	416.7	22.41	21.49	0.93
102	66.6	422.0	22.83	22.89	-0.06
103	265.1	434.5	22.50	22.01	0.48
104	54.2	441.5	22.84	22.66	0.18
105	88.4	441.3	22.40	22.11	0.28
106	234.4	450.6	21.60	22.15	-0.55
107	128.9	471.1	22.32	22.31	0.01
108	307.1	471.7	20.90	19.90	1.00
109	116.4	476.9	22.27	22.35	-0.08
110	214.6	477.9	22.41	22.09	0.32
111	210.1	478.4	21.00	21.50	-0.50
112	58.4	2.8	23.14	21.87	1.26
113	15.5	3.3	22.43	20.80	1.63
114	16.1	6.3	22.04	22.21	-0.17
115	255.0	3.8	22.28	21.87	0.41
116	307.6	7.6	22.54	22.49	0.06
117	308.1	9.7	22.77	21.85	0.92
118	41.5	9.1	22.90	22.11	0.80
119	42.6	11.3	23.02	22.64	0.38
120	5.1	13.4	22.47	21.34	1.13
121	8.3	14.9	23.03	22.32	0.71
122	180.5	13.6	23.00	22.40	0.60
123	178.4	13.9	23.04	22.68	0.36
124	94.5	23.5	21.55	21.22	0.32
125	68.6	35.1	21.94	21.77	0.17
126	297.2	42.0	22.57	21.27	1.30
127	3.5	41.1	24.04	22.86	1.19
128	269.6	44.9	22.20	22.50	-0.30
129	270.6	47.2	22.50	22.17	0.33
130	53.9	45.4	18.70	18.66	0.04
131	54.3	47.7	19.43	19.38	0.05
132	153.9	48.6	23.48	22.64	0.84
133	288.8	63.5	23.04	23.07	-0.03
134	13.7	67.8	23.38	21.76	1.62
135	15.1	69.3	23.26	22.52	0.74
136	235.8	69.2	21.01	21.27	-0.26
137	233.8	69.5	22.23	23.05	-0.82
138	6.7	70.8	23.17	22.23	0.95
139	7.5	72.5	23.69	22.23	1.46
140	111.3	74.3	22.23	21.74	0.50
141	108.9	74.7	21.95	21.87	0.08
142	114.5	81.2	21.77	22.06	-0.28
143	142.9	81.9	22.85	22.37	0.47
144	169.1	104.8	22.43	22.00	0.44
145	171.5	105.2	22.88	22.09	0.79
146	25.8	111.1	22.68	22.84	-0.16
147	23.9	113.8	22.16	21.77	0.39
148	307.6	111.5	23.06	22.57	0.49
149	306.1	112.8	23.35	23.05	0.31
150	5.2	112.4	22.45	22.45	0.00
151	262.9	122.8	21.88	21.91	-0.03
152	263.6	126.3	22.43	22.02	0.41
153	87.7	135.4	23.15	22.07	1.08
154	130.9	133.3	22.74	22.49	0.25
155	132.7	133.7	22.25	22.56	-0.31
156	247.0	136.7	22.30	22.23	0.06
157	245.5	138.8	20.77	20.32	0.46
158	5.1	142.0	22.83	21.42	1.41
159	2.8	145.7	24.34	22.37	1.97
160	273.6	147.2	23.25	21.98	1.26

Num	X	Y	B	V	$B-V$
161	92.6	148.9	23.00	22.96	0.04
162	18.1	151.6	23.24	22.17	1.07
163	16.8	154.0	22.56	22.22	0.35
164	87.5	155.7	22.79	21.86	0.93
165	86.4	157.9	21.75	21.86	-0.11
166	185.9	158.3	21.33	21.47	-0.13
167	188.3	158.4	22.00	20.12	1.88
168	306.7	172.0	22.27	21.53	0.75
169	246.4	172.1	21.72	21.50	0.22
170	167.4	174.9	22.86	22.56	0.29
171	168.6	176.4	22.51	22.42	0.09
172	250.8	178.2	22.06	22.10	-0.04
173	254.2	180.4	22.69	22.03	0.65
174	118.2	186.2	22.48	21.68	0.79
175	118.7	189.4	20.93	21.12	-0.19
176	129.9	194.4	19.44	19.48	-0.04
177	211.8	195.7	20.88	21.61	-0.73
178	210.2	196.0	22.08	21.99	0.09
179	214.3	202.5	20.05	20.07	-0.02
180	127.0	208.4	21.77	22.01	-0.25
181	124.4	211.1	23.09	21.15	1.94
182	142.3	218.6	21.55	21.69	-0.14
183	143.7	218.8	22.36	21.53	0.83
184	199.5	220.0	20.58	19.74	0.85
185	197.0	221.0	21.46	21.09	0.36
186	148.1	225.5	19.96	19.95	0.01
187	293.0	231.3	22.42	22.47	-0.05
188	307.5	237.0	22.05	22.19	-0.14
189	307.4	240.1	20.24	20.45	-0.22
190	83.0	250.2	22.80	23.12	-0.33
191	14.7	250.7	23.39	22.35	1.04
192	18.1	250.7	21.09	20.77	0.31
193	155.9	265.5	20.43	20.26	0.18
194	157.5	266.8	21.97	21.34	0.63
195	266.3	279.2	21.71	21.19	0.52
196	269.9	280.3	22.35	22.90	-0.55
197	178.0	282.5	22.68	22.31	0.37
198	179.1	284.0	21.15	20.73	0.42
199	171.7	283.2	22.16	22.00	0.16
200	171.2	285.7	21.71	22.00	-0.29
201	11.6	283.3	20.31	20.84	-0.53
202	14.4	285.1	22.89	22.16	0.73
203	81.3	285.2	21.85	22.05	-0.20
204	82.7	286.6	22.36	21.58	0.79
205	205.5	288.4	21.17	21.29	-0.12
206	75.4	292.9	22.45	22.01	0.44
207	75.6	294.8	22.81	23.01	-0.20
208	303.4	295.4	22.98	21.83	1.15
209	112.4	306.6	22.38	21.61	0.76
210	110.4	308.4	21.81	21.85	-0.04
211	167.2	315.8	22.93	21.74	1.20
212	169.8	318.9	22.99	21.80	1.19
213	257.9	316.4	21.87	21.43	0.44
214	227.8	329.5	20.90	21.15	-0.25
215	228.8	331.0	21.20	20.94	0.26
216	193.7	335.6	20.18	20.50	-0.32
217	77.8	345.0	21.63	21.27	0.35
218	299.7	348.7	20.48	20.17	0.31
219	299.6	350.3	21.62	21.10	0.52
220	234.2	351.9	21.85	21.49	0.36
221	5.4	352.1	21.55	22.13	-0.58
222	38.9	360.5	22.85	22.83	0.02
223	36.9	361.3	23.21	22.63	0.58
224	299.1	366.1	22.01	21.99	0.02
225	299.6	368.2	22.44	21.66	0.78
226	4.3	373.1	20.78	20.39	0.39
227	293.3	386.8	22.48	22.04	0.44
228	277.5	395.2	22.52	22.47	0.05
229	275.8	396.6	22.98	22.55	0.43
230	304.5	413.0	21.78	22.08	-0.30
231	285.6	420.8	21.44	21.78	-0.34
232	287.6	422.0	22.05	21.50	0.55
233	69.2	429.4	22.73	21.41	1.32
234	73.8	433.1	23.10	22.71	0.39
235	51.0	433.9	22.94	22.36	0.57
236	51.6	436.2	22.96	22.67	0.29
237	90.2	434.3	21.62	21.74	-0.11
238	92.8	435.7	19.93	19.83	0.10
239	92.6	454.3	22.67	22.66	0.01
240	267.5	452.7	21.10	21.25	-0.15

Num	X	Y	B	V	$B-V$
241	256.2	465.1	21.67	21.53	0.15
242	26.9	465.0	22.13	22.79	-0.67
243	116.5	472.2	22.85	21.51	1.35
244	212.1	470.8	21.37	21.36	0.01
245	212.7	473.3	22.70	22.80	-0.10
246	194.3	475.7	17.97	18.48	-0.50
247	223.7	475.5	23.15	22.30	0.85
248	49.4	476.9	21.99	22.46	-0.48
249	47.7	7.1	22.96	21.96	1.00
250	46.5	10.5	22.99	23.31	-0.32
251	49.4	13.2	22.62	21.93	0.69
252	119.2	25.3	23.53	22.29	1.25
253	276.8	39.4	21.74	21.34	0.40
254	278.9	40.0	22.76	22.25	0.51
255	296.9	49.9	23.62	23.26	0.36
256	240.8	58.4	22.81	21.61	1.20
257	237.5	59.2	18.58	18.60	-0.02
258	241.0	62.3	23.03	21.37	1.66
259	139.4	59.6	21.60	21.23	0.37
260	142.5	61.2	21.42	20.36	1.06
261	306.2	63.2	20.43	19.97	0.46
262	1.9	62.0	22.05	21.62	0.42
263	2.6	64.3	23.49	22.75	0.74
264	273.4	73.5	21.93	21.52	0.41
265	274.5	75.4	23.05	22.41	0.63
266	273.8	79.2	21.41	20.71	0.71
267	162.2	75.3	20.30	20.16	0.14
268	163.6	79.5	23.24	22.14	1.10
269	181.8	79.9	22.56	22.51	0.05
270	182.1	83.1	22.82	22.47	0.35
271	182.1	85.7	23.71	21.93	1.78
272	201.7	80.2	20.73	20.76	-0.02
273	205.8	91.5	20.98	21.00	-0.01
274	203.5	96.1	23.37	21.67	1.69
275	56.1	95.0	22.84	22.42	0.42
276	53.9	96.3	22.82	22.25	0.58
277	173.9	100.3	22.34	22.81	-0.46
278	177.6	106.1	23.07	22.27	0.80
279	176.7	107.6	23.11	22.36	0.75
280	301.9	114.1	22.51	22.62	-0.10
281	301.5	117.3	21.06	21.41	-0.35
282	301.8	120.6	22.11	21.68	0.43
283	262.2	115.7	22.33	22.26	0.07
284	263.5	117.4	22.57	21.87	0.70
285	196.9	129.3	21.24	21.34	-0.10
286	195.6	131.9	22.27	21.56	0.72
287	28.4	151.9	21.77	21.38	0.39
288	23.3	152.7	22.75	21.68	1.07
289	171.9	162.2	21.43	21.53	-0.10
290	173.5	162.7	22.32	21.91	0.41
291	204.5	175.6	21.78	21.38	0.40
292	203.5	177.4	22.02	22.50	-0.47
293	204.5	179.3	22.78	21.99	0.79
294	212.7	176.1	21.83	21.58	0.25
295	211.5	177.9	22.52	21.92	0.60
296	210.5	180.2	21.07	20.99	0.08
297	102.3	200.9	21.71	22.29	-0.58
298	104.5	203.2	22.43	21.96	0.47
299	101.7	204.8	22.72	22.06	0.67
300	70.9	213.7	21.79	21.63	0.16
301	70.1	216.4	21.95	22.10	-0.15
302	230.2	222.4	21.13	21.51	-0.38
303	229.4	224.3	22.84	21.39	1.45
304	161.3	235.2	22.93	22.46	0.47
305	214.5	243.2	20.24	20.27	-0.03
306	83.0	244.7	22.29	21.97	0.31
307	79.1	244.9	22.63	22.40	0.23
308	106.4	248.7	22.17	20.47	1.71
309	109.5	249.1	23.41	21.57	1.83
310	66.5	259.6	19.46	19.55	-0.09
311	302.3	267.1	21.03	20.93	0.10
312	305.5	268.1	20.98	21.15	-0.17
313	271.6	271.0	22.95	22.41	0.53
314	245.4	281.2	22.38	22.79	-0.41
315	248.8	283.6	22.18	22.19	-0.01
316	265.3	286.2	20.08	20.38	-0.30
317	201.6	291.5	21.61	22.19	-0.58
318	236.3	304.7	19.03	19.24	-0.21
319	89.0	304.7	20.52	20.27	0.25
320	87.8	305.7	19.85	19.66	0.19

Num	X	Y	B	V	$B-V$
321	297.7	373.2	21.72	21.04	0.67
322	295.8	374.4	24.19	23.31	0.89
323	267.6	392.7	18.67	19.00	-0.33
324	271.7	393.6	21.30	21.20	0.10
325	266.7	441.2	22.73	22.52	0.21
326	266.5	443.2	22.12	21.87	0.25
327	124.7	466.2	21.97	21.41	0.56
328	244.6	477.9	22.90	22.38	0.52
329	246.7	478.3	21.63	21.80	-0.17
330	100.8	3.5	21.69	21.88	-0.19
331	100.6	7.8	21.91	21.63	0.29
332	98.2	9.2	22.00	22.08	-0.08
333	85.4	4.3	21.89	21.74	0.15
334	82.2	6.2	22.85	21.14	1.71
335	79.7	5.8	22.41	22.42	-0.01
336	160.8	4.4	23.07	22.57	0.49
337	157.6	4.4	21.08	20.98	0.10
338	160.7	7.5	22.49	22.22	0.28
339	67.3	50.4	21.41	21.71	-0.30
340	65.2	51.2	20.44	20.09	0.35
341	52.7	57.6	22.83	22.63	0.20
342	5.7	77.3	22.92	22.51	0.41
343	4.2	79.0	23.23	21.80	1.43
344	4.9	82.8	22.66	22.21	0.45
345	2.5	84.0	23.01	21.75	1.26
346	303.1	79.4	22.68	21.99	0.69
347	305.4	80.5	23.48	22.45	1.03
348	308.4	82.5	23.69	22.59	1.10
349	90.5	80.4	23.46	23.37	0.09
350	89.4	82.1	21.99	22.17	-0.18
351	85.1	83.7	18.30	18.33	-0.03
352	279.4	83.3	23.44	22.13	1.31
353	278.8	86.5	22.80	22.31	0.49
354	275.8	88.7	23.09	22.70	0.38
355	60.6	83.4	22.04	21.67	0.36
356	60.1	87.1	21.73	20.56	1.17
357	58.7	88.3	22.31	20.72	1.59
358	300.5	99.1	21.15	20.86	0.29
359	24.5	98.3	23.25	22.01	1.24
360	21.9	104.9	19.50	19.15	0.36
361	23.4	105.9	21.51	21.01	0.50
362	28.8	106.4	22.15	22.12	0.04
363	33.9	108.3	21.27	20.97	0.30
364	43.9	145.1	22.65	22.06	0.59
365	46.0	147.4	22.94	22.32	0.62
366	43.7	148.7	23.15	22.36	0.80
367	47.7	149.5	22.28	21.94	0.34
368	69.6	156.8	22.80	22.23	0.57
369	65.1	156.4	22.97	21.58	1.39
370	87.3	162.7	21.00	20.95	0.05
371	84.3	163.1	23.22	21.92	1.30
372	86.0	165.6	22.74	22.24	0.50
373	89.0	167.6	22.10	20.81	1.29
374	266.3	171.0	21.52	21.26	0.27
375	263.7	172.0	22.51	22.19	0.32
376	227.2	174.8	20.93	20.35	0.58
377	228.6	176.6	20.22	20.56	-0.34
378	232.1	177.5	21.77	21.32	0.46
379	232.0	181.5	22.10	21.53	0.56
380	232.6	211.8	22.42	22.18	0.23
381	228.2	216.4	22.16	22.00	0.15
382	266.0	212.3	21.44	21.12	0.32
383	268.5	212.4	21.38	21.34	0.03
384	263.0	212.7	22.72	21.08	1.64
385	259.0	212.7	21.06	20.68	0.38
386	170.6	223.1	20.85	21.05	-0.20
387	170.1	225.9	22.38	20.70	1.68
388	170.4	229.5	21.83	21.79	0.04
389	167.3	232.7	22.68	21.55	1.13
390	141.5	224.2	20.95	20.19	0.75
391	94.4	226.7	21.58	21.26	0.32
392	95.9	231.2	22.09	22.24	-0.15
393	301.0	231.4	21.80	21.88	-0.08
394	297.9	231.7	22.25	22.81	-0.56
395	298.5	234.4	20.19	20.62	-0.43
396	153.2	234.8	22.52	21.69	0.83
397	152.8	237.3	19.14	19.40	-0.26
398	19.4	244.6	23.24	22.54	0.70
399	21.9	246.6	21.80	21.74	0.06
400	24.6	247.0	21.56	22.00	-0.44

Num	X	Y	B	V	$B-V$
401	23.5	248.4	21.47	22.39	-0.92
402	285.7	253.5	20.50	20.82	-0.31
403	282.8	253.4	22.18	22.04	0.14
404	254.9	263.2	22.61	22.29	0.32
405	259.5	268.1	21.52	22.03	-0.51
406	283.5	289.5	20.84	20.39	0.46
407	289.6	293.1	22.67	22.20	0.47
408	285.6	292.2	19.49	19.52	-0.02
409	179.4	306.1	22.14	21.79	0.35
410	179.1	308.8	21.50	21.94	-0.44
411	175.9	309.2	22.90	22.34	0.55
412	183.1	309.7	20.08	20.38	-0.30
413	279.6	313.9	20.66	20.63	0.03
414	280.8	316.0	22.88	21.84	1.03
415	277.2	315.9	20.94	20.77	0.17
416	4.0	335.8	21.94	21.28	0.66
417	4.4	338.6	20.73	21.91	-1.18
418	2.8	343.8	17.77	17.51	0.26
419	293.3	342.7	20.08	20.25	-0.18
420	296.9	344.4	22.11	22.12	-0.01
421	81.8	349.3	20.63	20.94	-0.31
422	80.7	351.2	23.48	22.67	0.81
423	220.7	353.5	22.49	21.92	0.57
424	228.3	352.1	21.75	20.98	0.77
425	264.8	354.2	22.74	21.72	1.02
426	267.8	358.1	22.59	21.93	0.66
427	197.7	381.6	22.47	22.29	0.18
428	194.8	382.2	22.91	22.47	0.44
429	199.2	385.0	21.51	21.45	0.05
430	15.2	381.3	21.61	21.93	-0.32
431	17.1	383.5	20.19	19.98	0.21
432	16.6	385.5	21.71	20.73	0.99
433	12.1	385.7	20.94	21.80	-0.85
434	269.3	382.7	21.66	21.23	0.42
435	266.3	383.9	20.47	20.34	0.13
436	303.8	385.0	21.43	21.19	0.24
437	301.7	389.1	21.72	22.03	-0.31
438	284.0	396.9	20.31	20.47	-0.16
439	289.2	397.9	18.69	19.18	-0.49
440	33.2	404.7	20.64	20.89	-0.25
441	30.3	406.5	21.49	21.13	0.36
442	157.3	443.0	20.42	20.82	-0.40
443	159.6	445.7	22.09	22.14	-0.05
444	167.6	445.0	22.11	21.89	0.23
445	168.9	447.1	23.31	22.18	1.13
446	26.3	457.8	22.19	22.19	0.01
447	28.2	460.3	21.83	22.17	-0.34
448	30.7	461.0	21.04	21.71	-0.67
449	168.8	467.1	22.31	21.97	0.33
450	170.2	467.9	20.51	20.59	-0.08
451	169.0	472.0	18.70	19.13	-0.43
452	173.1	473.2	20.53	20.63	-0.10
453	204.4	470.1	22.23	21.83	0.40
454	205.1	473.1	20.37	20.16	0.21
455	288.0	473.3	21.93	21.68	0.25
456	284.9	477.4	21.34	21.25	0.09
457	26.3	476.0	20.50	20.78	-0.29
458	23.1	477.1	22.03	21.56	0.48
459	30.4	477.5	21.65	22.28	-0.63
460	235.6	7.4	22.30	22.65	-0.36
461	236.9	9.0	22.18	22.37	-0.19
462	242.1	15.5	23.79	22.66	1.13
463	240.5	11.8	22.32	22.07	0.25
464	277.7	11.4	23.21	22.66	0.55
465	276.7	13.5	23.81	22.71	1.10
466	105.8	21.4	21.74	20.59	1.15
467	102.6	25.6	21.02	21.07	-0.05
468	101.3	23.9	21.64	21.43	0.20
469	291.6	44.4	23.30	22.46	0.84
470	204.4	67.0	22.08	21.84	0.24
471	205.5	69.0	22.04	22.28	-0.24
472	200.9	69.3	22.27	21.96	0.31
473	107.9	83.3	20.83	20.46	0.36
474	102.6	88.0	18.67	18.61	0.06
475	209.5	99.1	22.97	22.35	0.62
476	207.9	100.1	22.85	21.91	0.95
477	297.8	151.4	21.02	21.32	-0.31
478	293.3	155.8	20.77	20.69	0.07
479	290.3	154.2	22.27	22.05	0.22
480	292.8	157.9	23.42	22.49	0.93

Num	X	Y	B	V	$B-V$
481	39.2	173.6	22.97	21.66	1.30
482	39.3	176.4	22.45	22.43	0.02
483	44.4	177.4	22.99	22.00	1.00
484	47.6	177.4	22.25	22.13	0.12
485	132.3	201.2	21.14	21.61	-0.48
486	130.1	204.8	20.97	20.92	0.06
487	134.8	206.1	19.59	19.41	0.18
488	131.9	208.7	21.62	22.17	-0.55
489	139.0	206.4	21.59	21.50	0.10
490	31.2	238.3	22.59	22.40	0.20
491	29.9	240.3	23.33	21.85	1.49
492	25.5	239.0	20.98	21.46	-0.48
493	275.1	241.6	20.81	20.15	0.67
494	279.3	241.7	21.38	21.84	-0.47
495	275.2	244.2	21.60	21.39	0.22
496	278.9	243.8	22.76	22.30	0.46
497	273.4	248.0	19.42	19.68	-0.25
498	99.6	242.4	20.84	21.12	-0.28
499	100.2	244.6	23.82	22.24	1.58
500	100.6	247.0	20.55	20.83	-0.28
501	101.3	249.1	22.68	21.59	1.09
502	98.6	249.3	23.12	21.88	1.25
503	161.9	255.6	22.74	21.80	0.94
504	165.5	256.9	22.41	21.88	0.53
505	160.8	258.4	22.12	21.19	0.94
506	162.7	262.6	21.56	21.75	-0.19
507	10.6	263.3	22.07	22.07	0.00
508	8.5	264.4	22.58	22.33	0.26
509	10.6	267.6	21.66	22.04	-0.38
510	8.0	268.0	23.15	22.05	1.11
511	252.7	358.3	22.12	21.81	0.31
512	255.3	359.6	21.89	21.98	-0.08
513	252.6	363.0	23.19	22.05	1.14
514	254.7	366.6	21.78	22.03	-0.26
515	269.6	408.0	22.41	21.53	0.88
516	267.7	408.2	21.49	21.66	-0.17
517	268.3	410.6	21.93	21.47	0.46
518	265.3	409.2	21.53	21.17	0.36
519	259.8	419.1	22.79	22.86	-0.07
520	256.3	419.1	22.91	22.19	0.72
521	97.4	439.3	19.77	20.06	-0.29
522	95.0	445.4	21.27	22.55	-1.28
523	96.9	445.6	20.03	20.21	-0.18
524	5.0	450.0	22.02	21.58	0.44
525	8.3	454.3	20.28	20.33	-0.05
526	3.5	454.9	21.99	22.90	-0.91
527	5.6	457.3	22.21	22.44	-0.23
528	77.5	472.8	21.48	21.38	0.10
529	78.7	477.3	21.91	21.75	0.16
530	123.5	9.9	21.74	21.30	0.44
531	118.4	13.4	21.85	21.70	0.15
532	114.0	13.8	20.37	19.87	0.50
533	113.2	16.0	21.72	21.65	0.07
534	109.4	15.8	22.08	21.79	0.29
535	252.4	19.7	21.47	20.14	1.33
536	250.4	24.1	22.24	22.28	-0.04
537	248.8	24.3	20.70	20.99	-0.29
538	252.4	27.5	22.16	22.24	-0.08
539	245.4	22.0	22.42	21.67	0.76
540	248.7	40.5	21.09	21.16	-0.07
541	253.5	41.8	23.44	22.41	1.03
542	251.8	42.9	22.88	22.41	0.47
543	248.0	43.6	23.11	22.42	0.69
544	247.0	45.3	22.63	21.77	0.86
545	237.9	44.6	22.93	22.60	0.33
546	236.6	48.2	22.79	22.49	0.29
547	235.1	52.5	21.98	21.36	0.62
548	240.9	51.0	22.97	22.57	0.40
549	303.4	55.2	23.98	22.92	1.05
550	307.5	55.4	23.32	23.49	-0.17
551	302.0	58.2	21.89	21.71	0.19
552	79.7	88.5	21.55	21.24	0.31
553	80.5	90.4	22.73	22.49	0.24
554	81.9	91.9	21.88	20.75	1.13
555	80.1	94.2	22.68	22.61	0.07
556	133.3	90.9	22.30	21.72	0.58
557	136.4	97.0	21.76	21.69	0.07
558	136.3	98.9	20.57	20.19	0.38
559	117.0	179.2	22.31	21.35	0.96
560	122.0	181.1	22.32	21.92	0.40

Num	X	Y	B	V	$B-V$
561	115.7	180.2	22.29	22.29	0.00
562	123.7	181.2	22.24	21.90	0.33
563	102.3	228.2	20.90	21.06	-0.16
564	107.8	230.9	21.10	20.84	0.26
565	110.5	231.3	22.55	22.21	0.33
566	272.5	232.0	21.65	22.14	-0.49
567	272.9	235.8	21.59	21.55	0.04
568	270.8	236.3	22.99	22.25	0.74
569	268.4	235.1	21.50	21.72	-0.22
570	158.4	242.7	21.93	22.20	-0.26
571	159.4	249.9	21.75	21.51	0.24
572	66.7	291.5	22.22	21.00	1.22
573	64.1	295.1	20.35	20.64	-0.29
574	68.3	297.3	22.26	21.88	0.38
575	61.4	292.9	22.36	21.52	0.84
576	91.5	428.9	21.64	21.97	-0.32
577	87.8	426.5	22.27	22.00	0.27
578	95.4	430.8	21.39	21.73	-0.34
579	86.4	424.9	21.54	21.96	-0.41
580	85.8	429.4	21.05	21.44	-0.39
581	100.9	431.1	19.23	19.94	-0.72
582	106.8	430.7	21.20	21.56	-0.36
583	102.5	432.3	20.05	20.30	-0.26
584	177.7	448.9	21.54	21.46	0.08
585	178.1	451.7	19.65	19.73	-0.08
586	178.3	459.1	22.76	22.57	0.19
587	245.2	457.7	22.25	22.48	-0.23
588	242.0	458.3	22.14	22.56	-0.43
589	244.5	460.6	21.41	21.89	-0.48
590	250.9	460.5	21.72	22.51	-0.79
591	87.7	467.8	20.64	20.85	-0.21
592	90.2	470.7	21.92	22.08	-0.16
593	86.6	470.9	21.70	21.31	0.39
594	87.7	474.5	22.12	22.04	0.08
595	160.6	28.2	23.01	22.73	0.28
596	163.3	30.7	22.20	20.69	1.51
597	161.1	38.2	22.80	20.99	1.81
598	251.0	68.6	23.39	23.11	0.28
599	250.8	72.7	22.37	22.04	0.34
600	252.6	74.7	22.56	22.23	0.33
601	256.5	73.5	22.89	22.34	0.55
602	208.8	79.4	22.72	22.36	0.36
603	206.7	81.8	21.55	21.53	0.02
604	209.4	86.0	22.16	22.87	-0.71
605	211.8	82.2	22.53	22.65	-0.12
606	214.2	82.7	21.05	21.01	0.05
607	269.0	81.0	23.37	22.29	1.08
608	262.6	84.1	22.74	21.88	0.86
609	264.9	87.3	20.96	21.28	-0.32
610	259.7	85.9	20.50	20.47	0.03
611	11.5	93.7	23.13	22.14	0.99
612	9.6	97.3	20.62	20.65	-0.04
613	13.6	96.4	23.21	22.52	0.69
614	3.6	152.2	21.50	21.64	-0.15
615	6.5	155.4	21.97	22.25	-0.28
616	10.5	156.8	22.71	22.58	0.14
617	7.7	159.5	22.68	22.31	0.38
618	4.3	160.3	22.71	22.00	0.71
619	94.5	160.0	23.00	22.19	0.81
620	92.2	161.6	21.63	20.58	1.05
621	93.2	163.7	22.07	21.60	0.47
622	96.3	167.5	23.89	22.48	1.42
623	93.7	170.1	22.32	22.04	0.28
624	258.8	284.0	21.33	21.57	-0.23
625	40.5	274.9	22.32	22.19	0.12
626	44.1	279.9	22.07	22.15	-0.08
627	41.7	279.7	21.81	22.04	-0.22
628	36.8	279.1	21.23	20.05	1.17
629	179.9	291.2	22.79	21.98	0.82
630	177.0	294.8	20.46	20.38	0.08
631	178.7	296.1	22.19	21.17	1.02
632	173.5	297.3	22.49	22.37	0.12
633	228.7	341.2	21.66	22.08	-0.42
634	232.4	342.9	22.39	21.88	0.51
635	230.3	346.2	21.75	22.65	-0.90
636	232.6	338.5	22.91	21.86	1.05
637	234.6	340.9	21.48	21.61	-0.14
638	227.1	346.2	21.12	21.06	0.06
639	159.9	404.1	21.76	22.15	-0.38
640	163.1	407.0	20.51	21.00	-0.49

Num	X	Y	B	V	$B-V$
641	164.1	409.3	21.45	21.75	-0.30
642	168.4	410.7	20.20	20.69	-0.49
643	262.3	450.3	20.67	21.13	-0.46
644	260.9	454.1	23.03	22.80	0.23
645	260.6	457.9	22.04	22.28	-0.24
646	110.7	4.2	22.25	22.40	-0.14
647	112.2	8.4	19.80	19.91	-0.11
648	106.5	10.6	21.86	21.90	-0.04
649	117.7	6.4	21.24	21.51	-0.28
650	104.2	12.5	22.78	22.10	0.69
651	121.8	5.4	21.60	21.57	0.02
652	239.7	4.4	21.65	21.66	-0.01
653	244.5	7.0	23.01	21.57	1.43
654	246.9	8.7	22.71	22.85	-0.14
655	246.2	11.2	22.20	20.53	1.67
656	249.0	11.4	22.27	23.02	-0.76
657	248.8	15.1	22.41	22.01	0.40
658	94.5	69.4	20.21	20.15	0.07
659	90.7	71.8	22.09	22.11	-0.02
660	88.9	71.8	21.45	21.35	0.10
661	87.3	76.4	21.29	21.41	-0.12
662	139.1	164.0	21.20	21.11	0.09
663	143.1	168.4	22.05	21.45	0.60
664	144.5	170.9	20.09	19.73	0.36
665	149.1	168.6	21.32	21.10	0.22
666	150.3	165.6	21.94	21.06	0.88
667	151.1	167.6	21.04	21.15	-0.10
668	294.7	220.9	21.59	21.89	-0.29
669	293.7	223.2	20.47	20.62	-0.15
670	304.8	225.3	21.41	21.29	0.12
671	300.2	226.8	22.68	22.37	0.31
672	302.0	224.5	21.30	21.53	-0.23
673	163.2	229.6	23.02	22.02	1.00
674	155.3	226.1	22.40	21.42	0.98
675	154.9	230.3	22.49	21.79	0.70
676	96.6	236.1	23.02	22.00	1.02
677	97.1	238.2	22.61	21.63	0.99
678	93.6	238.2	22.82	22.14	0.68
679	89.6	239.5	22.50	22.68	-0.18
680	87.9	237.8	21.82	21.68	0.14
681	85.6	237.3	23.49	22.22	1.28
682	84.1	240.5	21.46	21.80	-0.34
683	171.1	236.4	21.71	21.72	-0.01
684	170.8	240.3	19.97	20.18	-0.22
685	166.6	239.5	21.03	21.47	-0.43
686	260.7	430.8	22.38	21.43	0.95
687	256.7	432.0	21.89	22.20	-0.31
688	256.7	435.5	22.61	22.56	0.05
689	260.7	437.3	22.61	22.05	0.56
690	226.9	3.5	22.23	22.05	0.18
691	220.9	5.4	22.58	22.42	0.16
692	217.8	7.7	20.74	20.42	0.32
693	215.5	8.7	22.79	21.95	0.84
694	213.7	5.1	23.74	23.10	0.64
695	212.0	4.2	23.23	22.50	0.73
696	209.4	4.3	23.18	22.48	0.69
697	205.7	4.6	22.62	22.06	0.56
698	150.8	38.8	22.00	21.62	0.38
699	148.5	37.5	22.58	21.86	0.72
700	144.5	35.1	22.89	21.96	0.93
701	139.4	33.8	23.30	22.32	0.98
702	99.6	68.6	22.71	22.71	-0.01
703	102.0	72.9	20.33	20.40	-0.06
704	106.4	70.6	23.08	22.40	0.69
705	103.6	78.0	19.17	19.03	0.14
706	214.2	93.2	22.33	20.97	1.37
707	210.7	94.0	22.25	21.74	0.51
708	213.6	96.7	21.73	22.13	-0.40
709	219.3	97.3	21.14	21.04	0.10
710	219.6	100.4	22.03	22.01	0.02
711	273.9	224.5	22.07	22.26	-0.19
712	271.2	225.9	22.09	22.06	0.03
713	274.6	227.1	21.59	22.25	-0.66
714	278.9	228.8	22.17	21.59	0.57
715	278.0	233.0	21.62	21.45	0.17
716	281.8	237.0	19.10	19.17	-0.07
717	180.4	273.0	21.61	21.86	-0.25
718	183.5	275.9	21.48	22.11	-0.63
719	186.2	277.6	21.50	22.35	-0.86
720	189.0	280.1	21.56	21.37	0.19

Num	X	Y	B	V	$B-V$
721	190.8	283.9	19.96	19.92	0.04
722	294.0	105.4	22.67	21.25	1.43
723	290.8	106.3	22.93	22.16	0.78
724	285.5	106.3	21.68	21.58	0.10
725	284.6	104.1	22.80	22.43	0.38
726	282.6	105.6	22.83	22.35	0.49
727	113.5	238.1	20.97	21.16	-0.19
728	113.9	244.3	18.46	18.71	-0.25
729	110.8	244.0	20.51	20.52	-0.02
730	115.3	249.6	22.52	22.22	0.30
731	108.5	240.2	21.02	21.25	-0.22
732	118.6	251.0	21.74	21.82	-0.09
733	116.9	252.4	19.74	20.02	-0.28
734	187.2	291.2	21.55	21.76	-0.21
735	185.9	296.2	19.89	20.02	-0.12
736	183.6	297.6	22.84	21.98	0.86
737	182.5	300.6	22.48	22.21	0.28
738	183.6	303.2	21.43	21.56	-0.12
739	188.3	303.1	19.05	19.80	-0.75
740	187.5	307.0	20.35	20.95	-0.60
741	279.6	387.3	22.66	21.63	1.03
742	277.7	389.7	22.60	22.33	0.27
743	282.6	385.9	22.67	22.58	0.10
744	286.2	387.3	21.23	21.53	-0.31
745	284.0	389.0	22.66	22.46	0.20
746	287.3	385.6	22.18	22.02	0.17
747	62.1	8.2	23.36	22.99	0.38
748	64.0	15.5	22.71	22.96	-0.25
749	62.3	16.9	22.68	21.75	0.93
750	55.8	10.7	22.58	21.80	0.77
751	53.4	10.8	21.93	21.84	0.09
752	5.3	193.0	22.20	21.60	0.60
753	2.5	196.2	22.21	22.75	-0.55
754	8.3	198.6	21.32	22.04	-0.72
755	3.7	202.4	21.57	21.65	-0.08
756	2.5	204.2	21.13	21.05	0.08
757	288.5	218.9	22.67	21.34	1.33
758	288.3	221.6	21.30	21.30	0.00
759	287.6	224.4	20.76	21.88	-1.12
760	287.8	225.9	20.87	20.48	0.39
761	5.1	235.4	21.54	21.92	-0.38
762	9.2	235.6	21.57	21.76	-0.19
763	7.0	237.1	21.22	21.28	-0.06
764	10.8	237.8	20.68	20.80	-0.12
765	6.2	241.5	22.51	22.04	0.47
766	7.7	243.0	22.26	22.72	-0.46
767	262.3	475.8	20.55	21.24	-0.69
768	255.2	471.8	21.76	21.00	0.76
769	269.6	473.8	21.39	21.52	-0.13
770	268.2	476.1	21.17	21.84	-0.67
771	252.2	473.3	21.08	21.62	-0.54
772	268.6	472.1	22.15	22.05	0.10
773	273.2	475.7	19.78	19.80	-0.01
774	305.3	20.6	23.04	21.69	1.36
775	304.3	25.2	22.38	22.03	0.35
776	301.9	23.7	23.00	22.25	0.75
777	301.5	30.8	22.42	22.26	0.16
778	306.0	32.9	21.96	21.84	0.12
779	305.9	35.0	21.36	20.91	0.45
780	297.8	33.0	22.92	22.20	0.72
781	304.5	40.5	23.16	22.10	1.06
782	13.8	159.9	22.24	22.71	-0.47
783	16.6	162.9	21.77	21.58	0.19
784	14.6	165.7	21.78	22.33	-0.55
785	18.4	165.9	23.39	22.85	0.54
786	12.0	168.8	23.25	21.75	1.50
787	8.4	167.8	22.69	22.36	0.34
788	7.7	170.5	21.83	21.67	0.16
789	6.2	173.0	22.17	22.16	0.01
790	3.6	175.1	22.18	22.65	-0.47
791	8.6	178.7	21.73	21.93	-0.20
792	5.6	180.3	20.89	21.03	-0.14
793	80.4	167.6	23.91	22.58	1.33
794	81.7	169.3	21.08	21.17	-0.09
795	81.9	172.4	22.69	21.32	1.37
796	80.3	176.3	21.28	21.45	-0.17
797	86.7	175.9	23.64	21.77	1.87
798	259.0	188.3	22.11	22.06	0.05
799	255.3	188.9	21.42	20.94	0.48
800	260.9	189.2	21.82	22.36	-0.55

Num	X	Y	B	V	$B-V$
801	257.9	191.6	21.57	21.17	0.40
802	265.0	204.5	22.85	22.07	0.78
803	262.6	206.4	23.74	22.91	0.83
804	276.9	271.0	21.37	21.31	0.07
805	275.6	274.1	22.15	21.67	0.48
806	281.4	276.5	23.18	21.85	1.33
807	279.6	278.9	20.14	20.39	-0.25
808	280.1	283.1	21.75	22.34	-0.59
809	286.7	282.4	21.55	21.52	0.03
810	278.0	285.9	21.16	21.22	-0.06
811	285.7	284.5	23.39	23.01	0.37
812	277.5	289.0	18.75	18.73	0.01
813	85.0	437.1	22.36	22.73	-0.37
814	79.7	440.0	22.46	22.02	0.44
815	79.2	443.4	23.97	22.48	1.49
816	83.8	444.4	22.58	21.96	0.62
817	76.2	445.9	20.05	20.11	-0.06
818	84.2	447.6	20.27	20.47	-0.20
819	86.1	8.7	22.54	22.22	0.32
820	89.4	11.4	19.26	19.10	0.16
821	84.5	12.0	22.25	20.72	1.52
822	92.5	18.2	21.89	22.07	-0.18
823	79.4	14.9	21.61	20.92	0.68
824	79.9	17.5	22.69	22.31	0.38
825	167.6	41.2	22.03	21.67	0.37
826	167.7	44.1	21.33	21.27	0.06
827	176.6	44.2	22.57	22.99	-0.43
828	179.1	44.8	19.40	19.39	0.01
829	176.1	47.6	21.49	21.28	0.21
830	179.1	50.4	19.35	20.06	-0.71
831	182.4	55.0	22.48	22.93	-0.45
832	42.6	109.8	23.61	23.69	-0.08
833	39.7	113.1	22.51	22.11	0.40
834	45.6	110.7	21.55	21.10	0.44
835	42.4	112.4	23.33	23.07	0.26
836	45.9	113.7	21.90	22.17	-0.27
837	42.6	117.3	23.42	22.17	1.25
838	42.7	119.7	21.89	21.16	0.73
839	48.0	117.6	21.66	21.57	0.09
840	45.4	121.5	22.92	22.48	0.43
841	49.3	120.3	22.01	21.97	0.03
842	53.2	118.0	22.44	21.67	0.77
843	55.2	122.3	20.40	20.54	-0.14
844	60.4	125.1	22.55	22.27	0.28
845	56.7	127.3	22.86	22.05	0.81
846	55.5	131.6	23.81	22.85	0.96
847	52.4	132.2	21.20	21.47	-0.27
848	51.5	128.4	22.67	21.88	0.80
849	275.5	141.9	22.39	22.46	-0.07
850	276.4	143.7	21.66	21.58	0.08
851	278.1	144.2	22.92	22.68	0.24
852	280.2	145.2	22.32	21.85	0.46
853	279.6	147.2	23.06	22.02	1.04
854	282.5	142.2	22.86	22.20	0.66
855	284.4	143.6	22.32	22.33	-0.01
856	286.7	145.6	21.08	21.21	-0.13
857	287.4	148.3	21.85	21.19	0.66
858	285.0	154.1	21.89	22.00	-0.11
859	171.6	3.8	23.55	22.72	0.83
860	168.6	4.0	23.13	22.00	1.12
861	173.9	5.3	21.82	21.56	0.27
862	169.6	5.6	22.21	21.94	0.27
863	176.7	4.1	22.62	22.17	0.45
864	180.1	6.3	22.38	22.39	-0.01
865	170.9	14.7	22.94	22.39	0.55
866	166.4	15.6	22.72	21.32	1.40
867	174.3	16.1	23.09	22.28	0.81
868	270.5	6.7	21.07	21.07	-0.01
869	265.9	10.1	22.97	22.58	0.38
870	264.4	7.0	23.37	22.20	1.17
871	265.2	13.9	22.92	22.24	0.68
872	261.5	7.0	23.10	21.59	1.52
873	264.4	15.6	21.85	21.87	-0.02
874	263.8	17.1	22.92	22.41	0.51
875	260.5	15.6	22.37	21.60	0.76
876	262.5	20.9	22.10	20.77	1.33
877	259.6	12.5	22.44	22.44	0.00
878	257.8	15.3	22.94	23.06	-0.12
879	9.3	24.9	21.71	21.94	-0.23
880	12.2	25.4	22.26	21.44	0.82

Num	X	Y	B	V	$B-V$
881	16.0	25.5	22.94	22.20	0.74
882	18.2	30.6	23.03	22.29	0.74
883	23.1	29.5	23.45	22.73	0.73
884	19.4	33.1	22.14	21.93	0.21
885	69.5	29.4	22.12	21.68	0.44
886	60.0	30.2	22.92	22.10	0.82
887	59.8	33.3	22.76	22.32	0.44
888	58.0	31.3	23.59	22.38	1.21
889	57.2	35.3	22.99	23.47	-0.48
890	55.4	36.5	22.99	22.75	0.24
891	63.1	39.6	20.14	20.17	-0.03
892	301.7	239.7	20.74	20.60	0.14
893	302.4	243.1	22.33	22.13	0.20
894	303.4	245.4	22.27	22.62	-0.35
895	300.5	248.8	22.60	21.95	0.65
896	303.2	249.7	18.82	19.11	-0.29
897	298.2	247.8	22.13	21.99	0.14
898	299.0	249.1	22.36	22.41	-0.05
899	294.8	243.1	19.96	20.18	-0.22
900	293.4	246.6	22.93	23.07	-0.14
901	292.9	241.5	21.33	21.44	-0.10
902	303.8	331.7	22.20	22.00	0.19
903	306.7	333.7	22.10	22.43	-0.33
904	304.4	336.6	22.01	21.65	0.36
905	305.6	338.2	22.19	21.84	0.36
906	298.9	335.6	19.80	19.99	-0.19
907	296.6	338.4	19.05	19.18	-0.13
908	296.7	332.5	22.47	21.94	0.53
909	263.0	365.9	20.97	21.37	-0.40
910	259.7	367.4	22.13	21.90	0.23
911	262.4	369.5	22.05	22.39	-0.34
912	264.0	370.1	21.37	21.83	-0.46
913	266.0	377.7	21.23	22.10	-0.88
914	268.7	376.1	21.70	21.66	0.04
915	271.8	377.0	21.24	22.23	-1.00
916	273.5	374.5	22.96	22.01	0.95
917	212.1	444.8	21.10	21.21	-0.11
918	217.0	445.0	22.41	21.82	0.59
919	209.0	446.2	22.51	21.77	0.74
920	209.9	448.7	21.30	20.86	0.44
921	213.5	449.1	20.88	21.17	-0.29
922	217.9	447.2	21.06	21.23	-0.17
923	221.5	448.4	23.20	22.56	0.64
924	219.4	450.2	22.02	22.09	-0.07
925	222.3	452.6	23.36	23.73	-0.37
926	293.2	19.7	21.74	21.70	0.04
927	295.9	21.7	23.67	22.88	0.79
928	290.0	29.3	23.10	21.65	1.45
929	289.5	25.8	23.07	21.55	1.52
930	287.8	29.6	22.85	22.92	-0.07
931	283.4	32.8	21.66	21.80	-0.15
932	281.4	35.7	22.10	22.14	-0.04
933	283.7	41.2	21.75	21.48	0.26
934	144.7	44.1	22.27	22.14	0.14
935	150.5	44.6	22.55	22.01	0.54
936	147.7	49.7	21.06	20.70	0.36
937	145.1	50.2	21.50	21.58	-0.08
938	142.2	51.5	22.87	22.95	-0.08
939	139.0	52.0	22.50	22.81	-0.31
940	135.8	52.4	21.92	22.04	-0.12
941	134.6	48.5	23.08	21.96	1.12
942	160.8	45.1	23.43	22.47	0.96
943	161.4	48.4	21.94	22.52	-0.58
944	159.5	53.4	22.39	21.74	0.65
945	167.8	51.9	21.93	21.83	0.10
946	158.4	55.0	22.32	21.52	0.80
947	170.3	48.4	21.99	22.08	-0.09
948	154.5	57.1	22.93	21.40	1.53
949	158.4	57.9	22.33	21.96	0.38
950	152.0	53.9	21.38	21.53	-0.15
951	150.5	58.9	23.75	22.62	1.13
952	149.5	56.2	23.15	22.96	0.19
953	75.6	84.6	22.74	22.32	0.42
954	74.0	87.1	21.81	22.07	-0.26
955	74.5	88.6	22.15	21.85	0.30
956	70.6	88.1	21.98	22.39	-0.41
957	68.2	86.4	22.45	22.24	0.21
958	68.4	91.9	20.56	19.99	0.57
959	68.9	93.2	20.12	20.00	0.12
960	72.5	93.8	23.12	22.10	1.03

Num	X	Y	B	V	$B-V$
961	70.3	97.7	22.00	21.40	0.60
962	73.7	98.0	22.31	22.18	0.13
963	68.7	101.5	22.07	21.92	0.15
964	61.5	159.2	23.28	22.21	1.08
965	64.1	162.9	22.50	21.94	0.55
966	56.3	162.7	19.34	19.53	-0.19
967	66.3	162.4	22.60	22.76	-0.16
968	64.5	166.3	22.39	22.41	-0.02
969	53.8	163.9	21.17	21.25	-0.08
970	68.9	165.2	22.99	22.28	0.71
971	64.0	168.8	22.53	21.39	1.14
972	51.3	167.3	19.69	19.63	0.06
973	64.1	173.8	22.24	21.62	0.62
974	61.5	173.1	22.22	22.53	-0.30
975	137.5	177.9	21.22	21.35	-0.13
976	138.3	180.6	22.64	21.23	1.42
977	131.1	178.5	21.48	21.41	0.06
978	128.9	181.4	21.93	21.96	-0.02
979	134.9	185.4	21.72	21.33	0.40
980	131.5	183.7	22.45	21.74	0.71
981	140.8	190.4	22.67	22.34	0.32
982	138.1	190.3	21.63	21.91	-0.28
983	14.0	271.3	21.38	21.25	0.13
984	13.5	273.6	20.52	20.67	-0.15
985	15.0	278.5	21.98	21.66	0.32
986	17.6	276.6	23.28	22.96	0.32
987	17.4	279.5	22.29	21.45	0.83
988	21.6	280.4	21.48	21.81	-0.34
989	26.1	280.4	21.86	21.50	0.37
990	22.6	282.2	21.43	20.76	0.67
991	25.5	276.0	21.29	21.07	0.21
992	27.1	283.8	21.39	21.86	-0.47
993	25.1	287.7	22.01	22.21	-0.19
994	231.8	357.4	22.86	21.78	1.08
995	231.2	360.6	22.64	22.13	0.50
996	227.9	360.1	21.95	21.79	0.16
997	224.3	367.7	22.13	21.95	0.17
998	224.0	361.0	22.34	21.22	1.12
999	233.1	369.0	21.05	21.31	-0.26
1000	230.8	370.5	21.19	21.34	-0.15
1001	233.7	371.3	22.68	22.19	0.49
1002	218.3	364.2	21.11	20.54	0.57
1003	219.6	365.4	22.36	21.72	0.64
1004	290.8	349.2	22.31	21.73	0.57
1005	292.6	349.5	21.41	21.80	-0.39
1006	293.5	351.2	22.75	22.30	0.45
1007	289.1	352.6	23.27	21.64	1.63
1008	289.4	357.7	22.69	21.89	0.80
1009	295.8	356.2	22.71	23.15	-0.44
1010	298.6	357.8	22.48	22.14	0.34
1011	291.7	365.0	22.65	22.39	0.26
1012	290.3	367.5	21.42	20.95	0.48
1013	100.2	410.1	19.85	20.53	-0.68
1014	98.9	410.9	20.03	19.95	0.08
1015	100.0	414.9	18.92	19.08	-0.16
1016	95.3	414.0	21.25	21.86	-0.61
1017	92.1	415.1	21.06	21.13	-0.07
1018	96.7	425.8	21.28	21.42	-0.15
1019	87.7	413.2	21.76	21.75	0.01
1020	89.1	417.1	21.04	21.26	-0.22
1021	94.4	421.4	22.67	22.42	0.25
1022	97.8	421.2	21.02	20.78	0.24
1023	100.9	422.9	20.29	20.65	-0.36
1024	99.7	424.9	20.44	20.69	-0.25
1025	269.7	252.7	21.43	21.98	-0.55
1026	269.4	255.3	22.05	22.49	-0.43
1027	268.5	258.2	19.21	19.32	-0.12
1028	263.9	262.4	20.70	21.09	-0.39
1029	274.8	254.7	21.47	21.65	-0.18
1030	277.0	262.3	21.84	22.10	-0.26
1031	278.8	259.0	22.01	22.32	-0.31
1032	281.7	267.6	22.25	22.18	0.06
1033	269.7	352.7	22.63	22.32	0.31
1034	277.6	355.0	22.09	21.35	0.73
1035	277.7	359.5	20.79	20.77	0.02
1036	281.5	362.5	22.06	21.99	0.07
1037	275.7	368.6	22.14	22.69	-0.55
1038	282.8	370.0	19.78	20.07	-0.29
1039	276.3	371.2	22.78	23.15	-0.37
1040	271.5	366.9	22.04	21.63	0.42

Num	X	Y	B	V	$B-V$
1041	273.7	363.1	21.09	21.05	0.05
1042	272.7	364.2	20.97	20.95	0.02
1043	201.3	433.1	21.12	21.27	-0.15
1044	199.8	436.0	21.23	21.27	-0.04
1045	200.9	439.7	21.87	21.83	0.03
1046	204.2	440.6	22.55	21.73	0.82
1047	200.2	442.6	22.32	21.88	0.43
1048	204.9	436.3	22.08	21.64	0.44
1049	204.3	446.1	21.42	21.68	-0.26
1050	198.8	446.2	22.62	22.37	0.25
1051	206.5	433.2	23.28	22.98	0.30
1052	208.3	434.7	22.61	22.12	0.50
1053	195.8	443.7	22.31	21.44	0.87
1054	71.3	451.8	21.68	21.91	-0.23
1055	69.6	455.1	21.85	21.42	0.43
1056	67.0	465.3	21.51	21.93	-0.41
1057	63.6	467.4	23.46	22.94	0.52
1058	60.0	466.1	20.37	21.04	-0.68
1059	64.8	469.8	22.39	22.16	0.23
1060	62.7	470.5	22.34	21.39	0.95
1061	58.9	471.5	22.47	21.43	1.05
1062	15.5	459.2	21.73	22.32	-0.59
1063	14.7	465.2	21.91	22.15	-0.24
1064	16.6	469.5	21.57	21.57	0.00
1065	21.2	468.6	23.12	22.33	0.79
1066	15.6	473.9	22.52	23.14	-0.62
1067	23.2	470.0	23.18	21.92	1.26
1068	20.8	471.9	23.00	22.90	0.10
1069	12.4	477.8	22.53	21.90	0.63
1070	10.6	468.0	22.91	22.25	0.67
1071	6.5	469.6	21.73	22.15	-0.42
1072	176.9	89.0	22.52	22.61	-0.09
1073	175.8	91.3	23.50	22.39	1.11
1074	185.4	91.5	23.26	22.45	0.81
1075	183.7	94.8	22.37	21.90	0.47
1076	185.4	97.5	22.74	23.26	-0.52
1077	189.0	97.9	22.58	21.65	0.93
1078	182.0	99.2	22.75	22.43	0.32
1079	191.3	97.2	22.44	22.37	0.07
1080	193.7	101.4	22.89	22.48	0.41
1081	196.7	102.6	21.54	21.64	-0.10
1082	200.6	101.9	22.70	23.06	-0.35
1083	202.9	102.0	21.71	21.85	-0.14
1084	281.4	202.5	23.18	22.75	0.43
1085	279.9	204.1	21.99	21.77	0.22
1086	281.4	205.9	21.69	22.00	-0.31
1087	280.5	208.4	20.84	21.34	-0.50
1088	279.4	210.5	21.52	20.36	1.16
1089	284.0	211.1	21.62	21.75	-0.13
1090	277.1	208.5	22.29	22.98	-0.69
1091	275.1	212.2	21.14	21.09	0.06
1092	282.2	213.2	21.28	21.52	-0.24
1093	278.9	214.5	21.45	21.76	-0.31
1094	285.8	212.2	23.05	22.39	0.66
1095	275.4	216.6	21.64	22.10	-0.47
1096	280.3	215.9	22.34	22.18	0.17
1097	283.8	216.4	21.77	21.53	0.24
1098	272.8	218.6	21.90	21.84	0.06
1099	185.1	447.3	21.62	21.65	-0.03
1100	186.2	448.8	20.84	20.58	0.26
1101	188.0	451.2	22.61	22.44	0.17
1102	183.3	454.7	21.67	21.75	-0.08
1103	194.5	461.2	23.15	22.38	0.77
1104	197.5	464.2	21.23	21.59	-0.37
1105	194.5	469.5	19.04	19.35	-0.32
1106	185.4	60.2	21.15	21.63	-0.47
1107	183.7	60.6	22.47	22.47	0.00
1108	181.3	62.7	20.84	20.97	-0.13
1109	180.8	64.6	22.11	21.54	0.57
1110	176.7	60.3	23.13	22.23	0.90
1111	173.4	58.3	22.86	22.90	-0.04
1112	172.6	63.2	19.74	19.68	0.06
1113	169.4	59.0	21.30	21.32	-0.02
1114	170.9	61.0	24.04	22.45	1.59
1115	169.8	66.6	21.82	21.98	-0.16
1116	167.4	66.5	21.37	21.50	-0.13
1117	164.3	64.8	21.73	21.97	-0.25
1118	165.6	68.2	22.48	21.97	0.52
1119	161.9	63.0	22.65	21.73	0.92
1120	236.2	379.2	21.02	21.41	-0.39

Num	X	Y	B	V	$B-V$
1121	237.7	380.4	22.59	21.92	0.68
1122	229.5	382.4	21.72	21.49	0.23
1123	231.9	387.3	20.90	21.35	-0.45
1124	226.8	378.5	22.01	21.91	0.10
1125	225.7	380.8	21.60	21.24	0.36
1126	226.5	384.0	21.96	21.25	0.72
1127	226.8	389.2	21.05	21.16	-0.11
1128	221.4	387.4	21.34	21.49	-0.14
1129	225.0	392.8	21.78	22.36	-0.58
1130	34.6	151.4	22.32	22.58	-0.26
1131	39.4	155.1	21.66	19.97	1.70
1132	41.8	159.5	22.49	21.85	0.63
1133	33.2	156.9	22.38	22.58	-0.21
1134	44.1	160.0	21.46	21.60	-0.14
1135	36.4	162.0	23.24	22.05	1.19
1136	46.8	158.1	21.63	21.71	-0.08
1137	46.9	162.0	21.52	21.69	-0.17
1138	31.9	161.8	22.28	21.31	0.97
1139	49.6	159.3	21.13	21.33	-0.20
1140	29.5	160.0	22.31	22.07	0.24
1141	31.2	160.7	22.03	21.83	0.20
1142	27.2	161.4	20.76	20.77	-0.01
1143	24.2	158.0	22.81	22.18	0.63
1144	77.2	409.6	21.61	21.54	0.06
1145	79.0	409.8	21.44	21.90	-0.46
1146	74.6	410.3	21.68	21.84	-0.16
1147	70.4	408.9	22.13	21.75	0.37
1148	74.7	412.6	20.99	21.92	-0.93
1149	78.1	413.1	21.25	21.54	-0.29
1150	82.2	409.9	21.86	21.24	0.62
1151	81.4	413.8	21.64	22.24	-0.60
1152	75.9	416.5	21.56	22.26	-0.70
1153	80.0	416.9	21.18	22.25	-1.07
1154	76.4	419.7	21.02	21.33	-0.31
1155	82.4	419.4	21.50	22.23	-0.73
1156	79.4	421.4	21.10	21.61	-0.52
1157	75.4	421.1	22.35	22.25	0.11
1158	81.3	424.9	20.85	20.57	0.28
1159	71.7	418.9	21.85	22.10	-0.25
1160	70.0	414.8	19.38	19.67	-0.29
1161	37.3	84.8	21.24	21.19	0.05
1162	39.5	83.2	22.09	21.62	0.47
1163	38.2	88.1	21.67	21.86	-0.19
1164	34.3	88.4	22.43	21.72	0.71
1165	45.5	88.5	22.31	22.05	0.26
1166	34.0	94.5	21.53	21.33	0.20
1167	50.8	83.7	21.27	19.92	1.36
1168	51.5	88.3	23.02	23.25	-0.23
1169	30.5	98.3	22.73	21.97	0.76
1170	50.2	90.6	21.92	20.78	1.14
1171	52.6	91.8	22.92	21.82	1.10
1172	282.6	117.3	22.53	22.33	0.20
1173	284.0	119.2	22.07	20.60	1.47
1174	277.8	136.7	22.32	22.14	0.18
1175	285.2	124.8	21.42	20.78	0.64
1176	282.4	127.2	22.70	22.30	0.40
1177	282.1	131.5	20.85	20.86	-0.01
1178	274.4	120.3	21.38	21.93	-0.55
1179	273.3	116.3	23.23	22.47	0.76
1180	271.5	118.2	22.93	22.85	0.08
1181	281.3	136.7	22.10	22.21	-0.11
1182	283.3	137.3	21.91	22.09	-0.17
1183	269.8	117.7	22.26	22.19	0.08
1184	59.7	131.5	23.51	22.27	1.24
1185	61.4	131.5	22.67	21.70	0.97
1186	61.3	136.3	23.59	22.58	1.01
1187	60.5	139.7	19.17	19.10	0.06
1188	60.1	145.1	23.02	22.54	0.48
1189	63.5	146.9	23.21	22.16	1.05
1190	52.1	144.4	18.97	18.92	0.05
1191	60.9	152.0	22.64	21.54	1.10
1192	51.1	145.8	20.00	19.93	0.07
1193	53.0	152.2	22.65	22.83	-0.18
1194	54.2	153.1	22.84	21.50	1.35
1195	47.6	136.6	22.36	22.54	-0.18
1196	243.1	290.1	22.35	20.93	1.42
1197	242.7	292.2	21.76	21.97	-0.20
1198	245.5	292.8	21.98	21.99	-0.01
1199	240.2	295.7	22.00	22.35	-0.35
1200	249.6	295.2	21.62	22.14	-0.51

Num	X	Y	B	V	$B-V$
1201	250.7	297.0	22.97	22.90	0.07
1202	246.5	300.9	22.52	21.40	1.12
1203	242.6	299.8	21.57	22.03	-0.46
1204	248.6	305.9	21.54	21.39	0.15
1205	244.4	307.2	22.27	21.61	0.67
1206	247.2	307.9	23.11	22.18	0.93
1207	246.4	310.6	20.93	21.19	-0.26
1208	242.3	316.1	22.10	20.46	1.64
1209	247.3	318.0	23.40	22.65	0.75
1210	250.6	317.6	21.65	21.40	0.25
1211	252.7	319.2	22.15	22.13	0.01
1212	233.0	309.9	19.87	19.95	-0.08
1213	234.9	314.7	21.65	22.20	-0.56
1214	232.8	333.3	21.85	20.98	0.87
1215	231.0	322.3	21.81	20.13	1.68
1216	225.1	319.3	22.28	22.65	-0.36
1217	225.4	321.4	21.46	21.40	0.06
1218	228.8	322.6	21.91	21.23	0.68
1219	220.9	317.5	21.51	21.63	-0.12
1220	221.5	322.3	22.09	22.19	-0.09
1221	238.1	322.3	20.22	20.21	0.00
1222	235.8	330.2	22.22	21.59	0.63
1223	239.7	329.3	22.51	21.88	0.64
1224	215.4	29.1	22.18	22.27	-0.10
1225	215.0	31.2	22.05	22.08	-0.03
1226	213.1	39.8	21.49	22.48	-0.99
1227	213.9	43.9	20.83	20.86	-0.03
1228	211.3	45.0	20.94	20.93	0.01
1229	219.2	40.1	20.22	20.18	0.04
1230	222.6	41.6	22.36	21.57	0.79
1231	223.1	33.2	19.31	19.35	-0.04
1232	226.1	32.9	22.51	22.97	-0.45
1233	227.6	35.8	23.00	22.68	0.32
1234	232.8	36.0	22.80	22.25	0.55
1235	185.8	68.2	21.44	21.40	0.05
1236	190.6	73.9	21.50	21.41	0.09
1237	192.7	77.4	21.73	21.66	0.08
1238	196.4	73.5	19.76	19.70	0.06
1239	198.6	75.6	22.32	21.36	0.96
1240	188.5	77.8	22.35	22.09	0.26
1241	189.1	80.4	23.24	21.94	1.30
1242	185.0	76.0	21.78	21.48	0.30
1243	185.7	78.6	23.44	22.77	0.66
1244	178.6	72.1	22.59	22.38	0.22
1245	181.1	72.8	22.39	21.77	0.62
1246	177.6	69.9	21.89	21.95	-0.06
1247	176.8	73.6	22.67	22.08	0.59
1248	176.2	67.7	22.35	22.80	-0.46
1249	172.9	73.0	23.74	22.61	1.13
1250	177.6	77.8	23.46	22.77	0.69
1251	296.0	122.5	21.99	20.48	1.51
1252	297.6	125.1	20.35	20.23	0.13
1253	306.9	125.8	22.40	22.78	-0.37
1254	305.2	126.8	21.47	21.26	0.21
1255	307.5	129.6	22.19	21.78	0.40
1256	305.9	132.3	20.43	20.81	-0.38
1257	302.1	138.6	20.28	20.42	-0.14
1258	298.5	135.4	18.98	19.08	-0.11
1259	299.4	140.5	22.20	22.40	-0.20
1260	296.8	133.0	21.13	21.45	-0.32
1261	294.5	143.5	21.98	21.94	0.04
1262	290.5	137.5	20.33	20.97	-0.64
1263	288.8	134.3	20.98	21.23	-0.25
1264	69.2	19.2	20.19	19.98	0.21
1265	74.8	23.0	21.51	20.91	0.60
1266	79.0	23.5	22.33	23.01	-0.68
1267	74.8	27.4	22.55	22.46	0.09
1268	60.7	24.7	21.85	21.85	0.00
1269	75.8	29.3	21.61	21.03	0.58
1270	76.9	31.1	21.92	21.88	0.04
1271	58.5	26.1	22.80	22.54	0.26
1272	83.4	27.1	21.66	21.94	-0.28
1273	83.1	29.2	22.39	22.56	-0.17
1274	81.8	33.0	23.31	22.36	0.95
1275	82.6	34.8	21.33	21.59	-0.27
1276	92.6	29.0	19.51	19.45	0.06
1277	86.2	35.4	23.27	22.71	0.56
1278	19.9	65.3	22.60	22.64	-0.04
1279	20.4	67.8	21.51	21.37	0.15
1280	23.1	70.7	23.38	23.26	0.12

Num	X	Y	B	V	$B-V$
1281	20.8	73.5	23.35	22.46	0.90
1282	22.6	74.2	22.25	21.59	0.66
1283	19.9	76.2	21.85	21.95	-0.10
1284	26.9	73.9	20.68	20.88	-0.19
1285	18.3	79.5	22.51	22.14	0.37
1286	28.0	79.6	23.52	22.51	1.01
1287	25.1	81.0	23.43	22.47	0.96
1288	18.0	84.1	21.54	21.22	0.32
1289	15.4	88.4	22.19	21.72	0.47
1290	15.6	90.1	21.75	21.68	0.07
1291	21.3	91.3	22.43	21.68	0.76
1292	13.5	85.3	22.25	21.90	0.36
1293	12.5	89.1	23.03	22.69	0.35
1294	296.4	71.9	20.44	19.91	0.54
1295	293.0	73.6	21.76	21.27	0.49
1296	290.6	76.1	23.34	22.26	1.08
1297	293.4	76.6	23.37	22.13	1.25
1298	287.1	76.8	22.62	22.11	0.51
1299	285.3	77.1	23.05	22.97	0.08
1300	287.0	79.7	23.25	22.28	0.97
1301	294.1	88.9	21.15	20.90	0.25
1302	291.3	93.7	20.60	20.68	-0.08
1303	295.9	85.3	21.60	20.88	0.72
1304	295.5	83.8	22.20	21.97	0.23
1305	301.5	90.7	22.40	21.61	0.79
1306	301.7	92.8	22.30	22.09	0.21
1307	153.7	251.1	22.61	21.85	0.76
1308	156.7	255.6	21.49	21.43	0.06
1309	151.9	255.6	21.09	21.13	-0.04
1310	152.8	260.1	22.31	21.62	0.69
1311	146.9	265.1	21.80	21.43	0.36
1312	146.8	269.1	21.78	20.47	1.31
1313	148.4	272.3	20.47	20.48	-0.01
1314	155.4	273.3	21.33	21.50	-0.17
1315	158.6	272.8	21.59	20.80	0.79
1316	161.3	275.1	21.05	21.35	-0.29
1317	162.5	277.4	22.32	22.16	0.16
1318	166.9	279.6	21.93	21.98	-0.05
1319	166.9	282.7	22.00	21.76	0.24
1320	170.8	273.9	21.26	21.44	-0.18
1321	168.8	273.4	22.44	21.97	0.47
1322	173.4	275.8	21.26	21.07	0.19
1323	260.6	296.3	22.27	21.83	0.44
1324	265.9	300.8	20.82	20.50	0.32
1325	259.5	300.8	23.01	22.49	0.52
1326	260.1	302.4	22.23	22.31	-0.08
1327	265.1	306.6	22.32	22.25	0.07
1328	269.1	307.0	22.22	22.01	0.21
1329	265.2	308.9	21.85	22.61	-0.76
1330	263.5	309.5	22.07	21.18	0.89
1331	271.9	306.9	21.78	21.83	-0.05
1332	262.8	313.9	22.29	22.00	0.29
1333	274.8	306.0	21.20	21.94	-0.74
1334	270.8	311.5	21.60	22.01	-0.42
1335	272.3	302.0	21.04	21.01	0.03
1336	263.8	320.0	21.95	21.58	0.37
1337	84.5	204.6	22.52	21.84	0.68
1338	82.4	205.9	22.46	22.03	0.42
1339	86.3	207.0	21.32	21.46	-0.15
1340	88.4	209.7	22.33	22.21	0.12
1341	97.8	211.3	21.45	21.54	-0.09
1342	99.3	211.6	22.27	21.50	0.78
1343	92.7	214.7	22.34	22.51	-0.16
1344	90.8	215.0	22.66	22.91	-0.25
1345	102.9	212.7	22.02	22.48	-0.46
1346	89.5	217.4	22.17	21.82	0.35
1347	103.6	215.6	22.30	22.30	0.00
1348	95.5	219.3	22.77	21.96	0.81
1349	97.6	216.7	23.03	22.55	0.48
1350	105.1	220.4	22.39	22.08	0.31
1351	105.9	222.7	23.28	22.22	1.06
1352	201.1	296.5	23.02	22.66	0.35
1353	197.9	297.6	22.50	21.82	0.68
1354	203.7	298.6	22.22	21.98	0.24
1355	203.6	300.6	23.47	22.69	0.78
1356	209.0	303.8	22.08	21.59	0.49
1357	212.6	301.8	23.38	23.09	0.30
1358	212.4	305.3	22.58	22.34	0.24
1359	210.6	307.1	21.97	22.36	-0.40
1360	214.9	302.1	23.42	22.07	1.34

Num	X	Y	B	V	$B-V$
1361	208.1	309.3	20.97	21.35	-0.38
1362	204.7	309.9	22.24	21.93	0.31
1363	202.3	312.1	21.16	21.42	-0.25
1364	194.5	314.9	20.23	20.49	-0.26
1365	196.2	316.3	22.05	22.00	0.05
1366	195.3	320.1	20.89	20.64	0.25
1367	193.9	323.8	21.66	21.75	-0.09
1368	192.4	327.1	21.46	22.15	-0.70
1369	188.0	330.1	20.67	21.14	-0.47
1370	253.1	328.9	23.30	22.10	1.20
1371	254.3	333.2	21.53	21.81	-0.28
1372	252.8	335.6	21.54	21.81	-0.27
1373	259.1	339.1	21.61	21.20	0.41
1374	256.6	343.3	21.40	20.94	0.46
1375	252.9	345.0	22.56	21.88	0.68
1376	259.3	343.9	21.02	20.99	0.02
1377	244.4	341.0	19.03	19.04	-0.01
1378	251.0	348.7	21.52	21.57	-0.06
1379	243.3	337.1	22.33	21.64	0.69
1380	241.4	338.6	21.71	21.08	0.62
1381	240.4	342.5	22.11	22.26	-0.15
1382	238.8	334.7	21.21	21.44	-0.23
1383	257.2	353.0	22.21	21.57	0.64
1384	254.8	353.7	22.66	22.35	0.31
1385	279.9	402.6	21.64	21.65	-0.02
1386	281.5	406.6	22.13	21.80	0.33
1387	285.6	405.2	21.18	20.61	0.56
1388	281.6	409.7	21.92	21.60	0.31
1389	279.8	410.7	21.08	21.28	-0.20
1390	290.3	408.8	19.59	19.74	-0.16
1391	284.5	413.1	20.95	21.44	-0.49
1392	292.5	404.3	21.91	22.76	-0.86
1393	297.5	410.3	21.11	21.30	-0.19
1394	293.6	415.3	22.72	21.74	0.98
1395	292.7	418.4	22.27	22.39	-0.12
1396	294.7	419.7	23.14	22.65	0.48
1397	224.2	12.6	23.23	22.49	0.74
1398	226.8	13.0	22.24	21.52	0.72
1399	222.2	13.9	22.17	21.84	0.34
1400	219.7	17.0	21.51	21.15	0.36
1401	223.8	18.0	23.02	22.33	0.69
1402	233.7	13.9	23.63	22.11	1.52
1403	216.4	15.3	21.31	21.41	-0.10
1404	225.7	18.4	21.52	20.43	1.09
1405	212.1	17.2	21.36	21.43	-0.07
1406	211.6	20.0	22.89	22.66	0.23
1407	229.0	23.1	22.05	21.83	0.22
1408	236.5	21.7	22.65	22.30	0.36
1409	234.2	22.9	22.22	22.06	0.17
1410	230.0	27.1	22.20	21.66	0.54
1411	239.2	21.0	22.82	23.12	-0.30
1412	223.7	302.8	21.85	21.85	0.00
1413	220.3	303.4	22.66	22.74	-0.08
1414	223.7	307.0	21.91	22.22	-0.31
1415	219.5	304.9	22.07	21.58	0.49
1416	219.8	309.7	21.87	20.99	0.88
1417	215.7	310.4	19.24	18.97	0.28
1418	212.7	313.8	22.34	22.19	0.14
1419	214.4	315.7	20.89	20.57	0.32
1420	211.8	316.7	22.39	23.44	-1.05
1421	211.5	321.2	21.13	21.06	0.08
1422	208.3	322.6	20.98	21.40	-0.42
1423	212.3	324.3	21.44	21.39	0.04
1424	206.1	323.7	22.29	22.44	-0.15
1425	210.0	326.1	20.97	20.27	0.70
1426	203.9	321.3	21.47	21.80	-0.33
1427	201.1	322.8	21.72	21.67	0.05
1428	205.6	331.6	22.23	21.44	0.79
1429	202.2	328.2	22.50	22.43	0.07
1430	201.9	335.3	19.86	20.25	-0.39
1431	204.1	336.5	20.15	20.66	-0.50
1432	78.1	42.1	21.66	21.86	-0.19
1433	86.9	42.1	22.77	22.86	-0.09
1434	73.7	43.1	22.97	22.51	0.45
1435	71.1	47.0	20.27	20.12	0.15
1436	74.9	49.1	23.08	22.80	0.27
1437	78.0	51.8	19.92	20.01	-0.09
1438	71.7	53.1	22.32	22.06	0.26
1439	82.0	50.0	21.39	21.63	-0.24
1440	74.0	56.9	21.09	21.30	-0.21

Num	X	Y	B	V	$B-V$
1441	85.3	48.4	21.59	21.44	0.15
1442	83.3	51.0	20.16	20.09	0.08
1443	78.2	58.4	20.50	20.32	0.18
1444	75.2	58.2	22.09	22.09	0.00
1445	68.8	59.4	22.52	21.82	0.70
1446	297.5	253.4	21.19	21.56	-0.37
1447	295.4	257.3	21.11	20.83	0.28
1448	298.5	257.5	21.56	21.38	0.19
1449	296.5	261.7	21.60	21.78	-0.17
1450	290.4	256.9	22.33	22.04	0.29
1451	289.6	260.9	21.94	21.93	0.00
1452	303.1	259.6	22.02	21.89	0.14
1453	285.8	263.3	22.00	21.79	0.20
1454	290.8	266.9	22.96	22.18	0.78
1455	287.6	272.2	22.32	21.84	0.48
1456	289.3	273.2	20.84	21.11	-0.27
1457	293.3	275.9	21.42	20.53	0.89
1458	290.9	276.2	20.80	21.11	-0.31
1459	296.5	279.0	23.67	22.43	1.24
1460	293.6	270.8	22.43	21.59	0.84
1461	296.7	270.9	19.94	20.00	-0.06
1462	298.4	271.7	22.23	21.08	1.15
1463	302.6	271.8	22.08	22.51	-0.43
1464	254.6	215.3	22.48	22.31	0.17
1465	253.0	217.0	19.92	19.97	-0.05
1466	248.8	218.4	21.74	22.27	-0.53
1467	253.5	221.9	21.02	21.54	-0.52
1468	249.6	223.3	20.95	20.85	0.10
1469	257.2	221.2	22.30	21.70	0.60
1470	255.6	223.9	20.83	20.46	0.37
1471	256.0	226.8	21.34	21.27	0.07
1472	262.3	221.6	22.16	21.89	0.28
1473	258.7	228.4	21.70	21.41	0.30
1474	256.5	231.0	22.30	22.18	0.12
1475	241.8	229.7	22.60	22.16	0.44
1476	264.6	224.3	22.50	22.06	0.44
1477	259.8	231.4	21.71	21.90	-0.19
1478	245.9	231.3	20.73	21.00	-0.27
1479	246.6	234.4	18.99	19.06	-0.06
1480	251.0	234.3	21.82	20.55	1.26
1481	200.5	108.5	23.08	22.18	0.90
1482	195.7	110.0	22.30	22.46	-0.16
1483	200.5	112.9	21.96	21.62	0.34
1484	193.4	111.1	22.45	22.70	-0.25
1485	194.6	114.5	23.54	23.02	0.52
1486	192.5	113.4	22.69	22.15	0.54
1487	193.7	118.5	22.56	21.58	0.99
1488	189.8	116.5	21.97	21.49	0.48
1489	200.4	120.6	22.47	22.56	-0.08
1490	196.3	122.3	21.67	21.52	0.16
1491	188.1	115.4	23.55	22.27	1.28
1492	201.4	122.1	22.95	22.28	0.67
1493	196.4	124.7	22.87	22.74	0.13
1494	212.3	123.0	21.77	21.50	0.27
1495	212.9	114.9	22.26	21.64	0.62
1496	211.1	117.2	23.28	21.81	1.47
1497	211.5	111.4	21.60	21.56	0.05
1498	216.2	113.7	22.23	22.42	-0.19
1499	292.2	300.1	19.08	18.98	0.11
1500	289.4	303.2	21.99	23.22	-1.24
1501	292.0	305.5	21.21	21.37	-0.16
1502	293.8	306.7	19.66	19.89	-0.23
1503	285.7	305.7	22.15	22.25	-0.09
1504	287.7	307.7	21.46	21.39	0.07
1505	287.1	309.1	22.38	21.91	0.47
1506	287.6	311.3	21.40	21.56	-0.16
1507	297.9	306.0	22.15	21.96	0.19
1508	296.6	309.5	21.67	21.78	-0.10
1509	283.5	303.9	21.26	21.39	-0.13
1510	298.8	313.4	21.30	21.50	-0.20
1511	302.8	315.0	22.41	21.67	0.74
1512	301.2	317.5	20.23	19.85	0.38
1513	303.8	311.5	22.54	22.14	0.40
1514	297.7	318.6	23.01	21.95	1.05
1515	304.3	306.0	20.52	20.48	0.03
1516	304.3	301.4	21.11	20.93	0.18
1517	300.9	299.6	21.93	21.33	0.60
1518	301.3	301.2	22.52	21.71	0.81
1519	26.1	168.8	21.52	21.39	0.13
1520	25.5	172.9	20.28	20.45	-0.17

Num	X	Y	B	V	$B-V$
1521	17.2	175.7	19.54	19.43	0.11
1522	22.8	179.5	21.97	21.94	0.03
1523	17.3	170.5	23.11	22.53	0.58
1524	26.5	178.5	23.01	22.10	0.91
1525	30.5	180.1	21.56	21.33	0.23
1526	28.9	181.7	20.77	21.11	-0.34
1527	12.6	186.6	22.30	22.09	0.21
1528	32.7	178.6	22.18	21.97	0.22
1529	32.7	184.0	23.06	22.25	0.80
1530	29.0	184.4	19.32	19.16	0.17
1531	27.7	185.8	21.75	21.59	0.17
1532	9.2	185.2	22.09	22.64	-0.55
1533	34.6	175.1	22.75	21.60	1.15
1534	13.5	191.8	22.42	22.17	0.25
1535	34.2	170.9	22.25	22.00	0.24
1536	78.5	129.6	22.91	22.28	0.62
1537	77.7	131.4	22.86	22.32	0.54
1538	80.6	131.8	24.07	23.04	1.03
1539	80.9	135.3	21.88	21.75	0.13
1540	81.3	140.0	22.21	21.46	0.76
1541	77.4	141.1	22.67	21.44	1.23
1542	81.4	143.7	22.68	22.01	0.67
1543	79.9	143.7	22.40	21.91	0.50
1544	77.7	144.3	22.53	21.81	0.71
1545	71.8	142.6	22.42	22.54	-0.12
1546	73.1	144.6	22.89	22.08	0.81
1547	69.8	145.1	22.49	22.50	-0.01
1548	72.8	148.9	21.79	21.74	0.05
1549	75.6	151.3	23.46	21.99	1.47
1550	72.8	151.5	23.39	22.23	1.16
1551	81.0	154.1	22.05	21.97	0.08
1552	77.3	156.5	21.35	20.86	0.49
1553	78.7	158.7	22.29	21.54	0.75
1554	81.9	159.1	22.32	22.43	-0.12
1555	282.3	50.7	21.37	21.59	-0.22
1556	282.8	53.4	23.72	22.31	1.42
1557	278.6	56.6	22.71	22.23	0.47
1558	282.7	62.8	22.84	21.43	1.42
1559	277.8	51.1	22.35	22.05	0.31
1560	273.8	57.7	22.52	21.46	1.07
1561	278.5	64.0	22.74	21.50	1.25
1562	274.6	63.6	23.30	22.07	1.24
1563	278.3	67.7	22.71	21.78	0.92
1564	270.1	63.6	22.56	20.57	1.98
1565	276.9	69.7	21.79	21.77	0.02
1566	278.6	72.1	23.17	22.25	0.93
1567	263.9	74.5	22.79	21.11	1.69
1568	268.9	59.7	21.51	21.36	0.15
1569	269.9	66.8	22.47	22.26	0.21
1570	271.3	67.9	23.52	22.32	1.20
1571	264.5	66.1	23.25	22.57	0.68
1572	267.4	73.2	23.49	22.86	0.63
1573	259.7	70.2	23.19	22.77	0.42
1574	232.0	456.1	22.42	22.14	0.29
1575	234.4	461.2	21.05	21.07	-0.02
1576	230.6	461.8	21.97	22.45	-0.48
1577	235.6	462.2	22.89	21.56	1.33
1578	237.4	457.7	22.60	22.72	-0.12
1579	234.6	464.3	22.92	22.65	0.28
1580	206.8	460.1	18.89	19.46	-0.56
1581	236.8	473.2	20.35	20.73	-0.39
1582	232.6	473.3	22.38	21.92	0.45
1583	229.3	471.6	21.92	21.59	0.34
1584	229.0	469.0	20.38	20.50	-0.13
1585	226.5	470.6	21.98	21.95	0.03
1586	220.2	468.7	22.29	21.57	0.72
1587	218.3	467.3	21.80	21.30	0.49
1588	218.7	464.0	23.10	21.89	1.21
1589	208.5	460.6	20.21	20.51	-0.30
1590	154.9	11.1	22.10	22.02	0.08
1591	151.8	11.6	20.81	21.17	-0.36
1592	156.9	14.2	22.17	21.56	0.61
1593	148.2	14.1	20.74	20.61	0.12
1594	159.6	11.4	23.34	23.18	0.16
1595	159.5	17.0	23.13	22.00	1.13
1596	156.7	18.3	22.39	22.59	-0.20
1597	162.8	12.0	21.61	19.94	1.67
1598	162.0	17.1	23.23	21.76	1.47
1599	152.9	17.0	22.95	22.45	0.49
1600	163.5	25.2	22.18	22.14	0.05

Num	X	Y	B	V	$B-V$
1601	165.1	23.3	22.88	21.99	0.88
1602	171.0	25.9	20.10	19.60	0.50
1603	172.7	23.9	23.51	23.36	0.15
1604	172.5	28.5	23.48	23.40	0.08
1605	173.1	32.9	21.88	21.49	0.38
1606	178.4	21.1	23.08	22.83	0.24
1607	179.0	24.2	21.90	21.75	0.16
1608	177.9	31.5	20.26	19.92	0.35
1609	175.4	34.5	22.19	22.44	-0.25
1610	181.0	34.1	21.25	20.78	0.47
1611	178.1	34.5	23.19	23.23	-0.04
1612	171.1	37.0	21.69	21.63	0.06
1613	98.2	144.2	22.57	21.57	1.00
1614	99.7	144.9	22.59	21.80	0.80
1615	101.1	151.1	23.61	22.23	1.39
1616	98.2	153.6	22.67	21.74	0.93
1617	106.6	154.5	23.27	22.02	1.25
1618	94.4	153.6	22.46	22.17	0.29
1619	91.6	153.1	22.68	22.00	0.68
1620	105.8	159.7	23.17	22.25	0.93
1621	99.8	160.4	22.21	21.92	0.29
1622	108.4	161.6	23.20	21.94	1.26
1623	107.2	163.0	21.22	20.95	0.28
1624	107.4	165.9	22.16	21.69	0.47
1625	112.5	164.5	22.58	21.78	0.80
1626	114.6	165.6	23.56	22.46	1.11
1627	109.9	171.9	23.17	22.16	1.01
1628	103.0	170.7	22.55	22.50	0.05
1629	112.2	174.6	21.69	21.17	0.51
1630	106.7	174.7	22.92	21.56	1.37
1631	99.8	170.2	23.22	21.96	1.26
1632	114.7	171.2	22.31	22.24	0.07
1633	107.0	178.1	22.26	21.68	0.57
1634	76.8	299.5	22.05	22.46	-0.41
1635	72.6	300.0	21.51	21.29	0.22
1636	72.5	303.8	21.89	22.28	-0.39
1637	72.3	307.5	23.00	22.54	0.45
1638	71.4	312.0	21.75	21.16	0.59
1639	76.6	307.0	22.62	22.28	0.33
1640	68.6	313.3	20.41	20.63	-0.22
1641	80.3	310.3	20.79	20.95	-0.16
1642	65.2	312.7	21.36	21.56	-0.20
1643	69.4	317.9	20.19	20.49	-0.30
1644	77.2	314.0	21.67	21.19	0.47
1645	62.5	312.6	22.48	21.27	1.21
1646	71.4	319.9	22.31	21.59	0.72
1647	68.9	322.6	21.87	22.06	-0.19
1648	83.7	313.9	20.51	20.61	-0.10
1649	62.4	308.2	20.71	20.57	0.14
1650	64.4	322.9	22.37	21.56	0.81
1651	63.9	305.0	22.05	21.95	0.09
1652	60.8	305.8	21.44	20.29	1.14
1653	57.7	307.8	21.22	21.64	-0.42
1654	65.3	326.6	19.59	19.66	-0.07
1655	65.8	302.6	21.76	21.63	0.14
1656	59.9	302.1	21.10	21.32	-0.22
1657	65.1	329.0	20.47	20.76	-0.29
1658	167.9	248.5	22.11	21.58	0.53
1659	171.0	252.9	20.21	20.50	-0.29
1660	174.4	259.9	21.68	20.75	0.93
1661	176.9	259.8	21.86	22.30	-0.44
1662	171.5	260.9	22.14	22.08	0.06
1663	179.2	262.0	21.77	21.89	-0.12
1664	184.1	256.6	21.72	21.59	0.13
1665	187.9	257.0	20.95	21.14	-0.19
1666	184.7	260.9	21.59	21.99	-0.40
1667	174.2	265.1	21.31	22.01	-0.70
1668	174.2	268.1	21.20	22.04	-0.83
1669	182.5	267.1	21.49	21.78	-0.29
1670	191.2	255.4	21.30	21.68	-0.37
1671	190.6	260.9	21.47	21.85	-0.38
1672	187.0	262.0	21.11	21.11	0.00
1673	185.5	265.0	21.08	21.61	-0.53
1674	171.4	265.4	22.77	22.06	0.71
1675	192.8	255.8	22.60	22.67	-0.06
1676	193.9	258.3	20.70	20.99	-0.29
1677	193.4	265.0	19.12	19.14	-0.02
1678	167.7	266.6	21.14	21.61	-0.47
1679	169.5	268.5	21.87	21.87	0.00
1680	165.9	269.2	22.78	21.34	1.45

Num	X	Y	B	V	$B-V$
1681	181.2	179.4	22.19	22.08	0.11
1682	176.2	179.6	21.71	21.76	-0.05
1683	180.8	184.1	20.84	21.14	-0.30
1684	171.3	184.7	21.88	21.81	0.07
1685	179.5	189.7	18.95	18.81	0.14
1686	168.4	184.5	21.64	21.79	-0.15
1687	172.3	187.3	21.16	21.30	-0.14
1688	170.0	189.3	20.77	21.18	-0.41
1689	178.1	189.3	19.51	19.35	0.16
1690	174.5	191.5	21.40	22.00	-0.60
1691	166.5	185.8	21.29	21.54	-0.25
1692	170.7	191.3	22.79	22.73	0.06
1693	169.2	194.5	19.26	19.34	-0.08
1694	167.4	195.7	20.61	20.04	0.57
1695	163.5	192.1	20.87	20.67	0.20
1696	160.1	189.5	21.58	21.54	0.04
1697	161.6	194.4	21.45	21.64	-0.19
1698	155.9	185.7	19.46	19.62	-0.16
1699	89.5	245.3	23.53	22.16	1.37
1700	95.4	245.8	22.78	22.48	0.31
1701	88.9	249.7	23.32	22.53	0.79
1702	91.5	250.7	22.13	21.84	0.29
1703	92.7	256.4	21.38	21.36	0.02
1704	86.1	257.8	21.65	22.45	-0.80
1705	83.3	258.9	22.17	21.94	0.23
1706	84.7	260.8	22.73	22.12	0.61
1707	90.4	264.9	21.45	21.87	-0.42
1708	84.1	264.9	19.30	19.19	0.12
1709	80.4	264.0	22.68	22.21	0.46
1710	86.7	268.6	22.48	21.97	0.51
1711	76.3	262.8	22.30	21.85	0.44
1712	85.5	271.8	21.43	21.99	-0.56
1713	75.0	258.5	22.69	21.78	0.91
1714	73.7	260.6	23.35	22.11	1.24
1715	75.6	266.4	22.44	21.49	0.95
1716	83.7	274.6	23.03	21.83	1.20
1717	74.3	272.0	17.46	17.54	-0.08
1718	87.1	276.2	22.13	21.57	0.56
1719	70.8	268.2	22.99	22.26	0.72
1720	79.8	270.3	21.67	21.42	0.25
1721	77.1	276.3	21.85	21.98	-0.13
1722	80.4	278.4	22.24	22.17	0.07
1723	47.2	44.3	22.54	22.48	0.06
1724	44.6	46.5	21.52	21.32	0.20
1725	44.6	49.0	22.74	21.84	0.90
1726	43.3	51.7	22.12	20.44	1.68
1727	40.1	51.7	22.94	22.83	0.11
1728	39.1	54.6	23.15	21.25	1.89
1729	37.5	56.1	23.31	21.86	1.45
1730	40.7	57.3	21.56	21.32	0.24
1731	32.5	50.4	20.45	20.07	0.39
1732	33.8	50.9	20.50	20.56	-0.06
1733	32.4	56.2	22.79	21.88	0.91
1734	37.8	60.4	22.27	22.55	-0.28
1735	41.9	60.0	22.88	21.28	1.61
1736	27.8	50.9	22.39	22.85	-0.46
1737	30.4	54.8	23.67	22.49	1.18
1738	25.5	52.7	22.60	22.96	-0.36
1739	25.0	55.7	23.75	22.23	1.52
1740	17.8	58.4	22.18	21.77	0.41
1741	21.3	59.9	22.65	22.39	0.26
1742	18.8	50.8	22.85	22.30	0.54
1743	11.8	54.1	22.08	21.69	0.39
1744	10.9	56.9	21.94	21.56	0.39
1745	12.9	59.7	22.40	22.24	0.16
1746	16.6	47.9	21.75	21.37	0.38
1747	12.8	49.9	23.64	22.72	0.92
1748	9.2	55.3	23.13	22.48	0.64
1749	13.9	62.1	22.97	22.44	0.53
1750	14.5	46.1	23.31	22.87	0.44
1751	5.2	51.8	19.04	18.43	0.61
1752	33.0	247.6	23.09	21.93	1.16
1753	28.8	251.3	20.71	21.13	-0.42
1754	32.7	252.4	22.96	22.36	0.60
1755	32.3	254.6	22.11	22.11	0.00
1756	34.3	259.1	22.06	21.86	0.20
1757	26.8	257.1	22.78	21.83	0.96
1758	29.0	260.4	22.36	22.76	-0.39
1759	23.6	257.5	21.64	21.85	-0.21
1760	24.9	262.8	20.15	20.27	-0.13

Num	X	Y	B	V	$B-V$
1761	37.5	263.1	22.69	22.50	0.19
1762	40.8	263.1	23.07	22.30	0.77
1763	21.3	257.0	21.64	21.90	-0.26
1764	26.9	265.1	21.91	21.80	0.11
1765	37.6	266.0	22.61	22.00	0.61
1766	41.6	267.4	22.36	22.95	-0.59
1767	15.1	256.4	21.86	22.10	-0.24
1768	15.5	260.6	21.53	21.40	0.14
1769	28.1	270.2	23.15	21.55	1.59
1770	18.8	264.1	23.00	22.31	0.69
1771	11.4	253.6	21.91	22.42	-0.51
1772	9.2	251.3	21.83	21.45	0.37
1773	6.6	254.6	22.38	22.48	-0.10
1774	6.4	257.7	21.52	21.35	0.16
1775	3.6	259.0	20.52	20.25	0.27
1776	49.4	267.1	22.01	22.45	-0.43
1777	51.2	268.5	22.14	22.53	-0.39
1778	57.8	271.9	21.67	22.21	-0.55
1779	59.9	273.4	22.58	22.26	0.32
1780	61.7	273.9	22.39	20.68	1.71
1781	51.0	272.7	22.63	22.32	0.31
1782	59.8	277.3	22.58	22.16	0.42
1783	47.7	274.4	21.89	21.82	0.07
1784	49.8	277.1	22.42	22.16	0.26
1785	53.6	276.7	22.46	21.54	0.92
1786	54.1	278.6	20.63	20.68	-0.06
1787	65.8	279.5	22.72	22.19	0.53
1788	61.3	284.3	20.53	20.67	-0.15
1789	68.2	280.9	21.51	21.77	-0.26
1790	59.4	285.3	19.14	19.26	-0.12
1791	70.6	279.0	20.65	20.83	-0.18
1792	70.9	283.8	21.73	21.81	-0.08
1793	57.7	288.2	21.81	21.86	-0.05
1794	72.6	278.6	22.97	22.03	0.94
1795	74.0	285.0	22.52	22.15	0.38
1796	53.3	285.2	22.02	22.19	-0.16
1797	76.5	283.4	23.26	22.26	1.00
1798	51.7	288.9	21.99	22.01	-0.02
1799	46.5	288.5	21.47	21.06	0.40
1800	50.0	292.2	21.70	21.34	0.36
1801	42.7	288.2	21.88	22.00	-0.12
1802	144.4	179.9	19.94	20.16	-0.22
1803	146.3	181.0	21.14	20.73	0.41
1804	149.9	182.8	22.29	21.95	0.34
1805	149.4	190.4	20.76	20.58	0.18
1806	148.0	193.0	22.29	22.27	0.02
1807	144.3	193.6	22.11	21.87	0.24
1808	147.3	195.9	23.35	21.81	1.54
1809	148.7	200.3	21.25	20.87	0.38
1810	155.1	196.8	21.64	21.90	-0.27
1811	155.6	199.1	21.71	22.61	-0.91
1812	152.9	203.3	21.00	20.55	0.45
1813	152.0	205.1	22.04	21.86	0.18
1814	155.1	207.1	20.91	21.07	-0.16
1815	156.4	208.4	21.54	21.40	0.14
1816	151.3	209.9	20.47	20.78	-0.31
1817	154.9	212.3	20.73	20.84	-0.11
1818	144.2	208.0	20.84	19.87	0.96
1819	144.8	202.8	21.90	20.98	0.93
1820	143.6	201.8	20.58	20.58	0.00
1821	141.5	214.0	22.39	21.29	1.10
1822	155.8	221.4	21.95	21.84	0.11
1823	152.0	222.1	21.66	20.69	0.97
1824	76.0	210.0	20.96	21.36	-0.40
1825	76.6	213.6	21.46	21.92	-0.46
1826	77.2	221.5	22.02	22.45	-0.43
1827	80.4	221.6	21.92	20.00	1.93
1828	81.8	225.3	21.83	21.57	0.26
1829	79.3	227.4	22.82	22.22	0.61
1830	80.3	229.6	21.30	21.63	-0.33
1831	80.1	233.0	21.90	22.52	-0.62
1832	73.8	231.7	22.77	22.49	0.28
1833	76.3	233.1	21.34	20.49	0.85
1834	81.8	235.9	22.37	22.78	-0.41
1835	79.4	235.9	23.35	22.45	0.91
1836	70.2	235.5	21.05	19.37	1.68
1837	74.0	235.8	21.69	21.50	0.19
1838	84.6	230.6	22.93	23.08	-0.15
1839	69.0	227.3	21.30	21.36	-0.07
1840	71.4	239.8	21.26	21.48	-0.21

Num	X	Y	B	V	$B-V$
1841	85.6	228.6	22.21	22.22	-0.01
1842	71.5	223.8	22.49	21.39	1.10
1843	70.3	244.2	21.06	21.40	-0.33
1844	73.9	243.4	21.77	21.58	0.20
1845	72.4	221.8	23.18	22.51	0.67
1846	73.6	223.9	22.58	22.61	-0.03
1847	73.8	246.1	22.47	21.65	0.82
1848	75.4	250.7	21.80	21.61	0.18
1849	61.3	237.6	20.96	21.44	-0.49
1850	75.6	253.1	22.81	21.89	0.92
1851	72.0	253.8	22.02	20.87	1.15
1852	68.9	251.9	22.59	22.23	0.36
1853	70.3	253.0	21.18	20.42	0.76
1854	142.8	4.6	22.31	21.93	0.38
1855	136.7	5.6	20.73	20.78	-0.05
1856	138.1	9.4	23.45	22.89	0.57
1857	132.4	9.6	22.22	22.11	0.11
1858	133.9	12.4	19.70	19.51	0.19
1859	138.4	14.6	22.62	21.73	0.88
1860	130.6	5.3	23.08	21.20	1.89
1861	133.2	17.1	20.97	20.87	0.10
1862	130.3	16.6	20.08	19.73	0.35
1863	135.8	19.1	21.61	22.00	-0.39
1864	129.6	21.1	22.25	22.22	0.03
1865	137.9	20.4	22.24	22.21	0.03
1866	132.3	22.0	22.62	22.05	0.58
1867	141.9	17.6	21.54	21.72	-0.18
1868	143.8	19.4	21.87	22.39	-0.52
1869	144.6	25.2	22.09	21.77	0.32
1870	142.5	26.5	22.64	22.83	-0.19
1871	146.7	20.9	23.22	21.64	1.58
1872	147.3	28.5	23.16	23.00	0.15
1873	137.9	28.2	22.50	22.20	0.29
1874	135.8	30.9	22.45	22.22	0.23
1875	133.1	33.0	21.63	21.25	0.38
1876	131.4	34.9	22.35	22.34	0.01
1877	127.2	37.4	20.37	20.31	0.06
1878	135.7	39.6	22.87	22.38	0.49
1879	126.1	32.9	23.35	22.63	0.72
1880	127.9	29.9	22.72	20.80	1.92
1881	127.7	26.9	23.55	23.13	0.42
1882	245.7	78.4	20.71	20.74	-0.03
1883	248.8	81.1	22.00	21.58	0.43
1884	246.3	84.4	21.46	21.20	0.25
1885	242.9	83.5	22.67	22.33	0.34
1886	244.6	85.1	20.66	20.57	0.09
1887	242.6	88.9	22.94	22.83	0.11
1888	250.2	87.9	22.25	21.92	0.32
1889	245.1	89.9	22.30	22.24	0.06
1890	251.1	90.2	22.63	21.53	1.10
1891	254.5	97.5	21.96	22.11	-0.15
1892	257.5	101.3	22.53	21.70	0.83
1893	259.9	99.1	21.74	21.56	0.18
1894	259.6	102.7	21.81	20.83	0.98
1895	256.8	104.6	22.47	23.02	-0.55
1896	259.5	95.5	21.93	21.95	-0.01
1897	263.7	98.9	22.56	22.15	0.41
1898	263.8	103.8	22.89	22.67	0.22
1899	256.5	108.3	22.92	21.09	1.84
1900	256.7	93.2	21.95	21.93	0.01
1901	267.0	97.3	21.50	21.14	0.36
1902	263.4	106.4	19.94	19.83	0.11
1903	257.5	112.6	21.36	21.42	-0.06
1904	268.9	99.9	22.10	22.17	-0.06
1905	263.5	109.2	21.45	21.15	0.30
1906	274.9	97.0	22.29	22.08	0.21
1907	274.3	101.4	22.57	22.11	0.46
1908	276.5	104.0	22.58	21.90	0.68
1909	239.1	80.9	22.70	22.34	0.35
1910	236.5	81.8	21.73	21.80	-0.06
1911	233.7	82.0	22.27	22.45	-0.17
1912	233.8	84.4	22.10	22.82	-0.71
1913	229.4	85.0	20.63	20.51	0.11
1914	226.9	86.7	23.49	22.37	1.12
1915	234.6	89.3	21.91	22.05	-0.14
1916	235.5	92.3	22.90	22.31	0.58
1917	231.7	91.1	23.18	22.30	0.88
1918	231.7	96.5	21.75	21.90	-0.15
1919	228.7	94.8	23.22	21.91	1.31
1920	234.0	97.3	22.53	21.46	1.07

Num	X	Y	B	V	$B-V$
1921	237.1	98.9	21.57	21.78	-0.22
1922	241.2	103.6	21.65	22.09	-0.44
1923	239.3	104.0	21.04	20.73	0.31
1924	236.5	109.2	21.92	21.42	0.50
1925	246.4	107.3	22.50	21.99	0.51
1926	244.8	109.3	22.89	21.89	1.00
1927	246.0	113.6	21.26	21.49	-0.23
1928	249.2	112.8	21.47	21.42	0.05
1929	241.9	115.0	21.73	21.18	0.56
1930	252.7	114.4	22.31	21.72	0.59
1931	250.7	115.2	22.12	20.51	1.60
1932	240.4	113.1	21.60	20.85	0.75
1933	241.5	118.0	21.47	21.07	0.40
1934	251.8	119.8	22.72	22.51	0.21
1935	238.2	118.3	22.59	23.18	-0.59
1936	251.0	121.1	22.43	22.56	-0.12
1937	248.1	129.2	23.52	22.10	1.42
1938	246.7	122.4	22.34	22.91	-0.57
1939	244.6	123.8	22.44	22.24	0.20
1940	245.8	119.7	21.99	22.26	-0.27
1941	278.5	323.3	21.17	21.04	0.14
1942	280.6	325.7	22.17	21.97	0.20
1943	278.3	326.5	20.15	19.79	0.36
1944	284.8	327.7	22.04	21.89	0.15
1945	279.5	329.1	20.88	20.92	-0.04
1946	282.6	331.4	21.27	21.58	-0.31
1947	281.7	333.8	21.01	21.15	-0.14
1948	288.6	331.1	21.46	21.85	-0.40
1949	284.5	332.7	21.37	22.51	-1.14
1950	270.5	328.5	21.69	21.25	0.45
1951	292.2	329.5	21.47	21.91	-0.44
1952	266.4	330.0	20.92	21.91	-0.99
1953	295.2	327.5	21.39	21.33	0.06
1954	263.7	335.1	22.26	22.26	0.00
1955	291.9	323.3	21.77	22.32	-0.55
1956	299.8	325.4	21.08	21.68	-0.60
1957	263.6	339.1	21.99	22.29	-0.31
1958	266.1	342.4	22.44	21.38	1.06
1959	270.0	343.2	21.99	22.08	-0.09
1960	269.5	338.7	20.62	20.68	-0.06
1961	275.7	343.7	22.73	21.85	0.88
1962	279.6	345.5	22.39	22.51	-0.12
1963	281.8	348.5	22.03	22.35	-0.32
1964	284.1	342.9	21.35	21.05	0.30
1965	275.7	349.0	23.06	22.58	0.47
1966	274.3	347.9	22.51	22.19	0.32
1967	181.7	217.1	22.58	21.45	1.13
1968	176.9	218.0	21.37	22.16	-0.79
1969	178.6	219.3	21.25	21.30	-0.06
1970	183.1	218.5	20.78	21.15	-0.37
1971	181.6	222.4	21.96	22.15	-0.19
1972	186.4	218.3	22.89	22.32	0.58
1973	183.7	223.0	22.38	22.67	-0.29
1974	179.8	225.4	21.89	22.26	-0.38
1975	187.6	216.8	23.40	22.90	0.50
1976	190.0	217.9	23.23	22.93	0.31
1977	189.1	224.7	22.49	22.23	0.27
1978	175.2	225.6	20.87	21.00	-0.12
1979	180.6	227.5	22.82	22.38	0.44
1980	175.9	230.1	21.86	21.78	0.08
1981	190.7	228.8	22.53	22.53	0.01
1982	196.4	227.5	20.27	20.14	0.13
1983	197.3	229.9	21.94	21.99	-0.05
1984	199.0	234.0	22.28	21.36	0.92
1985	200.6	233.5	21.29	21.36	-0.07
1986	201.7	236.4	22.62	22.61	0.01
1987	191.7	234.4	21.73	22.64	-0.90
1988	194.4	238.9	21.48	21.47	0.01
1989	199.4	238.6	21.59	21.89	-0.31
1990	188.7	234.6	22.75	22.46	0.29
1991	195.0	242.6	20.60	20.33	0.27
1992	189.2	241.1	21.97	20.96	1.01
1993	192.5	245.6	21.97	22.17	-0.20
1994	186.2	238.6	21.91	21.22	0.69
1995	196.5	248.1	21.58	21.97	-0.39
1996	187.6	248.4	21.76	22.02	-0.26
1997	182.3	246.2	19.07	19.25	-0.18
1998	182.8	251.0	22.25	22.04	0.22
1999	180.2	251.3	20.77	20.95	-0.18
2000	176.5	244.8	21.07	20.75	0.31

Num	X	Y	B	V	$B-V$
2001	62.2	225.0	20.38	20.14	0.24
2002	59.6	222.8	22.78	22.10	0.68
2003	56.5	221.0	21.45	21.29	0.16
2004	51.7	222.4	21.98	21.90	0.08
2005	52.3	224.6	22.77	23.10	-0.34
2006	50.6	225.4	22.89	22.28	0.61
2007	51.8	229.5	22.08	21.60	0.49
2008	56.4	230.7	23.35	22.79	0.56
2009	53.2	233.0	23.21	22.80	0.41
2010	58.7	233.5	21.87	23.11	-1.24
2011	56.5	234.8	22.11	22.18	-0.07
2012	55.7	237.7	21.72	22.06	-0.34
2013	55.8	240.1	21.12	21.73	-0.61
2014	54.9	243.1	22.73	21.94	0.79
2015	52.5	242.5	21.44	21.54	-0.10
2016	56.7	245.3	22.36	22.96	-0.61
2017	57.0	248.3	21.86	22.36	-0.50
2018	50.3	248.4	21.52	22.00	-0.47
2019	51.7	250.9	22.81	22.62	0.19
2020	47.5	251.3	21.43	21.42	0.01
2021	53.1	254.1	22.18	22.67	-0.49
2022	61.0	248.9	22.42	21.83	0.58
2023	65.3	249.5	22.49	22.49	0.00
2024	41.2	253.3	22.41	21.50	0.91
2025	42.5	255.4	22.69	22.59	0.10
2026	49.4	259.2	22.39	21.55	0.84
2027	40.2	249.9	22.61	22.28	0.32
2028	38.3	256.0	21.65	21.85	-0.21
2029	45.9	259.8	19.93	20.35	-0.42
2030	40.4	245.4	22.68	21.73	0.95
2031	281.3	180.1	22.03	21.85	0.18
2032	277.9	182.7	20.40	20.34	0.05
2033	302.9	218.7	21.89	21.93	-0.05
2034	273.6	187.1	21.06	21.12	-0.06
2035	286.9	187.0	22.35	22.41	-0.07
2036	270.7	189.6	21.99	21.34	0.65
2037	272.0	190.4	22.40	21.68	0.72
2038	294.5	187.2	21.16	21.32	-0.16
2039	291.8	188.0	22.47	22.18	0.29
2040	296.1	183.9	20.92	20.84	0.07
2041	294.9	191.7	23.18	22.79	0.39
2042	300.8	184.9	20.82	20.45	0.37
2043	291.7	193.0	22.21	22.26	-0.05
2044	278.4	196.9	23.32	22.56	0.76
2045	302.5	184.7	21.08	21.10	-0.02
2046	301.3	189.1	22.05	22.29	-0.25
2047	292.0	197.3	21.46	21.68	-0.22
2048	280.5	193.5	22.29	22.10	0.19
2049	303.7	192.1	20.72	21.02	-0.30
2050	295.7	197.9	23.22	22.05	1.17
2051	284.6	192.9	22.90	21.67	1.24
2052	298.5	195.9	22.58	21.69	0.88
2053	298.3	201.4	21.79	20.00	1.79
2054	303.8	201.5	19.69	19.72	-0.03
2055	305.7	200.7	21.43	21.28	0.15
2056	298.7	206.6	21.46	21.27	0.19
2057	304.5	211.4	21.41	21.73	-0.31
2058	294.7	210.7	22.59	22.36	0.23
2059	294.1	207.1	21.94	22.00	-0.05
2060	308.8	215.0	21.65	21.58	0.06
2061	308.5	218.1	21.38	21.35	0.02
2062	290.2	205.0	20.84	19.46	1.38
2063	290.9	206.7	22.13	21.45	0.68
2064	233.6	409.4	22.24	22.39	-0.15
2065	238.0	411.0	21.76	21.30	0.46
2066	239.4	415.9	21.37	21.17	0.20
2067	231.3	417.0	21.90	22.02	-0.12
2068	232.6	420.8	21.42	22.03	-0.60
2069	234.0	422.1	20.29	20.66	-0.37
2070	229.5	422.8	23.57	23.49	0.09
2071	224.6	422.0	19.47	19.63	-0.16
2072	225.7	425.5	21.41	22.23	-0.82
2073	228.8	425.9	21.89	20.98	0.91
2074	221.8	420.0	21.58	22.52	-0.94
2075	227.3	428.8	20.00	20.21	-0.21
2076	234.5	432.2	22.00	21.77	0.23
2077	225.3	435.5	21.79	20.69	1.10
2078	220.8	435.0	21.60	21.58	0.02
2079	239.1	427.0	21.10	20.91	0.20
2080	230.4	436.1	21.90	21.56	0.34

Num	X	Y	B	V	$B-V$
2081	243.3	425.7	21.25	21.30	-0.05
2082	241.7	428.3	21.99	21.79	0.20
2083	241.2	421.8	20.95	20.97	-0.02
2084	247.1	423.8	21.61	20.86	0.75
2085	246.6	426.5	21.73	21.53	0.19
2086	249.1	421.0	22.29	21.66	0.63
2087	243.0	434.0	21.04	20.93	0.11
2088	248.4	416.8	22.09	22.14	-0.05
2089	244.4	436.5	20.87	21.36	-0.48
2090	246.4	414.1	22.26	22.31	-0.05
2091	245.3	445.4	22.49	22.04	0.45
2092	238.9	442.8	22.89	21.33	1.56
2093	247.6	445.7	23.51	22.17	1.34
2094	246.7	448.5	22.45	23.07	-0.62
2095	239.6	439.0	23.22	22.11	1.11
2096	243.5	450.6	21.21	22.05	-0.83
2097	242.2	453.4	22.31	22.04	0.26
2098	239.0	447.7	23.22	22.85	0.36
2099	217.9	381.6	21.13	21.06	0.07
2100	211.9	385.2	20.47	20.35	0.12
2101	207.5	381.2	22.02	21.75	0.27
2102	204.1	382.3	22.60	22.40	0.20
2103	206.7	385.0	21.81	21.77	0.03
2104	205.3	386.4	20.97	21.07	-0.10
2105	209.1	391.0	20.26	20.41	-0.15
2106	213.0	390.8	20.26	19.65	0.61
2107	204.8	394.0	23.09	23.12	-0.03
2108	207.9	396.8	22.61	21.78	0.83
2109	213.0	399.3	21.23	21.20	0.03
2110	209.9	400.9	21.84	21.45	0.39
2111	213.5	403.0	21.00	21.23	-0.23
2112	208.2	403.8	22.37	21.93	0.44
2113	210.6	405.3	21.26	21.22	0.04
2114	213.4	407.0	20.43	20.54	-0.10
2115	209.7	407.4	22.76	22.26	0.50
2116	218.1	409.0	22.12	21.96	0.16
2117	216.5	411.0	22.09	22.33	-0.24
2118	220.7	408.0	22.41	22.42	-0.02
2119	210.7	411.6	21.60	21.70	-0.10
2120	213.0	416.0	21.79	21.81	-0.02
2121	217.0	418.2	22.49	22.25	0.24
2122	215.4	424.1	21.76	22.31	-0.54
2123	213.3	425.9	21.25	21.08	0.17
2124	206.5	426.3	22.41	22.07	0.34
2125	208.7	427.8	22.27	22.28	-0.01
2126	214.6	429.8	23.09	22.31	0.79
2127	202.0	427.2	19.61	19.77	-0.15
2128	198.5	424.5	21.87	22.07	-0.20
2129	196.4	424.2	21.90	21.60	0.30
2130	194.0	427.7	22.45	21.84	0.61
2131	193.9	430.1	21.33	19.88	1.45
2132	296.3	6.2	20.50	20.76	-0.25
2133	289.3	8.6	22.23	21.92	0.31
2134	194.1	11.5	22.70	22.64	0.06
2135	198.1	11.6	20.57	20.52	0.05
2136	295.7	12.0	22.32	21.94	0.38
2137	294.2	13.7	22.08	21.92	0.15
2138	22.2	15.3	23.68	22.79	0.89
2139	285.9	15.0	22.47	21.81	0.66
2140	288.1	16.0	21.80	21.83	-0.03
2141	275.6	18.4	22.66	21.89	0.77
2142	276.9	19.6	22.49	21.82	0.67
2143	271.0	22.1	22.90	22.10	0.80
2144	210.2	25.1	22.80	22.10	0.70
2145	113.7	24.5	22.34	22.08	0.26
2146	194.9	25.2	22.47	22.75	-0.28
2147	38.9	27.0	23.47	21.91	1.56
2148	40.9	28.7	23.57	21.90	1.67
2149	272.3	31.5	21.71	21.70	0.01
2150	43.8	32.1	22.84	21.92	0.93
2151	258.1	33.3	21.84	21.51	0.33
2152	41.9	34.3	22.39	21.80	0.58
2153	206.0	36.8	21.58	21.78	-0.21
2154	16.0	37.5	22.86	21.61	1.25
2155	28.3	38.5	18.69	17.33	1.37
2156	97.9	40.2	23.02	22.08	0.95
2157	206.9	47.6	21.13	21.26	-0.13
2158	252.2	55.0	22.87	22.14	0.73
2159	134.2	57.9	21.85	21.78	0.07
2160	119.5	57.9	20.75	20.68	0.06

Num	X	Y	B	V	$B-V$
2161	84.6	59.6	22.24	21.97	0.27
2162	215.5	60.1	22.43	21.46	0.97
2163	248.2	61.2	23.19	22.59	0.60
2164	51.7	62.0	22.71	22.23	0.49
2165	76.1	68.3	22.00	21.69	0.31
2166	229.1	69.0	21.95	21.95	0.00
2167	71.3	69.1	20.39	20.31	0.08
2168	126.7	69.6	23.22	21.69	1.52
2169	209.6	71.3	22.20	21.70	0.50
2170	124.1	72.1	21.31	21.07	0.23
2171	143.1	72.9	22.88	22.59	0.29
2172	220.0	74.2	22.66	22.06	0.60
2173	44.6	74.5	21.71	21.78	-0.07
2174	69.1	77.1	23.17	21.90	1.27
2175	45.6	78.3	22.54	22.09	0.45
2176	61.6	78.7	23.43	21.69	1.74
2177	65.8	79.2	23.13	22.37	0.76
2178	133.7	82.5	23.30	21.84	1.46
2179	119.2	85.3	23.09	22.58	0.50
2180	139.2	88.7	22.27	21.60	0.67
2181	117.0	93.2	22.08	21.77	0.32
2182	151.0	94.9	22.24	22.07	0.17
2183	159.6	95.1	22.18	21.83	0.35
2184	149.0	96.8	22.23	22.23	0.00
2185	105.7	98.1	22.83	21.95	0.88
2186	147.5	98.8	22.27	22.07	0.20
2187	117.7	99.4	22.68	22.07	0.61
2188	127.5	99.9	22.92	22.05	0.88
2189	55.4	101.7	22.40	22.70	-0.31
2190	90.4	103.1	21.14	20.01	1.13
2191	147.6	103.8	22.76	22.06	0.70
2192	49.0	106.0	21.79	22.08	-0.29
2193	148.0	107.6	22.69	22.22	0.47
2194	186.6	108.1	22.24	22.30	-0.06
2195	66.2	108.2	22.23	21.67	0.56
2196	97.0	108.6	22.53	22.30	0.23
2197	105.0	109.2	21.60	21.63	-0.03
2198	80.2	110.6	22.65	22.29	0.36
2199	166.4	110.9	23.66	22.40	1.26
2200	184.0	111.5	22.00	21.91	0.10
2201	174.7	112.9	22.41	21.75	0.66
2202	183.5	114.7	22.83	22.41	0.43
2203	167.1	115.1	23.61	22.42	1.19
2204	58.3	115.4	21.58	21.40	0.18
2205	10.6	115.8	22.89	22.04	0.85
2206	229.7	117.7	23.36	22.14	1.22
2207	151.6	119.6	22.16	22.21	-0.05
2208	100.2	119.6	21.37	21.66	-0.29
2209	67.3	120.2	22.03	22.16	-0.13
2210	140.6	121.0	21.59	21.58	0.01
2211	125.8	121.9	23.39	22.82	0.57
2212	109.5	122.2	20.01	20.12	-0.11
2213	269.6	122.3	22.60	22.18	0.43
2214	180.8	122.7	18.16	18.09	0.07
2215	170.0	123.4	22.84	22.42	0.42
2216	5.7	123.1	23.23	22.33	0.89
2217	240.7	124.3	22.44	22.11	0.33
2218	268.3	125.1	22.38	22.25	0.13
2219	41.8	125.2	21.69	21.73	-0.04
2220	227.6	126.1	22.69	22.32	0.37
2221	222.4	126.2	22.86	22.45	0.40
2222	99.7	127.9	22.43	22.69	-0.26
2223	155.8	128.5	22.61	22.63	-0.02
2224	32.6	130.1	22.09	21.93	0.16
2225	263.8	130.8	22.44	22.18	0.26
2226	253.0	131.6	23.00	22.18	0.81
2227	186.6	131.9	20.17	20.02	0.15
2228	115.1	132.2	22.82	21.15	1.67
2229	125.4	132.3	22.91	21.66	1.25
2230	28.5	132.4	23.59	22.90	0.70
2231	142.8	132.8	22.38	22.34	0.03
2232	22.5	133.1	22.87	21.66	1.21
2233	235.5	133.5	23.01	22.23	0.78
2234	18.5	134.0	22.32	22.16	0.16
2235	263.4	134.9	22.11	21.25	0.87
2236	210.7	135.5	21.75	21.72	0.03
2237	112.5	135.6	22.34	22.41	-0.07
2238	37.1	137.1	22.66	22.31	0.35
2239	231.1	137.3	22.07	22.30	-0.23
2240	261.2	138.4	22.08	21.44	0.65

Num	X	Y	B	V	$B-V$
2241	137.9	139.0	22.07	22.67	-0.60
2242	26.8	140.7	23.48	22.16	1.32
2243	36.5	140.7	23.59	22.41	1.18
2244	214.9	143.0	22.62	21.55	1.07
2245	222.4	144.9	21.17	20.88	0.30
2246	257.2	145.4	21.77	21.44	0.32
2247	18.0	146.0	23.16	22.35	0.81
2248	146.0	146.0	21.58	21.28	0.29
2249	217.9	147.2	22.26	21.53	0.74
2250	202.9	147.7	22.16	21.64	0.51
2251	123.9	148.2	22.63	22.31	0.32
2252	147.4	150.0	21.05	21.06	-0.02
2253	221.6	150.2	21.35	21.45	-0.10
2254	235.3	150.6	21.39	21.39	0.00
2255	123.6	151.6	23.31	22.04	1.27
2256	256.0	151.9	22.01	21.41	0.60
2257	132.9	152.4	21.75	21.48	0.27
2258	164.5	154.8	22.41	21.77	0.64
2259	162.5	158.7	22.37	21.75	0.63
2260	276.9	160.6	22.35	22.06	0.29
2261	121.7	161.1	18.72	18.83	-0.12
2262	163.0	161.6	22.32	21.78	0.53
2263	130.8	163.1	22.76	22.22	0.54
2264	273.1	165.1	20.40	20.65	-0.25
2265	234.9	167.4	21.89	22.09	-0.20
2266	255.6	171.6	22.04	22.09	-0.05
2267	199.8	172.0	22.08	21.93	0.15
2268	73.5	175.0	22.51	21.63	0.88
2269	51.5	180.7	21.92	21.84	0.08
2270	201.4	182.9	21.24	21.19	0.05
2271	60.8	186.4	21.76	21.12	0.64
2272	223.5	187.8	21.56	21.45	0.11
2273	81.1	190.8	22.53	21.75	0.78
2274	57.9	192.4	22.32	21.92	0.41
2275	82.9	193.5	23.34	21.72	1.62
2276	237.0	194.9	21.44	21.18	0.26
2277	56.2	195.2	22.70	21.94	0.76
2278	109.2	195.1	22.22	22.33	-0.10
2279	39.5	195.2	21.07	20.66	0.41
2280	18.0	195.2	23.10	22.63	0.47
2281	76.8	196.1	21.61	21.86	-0.25
2282	81.3	197.2	21.74	21.79	-0.05
2283	78.1	199.2	21.84	22.39	-0.55
2284	93.4	199.1	22.68	21.91	0.77
2285	41.7	199.6	22.62	22.40	0.22
2286	198.6	200.2	20.99	21.30	-0.31
2287	114.1	201.0	21.00	20.75	0.25
2288	194.7	202.5	22.39	22.32	0.07
2289	54.5	205.9	21.42	21.54	-0.12
2290	197.2	206.6	20.94	20.86	0.09
2291	57.9	206.6	22.48	22.70	-0.22
2292	229.7	207.7	22.01	21.48	0.53
2293	35.1	209.8	22.25	22.72	-0.47
2294	6.6	210.5	22.73	22.54	0.19
2295	191.3	211.3	22.08	22.03	0.06
2296	195.6	212.7	21.40	21.46	-0.06
2297	215.5	213.0	21.90	21.68	0.22
2298	203.9	216.2	21.43	20.19	1.24
2299	45.9	228.4	21.21	20.96	0.25
2300	207.3	231.4	21.66	21.63	0.03
2301	39.1	232.1	21.44	21.17	0.27
2302	147.0	232.8	21.73	21.44	0.30
2303	228.5	238.9	22.02	22.60	-0.58
2304	125.0	240.6	22.88	21.70	1.18
2305	205.7	241.4	22.28	21.87	0.41
2306	232.0	241.9	22.10	22.14	-0.04
2307	256.8	243.5	21.62	21.92	-0.29
2308	207.8	245.2	21.63	21.84	-0.21
2309	139.8	249.6	22.42	22.95	-0.53
2310	232.8	251.7	22.48	21.31	1.17
2311	204.8	255.4	21.48	21.65	-0.17
2312	207.2	268.4	21.27	21.81	-0.54
2313	250.6	268.9	22.31	21.94	0.36
2314	97.4	272.1	21.28	21.53	-0.25
2315	103.7	273.4	21.75	22.03	-0.28
2316	148.6	277.4	21.78	21.75	0.03
2317	5.2	277.9	20.94	21.35	-0.41
2318	219.4	283.1	22.43	22.18	0.24
2319	33.5	285.3	21.58	22.32	-0.74
2320	215.1	287.4	22.72	22.21	0.50

Num	X	Y	B	V	$B-V$
2321	215.9	292.1	22.30	20.57	1.74
2322	94.5	293.8	22.80	21.85	0.95
2323	152.1	297.1	21.41	21.64	-0.23
2324	145.1	297.4	21.03	21.14	-0.10
2325	223.2	298.1	21.90	22.37	-0.47
2326	85.8	299.6	21.89	22.26	-0.37
2327	103.0	303.9	21.89	22.23	-0.34
2328	165.5	308.6	20.92	21.24	-0.33
2329	46.7	309.0	23.11	22.55	0.56
2330	86.0	319.1	21.34	21.34	0.00
2331	9.0	319.7	21.93	22.13	-0.20
2332	78.5	321.6	21.70	21.62	0.08
2333	53.4	321.7	21.37	21.81	-0.43
2334	75.3	322.7	21.73	21.35	0.38
2335	98.4	322.9	21.51	19.98	1.53
2336	121.3	323.2	20.75	19.69	1.06
2337	90.5	323.0	21.31	21.80	-0.49
2338	84.8	325.0	21.01	21.37	-0.36
2339	78.2	325.9	22.00	21.36	0.64
2340	119.0	329.0	21.35	21.50	-0.15
2341	86.7	329.1	20.92	20.67	0.25
2342	23.0	329.5	21.08	20.97	0.10
2343	76.7	330.1	22.52	22.25	0.27
2344	90.5	330.4	20.95	21.23	-0.28
2345	92.5	333.9	20.13	20.40	-0.27
2346	25.2	338.1	22.06	22.53	-0.47
2347	19.6	341.1	21.44	21.99	-0.55
2348	99.2	343.3	21.82	21.98	-0.16
2349	44.9	344.4	21.89	21.83	0.05
2350	129.0	345.4	21.58	22.02	-0.44
2351	124.5	346.1	21.19	21.05	0.15
2352	53.3	347.0	21.44	21.19	0.26
2353	49.3	347.2	23.27	22.44	0.83
2354	179.0	347.9	22.37	20.94	1.43
2355	30.3	348.2	20.67	21.20	-0.53
2356	182.2	350.4	23.21	21.95	1.26
2357	138.6	353.4	21.53	21.83	-0.30
2358	184.2	355.3	23.01	22.35	0.66
2359	129.8	355.8	20.85	21.25	-0.40
2360	22.4	358.6	21.77	21.37	0.41
2361	79.9	361.1	21.27	22.40	-1.13
2362	104.3	362.1	21.46	21.84	-0.38
2363	191.1	365.1	23.01	22.45	0.56
2364	170.7	368.7	22.01	21.73	0.28
2365	127.1	369.5	21.11	21.56	-0.46
2366	167.2	371.4	22.65	22.45	0.19
2367	257.1	370.8	21.31	21.41	-0.10
2368	104.1	372.9	21.41	21.55	-0.14
2369	127.5	373.5	20.40	20.78	-0.39
2370	253.6	373.9	22.06	22.07	-0.02
2371	20.5	378.5	20.76	21.21	-0.45
2372	63.2	380.1	21.45	21.78	-0.33
2373	190.1	383.6	21.67	21.37	0.29
2374	154.0	385.6	22.60	21.92	0.68
2375	100.0	390.0	20.84	22.11	-1.26
2376	90.5	392.4	20.08	20.58	-0.50
2377	241.5	396.6	23.02	22.05	0.98
2378	16.8	400.4	21.80	22.34	-0.54
2379	252.4	400.4	22.49	23.16	-0.67
2380	155.1	405.5	21.42	21.08	0.34
2381	225.4	407.7	21.59	21.47	0.12
2382	174.3	408.6	21.06	21.60	-0.54
2383	7.1	415.8	20.51	21.01	-0.50
2384	25.6	417.9	21.56	21.82	-0.25
2385	3.1	417.7	20.02	20.43	-0.42
2386	114.1	418.1	22.05	21.47	0.58
2387	304.2	418.5	20.98	20.83	0.15
2388	191.5	419.4	22.22	21.63	0.58
2389	28.1	420.6	21.23	21.13	0.10
2390	171.8	420.8	21.05	21.22	-0.17
2391	144.7	422.6	21.38	22.01	-0.63
2392	174.3	424.4	21.95	22.04	-0.09
2393	279.0	425.2	22.17	21.67	0.50
2394	177.4	425.3	22.52	22.09	0.43
2395	25.3	432.4	21.85	21.89	-0.04
2396	4.0	433.5	21.27	19.91	1.37
2397	108.2	436.6	21.59	21.91	-0.32
2398	132.5	436.8	21.69	22.09	-0.40
2399	5.3	438.1	22.46	20.71	1.74
2400	14.6	445.6	22.28	22.44	-0.16

Num	X	Y	B	V	$B-V$
2401	64.8	446.2	21.93	22.27	-0.34
2402	18.0	446.1	21.36	21.44	-0.08
2403	141.6	446.6	21.65	22.13	-0.48
2404	156.0	449.2	21.54	21.85	-0.31
2405	281.1	450.0	22.22	21.91	0.31
2406	154.7	452.8	22.11	21.71	0.40
2407	118.9	455.5	21.35	21.73	-0.38
2408	286.4	457.6	21.94	22.14	-0.20
2409	271.6	457.9	22.31	22.03	0.27
2410	39.8	457.8	20.60	20.03	0.57
2411	306.3	458.3	21.92	21.35	0.57
2412	267.6	460.0	22.00	22.31	-0.31
2413	273.4	460.1	22.40	21.93	0.48
2414	284.6	460.4	21.61	22.33	-0.71
2415	49.1	462.3	21.31	21.32	-0.01
2416	161.1	475.4	18.59	17.56	1.03
2417	200.4	2.5	21.35	21.35	-0.01
2418	292.2	5.7	21.73	21.84	-0.10
2419	292.7	9.6	22.77	22.00	0.77
2420	16.6	13.4	23.79	22.49	1.30
2421	18.4	14.5	24.22	22.52	1.70
2422	31.0	22.8	22.72	21.65	1.06
2423	32.0	24.4	23.37	23.13	0.25
2424	50.7	24.4	21.94	21.97	-0.03
2425	276.6	26.0	22.78	22.69	0.08
2426	275.0	27.9	22.35	22.38	-0.04
2427	47.1	31.3	22.89	22.57	0.32
2428	269.2	32.5	21.63	21.81	-0.18
2429	270.8	35.6	21.02	21.07	-0.05
2430	198.4	36.0	20.72	20.63	0.09
2431	120.7	34.2	21.46	21.11	0.35
2432	21.6	38.4	22.52	22.11	0.41
2433	22.5	41.1	22.95	22.26	0.69
2434	257.8	40.4	22.20	22.06	0.14
2435	260.2	41.5	22.14	22.49	-0.35
2436	123.1	40.9	21.83	21.57	0.26
2437	206.8	40.7	21.07	21.34	-0.27
2438	206.6	44.0	22.65	22.17	0.48
2439	100.7	48.8	21.57	21.47	0.10
2440	97.3	49.0	20.47	20.00	0.46
2441	91.6	48.9	22.25	22.26	-0.02
2442	91.8	51.0	23.23	21.88	1.35
2443	113.1	51.8	23.35	22.08	1.28
2444	115.4	52.4	22.70	22.26	0.44
2445	207.0	56.1	22.34	21.57	0.78
2446	203.4	57.3	20.55	20.99	-0.44
2447	115.7	57.0	23.30	22.47	0.83
2448	114.0	58.3	23.15	21.69	1.47
2449	254.4	57.2	22.40	22.36	0.05
2450	134.0	66.2	23.36	22.41	0.95
2451	153.9	65.7	22.15	22.45	-0.31
2452	220.1	65.8	23.33	22.42	0.90
2453	219.4	67.9	22.67	22.73	-0.07
2454	37.7	67.3	22.33	22.05	0.28
2455	141.2	66.5	21.39	21.57	-0.19
2456	141.7	68.2	21.66	21.70	-0.04
2457	135.1	69.1	22.30	21.63	0.67
2458	136.3	72.0	21.32	21.40	-0.08
2459	224.1	74.4	22.12	22.25	-0.12
2460	83.7	72.7	22.59	22.18	0.41
2461	82.4	73.7	23.00	22.97	0.04
2462	58.7	73.5	23.24	22.11	1.13
2463	55.7	75.2	22.38	21.37	1.01
2464	62.5	74.8	22.17	22.30	-0.13
2465	64.2	75.9	23.39	22.81	0.58
2466	157.1	77.4	21.63	21.97	-0.34
2467	155.7	80.0	20.61	20.65	-0.05
2468	139.9	77.5	19.69	19.86	-0.17
2469	71.6	80.7	23.17	22.06	1.11
2470	69.4	80.5	22.67	22.16	0.50
2471	136.1	84.5	22.28	21.67	0.61
2472	122.2	87.4	23.12	21.92	1.20
2473	156.6	91.4	23.32	22.58	0.74
2474	162.2	96.1	22.58	22.15	0.43
2475	102.2	96.8	21.98	21.76	0.22
2476	144.6	100.8	22.46	21.77	0.68
2477	78.6	101.6	22.33	20.43	1.90
2478	130.9	101.9	21.54	21.33	0.21
2479	130.6	105.1	23.21	21.54	1.67
2480	126.1	105.3	22.02	21.34	0.68

Num	X	Y	B	V	$B-V$
2481	124.2	106.1	22.06	21.62	0.44
2482	60.3	106.8	22.77	21.25	1.52
2483	126.7	112.1	22.73	21.82	0.91
2484	133.7	111.9	22.58	21.72	0.85
2485	78.2	112.8	22.22	22.58	-0.36
2486	76.8	114.4	22.45	22.68	-0.23
2487	139.6	114.9	20.98	20.69	0.29
2488	81.7	114.8	22.62	22.38	0.24
2489	79.7	114.6	22.91	22.09	0.82
2490	164.5	118.0	21.04	21.29	-0.25
2491	165.1	119.7	21.30	21.44	-0.15
2492	224.6	120.7	22.99	22.17	0.82
2493	226.3	121.6	22.01	21.32	0.69
2494	155.8	120.6	22.43	22.24	0.19
2495	154.1	121.8	21.21	21.66	-0.44
2496	22.6	121.8	22.47	22.06	0.41
2497	143.5	124.5	21.91	22.26	-0.35
2498	142.1	126.1	20.82	21.06	-0.24
2499	23.7	127.4	22.04	22.32	-0.28
2500	16.7	127.9	22.19	20.76	1.43
2501	18.4	130.1	22.07	21.91	0.16
2502	11.4	130.2	22.01	21.45	0.56
2503	136.1	129.1	21.38	21.38	0.00
2504	136.6	131.4	22.62	22.09	0.53
2505	208.4	131.3	23.60	22.97	0.63
2506	209.1	133.1	23.58	22.54	1.03
2507	204.4	136.6	19.95	19.81	0.15
2508	26.5	134.9	22.85	23.00	-0.15
2509	26.4	137.2	22.48	22.03	0.45
2510	214.9	135.1	22.41	21.73	0.67
2511	214.6	138.0	22.61	22.78	-0.17
2512	174.7	137.5	22.03	21.13	0.90
2513	138.0	135.7	21.80	21.83	-0.03
2514	257.0	135.9	19.54	19.19	0.35
2515	256.7	137.3	20.82	20.97	-0.16
2516	190.9	135.8	22.11	22.20	-0.09
2517	192.9	137.1	22.18	22.89	-0.71
2518	29.7	136.1	22.13	21.88	0.25
2519	30.0	139.5	23.43	22.74	0.69
2520	266.9	136.5	21.75	21.66	0.09
2521	265.7	139.3	21.12	21.36	-0.24
2522	169.8	140.9	21.89	21.84	0.05
2523	168.1	142.2	21.36	21.36	0.00
2524	31.1	142.1	22.22	21.88	0.34
2525	33.6	142.3	23.01	22.45	0.56
2526	137.7	142.7	22.69	22.42	0.27
2527	260.7	143.5	21.94	22.02	-0.08
2528	264.6	144.4	22.42	21.98	0.43
2529	265.2	146.6	22.87	21.73	1.15
2530	172.4	145.2	22.16	22.64	-0.48
2531	171.5	148.1	22.28	21.21	1.07
2532	246.0	146.6	22.49	21.59	0.89
2533	161.6	148.8	22.08	22.05	0.03
2534	161.3	151.1	22.55	22.09	0.46
2535	214.8	150.1	22.38	21.43	0.94
2536	117.4	150.8	23.15	22.53	0.61
2537	226.2	152.9	21.48	21.24	0.24
2538	224.3	154.0	21.10	20.85	0.25
2539	260.5	157.3	21.08	21.28	-0.20
2540	263.1	154.7	20.61	20.49	0.12
2541	264.6	155.9	22.44	22.30	0.14
2542	120.3	155.9	23.61	22.08	1.53
2543	217.5	155.8	22.66	22.37	0.29
2544	215.8	157.5	21.51	21.81	-0.30
2545	198.6	156.6	22.24	21.16	1.08
2546	197.2	159.4	22.91	22.23	0.69
2547	269.1	157.8	21.71	22.14	-0.43
2548	203.0	158.1	20.71	20.81	-0.10
2549	202.1	161.5	21.24	20.71	0.53
2550	266.6	164.6	19.68	19.75	-0.08
2551	74.8	167.6	22.04	21.90	0.14
2552	72.4	168.6	22.75	21.62	1.13
2553	218.6	171.5	22.55	21.64	0.91
2554	235.9	172.8	22.27	21.58	0.69
2555	54.3	179.4	21.59	22.30	-0.71
2556	57.6	181.2	18.78	18.81	-0.03
2557	78.7	185.7	22.52	22.13	0.40
2558	80.5	186.4	22.36	22.00	0.35
2559	28.6	194.2	22.41	21.95	0.46
2560	199.0	194.7	18.60	18.56	0.05

Num	X	Y	B	V	$B-V$
2561	201.4	195.6	20.64	20.27	0.37
2562	84.7	199.0	21.94	21.90	0.04
2563	86.6	199.5	21.33	21.50	-0.17
2564	207.4	202.8	21.87	22.22	-0.35
2565	162.1	201.2	19.70	19.65	0.06
2566	164.7	203.4	21.74	21.51	0.23
2567	203.4	204.1	20.80	20.83	-0.03
2568	162.3	206.7	21.73	22.10	-0.37
2569	162.3	210.0	21.47	21.56	-0.09
2570	186.8	208.9	22.26	22.15	0.11
2571	255.5	209.4	21.86	22.64	-0.78
2572	253.5	210.1	21.51	22.28	-0.78
2573	30.4	211.2	19.06	18.66	0.40
2574	32.9	216.1	22.01	22.44	-0.43
2575	23.3	217.5	21.65	20.62	1.03
2576	134.2	217.8	22.02	22.03	0.00
2577	17.5	218.5	21.28	21.81	-0.53
2578	18.8	219.0	21.48	21.87	-0.39
2579	222.7	220.3	22.53	22.05	0.48
2580	129.6	221.6	21.73	21.83	-0.10
2581	21.7	223.3	21.40	21.05	0.34
2582	22.6	224.6	23.02	22.13	0.89
2583	117.3	230.6	22.44	22.16	0.28
2584	116.7	233.1	22.94	21.97	0.98
2585	142.6	234.9	22.74	21.74	1.00
2586	144.8	235.7	21.93	21.49	0.44
2587	129.3	236.1	22.20	21.70	0.50
2588	250.8	243.9	22.00	22.49	-0.48
2589	132.4	253.1	20.79	20.67	0.12
2590	208.0	252.3	21.23	21.14	0.09
2591	201.6	253.5	22.90	22.24	0.66
2592	199.0	253.9	22.45	22.50	-0.05
2593	103.8	267.1	22.04	20.66	1.38
2594	105.7	270.0	21.23	21.04	0.19
2595	127.0	274.0	21.18	21.21	-0.03
2596	150.1	280.6	21.59	21.86	-0.26
2597	211.8	286.4	22.31	22.07	0.24
2598	93.9	286.7	21.75	20.56	1.20
2599	96.6	288.6	22.27	22.46	-0.19
2600	7.6	289.9	22.84	21.97	0.88
2601	226.5	287.9	21.84	21.85	-0.01
2602	225.1	291.0	21.03	21.42	-0.39
2603	146.9	293.0	21.92	22.12	-0.20
2604	149.2	295.0	22.02	21.13	0.89
2605	219.8	294.1	22.78	21.76	1.01
2606	222.6	294.5	20.98	21.42	-0.43
2607	155.9	297.9	22.86	21.82	1.03
2608	155.8	301.4	20.79	20.87	-0.08
2609	230.0	301.5	20.90	20.87	0.03
2610	134.5	306.0	22.19	20.96	1.24
2611	135.0	309.0	21.80	22.14	-0.34
2612	9.6	306.0	21.83	22.38	-0.55
2613	11.6	306.6	21.59	20.96	0.63
2614	94.6	307.5	22.13	22.39	-0.25
2615	94.1	309.5	21.07	21.12	-0.05
2616	6.0	310.7	19.01	19.19	-0.18
2617	34.3	314.3	19.66	19.71	-0.05
2618	36.7	315.4	22.23	21.92	0.31
2619	153.8	315.9	21.18	21.61	-0.42
2620	155.3	319.2	21.67	21.06	0.61
2621	105.7	316.9	20.84	21.15	-0.31
2622	106.7	319.4	20.81	20.95	-0.14
2623	36.4	319.5	22.09	21.98	0.11
2624	126.0	323.8	21.84	21.56	0.28
2625	107.1	323.8	21.00	20.04	0.96
2626	81.5	324.3	21.53	21.81	-0.28
2627	50.9	341.9	22.73	22.02	0.70
2628	66.7	341.6	21.58	21.61	-0.04
2629	41.9	346.0	21.38	22.02	-0.64
2630	42.2	348.2	22.20	22.31	-0.11
2631	67.2	347.2	22.13	22.36	-0.23
2632	195.2	351.5	20.12	20.39	-0.27
2633	165.4	351.8	21.53	21.47	0.06
2634	162.8	354.4	22.11	22.54	-0.43
2635	143.3	355.6	21.15	21.06	0.09
2636	97.4	360.0	20.95	21.31	-0.36
2637	180.8	364.9	21.80	22.70	-0.91
2638	178.0	365.0	22.32	21.82	0.50
2639	53.2	370.0	18.25	18.32	-0.07
2640	124.2	376.3	23.32	22.24	1.08

Num	X	Y	B	V	$B-V$
2641	122.6	378.3	22.13	21.96	0.17
2642	252.1	378.2	21.92	21.88	0.04
2643	30.1	381.9	21.78	21.26	0.53
2644	79.4	385.4	21.12	21.39	-0.27
2645	76.9	386.9	21.52	21.78	-0.26
2646	65.6	386.4	21.26	20.11	1.16
2647	66.4	388.5	19.63	20.03	-0.41
2648	244.2	387.5	20.97	21.22	-0.25
2649	94.1	390.3	19.84	20.10	-0.26
2650	96.7	392.1	21.18	21.72	-0.54
2651	198.2	390.8	20.72	20.93	-0.21
2652	196.3	392.8	21.94	23.00	-1.06
2653	232.7	396.1	22.43	21.82	0.61
2654	237.7	396.1	22.37	21.93	0.44
2655	227.5	398.6	21.66	21.30	0.36
2656	26.3	398.9	20.59	21.37	-0.78
2657	174.9	399.5	21.85	22.13	-0.28
2658	45.6	408.5	21.37	21.79	-0.41
2659	45.4	410.4	21.63	21.83	-0.20
2660	158.2	413.0	21.46	21.46	0.00
2661	156.1	414.7	20.22	19.38	0.83
2662	198.9	414.2	22.78	22.64	0.14
2663	268.5	417.2	22.98	22.77	0.21
2664	5.7	422.2	23.12	22.36	0.76
2665	181.7	423.5	21.22	21.77	-0.56
2666	260.3	424.4	20.03	20.61	-0.57
2667	263.6	424.6	20.80	21.11	-0.31
2668	54.3	424.9	21.99	21.79	0.19
2669	51.7	425.9	22.53	21.92	0.60
2670	274.2	428.5	21.71	22.39	-0.68
2671	145.6	433.8	22.44	22.23	0.22
2672	143.8	434.1	22.38	21.94	0.44
2673	66.2	433.8	21.23	21.31	-0.08
2674	20.8	435.5	21.15	21.87	-0.73
2675	43.3	435.6	21.42	21.53	-0.11
2676	127.4	435.0	19.76	19.47	0.29
2677	125.8	437.2	22.33	21.94	0.40
2678	113.9	437.2	21.38	22.09	-0.71
2679	111.6	438.9	21.34	19.80	1.55
2680	123.0	440.7	21.20	21.95	-0.75
2681	8.2	442.3	20.78	21.14	-0.35
2682	10.7	443.0	21.10	21.46	-0.37
2683	42.7	447.3	22.68	22.10	0.58
2684	42.2	450.8	21.97	21.42	0.56
2685	295.2	449.3	21.74	21.62	0.13
2686	297.8	450.1	20.76	20.75	0.01
2687	64.2	450.1	21.36	21.63	-0.28
2688	55.1	453.9	22.42	22.80	-0.39
2689	54.3	456.4	23.40	21.49	1.92
2690	118.1	461.4	19.26	19.23	0.03
2691	147.2	465.3	18.68	19.10	-0.42
2692	276.3	462.8	21.84	21.04	0.81
2693	110.7	465.7	22.13	22.02	0.11
2694	150.8	478.3	19.93	20.52	-0.59
2695	196.6	4.2	21.88	22.09	-0.21
2696	196.3	6.4	22.72	22.03	0.69
2697	287.9	6.4	22.75	22.05	0.70
2698	286.4	6.4	22.66	22.37	0.28
2699	12.8	15.7	22.77	22.23	0.54
2700	13.2	18.6	23.35	21.95	1.40
2701	48.2	20.8	22.22	22.36	-0.14
2702	49.6	21.2	23.14	22.36	0.78
2703	254.5	34.8	21.29	21.39	-0.10
2704	252.9	36.7	22.09	21.74	0.34
2705	117.7	39.8	22.25	21.33	0.91
2706	93.8	44.5	21.35	20.48	0.87
2707	197.7	45.1	21.93	22.31	-0.38
2708	198.3	49.0	21.91	20.38	1.53
2709	103.0	52.8	21.63	21.36	0.26
2710	105.6	54.2	21.99	22.53	-0.54
2711	104.7	56.1	21.40	21.29	0.11
2712	80.9	65.4	22.33	22.21	0.12
2713	83.0	66.0	22.98	21.46	1.51
2714	128.2	78.4	22.36	22.44	-0.08
2715	129.7	80.2	22.97	22.92	0.05
2716	157.3	84.0	21.84	21.79	0.05
2717	159.9	84.3	22.24	20.55	1.69
2718	168.8	92.2	21.21	20.49	0.72
2719	167.1	94.5	22.81	22.08	0.73
2720	92.2	93.4	23.04	23.00	0.04

Num	X	Y	B	V	$B-V$
2721	93.9	96.5	23.36	22.93	0.43
2722	61.8	97.3	21.70	21.50	0.20
2723	59.9	98.3	20.85	20.68	0.17
2724	59.1	100.2	21.58	21.02	0.56
2725	49.1	99.8	22.21	20.73	1.48
2726	52.2	100.8	22.83	22.87	-0.04
2727	163.3	102.3	22.03	21.30	0.74
2728	85.8	104.7	22.52	22.35	0.17
2729	85.3	107.5	22.09	20.41	1.68
2730	84.8	108.7	21.62	21.27	0.35
2731	189.5	104.8	23.00	21.99	1.01
2732	187.5	105.5	23.28	22.21	1.07
2733	133.8	106.6	21.87	22.80	-0.93
2734	137.2	106.8	22.99	22.65	0.34
2735	152.1	109.7	21.62	20.74	0.88
2736	158.1	111.9	18.66	18.69	-0.03
2737	156.1	113.5	20.65	20.77	-0.12
2738	156.6	117.2	21.28	21.31	-0.04
2739	179.8	113.0	22.89	22.75	0.14
2740	177.9	115.1	21.80	21.89	-0.09
2741	175.1	115.9	22.50	21.72	0.78
2742	83.8	118.5	22.18	22.05	0.13
2743	86.5	118.9	22.50	21.73	0.76
2744	86.0	121.1	22.03	22.27	-0.24
2745	183.6	118.9	22.46	21.98	0.48
2746	186.1	119.6	23.24	22.29	0.94
2747	70.1	121.2	21.72	22.14	-0.42
2748	72.6	121.7	21.98	21.91	0.07
2749	91.1	122.5	21.29	20.22	1.07
2750	88.1	125.3	19.76	19.55	0.21
2751	89.5	128.3	21.85	22.34	-0.50
2752	237.4	125.8	22.52	21.60	0.92
2753	237.6	128.9	22.19	22.03	0.16
2754	184.8	127.0	21.63	21.61	0.02
2755	183.4	128.1	19.38	19.42	-0.04
2756	180.0	127.6	23.16	22.41	0.75
2757	106.8	127.4	22.76	22.17	0.58
2758	109.2	128.4	22.58	22.01	0.57
2759	256.7	129.9	21.85	21.46	0.39
2760	255.0	131.7	22.58	22.07	0.52
2761	35.6	132.1	23.35	22.16	1.19
2762	37.5	133.9	22.70	21.74	0.96
2763	94.3	140.3	21.32	21.50	-0.18
2764	93.7	142.2	21.00	21.08	-0.08
2765	127.2	138.1	20.60	20.63	-0.03
2766	124.7	139.5	22.07	21.85	0.22
2767	204.0	142.7	21.16	21.02	0.14
2768	105.0	143.4	22.22	21.57	0.65
2769	13.1	143.1	21.38	20.06	1.32
2770	11.3	146.0	20.30	20.23	0.06
2771	14.4	146.4	23.64	22.40	1.23
2772	142.4	148.2	21.23	21.27	-0.04
2773	143.7	149.8	20.18	20.44	-0.26
2774	165.7	148.0	22.16	22.03	0.13
2775	167.9	150.1	21.94	21.55	0.38
2776	133.2	155.6	22.16	22.47	-0.31
2777	135.0	157.6	19.85	20.09	-0.24
2778	134.5	159.8	22.32	22.19	0.12
2779	130.3	157.9	22.39	22.49	-0.09
2780	126.7	160.9	23.29	22.32	0.97
2781	262.1	162.4	20.69	20.80	-0.11
2782	259.3	163.7	21.88	21.61	0.28
2783	128.6	166.8	21.06	21.45	-0.39
2784	131.8	167.9	23.53	22.90	0.64
2785	175.2	168.8	19.42	19.54	-0.12
2786	133.9	170.4	23.56	21.92	1.64
2787	136.3	170.6	20.95	20.25	0.70
2788	135.1	173.3	21.51	21.46	0.05
2789	281.2	175.1	22.11	22.15	-0.04
2790	268.2	182.6	19.61	19.87	-0.25
2791	270.4	183.1	21.82	21.86	-0.04
2792	228.5	186.8	20.85	20.83	0.02
2793	227.1	188.0	21.31	21.18	0.12
2794	57.0	188.2	22.33	21.96	0.36
2795	232.5	187.8	20.23	20.23	0.00
2796	88.6	190.9	23.25	22.09	1.16
2797	90.1	192.6	23.68	21.69	1.99
2798	87.4	192.8	22.77	22.16	0.62
2799	191.9	195.7	21.81	21.26	0.55
2800	31.4	203.3	22.32	22.46	-0.14

Num	X	Y	B	V	$B-V$
2801	28.6	204.4	22.32	21.73	0.59
2802	191.1	205.1	20.31	20.40	-0.08
2803	193.6	206.9	22.62	21.46	1.16
2804	170.6	204.6	22.13	21.86	0.27
2805	168.3	205.8	21.52	20.82	0.71
2806	167.0	208.4	21.80	21.21	0.59
2807	206.9	220.6	21.52	21.46	0.06
2808	212.8	219.1	20.82	20.80	0.03
2809	213.3	221.7	22.63	22.09	0.54
2810	203.6	224.9	20.18	19.95	0.23
2811	204.0	226.6	20.93	20.73	0.20
2812	203.7	229.8	21.93	21.96	-0.03
2813	209.1	226.8	20.32	20.23	0.09
2814	211.3	227.2	20.64	21.17	-0.53
2815	234.3	231.4	22.47	22.30	0.17
2816	233.2	233.4	22.76	22.38	0.38
2817	231.1	232.1	22.47	21.78	0.69
2818	35.6	233.4	22.31	22.24	0.07
2819	36.9	238.0	22.38	22.94	-0.56
2820	119.9	242.0	22.17	21.85	0.32
2821	120.4	244.8	22.76	21.13	1.63
2822	123.9	244.2	21.45	21.57	-0.11
2823	128.9	256.9	20.74	21.32	-0.58
2824	125.5	259.6	17.66	17.92	-0.25
2825	202.1	259.0	22.04	21.03	1.01
2826	198.2	260.9	22.28	21.80	0.48
2827	220.9	274.1	21.80	20.85	0.95
2828	195.3	274.6	21.77	21.92	-0.14
2829	98.2	276.0	21.65	21.92	-0.27
2830	143.8	276.5	21.50	21.25	0.25
2831	141.7	278.2	22.60	23.08	-0.49
2832	145.5	279.2	21.39	21.80	-0.40
2833	7.2	281.8	21.88	21.43	0.45
2834	5.6	284.0	21.28	21.16	0.12
2835	218.8	286.0	22.60	23.20	-0.61
2836	219.5	289.3	22.45	21.03	1.42
2837	34.6	288.9	21.82	21.35	0.47
2838	33.0	290.2	21.93	21.13	0.80
2839	125.9	296.4	21.88	22.31	-0.43
2840	123.6	297.5	22.07	22.50	-0.44
2841	124.6	299.2	21.51	21.78	-0.27
2842	113.3	298.9	20.73	20.90	-0.16
2843	113.4	301.8	22.43	22.72	-0.29
2844	91.9	299.3	20.34	20.71	-0.37
2845	93.6	299.9	21.63	21.75	-0.12
2846	94.2	303.0	21.72	21.93	-0.21
2847	168.7	301.2	21.05	20.75	0.30
2848	170.4	301.7	22.98	22.54	0.44
2849	139.7	312.4	18.50	18.56	-0.06
2850	59.2	327.2	22.01	21.47	0.54
2851	56.4	328.8	20.11	20.49	-0.37
2852	57.8	331.8	21.45	21.56	-0.11
2853	9.1	329.1	20.74	20.83	-0.09
2854	7.4	330.6	18.81	18.87	-0.06
2855	30.6	331.1	18.82	18.43	0.38
2856	33.8	333.0	22.44	21.63	0.82
2857	60.9	336.2	21.69	21.77	-0.09
2858	64.5	339.4	22.78	22.36	0.42
2859	38.6	340.3	21.76	21.53	0.24
2860	39.8	341.9	21.67	21.89	-0.23
2861	135.4	345.9	21.68	21.48	0.19
2862	139.4	348.2	20.01	20.36	-0.35
2863	187.0	346.5	19.78	19.53	0.25
2864	186.1	349.6	20.86	20.80	0.06
2865	44.8	351.0	21.83	21.68	0.15
2866	136.4	357.1	21.90	22.28	-0.38
2867	134.4	357.4	21.31	21.83	-0.53
2868	167.5	356.1	21.65	21.02	0.62
2869	26.2	359.2	20.80	20.87	-0.07
2870	26.6	359.8	20.39	21.03	-0.64
2871	132.2	361.1	22.34	22.18	0.16
2872	135.5	362.0	20.54	20.74	-0.20
2873	135.3	364.4	22.02	21.22	0.80
2874	181.1	361.1	23.68	22.98	0.70
2875	184.4	362.5	20.32	20.02	0.30
2876	186.0	362.0	22.69	21.82	0.87
2877	7.2	361.3	22.71	21.49	1.22
2878	6.6	362.9	21.52	21.83	-0.30
2879	46.0	363.5	21.13	21.27	-0.14
2880	44.4	373.0	20.99	21.34	-0.35

Num	X	Y	B	V	$B-V$
2881	117.6	372.6	20.86	21.05	-0.19
2882	117.2	376.6	18.97	19.08	-0.11
2883	22.6	382.8	20.07	20.15	-0.08
2884	22.6	384.8	20.74	21.05	-0.31
2885	52.7	386.0	20.48	20.74	-0.26
2886	54.3	388.1	19.02	18.81	0.21
2887	56.0	389.8	21.05	21.01	0.04
2888	83.2	389.2	20.77	20.89	-0.12
2889	85.4	392.4	19.66	19.45	0.21
2890	83.9	396.4	21.65	21.81	-0.16
2891	76.0	392.0	18.72	18.31	0.41
2892	70.4	393.2	18.95	19.18	-0.24
2893	72.2	395.9	18.73	18.91	-0.18
2894	172.4	394.5	21.37	22.16	-0.80
2895	173.4	396.0	21.12	21.59	-0.47
2896	108.0	397.6	20.57	20.92	-0.34
2897	105.0	400.0	18.57	18.01	0.56
2898	106.2	401.9	18.96	19.08	-0.12
2899	176.8	405.9	21.93	22.66	-0.73
2900	178.0	408.2	21.37	21.43	-0.06
2901	180.6	408.3	22.48	22.28	0.20
2902	49.2	414.4	21.88	22.19	-0.32
2903	29.8	417.2	20.50	21.05	-0.55
2904	31.5	418.1	20.73	21.24	-0.50
2905	149.4	422.5	22.80	21.10	1.69
2906	148.9	426.4	19.17	19.27	-0.10
2907	150.6	428.1	20.83	19.49	1.34
2908	155.1	428.7	20.68	20.17	0.51
2909	156.4	430.6	20.67	21.33	-0.67
2910	157.3	434.6	21.87	20.03	1.84
2911	53.5	429.6	22.10	21.64	0.46
2912	56.4	432.5	22.07	21.95	0.12
2913	162.6	434.5	20.67	20.51	0.16
2914	166.3	436.2	21.21	21.77	-0.56
2915	188.3	436.4	21.02	19.34	1.67
2916	185.7	435.3	21.72	22.11	-0.38
2917	52.2	450.3	21.30	20.14	1.16
2918	50.6	451.1	21.23	21.23	0.00
2919	288.9	459.9	22.22	21.59	0.63
2920	287.5	463.0	21.91	21.96	-0.05
2921	153.6	461.8	21.37	22.32	-0.95
2922	36.6	462.3	21.12	21.65	-0.53
2923	45.1	16.8	22.72	22.45	0.26
2924	44.1	21.4	22.70	20.82	1.88
2925	41.5	18.9	23.48	22.24	1.24
2926	194.9	28.5	21.58	21.77	-0.18
2927	191.8	30.3	20.08	20.20	-0.13
2928	186.3	42.0	23.02	22.20	0.81
2929	185.4	43.9	19.18	19.16	0.02
2930	106.8	46.9	21.72	21.36	0.36
2931	209.2	50.7	21.89	21.63	0.26
2932	211.6	55.5	17.81	17.60	0.21
2933	57.0	65.2	23.03	21.71	1.32
2934	57.9	67.3	23.60	22.88	0.72
2935	59.8	66.7	23.71	22.07	1.64
2936	157.3	69.1	21.48	21.38	0.10
2937	156.4	71.6	21.06	21.08	-0.02
2938	153.7	71.3	21.70	21.64	0.06
2939	130.6	69.8	21.57	21.53	0.04
2940	131.0	72.7	22.16	20.54	1.62
2941	133.3	73.5	21.66	21.43	0.23
2942	133.1	75.2	23.09	22.00	1.09
2943	121.8	78.3	22.07	21.99	0.09
2944	120.4	81.9	21.35	21.09	0.26
2945	152.5	85.4	22.68	21.78	0.90
2946	152.4	87.7	22.87	22.32	0.56
2947	154.0	89.7	23.58	22.35	1.23
2948	126.2	96.2	21.47	21.08	0.38
2949	122.6	98.3	21.25	21.32	-0.07
2950	120.6	95.6	22.38	22.19	0.19
2951	103.6	101.1	21.69	21.52	0.17
2952	115.4	102.6	22.20	20.90	1.30
2953	118.6	103.1	21.98	21.44	0.54
2954	112.0	103.2	22.70	22.32	0.38
2955	114.2	104.0	20.28	20.43	-0.15
2956	69.7	109.9	21.08	21.30	-0.22
2957	69.9	113.1	21.37	21.67	-0.31
2958	68.6	114.4	21.11	19.74	1.37
2959	71.4	116.6	21.12	21.50	-0.37
2960	64.0	110.9	22.25	21.66	0.59

Num	X	Y	B	V	$B-V$
2961	29.0	117.0	21.93	21.60	0.34
2962	30.5	119.5	23.57	22.84	0.73
2963	26.0	120.6	22.05	21.69	0.36
2964	103.2	119.1	22.32	22.56	-0.24
2965	105.8	122.6	21.36	21.43	-0.07
2966	9.1	117.9	21.85	22.14	-0.29
2967	9.6	119.9	23.79	22.49	1.30
2968	10.2	122.8	21.69	20.92	0.77
2969	8.4	124.9	23.13	22.80	0.33
2970	69.3	123.7	21.98	22.24	-0.26
2971	71.4	125.3	21.95	21.00	0.95
2972	73.5	126.1	22.06	21.29	0.77
2973	69.4	127.2	21.54	21.63	-0.09
2974	37.1	125.6	23.00	22.29	0.71
2975	41.2	128.9	22.36	21.62	0.74
2976	42.7	130.3	23.48	22.35	1.13
2977	175.9	131.9	22.10	22.53	-0.43
2978	178.4	135.0	20.18	20.26	-0.07
2979	104.1	137.3	20.07	20.25	-0.18
2980	107.3	139.3	21.58	21.58	0.00
2981	109.5	138.7	22.33	22.33	0.01
2982	8.9	135.2	22.27	21.01	1.26
2983	6.4	137.0	21.32	21.55	-0.23
2984	10.5	139.0	20.91	21.38	-0.46
2985	117.2	136.3	23.12	22.95	0.17
2986	116.0	137.6	22.26	22.02	0.24
2987	119.6	139.7	22.36	21.78	0.58
2988	219.9	139.8	20.96	20.39	0.57
2989	218.6	141.7	22.23	22.08	0.15
2990	251.7	146.7	21.63	21.70	-0.08
2991	249.9	149.9	21.36	22.17	-0.81
2992	306.4	149.7	21.49	21.80	-0.31
2993	307.6	152.1	22.51	21.73	0.78
2994	305.3	154.6	21.25	21.30	-0.05
2995	156.8	151.6	20.52	20.67	-0.15
2996	170.7	153.7	21.46	21.33	0.13
2997	173.5	155.3	21.83	20.32	1.52
2998	169.3	155.5	22.43	22.09	0.35
2999	116.4	155.0	21.11	21.01	0.10
3000	277.8	164.8	21.93	21.58	0.35
3001	48.1	199.0	23.12	21.85	1.27
3002	46.7	200.8	20.67	20.76	-0.08
3003	182.3	202.6	22.45	21.91	0.54
3004	185.4	204.0	19.76	19.52	0.25
3005	56.5	213.9	21.63	20.80	0.83
3006	54.6	212.1	22.53	21.54	0.99
3007	10.4	211.1	21.66	21.70	-0.03
3008	7.1	215.0	21.34	21.08	0.25
3009	39.8	216.2	21.50	21.55	-0.05
3010	42.6	217.8	21.27	20.86	0.41
3011	125.5	218.2	22.13	21.56	0.58
3012	123.6	220.6	22.11	22.28	-0.17
3013	125.8	221.9	22.50	21.79	0.71
3014	120.9	224.2	21.70	22.17	-0.47
3015	120.6	235.1	22.61	21.84	0.77
3016	123.6	234.2	20.80	21.01	-0.22
3017	125.6	236.6	22.30	21.93	0.37
3018	235.9	236.6	22.51	22.02	0.48
3019	230.7	237.4	21.22	22.59	-1.37
3020	128.8	249.2	21.40	21.47	-0.07
3021	126.9	252.2	21.35	21.64	-0.28
3022	102.7	260.6	22.39	21.97	0.42
3023	102.1	263.0	21.41	21.03	0.38
3024	99.2	263.8	23.09	21.56	1.54
3025	97.5	265.8	20.82	21.09	-0.27
3026	218.6	264.3	19.66	19.63	0.03
3027	222.3	265.8	18.79	19.00	-0.20
3028	219.8	265.8	20.61	21.05	-0.44
3029	139.9	271.0	20.76	20.86	-0.10
3030	136.5	274.2	20.70	19.99	0.71
3031	133.9	277.0	21.63	21.38	0.25
3032	133.3	281.4	21.01	20.22	0.79
3033	130.3	283.2	20.07	20.24	-0.16
3034	132.3	284.5	20.09	20.19	-0.09
3035	121.7	286.3	21.95	21.96	-0.02
3036	124.4	287.1	22.18	21.32	0.86
3037	127.9	286.3	21.75	21.36	0.40
3038	126.4	287.7	22.68	21.87	0.81
3039	5.6	297.1	21.23	21.51	-0.28
3040	7.2	299.9	20.69	20.59	0.10

Num	X	Y	B	V	$B-V$
3041	4.5	301.9	22.11	21.69	0.42
3042	5.9	304.6	21.31	21.81	-0.50
3043	23.1	299.0	22.50	22.89	-0.38
3044	22.3	301.1	22.05	21.77	0.28
3045	19.7	302.5	22.33	21.91	0.42
3046	20.6	305.0	21.38	21.52	-0.14
3047	134.2	299.2	22.27	22.56	-0.29
3048	129.4	306.3	22.14	22.59	-0.45
3049	127.6	309.0	19.54	19.90	-0.36
3050	131.4	310.2	22.21	22.35	-0.14
3051	120.7	309.5	22.09	21.71	0.38
3052	118.7	310.0	22.42	21.40	1.02
3053	118.9	312.7	22.70	22.23	0.47
3054	51.6	328.0	22.28	21.53	0.75
3055	52.1	330.4	22.43	20.96	1.47
3056	54.1	333.1	21.83	20.82	1.01
3057	176.8	326.0	23.08	22.31	0.77
3058	173.9	328.1	22.65	22.34	0.32
3059	174.6	334.3	21.49	21.74	-0.25
3060	175.2	336.4	22.33	22.11	0.22
3061	111.6	340.9	21.03	21.38	-0.35
3062	113.3	342.8	21.63	21.40	0.23
3063	112.1	344.3	22.01	21.43	0.58
3064	155.5	342.8	22.93	22.46	0.47
3065	155.7	345.4	21.99	21.64	0.34
3066	61.1	346.9	23.30	21.84	1.46
3067	63.5	347.7	22.78	22.00	0.79
3068	132.3	348.5	21.65	22.56	-0.92
3069	132.9	350.9	22.08	21.94	0.14
3070	86.3	355.6	23.19	21.87	1.32
3071	86.6	358.5	20.60	20.88	-0.28
3072	194.9	364.6	20.18	20.33	-0.16
3073	199.8	364.8	20.57	20.12	0.44
3074	191.8	375.3	19.93	20.33	-0.41
3075	193.3	377.8	22.20	22.79	-0.60
3076	71.1	373.5	21.29	20.79	0.50
3077	73.2	374.6	20.89	19.72	1.18
3078	70.4	377.1	19.98	20.26	-0.28
3079	249.5	376.5	22.33	21.86	0.47
3080	246.5	377.5	21.46	21.51	-0.05
3081	260.7	380.2	21.29	21.88	-0.59
3082	259.0	378.0	20.57	20.73	-0.17
3083	155.0	380.5	21.42	20.77	0.65
3084	156.1	381.5	20.56	20.07	0.50
3085	152.3	380.5	21.00	21.62	-0.62
3086	180.7	388.0	19.63	20.09	-0.46
3087	179.6	390.7	21.81	22.02	-0.21
3088	181.4	392.7	21.93	22.52	-0.59
3089	233.8	400.0	21.69	21.82	-0.13
3090	232.5	403.0	20.83	21.02	-0.19
3091	230.5	404.8	19.85	20.09	-0.25
3092	186.2	417.4	17.90	18.00	-0.10
3093	61.1	419.8	21.80	21.79	0.02
3094	61.6	423.0	20.20	20.50	-0.30
3095	58.3	422.8	22.88	22.18	0.69
3096	61.6	425.5	22.11	22.08	0.04
3097	138.1	423.7	21.95	22.01	-0.06
3098	140.8	424.2	21.27	21.44	-0.18
3099	136.9	426.3	21.16	21.29	-0.13
3100	26.4	424.3	22.19	20.95	1.24
3101	25.9	426.9	21.34	21.55	-0.21
3102	26.2	429.3	21.65	22.06	-0.41
3103	269.3	426.2	22.31	21.88	0.43
3104	265.6	428.8	21.67	22.10	-0.43
3105	266.2	430.1	21.93	21.92	0.01
3106	171.0	430.4	20.62	21.03	-0.41
3107	172.1	431.5	21.14	20.08	1.06
3108	60.6	445.6	22.29	22.17	0.12
3109	56.2	447.4	21.33	20.88	0.45
3110	137.7	448.8	19.68	19.99	-0.30
3111	134.7	448.0	20.95	22.07	-1.12
3112	283.6	447.1	21.50	20.99	0.51
3113	126.7	456.5	22.37	21.74	0.63
3114	123.8	458.5	19.87	20.45	-0.58
3115	128.0	459.2	21.62	20.92	0.71
3116	35.3	468.4	20.33	20.65	-0.33
3117	37.6	469.8	20.67	20.83	-0.16
3118	33.2	469.8	19.97	20.01	-0.04
3119	205.6	10.8	22.31	21.94	0.37
3120	202.8	15.9	20.73	20.56	0.17

Num	X	Y	B	V	$B-V$
3121	199.3	15.9	20.62	20.72	-0.10
3122	201.9	17.5	21.47	21.34	0.12
3123	203.2	42.5	21.96	21.37	0.60
3124	202.4	43.7	21.06	21.39	-0.34
3125	202.9	46.4	21.39	21.64	-0.25
3126	202.5	49.0	21.57	21.30	0.27
3127	201.7	51.2	21.22	21.16	0.06
3128	223.8	57.9	22.04	21.74	0.30
3129	225.4	60.3	22.42	21.96	0.46
3130	223.9	61.7	21.43	21.74	-0.31
3131	224.5	64.8	22.27	21.73	0.54
3132	223.1	67.8	22.76	22.74	0.01
3133	148.1	66.4	19.55	19.32	0.23
3134	144.1	65.6	22.78	22.53	0.25
3135	145.8	70.6	21.92	21.49	0.43
3136	151.4	76.6	21.16	21.32	-0.16
3137	146.9	76.7	23.47	22.17	1.30
3138	148.9	81.9	21.34	21.44	-0.10
3139	127.7	83.4	20.66	20.70	-0.04
3140	125.0	83.8	22.39	22.42	-0.04
3141	128.6	86.2	21.85	21.75	0.10
3142	147.9	92.0	22.15	22.13	0.02
3143	145.7	94.7	22.75	21.17	1.58
3144	142.9	92.0	21.15	21.15	0.00
3145	142.2	95.9	21.22	21.33	-0.10
3146	98.4	100.7	22.16	21.47	0.69
3147	96.6	103.8	22.69	22.49	0.20
3148	4.0	126.6	22.60	22.41	0.20
3149	2.8	128.5	23.61	23.17	0.44
3150	2.8	131.8	22.22	21.05	1.17
3151	5.3	130.6	22.14	22.24	-0.10
3152	98.7	131.3	22.29	21.92	0.37
3153	98.6	133.9	20.68	20.90	-0.22
3154	99.6	137.4	21.71	21.99	-0.28
3155	209.6	157.4	20.67	20.81	-0.14
3156	207.4	157.9	22.91	21.34	1.57
3157	211.7	158.0	22.08	21.62	0.46
3158	211.6	160.7	20.00	19.98	0.01
3159	284.6	161.1	20.71	20.67	0.04
3160	287.6	162.2	20.36	20.76	-0.40
3161	281.9	163.7	22.08	22.14	-0.06
3162	242.6	167.4	22.29	21.81	0.49
3163	241.7	168.7	21.76	22.13	-0.37
3164	238.7	171.4	22.03	21.94	0.09
3165	240.1	173.5	20.09	19.04	1.05
3166	197.7	174.9	22.83	21.77	1.06
3167	195.0	176.7	22.24	22.21	0.02
3168	196.3	179.0	21.10	21.31	-0.21
3169	195.5	183.9	20.81	20.40	0.42
3170	100.9	181.1	23.68	22.49	1.19
3171	101.4	183.3	20.76	20.86	-0.10
3172	104.2	185.0	20.26	20.25	0.01
3173	106.1	190.5	19.25	19.28	-0.03
3174	110.9	185.9	20.71	20.86	-0.15
3175	108.8	183.3	22.40	22.35	0.05
3176	112.0	188.7	20.45	20.21	0.25
3177	111.3	191.3	21.32	21.58	-0.25
3178	225.6	191.7	21.17	20.87	0.29
3179	223.6	192.6	20.92	21.08	-0.15
3180	222.9	194.8	22.02	21.71	0.31
3181	224.0	197.6	21.74	20.60	1.14
3182	220.1	198.9	21.72	22.70	-0.98
3183	22.1	194.2	19.72	19.62	0.10
3184	23.8	198.0	21.69	22.19	-0.49
3185	20.8	200.3	19.92	19.85	0.07
3186	106.5	197.8	21.98	22.08	-0.10
3187	109.6	199.7	22.37	22.29	0.08
3188	109.0	202.3	22.13	20.80	1.33
3189	174.0	203.2	21.16	20.40	0.76
3190	177.6	203.3	21.49	21.24	0.25
3191	179.0	202.5	21.11	21.28	-0.16
3192	22.9	206.6	19.50	19.42	0.08
3193	24.6	210.8	22.03	22.08	-0.04
3194	114.8	208.2	21.28	21.43	-0.16
3195	8.6	219.3	21.57	21.49	0.09
3196	7.8	222.2	21.99	22.61	-0.62
3197	9.8	223.7	22.07	21.69	0.39
3198	12.1	221.7	22.05	21.66	0.39
3199	13.1	223.6	21.68	21.89	-0.20
3200	130.7	227.0	23.26	22.88	0.37

Num	X	Y	B	V	$B-V$
3201	130.4	230.3	22.88	21.51	1.37
3202	130.1	231.8	21.85	21.58	0.27
3203	134.2	232.6	20.97	20.92	0.05
3204	46.7	235.3	22.20	20.97	1.23
3205	47.8	232.0	22.43	22.52	-0.09
3206	130.8	241.2	21.40	20.42	0.98
3207	134.4	241.5	21.98	21.12	0.86
3208	136.1	242.8	21.75	21.60	0.15
3209	140.5	245.4	21.60	21.74	-0.14
3210	135.7	264.4	20.66	20.90	-0.23
3211	131.4	265.0	19.99	19.90	0.09
3212	132.3	268.5	20.22	19.69	0.53
3213	205.1	265.3	22.42	22.52	-0.10
3214	202.0	265.7	20.01	19.45	0.56
3215	198.6	266.0	22.69	21.94	0.75
3216	197.8	268.3	20.90	20.93	-0.04
3217	198.2	270.8	21.41	21.05	0.36
3218	114.9	271.1	22.40	22.13	0.27
3219	113.4	273.1	21.51	21.28	0.22
3220	117.5	273.8	20.80	20.20	0.60
3221	117.7	276.9	22.09	21.91	0.18
3222	115.4	279.1	21.44	22.08	-0.64
3223	112.7	281.6	21.04	21.06	-0.02
3224	231.0	281.6	22.32	22.52	-0.19
3225	231.0	286.0	21.71	21.71	-0.01
3226	232.7	286.3	21.89	21.95	-0.06
3227	159.1	284.4	20.70	21.06	-0.36
3228	160.5	284.8	19.38	19.28	0.10
3229	159.4	288.8	21.30	21.30	0.00
3230	160.0	290.6	21.72	21.15	0.57
3231	156.3	288.2	21.24	21.31	-0.08
3232	153.1	289.0	20.46	20.60	-0.14
3233	149.9	289.0	22.00	21.69	0.31
3234	133.2	289.4	19.03	18.80	0.23
3235	129.0	290.8	21.90	22.08	-0.17
3236	136.3	295.2	21.05	21.22	-0.17
3237	9.3	292.6	21.99	21.92	0.08
3238	10.5	295.9	20.95	21.25	-0.30
3239	12.4	296.6	21.00	21.40	-0.40
3240	12.7	299.6	21.16	20.60	0.56
3241	98.6	293.9	22.89	22.62	0.27
3242	100.2	295.0	21.61	21.47	0.15
3243	107.3	294.2	20.52	19.98	0.55
3244	109.7	296.1	20.92	21.14	-0.21
3245	107.4	297.9	19.22	19.34	-0.12
3246	105.3	299.3	21.76	21.86	-0.10
3247	109.4	300.5	22.42	22.19	0.23
3248	159.3	304.5	22.28	21.97	0.31
3249	158.4	306.3	20.67	21.14	-0.47
3250	92.3	313.8	21.33	21.83	-0.49
3251	90.2	316.4	21.09	19.66	1.43
3252	92.0	319.9	22.01	21.59	0.42
3253	131.6	313.2	21.99	22.19	-0.20
3254	130.4	315.2	21.40	21.31	0.09
3255	128.1	312.4	22.00	21.91	0.09
3256	125.4	318.6	21.29	21.72	-0.43
3257	116.0	331.7	21.24	20.99	0.25
3258	116.5	337.7	19.89	20.29	-0.40
3259	119.1	334.9	21.70	21.51	0.19
3260	71.6	333.3	22.16	22.31	-0.14
3261	68.0	337.4	22.82	22.37	0.45
3262	163.8	341.3	21.81	22.20	-0.39
3263	161.0	343.4	19.17	19.41	-0.24
3264	163.6	346.6	21.79	22.14	-0.35
3265	115.6	346.6	20.80	20.83	-0.03
3266	117.6	349.4	22.27	21.91	0.36
3267	119.1	350.1	21.73	22.47	-0.74
3268	117.6	351.1	23.24	22.22	1.02
3269	112.1	352.0	21.77	21.63	0.13
3270	113.4	355.2	21.73	21.62	0.12
3271	192.3	354.8	20.85	20.93	-0.08
3272	189.8	355.0	21.90	22.36	-0.45
3273	192.1	359.0	21.92	21.86	0.06
3274	39.5	365.0	21.37	23.05	-1.67
3275	41.7	367.7	22.34	21.83	0.51
3276	38.1	370.0	21.88	22.06	-0.18
3277	193.7	403.7	22.35	22.04	0.30
3278	190.8	409.2	20.74	21.11	-0.37
3279	192.6	409.8	22.30	21.51	0.79
3280	179.4	415.8	21.36	21.44	-0.08

Num	X	Y	B	V	$B-V$
3281	177.9	418.0	21.73	21.31	0.43
3282	181.2	419.6	21.22	21.79	-0.57
3283	116.5	428.0	20.90	21.32	-0.43
3284	115.0	429.9	20.43	20.44	-0.01
3285	118.4	431.4	21.52	21.87	-0.34
3286	114.5	432.3	20.97	21.53	-0.56
3287	120.4	429.1	21.38	21.76	-0.38
3288	178.2	429.8	22.61	21.58	1.02
3289	181.6	433.9	21.96	20.88	1.07
3290	183.7	432.0	21.10	21.22	-0.12
3291	63.0	439.1	21.36	21.09	0.27
3292	59.5	440.7	20.10	20.54	-0.44
3293	66.9	439.3	22.29	22.23	0.06
3294	302.4	439.5	21.80	22.92	-1.12
3295	303.8	441.4	21.78	21.24	0.55
3296	301.5	444.1	21.29	20.85	0.44
3297	298.8	444.8	21.68	21.68	0.00
3298	297.5	442.0	20.40	21.04	-0.64
3299	129.3	449.5	19.01	18.78	0.23
3300	125.4	451.2	20.68	20.95	-0.27
3301	124.1	449.8	21.49	20.13	1.35
3302	135.9	458.5	19.21	19.73	-0.52
3303	95.9	460.7	20.31	20.73	-0.43
3304	92.9	459.5	22.05	22.07	-0.02
3305	37.6	19.2	23.47	21.81	1.66
3306	37.5	23.5	22.80	21.52	1.28
3307	40.8	25.2	23.59	22.35	1.24
3308	43.3	25.3	22.70	20.56	2.14
3309	36.6	36.5	22.19	21.89	0.30
3310	41.1	38.1	20.45	20.54	-0.09
3311	33.8	38.9	19.99	19.71	0.27
3312	39.6	37.3	22.98	22.27	0.71
3313	33.0	41.9	22.05	21.79	0.26
3314	78.9	67.8	23.20	21.74	1.47
3315	78.2	70.4	21.97	21.76	0.21
3316	77.3	73.0	21.88	21.58	0.30
3317	76.5	74.7	22.59	23.13	-0.55
3318	78.5	76.7	21.13	20.40	0.73
3319	81.1	78.2	22.20	21.93	0.28
3320	38.2	70.7	23.35	21.89	1.46
3321	40.8	71.8	21.72	21.13	0.58
3322	41.7	73.8	21.91	21.68	0.23
3323	40.4	76.7	20.48	20.48	0.00
3324	42.5	77.3	22.18	22.02	0.15
3325	54.3	109.5	21.91	21.37	0.54
3326	50.7	108.9	21.68	21.76	-0.09
3327	56.4	109.3	22.76	22.18	0.59
3328	52.5	109.8	21.77	21.57	0.21
3329	115.1	109.2	19.79	20.10	-0.31
3330	112.9	109.9	19.56	19.53	0.03
3331	110.3	111.5	20.94	21.07	-0.13
3332	110.8	114.0	21.93	21.32	0.61
3333	109.8	117.0	21.55	21.20	0.35
3334	112.0	118.7	21.73	21.57	0.16
3335	141.8	111.3	22.14	21.66	0.48
3336	144.6	113.7	22.24	22.16	0.08
3337	144.3	116.6	22.26	21.57	0.69
3338	17.6	115.7	23.52	22.18	1.33
3339	16.9	117.8	21.85	21.98	-0.12
3340	14.7	117.7	22.71	22.01	0.70
3341	17.5	123.2	21.38	19.45	1.93
3342	151.9	131.3	21.49	21.95	-0.46
3343	149.3	130.6	19.44	19.56	-0.12
3344	146.6	130.9	21.07	21.13	-0.06
3345	231.6	143.4	22.60	21.89	0.71
3346	229.3	148.8	19.32	19.50	-0.19
3347	229.7	152.7	21.64	21.59	0.05
3348	210.0	148.1	21.60	21.84	-0.24
3349	211.3	147.1	21.92	21.84	0.08
3350	210.1	151.1	22.36	22.70	-0.35
3351	207.9	152.8	21.47	19.82	1.65
3352	227.5	157.1	21.78	22.07	-0.29
3353	226.0	158.6	22.32	21.83	0.49
3354	223.0	162.2	18.67	18.69	-0.02
3355	220.5	159.0	21.73	21.41	0.31
3356	193.5	159.7	21.62	21.44	0.18
3357	196.1	165.1	21.19	21.70	-0.51
3358	198.1	163.5	21.91	21.59	0.32
3359	197.6	165.2	22.06	20.98	1.08
3360	200.7	166.9	21.02	21.35	-0.33

Num	X	Y	B	V	$B-V$
3361	217.0	182.1	20.30	20.39	-0.09
3362	215.0	183.8	20.26	20.50	-0.25
3363	215.8	186.8	20.83	21.17	-0.34
3364	209.9	205.4	21.85	22.08	-0.23
3365	210.6	207.2	23.17	22.16	1.01
3366	211.1	209.8	21.07	20.62	0.45
3367	206.6	208.9	22.17	21.88	0.29
3368	207.5	210.6	22.26	22.41	-0.14
3369	45.9	224.4	22.33	22.15	0.18
3370	39.4	226.6	22.41	21.57	0.84
3371	138.0	235.8	22.39	21.30	1.09
3372	135.3	237.9	21.08	21.15	-0.07
3373	137.8	238.8	22.23	22.02	0.21
3374	140.6	240.1	19.56	19.22	0.34
3375	144.6	240.5	20.25	20.12	0.14
3376	147.6	240.9	22.22	22.20	0.02
3377	125.5	269.2	20.74	21.00	-0.26
3378	124.1	271.8	21.64	21.37	0.27
3379	123.0	273.9	21.23	21.87	-0.64
3380	92.9	279.5	21.42	20.02	1.40
3381	118.1	300.2	21.00	21.63	-0.63
3382	119.7	302.4	22.05	21.97	0.08
3383	116.6	302.5	22.14	22.17	-0.03
3384	118.9	305.3	22.19	22.36	-0.17
3385	101.6	308.2	20.03	20.23	-0.20
3386	100.0	311.2	21.73	22.52	-0.79
3387	99.3	315.6	20.15	20.39	-0.24
3388	100.2	319.1	21.92	22.67	-0.74
3389	80.7	336.3	22.18	22.13	0.05
3390	85.3	336.5	20.76	19.71	1.04
3391	85.8	339.7	19.67	19.77	-0.09
3392	157.1	348.2	21.22	21.36	-0.14
3393	158.2	350.0	19.46	19.69	-0.23
3394	158.9	354.8	22.11	21.10	1.01
3395	160.7	357.1	21.95	22.28	-0.32
3396	119.5	360.7	21.78	21.82	-0.04
3397	119.0	362.2	20.66	21.31	-0.65
3398	121.7	364.7	20.89	21.25	-0.37
3399	115.0	366.9	19.62	19.88	-0.26
3400	138.8	364.8	20.91	21.04	-0.13
3401	141.5	366.4	22.02	21.93	0.09
3402	141.9	368.5	21.63	21.76	-0.13
3403	139.6	368.9	21.36	21.76	-0.40
3404	140.3	372.2	20.25	20.52	-0.27
3405	140.5	374.4	20.42	20.84	-0.42
3406	176.4	369.2	21.95	22.11	-0.16
3407	177.4	371.9	22.26	21.67	0.60
3408	173.5	372.6	21.69	21.93	-0.24
3409	77.3	379.1	21.13	20.47	0.66
3410	80.3	379.0	21.28	21.38	-0.10
3411	74.9	380.8	21.27	21.68	-0.41
3412	82.3	381.5	21.39	19.76	1.63
3413	76.4	383.4	21.39	22.16	-0.77
3414	82.3	383.0	20.84	20.89	-0.04
3415	138.4	391.7	21.03	21.42	-0.39
3416	141.5	392.7	19.33	19.57	-0.24
3417	143.6	395.3	20.80	21.12	-0.32
3418	255.0	394.0	21.14	21.46	-0.32
3419	254.4	396.1	20.22	20.75	-0.53
3420	258.0	398.5	22.13	20.78	1.35
3421	46.9	425.3	21.61	21.74	-0.13
3422	43.8	425.7	22.36	22.47	-0.10
3423	42.1	426.3	21.64	20.37	1.27
3424	17.9	439.6	20.68	20.72	-0.04
3425	16.9	442.0	22.94	21.65	1.29
3426	20.1	442.9	22.67	22.07	0.60
3427	22.6	443.0	22.88	21.15	1.73
3428	24.0	445.0	21.32	21.69	-0.37
3429	109.1	461.9	20.88	20.97	-0.09
3430	106.2	462.4	22.22	21.02	1.20
3431	105.4	469.4	18.61	17.97	0.64
3432	97.4	465.0	21.28	21.10	0.18
3433	99.2	466.6	20.15	20.01	0.14
3434	100.3	470.2	22.86	21.86	1.00
3435	97.8	470.3	21.92	22.29	-0.37
3436	38.5	474.8	20.21	20.32	-0.11
3437	41.8	476.2	19.75	20.04	-0.28
3438	36.0	478.0	19.19	19.31	-0.12
3439	285.6	19.5	22.47	21.70	0.76
3440	282.3	20.6	23.14	21.53	1.61

Num	X	Y	B	V	$B-V$
3441	284.3	22.9	20.99	20.93	0.06
3442	281.1	23.6	21.67	21.66	0.01
3443	284.2	26.6	23.00	22.08	0.92
3444	265.5	26.6	18.82	18.43	0.39
3445	269.9	27.1	22.28	21.63	0.65
3446	261.9	27.1	21.07	21.25	-0.18
3447	269.7	29.0	22.27	22.09	0.18
3448	264.1	31.1	18.63	18.37	0.26
3449	190.6	34.6	21.62	21.82	-0.20
3450	192.4	38.1	20.21	20.37	-0.16
3451	195.4	39.9	21.92	22.02	-0.10
3452	192.5	41.4	22.40	22.30	0.10
3453	154.5	100.3	20.69	20.88	-0.19
3454	154.7	103.9	22.34	23.11	-0.78
3455	157.2	107.8	22.29	22.30	-0.01
3456	164.2	106.6	22.37	21.78	0.59
3457	115.9	121.7	22.52	22.01	0.51
3458	112.4	125.4	20.61	20.61	0.00
3459	117.3	128.1	22.19	21.18	1.01
3460	114.7	127.5	22.10	21.57	0.54
3461	22.2	138.5	20.50	19.96	0.54
3462	20.0	138.2	22.54	21.58	0.96
3463	19.5	142.1	22.35	21.13	1.22
3464	16.4	140.8	22.12	22.32	-0.20
3465	132.3	138.5	22.81	22.10	0.71
3466	132.6	141.3	19.92	19.83	0.08
3467	131.6	144.6	22.25	21.38	0.87
3468	126.8	142.8	21.76	22.07	-0.31
3469	176.8	141.1	21.47	20.56	0.91
3470	179.6	142.9	20.95	21.10	-0.15
3471	178.0	145.8	20.66	20.19	0.47
3472	181.3	147.2	18.35	18.16	0.19
3473	183.5	151.3	21.66	21.02	0.65
3474	207.2	164.4	19.48	19.49	-0.02
3475	205.9	167.4	21.86	22.20	-0.34
3476	211.7	167.5	19.88	19.98	-0.09
3477	214.2	166.4	21.24	20.89	0.35
3478	209.0	170.2	22.70	21.82	0.88
3479	288.7	166.6	20.70	20.97	-0.27
3480	294.0	167.4	21.59	21.64	-0.05
3481	293.8	170.2	21.64	20.98	0.66
3482	221.0	177.5	21.60	20.21	1.39
3483	223.5	178.2	21.41	21.06	0.35
3484	223.1	183.0	20.76	20.82	-0.05
3485	220.6	183.8	21.17	21.04	0.13
3486	41.1	180.2	21.84	22.23	-0.40
3487	37.7	185.6	22.44	21.68	0.76
3488	39.0	191.1	21.98	21.23	0.75
3489	150.0	244.9	21.00	20.80	0.20
3490	149.0	247.5	19.82	20.08	-0.25
3491	145.8	249.7	21.59	21.55	0.04
3492	143.1	250.5	22.13	22.50	-0.37
3493	147.4	253.5	21.00	21.09	-0.09
3494	144.9	253.8	22.56	20.92	1.64
3495	15.1	290.8	21.44	21.50	-0.06
3496	18.2	291.6	21.37	21.58	-0.21
3497	20.8	292.6	20.53	20.34	0.19
3498	24.6	292.8	21.63	21.48	0.15
3499	28.1	292.3	22.25	21.27	0.98
3500	24.6	295.0	21.95	21.90	0.05
3501	16.1	309.0	21.29	22.40	-1.11
3502	16.5	313.1	20.66	20.80	-0.14
3503	15.4	315.0	22.35	21.76	0.58
3504	12.4	313.9	20.64	20.91	-0.26
3505	117.8	318.2	20.46	20.60	-0.14
3506	119.8	319.2	22.23	21.71	0.52
3507	116.4	319.3	21.79	21.86	-0.07
3508	114.7	320.7	20.94	21.18	-0.24
3509	112.1	319.8	20.72	20.71	0.01
3510	114.1	324.6	20.61	20.35	0.26
3511	116.7	326.9	21.65	21.90	-0.25
3512	140.6	319.0	22.52	21.45	1.08
3513	142.3	319.5	23.16	21.99	1.18
3514	144.1	321.9	21.17	20.98	0.18
3515	136.6	319.6	22.62	21.94	0.68
3516	137.7	322.5	21.98	21.76	0.21
3517	16.6	343.9	21.91	22.18	-0.26
3518	18.0	345.2	21.01	21.32	-0.31
3519	14.7	347.3	21.63	21.92	-0.29
3520	15.6	350.5	19.34	20.20	-0.86

Num	X	Y	B	V	$B-V$
3521	12.8	352.0	21.42	21.71	-0.29
3522	108.1	366.2	20.12	20.20	-0.08
3523	104.1	367.6	20.28	19.26	1.02
3524	111.5	371.4	20.64	21.13	-0.49
3525	169.9	372.5	21.21	21.69	-0.48
3526	169.1	380.2	22.10	21.11	0.99
3527	34.7	421.6	21.15	21.00	0.15
3528	32.3	423.8	20.52	20.87	-0.35
3529	36.7	425.1	20.98	21.19	-0.22
3530	31.9	427.4	20.92	21.22	-0.29
3531	35.1	428.9	21.86	21.24	0.63
3532	134.1	439.7	21.67	22.56	-0.89
3533	135.9	442.0	20.15	20.45	-0.30
3534	132.4	443.0	21.53	21.43	0.10
3535	135.6	443.4	21.29	21.26	0.04
3536	130.2	442.8	19.51	19.98	-0.47
3537	287.9	439.8	22.66	22.08	0.58
3538	286.7	443.9	21.72	21.65	0.06
3539	293.8	441.7	21.62	21.45	0.17
3540	291.9	445.8	20.93	21.11	-0.19
3541	305.0	447.8	22.28	21.71	0.56
3542	308.8	448.4	21.89	22.25	-0.36
3543	301.7	448.2	21.30	21.12	0.18
3544	302.9	450.4	23.52	21.39	2.14
3545	304.6	451.7	21.30	20.95	0.35
3546	34.5	451.0	20.76	19.41	1.35
3547	31.9	451.1	21.43	21.76	-0.33
3548	36.9	454.3	21.18	21.50	-0.32
3549	34.8	455.2	21.94	21.80	0.14
3550	54.0	467.8	20.38	20.39	-0.02
3551	48.4	467.9	21.90	20.53	1.37
3552	46.8	465.8	22.08	22.17	-0.10
3553	47.8	471.0	21.52	21.28	0.23
3554	44.8	472.1	19.58	19.89	-0.31
3555	207.0	26.4	20.92	18.75	2.17
3556	211.6	28.1	23.24	22.21	1.03
3557	206.1	32.9	20.47	20.59	-0.12
3558	201.8	32.2	22.57	21.80	0.76
3559	201.6	33.9	21.52	21.77	-0.26
3560	262.3	36.0	21.10	21.26	-0.16
3561	261.4	39.4	22.20	22.37	-0.17
3562	267.6	36.2	21.48	21.93	-0.46
3563	266.2	38.8	21.07	20.72	0.35
3564	264.8	41.1	20.90	20.98	-0.09
3565	266.8	41.7	21.47	22.31	-0.84
3566	263.7	46.9	22.71	21.81	0.90
3567	261.8	47.2	22.75	22.64	0.11
3568	256.4	47.7	21.98	20.84	1.13
3569	254.7	50.4	21.67	21.94	-0.27
3570	257.0	53.1	21.35	21.36	-0.01
3571	255.8	54.4	22.04	22.14	-0.10
3572	46.6	67.1	22.37	22.51	-0.14
3573	47.3	68.7	23.10	21.94	1.15
3574	50.3	70.3	19.46	19.29	0.17
3575	46.2	71.1	22.78	22.40	0.38
3576	269.5	129.0	19.87	19.96	-0.09
3577	276.3	130.5	20.74	20.63	0.11
3578	272.5	133.7	19.96	19.97	-0.02
3579	277.2	127.5	22.19	22.23	-0.04
3580	271.3	137.3	23.06	22.79	0.27
3581	163.7	165.3	21.67	21.91	-0.24
3582	163.1	168.4	19.25	19.16	0.09
3583	159.7	169.9	22.34	22.09	0.25
3584	164.6	171.6	21.85	22.31	-0.46
3585	158.9	172.8	21.75	21.77	-0.02
3586	157.1	175.6	21.39	21.15	0.23
3587	60.5	203.8	22.58	21.44	1.14
3588	63.0	205.9	21.34	21.55	-0.21
3589	59.1	203.2	22.19	22.19	0.00
3590	62.5	209.3	22.82	22.09	0.73
3591	65.0	209.4	20.86	20.87	-0.02
3592	67.3	206.9	21.27	21.87	-0.60
3593	65.4	212.4	21.72	21.90	-0.19
3594	109.7	257.0	21.47	21.87	-0.40
3595	111.8	258.9	22.45	22.28	0.17
3596	110.3	261.5	19.24	19.33	-0.09
3597	113.8	260.7	18.99	19.23	-0.25
3598	106.8	263.6	20.87	21.39	-0.52
3599	109.9	266.5	19.18	19.23	-0.05
3600	217.3	271.8	20.93	20.95	-0.02

Num	X	Y	B	V	$B-V$
3601	216.6	275.4	20.82	21.07	-0.25
3602	212.6	272.2	21.64	21.45	0.19
3603	217.6	277.9	22.54	22.39	0.16
3604	209.7	272.7	22.88	21.95	0.92
3605	211.4	273.8	21.49	21.12	0.38
3606	88.3	288.3	19.28	19.50	-0.22
3607	90.9	289.7	23.06	22.74	0.32
3608	91.4	292.1	22.67	21.90	0.77
3609	86.7	293.0	21.80	21.82	-0.02
3610	81.6	293.6	22.28	21.59	0.69
3611	140.7	294.0	21.01	21.54	-0.53
3612	140.6	296.7	22.12	22.21	-0.09
3613	142.1	302.8	20.68	20.78	-0.10
3614	136.0	302.7	22.23	21.65	0.58
3615	44.2	305.0	20.42	19.84	0.58
3616	40.8	305.7	20.97	20.82	0.15
3617	37.5	305.6	22.72	22.88	-0.16
3618	35.8	308.2	21.52	21.84	-0.32
3619	36.3	345.7	22.02	21.81	0.21
3620	38.5	347.6	22.06	21.51	0.54
3621	34.3	348.9	20.73	20.94	-0.20
3622	36.4	349.8	21.74	22.21	-0.47
3623	32.7	352.2	20.97	21.03	-0.06
3624	31.9	354.5	20.78	21.15	-0.37
3625	14.8	355.8	22.90	22.06	0.84
3626	18.4	360.5	20.77	20.78	0.00
3627	15.1	362.2	21.61	21.16	0.46
3628	19.9	364.1	22.64	22.36	0.28
3629	13.7	365.2	20.53	20.80	-0.28
3630	14.8	367.4	20.85	21.10	-0.25
3631	184.0	366.8	22.05	22.44	-0.39
3632	182.6	368.2	22.11	22.10	0.00
3633	180.7	369.3	22.85	23.48	-0.63
3634	184.7	370.9	21.23	21.63	-0.41
3635	188.4	369.2	21.04	21.33	-0.29
3636	187.6	373.0	21.82	21.75	0.07
3637	238.7	368.3	20.51	20.90	-0.39
3638	242.0	369.5	20.98	21.60	-0.62
3639	246.2	370.2	20.97	21.57	-0.60
3640	244.0	374.1	21.63	21.92	-0.28
3641	248.9	371.2	23.05	22.43	0.61
3642	129.6	376.8	20.89	21.60	-0.71
3643	129.7	379.1	22.17	20.71	1.46
3644	131.9	382.5	20.67	20.33	0.35
3645	131.2	383.7	18.71	19.03	-0.32
3646	133.4	385.1	20.96	21.02	-0.06
3647	136.9	386.4	18.95	18.92	0.03
3648	188.9	386.9	22.48	21.93	0.55
3649	185.6	387.8	22.42	21.78	0.65
3650	191.0	388.2	22.35	22.10	0.24
3651	188.6	392.6	22.19	21.81	0.38
3652	191.0	393.4	21.47	20.95	0.52
3653	181.9	396.2	22.01	21.97	0.05
3654	181.9	399.2	20.75	20.86	-0.11
3655	179.8	399.3	21.56	21.74	-0.18
3656	184.8	398.4	22.20	22.14	0.06
3657	184.6	402.5	20.71	21.15	-0.44
3658	183.9	405.0	18.75	18.53	0.22
3659	59.0	403.8	20.78	20.57	0.21
3660	56.2	405.1	21.24	21.78	-0.54
3661	59.5	408.4	22.14	20.91	1.23
3662	56.7	411.3	21.59	21.01	0.58
3663	242.9	403.7	21.01	21.50	-0.49
3664	241.9	405.2	22.22	21.81	0.41
3665	248.4	406.0	18.71	19.15	-0.43
3666	252.3	404.7	21.90	21.88	0.01
3667	41.0	412.6	19.52	18.35	1.16
3668	41.9	420.3	20.73	20.61	0.13
3669	45.8	418.9	21.82	21.79	0.03
3670	45.9	422.0	21.60	21.81	-0.21
3671	48.7	421.2	21.62	21.65	-0.03
3672	272.7	413.6	22.53	21.92	0.61
3673	272.3	418.3	22.19	22.32	-0.13
3674	276.8	418.9	21.60	21.92	-0.32
3675	281.5	419.7	22.44	22.51	-0.07
3676	9.5	429.2	22.44	22.27	0.17
3677	10.6	431.4	20.25	20.46	-0.20
3678	13.2	431.1	21.54	21.74	-0.19
3679	8.8	433.9	22.12	22.15	-0.03
3680	8.7	436.1	21.45	21.73	-0.28

Num	X	Y	B	V	$B-V$
3681	11.9	437.8	20.21	20.50	-0.29
3682	47.4	440.2	21.45	21.16	0.29
3683	45.8	440.9	21.67	21.63	0.04
3684	51.5	445.3	21.01	21.09	-0.08
3685	47.7	445.0	22.74	22.26	0.48
3686	139.6	440.3	19.98	20.35	-0.38
3687	145.1	439.0	21.25	20.82	0.43
3688	150.9	439.5	18.36	18.86	-0.49
3689	142.2	441.5	20.59	21.10	-0.51
3690	141.5	450.2	21.76	22.72	-0.95
3691	143.0	451.9	22.06	21.36	0.70
3692	142.2	454.2	21.16	21.49	-0.34
3693	148.5	456.9	22.12	22.37	-0.25
3694	148.5	459.1	21.58	22.13	-0.55
3695	223.7	107.5	22.45	22.45	0.01
3696	225.6	110.7	19.63	19.77	-0.15
3697	222.6	111.1	20.58	20.92	-0.34
3698	219.8	109.0	20.99	21.27	-0.28
3699	222.2	113.9	20.64	20.88	-0.24
3700	219.0	107.1	20.93	21.18	-0.25
3701	230.7	125.6	22.42	22.01	0.41
3702	231.8	127.5	22.50	21.75	0.75
3703	230.5	131.9	19.20	17.76	1.44
3704	221.5	133.4	18.95	19.01	-0.06
3705	225.5	135.1	22.54	21.89	0.65
3706	218.3	132.5	23.45	22.83	0.63
3707	275.8	170.0	21.40	21.35	0.05
3708	276.5	171.7	20.47	20.32	0.15
3709	278.2	172.3	21.48	22.23	-0.75
3710	275.5	177.1	22.02	21.42	0.59
3711	272.3	176.7	21.38	21.57	-0.19
3712	273.8	179.5	20.59	20.48	0.11
3713	270.6	178.8	21.62	21.79	-0.17
3714	48.6	183.9	21.65	20.19	1.46
3715	47.3	187.0	21.89	22.28	-0.39
3716	46.0	191.6	21.20	21.41	-0.21
3717	50.8	191.5	20.29	20.37	-0.08
3718	52.4	190.3	22.90	22.09	0.80
3719	54.2	190.4	23.13	21.89	1.24
3720	201.3	187.4	21.69	21.77	-0.08
3721	198.9	188.3	21.38	21.15	0.23
3722	203.5	189.6	22.43	21.65	0.78
3723	196.1	188.6	22.06	22.55	-0.49
3724	195.1	192.2	18.95	18.99	-0.04
3725	209.0	188.1	20.56	20.56	0.00
3726	191.4	190.8	21.59	21.52	0.06
3727	211.3	188.0	21.63	20.99	0.64
3728	48.4	205.0	21.95	21.30	0.65
3729	45.9	208.5	20.50	20.51	-0.01
3730	41.2	209.9	22.36	21.51	0.84
3731	49.8	210.9	21.71	21.63	0.08
3732	38.3	211.7	22.25	22.24	0.02
3733	30.4	226.2	22.45	21.62	0.83
3734	34.7	218.5	22.54	22.16	0.38
3735	32.4	222.1	19.16	19.38	-0.22
3736	30.6	221.0	20.29	20.17	0.13
3737	30.4	224.2	20.19	20.35	-0.16
3738	27.7	219.7	22.02	21.89	0.14
3739	49.6	316.5	20.70	21.09	-0.39
3740	53.9	315.6	20.22	20.59	-0.37
3741	56.7	317.5	21.34	21.21	0.13
3742	58.0	314.1	21.85	21.85	0.00
3743	58.4	318.1	21.47	21.54	-0.07
3744	58.7	321.6	22.01	22.48	-0.48
3745	185.3	314.9	19.88	20.23	-0.35
3746	183.8	316.5	21.02	20.66	0.36
3747	186.3	318.5	18.39	18.71	-0.32
3748	189.8	317.0	20.89	21.00	-0.11
3749	186.0	322.5	19.75	20.08	-0.32
3750	43.8	376.9	22.08	21.91	0.16
3751	45.1	379.6	20.64	20.12	0.52
3752	41.5	380.8	18.73	18.94	-0.21
3753	47.7	381.6	20.04	20.28	-0.25
3754	38.3	380.3	19.58	19.83	-0.25
3755	43.3	383.9	21.73	21.76	-0.03
3756	50.7	381.5	19.67	20.10	-0.43
3757	53.5	379.8	21.85	21.81	0.05
3758	107.9	415.4	18.64	18.89	-0.25
3759	106.0	420.1	20.84	21.08	-0.24
3760	108.5	422.5	20.35	20.83	-0.47

Num	X	Y	B	V	$B-V$
3761	107.8	424.8	21.09	20.36	0.73
3762	16.4	453.0	21.35	21.73	-0.38
3763	19.9	455.9	21.89	22.12	-0.23
3764	22.4	455.3	21.49	22.33	-0.84
3765	224.2	47.8	22.78	22.51	0.27
3766	222.6	50.6	21.35	20.77	0.59
3767	224.0	52.6	22.28	21.56	0.71
3768	227.7	53.6	21.64	21.76	-0.11
3769	218.6	54.2	21.26	21.07	0.19
3770	229.8	54.8	22.95	21.85	1.10
3771	120.4	115.0	21.68	21.49	0.19
3772	124.3	117.8	22.48	21.68	0.80
3773	126.5	118.0	21.83	21.89	-0.06
3774	129.3	118.9	22.66	21.74	0.92
3775	131.6	119.7	21.86	20.27	1.60
3776	132.9	118.2	22.77	22.72	0.06
3777	136.7	123.1	21.24	21.39	-0.14
3778	136.6	124.7	22.45	22.30	0.15
3779	238.6	151.6	22.81	22.36	0.45
3780	237.2	154.1	21.62	21.55	0.07
3781	239.7	154.6	22.53	22.25	0.29
3782	236.8	158.5	21.53	21.36	0.17
3783	236.5	163.0	20.14	20.37	-0.23
3784	178.4	160.1	23.15	22.34	0.81
3785	179.2	162.0	22.00	21.01	0.99
3786	181.2	164.4	21.87	21.99	-0.11
3787	182.6	167.1	21.58	21.59	-0.01
3788	179.6	167.7	21.33	22.01	-0.68
3789	184.6	168.9	21.70	21.50	0.20
3790	17.6	224.6	22.31	22.25	0.05
3791	17.1	227.0	23.03	21.52	1.51
3792	20.4	227.8	22.24	21.62	0.63
3793	18.6	229.3	19.71	19.98	-0.26
3794	15.2	231.0	22.26	22.29	-0.03
3795	19.5	232.6	22.24	22.18	0.06
3796	16.5	233.1	19.99	20.32	-0.33
3797	21.7	234.3	21.88	22.20	-0.32
3798	23.3	233.7	22.04	21.66	0.38
3799	22.4	231.5	23.25	22.08	1.18
3800	236.6	282.9	21.11	21.24	-0.13
3801	236.6	288.6	21.42	21.40	0.02
3802	234.8	291.3	20.70	21.00	-0.30
3803	234.1	294.6	21.31	21.81	-0.51
3804	230.8	291.1	22.08	22.31	-0.23
3805	230.3	294.8	20.03	20.16	-0.13
3806	103.4	283.3	23.27	21.42	1.85
3807	100.1	283.6	19.70	19.78	-0.08
3808	105.4	286.2	22.71	22.16	0.55
3809	104.2	289.7	20.23	20.18	0.05
3810	106.5	289.7	22.26	22.05	0.22
3811	113.6	286.7	21.79	21.59	0.21
3812	111.8	288.4	22.72	21.73	0.99
3813	110.7	291.3	22.57	22.48	0.09
3814	167.9	289.6	21.96	21.74	0.22
3815	168.8	291.4	21.18	21.10	0.08
3816	168.9	294.9	22.84	22.12	0.71
3817	166.6	296.3	21.57	21.88	-0.32
3818	162.5	297.8	21.40	22.22	-0.82
3819	161.9	300.9	21.62	21.13	0.48
3820	161.4	294.4	20.91	21.13	-0.22
3821	163.4	304.2	21.62	21.36	0.26
3822	29.6	303.4	21.67	22.06	-0.39
3823	28.2	305.3	21.53	21.66	-0.13
3824	26.2	307.7	21.28	21.03	0.24
3825	24.8	308.7	19.54	19.84	-0.30
3826	19.8	310.5	21.47	21.85	-0.38
3827	303.2	422.8	18.70	18.98	-0.28
3828	304.5	426.1	22.15	21.90	0.25
3829	301.0	426.6	21.44	21.20	0.25
3830	304.3	430.2	21.09	21.60	-0.51
3831	302.2	434.5	22.35	22.38	-0.02
3832	122.8	54.5	20.84	20.99	-0.15
3833	126.3	54.7	19.91	18.84	1.07
3834	123.5	58.2	24.12	23.24	0.88
3835	126.9	60.3	20.68	20.36	0.31
3836	128.5	59.4	22.91	22.35	0.56
3837	121.6	63.0	18.87	19.45	-0.58
3838	130.6	57.6	23.18	23.05	0.13
3839	91.9	107.8	22.73	22.30	0.42
3840	91.3	110.8	21.90	21.40	0.50

Num	X	Y	B	V	$B-V$
3841	94.8	110.6	22.11	22.13	-0.02
3842	91.6	113.6	22.30	22.37	-0.07
3843	94.3	114.2	21.08	21.17	-0.09
3844	91.4	116.4	21.84	22.13	-0.29
3845	93.3	118.8	22.13	21.31	0.82
3846	96.7	122.9	21.43	21.14	0.29
3847	95.6	124.8	20.73	20.82	-0.09
3848	95.2	128.3	23.17	22.29	0.88
3849	115.8	194.1	22.13	21.18	0.95
3850	113.7	194.6	22.02	21.89	0.13
3851	112.8	197.6	21.88	22.09	-0.21
3852	120.6	196.2	22.20	21.58	0.62
3853	124.2	197.0	20.50	20.24	0.25
3854	122.8	199.9	22.77	22.97	-0.20
3855	121.7	202.8	22.09	21.50	0.60
3856	123.4	202.9	22.14	22.42	-0.28
3857	222.5	204.2	20.58	20.67	-0.09
3858	223.1	207.6	21.32	21.73	-0.40
3859	221.1	210.1	22.42	21.46	0.95
3860	221.6	216.1	22.29	21.91	0.38
3861	217.6	217.1	22.36	22.20	0.16
3862	205.0	279.0	22.11	22.40	-0.29
3863	208.5	281.0	23.19	22.49	0.70
3864	213.5	279.4	21.79	21.43	0.36
3865	8.2	389.3	19.96	19.59	0.37
3866	9.2	391.9	18.46	18.09	0.37
3867	10.3	393.1	19.30	20.08	-0.78
3868	5.5	393.6	20.23	20.48	-0.25
3869	7.3	396.0	18.69	18.69	0.00
3870	4.5	397.3	21.62	21.54	0.08
3871	8.6	400.0	21.26	21.34	-0.08
3872	9.7	401.6	21.42	21.91	-0.49
3873	281.6	435.2	21.83	21.33	0.50
3874	284.5	433.7	20.13	20.66	-0.53
3875	286.5	430.9	21.85	22.38	-0.53
3876	288.0	434.3	20.92	21.54	-0.61
3877	291.6	434.0	19.59	19.65	-0.05
3878	294.1	436.0	19.80	19.45	0.35
3879	298.3	434.9	20.23	20.20	0.03
3880	297.4	437.0	18.65	19.12	-0.47
3881	28.9	431.4	22.59	21.99	0.60
3882	30.9	431.9	21.42	21.78	-0.35
3883	29.9	435.1	21.72	21.91	-0.19
3884	32.2	436.2	22.25	21.11	1.14
3885	27.8	440.5	20.96	22.03	-1.07
3886	28.2	443.1	21.56	21.33	0.23
3887	28.1	445.7	21.53	20.42	1.11
3888	26.9	6.4	22.91	22.01	0.89
3889	28.9	7.3	20.51	20.03	0.48
3890	22.9	8.1	22.68	21.97	0.71
3891	24.7	9.7	23.05	21.82	1.22
3892	30.4	9.3	23.26	21.82	1.44
3893	28.4	10.8	22.06	21.63	0.43
3894	29.6	12.2	23.53	22.33	1.21
3895	110.9	212.8	21.57	22.13	-0.56
3896	109.6	215.4	20.77	20.65	0.12
3897	108.9	216.8	22.04	21.94	0.11
3898	115.3	219.8	22.39	20.85	1.53
3899	119.0	215.8	22.96	21.67	1.28
3900	121.8	215.0	22.29	21.81	0.49
3901	262.6	244.6	21.42	20.72	0.70
3902	266.6	244.8	20.58	20.82	-0.24
3903	264.1	246.6	19.93	20.27	-0.34
3904	260.1	247.1	20.54	20.61	-0.07
3905	259.3	249.9	21.32	21.28	0.03
3906	263.1	251.4	20.91	21.43	-0.53
3907	40.8	293.5	21.54	21.91	-0.37
3908	38.0	294.2	21.73	21.05	0.67
3909	35.8	295.9	19.05	19.18	-0.13
3910	39.8	297.4	21.73	22.12	-0.39
3911	31.6	295.9	22.78	22.14	0.64
3912	31.6	297.6	21.46	21.74	-0.28
3913	29.3	299.3	21.86	21.16	0.70
3914	27.3	298.7	21.32	21.38	-0.06
3915	182.5	328.2	21.33	21.34	-0.01
3916	179.1	329.7	22.20	21.41	0.80
3917	181.5	334.1	21.55	21.88	-0.33
3918	180.4	338.1	21.16	21.08	0.08
3919	181.0	341.0	22.14	21.96	0.18
3920	162.2	380.7	21.25	21.57	-0.32

Num	X	Y	B	V	$B-V$
3921	161.4	383.9	19.51	19.39	0.12
3922	158.6	386.2	22.65	21.69	0.96
3923	162.1	388.3	18.52	18.77	-0.25
3924	165.2	390.3	18.52	18.72	-0.20
3925	169.2	391.1	22.24	21.28	0.97
3926	168.7	384.6	22.64	22.99	-0.36
3927	171.8	388.1	20.58	20.99	-0.41
3928	255.6	382.5	21.96	22.56	-0.60
3929	251.6	383.3	20.18	20.90	-0.72
3930	250.6	385.0	20.66	21.00	-0.35
3931	250.4	388.9	20.82	20.79	0.03
3932	247.0	391.9	21.71	21.84	-0.13
3933	250.0	393.5	21.33	21.58	-0.25
3934	167.6	418.2	22.06	22.01	0.05
3935	167.5	420.7	21.65	21.83	-0.18
3936	163.9	422.1	20.48	20.45	0.04
3937	168.9	423.2	22.81	22.17	0.64
3938	161.9	424.3	19.10	19.42	-0.32
3939	168.4	426.4	21.06	21.55	-0.49
3940	159.1	421.2	20.23	19.28	0.95
3941	157.9	425.2	21.15	21.90	-0.75
3942	170.8	426.3	22.22	21.90	0.31
3943	163.6	452.5	21.38	21.95	-0.57
3944	161.2	455.5	21.33	21.04	0.29
3945	160.6	457.9	20.49	20.46	0.03
3946	159.6	460.9	21.22	21.39	-0.17
3947	161.5	462.7	21.44	20.90	0.55
3948	163.8	462.9	20.04	20.10	-0.06
3949	158.9	464.4	19.94	21.02	-1.08
3950	165.9	459.5	21.51	21.58	-0.07
3951	99.3	57.5	20.55	20.28	0.27
3952	101.2	57.6	22.56	20.81	1.75
3953	96.1	58.6	21.96	21.83	0.13
3954	94.1	58.1	22.04	21.52	0.52
3955	93.1	55.7	22.87	22.36	0.51
3956	91.7	60.0	21.89	21.75	0.14
3957	90.2	61.8	22.35	22.55	-0.20
3958	88.4	62.5	21.77	21.74	0.03
3959	86.3	63.6	22.30	21.89	0.41
3960	83.6	62.4	22.37	22.60	-0.24
3961	304.5	158.8	20.89	20.76	0.13
3962	307.6	160.0	21.29	21.65	-0.37
3963	297.1	165.5	22.11	21.87	0.24
3964	299.2	161.1	19.71	19.24	0.46
3965	303.0	164.2	20.67	20.97	-0.30
3966	305.2	165.6	22.68	21.28	1.40
3967	303.2	167.1	20.48	20.65	-0.17
3968	307.8	166.1	20.89	20.99	-0.10
3969	299.5	167.4	21.49	21.61	-0.12
3970	302.5	168.9	21.06	21.35	-0.29
3971	246.5	179.1	22.08	22.18	-0.11
3972	243.6	180.2	19.93	19.90	0.04
3973	242.2	193.9	21.30	21.19	0.11
3974	244.7	184.1	20.18	20.20	-0.03
3975	244.4	186.9	19.57	19.55	0.02
3976	239.2	183.4	18.84	19.02	-0.19
3977	239.5	186.8	20.76	20.97	-0.21
3978	238.4	189.7	22.17	21.75	0.42
3979	240.9	192.2	20.86	20.93	-0.07
3980	95.3	181.9	21.36	21.87	-0.51
3981	94.8	184.1	20.76	21.15	-0.40
3982	97.0	185.6	21.92	22.15	-0.23
3983	93.6	185.9	20.92	21.06	-0.14
3984	96.1	188.9	20.83	20.92	-0.09
3985	99.4	188.7	20.82	21.07	-0.25
3986	93.0	190.6	20.90	21.22	-0.32
3987	91.6	189.4	23.34	21.72	1.63
3988	102.4	194.5	20.97	21.32	-0.35
3989	235.8	245.6	21.61	20.64	0.97
3990	234.4	247.7	22.33	22.79	-0.47
3991	236.2	250.0	21.86	21.25	0.61
3992	242.4	254.9	21.94	21.88	0.07
3993	241.9	260.9	21.82	21.28	0.53
3994	239.3	258.7	20.83	21.15	-0.32
3995	241.0	263.6	21.96	22.15	-0.19
3996	244.5	264.1	22.23	22.42	-0.19
3997	25.6	333.8	22.02	22.63	-0.61
3998	27.7	336.4	21.21	20.54	0.67
3999	31.0	336.1	20.75	20.33	0.43
4000	27.4	338.6	22.83	22.48	0.35

Num	X	Y	B	V	$B-V$
4001	25.5	342.6	19.45	19.52	-0.07
4002	23.0	342.7	21.44	21.48	-0.04
4003	26.7	347.1	21.58	21.62	-0.04
4004	24.7	349.6	22.32	21.76	0.55
4005	22.2	350.7	21.42	20.34	1.08
4006	23.0	352.3	21.83	22.11	-0.28
4007	21.3	354.4	22.02	22.32	-0.29
4008	209.0	60.2	21.46	21.01	0.45
4009	208.5	63.2	22.03	22.25	-0.22
4010	209.5	65.0	21.84	21.79	0.05
4011	211.6	65.8	22.36	22.48	-0.12
4012	213.9	67.6	21.80	21.26	0.54
4013	212.7	62.3	21.83	22.36	-0.53
4014	214.9	71.4	22.54	23.15	-0.61
4015	214.5	73.2	22.07	22.10	-0.03
4016	219.0	60.8	22.18	22.24	-0.06
4017	136.6	149.7	23.24	21.72	1.52
4018	138.2	151.0	19.82	19.92	-0.10
4019	142.9	156.9	22.03	21.89	0.14
4020	148.0	154.4	19.96	19.77	0.18
4021	150.3	152.9	22.56	22.31	0.25
4022	152.5	153.1	21.88	21.82	0.05
4023	146.0	160.2	21.73	21.12	0.61
4024	152.0	150.1	21.21	21.69	-0.47
4025	235.1	270.2	20.78	21.07	-0.29
4026	237.5	270.2	22.19	22.45	-0.26
4027	241.3	273.6	20.37	20.37	0.00
4028	245.3	273.5	21.02	21.27	-0.25
4029	245.8	270.9	21.28	21.63	-0.35
4030	248.1	273.4	22.75	22.53	0.21
4031	254.3	275.3	21.85	21.93	-0.08
4032	253.4	278.0	23.22	22.39	0.83
4033	250.6	278.1	22.87	22.08	0.79
4034	156.0	359.3	22.62	21.25	1.37
4035	156.1	364.2	20.27	20.48	-0.21
4036	158.4	365.8	21.84	21.66	0.18
4037	155.0	367.0	22.97	21.63	1.34
4038	150.4	364.2	20.97	20.57	0.40
4039	152.3	367.1	19.98	20.05	-0.08
4040	155.7	369.4	21.94	22.19	-0.25
4041	147.1	362.9	21.17	21.13	0.04
4042	152.4	370.6	21.37	21.43	-0.07
4043	141.1	361.5	20.26	20.44	-0.18
4044	139.2	360.5	20.59	20.90	-0.31
4045	241.0	238.9	21.82	22.91	-1.09
4046	244.8	242.4	22.19	22.13	0.06
4047	242.0	245.5	19.08	18.24	0.84
4048	246.2	248.9	20.30	20.54	-0.24
4049	251.7	250.2	22.28	21.86	0.42
4050	254.3	252.1	19.49	19.60	-0.11
4051	260.8	257.1	21.83	21.53	0.31
4052	254.6	257.6	21.68	20.99	0.69
4053	158.8	324.3	21.95	21.76	0.19
4054	159.8	331.3	21.74	21.70	0.05
4055	152.5	333.8	22.32	22.10	0.21
4056	150.8	337.8	22.99	22.12	0.87
4057	147.7	338.3	19.18	19.19	-0.01
4058	147.2	341.5	20.31	20.39	-0.08
4059	31.4	324.0	20.57	20.14	0.43
4060	33.0	326.5	22.27	22.80	-0.53
4061	35.7	328.4	21.51	21.29	0.23
4062	40.0	326.2	21.42	22.05	-0.63
4063	40.9	330.0	20.77	20.69	0.07
4064	44.6	330.3	22.78	21.19	1.59
4065	38.4	331.1	21.42	21.90	-0.48
4066	40.9	333.1	20.95	21.07	-0.12
4067	44.6	327.1	21.52	20.82	0.71
4068	47.8	331.3	21.82	21.75	0.07
4069	42.3	334.9	19.98	19.65	0.33
4070	46.5	324.7	21.96	22.02	-0.07
4071	48.0	326.3	22.19	22.18	0.02
4072	56.3	383.6	20.97	20.26	0.71
4073	58.6	385.5	21.09	21.37	-0.28
4074	60.2	387.5	18.73	18.86	-0.13
4075	60.9	391.6	20.03	20.27	-0.24
4076	64.0	396.4	20.25	19.59	0.66
4077	59.3	396.8	21.13	21.57	-0.44
4078	62.1	397.9	21.29	21.27	0.02
4079	63.1	404.0	20.73	20.84	-0.11
4080	66.5	403.3	21.47	20.17	1.30

Num	X	Y	B	V	$B-V$
4081	69.2	401.0	18.01	18.14	-0.13
4082	71.2	401.4	19.98	20.17	-0.19
4083	111.1	29.4	21.33	20.01	1.32
4084	113.9	32.5	19.59	19.52	0.08
4085	108.3	33.1	17.55	17.40	0.15
4086	107.1	41.1	19.01	18.86	0.15
4087	102.5	40.6	21.24	21.54	-0.29
4088	101.3	38.0	21.43	22.10	-0.67
4089	101.2	34.9	19.73	19.66	0.07
4090	98.7	34.4	21.89	22.09	-0.20
4091	186.2	141.9	20.29	21.41	-1.12
4092	187.4	144.6	22.68	21.68	1.00
4093	187.3	147.6	19.98	19.83	0.15
4094	192.1	149.1	19.96	19.91	0.05
4095	193.5	149.7	20.55	20.01	0.54
4096	195.9	145.5	21.47	20.38	1.08
4097	196.6	152.8	21.18	21.11	0.07
4098	199.4	147.6	21.94	21.41	0.53
4099	247.7	193.9	21.86	22.24	-0.38
4100	251.0	194.7	21.34	21.06	0.27
4101	252.4	195.7	21.35	21.51	-0.16
4102	244.7	196.8	21.26	21.54	-0.28
4103	249.2	199.1	21.45	20.96	0.48
4104	250.7	203.0	20.80	20.97	-0.17
4105	240.6	200.3	21.60	21.98	-0.38
4106	253.8	201.9	23.10	21.86	1.24
4107	238.4	201.7	21.83	21.81	0.02
4108	254.9	204.5	22.69	22.38	0.31
4109	103.4	339.9	20.08	20.15	-0.07
4110	106.5	341.3	21.71	21.48	0.24
4111	106.4	344.0	20.29	20.49	-0.20
4112	109.0	346.6	20.48	20.57	-0.10
4113	105.4	348.2	20.73	21.11	-0.38
4114	109.3	349.0	21.46	20.94	0.52
4115	103.5	349.8	21.02	21.41	-0.38
4116	102.0	346.2	20.50	21.18	-0.68
4117	96.9	348.9	20.30	20.30	0.00
4118	100.7	353.2	21.52	20.30	1.22
4119	296.7	454.3	21.37	21.26	0.11
4120	296.4	456.0	21.20	21.44	-0.25
4121	296.7	459.8	22.04	21.38	0.66
4122	299.4	459.0	21.63	20.98	0.65
4123	295.8	464.6	20.80	20.65	0.16
4124	299.5	465.8	20.28	20.55	-0.27
4125	292.9	464.9	22.15	20.90	1.24
4126	302.4	475.2	20.78	20.81	-0.03
4127	69.9	178.3	19.39	19.23	0.16
4128	68.4	180.9	22.56	21.03	1.54
4129	69.8	185.6	18.16	18.08	0.09
4130	64.7	182.4	22.40	22.43	-0.02
4131	69.1	187.6	21.64	21.11	0.53
4132	73.6	190.4	20.00	20.22	-0.22
4133	70.4	193.0	20.83	20.46	0.37
4134	76.9	188.6	21.97	22.36	-0.39
4135	69.1	195.4	21.99	21.73	0.27
4136	66.4	197.4	22.30	21.47	0.82
4137	69.2	198.6	22.84	22.16	0.68
4138	101.7	325.7	19.87	20.29	-0.42
4139	104.3	326.8	20.08	20.36	-0.28
4140	102.8	328.5	21.55	21.81	-0.27
4141	99.5	330.3	21.09	21.17	-0.09
4142	102.4	333.1	19.31	18.74	0.58
4143	98.0	336.0	21.09	21.08	0.01
4144	101.4	335.0	19.93	20.03	-0.10
4145	107.7	330.5	18.02	18.32	-0.29
4146	109.1	333.9	20.43	18.38	2.06
4147	94.4	338.8	20.49	20.94	-0.44
4148	94.5	341.8	17.94	18.02	-0.08
4149	94.2	345.2	20.67	20.82	-0.15
4150	139.2	462.6	22.03	21.81	0.22
4151	138.4	464.7	20.22	20.40	-0.18
4152	135.7	464.9	22.18	22.57	-0.39
4153	134.6	467.2	21.38	20.99	0.38
4154	131.5	463.1	21.54	22.15	-0.61
4155	132.8	468.6	21.79	21.97	-0.17
4156	136.3	474.7	18.68	19.05	-0.37
4157	139.4	476.1	18.72	19.44	-0.72
4158	144.4	474.9	17.06	17.41	-0.35
4159	146.2	478.5	18.60	19.03	-0.42
4160	142.7	469.1	20.73	21.08	-0.35

Num	X	Y	B	V	$B-V$
4161	100.1	374.0	21.38	21.60	-0.21
4162	97.1	376.1	21.37	20.92	0.45
4163	98.5	376.8	20.38	20.71	-0.33
4164	105.5	379.1	18.90	19.29	-0.40
4165	101.2	379.4	19.53	19.66	-0.13
4166	99.2	382.6	20.49	20.82	-0.33
4167	106.6	383.0	17.94	18.52	-0.58
4168	98.2	386.4	21.94	22.36	-0.42
4169	110.9	378.6	18.59	18.93	-0.34
4170	114.1	382.0	18.46	18.58	-0.11
4171	117.9	381.1	22.31	21.55	0.76
4172	114.4	384.3	19.92	19.71	0.21
4173	188.6	7.0	22.78	22.63	0.16
4174	190.9	24.9	21.58	21.43	0.15
4175	190.9	8.2	21.92	20.76	1.16
4176	186.4	10.9	20.17	20.30	-0.13
4177	193.9	8.1	22.81	22.74	0.08
4178	186.4	15.5	21.01	20.66	0.35
4179	185.4	17.2	21.74	22.12	-0.38
4180	191.5	18.7	21.43	21.14	0.28
4181	193.6	16.3	22.09	22.07	0.03
4182	190.7	20.6	21.57	21.46	0.11
4183	195.4	17.3	21.52	21.15	0.37
4184	196.1	19.5	21.22	20.82	0.40
4185	241.6	149.8	22.16	22.16	0.00
4186	242.7	151.3	22.40	21.76	0.64
4187	244.5	153.6	22.45	22.55	-0.10
4188	246.8	155.6	21.39	21.12	0.27
4189	251.2	157.3	20.43	20.63	-0.19
4190	248.9	160.0	21.55	21.06	0.50
4191	253.4	159.5	22.01	21.97	0.05
4192	251.0	162.0	21.35	21.66	-0.30
4193	254.7	161.1	21.45	20.73	0.72
4194	250.6	165.3	21.53	21.87	-0.34
4195	246.1	162.5	22.38	22.60	-0.22
4196	255.7	157.3	21.54	22.24	-0.70
4197	251.4	167.8	21.10	21.26	-0.16
4198	25.3	316.9	21.03	21.08	-0.05
4199	23.8	318.1	21.78	21.16	0.62
4200	25.1	321.4	21.62	20.23	1.39
4201	25.2	323.8	21.02	21.41	-0.39
4202	22.5	325.5	21.88	21.42	0.46
4203	20.0	321.8	20.40	20.19	0.21
4204	15.6	322.7	21.08	20.31	0.77
4205	16.1	325.1	22.06	21.34	0.72
4206	13.0	319.7	21.11	20.34	0.77
4207	17.3	327.3	20.63	20.35	0.28
4208	19.0	332.2	22.97	21.85	1.12
4209	16.5	334.1	21.94	22.18	-0.24
4210	20.2	334.1	20.72	20.30	0.42
4211	14.6	332.2	21.95	21.39	0.56
4212	12.7	332.8	21.33	21.72	-0.40
4213	165.6	129.4	22.31	21.68	0.62
4214	170.1	130.8	21.55	21.69	-0.14
4215	168.3	132.4	23.19	22.75	0.45
4216	159.5	131.5	22.26	21.50	0.76
4217	158.3	133.5	21.85	22.09	-0.25
4218	156.3	132.3	21.77	22.23	-0.45
4219	154.8	133.7	22.03	21.25	0.77
4220	153.1	137.0	21.22	21.47	-0.25
4221	153.9	139.6	21.73	21.46	0.26
4222	155.7	141.5	20.71	20.86	-0.14
4223	153.4	143.0	21.78	22.47	-0.69
4224	158.9	140.2	21.67	21.55	0.12
4225	159.2	137.2	22.37	22.08	0.28
4226	161.0	138.2	22.92	21.50	1.42
4227	161.3	141.9	23.25	22.96	0.30
4228	123.8	385.0	21.37	20.42	0.95
4229	121.5	388.1	21.52	21.32	0.21
4230	119.8	388.2	21.05	19.61	1.44
4231	116.4	388.9	21.31	21.49	-0.18
4232	114.2	391.0	19.14	19.56	-0.42
4233	113.2	396.3	18.93	19.21	-0.27
4234	116.8	397.4	20.02	20.34	-0.32
4235	113.9	399.3	21.07	21.34	-0.27
4236	119.7	400.9	17.33	17.49	-0.17
4237	112.2	401.6	21.10	21.17	-0.07
4238	110.6	403.4	21.68	21.76	-0.09
4239	113.3	406.0	18.65	18.74	-0.09
4240	108.9	407.2	18.91	19.58	-0.67

Num	X	Y	B	V	$B-V$
4241	111.8	412.9	19.69	20.26	-0.57
4242	114.2	410.5	19.19	19.52	-0.32
4243	106.1	407.5	20.75	20.06	0.69
4244	128.7	323.4	21.99	21.84	0.15
4245	128.7	327.6	20.95	21.17	-0.21
4246	125.6	329.0	21.25	20.65	0.60
4247	130.7	329.9	22.09	21.21	0.87
4248	126.1	333.1	19.94	20.09	-0.16
4249	133.4	329.8	22.08	21.68	0.40
4250	125.9	335.1	19.09	19.33	-0.23
4251	135.9	331.1	21.91	21.48	0.43
4252	133.5	333.1	22.40	22.00	0.39
4253	122.9	336.6	19.97	20.22	-0.26
4254	137.8	333.2	22.11	22.10	0.02
4255	141.5	334.0	20.22	20.10	0.12
4256	137.5	335.8	21.98	21.63	0.35
4257	124.5	341.8	21.90	21.11	0.79
4258	141.0	332.3	21.65	21.70	-0.05
4259	135.7	337.9	22.31	22.11	0.20
4260	126.7	342.6	22.76	23.03	-0.27
4261	139.7	330.1	20.92	21.25	-0.33
4262	105.5	390.4	18.00	18.36	-0.35
4263	103.3	392.9	19.04	19.37	-0.33
4264	100.3	393.8	21.68	21.90	-0.22
4265	100.9	396.7	19.01	19.30	-0.29
4266	97.5	395.8	20.82	21.26	-0.44
4267	96.4	399.6	19.72	19.55	0.18
4268	87.9	399.4	21.01	21.31	-0.30
4269	87.6	403.2	20.99	21.58	-0.58
4270	85.2	404.5	21.61	21.47	0.14
4271	83.5	403.9	20.41	20.55	-0.14
4272	79.6	400.2	20.87	19.86	1.01
4273	78.8	398.4	20.66	20.74	-0.08
4274	107.6	440.1	21.72	21.47	0.24
4275	104.9	441.8	20.66	20.50	0.16
4276	108.8	443.6	22.47	21.35	1.12
4277	111.5	443.0	20.40	20.98	-0.57
4278	112.8	445.7	20.34	20.84	-0.49
4279	110.8	451.6	17.38	17.59	-0.22
4280	108.1	453.9	19.49	20.17	-0.69
4281	104.0	449.0	20.28	20.43	-0.14
4282	106.4	455.2	19.68	19.73	-0.05
4283	101.8	447.6	21.82	22.26	-0.44
4284	117.5	447.8	21.26	21.92	-0.66
4285	113.8	458.8	21.28	20.86	0.42
4286	111.8	458.1	21.11	21.27	-0.16
4287	92.7	354.0	20.07	20.44	-0.37
4288	94.8	356.2	21.73	21.76	-0.03
4289	93.5	358.4	20.46	20.69	-0.23
4290	94.0	361.8	21.31	21.70	-0.39
4291	91.6	365.1	20.58	20.90	-0.32
4292	92.5	370.0	21.58	21.43	0.15
4293	90.7	370.9	21.17	21.16	0.00
4294	93.5	372.5	20.84	21.22	-0.37
4295	88.0	372.9	21.01	21.69	-0.68
4296	85.6	374.7	21.05	21.39	-0.35
4297	90.1	375.5	22.04	22.12	-0.08
4298	87.4	376.6	19.93	20.14	-0.21
4299	98.3	369.2	19.90	20.34	-0.44
4300	96.8	370.0	19.85	20.14	-0.29
4301	85.9	377.9	20.92	21.33	-0.40
4302	89.2	379.1	20.72	21.09	-0.37
4303	86.5	382.0	20.50	20.90	-0.41
4304	86.2	384.9	19.85	20.21	-0.35
4305	33.8	367.1	22.02	21.99	0.03
4306	33.0	371.4	19.39	19.50	-0.11
4307	25.9	370.7	20.84	20.50	0.34
4308	34.2	374.0	20.43	20.50	-0.07
4309	30.9	377.0	20.79	21.47	-0.68
4310	21.2	368.0	20.62	21.49	-0.87
4311	17.9	369.9	21.07	20.85	0.22
4312	21.2	372.0	20.87	20.95	-0.08
4313	15.2	374.8	19.04	18.78	0.26
4314	10.6	375.5	21.05	20.92	0.13
4315	9.0	380.0	19.08	19.58	-0.50
4316	7.2	382.2	18.98	18.99	-0.01
4317	22.9	407.0	20.77	20.27	0.50
4318	19.7	408.0	22.37	21.67	0.71
4319	16.8	408.0	20.39	20.02	0.37
4320	18.2	410.8	20.80	21.08	-0.28

Num	X	Y	B	V	$B-V$
4321	13.5	407.3	20.65	20.49	0.16
4322	16.1	413.6	21.43	21.53	-0.10
4323	17.3	414.9	21.75	21.73	0.02
4324	8.8	407.2	19.61	19.74	-0.13
4325	10.4	410.7	20.28	20.14	0.14
4326	21.7	415.1	20.33	20.15	0.18
4327	19.6	419.7	21.19	21.30	-0.10
4328	4.5	408.1	20.12	20.43	-0.32
4329	10.0	413.8	21.53	21.38	0.15
4330	22.2	420.0	22.28	21.03	1.25
4331	123.6	410.2	21.41	21.58	-0.17
4332	126.8	412.2	21.45	21.33	0.12
4333	120.5	411.0	20.62	20.65	-0.03
4334	121.3	414.0	19.97	19.61	0.36
4335	118.6	414.5	21.07	19.07	2.00
4336	129.8	414.4	20.51	20.73	-0.22
4337	123.5	415.7	20.45	20.53	-0.08
4338	133.1	414.2	20.04	19.38	0.66
4339	126.3	418.5	18.42	18.56	-0.14
4340	121.9	419.0	21.60	19.72	1.88
4341	133.8	417.0	20.86	21.01	-0.14
4342	123.2	421.0	20.10	19.90	0.21
4343	118.1	420.0	20.74	21.13	-0.39
4344	124.3	423.0	18.27	18.85	-0.58
4345	116.0	421.7	19.67	21.79	-2.12
4346	126.5	427.1	20.95	21.51	-0.56
4347	126.3	430.0	20.62	20.66	-0.04
4348	128.4	431.0	21.28	21.70	-0.41
4349	123.5	432.6	19.04	19.32	-0.28
4350	130.6	428.1	18.70	19.04	-0.33
4351	130.3	424.0	19.29	19.00	0.29
4352	56.3	353.5	23.03	22.69	0.34
4353	55.4	355.2	21.06	21.41	-0.34
4354	55.9	357.8	21.82	21.70	0.12
4355	58.1	357.9	20.96	20.87	0.09
4356	54.1	360.0	20.51	20.66	-0.16
4357	60.8	355.4	21.84	22.31	-0.46
4358	59.7	361.4	21.64	21.82	-0.18
4359	62.9	353.9	21.46	21.91	-0.45
4360	54.3	365.3	21.96	22.27	-0.31
4361	63.6	361.0	21.85	21.83	0.02
4362	62.8	367.3	21.66	21.38	0.28
4363	64.3	367.4	20.56	20.87	-0.31
4364	67.4	369.6	20.64	20.92	-0.28
4365	64.0	371.4	21.12	21.32	-0.20
4366	64.6	373.4	21.29	21.79	-0.50
4367	72.8	366.7	18.63	18.83	-0.19
4368	58.4	373.3	20.52	20.82	-0.31
4369	65.9	376.1	21.28	21.66	-0.38
4370	74.7	367.9	19.73	19.84	-0.12
4371	77.2	364.7	19.44	19.44	0.00
4372	79.2	368.0	20.76	21.25	-0.49
4373	219.9	229.8	20.89	21.02	-0.13
4374	223.5	231.6	19.01	18.89	0.13
4375	218.3	231.6	21.16	21.48	-0.32
4376	226.0	233.3	22.92	22.25	0.68
4377	215.3	232.1	21.32	21.52	-0.20
4378	219.0	235.5	18.60	18.37	0.23
4379	221.1	238.9	19.99	19.92	0.06
4380	225.1	240.6	21.53	21.82	-0.29
4381	222.5	244.7	21.47	21.77	-0.30
4382	227.0	243.0	22.26	22.68	-0.42
4383	220.8	245.6	21.75	21.69	0.06
4384	219.2	249.6	19.37	19.33	0.04
4385	215.1	249.1	21.39	20.86	0.53
4386	216.1	252.5	22.10	22.55	-0.44
4387	219.0	253.9	21.59	21.84	-0.25
4388	212.6	250.1	21.02	21.56	-0.54
4389	224.6	252.8	21.93	20.78	1.15
4390	213.9	254.6	20.99	21.38	-0.39
4391	211.2	247.2	21.60	22.59	-0.99
4392	226.7	251.6	22.10	22.24	-0.14
4393	227.8	253.4	20.09	20.25	-0.15
4394	224.6	256.7	21.21	20.92	0.29
4395	228.1	257.6	22.14	20.40	1.74
4396	230.9	256.6	22.06	22.16	-0.10
4397	230.2	261.1	18.81	18.60	0.22
4398	226.6	261.1	21.63	21.88	-0.25
4399	224.7	261.6	20.61	20.30	0.31
4400	230.0	263.5	21.69	21.96	-0.28

Num	X	Y	B	V	$B-V$
4401	234.6	260.5	21.37	20.89	0.48
4402	228.2	265.4	20.71	20.94	-0.23
4403	229.0	267.6	22.96	22.67	0.28
4404	46.3	385.4	21.68	22.08	-0.40
4405	45.7	389.1	19.89	20.02	-0.13
4406	48.8	390.7	20.73	19.49	1.24
4407	46.3	390.9	18.03	17.94	0.09
4408	51.4	392.8	21.23	20.14	1.09
4409	47.0	395.5	20.27	20.03	0.25
4410	54.5	394.5	20.92	21.34	-0.41
4411	40.8	390.9	20.65	21.10	-0.46
4412	37.7	392.1	20.41	20.85	-0.44
4413	38.7	398.9	20.25	20.85	-0.59
4414	38.6	387.5	20.92	21.01	-0.09
4415	40.2	401.1	19.22	18.98	0.24
4416	36.2	386.2	21.70	21.55	0.16
4417	41.0	405.6	20.72	20.73	-0.01
4418	34.3	388.6	21.02	21.12	-0.10
4419	45.3	399.4	21.24	21.14	0.10
4420	42.5	406.6	21.37	22.01	-0.64
4421	32.5	387.1	21.50	22.11	-0.61
4422	48.2	400.7	20.99	21.08	-0.09
4423	28.6	391.0	20.79	20.57	0.22
4424	48.7	404.3	19.51	19.71	-0.20
4425	51.8	403.7	20.96	21.73	-0.77
4426	157.6	392.6	20.75	21.34	-0.59
4427	158.6	395.1	21.55	21.42	0.13
4428	160.3	395.8	20.09	20.40	-0.31
4429	161.4	399.5	21.46	21.55	-0.09
4430	154.6	399.0	19.95	20.50	-0.55
4431	153.2	400.3	21.77	22.14	-0.37
4432	145.2	401.6	20.88	20.35	0.53
4433	143.8	404.8	20.89	21.65	-0.76
4434	126.9	400.1	19.10	19.15	-0.05
4435	150.8	404.2	19.50	19.81	-0.31
4436	139.3	403.8	20.00	19.89	0.11
4437	140.5	406.9	20.86	20.74	0.13
4438	145.6	407.7	20.21	19.61	0.60
4439	136.5	401.8	20.19	19.64	0.56
4440	137.5	408.1	20.76	21.04	-0.28
4441	141.3	410.5	20.69	20.82	-0.13
4442	134.7	400.8	20.31	20.76	-0.45
4443	136.7	409.3	19.96	20.52	-0.56
4444	144.9	412.5	18.97	18.88	0.08
4445	143.4	414.3	19.36	19.27	0.09
4446	135.0	396.8	18.63	19.44	-0.81
4447	132.0	405.2	19.79	20.49	-0.70
4448	140.3	416.1	20.02	19.83	0.20
4449	147.7	417.2	20.82	20.41	0.40
4450	132.8	395.3	18.53	18.70	-0.16
4451	140.6	418.2	20.64	21.11	-0.47
4452	130.3	398.6	19.86	20.26	-0.40
4453	151.9	416.6	20.14	20.64	-0.49

Appendix C

Image Sharpening Software Package

The IPD data on which the technical image-sharpening results in chapter 6 were based, consists of the (x, y) positions of photon arrival events binned into 1ms frames. In order to facilitate the analysis of this data a suite of programs were written covering the following areas:

- routines to convert the single byte integer raw data, into a customised HDS (Warren-Smith and Lawden 1991) 'frame' file.

  CVT_SDF - convert RAW data to frame file, also bins data.

  CVT_ROT - converts RAW data, and also derotates the coordinate system in the process.

- routine to perform the function of artificial 'beam-splitter' to eliminate effect of artificial sharpening.

  BEAM_SPLIT - performs function of beamsplitter.

- routines to define spatial windows on the data.

  WINDAT - flags events which are within window. The inertia of the window can be set.

NEW_WIN - resets window flags according to window defined by the filtered centroid positions.

PYRAWIN - as WINDAT but weights linearly with radius out to the full window radius.

BELLWIN - as WINDAT but weights with a gaussian of given FWHM.

CC_CEN - alternative to window philosophy: uses a mask to cross correlate with the photon positions to get the offsets (good for situation of several monitors but may add noise otherwise?)

- basic statistics off a single frames.

  ONE_CEN - calculates the centroids of each frame.

  NEW_SIG - calculates the dispersion of the flagged window events about the filtered centroid positions.

- filtering routines to smooth the time-series of centroid positions.

  TOPHAT - performs a top-hat filter of the data.

  LONGHAT - as with TOPHAT, but more efficient for long filter.

  FILTER - applies double sided exponential filter to the centroids.

  VTAU - uses fixed cut exponential, but varies the decay constant heuristically.

- frame-selection routines.

  FSELECT - sets frame selection flags according to sigma criterion.

- real-time experiments

  CUSPS - simulates the MARTINI sharpening algorithm.

- correlation routines.

  XCOR - cross correlates fields from two files.

  ACOR - autocorrelates data in a list.

- conversion to images.

  TOPIC - converts time-series data to a Starlink NDF/HDS image file.

- utilities to examine the data graphically and numerically.

  LIST - writes ASCII list of one or more fields versus time in seconds; may be sparsely sampled or averaged.

  ANALIST - creates a histogram of information from a list.

  EXAMINE - allows the examination of the contents of a frame file.

  SCROLL - uses terminal scrolling to show graphically the variation of centroid positions.

  CALCAV - calculates the global average value of a field.

  VIDEO - movie of events (also shows window, and centroids).

  PFIT - reads in a cursor position and estimates the FWHM of the profile in pixels. Outputs both the X and Y results to the user.

  CURSFIT - uses cursor positions to define end points for a profile, which is output to a ASCII file.

Appendix D

Standard Cosmological Models

Einstein's General Theory of Relativity (1916) provides us with an elegant and compelling theory of gravity. In applying this theory to the evolution of the universe as a whole it is conventional, in the first instance for reasons of tractability, to make some simplifying assumptions. Our observations seem to tell us that, when averaged over very large length scales, the universe is essentially homogeneous and isotropic. This has become enshrined as the Cosmological Principle, and provides us with the simplest models of the universe, the Friedmann models. Here we provide a brief outline of these models, following Einstein's preference for a zero cosmological constant. For a detailed treatment see Weinberg (1972).

Making the above simplifying assumptions we find that the field equations reduce to the following expressions governing the evolution of the scale factor R:

$$3\ddot{R} = -4\pi G(\rho + \frac{3p}{c^2})R$$

and

$$\dot{R}^2 = 8\pi G\rho R^2/3 - kc^2$$

where

- G and c have their usual meanings.

- ρ is the density.
- p is the pressure.
- k is the curvature constant (+1 for a closed universe, 0 for a flat universe and -1 for an open universe).

Now let us define the following constants, which are dimensionless forms of the expansion rate and the deceleration, at the present epoch:

$$H_0 = \frac{\dot{R}(t_0)}{R(t_0)}$$

$$q_0 = -\ddot{R}(t_0)\frac{R(t_0)}{\dot{R}^2(t_0)}$$

These are the Hubble constant and the deceleration parameter, respectively.

We see that:

$$\rho_0 = \frac{3}{8\pi G}\left(\frac{kc^2}{{R_0}^2} + {H_0}^2\right)$$

and

$$p_0 = -\frac{1}{8\pi G}\left(\frac{kc^2}{{R_0}^2} + {H_0}^2(1 - 2q_0)\right)$$

Now, we can formulate the critical density, when $k = 0$ and we have a 'flat' universe:

$$\rho_c = \frac{3{H_0}^2}{8\pi G}$$

Further, if we take the pressure at the present day to be very low:

$$\frac{kc^2}{{R_0}^2} = (2q_0 - 1){H_0}^2$$

Thus, the ratio of the density of the universe to the critical density:

$$\Omega_0 = \frac{\rho_0}{\rho_c} = 2q_0$$

The flat (Einstein-de Sitter) universe, represents the borderline case between an open universe, which expands forever, and a closed universe which will ultimately recollapse. Apart from aesthetic considerations, a flat universe is also the main prediction of the inflation models, which seek to resolve the fine-tuning and horizon problems.

Appendix E

Cepheid PL Relationships

In this thesis, we use the period-luminosity relations presented in Madore and Freedman (1991), derived from the LMC Cepheids.

$$M_B = -2.43 \log P - 1.07$$

$$M_V = -2.76 \log P - 1.40$$

$$M_R = -2.94 \log P - 1.58$$

$$M_I = -3.06 \log P - 1.81$$

These are based on an adopted LMC distance modulus of $\mu_0 = 18.50$. This compares to a more recent estimate by Feast (1991) of $\mu_0 = 18.55 \pm 0.15$ on the basis of the Cepheid, RR Lyrae and main-sequence fitting techniques. We note however, that there is still some uncertainty in the value of the Hyades distance modulus, which is one of the main first stepping stones for all of these techniques. For example, recent determinations of the distance to the Hyades are given by Patterson and Ianna (1991) who find $\mu_0(HYADES) = 3.18 \pm 0.09$, using trigonometric parallax, whilst Schwan (1991) obtains $\mu_0(HYADES) = 3.40 \pm 0.04$, using the moving cluster method.

However, some reassurance in the above values for the LMC distance can be taken from the

geometrical distance estimated from observations of the circumstellar ring around SN1987A of $\mu_0 = 18.50 \pm 0.13$ (Panagia *et al.* 1991).

Appendix F

Standard Reddening Relations

Extinction is quantified in terms of magnitudes in the particular passband, written A_λ. The difference in extinction in two different passbands is denoted by a colour excess, eg. $E_{B-V} = A_B - A_V$ In this thesis we will always use values for the extinction and reddening derived from Cardelli, Clayton and Mathis (1989). These are summarised in the table below:

Filter	A_λ/A_V	A_λ/E_{B-V}	$E_{V-\lambda}/E_{B-V}$
B	1.337	4.0	-1.00
V	1.000	3.1	0.00
R	0.751	2.2	0.74
I	0.479	1.4	1.55

Table F.1: Summary of extinction relations in the optical and near infra-red passbands. The ratio of total to selective extinction $R_V = A_V/E_{B-V}$ is taken as the standard value for the interstellar medium of 3.1 (eg. Rieke and Lebofsky 1985).

Bibliography

Aaronson, M., Mould, J., 1986, *Ap.J.*, **303**, 1.

Aitken, G.J.M., 1989, *Pub.Ast.Soc.Pac.*, **101**, 471.

Allen, C.W., 1973, *Astrophysical Quantities*, Athlone.

Arnett, W.D., Branch, D., Wheeler, J.C., 1985, *Nature*, **314**, 337.

Baade, W., 1956, *Pub.Ast.Soc.Pac.*, **68**, 5.

Baade, W., Swope, H.H., 1963, *Ast.J.*, **68**, 435.

Bahcall, J.N., Casertano, S., Ratnatunga, K.U., *Ap.J.*, **320**, 515.

Bahcall, J.N., Soneira, R.M., 1984, *Ap.J.Sup.*, **55**, 67.

Becker, S.A., Iben, I., Tuggle, R.S., 1977, *Ap.J.*, **218**, 633.

Beckers, J.M., 1990, *ESO Messenger*, **60**, 1.

Berkhuijsen, E.M., Humphreys, R.M., Ghigo, F.D., Zumach, W., 1988, *Ast.Ap.Sup.*, **76**, 65.

Berry, D.S., 1991, *Starlink User Note 117.2.*

Bertelli, G., Betto, R., Bressan, A., Chiosi, C., Nasi, E., Vallenari, A., 1990, *Ast.Ap.Sup.*, **85**, 845.

Bianchi, L., Hutchings, J.B., Massey, P., 1991, *Ast.Ap.*, **249**, 14.

Biviano, A., Giuricin, G., Mardirossian, F., Mezzetti, M., 1990, *Ap.J.Sup.*, **74**, 325.

Blair, W.P., Kirshner, R.P., Chevalier, R.A., 1981, *Ap.J.*, **247**, 879.

Blair, W.P., Kirshner, R.P., Chevalier, R.A., 1982, *Ap.J.*, **254**, 50.

Boesgaard, A.M., Steigman, G., 1985, *Ann.Rev.Ast.Ap.*, **23**, 319.

Böhm-Vitense, E., 1981, *Ann.Rev.Ast.Ap.*, **19**, 295.

Böhm-Vitense, E., 1988, *Ap.J.*, **324**, L27.

Branch, D., 1979, *Mon.Not.Roy.Ast.Soc.*, **186**, 609. **71**, 25.

Buonanno, R., Iannicola, G., 1989, *Pub.Ast.Soc.Pac.*, **101**, 294.

Buscher, D.F., Haniff, C.A., Baldwin, J.E., Warner, P.J., 1990, *Mon.Not.Roy.Ast.Soc.*, **245**, 7p.

Burstein, D., Heiles, C., 1978, *Ap.J.*, **225**, 40.

Burstein, D., Heiles, C., 1982, *Ast.J.*, **87**, 1165.

Burstein, D., Heiles, C., 1984, *Ap.J.Sup.*, **54**, 33.

Capaccioli, M., Cappellaro, E., Della Valle, M., D'Onofrio, M., Rosino, L., Turatto M., 1990, *Ap.J.*, **350**, 110.

Cardelli, J.A., Clayton, G.C., Mathis, J.S., 1989, *Ap.J.*, **345**, 245.

Chiosi, C., Maeder, A., 1986, *Ann.Rev.Ast.Ap.*, **24**, 329.

Christian, C.A., Racine, R., 1985, *Pub.Ast.Soc.Pac.*, **97**, 1215.

Christian, C.A., Schommer, R.A., 1987, *Ast.J.*, **93**, 557.

Cohen, J.G., 1985, *Ap.J.*, **292**, 90.

Cohen, J.G., 1987, *The Extragalactic Distance Scale*, eds. van den Bergh, S., Pritchet, C.J., A.S.P. conf. proc. 4, 114.

Cook, K.H., Aaronson, M., Illingworth, G., 1986, *Ap.J.*, **301**, L45.

Coulman, C.E., 1986, *Identification, Optimisation and Protection of Optical Telescope Sites*, eds. Millis, R.L., Franz, O.G., Ables, H.D., Dahn, C.C., Lowell Observatory.

Crotts, A.P.S., 1986, *Ast.J.*, **92**, 292.

de Loore, C., 1988, *Ast.Ap.*, **203**, 71.

de Vaucouleurs, G., 1983, *Mon.Not.Roy.Ast.Soc.*, **202**, 367.

Devaney, M.N., 1989, *Ph.D. Thesis*, National University of Ireland.

Doel, A.P., 1990, *Ph.D. Thesis*, University of Durham.

Doel, A.P., Dunlop, C.N., Major, J.V., Myers, R.M., Purvis, A., Thompson, M.G., 1990, SPIE **1236**, 179.

Doom, C., De Greve, J.P., de Loore, C., 1986, *Ap.J.*, **303**, 136.

Dressler, A., Lynden-Bell, D., Burstein, D., Davies, R.L., Faber, S.M., Terlevich, R.J., Wegner, G., 1987, *Ap.J.*, **313**, 42.

Duncan, J.C., 1922, *Pub.Ast.Soc.Pac.*, **34**, 290.

Eaton, N., 1992, *Starlink User Note 45.4*.

Einstein, A., 1916, *Annalen der Phys.*, **49**, 769.

Faber, S.M., Wegner, G., Burstein, D., Davies, R.L., Dressler, A., Lynden-Bell, D., Terlevich, R.J., 1989, *Ap.J.Sup.*, **69**, 763.

Feast, M.W., 1991, *Observational Tests of Cosmological Inflation*, eds. Shanks, T., Banday, A.J., Ellis, R.S., Frenk, C.S., Wolfendale, A.W., NATO ASI C348.

Fernie, J.D., 1983, *Pub.Ast.Soc.Pac.*, **95**, 782.

FitzGerald, M.P., 1970, *Ast.Ap.*, **4**, 234.

Flower, P.J., 1977, *Ast.Ap.*, **54**, 31.

Fong, R., Jones, L.R., Shanks, T., Stevenson, P.R.F., Strong, A.W., Dawe, J.A., Murray, J.D., 1987, *Mon.Not.Roy.Ast.Soc.*, **224**, 1059.

Ford, H.C., Ciardullo, R., 1988, *The Extragalactic Distance Scale*, eds. van den Bergh, S., Pritchet, C.J., A.S.P. conf. proc. 4, 128.

Freedman, W.L., 1988, *Ap.J.*, **326**, 691.

Freedman, W.L., Madore, B.F., 1990, *Ap.J.*, **365**, 186.

Freedman, W.L., Wilson, C.D., Madore, B.F., 1991, *Ap.J.*, **372**, 455.

Fried, D.L., 1965, *J.Opt.Soc.Am.*, **55**, 1427.

Fried, D.L., 1966, *J.Opt.Soc.Am.*, **56**, 1372.

Fried, D.L., 1978, *J.Opt.Soc.Am.*, **68**, 1651.

Frogel, J.A., Cohen, J.G., Persson, S.E., 1983, *Ap.J.*, **275**, 773.

Fukugita, M., Hogan, C.J., 1991, *Ap.J.*, L11.

Green, E.M., Bessel, M.S., Demarque, P., King, C.R., Peters, W.L., 1987, *The Revised Yale Isochrones and Luminosity Functions*, Yale University Observatory, New Haven.

Groth, E.J., 1991, *IInd Rencontres de Blois:Physical Cosmology*, eds. Blanchard, A., Celnikier, L., Lachièze-Rey, M., Trân Thanh Vân, J., Editions Frontières..

Guryanov, A.E., *Sov. Ast.*, **28**, 343.

Guth, A.H., 1991, *Observational Tests of Cosmological Inflation*, eds. Shanks, T., Banday, A.J., Ellis, R.S., Frenk, C.S., Wolfendale, A.W., NATO ASI C348

Harris, W.E., 1990, *Pub.Ast.Soc.Pac.*, **102**, 949.

Henry, J.P., Heyer, I., Cecil, G., Barnes, B., Cheigh, F., 1987, *Pub.Ast.Soc.Pac.*, **99**, 1354.

Heydari-Malayeri, M., Hutsemékers, D., 1991, *Ast.Ap.*, **243**, 401.

Hildtich, R.W., Hill, G., Barnes, J.V., 1983, *Mon.Not.Roy.Ast.Soc.*, **204**, 241.

Hodge, P., Lee, M.G., Mateo, M., 1988. *Ap.J.*, **324**, 172.

Hubble, E.P., 1925, *Observatory*, **48**, 139.

Hubble, E.P., 1926, *Ap.J.*, **63**, 236.

Hubble, E.P., Humason, M.L., 1931, *Ap.J.*, 74, 43.

Hubble, E.P., 1936, *The Realm of the Nebulae*, (Dover).

Hufnagel, R.E., 1974, *Digest of Topical Meeting on Optical Propogation Through Turbulence*, Optical Society of America.

Humphreys, R.M., 1979, *Ap.J.*, **234**, 854.

Humphreys, R.M., 1980, *Ap.J.*, **241**, 587.

Humphreys, R.M., 1983, *Ap.J.*, **269**, 335.

Humphreys, R.M., 1988, *The Extragalactic Distance Scale*, eds. van den Bergh, S., Pritchet, C.J., A.S.P. conf. proc. 4, 103.

Humphreys, R.M., Aaronson, M., 1987, *Ap.J.*, **318**, L69.

Humphreys, R.M., Davidson, K., 1979, *Ap.J.*, **232**, 409.

Humphreys, R.M., Massey, P., Freedman, W.L., 1990, *Ast.J.*, **99**, 84.

Humphreys, R.M., Pennington, R.L., Jones, T.J., Ghigo, F.D., 1988, *Ast.J.*, **96**, 1884.

Humphreys, R.M., Sandage, A., 1980, *Ap.J.Sup.*, **44**, 319.

Humphreys, R.M., Sitko, M.L., Sitko, A.K., 1987, *Pub.Ast.Soc.Pac.*, **99**, 380.

Iben, I., Tuggle, R.S., 1975, *Ap.J.*, **197**, 39.

Iye, M., Noguchi, T., Torii, Y., Mikami, Y., Ando, H., 1991, *Pub.Ast.Soc.Pac.*, **103**, 712.

Jacoby, G.H., Ciardullo, R., Ford, H.C., 1990, *Ap.J.*, **356**, 332.

Johnson, H.L., 1966, *Ann.Rev.Ast.Ap.*, **4**, 193.

Johnson, S.B., Joner, M.D., 1987, *Ast.J.*, **94**, 324.

King, I.R., 1971, *Pub.Ast.Soc.Pac.*, **83**, 199.

Knude, J., 1985, *Matematisk-Fysiske Meddelelser*, **41**, 71.

Kolmogorov, A., 1961, *Turbulence - Classic Papers in Statistical Theory*, Interscience Publishers Inc.

Kraan-Korteweg, R.C., Cameron, L.M., Tammann, G.A., 1988, *Ap.J.*, **331**, 620.

Labeyrie, A., 1970, *Ast.Ap.*, **6**, 85.

Laird, J.B., Rupen, M.P., Carney, B.W., Lathem, D.W., 1988, *Ast.J.*, **96**, 1908.

Lamers, H.J.G.L.M., Fitzpatrick, E.L., 1988, *Ap.J.*, **324**, 279.

Landolt, A.U., 1983A, *Ast.J.*, **88**, 439.

Landolt, A.U., 1983B, *Ast.J.*, **88**, 853.

Lattanzio, J.C., 1991, *Ap.J.Sup.*, **76**, 215.

Lelièvre, G., Nieto, J.L., Salmon, D., Llebaria, A., Thouvenot, E., Boulesteix, J., Le Coarer, E., Arnaud, J., 1988, *Ast.Ap.*, **200**, 301.

Léna, P., 1991, *IInd Rencontres de Blois:Physical Cosmology*, eds. Blanchard, A., Celnikier, L., Lachièze-Rey, M., Trân Thanh Vân, J., Editions Frontières..

Madore, B.F., 1977, *Mon.Not.Roy.Ast.Soc.*, **178**, 505.

Madore, B.F., McAlary, C.W., McLaren, R.A., Welch, D.L., Neugebauer, G., Mathews, K., 1985, *Ap.J.*, **294**, 560.

Madore, B.F., Freedman, W.L., 1991, *Pub.Ast.Soc.Pac.*, **103**, 933.

Maeder, A., 1983, *Ast.Ap.*, **120**, 113.

Maeder, A., Mermilliod, J.C., 1991, *Ast.Ap.Sup.*, **89**, 451.

Massey, P., Armandroff, T.E., Conti, P.S., 1986, *Ast.J.*, **92**, 1303.

Mather, J.C. *et al.* , 1990, *I.A.U. Symposium 123*, ed. Kondo, Y., Kluwer, Dordrecht.

McCall, M.L., Rybski, P.M., Shields, G.A., 1985, *Ap.J.Sup.*, **57**, 1.

McClure, R.D., Racine, R., 1969, *Ast.J.*, **74**, 1000.

McClure, R.D., Grundmann, W.A., Rambold, W.N., Fletcher, J.M., Richardson, E.H., Stilburn, J.R., Racine, R., Christian, C.A., Waddell, P., 1989, *Pub.Ast.Soc.Pac.*, **101**, 1156.

McClure, R.D., Arnaud, J., Fletcher, J.M., Nieto, J.L., Racine, R., 1991, *Pub.Ast.Soc.Pac.*, **103**, 570.

Mermilliod, J.C., 1981, *Ast.Ap.*, **97**, 235.

Metcalfe, N., Shanks, T., 1991, *Mon.Not.Roy.Ast.Soc.*, **250**, 438.

Metcalfe, N., Shanks, T., Fong, R., Jones, L.R., 1991, *Mon.Not.Roy.Ast.Soc.*, **249**, 498.

Mighell, K.J., 1989, *Mon.Not.Roy.Ast.Soc.*, **238**, 807.

Moffat, A.F.J., 1969, *Ast.Ap.*, **3**, 455.

Mould, J., Kristian, J., 1986, *Ap.J.*, **305**, 591.

Mould, J., Kristian, J., Da Costa, G.S., 1983, *Ap.J.*, **270**, 471.

Narayan, R., Nityananda, R., 1986, *Ann.Rev.Ast.Ap.*, **24**, 127.

Newberry, M.V., 1991, *Pub.Ast.Soc.Pac.*, **103**, 122.

Nieto, J.L., Llabaria, A., di Serego Alighieri, S., 1987, *Ast.Ap.*, **178**, 301.

Nightingale, N.S., Buscher, D.F., 1991, *Mon.Not.Roy.Ast.Soc.*, **251**,155.

Panagia, N., Gilmozzi, R., Macchetto, F., Adorf, H.M., Kirshner, R.P., 1991, *Ap.J.*, **380**, L23.

Parker, J.W., 1991, *Pub.Ast.Soc.Pac.*, **103**, 243.

Patterson, R.J., Ianna, P.A., 1991, *Ast.J.*, **102**, 1091.

Peebles, P.J.E., Ratra, B., 1988, *Ap.J.*, **325**, 17.

Penny, A.J., Dickens, R.J., 1986, *Mon.Not.Roy.Ast.Soc.*, **220**, 845.

Pierce, M.J., Tully, R.B., 1988, *Ap.J.*, **330**, 579.

Pritchet, C.J., 1987, *The Extragalactic Distance Scale*, eds. van den Bergh, S., Pritchet, C.J., A.S.P. conf. proc. 4, 517.

Pritchet, C.J., van den Bergh, S., 1987A, *Ap.J.*, **316**, 517.

Pritchet, C.J., van den Bergh, S., 1987B, *Ap.J.*, **318**, 507.

Pritchet, C.J., van den Bergh, S., 1988, *Ap.J.*, **331**, 135.

Racine, R., McClure, R., Christian, C., 1989, *Pub.Ast.Soc.Pac.*, **101**, 731.

Racine, R., Salmon, D., Cowley, D., Sovka, J., 1991, *Pub.Ast.Soc.Pac.*, **103**, 1020.

Ratnatunga, K.U., Bahcall, J.N., 1985, *Ap.J.Sup.*, **59**, 63.

Redfern, R.M., Devaney, M.N., O'Kane, P., Ballesteros Ramirez, E., Gomez Reñasco, R., Rosa, F., 1989, *Mon.Not.Roy.Ast.Soc.*, **238**, 791.

Reid, N., Mould, J., Thompson, I., 1987, *Ap.J.*, **323**, 433.

Renzini, A., 1991, *Observational Tests of Cosmological Inflation*, eds. Shanks, T., Banday, A.J., Ellis, R.S., Frenk, C.S., Wolfendale, A.W., NATO ASI C348

Rich, R.M., Mould, J., Picard, A., Frogel, J.A., Davies, R., 1989, *Ap.J.*, **341**, L51.

Richer, H.B., Crabtree, D.R., 1985, *Ap.J.*, L13.

Rieke, G.H., Lebofsky, M.J., 1985, *Ap.J.*, **288**, 618.

Roddier, F., 1981, *Progress in Optics XIX*, ed. Wolf, E., , North-Holland, p.283.

Roddier, F., Northcott, M., Graves, E.J., 1991, *Pub.Ast.Soc.Pac.*, **103**, 131.

Rowan-Robinson, M., 1985, *The Cosmological Distance Ladder*, Freeman.

Rowan-Robinson, M., Hughes, J., Jones, M., Leech, K., Vedi, K., Walker, D.W., 1991, *Mon.Not.Roy.Ast.Soc.*, **249**, 729.

Sandage, A.R., 1958, *Ap.J.*, **127**, 513.

Sandage, A.R., 1971, *Ap.J.*, **166**, 13.

Sandage, A.R., 1983, *Ast.J.*, **88**, 1108.

Sandage, A.R., 1986, *Ast.J.*, **91**, 496.

Sandage, A.R., 1988, *Pub.Ast.Soc.Pac.*, **100**, 935.

Sandage, A.R., Bedke, J., 1985, *Ast.J.*, **90**, 2006.

Sandage, A.R., Carlson, G., 1988, *Ast.J.*, **96**, 1599.

Sandage, A.R., Tammann, G.A., 1990, *Ap.J.*, **365**, 1.

Schild, R.E., 1983, *Pub.Ast.Soc.Pac.*, **95**, 1021.

Schommer, R.A., Olszewski, E.W., Aaronson, M., 1984, *Ap.J.*, **285**, L53.

Schwan, H., 1991, *Ast.Ap.*, **243**, 386.

Shanks, T., 1985, *Vistas in Astr.*, **28**, 595.

Stetson, P.B., 1987, *Pub.Ast.Soc.Pac.*, **99**, 191.

Stetson, P.B., 1987, *DAOPHOT USERS GUIDE.*

Stetson, P.B., 1990, *Pub.Ast.Soc.Pac.*, **102**, 932.

Steward, E.G., 1983, *Fourier Optics: an introduction*, Ellis Horwood.

Stothers, R.B., 1988, *Ap.J.*, **329**, 712.

Stothers, R.B., Chin, C.W., 1991, *Ap.J.*, L67.

Tammann, G.A., Sandage, A.R., 1968, *Ap.J.*, **151**, 825.

Tartarski, V.I., 1961, *Wave Propogation in a Turbulent Medium*, McGraw-Hill.

Tonry, J.L., 1991, *Ap.J.*, **373**, L1.

Tully, R.B., Fisher, J.R., 1977, *Ast.Ap.*, **54**, 661.

Valley, G.C., 1979, *App.Opt.*, **18**, 984.

Valley, G.C., 1980, *App.Opt.*, **19**, 574.

Valley, G.C., Wandzura, S.M., 1979, *J.Opt.Soc.Am.*, **69**, 712.

VandenBerg, D.A., 1985, *Ap.J.Sup.*, **58**, 711.

VandenBerg, D.A., 1988, *The Extragalactic Distance Scale*, eds. van den Bergh, S., Pritchet, C.J., A.S.P. conf. proc. 4, 189.

van den Bergh, S., 1964, *Ap.J.Sup.*, **9**, 65.

van den Bergh, S., 1991, *Pub.Ast.Soc.Pac.*, **103**, 609.

Wang, J.Y., 1977, *J.Opt.Soc.Am.*, **67**, 383

Warren-Smith, R.F., Lawden, M.D., 1991, *Starlink User Note 92.8.*

Weinberg, S., 1972, *Gravitation and Cosmology*, Wiley.

Weir, N, 1991, *Proceedings of the ESO/ST-ECF Data Analysis Workshop.*

Welch, D.L., McAlary, C.W., McLaren, R.A., Madore, B.F., 1986, *Ap.J.*, **305**, 583.

Welch, D.L., McLaren, R.A., Madore, B.F., McAlary, C.W., 1987, *Ap.J.*, **321**, 162.

Wilson, C.D., Freedman, W.L., Madore, B.F., 1990, *Ast.J.*, **99**, 149.

Wolf, M., 1923, *Astr.Nach.*, **217**, 476.

Woolf, N.J., 1982, *Ann.Rev.Ast.Ap.*, **20**, 367.

Young, A.T., 1974, *Ap.J.*, **189**, 587.

Acknowledgements

I wish to thank my supervisors, Dick Fong and Tom Shanks, without whom this work would never have gotten started, let alone been finished. I am also grateful to my other collaborators, Nigel Metcalfe, Nick Devaney, Mike Redfern, Peter O'Kane, Pete Doel, Dick Myers, John Major and Colin Dunlop, for their contributions to these projects and for remaining amicable during many (usually whilst observing) crises.

A very important aspect of scientific research is the interaction with colleagues on an day-by-day basis, and I have been fortunate in Durham to have had plenty of it. Ioannis, John, Ian(s), Esperanza, Karl, Gordon, Richard, Steve, Rafael, Alfonso, Nick, Alan, Jeremy, Ray,... Thank you all.

Finally, I owe a great debt to my family, teachers and friends who have encouraged and supported me, not only during the period of working towards this thesis, but also through my previous education. Dad and Jim, in particular, were responsible for stimulating my interest in science at an early age.

Very special thanks go to my wife Claire and elder son, Thomas, who have bought so much to my life, and who also bore the brunt of the many evenings and weekends spent "in the department". Last, but not least, I am grateful to my younger son, Seán, who prevented disaster by holding off his birth till four days after this thesis was completed!